



# Konya Mühendislik Bilimleri Dergisi

## Konya Journal of Engineering Sciences



**(KONJES)**  
E-ISSN: 2667-8055



2025 - Cilt: 13 - Sayı: 1  
2025 - Volume: 13 - Issue: 1

---

# KONYA JOURNAL OF ENGINEERING SCIENCES (KONJES)

## KONYA MÜHENDİSLİK BİLİMLERİ DERGİSİ

---

Peer-Reviewed Journal

OWNER

Owner on Behalf of Engineering and Natural Sciences Faculty of Konya Technical University Prof. Ali KÖKEN

Editor-in-Chief

Prof. Mustafa TABAKCI

Associate Editors

Prof. Halife KODAZ

Assoc. Prof. Ömer Kaan BAYKAN

Section Editors

Prof. Muharrem Kemal ÖZFIRAT

Prof. Mustafa KORKANÇ

Prof. Niyazi B L M

Prof. Orhan BAYTAR

Prof. Rıdvan SARAÇOĞLU

Prof. Volkan KALEM

Assoc. Prof. Abdülkerim OKBAZ

Asst. Prof. Enes ÖZKÖK

Assoc. Prof. Farabi TEMEL

Assoc. Prof. Smail NCE

Assoc. Prof. Muharrem Hilmi AKSOY

Assoc. Prof. Ömer Kaan BAYKAN

Assoc. Prof. Selim DOĞAN

Assoc. Prof. Sercan BÜLBÜL

Asst. Prof. Alper DÖYEN

Asst. Prof. Burhaneddin BİLGEN

Asst. Prof. Cihangir KÖYCEZ

Asst. Prof. Kemal ERDOĞAN

Asst. Prof. Mehmet Ali TOPÇU

Asst. Prof. Mehmet UZUN

Asst. Prof. Monika MAZIUKIENĖ

Asst. Prof. Muhammed Arif ÇEN

Asst. Prof. Selim SOYLU

Asst. Prof. Taylan DOLU

Dr. Smail BAĞOĞLU

Language Editing/Yabancı Dil Editörü

Instructor Emre ÜN

Secretary/Sekreter

Asst. Prof. Dr. Sema KÖZ

Composition and Printing/Baskı ve Dizgi

Assoc. Prof. Smail KOÇ

Res. Asst. Emir Ali DİNSEL

Res. Asst. Aybüke BABADA

Correspondance Address/ Yazışma Adresi

Konya Teknik Üniversitesi Mühendislik ve Doğa Bilimleri Fakültesi  
Dekanlık Binası 42075-Kampüs, Selçuklu, Konya-TÜRKİYE

Tel : +90 332 205 15 00

Fax : +90 332 241 06 35

E-mail: konjes@ktun.edu.tr

Web : <http://dergipark.org.tr/konjes>

## **EDITORIAL ADVISORY BOARD**

**Prof. Ahmet Afşin KULAKSIZ**

Konya Technical University, Türkiye

**Prof. Fahrettin ÖZTÜRK**

Istanbul Technical University, Türkiye

**Prof. Ali KOÇAK**

Yıldız Technical University, Türkiye

**Assoc. Prof. Alpaslan YARAR**

Konya Technical University, Türkiye

**Prof. H. Kürşad ERSOY**

Konya Technical University, Türkiye

**Prof. Hi-ryong BYUN**

Pukyong National University, South Korea

**Prof. Hüseyin DEVECİ**

Konya Technical University, Türkiye

**Prof. İhsan ÖZKAN**

Konya Technical University, Türkiye

**Prof. Kerim KOÇAK**

Konya Technical University, Türkiye

**Lecturer Loredana Emanuela JUDELE**

Gheorghe Asachi Technical University of Iaşi, Romania

**Prof. Bouabaz MOHAMED**

University of 20 August 1955 Skikda, Algeria

**Prof. Murat KARAKUS**

University of Adelaide, Australia

**Prof. Selçuk Kürşat İŞLEYEN**

Gazi University, Türkiye

**Assoc. Prof. Selim DOĞAN**

Konya Technical University, Türkiye

**Prof. Spase SHUMKA**

Agricultural University of Tirana, Albania

**Prof. Zoran SAPURIC**

University American College, Macedonia

**KONYA JOURNAL OF ENGINEERING SCIENCES  
(KONJES)  
KONYA MÜHENDİSLİK BİLİMLERİ DERGİSİ**

ISSN 2667 – 8055 (Electronic)

---

Volume	13	March	2025	Issue	1
--------	----	-------	------	-------	---

---

**CONTENTS**

**Research Articles**

**MA-OFDM-SPM: A NEW MULTIPLE ACCESS TECHNIQUE FOR 3GPP-DEFINED REDCAP IOT DEVICES**

Ülkü GÜLEÇ, Jehad M. HAMAMREH, Seyfettin Sinan GÜLTEKİN ..... 1-10

**INVESTIGATION OF THE EFFECTS OF RIB APPLICATION ON COOLING IN A TURBINE BLADE**

Muhammed Emin TOLU, Osman BABAYİĞİT, Dilek Nur ÖZEN ..... 11-24

**ZnO-In<sub>2</sub>O<sub>3</sub>-SnO<sub>2</sub> THIN FILM TRANSPARENT HEATERS: TUNABLE ELECTROTHERMAL PROPERTIES THROUGH SUBSTRATE TEMPERATURE AND POSTGROWTH ANNEALING**

Hasan AKYILDIZ, Hilal Aybike CAN, Burak KIVRAK, Tayfur ÖZTÜRK ..... 25-43

**DETERMINATION OF TRAFFIC IMPACT LEVEL IN URBAN CYCLING**

Recep AYDAR, Osman Nuri ÇELİK ..... 44-58

**A COMPARATIVE STUDY OF DIVERSE AUTOENCODER MODELS IN LOCAL GEAR PITTING FAULT DIAGNOSIS**

Mustafa YURTSEVER, Rafet Can ÜMÜTLÜ, Hasan ÖZTÜRK ..... 59-73

**CHARACTERIZATION OF EPOXY RESIN AND SILLE STONE POWDER BASED COMPOSITE MORTARS**

Ahmet Cihat ARI, Mustafa TOSUN ..... 74-97

**AN ADAPTIVE AND HYBRID STATE OF CHARGE ESTIMATION METHOD INTEGRATING SEQUENCE-TO-POINT LEARNING AND COULOMB COUNTING FOR LI-ION BASED ENERGY STORAGE SYSTEMS**

Halil ÇİMEN ..... 98-109

**ONE-STATION, DOUBLE-STATION AND ARRAY ANALYSIS OF RAYLEIGH SURFACE WAVES APPLIED TO A COMMON-SHOT GATHER: A PROGRAMMED TECHNIQUE DESCRIBED THROUGH SYNTHETIC SEISMOGRAMS IN NEAR-SURFACE**

Özcan ÇAKIR ..... 110-131

**LAND ADMINISTRATION AND ITS DIGITAL SHIFT IN BANGLADESH AND TÜRKİYE: A COMPARATIVE ANALYSIS**

Md Moynul AHSAN ..... 132-146

<b>ANALYZING THE IMPACT OF THE 2023 GENERAL ELECTIONS ON LAND PRICES USING MACHINE LEARNING: A CASE STUDY IN ÇANAKKALE, TURKEY</b> Simge DOĞAN, Levent GENÇ, Sait Can YÜCEBAŞ, Şükran YALPIR .....	<b>147-164</b>
<b>IMPACT ANALYSIS OF PLUG-IN ELECTRIC VEHICLES ON THE REAL RESIDENTIAL DISTRIBUTION NETWORK</b> Muhammed Sait AYDIN .....	<b>165-179</b>
<b>OPTIMIZATION OF SHEAR AND PEEL STRESSES IN DOUBLE-L-BRACKET JOINTS USING RESPONSE SURFACE METHODOLOGY</b> Bertan BEYLERGİL .....	<b>180-203</b>
<b>INDUCED STRESSES &amp; DISPLACEMENTS CAUSED BY SINKHOLE DEVELOPMENT</b> Mehmet Kemal GOKAY, Mehmet MESUTOGLU .....	<b>204-219</b>
<b>REAL-TIME DETECTION OF TRAFFIC SIGNS WITH YOLO ALGORITHMS</b> Abdil KARAKAN .....	<b>220-237</b>
<b>IMAGE ENHANCEMENT IN INDUSTRIAL WELDING ENVIRONMENT WITH IMAGE PROCESSING TECHNIQUES</b> Levent CİVCİK, Muhammed Alperen AKSİN .....	<b>238-259</b>
<b>POSITION CONTROL OF HYDRAULIC SERVO CYLINDER FOR WAVE CHANNEL</b> Batın DEMİRCAN, Sabri BIÇAKÇI, Ersin AKYÜZ .....	<b>260-276</b>
<b>EXPERIMENTAL AND NUMERICAL INVESTIGATION ON THE EFFECT OF INFILL WALLS ON DYNAMIC BEHAVIOR IN RC STRUCTURES: SHAKE TABLE TESTS</b> Abdulhamit NAKİPOĞLU, M. Sami DÖNDÜREN .....	<b>277-293</b>
<b>COPPER EXTRACTION FROM DEEP EUTECTIC SOLVENT AS ATACAMITE BY HYDROLYSIS METHOD</b> Mehmet Ali TOPÇU .....	<b>294-306</b>
<b>URETHANE-MODIFIED ALKYD RESIN BASED PAINT PRODUCTION: DETERMINATION OF PAINT PROPERTIES</b> Ferda CİVAN ÇAVUŞOĞLU, Işıl ACAR .....	<b>307-320</b>
<b>IMPACT OF PARTIAL SHADING GEOMETRY ON THE ENERGY AND EXERGY PERFORMANCE OF PV MODULES</b> Saleh Musaed Saleh Musaed ALNAKHLANI, Selcuk SELIMLI .....	<b>321-335</b>

## MA-OFDM-SPM: A NEW MULTIPLE ACCESS TECHNIQUE FOR 3GPP-DEFINED REDCAP IOT DEVICES

<sup>1,\*</sup> Ülkü GÜLEÇ , <sup>2</sup> Jehad M. HAMAMREH , <sup>3</sup> Seyfettin Sinan GÜLTEKİN 

<sup>1,3</sup>Konya Technical University, Engineering and Natural Sciences Faculty, Electrical and Electronics Department, Konya, TÜRKİYE

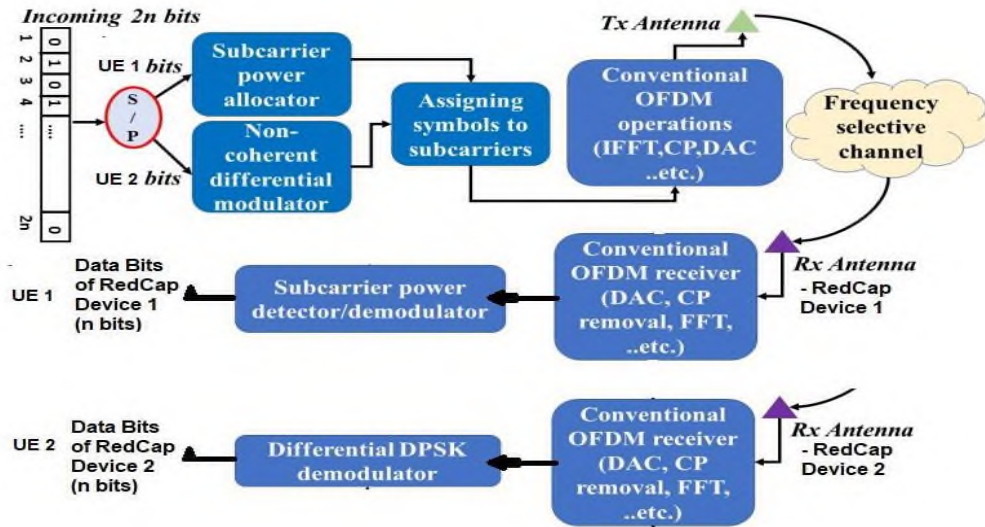
<sup>2</sup>Wislabi.com, Antalya Bilim University, Antalya, TÜRKİYE

<sup>1</sup> e188121002003@ktun.edu.tr, <sup>2</sup> jehad.hamamreh@antalya.edu.tr, <sup>3</sup> ssgultekin@ktun.edu.tr

### Highlights

- Non-coherent OFDM based a new multiple user waveform has been studied for 6g and beyond wireless communications.
- The performance of this new technique that is called MA-OFDM-SPM is compared with conventional OFDMA.
- The BER and throughput of this waveform are found to work well for RedCap devices and IOT.

### Graphical Abstract



Transmitter/Receiver of the proposed MA-OFDM-SPM. Unlike conventional OFDM, the proposed technique employs two separate modulations where half the incoming bit stream is modulated by DPSK and the other half is modulated through the power level (i.e., high and low pattern).



## MA-OFDM-SPM: A NEW MULTIPLE ACCESS TECHNIQUE FOR 3GPP-DEFINED REDCAP IOT DEVICES

<sup>1,\*</sup> Ülkü GÜLEÇ , <sup>2</sup> Jihad M. HAMAMREH , <sup>3</sup> Seyfettin Sinan GÜLTEKİN 

<sup>1,3</sup> Konya Technical University, Engineering and Natural Sciences Faculty, Electrical and Electronics Department, Konya, TÜRKİYE

<sup>2</sup> Wislabi.com, Antalya Bilim University, Antalya, TÜRKİYE

<sup>1</sup> e188121002003@ktun.edu.tr, <sup>2</sup> jehad.hamamreh@antalya.edu.tr, <sup>3</sup> ssgultekin@ktun.edu.tr

(Received: 08.08.2024; Accepted in Revised Form: 04.12.2024)

**ABSTRACT:** RedCap devices face challenges related to efficient multiple access techniques that can fully leverage their potential while adhering to their constraints. There are many multiple access techniques proposed in the literature recently, but none of them is deemed a good fit for the multi-facet requirements of RedCap devices. Motivated by that, this paper introduces a new multiple-access technique designed to address these challenges, aiming to optimize the performance and efficiency of RedCap devices in various application scenarios. The proposed technique seeks to enhance data rates, reduce latency, and extend battery life while maintaining the cost-effectiveness and simplicity essential for RedCap devices. Consequently, the proposed design effectively overcomes prior challenges and boosts system throughput by leveraging the power domain to transmit supplementary data bits, all while preserving a streamlined and uncomplicated transceiver design. In summary, with the same time, frequency, space, and power resources, it can be served an additional user with a stream of data bits equal to that of the main user, thus resulting in doubling the system's spectral efficiency.

**Keywords:** 6G, Coherent Transmission, IOT, Non-Coherent OFDM, Subcarrier Power Modulation, Wireless Communications

### 1. INTRODUCTION

Reduced Capability (RedCap) devices, as delineated by the 3rd Generation Partnership Project (3GPP) standards, represent a middle ground between high-end, full-featured 5G devices and low-power, low-complexity IoT devices. These devices are engineered to support use cases such as industrial IoT and remote drone control that necessitate moderate data rates and latency, while also benefiting from lower device complexity and extended battery life. RedCap devices are particularly relevant for applications where performance requirements are more demanding than those of low-end IoT devices but do not necessitate the full capabilities of 5G [1].

The main specifications of RedCap Devices include: 1) reduced peak data rates; 2) simplified and lower-order modulation and coding schemes; 3) reduced bandwidth with support for sub 6G Hz spectrum; 4) simplified MIMO configurations limited to 2x2 MIMO or single-antenna systems; 5) lower complexity with fewer receive and transmit chains and simplified RF design and baseband processing; 6) extended battery life with enhanced power-saving features and Support for extended DRX cycles and power-saving modes; 7) support for 5G core features including compatibility with key 5G core network features such as network slicing, service-based architecture, and edge computing.

The advantages of RedCap Devices include cost effectiveness due to reduced complexity which leads to lower production costs, extended battery life that is optimized for low power consumption, moderate performance suitable for applications requiring better performance than basic IoT but not the full capabilities of high-end 5G devices, and seamless integration that is compatible with existing 5G infrastructure, leveraging 5G's advanced features.

Despite these advantages, RedCap devices face challenges related to efficient multiple-access techniques that can fully leverage their potential while adhering to their constraints. There are many multiple access techniques both orthogonal and non-orthogonal proposed in the literature recently [2], [3], but none of them is deemed a good fit for the multifaceted requirements of RedCap devices, especially the one related to reducing complexity while improving efficiency. Motivated by that, this paper introduces a new multiple-access technique designed to address these challenges, aiming to optimize the performance and efficiency of RedCap devices in various application scenarios. The proposed technique seeks to reduce complexity, enhance data rates, reduce latency, and extend battery life while maintaining the cost-effectiveness and simplicity essential for RedCap devices.

The use of non-coherent-based multiple access approaches allows the use of low complexity detectors, which can reduce complexity remarkably and thus make it a better fit for RedCap devices. Although non-coherent-based multiple schemes and systems reduce complexity significantly, their performance in terms of reliability and throughput is usually suboptimal compared to their coherent counterparts [4]. To address the dilemma between coherent and non-coherent designs, the authors have proposed a solution involving Orthogonal Frequency-Division Multiplexing with Subcarrier Power Modulation (OFDM-SPM), and Differential Phase Shift Keying (DPSK) as initially introduced in references [5] and [6]. In [7], OFDM-SPM was generalized to quadrature signal constellations. A non-coherent adaptation of Orthogonal Frequency-Division Multiplexing (OFDM) with Subcarrier Power Modulation (OFDM-SPM) was proposed in [8] where the receiver complexity was reduced further using differential phase shift keying (DPSK) instead of coherent BPSK. OFDM-SPM exploits the power of the subcarriers within an OFDM block as an additional dimension to transmit extra information bits, resulting in reduced complexity and latency compared to conventional approaches. Furthermore, it was shown in [8] that OFDM-SPM operates under different power modes including power saving and power reassignment. This latter mode includes two policies, namely an optimized and a non-optimized reassignment mode. This publication comes under the scope of non-optimized power reassignment where it was found that, under this mode, the scheme achieves the same performance as coherent OFDM-BPSK. Motivated by this, the key contributions of this paper are outlined as follows:

- Presenting a novel non-coherent multiple access design that attains a bit error rate (BER) performance equivalent to that of coherent OFDMA.
- The power level is explored as an extra data dimension; thus, an additional data stream can be transmitted to serve an additional user by changing the subcarriers' power levels according to the user's data bits.
- Achieving twice the spectral efficiency of the overall system relative to conventional OFDMA, due to the inclusion of the two-dimensional data modulation aspects of the scheme.

The subsequent sections of this paper are outlined as follows: Section II provides a detailed description of the system model. Section III examines the performance characteristics of the proposed scheme. Section IV presents the simulation results, and Section V delineates the concluding remarks.

## 2. SYSTEM MODEL OF MA-OFDM-SPM SYSTEM

The transceiver structure of the proposed MA-OFDM-SPM system is illustrated in Figure 1. In the transmitter, the incoming stream of length  $2n$  bits is partitioned into two branches of  $n$  bits each, which are modulated independently afterwards to serve two distinct user equipment (UE1 and UE2) of RedCap-type devices. To serve UE1, the power allocation block determines the power levels for the subcarriers, with the  $i$ th bit indicating the power value assigned to the  $i$ th subcarrier used for data transmission. In other words, a bit '1' signifies that the subcarrier power is set to high (represented as H), whereas a bit '0'



indicates that the subcarrier power is set to low (represented as L). The second  $n$  bits are modulated using classical DPSK modulation to serve UE2.

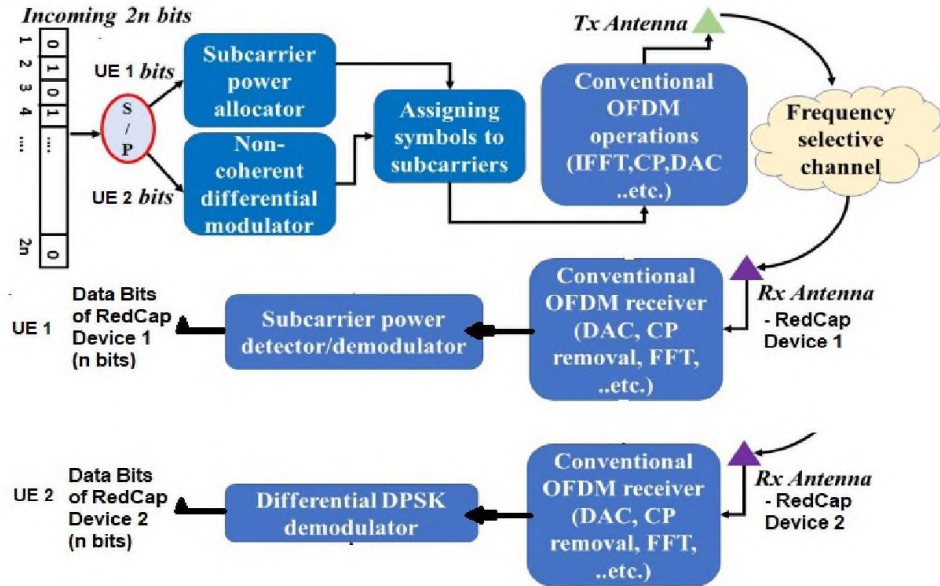


**Figure 1.** Transmitter/Receiver of the proposed MA-OFDM-SPM. In contrast to conventional OFDMA, the proposed approach uses two distinct modulations: one half of the incoming bit stream is modulated using DPSK, while the other half is modulated based on the power levels (i.e., high and low values).

At the receiving RedCap Device 1 (UE1), the power bits are detected from the incoming combined stream. More specifically, the values essentially the levels of power detection are performed by straightforwardly comparing each subcarrier's received power level with a pre-determined optimal threshold  $T$  defined as the power level corresponding exactly to the central point between the high (H) and low (L) power values.

$$T = \left(\frac{H+L}{2}\right)^2 \quad (1)$$

On the other hand, at the receiving RedCap Device 2 (UE2), conventional DPSK demodulation is performed for the data symbols according to the difference of the symbols' phases and applying differential decoding for the bits having DPSK modulation. It is crucial to emphasize that the minor complexity in the detection of the power block through thresholding comparison, which is regarded as a non-coherent detection approach, makes the proposed scheme an excellent fit for Redcap device requirements. The resulting simplicity in the detection process of the proposed design makes it surpass existing methodologies such as OFDM-IM, OFDM-SNM, and SIM-OFDM, which commonly rely on either maximum likelihood (ML) detection for optimal performance or log-likelihood ratio (LLR) detection for decreased complexity [9].

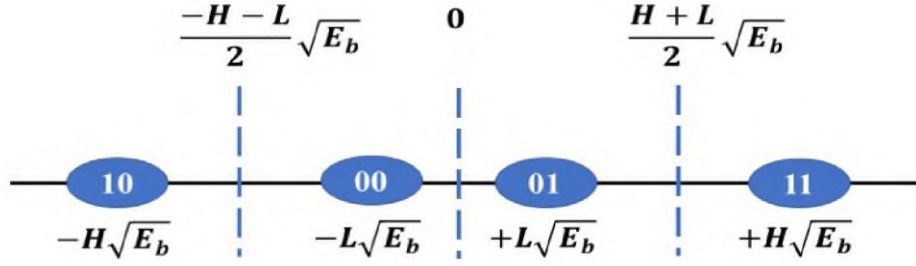


**Figure 2.** Constellation diagram of MA-OFDM-SPM, where the bit pair 'ij' is mapped to a subcarrier with power modulation (high if 'i' = 1 and low if 'i' = 0) and carries a bit 'j' modulated using two-bit (2)-DPSK

### 3. PERFORMANCE ANALYSIS OF THE PROPOSED MULTI-USER SYSTEM: MA-OFDM-SPM

Unlike conventional OFDMA, MA-OFDM-SPM combines two modulations to serve two different users. As shown in the receiver in Fig.1, an error can occur during the power levels' detection for UE1 or DPSK symbols demodulation for UE2. This results from multipath channel fading and noise impact, which can either increase or decrease the subcarrier power. Consequently, a high-power subcarrier may be misinterpreted as a low-power subcarrier, and vice versa. This results in four constellation points as shown in the constellation diagram of Fig.2. Consequently, the aggregated bit error rate of the system supporting two users simultaneously is characterized as the average of the bit error rates for the power component associated with UE1 and the DPSK component linked to UE2:

$$BER_{MA} = \frac{1}{2}(BER_{DPSK-UE2} + BER_{Power-UE1}) \quad (2)$$

Particularly, the bit error rate expression for 2-DPSK in a Rayleigh fading environment, under the assumption that the channel phase remains relatively stable over the duration of a bit sequence, is as follows [10]:

$$BER_{DPSK,Conventional} = \frac{1}{2(1+\frac{E_b}{N_0})} \quad (3)$$

where  $E_b/N_0$  shows the signal to noise ratio. The derivation of the expression  $BER_{DPSK-UE2}$  can be computed by considering the variations resulting from high and low power levels. As such, the bit error rate of the bit stream modulated through DPSK follows the following expression:

$$BER_{DPSK-UE2} = \frac{1}{2} (BER_{DPSK|H} + BER_{DPSK|L}) \quad (4)$$

where

$$BER_{DPSK|H} = \frac{1}{2(1+H^2\frac{E_b}{N_0})} \quad (5)$$

and

$$BER_{DPSK|L} = \frac{1}{2(1+L^2\frac{E_b}{N_0})} \quad (6)$$

show the impact of the high and low power levels on the bit stream modulated by DPSK respectively.

For the bit stream modulated by the power levels, the BER can be expressed as follows:

$$BER_{Power-UE1} = \frac{1}{4}P_1 + \frac{1}{4}P_2 + \frac{1}{4}P_3 + \frac{1}{4}P_4 \quad (7)$$

where

$$P_1 = \frac{1}{2\left(1 + \left(\frac{H-L}{2}\right)^2 \frac{E_b}{N_0}\right)} \quad (8)$$

$$P_2 = \frac{1}{2\left(1 + \left(\frac{H+3L}{2}\right)^2 \frac{E_b}{N_0}\right)} \quad (9)$$

$$P_3 = \frac{1}{2\left(1 + \left(\frac{H-L}{2}\right)^2 \frac{E_b}{N_0}\right)} \quad (10)$$

$$P_4 = \frac{1}{2\left(1 + (H+L)^2 \frac{E_b}{N_0}\right)} \quad (11)$$

For the case of non-optimized power reassignment, through a successive series of exhaustive trial-and-error experiments, the values of high and low power were determined to be:

$$H = \sqrt{3}, L = 1 \quad (12)$$

By substituting the specific values of H and L identified in equation (12) into equation (4),

It was found that this expression approaches the bit error rate of coherent conventional OFDM-BPSK very closely as confirmed by the bit error rate simulation results. The expression for conventional OFDM with BPSK used in the simulations is as follows:

$$BER_{Coherent-BPSK} = \frac{1}{2} \left( 1 - \sqrt{\frac{\frac{E_b}{N_0}}{1 + \frac{E_b}{N_0}}} \right) \quad (13)$$

#### 4. SIMULATION RESULTS

Simulation results displaying the performance of the proposed multiple access technique named MA-OFDM-SPM are exhibited. In the simulator, non-coherent subcarrier power modulation is used to serve UE 1, and non-coherent differential phase shift keying is used to serve UE2. The evaluation is expressed as bit error rate (BER) and throughput of the system. Table 1 shows a complete list of the simulation parameters.

Figure 3 illustrates the results of the simulations for BER for both U2 and U1 which are served by bit sequences modulated by DPSK and power level of the subcarriers respectively. Besides, the derived BER curve for the DPSK-UE2 is plotted. Furthermore, theoretical BER curves for conventional OFDM with DPSK and conventional OFDM with BPSK are displayed for comparison purposes. As shown in this plot, the BER curve for UE2 as a result of using MA-OFDM-SPM surpasses conventional OFDM with DPSK and achieves almost the same performance as coherent OFDM-BPSK.

**Table 1:** Parameters of Simulations with Rayleigh Channel Model

Modulation Parameters	Values
IFFT / FFT size	64
Number of subcarriers for data n	52
Number of symbols for CP	16
Number of inactive sub-carriers for OOB	12
Number of OFDM symbols	$10^4$
Delay samples positions ( Multipath channel)	[0 3 5 6 8]
Multipath channel tap power profile (dBm)	[0 -8 -17 -21 -25]

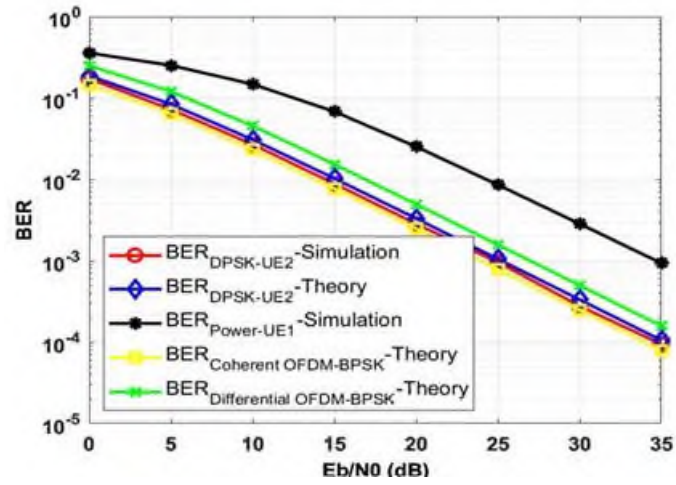


**Figure 3.** BER (Bit error rate) of MA-OFDM-SPM method. As observed, the bit error rate for groups of bits modulated with DPSK approaches the curve of coherent OFDM-BPSK very closely.

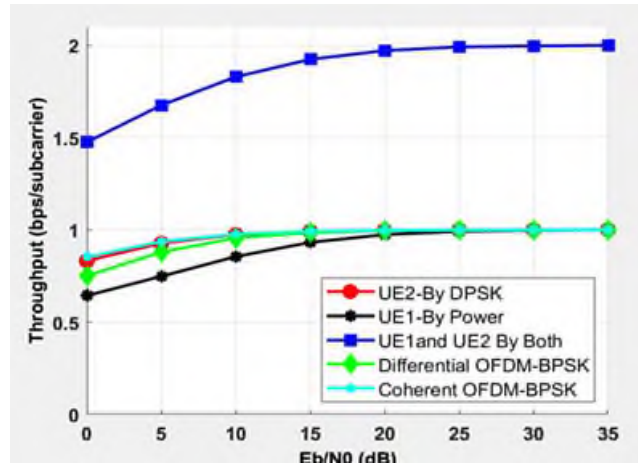


**Figure 4.** Throughput of MA-OFDM-SPM relative to conventional OFDM with coherent BPSK and non-coherent BPSK (i.e. DPSK). The 2-D modulation aspect (i.e., the DPSK dimension and the power dimension) of MA-OFDM-SPM gives it the benefit of doubling the system throughput compared to conventional OFDM with BPSK or DPSK

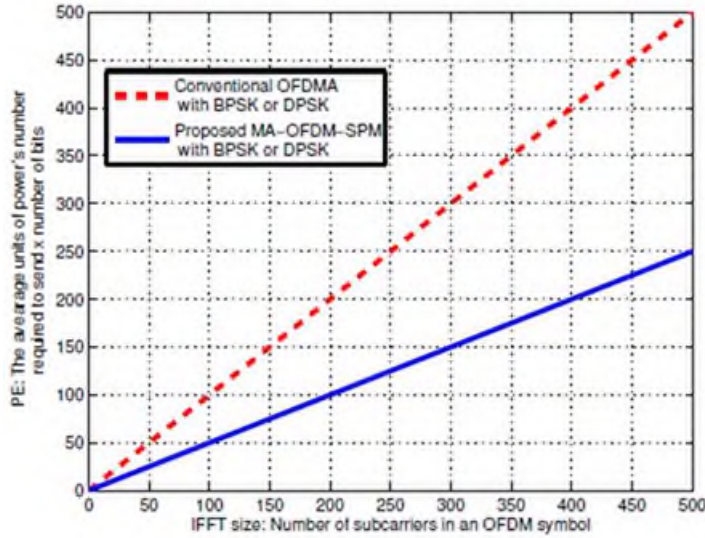


**Figure 5:** MA-OFDM-SPM compared to OFDM in terms of Power Efficiency (PE) versus number of subcarriers in an OFDM symbol (IFFT size).

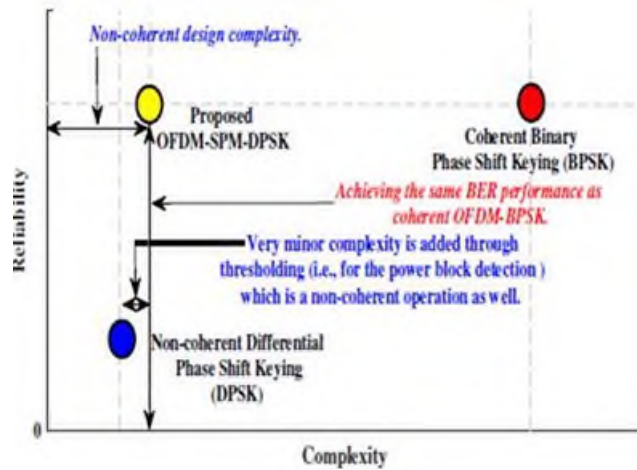


**Figure 6:** OFDM-SPM-DPSK compared to coherent and noncoherent BPSK in terms of design complexity and reliability. The figure shows that OFDM-SPM-DPSK combines the benefits of both non-coherent modulations (i.e., low-complexity) and coherent modulations (i.e., high performance).

Moreover, since MA-OFDM-SPM explores the power characteristic of the subcarriers as an additional data-carrying dimension, it allows for the transmission of an extra bit sequence using the power levels of the subcarriers. However, as shown in Figure 3, the detection of this additional stream is less reliable compared to conventional OFDM-DPSK. This erroneous bit sequence can be allocated to some user applications such as audio or video streaming services that don't demand ultra-reliability.

In Figure 4, the throughput of MA-OFDM-SPM is displayed individually and collectively for both UE1 and UE2. It is clear that, at high SNR values, the aggregated data rate of the scheme is twice as high as that of conventional OFDMA with DPSK/BPSK. This is due to the fact that MA-OFDM-SPM utilized the power of subcarriers in OFDM as an extra dimension to serve an additional user, thus outperforming conventional OFDMA in terms of data rate. It is known in the literature, coherent schemes are recognized as surpassing non-coherent systems in terms of reliability; however, non-coherent schemes are less complex in terms of receiver design because of the absence of phase estimation.

In Fig. 5, the power efficiency<sup>1</sup> of MA-OFDM-SPM is compared with coherent and non-coherent OFDMA modulations considering the use of binary phase shift keying with different number of

subcarriers (i.e., IFFT size)<sup>1</sup>. This plot represents the huge benefits that MA-OFDM-SPM offers, as being a non-coherent multi-access design which can provide twice the performance in terms of power efficiency as that of conventional coherent or non-coherent OFDMA based designs, which are currently being used in LTE, 5G, and WiFi networks. In other words, MA-OFDM-SPM needs half the power as that of OFDMA to send the same number of bits. This is with the benefit of having an additional stream that can be transmitted through the power subcarriers.

It is known in the literature that coherent systems surpass non-coherent systems in terms of reliability; however, noncoherent schemes are less complex in terms of receiver design because of the absence of phase estimation [11]–[14]. In Fig.6, OFDM-SPM-DPSK is compared with coherent and noncoherent binary phase shift keying modulations in terms of complexity and reliability. This plot is a presentation for the great benefits which OFDM-SPM-DPSK offers, in the nonoptimized power reassignment mode, as being a non-coherent design with the same performance as coherent OFDM with BPSK. This is with the benefit of having an additional stream that can be transmitted through the power subcarriers. As such, OFDM-SPM-DPSK is a good fit for applications requiring low-complexity, ultra-reliability and high data rate.

In addition, we used logical numerical and theoretical analysis to investigate the effect of the number of users on the amount of spectrum measured in IFFT size, which is required to be allocated among users so that similar spectral efficiency can be achieved, and noticed that MA-OFDM-SPM is twice superior than that of conventional OFDMA. It's also anticipated by logic that the BER performance to remain the same regardless of the number of users in the system because the new additional users can be allocated different new resources. Also, the system spectral efficiency of MA-OFDMSPM will stay twice or double that of conventional OFDMA based systems even when the number of users increases in the system setup. Moreover, future studies will conduct actual practical implementation of MA-OFDM-SPM to verify and solidify its superiority against competitive schemes in real life network setups. Given the above detailed analysis of the results, it is shown that MA-OFDM-SPM can be a good fit for applications requiring low complexity, ultra-reliability, and high spectral efficiency performance. Future studies will focus on improving the performance of MA-OFDM-SPM further using AI/ML based methods and techniques like deep learning and neural networks in a way that is similar to what has been done in [15], [16].

## 5. CONCLUSION

RedCap devices face significant challenges in achieving efficient multiple access techniques that fully leverage their potential while adhering to their constraints. Despite numerous proposed techniques in recent literature, none have satisfactorily met the multi-faceted requirements of RedCap devices. This paper introduced a novel multiple-access technique designed specifically to address these challenges, optimizing the performance and efficiency of RedCap devices across various application scenarios. The proposed technique enhances data rates, reduces latency, and extends battery life while maintaining the cost-effectiveness and simplicity crucial for RedCap devices. By utilizing the power domain as an extra dimension for delivering additional data bits, the design not only overcomes previous challenges but also provides higher system throughput. This approach effectively doubles the system's spectral efficiency, allowing an additional user to be served with a stream of data bits equal to that of the main user, without increasing transceiver design complexity.

---

<sup>1</sup> Power efficiency (PE) is measured as the average units of power's number required to send x number of bits; and this is equal to the number of subcarriers in an OFDM symbol (the IFFT size) times the the unit of power in average per subcarrier divided by the number of bits per symbols per subcarrier that can be sent by OFDMA or MA-OFDMA-SPM.

### Declaration of Ethical Standards

The authors declare that all ethical guidelines including authorship, citation, data reporting, and publishing original research are followed.

### Declaration of Competing Interest

The authors declare that there is no conflict of interest.

### Funding / Acknowledgements

This research received no specific grant from any funding agency in the public, commercial, or not-for-profit sectors.

### Data Availability

The data that support the findings of this study are available from the corresponding author upon reasonable request.

### REFERENCES




- [1] S. N. K. Veedu *et al.*, "Toward smaller and lower-cost 5G devices with longer battery life: An overview of 3GPP Release 17 RedCap," *IEEE Commun. Stand. Mag.*, vol. 6, no. 3, Sep., pp. 84–90, 2022.
- [2] L. Dai, B. Wang, Z. Ding, Z. Wang, S. Chen, and L. Hanzo, "A survey of non-orthogonal multiple access for 5G," *IEEE Commun. Surv. Tutor.*, vol. 20, no. 3, pp. 2294–2323, 3rd Quart., 2018.
- [3] J. M. Hamamreh, M. Abewa, and J. P. Lemayian, "New non-orthogonal transmission schemes for achieving highly efficient, reliable, and secure multi-user communications," *RS Open J. Innov. Commun. Technol.*, vol. 1, no. 2, 2020.
- [4] C. Xu *et al.*, "Sixty years of coherent versus non-coherent tradeoffs and the road from 5G to wireless futures," *IEEE Access*, vol. 7, pp. 178246–178299, 2019.
- [5] A. Hajar, J. M. Hamamreh, M. Abewa, and Y. Belallou, "A spectrally efficient OFDM-based modulation scheme for future wireless systems," in *2019 Scientific Meeting on Electrical-Electronics Biomedical Engineering and Computer Science (EBBT)*, Apr. 2019, pp. 1–4.
- [6] J. M. Hamamreh, A. Hajar, and M. Abewa, "Orthogonal frequency division multiplexing with subcarrier power modulation for doubling the spectral efficiency of 6G and beyond networks," *Trans. Emerg. Telecommun. Technol.*, vol. 31, p. e3921, 2020.
- [7] A. Hajar and J. M. Hamamreh, "The generalization of orthogonal frequency division multiplexing with subcarrier power modulation to quadrature signal constellations," *RS Open J. Innov. Commun. Technol.*, vol. 1, no. 1. [Online]. Available: <https://doi.org/10.21428/03d8ffbd.4948e89e>. [Accessed May 24, 2024].
- [8] M. Abewa and J. M. Hamamreh, "Non-coherent OFDM-subcarrier power modulation for low complexity and high throughput IoT applications," *RS Open J. Innov. Commun. Technol.*, vol. 1, no. 1, 2020. [Online]. Available: <https://doi.org/10.46470/03d8ffbd.2a45a9a1>. [Accessed May 30, 2024].
- [9] J. A. Jaradat, J. Hamamreh, and H. Arslan, "Modulation options for OFDM-based waveforms: Classification, comparison, and future directions," *IEEE Access*, vol. 7, pp. 17263–17278, 2019.
- [10] A. Goldsmith, *Wireless Communications*. Cambridge, U.K.: Cambridge Univ. Press, 2005.
- [11] M. Abewa and J. M. Hamamreh, "NC-OFDM-SPM: A two-dimensional non-coherent modulation scheme for achieving the coherent performance of OFDM along with sending an additional datastream," *RS Open J. Innov. Commun. Technol.*, vol. 2, no. 3, 2021. [Online]. Available: <https://doi.org/10.46470/03d8ffbd.a97a5236>. [Accessed June 13, 2024].

- [12] M. Hijazi and J. M. Hamamreh, "Signal space diversity for improving the reliability performance of OFDM with subcarrier power modulation," *RS Open J. Innov. Commun. Technol.*, vol. 2, no. 3, 2021. [Online]. Available: <https://doi.org/10.46470/03d8ffbd.7f32914f>. [Accessed June 27, 2024].
- [13] M. Hijazi and J. M. Hamamreh, "Signal space diversity for improving the reliability performance of OFDM with subcarrier power modulation," *RS Open J. Innov. Commun. Technol.*, vol. 2, no. 3, 2021. [Online]. Available: <https://doi.org/10.46470/03d8ffbd.7f32914f>. [Accessed June 30, 2024].
- [14] A. Abuqamar, J. M. Hamamreh, and M. Abewa, "STBC-assisted OFDM with subcarrier power modulation," *RS Open J. Innov. Commun. Technol.*, vol. 2, no. 4, 2021. [Online]. Available: <https://doi.org/10.46470/03d8ffbd.275ae770>. [Accessed July 01, 2024].
- [15] M. Hijazi and J. M. Hamamreh, "Convolutional neural network-based equalizer for improving the reliability performance of OFDM with subcarrier power modulation," *RS Open J. Innov. Commun. Technol.*, vol. 2, no. 5, 2021. [Online]. Available: <https://doi.org/10.46470/03d8ffbd.48b1d1c8>. [Accessed July 01, 2024].
- [16] A. Abuqamar and J. M. Hamamreh, "Back propagation artificial neural network for improving the performance of STBC-based OFDM with subcarrier power modulation," *RS Open J. Innov. Commun. Technol.*, vol. 2, no. 4, 2021. [Online]. Available: <https://doi.org/10.46470/03d8ffbd.7aff4a62>. [Accessed July 01, 2024].





## INVESTIGATION OF THE EFFECTS OF RIB APPLICATION ON COOLING IN A TURBINE BLADE

<sup>1,2,\*</sup> Muhammed Emin TOLU , <sup>2</sup> Osman BABAYİĞİT , <sup>3</sup> Dilek Nur ÖZEN 

<sup>1,2</sup> Necmettin Erbakan University, The Graduate School of Natural and Applied Science, Mechanical Engineering Department, Konya, TÜRKİYE

<sup>2</sup> Karamanoğlu Mehmetbey University, Engineering Faculty, Mechanical Engineering Department, Konya, TÜRKİYE




<sup>3</sup> Necmettin Erbakan University, Engineering Faculty, Mechanical Engineering Department, Konya, TÜRKİYE  
<sup>1,2</sup> [metolu@kmu.edu.tr](mailto:metolu@kmu.edu.tr), <sup>2</sup> [obabayigit@kmu.edu.tr](mailto:obabayigit@kmu.edu.tr), <sup>3</sup> [dnozen@erbakan.edu.tr](mailto:dnozen@erbakan.edu.tr)

### Highlights

- A rib turbulator cooling design was developed, and the solid model was created
- The mesh structure required for flow and heat transfer analyses was generated
- CFD analyses were conducted for both the ribbed and non-ribbed turbine blades
- Nondimensional temperature parameter ( $T/T_0$ ) for both turbine blades were compared



## INVESTIGATION OF THE EFFECTS OF RIB APPLICATION ON COOLING IN A TURBINE BLADE

<sup>1,2,\*</sup>Muhammed Emin TOLU , <sup>2</sup>Osman BABAYİĞİT , <sup>3</sup>Dilek Nur ÖZEN 

<sup>1,2</sup>Necmettin Erbakan University, The Graduate School of Natural and Applied Science, Mechanical Engineering Department, Konya, TÜRKİYE

<sup>2</sup>Karamanoğlu Mehmetbey University, Engineering Faculty, Mechanical Engineering Department, Konya, TÜRKİYE

<sup>3</sup>Necmettin Erbakan University, Engineering Faculty, Mechanical Engineering Department, Konya, TÜRKİYE  
<sup>1,2</sup>[metolu@kmu.edu.tr](mailto:metolu@kmu.edu.tr), <sup>2</sup>[obabayigit@kmu.edu.tr](mailto:obabayigit@kmu.edu.tr), <sup>3</sup>[dnozen@erbakan.edu.tr](mailto:dnozen@erbakan.edu.tr)

(Received: 24.10.2024; Accepted in Revised Form: 22.02.2025)

**ABSTRACT:** Turbine blades are system components exposed to extremely high temperatures. Effective cooling of turbine blades is essential to enhance efficiency and extend the operational lifespan of gas turbines. In this study, a new rib turbulator cooling design was tested for the NASA C3X turbine blade. The analyses were compared with those conducted on non-ribbed blades. According to the findings, an average surface temperature of 574.6 K and a maximum surface temperature of 661.8 K were achieved. These values indicate a cooling efficiency of 19.1% for the leading edge, which is exposed to the maximum temperature, and 29.75% for the average surface temperature. All data obtained from the study have been shared in the form of figures and graphs.

**Keywords:** CFD Analysis, Ribbed Turbulators, Turbine Blade Cooling

### 1. INTRODUCTION

Throughout history, mankind, requiring increasing amounts of energy and power at each stage, has perpetually aimed to exert greater control over nature to sufficiently meet these needs. Humanity who had to produce various solutions to achieve this has scrutinized the functioning of nature and, pioneered numerous innovations, in the light of the information they acquired.

Presently, among the myriad mechanisms devised by humanity to fulfill its needs, gas turbines stand as prominent contributors. Gas turbines find application not only in electricity generation facilities but also in transportation. While their usage in land transportation is encountered, they are notably more extensively employed in aviation and maritime transport. Turbojet, turboprop, turboshaft, and turbofan engines utilized in transportation are specialized variants of gas turbine engines.

Gas turbines, fundamentally, are systems operating according to Newton's third law of motion, the principle of action and reaction. In gas turbines operating based on the Brayton cycle, the air compressed in the compressors reaches high pressure and high temperature. Subsequently, the air transferred to the combustion chamber is ignited with fuel. The resulting high energy is transferred to the turbine blades, facilitating the conversion of heat energy into mechanical energy. Then, the exhaust air is expelled from the exhaust.

Turbines consist of stationary blades (stator) and moving blades (rotor). Stationary blades intercept the flow before it reaches the moving blades, directing the airflow most efficiently towards the moving blades. Moving blades, on the other hand, facilitate the conversion of the heat energy acquired by the air in the combustion chamber into mechanical energy.

In gas turbines, turbine blades are particularly exposed to extremely high temperatures. The turbine inlet temperature is crucial not only for the power output and efficiency of the turbine but also significantly impacts the lifespan of turbine components. To achieve higher power and efficiency, it is increasingly desirable for gas turbines to operate at higher temperatures. The primary means to accomplish this is by enabling turbine blades to withstand these elevated temperatures.

\*Corresponding Author: Muhammed Emin Tolu, [metolu@kmu.edu.tr](mailto:metolu@kmu.edu.tr)

For turbine blades to operate under higher temperatures, it is essential to reduce the thermal stresses they experience. Therefore, cooling of turbine blades, particularly the efficient cooling of stationary turbine blades (stators) which first encounter the high-temperature fluid, is critical. Efficient cooling of turbine blades not only increases their lifespan but also enhances system efficiency by enabling operation at higher temperatures.

Efficiently cooled turbine blades will have an extended service life, reduced maintenance costs, and enhanced turbine efficiency, enabling higher power output.

There are also some disadvantages associated with cooling applications in turbine blades. The air used for cooling is extracted from the compressor, which can reduce the power output obtained at the turbine exit. The introduction of cold air obtained from the compressor into the high-temperature fluid decreases the enthalpy and pressure values of the fluid, which can slightly impact turbine efficiency in a negative manner. Cooling applications also present various manufacturing challenges and lead to increased costs. Designing a cooling application that takes into account all these advantages and disadvantages will ensure the most efficient results.

Experimental studies on this subject in the literature are limited due to very high costs and a complex process. Despite this, the fact that humanity need more power day by day increases the importance of studies on cooling turbine blades and prompting scientists to focus more and more on this issue.

One of the pioneering studies on cooling turbine blades was undertaken by Hylton et al. [1]. In this experimental study, Hylton et al. selected three C3X turbine blades to simulate the first stage of a gas turbine and examined the effects of the channels on the cooling of the blade. Subsequent studies have referenced this experimental study and compared their own numerical data with the experimental data obtained by Hylton and colleagues for validation purposes.

In numerical simulations, selecting an appropriate turbulence model is crucial for simulating the flow. In a study by Menter et al. [2] in 1994, the SST  $k-\omega$  turbulence model was first proposed as a blend of the  $k-\omega$  and  $k-\varepsilon$  turbulence models, aiming to combine the strengths of both models while avoiding their respective disadvantages.

In a study conducted by Faccini et al., [3] the thermal behavior of a NASA-C3X gas turbine blade, cooled radially by fluid passing through 10 cooling channels, was simulated using three-dimensional conjugate heat transfer simulations with the STAR-CD™ code. The study modeled the hot external flow volume and obtained the metal temperature distribution of the blade. The obtained data were compared with the results of experimental study, and the comparison results were presented graphically.

Referencing the study by Hylton et al., Zheng et al., [4] investigated five different turbulence models (standard  $k-\varepsilon$ , realizable  $k-\varepsilon$ , SST  $k-\omega$ , transitional  $k-k\ell-\omega$ , and  $v^2f$ ) to simulate the airflow and heat transfer of a turbine guide vane. Based on the results obtained, it was noted that the SST  $k-\omega$  turbulence model performed very well in accurately predicting heat transfer.

In a study conducted in 2016, Mazaheri et al., [5] optimized the shape and position of cooling channels in a C3X turbine blade. Their objective was to minimize the maximum temperature gradient and maximum temperature along the three-dimensional span of the blade. They modeled the shape of the cooling channels using a new method based on Bezier curves and utilized forty design variables in their study.

In their study titled "Optimization of Turbine Blade Cooling for Enhanced Turbine Performance," Mousavi et al., [6] simulated a simplified 2D model of the C3X blade to improve turbine performance. They conducted simulations using four different turbulence models, and the resulting data were compared with experimental data obtained by Hylton et al. in 1983. This comparison served as a validation study for their simulations.

Yousefi et al., [7] conducted research using computer-aided simulations to investigate the effects of ribbed channels on a modified NASA C3X gas turbine blade. In their study referencing the baseline design with ten cooling channels used by Hylton et al., they proposed a new model aimed to improve cooling performance by incorporating ribs of specific dimensions into the cooling channels. They studied the temperature distribution, convective heat transfer coefficient of the blade surface, performance factor, and

friction coefficient. Researchers examined six different configurations of longitudinally placed ribs within the cooling channels. They compared the obtained results with experimental results of Hylton et al., and numerical results of another previous study of Faccini et al. They found that these ribs increased heat transfer within the cooling channels by 25% while only increasing the friction factor by 3%. Additionally, the performance factor improved by 24%, and the maximum temperature was reduced by 25 K°.

In another study conducted in 2021, Karimi et al., [8] aimed to optimize an internally cooled gas turbine blade by enhancing cooling performance and reducing sensitivity to operational uncertainties. Using the  $v^2f$  turbulence model to minimize simulation errors, the researchers employed polynomial chaos methods for quantifying uncertainties. Their primary objective was to minimize the maximum temperature and maximum temperature gradient of the blades to extend their service life.

Vo et al., [9] simulated the combined heat transfer in the first-stage cooling blade of a W501F engine in their study, where they examined the effects of thermal barrier coating thickness and the ratio of the coolant flow to the mainstream hot gas pressure and temperature in blade film cooling. They found that a 100 K decrease in the coolant temperature resulted in an average blade temperature decrease of 58 K. Additionally, they determined that the presence of a thermal barrier coating with a thickness of 0.8 mm led to a 35% reduction in the heat transfer coefficient on the blade surface.

Goktepel and Atmaca [10] investigated the phenomena of flow separation and reattachment over a backward-facing step through numerical modeling. They conducted the analysis at a Reynolds number of  $Re=5000$ , referencing a prior experimental study and employing the RNG  $k-\epsilon$  turbulence model. As a result, they identified the reattachment length as 5,92 which aligns with the experimental data.

In this study, a new design of C3X turbine blade which features rib turbulators applied along the entire inner wall, was examined and the impact of the pressure and temperature of the coolant on blade cooling was investigated in a blade. The contributions to the literature resulting from this study are listed below:

- Cooling channels are used for the cooling of turbine blades. In this study, unlike other studies reviewed in the literature, the entire internal surface of the NASA C3X turbine blade has been modeled as a cooling channel for the cooling of the turbine blade.
- The ribbed cooling design used for the cooling of turbine blades was applied to the entire internal surface of the turbine blade, which was modeled as a cooling channel in a manner that has not been studied before.
- The obtained results were presented in the form of diagrams, tables, and graphs.

## 2. DESCRIPTION OF SYSTEM

Since the airflow reaching the turbine blades has extremely high temperatures, designing turbine blades to withstand such high temperatures is crucial for both the efficiency of the system and the operational lifespan of the blades. Numerous studies are being conducted across various fields to enhance the ability of turbine blades to withstand high temperatures. Some of these studies focus on manufacturing turbine blades from materials that can endure higher temperatures or coating the turbine blades with materials that are resistant to high temperatures, while others concentrate on cooling the blades to enable their operation even at extremely high temperatures.

As a result of numerous studies on turbine blade cooling, alternative cooling methods have been developed that can be applied under different operating conditions. Alnaeli et al., [11] adverted that the cooling process in turbine blades can be implemented through various methods which can generally be categorized into two main types as internal cooling and external cooling. The internal cooling methods that can be applied to a turbine blade are shown in the Figure 1.

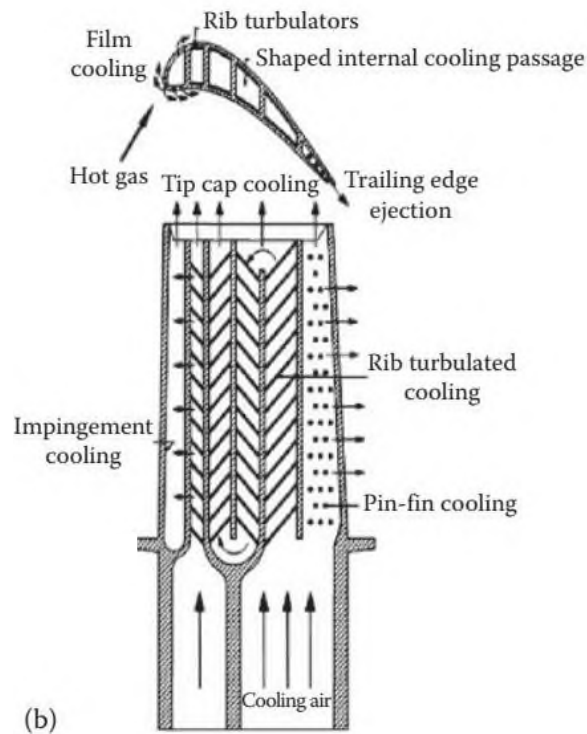


**Figure 1.** Various internal cooling methods used for cooling turbine blades [11]

The turbine blade to be used in this study was selected as the NASA C3X type, which has been used in numerous studies in the literature. Subsequently, a solid model of the turbine blade was created using the coordinate data obtained from the literature and with the aid of computer-aided solid modeling software, a ribbed turbulator design was applied to the internal surface of the blade, and flow domains for both the hot external flow and the cold internal flow were generated as can be observed in Figure 2.

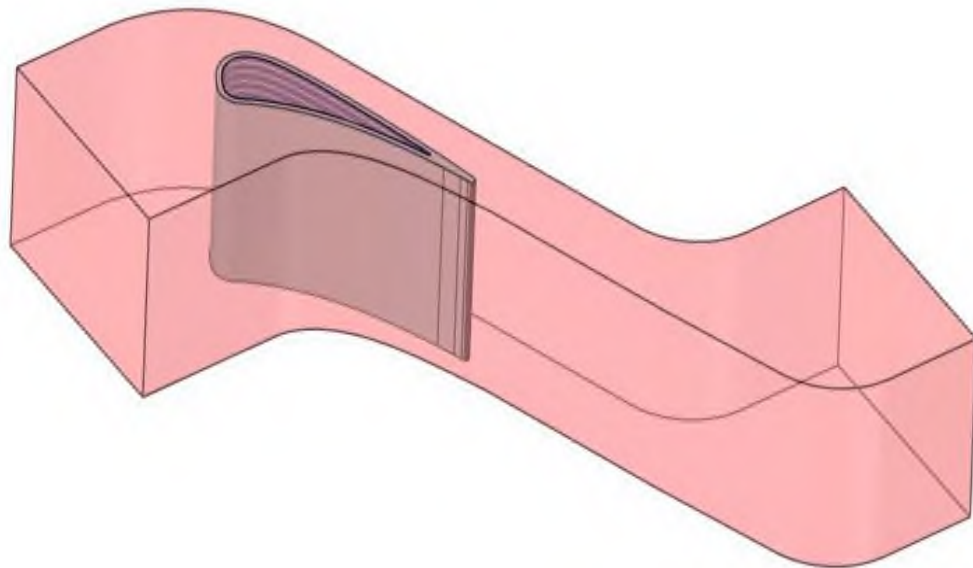


**Figure 2.** Turbine blade, hot external flow domain and cold internal flow domain

The flow analyses of the final design, which includes the solid model of the turbine blade with an

applied ribbed turbulator cooling design, as well as the internal and external flow volumes, were conducted using computer-aided simulations.

All the data obtained from the analyses, which examined heat transfer and pressure drops, were compiled in the form of graphs and diagrams.

### 3. MATERIAL AND METHOD

In this study, a NASA C3X type turbine blade was used, and a cooling design was investigated for this blade. The coordinates used for modeling the NASA C3X turbine blade were presented in the study conducted by Hylton et al. [1]. The geometric parameters of the NASA C3X turbine blade are provided in Table 1 [4].

**Table 1.** The geometrical parameters of NASA C3X turbine blade [4].

Blade Chord (mm)	Setting Angle (°)	Air Exit Angle (°)	Axial Chord (mm)	Vane Spacing (mm)	Throat (mm)
144.93	59.89	72.38	78.16	117.73	32.92

#### 3.1. Design of the Cooling Method

As a result of the literature review, no study was found in which the entire internal surface of the turbine was designed as a cooling channel. In order to address this gap in the literature and introduce a novel cooling design, the entire internal surface of the turbine blade was conceptualized as a cooling channel, and rib turbulator design were applied along the inner surface of the blade. This approach aims to enhance cooling efficiency by maximizing heat transfer across the entire internal surface. The solid modeling of this design was created using the SolidWorks® design software and can be seen in Figure 3.

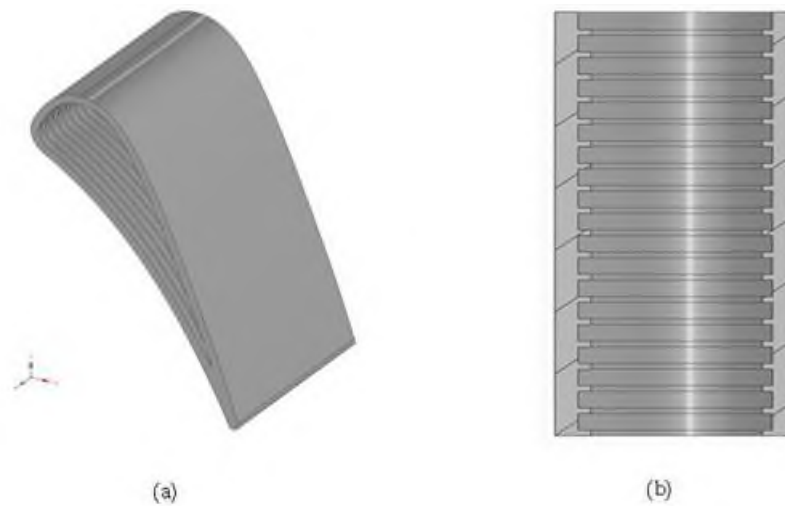


**Figure 3.** (a) turbine blade with rib turbulator, (b) cross-section of rib turbulator design.

There are several critical geometric parameters and design constraints that play a significant role in the design of ribbed turbulator cooling applications. These include the rib pitch-to-height ratio ( $p/e$ ) and rib height-to-hydraulic diameter ratio ( $e/D$ ). Each of these parameters must be optimized to balance between maximizing heat transfer and minimizing pressure drop.

As a result of the literature review [12], the geometric parameters were selected as follows: the "p" value, which represents the distance between two ribs, was chosen as 4 mm, and the "e" value, representing the rib height, was set to 1 mm. Accordingly, the rib pitch-to-height ratio ( $p/e$ ) was determined to be 4.

The hydraulic diameter, which is required to calculate the  $e/D$  ratio, another design constraint

representing the ratio of rib height to hydraulic diameter, was determined using the following formula (1):

$$D = \frac{4A}{W} \quad (1)$$

Here;  $D$ ,  $A$  and  $W$  are the hydraulic diameter, the cross-sectional area of the flow channel and the wetted perimeter of the channel respectively.

Both the  $A$  (cross-sectional area) and  $W$  (wetted perimeter) values were measured using the solid modeling program interface, with values of  $1881.75 \text{ mm}^2$  and  $260 \text{ mm}$ , respectively.

The  $p/e$  ratio and the  $e/D$  ratio are crucial for the rib turbulator cooling channel design to ensure efficient cooling [12] and they are presented in Table 2.

**Table 2.** Design parameters of the rib turbulator application.

$p/e$	4
$e/D$	0.035

Additionally, the technical drawing and the geometric parameters of the rib turbulator cooling channel design can also be seen in Figure 4.

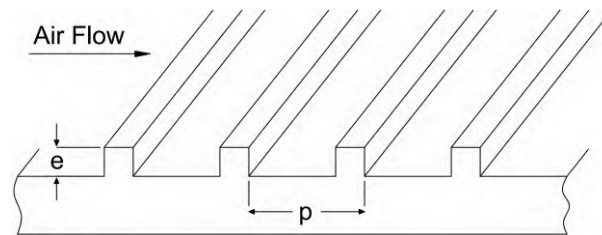


**Figure 4.** Geometric parameters of rib turbulator cooling channel

### 3.2. Design of the Analysis Domain

In order to perform the flow analysis, it is necessary to model the flow domain of the hot external flow coming onto the turbine blade. Based on the literature review, the design parameters used for the hot external flow domain in a study conducted by Zheng et al. using the NASA C3X turbine blade were referenced [4]. The domains of hot flow and cold flow are shown in Figure 5.

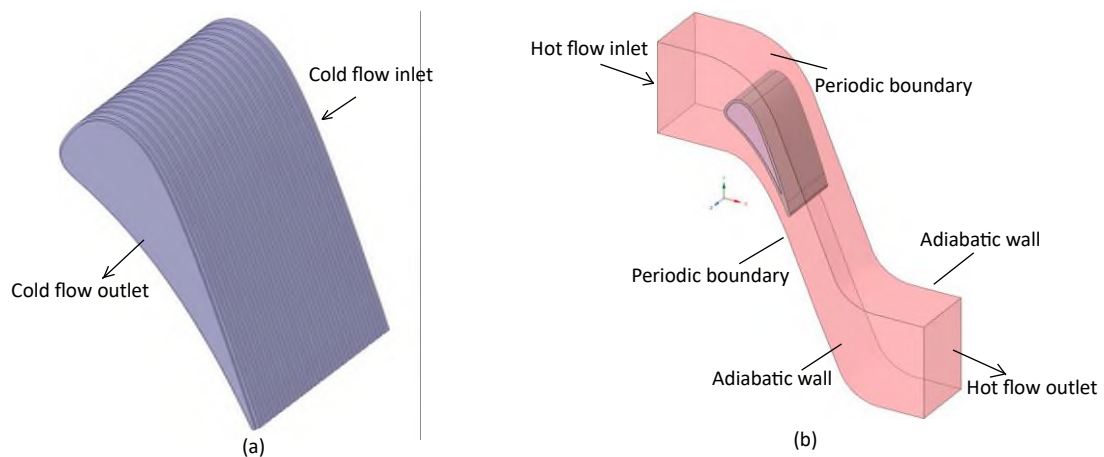


**Figure 5.**(a) Domain for internal flow, (b) external and internal flow domains with turbine blade

Cooling with rib turbulators is one of the most commonly used cooling techniques, which is an internal cooling method and employed in this study. In such cooling applications, an increase in cooling and heat transfer is expected by creating turbulence in the blade cooling canals [13]. The ribbed structure that creates turbulence is prepared as part of the manufacturing process and integrated into the blade during casting.

### 3.3. Computational Model

Modeled turbine blade and flow domains have been imported into the Ansys Fluent® program. Proper setup of the model within the program and accurate creation of the mesh structure are crucial for obtaining reliable analysis results.

The mesh structure was created using the Fluent Meshing module in the Ansys software. A poly-hexcore mesh was chosen to achieve a higher-quality flow analysis with a reduced number of elements. Based on the mesh independence study, an element count of 1371379 was selected as it provides the most efficient results with the lowest computational cost. The maximum skewness value of the generated mesh was 0.8285. A visual representation of the generated mesh structure is provided in Figure 6.

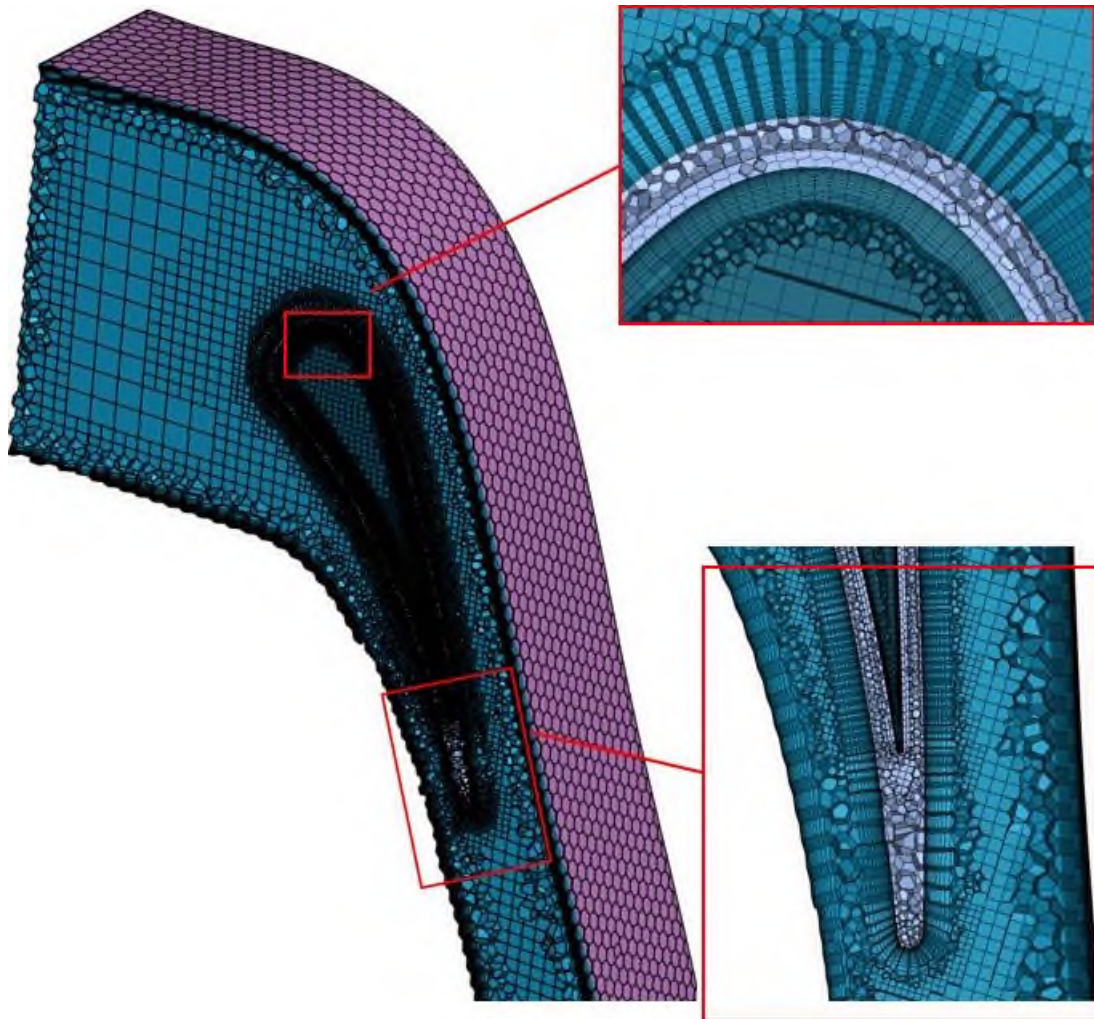


**Figure 6.** Mesh structure created for flow and heat transfer analyses

The flow analyses were conducted using the realizable  $k-\epsilon$  turbulence model with the Menter-Lechner near-wall treatment method, achieving a  $y^+$  value close to 30. The realizable  $k-\epsilon$  model is a more realistic model which better represents the distribution of turbulent kinetic energy and energy dissipation [14]. In



addition, the realizable  $k$ - $\epsilon$  model provides greater accuracy near the wall and yields more consistent results in flow separation, reattachment, and recirculation regions [15].

At this stage of the study, the following assumptions and definitions have been made:

- Periodic boundaries have been defined, and adiabatic wall assumptions have been applied for the hot external flow domain.
- For the surfaces in contact with the flow, smooth surface and no-slip condition assumptions have been applied.
- The NASA C3X turbine blade is made of ASTM-310 stainless steel (OCr25Ni20), with a constant density of 8030 kg/m<sup>3</sup> and a specific heat capacity of 502 J/kg·K [16]. The thermal conductivity value of blade ( $k_b$ ) varies with temperature and is calculated using the linear equation (2) provided below

$$k_b = 0,0115T + 9,9105 \quad (2)$$

- Air is used as the cooling fluid and is assumed to behave as an ideal gas. Since the thermal conductivity ( $k_A$ ), specific heat ( $C_{p,A}$ ), and viscosity ( $\mu_A$ ) of air vary with temperature, these values were not entered as constants but were instead calculated using equations.

The thermal conductivity of air was calculated using the Sutherland's Formula (3) [17].

$$k_A = k_0 \cdot \left( \frac{T}{T_0} \right)^{3/2} \cdot \left( \frac{T_0 + S}{T + S} \right) \quad (3)$$

where  $k_A$ ,  $k_0$ ,  $T$ ,  $T_0$  and  $S$  are; thermal conductivity at temperature, thermal conductivity at the reference temperature, temperature of the fluid, reference temperature and Sutherland constant respectively. A User Defined Function (UDF) code was written to implement the formula for calculating the thermal conductivity of air in the flow and heat transfer analyses. This code was embedded into the library of the analysis software.

The dynamic viscosity ( $\mu_A$ ) of air was calculated using the Sutherland's Formula (4) [17].

$$\mu_A = \mu_0 \cdot \left( \frac{T}{T_0} \right)^{3/2} \cdot \left( \frac{T_0 + S}{T + S} \right) \quad (4)$$

where  $\mu_0$  is Dynamic Viscosity at the reference temperature  $T_0$ .

The specific heat capacity of air was calculated using the equation (5) provided below [4]:

$$C_{p,A} = a_0 + a_1 \cdot T + a_2 \cdot T^2 + a_3 \cdot T^3 + a_4 \cdot T^4 \quad (5)$$

The coefficients used in the calculation of specific heat are given in Table 3.

**Table 3 .** The coefficients used in the calculation of specific heat

$a_0$	$a_1$	$a_2$	$a_3$	$a_4$
957.110256	0.2365234	$5.141114 \cdot 10^{-6}$	$-3.3917446 \cdot 10^{-9}$	$-6.0929646 \cdot 10^{-12}$

- The boundary conditions for the hot external flow and cold internal flow, obtained from the literature review, are provided in the Table 4 below.  $P_{Hin}$ ,  $T_{Hin}$ ,  $Tu$ ,  $Tv$ ,  $P_{Hout}$  are inlet pressure, inlet temperature, turbulence intensity, viscosity ratio and outlet pressure of hot flow respectively. For the cold flow,  $V_{Cin}$ ,  $T_{Cin}$ ,  $Tu$ ,  $D_H$  and  $P_{Cout}$  represent the inlet velocity, inlet temperature, turbulence intensity, hydraulic diameter, and outlet pressure, respectively.

**Table 4.** The boundary conditions of hot external flow and cold internal flow

	$P_{\text{Hin}}$ (Pa)	$T_{\text{Hin}}$ (K)	Tu (%)	Tv	$P_{\text{Hout}}$ (Pa)
<b>Hot external flow</b>	413286	818	8.3	30	101325
	$V_{\text{Cin}}$ (m/s)	$T_{\text{Cin}}$ (K)	Tu (%)	$D_{\text{H}}$ (mm)	$P_{\text{Cout}}$ (Pa)
<b>Cold internal flow</b>	65.77	349.2	10	25.7	101325

### 3.4. Mathematical Model

The governing equations of motion for a continuous, viscous fluid are three-dimensional, time-dependent, compressible Navier-Stokes equations [18], [19], [20]. These equations are the continuity equation (6) [12];

$$\nabla \cdot (\rho \cdot \vec{V}) = 0 \quad (6)$$

the momentum equation (7) [12];

$$\nabla \cdot \left[ (\rho \cdot v_i \cdot \vec{V}) - (\mu_{\text{eff}} \cdot \nabla v_i) \right] = \frac{\partial p}{\partial x_i} + S_{v_i} \quad (7)$$

and the energy equation (8) [12];

$$\nabla \cdot \left[ (\rho \cdot T \cdot V) - (\alpha_{\text{eff}} \cdot \nabla T) \right] = S_T \quad (8)$$

where  $S_{v_i}$  and  $S_T$  are source term for the momentum transport equation in the  $i$  direction and source term for energy transport respectively.

The realizable k- $\epsilon$  turbulence model, chosen for flow analyses, includes transport equations for the turbulence kinetic energy (k) and the rate of turbulence dissipation ( $\epsilon$ ). The turbulence kinetic energy equation (9) is;

$$\frac{\partial(\rho \cdot k)}{\partial t} + \nabla \cdot (\rho \cdot k \cdot \vec{V}) = \nabla \cdot \left[ \left( \frac{\mu + \mu_t}{\sigma_k} \right) \cdot \nabla k \right] + P_k - (\rho \cdot \epsilon) \quad (9)$$

where  $P_k$  is production term of turbulence kinetic energy.

$\epsilon$  is rate of turbulence dissipation and found with equation (10).

$$\frac{\partial(\rho \cdot \epsilon)}{\partial t} + \nabla \cdot (\rho \cdot \epsilon \cdot \vec{V}) = \nabla \cdot \left[ \left( \frac{\mu + \mu_t}{\sigma_\epsilon} \right) \cdot \nabla \epsilon \right] + \left[ (\rho \cdot C_1 \cdot S_\epsilon) - \left( \rho \cdot C_2 \cdot \frac{\epsilon^2}{k + \sqrt{v \cdot \epsilon}} \right) \right] \quad (10)$$

## 4. RESULTS AND DISCUSSION

The solid modeling of the NASA C3X ribbed turbulator turbine blade was performed using the SolidWorks CAD software, while the flow and heat transfer analyses were conducted in Ansys Fluent.

Figure 7 shows the pressure distribution of the refrigerant in the ribbed turbulator cooling channel. The rib turbulators within the cooling channel enhance cooling performance by increasing turbulence in the coolant, thereby improving heat transfer. However, the rib turbulators also cause a pressure drop in the coolant. The pressure drop in the coolant flow within the cross-sectional view of the cooling channel is can be seen in Figure 7.

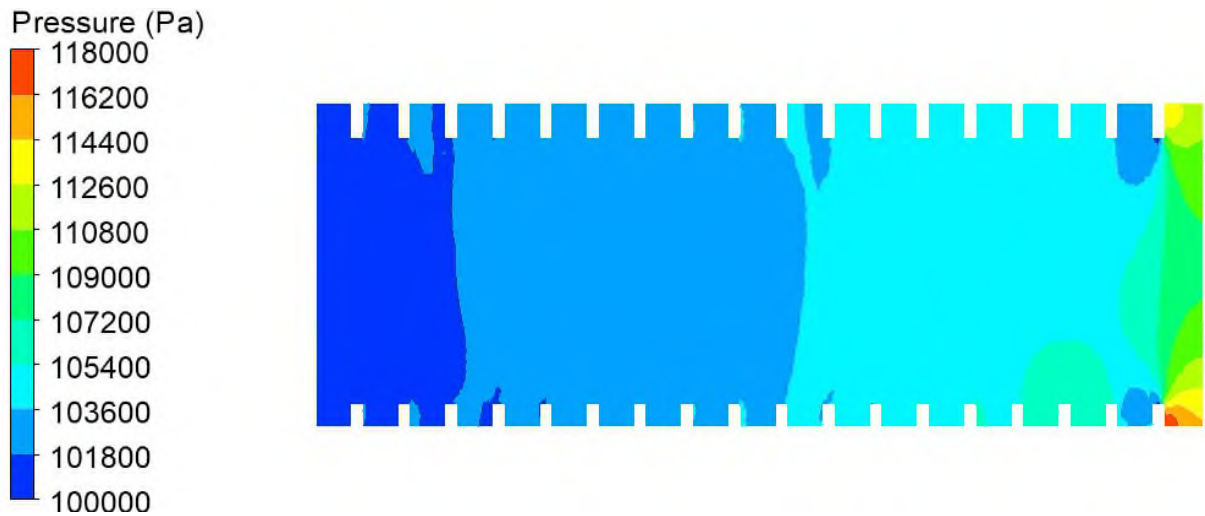


**Figure 7.** Pressure distribution of the coolant flow within the ribbed turbulator cooling channel

The inlet pressure and outlet pressure were measured and a pressure drop of 8100 Pa was recorded within the ribbed cooling channel, indicating a 7.4% pressure loss.

The pressure contour for the hot external flow is presented in Figure 8. The contour indicates that the leading edge of the blade is subjected to the highest pressure. In addition, as expected, the pressure values on the pressure side of the turbine blade remain significantly higher than those on the suction side. It can be observed that around the trailing edge, where the flow velocity is expected to reach its highest value, the pressure values decrease accordingly.

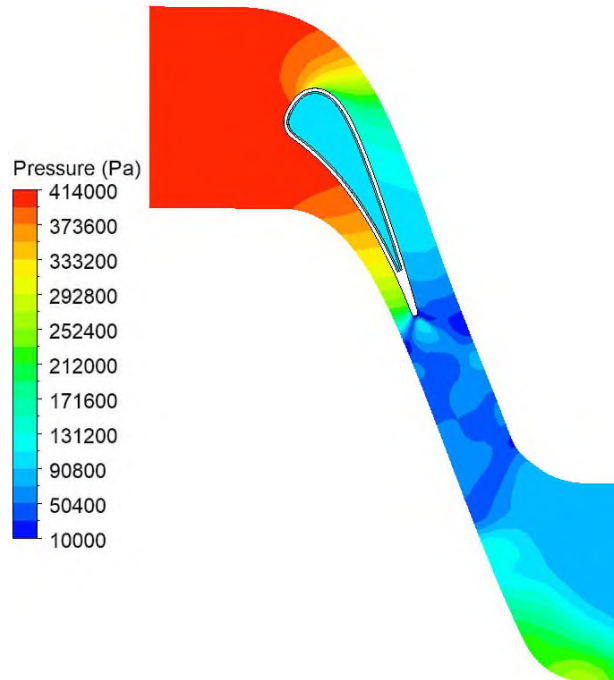


**Figure 8.** Pressure contour of the hot external flow obtained from flow analysis

The velocity contour obtained from the flow analyses is presented in Figure 9. It can be observed that at the leading edge, where pressure values are highest, velocity values are at their lowest. Conversely, at the trailing edge, as expected, the flow velocity reaches its maximum values. Additionally, in accordance with the no-slip condition, the velocity at the surfaces is observed to be zero. For the coolant, velocity values are also very low in the ribbed region.

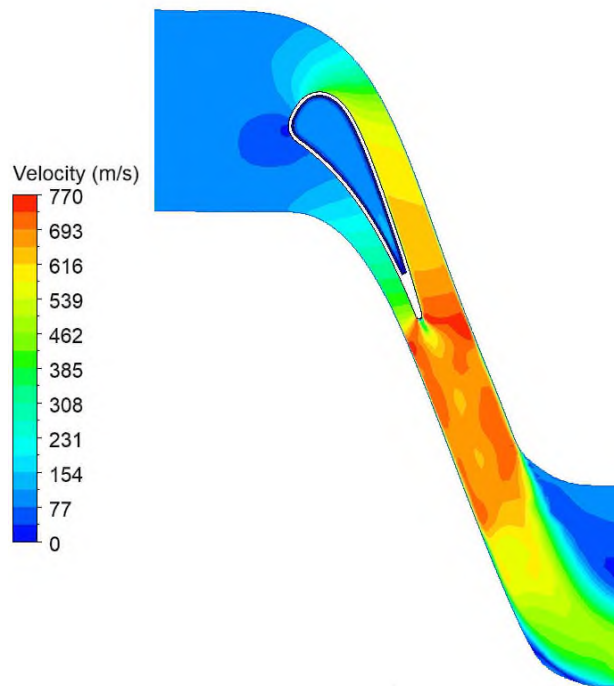


**Figure 9.** Velocity contour of the hot external flow and cold internal flow

The temperature contour obtained from the heat transfer analysis is shown in Figure 10. High temperature values are observed along the pressure side of the blade, where the flow adheres to the blade surface, while significant temperature drops are seen on the suction side, where flow separation occurs.

Examining the temperature contour of the turbine blade reveals that the coolant is highly effective in cooling the turbine blade. The area with the weakest cooling effect is the trailing edge, where rib turbulators could not be applied due to design constraints.

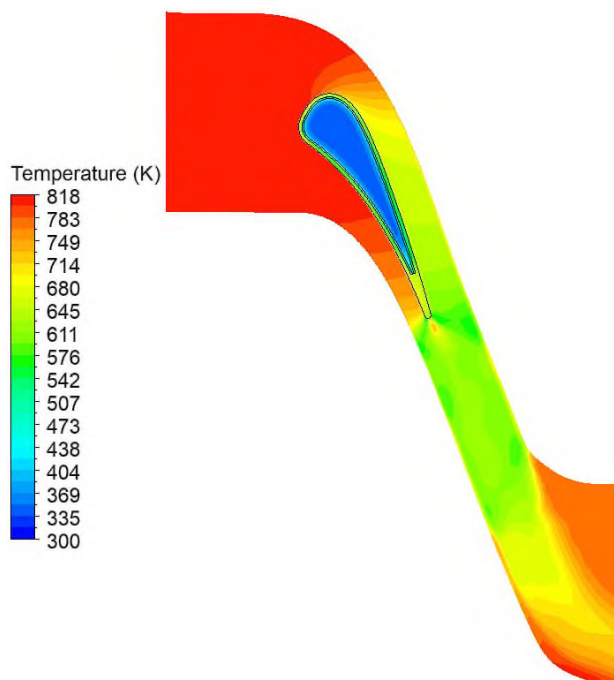


**Figure 10.** Temperature contour of the hot external flow and cold internal flow

The average surface temperature ( $T_{ave}$ ) of the ribbed turbine blade was measured as 574.6 K, while

the maximum surface temperature ( $T_{max}$ ) was determined to be 661.8 K. Given that the temperature of the hot external flow ( $T_{Hin}$ ) is known to be 818 K, a temperature difference of 156.2 K is observed between the hot flow and the maximum surface temperature. This indicates a cooling performance of 19.1% even at the maximum surface temperature. For the average surface temperature of the blade, the cooling performance is 29.75%.

The comparison between the normalized temperature value graph of the turbine blade with a ribbed turbulator cooling channel and the normalized temperature value graph of the turbine blade cooled with a non-ribbed cooling channel is presented in Figure 11.

The normalized temperature value graphs were obtained by calculating the ratio of the temperature at any point on the blade surface ( $T$ ) to the reference temperature ( $T_0=818$  K) for both blades.

The graph shows that the greatest difference in cooling efficiency between the turbine blade with a ribbed turbulator cooling channel and the one without is observed at the leading edge and nearby regions. As the trailing edge, where ribs could not be applied, is approached, the cooling values for both turbine blades become nearly identical.

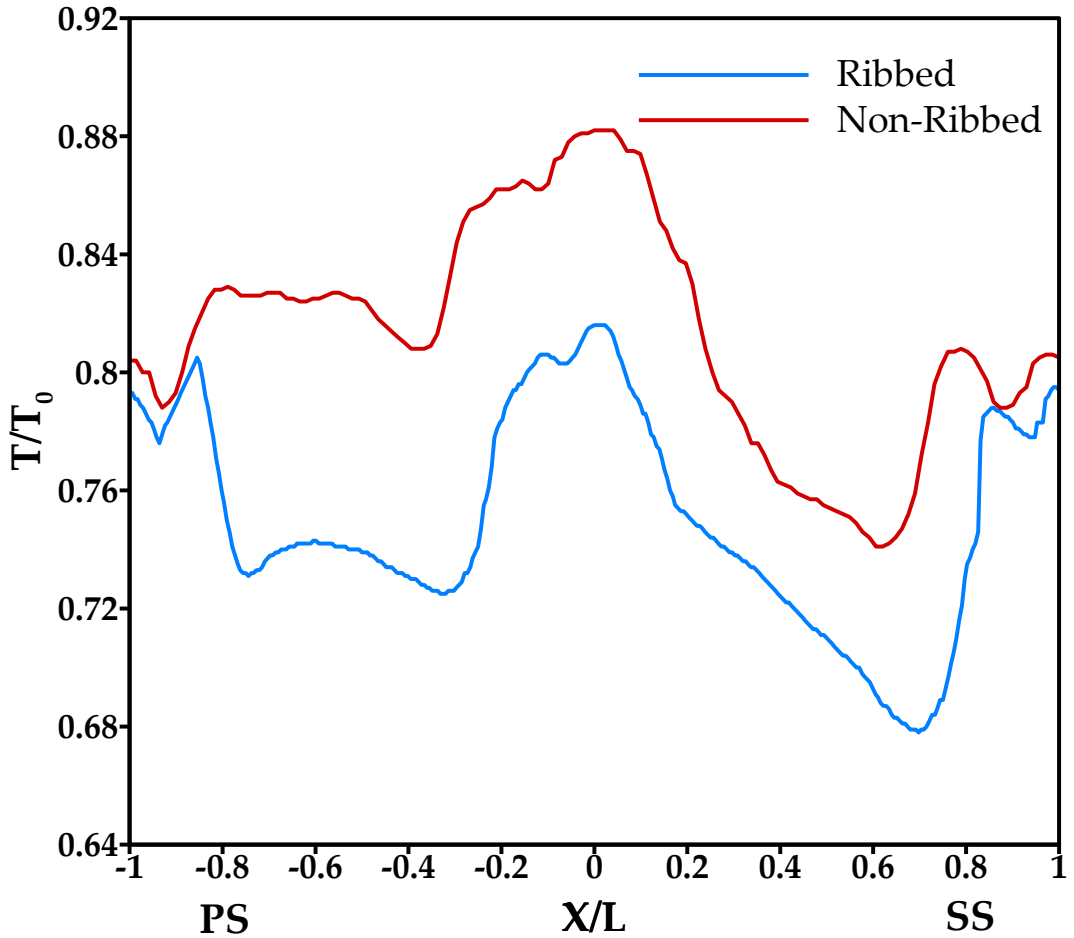


**Figure 11.** Comparison of normalized temperature values along the pressure and suction sides for ribbed and non-ribbed channels

## 5. CONCLUSION

In this study, flow and heat transfer analyses were conducted on a NASA C3X turbine blade made of ASTM-310 stainless steel. In these analyses, where the entire internal region of the turbine blade was designed as a cooling channel, pressure drop and heat transfer were examined for turbine blades with ribbed and non-ribbed cooling channels. The obtained data have been provided within the text and

presented in the form of figures and graphs.

1. The results indicate that the rib turbulators cause a 7.4% pressure drop in the cooling channel, while providing a 29.75% improvement in average surface cooling.
2. Due to design constraints, the trailing edge, where rib turbulators could not be applied, was observed to be the least cooled region of the blade. It is anticipated that if this region could be effectively cooled, the overall cooling efficiency would be significantly enhanced.
3. While the pressure drop caused by the rib turbulators is not overly significant compared to the cooling efficiency they provide, it is possible to reduce this pressure drop by making various design adjustments and optimization efforts in the rib design.

In our next study, further research on innovative blade and cooling channel designs to improve cooling efficiency in turbine blades is planned.

### **Declaration of Ethical Standarts**

Authors declare that all ethical standards have been complied with.

### **Credit Authorship Contribution Statement**

**Muhammed Emin Tolu:** Investigation, Modeling, Analyses, Writing.

**Osman Babayiğit:** Investigation, Supervision, Review, Editing.

**Dilek Nur Özen:** Investigation, Supervision, Review, Editing.

### **Declaration of Competing Interest**

The authors declare that there are no declarations of interest.

### **Funding / Acknowledgements**

The authors have not disclosed any funding. The authors acknowledged that this study is derived from the PhD Thesis of Muhammed Emin Tolu.

### **Data Availability**

The data obtained from this study are available from the corresponding author upon reasonable request.

### **REFERENCES**

- [1] L. D. Hylton, M. S. Mihelc, E. R. Turner, D. A. Nealy, and R. E. York, "Analytical and experimental evaluation of the heat transfer distribution over the surfaces of turbine vanes," NASA Lewis Research Centre, NASA-CR-168015, 1983.
- [2] F. R. Menter, "Two-equation eddy viscosity turbulence models for engineering applications," *AIAA Journal*, vol. 32, no. 8, pp. 1598–1605, 1994.
- [3] B. Facchini, A. Magi, and A. Scotti Del Greco, "Conjugate heat transfer simulation of a radially cooled gas turbine vane," in *ASME Turbo Expo 2004: Power for Land, Sea, and Air*, Vienna, Austria, Jun. 2004, pp. 951-961, vol. 3.
- [4] S. Zheng, Y. Song, G. Xie, and B. Sunden, "An assessment of turbulence models for predicting conjugate heat transfer for a turbine vane with internal cooling channels," *Heat Transfer Research*, vol. 46, no. 11, pp. 1039-1064, 2015.
- [5] K. Mazaheri, M. Zeinalpour, and H. R. Bokaei, "Turbine blade cooling passages optimization using reduced conjugate heat transfer methodology," *Applied Thermal Engineering*, vol. 103, pp. 1228-1236, 2016.

- [6] S. M. Mousavi, A. Nejat, and F. Kowsary, "Optimization of turbine blade cooling with the aim of overall turbine performance enhancement," *Energy Equipment and Systems*, vol. 5, no. 1, pp. 71-83, 2017.
- [7] A. Yousefi, A. Nejat, and M. H. Sabour, "Ribbed channel heat transfer enhancement of an internally cooled turbine vane using cooling conjugate heat transfer simulation," *Thermal Science and Engineering Progress*, vol. 19, Art. no. 100641, 2020.
- [8] M. S. Karimi, M. Raisee, S. Salehi, P. Hendrick, and A. Nourbakhsh, "Robust optimization of the NASA C3X gas turbine vane under uncertain operational conditions," *International Journal of Heat and Mass Transfer*, vol. 164, Art. no. 120537, 2021.
- [9] D. T. Vo, D. T. Mai, B. Kim, and J. Ryu, "Numerical study on the influence of coolant temperature, pressure, and thermal barrier coating thickness on heat transfer in high-pressure blades," *International Journal of Heat and Mass Transfer*, vol. 189, Art. no. 122715, 2022.
- [10] İ. Göktepe and U. Atmaca, "Numerical modeling of backward-facing step flow via computational fluid dynamics," *Journal of Scientific Reports-A*, vol. 054, pp. 176-193, 2023.
- [11] M. Alnaeli et al., "High-temperature materials for complex components in ammonia/hydrogen gas turbines: a critical review," *Energies*, vol. 16, no. 19, Art. no. 6973, 2023.
- [12] J.-C. Han, S. Dutta, and S. Ekkad, *Gas Turbine Heat Transfer and Cooling Technology*.
- [13] K. Tekin, "Gaz türbinleri kanatlarındaki soğutma tekniklerinin araştırılması," Master's Thesis, Sakarya Üniversitesi, 2020.
- [14] D. C. Wilcox, *Turbulence Modeling for CFD*. DCW Industries, 1998.
- [15] T. H. Shih, W. W. Liou, A. Shabbir, Z. Yang, and J. Zhu, "A new  $k-\epsilon$  eddy viscosity model for high Reynolds number turbulent flows," *Computers & Fluids*, vol. 24, no. 3, pp. 227-238, 1995, doi: 10.1016/0045-7930(94)00032-T.
- [16] A. Goldsmith, T. E. Waterman, and H. J. Hirshhorn, *Handbook of Thermophysical Properties of Solid Materials*, vol. II: Alloys, New York: The Macmillian Company, 1961.
- [17] M. Lappa, "A mathematical and numerical framework for the analysis of compressible thermal convection in gases at very high temperatures," *Journal of Computational Physics*, vol. 313, pp. 687-712, 2016, doi: 10.1016/j.jcp.2016.02.062.
- [18] H. Schlichting, *Boundary Layer Theor*, McGraw-Hill Book Company, Inc., 1960.
- [19] J. E. Bardina, P. G. Huang, and T. Coakley, "Turbulence modeling validation," in *28th Fluid Dynamics Conference*, Jun. 1997, p. 2121.
- [20] Y. M. Ahmed and A. H. Elbatran, "Numerical study of the flow field characteristics over a backward facing step using  $k-k_l-\omega$  turbulence model: comparison with different models," *World Journal of Engineering*, vol. 15, no. 1, pp. 173-180, 2018.



## ZnO-In<sub>2</sub>O<sub>3</sub>-SnO<sub>2</sub> THIN FILM TRANSPARENT HEATERS: TUNABLE ELECTROTHERMAL PROPERTIES THROUGH SUBSTRATE TEMPERATURE AND POSTGROWTH ANNEALING

<sup>1,3,\*</sup>Hasan AKYILDIZ<sup>ID</sup>, <sup>2</sup>Hilal Aybike CAN<sup>ID</sup>, <sup>3</sup>Burak KIVRAK<sup>ID</sup>, <sup>4</sup>Tayfur ÖZTÜRK<sup>ID</sup>

<sup>1,3</sup> Konya Technical University, Engineering and Natural Sciences faculty, Metallurgical and Materials Engineering Department, Konya, TÜRKİYE

<sup>2,4</sup> Middle East Technical University, Engineering Faculty, Metallurgical and Materials Engineering Department, Ankara, TÜRKİYE

<sup>3</sup> Konya Technical University, Nanotechnology and Advanced Materials Development Application and Research Center, Konya, TÜRKİYE

<sup>1,3</sup>hakyildiz@ktun.edu.tr, <sup>2</sup>hilal.can@epfl.ch, <sup>3</sup>bkivrak@ktun.edu.tr, <sup>4</sup>ozturk@metu.edu.tr

### Highlights

- Amorphous ZnO-In<sub>2</sub>O<sub>3</sub>-SnO<sub>2</sub> thin film transparent heaters were produced with a specific composition via magnetron sputtering
- The films produced at 150 °C showed exceptional electrothermal response
- The saturation surface temperature was measured as 112 °C
- The areal power density was calculated as 0.4635 Watt/cm<sup>2</sup> for an applied potential of 12V
- The heater melted all ice and evaporated the residual water droplets within 173 s





## ZnO-In<sub>2</sub>O<sub>3</sub>-SnO<sub>2</sub> THIN FILM TRANSPARENT HEATERS: TUNABLE ELECTROTHERMAL PROPERTIES THROUGH SUBSTRATE TEMPERATURE AND POSTGROWTH ANNEALING

<sup>1,3,\*</sup>Hasan AKYILDIZ<sup>ID</sup>, <sup>2</sup>Hilal Aybike CAN<sup>ID</sup>, <sup>3</sup>Burak KIVRAK<sup>ID</sup>, <sup>4</sup>Tayfur ÖZTÜRK<sup>ID</sup>

<sup>1,3</sup>Konya Technical University, Engineering and Natural Sciences faculty, Metallurgical and Materials Engineering Department, Konya, TÜRKİYE

<sup>2,4</sup>Middle East Technical University, Engineering Faculty, Metallurgical and Materials Engineering Department, Ankara, TÜRKİYE

<sup>3</sup>Konya Technical University, Nanotechnology and Advanced Materials Development Application and Research Center, Konya, TÜRKİYE

<sup>1,3</sup>[hakyildiz@ktun.edu.tr](mailto:hakyildiz@ktun.edu.tr), <sup>2</sup>[hilal.can@epfl.ch](mailto:hilal.can@epfl.ch), <sup>3</sup>[bkivrak@ktun.edu.tr](mailto:bkivrak@ktun.edu.tr), <sup>4</sup>[ozturk@metu.edu.tr](mailto:ozturk@metu.edu.tr)

(Received: 25.11.2024; Accepted in Revised Form: 16.12.2024)

**ABSTRACT:** Amorphous thin films of ZnO-In<sub>2</sub>O<sub>3</sub>-SnO<sub>2</sub> (a-ZITO) were manufactured using magnetron sputtering technique for the applications of thin film transparent heaters (TFTHs). For this purpose, a custom-made 3" sputtering target was prepared with a specific composition in terms of the atomic percentages (at.%) of Zn, In, and Sn cations. The impact of varying substrate temperatures on the characteristics of the samples investigated by depositing the films on glass substrates maintained at room temperature, 150 °C, and 250 °C. To improve the optical and electrical properties, post-growth annealing was carried out under forming gas atmosphere at 400 °C. Structural, morphological, optical, and electrical properties of the samples were thoroughly examined. Electrothermal characterization was performed on samples at room temperature and -40 °C to evaluate response time, saturation temperature, thermal homogeneity, stability, recyclability, thermal resistance, and the defogging/deicing capability of the produced TFTHs. The films produced at 150 °C demonstrated an exceptional electrothermal response, with the thermal resistance calculated to be 181.7 °C·cm<sup>2</sup>/W under 12 V input. With a measured power density of 0.4635 Watt/cm<sup>2</sup>, this heater was able to melt all ice and evaporate water droplets on the surface within 173 s, indicating a promising performance for commercial defogging/deicing applications.

**Keywords:** ZnO, In<sub>2</sub>O<sub>3</sub>, SnO<sub>2</sub>, Transparent Heater, Sputtering, Thin Film, Postgrowth Annealing

### 1. INTRODUCTION

Numerous transparent conductive oxide (TCO) compositions identified within the ternary ZITO system are of significant importance as alternatives to Tin-doped Indium Oxide (ITO) in various optoelectronic applications [1-3]. Over the past two decades, crystalline/amorphous thin films of ZITO have been studied for diverse applications, such as active channel layer in thin film transistor (TFT) and nonvolatile memory applications [4-12], as an anode material in organic light-emitting diodes (OLEDs) [13-17], as transparent electrode in organic photovoltaic devices [18-20], dye-sensitized solar cells [21], and polymer dispersed liquid-crystal smart windows [22, 23], as radiating element for optically transparent antennas [24], and as thermoelectric material in transparent display devices [25].

In parallel with the aforementioned studies, the processing parameters, as well as the structural, morphological, optical, and electrical properties including refractive index, extinction coefficient, Fermi level and work function of ZITO thin films were reviewed [26-33]. In addition, Kim et al., have demonstrated that ZITO thin films with Zn-cation concentration above 8.8 at.% are physically stable against hydrogen plasma [34]. Furthermore, Proffit et al., revealed that the crystallization onset temperature of an a-ZITO thin film strongly depends on the cation composition, and requires higher activation energy for crystallization than amorphous ITO [35]. This makes the ternary composition more suitable for applications requiring an amorphous arrangement. Additionally, thin films of a-ZITO have shown promising performance as transparent electrode material in flexible optoelectronic applications

\*Corresponding Author: Hasan AKYILDIZ, [hakyildiz@ktun.edu.tr](mailto:hakyildiz@ktun.edu.tr)

owing to their high visible transmittance, low sheet resistance, high work function, mechanical durability, and lower processing temperatures compatible with numerous polymeric substrates [36-39]. Besides external inner/outer bending, uniaxial stretching, and twisting test results showed that a-ZITO thin films exhibit better mechanical durability than ITO [40]. Therefore, the material was employed as a transparent conducting layer for WO<sub>3</sub>-based flexible electrochromic devices [41]. This device functioned for about 450 cycles without any reduction in electrochromic performance and displayed wider optical modulation and higher coloration efficiency compared to a device with a glass substrate and ITO conducting layer. In another study, an ultra-flexible organic photovoltaic cell was fabricated as a power source for wearable devices, using a layer of a-ZITO as the transparent electrode [42]. It was reported that 94.8% of the initial value of photo conversion efficiency was retained even after 1000 cycles of compression and relaxation test. Recently, Biswas et al., showed that the bending-induced effects on the optical and electrical properties of ZITO transparent electrode could be reduced substantially by inserting an organic semiconductor layer between the electrode and the active layer, maintaining performance up to 20,000 cycles [43]. These results provide strong evidence for the suitability of a-ZITO compositions in future flexible optoelectronic devices.

At this point it is worth remembering that the ternary system of ZnO-In<sub>2</sub>O<sub>3</sub>-SnO<sub>2</sub> includes various well identified compositions such as In<sub>2-2x</sub>Sn<sub>x</sub>Zn<sub>x</sub>O<sub>3</sub> solid solution or layered homologous series compounds of (ZnO)<sub>k</sub>-(In<sub>2</sub>O<sub>3</sub>):Sn [2, 3]. It can be inferred from the literature that the preferred compositions for TFT applications are generally composed of slightly Zn-rich compositions, with In:Zn:Sn atomic ratios of 1:1.25:0.25, 1:1.2:0.5 or 1:4.2:1.5 and In:Zn:Sn:P = 1.1:1:0.1:0.01 at.% [5, 6, 9-11]. In contrast, In-rich thin films (~55 to 74 at.% In) have been widely studied for OLED applications [14-17]. For flexible optoelectronic devices, ZITO transparent electrodes were produced from ceramic targets consisting of 70-80 at. % In<sub>2</sub>O<sub>3</sub> [39, 41, 42], while the compositions ranging from 30 to 60 at.% In have been investigated for organic photovoltaics [18-20]. The use of varied compositions for different applications is expected due to the unique requirements of each application. It is well documented that the structural, optical, and electrical properties of ZITO strongly depends on the corresponding cations (i.e., In, Zn, and Sn) ratio and as well as to the oxygen content [14, 15, 20, 25, 28-31, 35]. In fact, this compositional flexibility is advantageous for manipulating the properties of the ZITO thin films for specific applications. On the other hand, for thin film production methods such as in sputtering, one must prepare numerous different targets having different compositions to achieve or determine the thin film with the best atomic ratio that is suitable for any particular application. Thus, research on techniques that is expected to allow reduction in necessary time and sintering temperature as well as In-loss during the target preparation is continue [44, 45]. But the improvements in the synthesis of those ceramic targets do not directly solve the problem related to the identification of the perfect film composition for any specific application. Therefore, the combinatorial method may be considered as the best, fastest, and low-cost approach to establish any potential composition in this ternary system by constructing a thin film library with compositional gradient within a few deposition experiments [46, 47]. Following this approach, compositionally gradient ZITO thin films were produced by co-sputtering of high purity individual In<sub>2</sub>O<sub>3</sub>, ZnO, and SnO<sub>2</sub> targets [48, 49]. The effects of sputtering pressure, deposition time, substrate temperature, and various post-growth annealing atmospheres on the morphological, structural, optical, and electrical properties were examined in detail. As a result of these studies, a few potential crystalline/amorphous film compositions have been determined with optimal electrical and optical properties for different optoelectronic applications. However, we have identified that there is no study in literature showing the transparent thin film heater properties of ZITO thin films.

In this paper, one of those potential compositions (i.e., 49.6 at.% Zn, 44.5 at.% In, and 5.9 at.% Sn) was selected as the base composition for a 3" sputtering target. ZITO-TFTHs with 37.5 cm<sup>2</sup> area were deposited onto the glass substrates at three different substrate temperatures using magnetron sputtering. The visual, structural, morphological, optical, electrical, and electrothermal properties of these transparent heaters were examined and compared in both their as-deposited and annealed states. The study has shown that ZITO thin films are good candidates for replacing the commercially available TFTHs, offering significantly

lower In content than ITO and providing sufficiently high-power density for moderate size deicing applications.

## 2. EXPERIMENTAL

### 2.1 Thin Film Production

To achieve a single composition ZITO thin films, initially a 3" sputtering target was prepared with In:Zn:Sn cation at.% of 44.5:49.6:5.9. For this purpose, ZnO (45 μm, 99.999%, Sigma Aldrich), In<sub>2</sub>O<sub>3</sub> (45 μm, 99.99%, Nanografi), and SnO<sub>2</sub> (45 μm, 99.9%, Nanografi) powders were mixed, compacted and then sintered. The details of the method can be found elsewhere [50]. Prior to deposition, all substrates were cleaned using a sonication bath and hot alkaline detergent, acetone, and absolute alcohol mediums. The 3" sputtering target was located 15 cm away from a circular substrate holder (Ø=15 cm) carrying up to two 1.5 mm thick and 37.5 cm<sup>2</sup> microscope slide glass substrates. The base pressure was adjusted to 1x10<sup>-6</sup> Torr. The sputtering gas (99.999% Ar) pressure was set to 3 mTorr using a flow rate of 20 Sccm. After a 10 min of pre-sputtering under closed-shutter configuration, ZITO thin films were deposited on the glass substrates maintained at RT, 150 °C or 250 °C. The radio frequency sputtering power was fixed to a constant value of 100 W. During the deposition process, the substrate holder was rotated at 30 rpm and the film thicknesses were limited to 750 nm using a quartz crystal micro balance thickness monitor. For various characterization techniques, thin films on 18 mm diameter glass substrates were also produced using identical deposition parameters.

Once the samples cooled to room temperature under vacuum, films were transferred to an atmosphere-controlled furnace for post-growth annealing. The films were heated to 400 °C at a rate of 2 °C/min in a flowing Ar + 4% H<sub>2</sub> atmosphere and held at this temperature for 90 min. Subsequently, the samples were furnace-cooled ensuring the forming gas environment remained undisturbed.

### 2.2 Characterization

The crystalline/amorphous states of as-deposited and annealed films were identified using X-ray diffraction (XRD) method via a Bruker D8 Advance diffractometer equipped with a Cu X-ray tube (λ=1.5406 Å). The patterns were obtained in Bragg-Brentano mode with a step-size of 0.02° in the range of 2θ = 20-80°. Morphological and topographical examinations were carried out on both surface and cross-sectional areas of the films using FEI Nova NanoSem 430 model field emission scanning electron microscope (FE-SEM) and Veeco Multi-Mode V model atomic force microscope (AFM), operating in non-contact mode for the construction of 3D surface topography of ZITO thin films. Surface roughness values were determined from the scans over a 2 μm x 2 μm area. The atomic ratios of the cations in the prepared samples were estimated using Energy-dispersive X-ray spectroscopy (EDX). Additionally, a VWR 3100-PC model UV-Vis (ultraviolet-visible) spectrophotometer was employed to measure visible transmittance of ZITO thin films. Spectra were recorded in the wavelength ranges between 350-900 nm, however the data was evaluated between 400 to 700 nm for the calculation of average visible light transmittance ( $T_{vis}$ ) of the samples. Band gap values were estimated using  $(\alpha hv)^2 = A(hv - E_g)^{1/2}$  equation and Tauc plots. In the equation, the terms  $\alpha$ ,  $hv$ , and  $A$  stand for absorption coefficient, photon energy, and a constant, respectively. The optical bandgap energy ( $E_g$ ) was extracted from  $(\alpha hv)^2$  vs  $hv$  plots by intersecting the extrapolated linear region of the  $(\alpha hv)^2$  to the energy axis. Hall-effect measurements (Nanomagnetic Instruments, ezHEMS model) were carried out to determine the electrical properties. For this purpose, thin films were reproduced under identical deposition conditions on 18 mm diameter glass substrates. The measurements were performed on these samples. I-V measurements were conducted at room temperature on as-deposited and annealed thin films using the Van der Pauw configuration and 10 mA current. Measurements were repeated three times. To calculate the Figure of merit (FOM) values, Haacke

equation ( $\varphi_{TC} = T_{550\text{ nm}}^{10}/R_s$ ) was used. In this equation,  $T_{550}$  refers to the transmittance at 550 nm wavelength, and  $R_s$  ( $\Omega/\square$ ) is the sheet resistance of the ZITO thin film sample.

Electrothermal behavior of ZITO thin films were characterized using a custom-made measurement set up described in detail elsewhere [51]. Briefly, this setup includes a DC power supply (Tektronix PWS4602), an infrared camera (Optris Xi 400), a computer for image processing and a sample holder. The images were recorded at 55 cm distance from the film surfaces. ZITO TFTHs were subjected to constant DC voltages (i.e., 3, 6, 9, and 12 V) at RT to determine the response time, saturation temperature, temperature homogeneity and stability, recyclability, and thermal resistance of the samples. To assess the defogging/deicing capability, the heaters were first placed in a thermally insulated box cooled with dry-ice for 1 h. A humidifier was used to supply the vapor to the environment, creating conditions for ice condensation on the surface. After the sample was removed from the box, the power supply was turned on at 6, 9 or 12 V when the infrared camera indicated a mean surface temperature of  $-40$  °C. The increase in the surface temperature was recorded for each test using the camera. The deicing time was defined as the total duration elapsed for melting and subsequent evaporation of water droplets from the surface. The electrical connection between the power source and the film is provided by duck mouth Cu crocodile clips and Ag electrodes applied to the film surface.

The spatial distribution or the homogeneity of the surface temperature was calculated using the equation  $T_U = [(T_H - T_L)/2T_{avg}] \times 100$ .  $T_H$ ,  $T_L$ , and  $T_{avg}$  refer to highest, lowest and average temperatures recorded from the surface of the sample during the stability test, respectively. The highest and lowest temperatures were determined using an area of  $1\text{ mm} \times 1\text{ mm}$ , whereas the entire active area was used to compute the average value.

The areal power density of the TFTHs was determined by using the basic electrical formula  $P/A$ . Here,  $P$  refers to electrical power ( $P=I^2R$ ) and  $A$  denotes to the total heater area between the Ag-electrodes. While the current ( $I$ ) passing through the film is monitored from the power supply, the resistance ( $R$ ) was calculated by solving the  $R=\rho(L/W_e d_k)$  equation. In this equation,  $\rho$  ( $\Omega\text{cm}$ ) refers to resistivity,  $d_k$  (cm) the thickness,  $L$  (cm) the length, and  $W_e$  (cm) the distance between the Ag-electrodes.

### 3. RESULTS AND DISCUSSION

#### 3.1 Visual Examination

Figure 1a and b demonstrate the digital images of ZITO thin films in their as-deposited state and after annealing at  $400$  °C under forming gas atmosphere, respectively. The values given as inset on the upper left corners in Fig 1a indicate the employed substrate temperatures during depositions. It is obvious that the films exhibit visual transparency across all substrate temperatures suggesting that the influence of substrate temperature on visible transmittance is negligible. However, the film deposited at  $150$  °C (the one in the middle) appears slightly different than others, i.e., being particularly transparent, and colorless. It is apparent from Fig. 1b that the postgrowth annealing process can eliminate the partial coloration observed in the as-deposited samples. Further, the sample produced at  $150$  °C still looks the most transparent among others by visual inspection.

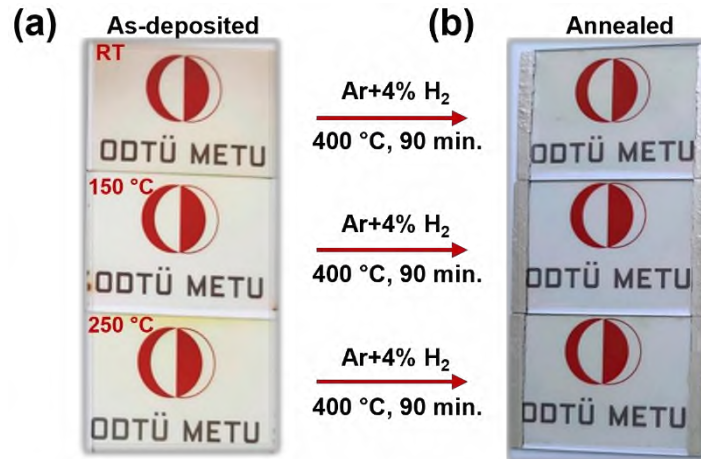


**Figure 1.** Digital images of ZITO thin films deposited at various substrate temperatures on 5 cm x 7.5 cm glass substrates, a) as-deposited, b) after annealing at 400 °C under Ar+4% H<sub>2</sub> atmosphere for 1.5 h

### 3.2 Structural Examination

Figure 2 (a) shows the XRD patterns of ZITO thin films deposited at various substrate temperatures. The broad and low intensity humps observed around  $2\theta = 25^\circ - 35^\circ$ , without any detectable peaks, indicate the amorphous nature of the ZITO samples, regardless of the deposition temperature. The existing literature on ZITO reveals inconsistent results about the onset temperature of crystallization [21, 31, 48, 52]. The formation of crystalline state is directly related to the substrate temperature, but it is also influenced by other parameters, such as film composition, sputtering power, and the use of either single alloyed target or co-sputtering for deposition. Numerous studies state that high Zn content in the composition induces amorphization in films [46, 52, 53]. This might be also valid for the current study due to the concentration of Zn-cation in the manufactured thin films, (See Table 1). However, our recent study on the combinatorial production of ZITO thin films revealed that this condition is not always true. In contrast, ZITO films with very high Zn component can display crystallization, whereas those with a lower zinc content may remain amorphous. [49]. Furthermore, the diffraction data of the annealed samples (Fig. 2b) indicates that the amorphous nature of the films can be maintained even after subjecting the samples to moderately high temperatures. These findings suggest that the film composition under consideration is highly resistant to crystallization and may be suitable for flexible or bendable applications [39]. Besides, the absence of grain boundaries can be advantageous for low sheet resistance transparent heaters due to high mobility of charge carriers without interruption of grain boundary barriers.

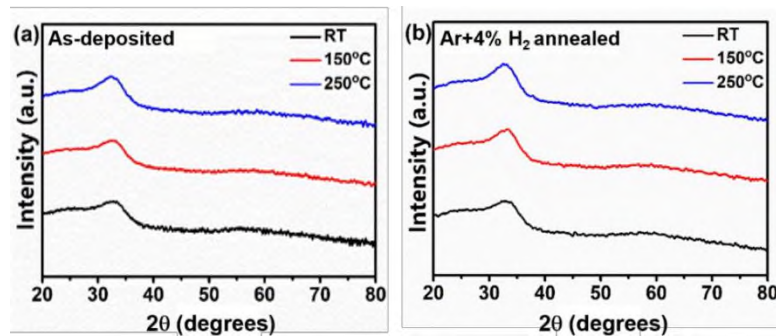


**Figure 2.** XRD patterns of a-ZITO thin films deposited at various substrate temperatures on 5 cm x 7.5 cm glass substrates, (a) as-deposited, (b) after annealing under Ar+4% H<sub>2</sub> atmosphere for 1.5 h at 400 °C

### 3.2 Morphological and Compositional Examination

Figures 3a1, b1, and c1 illustrate the high-magnification surface FE-SEM micrographs of a-ZITO thin films that were produced on substrates maintained at RT, 150 °C, and 250 °C, respectively. The inset images correspond to the low magnification, larger area observations of the same samples. Although the images of RT and 150 °C deposited thin films demonstrate some hill-like protrusions, the film surfaces can be acceptable as featureless in general. These formations are also visible from the 3D AFM surface topography images demonstrated in Figs. 3a5 and b5. It is apparent that the protrusions are much smaller in diameter ( $\leq 80$  nm) in the RT deposited sample, but their areal density is high. On the contrary the diameters can approach 300 nm for 150 °C deposited sample, but they are highly dispersed. Moreover, the height of the hills on the surface of both samples are not greater than 25-30 nm. On the other hand, the surface of the sample deposited at 250 °C is free from these protrusions (see Figs. 3c1 and c5). Therefore, these formations may be attributed to low adatom mobility at lower substrate temperatures, lack of crystallinity and shadowing effects. According to the inset images given in Figs. 3a1, b1, and c1, it can be stated that the as-deposited a-ZITO samples are homogenous with no evidence of cracks, voids and peeling.

The root mean square (RMS) values of the as-deposited samples were calculated as 1.83, 3.12, and 0.453 nm over a  $2 \mu\text{m} \times 2 \mu\text{m}$  surface area via AFM measurements, indicating the film's surfaces are practically smooth despite the presence of local hill-like feature formations. Figs. 3a2, b2, and c2 illustrate the surface FE-SEM images of samples after post-growth annealing. The high magnification SEM observation of the annealed samples did not provide significant detail about the effect of the heat treatments on surface morphology due to the featureless nature of the films. On the other hand, inset images revealed that the surface homogeneities were preserved after annealing. Additionally, 3D AFM surface images (Figs. 3a6 and 3b6) revealed that annealing had a noticeable effect on the protrusions present on the surface of as-deposited samples, leading to reduction in their number (for RT deposited sample) and decrease in sizes (for 150 °C deposited sample). Furthermore, the surface roughness decreased almost 50% for all samples with annealing. RMS values were identified as 0.808, 1.98, and 0.294 nm for RT, 150 °C, and 250 °C deposited thin films, respectively. These surface modifications probably stem from the surface reactions occurred at 400 °C annealing temperature. Obviously, increased smoothness is advantageous for mechanical and chemical inertness of a heater designed for use in ambient environments.

Figs. 3a3-4, b3-4, and c3-4 show the cross-sectional FE-SEM images of as-deposited and annealed samples. The thickness of the as deposited samples appears to be identical. This was achieved by tuning the deposition rates for all deposition temperatures. In addition, no alteration in the thickness was detected after annealing. Therefore, the electrothermal characteristics of the samples produced at various temperatures can be comparable. The cross-sections of both as-deposited and annealed thin films present no recognizable features, probably due to amorphous nature. Moreover, the inset images given in each figure imply that the films were obtained with uniform thickness and absence of any peeling from the substrate even after moderately high temperature annealing.

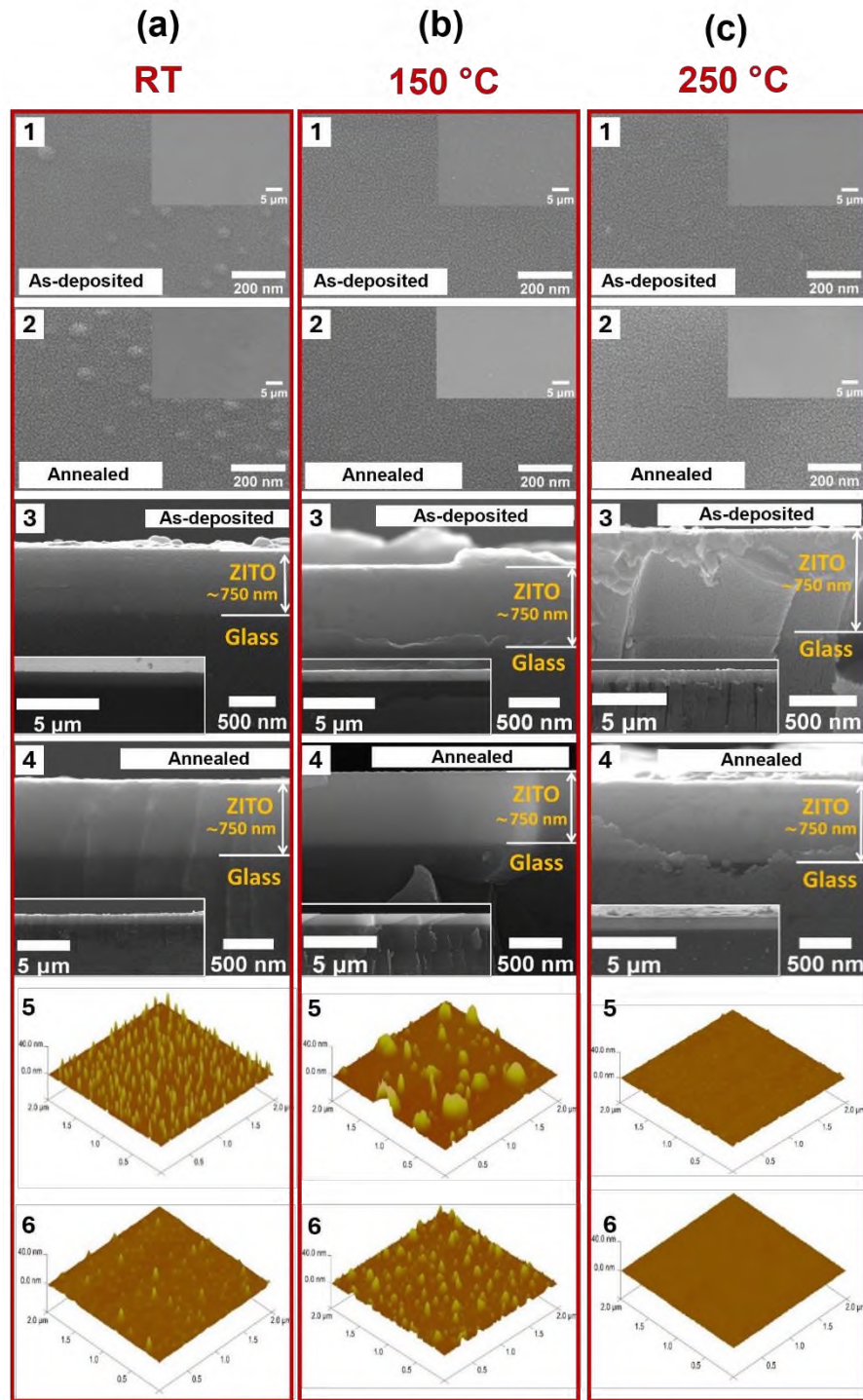


**Figure 3.** FE-SEM surface, through thickness and 3D AFM surface images of a) RT deposited, b) 150 °C deposited, c) 250 °C deposited a-ZITO thin films in as-deposited and annealed states (The surface SEM images and the insets were recorded at  $\times 400000$  and  $\times 10000$  magnifications, respectively. The cross-sectional SEM images and the insets were recorded at  $\times 100000$  and  $\times 10000$  magnifications, respectively)

**Table 1.** EDX analyses of a-ZITO thin films produced at various substrate temperatures and annealed under Ar+4% H<sub>2</sub> atmosphere for 1.5 h at 400 °C

Deposition temperature	As-deposited samples (at.%)			Postgrowth annealed samples (at.%)		
	Indium	Zinc	Tin	Indium	Zinc	Tin
RT	47.18	48.13	4.69	44.22	50.51	5.26
150 °C	46.76	45.84	7.39	41.73	51.93	6.34
250 °C	47.01	46.04	6.95	46.43	47.87	5.7

As discussed in Section 2.1, a-ZITO thin films were deposited on substrates held at RT, 150 °C, and 250 °C by sputtering of a 3" target consists of In:Zn:Sn cation at.% of 44.5:49.6:5.9. Table 1 shows the atomic ratios of these cations measured in the as-deposited and annealed samples via EDX. The result shows that the as-deposited thin films are slightly enriched by In-cations (~47 at.%) compared to In-content (44.5 at.%) of the target composition. This enrichment was compensated by 1-2 at. % variations between the amount of Zn and Sn cations in the films as a function of used substrate temperatures. Considering the accuracy range of EDX method, it can be stated that the films obtained at various substrate temperatures displayed practically the same composition as the target. After annealing, the distribution of the constituent cations slightly modified and approximated to the desired chemical make-up. When compared to their as-deposited compositions, annealed thin films were slightly enriched by Zn and depleted by In. This suggests that the annealing temperature was high enough for diffusion and rearrangement of the elements in the films, however remains below threshold for crystallization.

### 3.3 Optical Examination

Fig. 4a demonstrates the transmittance spectra of as-deposited a-ZITO thin films as a function of substrate temperature. For visual aid, the threshold for 75% transmittance is indicated with a dashed red line and the visible range is marked with a shaded area. It can be inferred from the images that all films exhibited high transmittance (e.g. > 80%) in the visible range regardless of the deposition temperature. Furthermore,  $T_{vis}$  values of the samples deposited at RT, 150 °C, and 250 °C were calculated as 82.5 %, 85.9 %, and 84.0 %, respectively, as presented in Table 2.

Fig. 4b reveals that the postgrowth annealing has no significant impact on average visible transmittances of the films which were determined as 85.6%, 85.6%, and 85.5% (see Table 2). Similar observations, or even reductions in the optical transmittance of ZITO thin films annealed in a forming gas atmosphere have been reported by others [20, 21]. On the contrary, significant improvement in the visible region transmittance after Ar+H<sub>2</sub> atmosphere annealing have been observed for RT deposited ZITO thin films with various compositions [48]. Furthermore, the absorption edges of the films displayed changes depending on the substrate temperature employed during the deposition. In the as-deposited state, the absorption edges were found to be 377, 372, and 379 nm for RT, 150 °C, and 250 °C, respectively. Upon annealing under forming gas, a blue shift occurred, and the absorption edges of the annealed films were measured as 365, 364, and 371 nm. The shift towards near UV was attributed to an increase in carrier concentration [21]. As listed in Table 2, the sample deposited at 150 °C exhibited the highest band gap values of 3.17 eV in the as-deposited state and 3.26 eV after annealing. The broadening of the band gap after annealing was ascribed to increase in carrier concentration and generally defined by the Burstein–Moss effect [20, 54]. These results confirm that the manufactured a-ZITO thin films exhibit sufficient transparency and appropriate band gap for the targeted transparent heater applications.



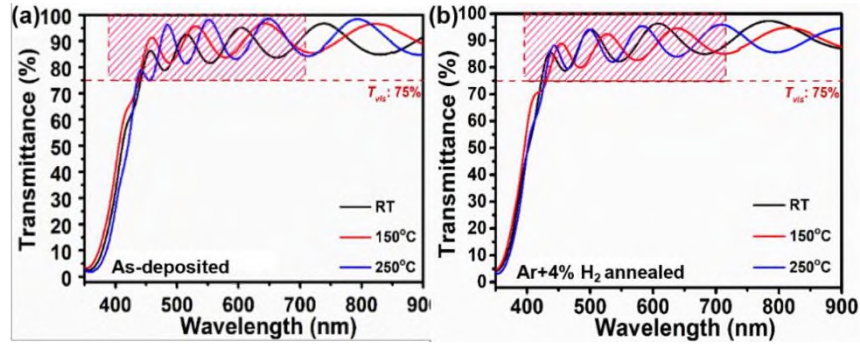


**Figure 4.** Transmittance spectra of a-ZITO thin films deposited at various substrate temperatures on 5 cm x 7.5 cm glass substrates: a) as-deposited and b) after annealing under Ar+4% H<sub>2</sub> atmosphere for 1.5 h at 400 °C (the shaded region in the figures denote the transmittance above 75% in the visible range and given for visual aid)

**Table 2.** Optical properties of a-ZITO thin films produced at various substrate temperatures and annealed under Ar+4% H<sub>2</sub> atmosphere for 1.5 h at 400 °C

Deposition temperature	As-deposited samples			Postgrowth annealed samples		
	T <sub>vis</sub> (%)	Absorption edge (nm)	E <sub>g</sub> (eV)	T <sub>vis</sub> (%)	Absorption edge (nm)	E <sub>g</sub> (eV)
RT	82.5	377	3.13	85.6	365	3.23
150 °C	85.9	372	3.17	85.6	364	3.26
250 °C	84.0	379	3.09	85.5	371	3.19

### 3.4 Electrical Examination

The thin films were subjected to Hall Effect measurements in the as-deposited and annealed states in order to determine the type of conductivity, sheet resistance ( $R_s$ ,  $\Omega/\square$ ), carrier concentration ( $\eta$ ,  $\text{cm}^{-3}$ ), Hall mobility ( $\mu$ ,  $\text{cm}^2/\text{Vs}$ ), and electrical resistivity ( $\rho$ ,  $\Omega\cdot\text{cm}$ ) of the produced samples. All samples showed n-type conductivity allowing the discussion of their electrical conductivity in terms of electron charge, carrier concentration, and mobility. Figures 5a-c presents the  $R_s$ ,  $\eta$ ,  $\mu$ , and  $\rho$  as a function of substrate temperature for both as-deposited and annealed samples. In addition, Table 3 provides numerical values for these properties. The dependency of the electrical properties to deposition temperature is obvious from Figs. 5a and b and the results are consistent with the optical properties. The carrier concentration of the as-deposited samples first showed a slight increase (~8%) when the deposition temperature is raised from RT to 150 °C, but then substantially decreased (~55%) followed by the increase in substrate temperature. On the other hand, the mobility exhibited proportional dependence on temperature and raised from 36.77  $\text{cm}^2/\text{Vs}$  to 42.01  $\text{cm}^2/\text{Vs}$  for RT and 150 °C deposited samples and eventually reached 44.56  $\text{cm}^2/\text{Vs}$  for the sample deposited at 250 °C. The high mobility of the films further indicates the absence of long-range order and grain boundaries in the as-deposited samples, both of these are known to adversely affect the mobility of charge carriers [55]. This direct correlation between the mobility and temperature may seem contradictory, as one would expect the lowest deposition temperature is usually associated with the more disordered structure, which should enhance the mobility. However, it is known that the mobility of the charge carriers in amorphous transparent conducting oxides not only affected by this factor but also affected from the ratio of cations, the corresponding local bonding and the presence of oxygen deficiencies in the structure [56, 57]. Further, 250 °C deposited sample exhibited the lowest carrier density among others, which might contribute to its high mobility value. Additionally, the sample deposited at 150 °C displayed the lowest  $R_s$  among the as-deposited samples (24.2  $\Omega/\square$ ), compared to the values of 30  $\Omega/\square$  and 41.4  $\Omega/\square$  for the RT and 250 °C samples, respectively.

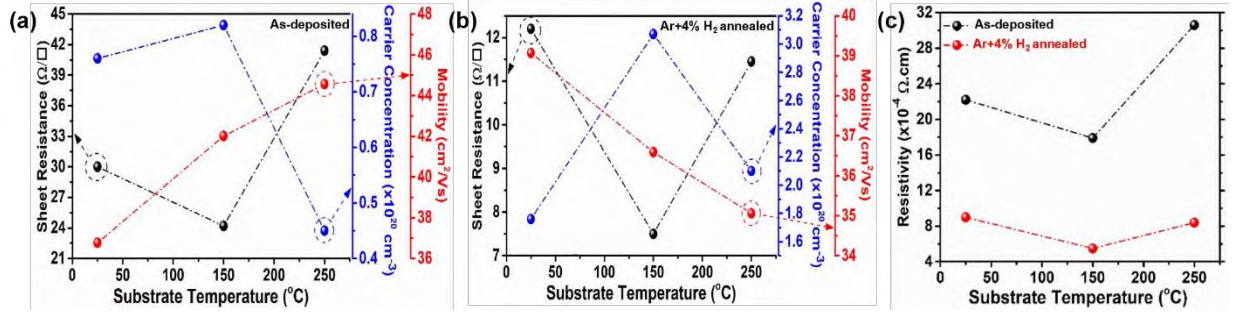


**Figure 5.** Electrical properties of a-ZITO thin films as a function of substrate temperature in as-deposited and post-growth annealed states: a) as-deposited sheet resistance, carrier concentration and mobility, b) annealed sheet resistance, carrier concentration and mobility, c) electrical resistivity in as-deposited and annealed states.

**Table 3.** Electrical properties of a-ZITO thin films produced at various substrate temperatures and annealed under Ar+4% H<sub>2</sub> atmosphere for 1.5 h at 400 °C

Sample		$\rho^*10^{-4}$ ( $\Omega\text{cm}$ )	$R_s$ ( $\Omega/\square$ )	$\eta^*10^{20}$ ( $\text{cm}^{-3}$ )	$\mu$ ( $\text{cm}^2/\text{Vs}$ )
As-deposited Samples	RT	22.2 ( $\pm 1.5 \times 10^{-4}$ )	30	0.76 ( $\pm 2.5 \times 10^{-4}$ )	36.77 ( $\pm 1.1 \times 10^{-2}$ )
	150 °C	17.9 ( $\pm 2.5 \times 10^{-4}$ )	24.2 ( $\pm 5.7 \times 10^{-4}$ )	0.82 ( $\pm 5.7 \times 10^{-5}$ )	42.01 ( $\pm 2.0 \times 10^{-3}$ )
	250 °C	30.6 ( $\pm 8.6 \times 10^{-3}$ )	41.4 ( $\pm 1.1 \times 10^{-2}$ )	0.45 ( $\pm 4.9 \times 10^{-4}$ )	44.56 ( $\pm 3.8 \times 10^{-2}$ )
Postgrowth Annealed Samples	RT	9.0 ( $\pm 7.2 \times 10^{-4}$ )	12.2 ( $\pm 1.1 \times 10^{-3}$ )	1.76 ( $\pm 5.7 \times 10^{-4}$ )	39.07 ( $\pm 2.0 \times 10^{-2}$ )
	150 °C	5.5 ( $\pm 5.7 \times 10^{-5}$ )	7.5	3.07 ( $\pm 1.0 \times 10^{-3}$ )	36.59 ( $\pm 1.4 \times 10^{-2}$ )
	250 °C	8.4 ( $\pm 1.1 \times 10^{-4}$ )	11.45	2.10 ( $\pm 5.7 \times 10^{-4}$ )	35.06 ( $\pm 7.5 \times 10^{-3}$ )

Fig. 5b and Table 3 illustrates the electrical properties of the samples, which underwent considerable modification after annealing in contrast to negligible change in the optical transmittance. In comparison to the as-deposited states, forming gas annealing enhanced the sheet resistance of all samples. Although the lowest  $R_s$  was achieved with the annealing of 150 °C deposited thin film (7.5  $\Omega/\square$ ), the highest improvement as compared to as-deposited state was observed for 250 °C deposited sample with a reduction of 3.6-fold in its sheet resistance value (11.45  $\Omega/\square$ ). In addition, RT deposited sample also showed a very low sheet resistance (12.21  $\Omega/\square$ ) after thermal treatment. The enhancement in the  $R_s$  of thin films after post-growth annealing can primarily be attributed to a noticeable increase in their carrier concentrations. After annealing, the carrier concentrations of the samples deposited at RT, 150 °C, and 250 °C increased around 131%, 274%, and 366%, respectively. Ndione et al., stated that the conductivity of a-ZITO depend on the cation composition and partial pressure of oxygen during deposition [47]. Others emphasized the effect of electron, hole or oxygen vacancy formation as a result of the substitution of Zn<sup>2+</sup> and Sn<sup>4+</sup> into In<sup>3+</sup> sites [58, 59]. Although the films in this study were produced under near-zero oxygen partial pressure and displayed similar cation compositions, the extend of atomic substitutions and the number of oxygen vacancies likely vary with the substrate temperature. Thus, the conductivity of as-deposited samples differs from each other. Further, the significant increase in the carrier concentrations with annealing can be attributed to the incorporation of hydrogen into the structure [60] as well as to the

suppression of localized defects and rearrangement of disordered charge distribution due to modification of amorphous network during annealing [61].

In contrast to the observations on the direct relationship between the mobility and substrate temperature for the as-deposited samples, the mobility of the films exhibited an inverse proportion with the employed deposition temperature for the films annealed at 400 °C. The highest mobility was achieved for the annealed state of the sample deposited at RT as 39.07 cm<sup>2</sup>/Vs. This value is higher than that of as-deposited counterpart. As the mobility of the films increased during film deposition under high purity Ar gas (practically  $P_{O_2} \cong 0$ ) with an increasing deposition temperature, the enhancement of the mobility of the RT deposited thin film after Ar + H<sub>2</sub> (practically  $P_{O_2} \cong 0$ ) annealing at 400 °C can be predicted. Interestingly, other samples exhibited decline in mobility after annealing. The annealed samples deposited at 150 °C and 250 °C exhibited mobility values of 36.59 cm<sup>2</sup>/Vs and 35.06 cm<sup>2</sup>/Vs, respectively. This decrease in the mobilities of 150 °C and 250 °C deposited samples after annealing can be ascribed to significant increase in their carrier concentration (274% and 366%, respectively) due to inverse relationship between these two properties. However, it is important to highlight that the mobility in amorphous oxide semiconductors depends on various parameters such as bonding energy difference of oxygen with the constituent cations, metal-oxygen local coordination's and the change of coordination states with annealing, modifications in the local distortions of metal-oxygen polyhedrons, formation of MO<sub>6</sub> chain structure and random distribution of MO<sub>4</sub> tetrahedrons, and structural differences at local or medium-range ordering [56]. Therefore, the aforementioned discussion on the mobility of annealed a-ZITO thin films just depends on the experimental observations and may require further investigation. In contrast, this research centers on the fabrication of TFTHs with a specific ZITO composition, highlighting that forming gas annealing serves as a beneficial technique for enhancing the electrical properties of the samples.

Figure 5c demonstrates the electrical resistivity of the annealed samples compared to their as-deposited state. The specific values can be followed from Table 3. The lowest resistivity was achieved via the annealing of 150 °C deposited sample as  $5.5 \times 10^{-4} \Omega \cdot \text{cm}$ . The conductivity of the films was calculated using  $\sigma = 1/\rho$  relation and determined as 1111 S/cm, 1818 S/cm, and 1190 S/cm, respectively for RT, 150 °C and 250 °C deposited samples. Accordingly, the FOM values were obtained as  $11.79 \times 10^{-3} \Omega^{-1}$ ,  $34.21 \times 10^{-3} \Omega^{-1}$ , and  $17.35 \times 10^{-3} \Omega^{-1}$  as in the same order.

### 3.5 Electrothermal Examination

Post-growth annealed a-ZITO TFTHs were subjected to 12 V to assess their heating response. The resulting data were plotted as a function of time and presented in Fig. 6a. As illustrated, all samples exhibited an increasing trend in terms of average surface temperature with the application of 12 V. Among these, the highest heating rate and maximum temperature was observed for the sample deposited at 150 °C. The response time i.e., the time that elapsed to attain 90% of the surface saturation temperature was measured as 102 s. Additionally, the heating response of 150 °C produced a-ZITO thin film to various applied voltage input was examined with the sample kept under ambient conditions. Fig. 6b shows the response of as-deposited thin film to 3, 6, 9, and 12 V inputs. The insets display the maximum average surface temperature of the sample after 500 seconds, along with the corresponding infrared camera image of the surface. As is obvious from the shape of the curves that the surface temperature of the TFTH initially increases and then saturates at a higher temperature. Further, the saturation temperature was found to increase proportional to the increasing input voltage. For the measurements conducted at applying 3, 6, 9, and 12 V, the mean saturation temperatures were recorded as 30, 47, 69, and 89 °C, respectively. This almost corresponds to 20 °C increase in the maximum achievable temperature for each 3V increments, suggesting that the saturation temperature depends on the power supplied to the heater [54].

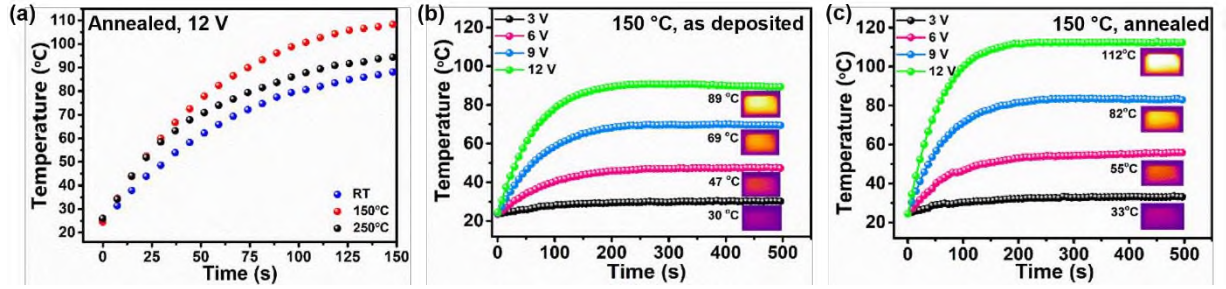


**Figure 6.** Electrothermal responses of a) post-growth annealed a-ZITO thin films to 12 V input, 150 °C deposited a-ZITO thin film to various applied voltages b) as-deposited, c) annealed (the inset images given in each figure refers to the thermal camera image of the sample at the corresponding saturation temperature)

Figure 6c displays the results of the same tests conducted using the annealed sample. In this case, the saturation temperatures were measured as 33, 55, 82, and 112 °C for input voltages of 3, 6, 9, and 12 V, respectively. These improvements in the heating behavior are expected as the annealing process significantly reduced the sheet resistance of the samples. In addition, the response time of the samples in the case of 6, 9, and 12 V inputs were calculated as 124, 114, and 102 s. These can be considered as moderate values for transparent heaters and might be attributed to sluggish heat conduction in the case of amorphous thin films [62]. On the other hand, the decreasing trend in the response time of the sample with the increasing input voltage can be defined by the increase in the specific heat of the film with increasing input power [63].

Electrothermal response of 150 °C deposited and annealed a-ZITO TFTH with respect to various electrical input conditions are illustrated in Fig. 7a, b and c. The behavior of the sample against voltage increase (+2V in every 60 s) up to 12 V is displayed in Fig. 7a. It is obvious that the sample exhibited linear response to voltage increases beyond 4 V. Further, the surface temperature enhanced after each increment as can be followed from the inset images. At an input of 12 V, the temperature reached approximately 96 °C after 60 s, and the sample demonstrated rapid cooling when the power supply was turned off.

The stability test was conducted by observing the change in the surface temperature for an extended period of time (e.g., 3600 s) under a specified voltage input. The test was performed at 60 °C surface temperature, achieved by applying 7 V, as shown in Fig. 7b. Under ambient atmospheric conditions, the deviation in temperature was negligible ( $\pm 0.4$  °C) indicating stable performance of the a-ZITO TFTH. The spatial distribution or the homogeneity of the surface temperature was calculated to be 19.66%. The uniformity value of the current TFTH is superior compared to that of wire-patterned deicing system suggested for car windshields and metallic quantum nanoparticle layered Ni/FTO transparent heaters [64, 65]. Moreover, the sample provided almost equivalent uniformity to that of NiCr/FTO (19.2 %) and bare FTO (19.7 %), but poorer homogeneity than Cr/FTO (14.65 %), AZO/SiO<sub>2</sub> (13.66 %), FTO/AZO (11.42 %), and AZO (17.70 %) TFTHs reported in literature [51, 54, 65, 66].

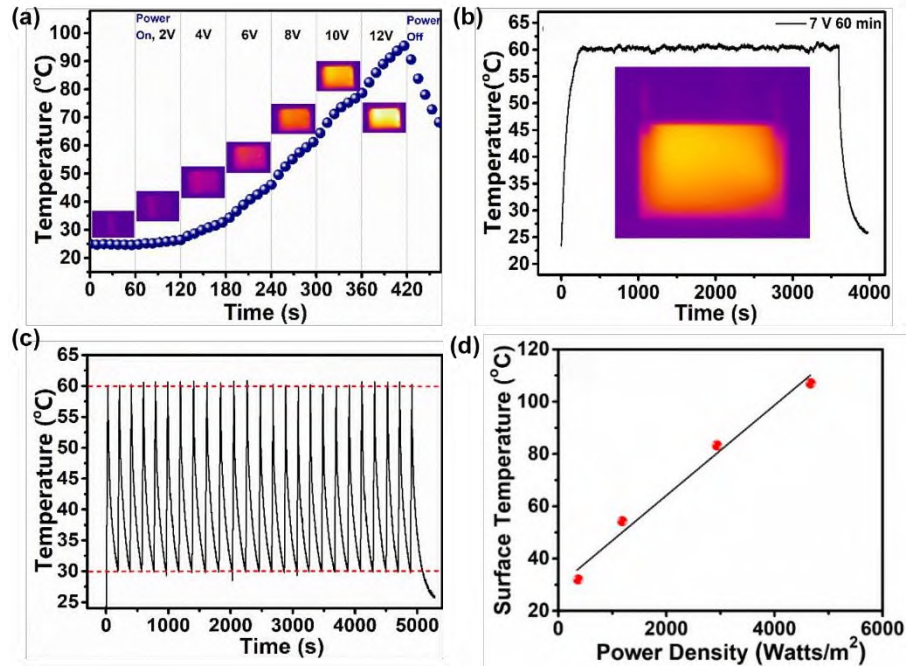


**Figure 7.** Electrothermal response of 150 °C deposited and forming gas annealed a-ZITO thin film to a) accumulative input voltage, b) constant input voltage stability, c) cyclic input voltage response, d) power density vs. surface saturation temperature relation (the inset images given in (a) and (b) refers to the thermal camera image of the sample at the corresponding temperature)

The cyclic voltage response of the sample was tested using 0-12 V on/off condition and illustrated in Fig. 7c. The surface temperature of the TFTH was first allowed to reach 60 °C by implementing 12 V, then the power supply was turned off to allow the heater to cool to 30 °C. This heating/cooling cycle was repeated 25 times. The horizontal red dashed lines in the figure show the upper and lower limits of the test. The peak temperature consistently attained around 25 s, indicating a heating rate of 1.2 °C/s.

The surface saturation temperature of the heater was recorded as a function of power density (electrical power/total active area) for 3, 6, 9, and 12 V inputs. The corresponding data points along with the fitted line plot is presented in Fig. 7d. Using the linear relationship between the power density and achieved saturation temperatures, the thermal resistance of the sample was calculated as 181.7 °C.cm<sup>2</sup>/Watt from  $dT/dP$ . In addition, the power consumption and power density of the sample (with an active area of 32.2 cm<sup>2</sup>) was calculated to be 3.95 W and 0.4635 Watt/cm<sup>2</sup>, respectively in case of 12 V input. A transparent heater is expected to provide heating power density values around 0.4 Watt/cm<sup>2</sup> to meet specifications for deicing applications in sea or air vehicles [67]. This implies that the a-ZITO heater prepared in this study has the potential to be used as an effective TFTHs device.

Deicing efficiency of 150 °C deposited and annealed a-ZITO TFTH was examined under different voltage input conditions and data are displayed in Fig. 8a. The maximum achieved temperature and the corresponding time for complete evaporation of water from the surface are presented as inset next to each curve. The overall deicing and complete evaporation time decreased with the increasing voltage input, as expected. Water droplets disappeared from the heater surface in 299, 195, and 173 s for 6, 9, and 12 V input. On the contrary, the maximum average surface temperature increased with the applied voltage reaching 50, 57, and 92 °C. For 12 V input, the camera recorded a surface temperature of 0 °C after ~23 s, and 30 °C in 50 s. Beyond this point, the temperature increased almost linearly with a heating rate of 0.68 °C/s. The inset images refer to the captures of the heater's surface by the camera during deicing at 0, 80, and 173 s under 12 V. The first image reveals a homogenous color resembling the initial condition of -40 °C. After 80 s, the temperature reached 50 °C. The dark spots highlight the remaining water droplets. After a while,

all the droplets evaporated, and the surface displayed a more homogenous temperature distribution as can be seen in the final inset image.

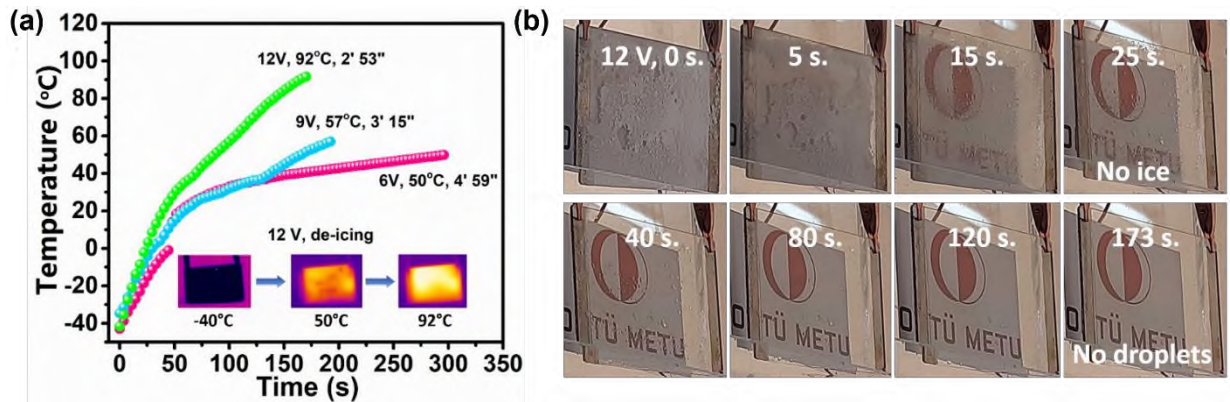


**Figure 8.** Deicing efficiency of 150 °C deposited 50 x 75 mm<sup>2</sup> a-ZITO thin film a) heating curves for 6, 9, and 12 V input starting from -40 °C, b) real-time digital deicing images of the heater as a function of time (inset images in (a) refer to the thermal camera captures of the sample during deicing at time 0, 80, and 173 s for 12 V input)

The digital images of the a-ZITO TFTH were collected at some points during the deicing process and presented in Fig. 8b in case of 12 V input. As can be seen from images, there is no clear visibility at the beginning due to condensed ice on the surface. However, a rapid melting occurred within 15 s improving the visibility as the ice layer melts. The translucent state turned to transparent almost within one minute. After this point the remaining droplets on the surface continued to evaporate and it took almost 3 min to remove all droplets from the surface via evaporation.

#### 4. CONCLUSIONS

ZnO-In<sub>2</sub>O<sub>3</sub>-SnO<sub>2</sub> thin film transparent heaters were manufactured using a 3" sputtering target with a specific cation composition of 49.6 at.% Zn, 44.5 at.% In, and 5.9 at.% Sn. The effects of substrate temperature and post-growth annealing on structural, morphological, optical, and electrical properties were investigated. The structural examination showed that the films were amorphous regardless of the substrate temperature in as-deposited state and this structure was maintained after annealing. Annealing under forming gas slightly increased the visible transmittance ( $T_{vis} \sim 85\%$ ) but substantially modified the electrical properties. The sample produced at a substrate temperature of 150 °C exhibited the lowest sheet resistance value (7.5  $\Omega/\square$ ) among the others. Electrothermal characterization results demonstrated that a-ZITO TFTHs exhibit power input-dependent, reproducible heating behavior with excellent stability and temperature homogeneity. The thermal resistance, power consumption, and areal power density of 150 °C deposited TFTH with an active area of 32.2 cm<sup>2</sup> were determined as 181.7 °C.cm<sup>2</sup>/Watt, 3.95 W, and 0.4635 Watt/cm<sup>2</sup> in case of 12 V input, respectively. Furthermore, this heater presented an outstanding deicing ability where defrosting and liquid phase removal steps were completed below 3 minutes with a heating rate of 0.68 °C/s. These findings revealed that the a-ZITO TFTHs produced in this study are suitable for various commercial defogging/deicing applications and their electrothermal properties can be tuned easily via modification of the substrate temperature.

#### Declaration of Ethical Standards

The authors declare that they have carried out this completely original study by adhering to all ethical rules including authorship, citation and data reporting

### Credit Authorship Contribution Statement

**H.A.:** Funding acquisition, Project administration, Supervision, Investigation, Methodology, Writing-review & editing, **H.A.C.:** Investigation, Data Curation, **B.K.:** Data Curation, Writing-review & editing, **T.Ö.:** Funding acquisition, Conceptualization, Supervision

### Declaration of Competing Interest

The authors declare that they have no conflict of interest.

### Data Availability

Data available on request from the author.

### Acknowledgements

This study was produced from the MSc thesis of Hilal Aybike CAN and supported financially by the Scientific and Technological Research Council of Turkey (TÜBİTAK; Project Number: 118M013), for which the authors are thankful.

### REFERENCES

- [1] S.P. Harvey, K.R. Poeppelmeier, and T.O. Mason, "Subsolidus Phase Relationships in the ZnO–In<sub>2</sub>O<sub>3</sub>–SnO<sub>2</sub> System," *Journal of the American Ceramic Society*, vol. 91, no. 11, pp. 3683-3689, 2008.
- [2] C.A. Hoel, T.O. Mason, J.-F. Gaillard, and K.R. Poeppelmeier, "Transparent Conducting Oxides in the ZnO-In<sub>2</sub>O<sub>3</sub>-SnO<sub>2</sub> System," *Chemistry of Materials*, vol. 22, no. 12, pp. 3569-3579, 2010.
- [3] T. Jantzen, K. Hack, E. Yazhenskikh, and M. Müller, "Thermodynamic assessment of oxide system In<sub>2</sub>O<sub>3</sub>-SnO<sub>2</sub>-ZnO," *Chimica Techno Acta*, vol. 5, no. 4, pp. 166-188, 2018.
- [4] M.H. Cho, C.H. Choi, and J.K. Jeong, "Recent progress and perspectives on atomic-layer-deposited semiconducting oxides for transistor applications," *Journal of the Society for Information Display*, vol. 30, no. 3, pp. 175-197, 2022.
- [5] I. Noviyana, A.D. Lestari, M. Putri, M.-S. Won, J.-S. Bae, Y.-W. Heo, and H.Y. Lee, "High mobility thin film transistors based on amorphous indium zinc tin oxide," *Materials*, vol. 10, no. 7, pp. 702, 2017.
- [6] J. Sheng, T. Hong, D. Kang, Y. Yi, J.H. Lim, and J.-S. Park, "Design of InZnSnO semiconductor alloys synthesized by supercycle atomic layer deposition and their rollable applications," *ACS applied materials & interfaces*, vol. 11, no. 13, pp. 12683-12692, 2019.
- [7] T. Kim, C.H. Choi, J.S. Hur, D. Ha, B.J. Kuh, Y. Kim, M.H. Cho, S. Kim, and J.K. Jeong, "Progress, challenges, and opportunities in oxide semiconductor devices: a key building block for applications ranging from display backplanes to 3D integrated semiconductor chips," *Advanced Materials*, vol. 35, no. 43, pp. 2204663, 2023.
- [8] T.E. Taouririt, A. Meftah, N. Sengouga, M. Adaika, S. Chala, and A. Meftah, "Effects of high-k gate dielectrics on the electrical performance and reliability of an amorphous indium–tin–zinc–oxide thin film transistor (a-ITZO TFT): an analytical survey," *Nanoscale*, vol. 11, no. 48, pp. 23459-23474, 2019.
- [9] H. Yang, W. Yang, J. Su, and X. Zhang, "Enhancement-mode thin film transistor using amorphous phosphorus-doped Indium–Zinc–Tin-Oxide channel layer," *Materials Science in Semiconductor Processing*, vol. 137, no. pp. 106228, 2022.
- [10] Y.G. Bak, J.W. Park, Y.J. Park, M.Z. Ansari, S. NamGung, B.Y. Cho, S.-H. Kim, and H.Y. Lee, "In-Zn-Sn-O thin film based transistor with high-k HfO<sub>2</sub> dielectric," *Thin Solid Films*, vol. 753, no. pp. 139290, 2022.

- [11] Y. Li, S. Yin, Y. Du, H. Zhang, J. Chen, Z. Wang, S. Wang, Q. Qin, M. Zhou, and L. Li, "Liquid-metal based flexible a-IZTO ultrathin films for electrical and optical applications," *Nanoscale*, vol. 14, no. 45, pp. 16797-16805, 2022.
- [12] C.P.T. Nguyen, T.T. Trinh, J. Raja, A.H.T. Le, K. Jang, Y.-J. Lee, and J. Yi, "High performance non-volatile memory with the control of charge trapping states in an amorphous InSnZnO active channel," *Semiconductor Science and Technology*, vol. 30, no. 7, pp. 075009, 2015.
- [13] J.-H. Bae, J.-M. Moon, S.W. Jeong, J.-J. Kim, J.-W. Kang, D.-G. Kim, J.-K. Kim, J.-W. Park, and H.-K. Kim, "Transparent conducting indium zinc tin oxide anode for highly efficient phosphorescent organic light emitting diodes," *Journal of The Electrochemical Society*, vol. 155, no. 1, pp. J1, 2007.
- [14] G.-S. Heo, Y. Matsumoto, I.-G. Gim, J.-W. Park, K.-Y. Kim, and T.-W. Kim, "Fabrication of cosputtered Zn-In-Sn-O films and their applications to organic light-emitting diodes," *Solid state communications*, vol. 149, no. 41-42, pp. 1731-1734, 2009.
- [15] T.-W. Kim, G.-S. Heo, H.-S. Kim, and J.-H. Lee, "Combinatorial exploration of new transparent conducting oxide films by using radio frequency sputtering and their application in optoelectronic devices," *MRS Online Proceedings Library (OPL)*, vol. 1425, no. pp. mrsf11-1425-uu01-04, 2012.
- [16] S.W. Heo, E.J. Lee, Y.W. Han, Y.S. Lee, W.J. Lee, S.-H. Choa, Y.S. Kim, and D.K. Moon, "Improved performance of flexible polymer light emitting diodes with an indium-zinc-tin-oxide transparent anode by controlling the thermal treatment temperature," *Journal of industrial and engineering chemistry*, vol. 53, no. pp. 68-76, 2017.
- [17] H.-K. Jeong and K.-M. Lee, "Effects of flow rate of atmosphere gases on the characteristics of Zn-doped ITO (ZITO) thin films for organic light emitting diodes," *Functional Materials Letters*, vol. 8, no. 03, pp. 1540007, 2015.
- [18] H.J. Lee, I. Noviyana, C.Y. Koo, J.-A. Lee, J.-J. Kim, A.D. Lestari, Y. Jeong, Y. Lee, and H.Y. Lee, "Organic Photovoltaics with Non-Stoichiometric InZnSnO Thin Film Cathodes," *Journal of Nanoscience and Nanotechnology*, vol. 17, no. 7, pp. 4822-4826, 2017.
- [19] H.J. Lee, I. Noviyana, M. Putri, C.Y. Koo, J.-A. Lee, J.-J. Kim, Y. Jeong, Y. Lee, and H.Y. Lee, "DC Magnetron Sputtered IZTO Thin Films for Organic Photovoltaic Application," *Journal of Nanoscience and Nanotechnology*, vol. 18, no. 2, pp. 1270-1273, 2018.
- [20] M. Putri, K.H. Kim, C.Y. Koo, J.-A. Lee, J.-J. Kim, I.D. Baikie, A.C. Grain, and H.Y. Lee, "Effect of annealing treatment on the properties of stoichiometric indium zinc tin oxide (IZTO) thin films," *Journal of Nanoelectronics and Optoelectronics*, vol. 12, no. 6, pp. 611-616, 2017.
- [21] H.C. Ma, Damisih, M. Putri, J.H. Cheon, J.H. Kim, and H.Y. Lee, "The effect of post-annealing treatment on the characteristics of a dye-sensitized solar cell with an indium zinc tin oxide electrode," *Journal of the Korean Physical Society*, vol. 61, no. pp. 1994-1999, 2012.
- [22] J.-D. Cho, Y.-B. Kim, G.-S. Heo, E.-M. Kim, and J.-W. Hong, "Optimization of Electro-Optical Properties of Acrylate-based Polymer-Dispersed Liquid Crystals for use in Transparent Conductive ZITO/Ag/ZITO Multilayer Films," *Applied Chemistry for Engineering*, vol. 31, no. 3, pp. 291-298, 2020.
- [23] E.M. Kim, I.-S. Choi, J.-P. Oh, Y.-B. Kim, J.-H. Lee, Y.-S. Choi, J.-D. Cho, Y.-B. Kim, and G.-S. Heo, "Transparent conductive ZnInSnO-Ag-ZnInSnO multilayer films for polymer dispersed liquid-crystal based smart windows," *Japanese Journal of Applied Physics*, vol. 53, no. 9, pp. 095505, 2014.
- [24] S. Syed Feroze Hussain and D. Thiripurasundari, "A review on optically transparent antenna fabricated with conductive nano-material oxides," *Journal of Electronic Materials*, vol. 51, no. 12, pp. 6707-6734, 2022.
- [25] H.Y. Lee, I.J. Yang, J.-H. Yoon, S.-H. Jin, S. Kim, and P.K. Song, "Thermoelectric properties of zinc-doped indium tin oxide thin films prepared using the magnetron co-sputtering method," *Coatings*, vol. 9, no. 12, pp. 788, 2019.
- [26] J.-A. Lee, Y.-W. Heo, J.-H. Lee, H.Y. Lee, and J.-J. Kim, "Structural and optical characteristics of Zn-rich In<sub>2</sub>O<sub>3</sub>-SnO<sub>2</sub>-ZnO (ITZO) thin films prepared by radio frequency magnetron sputtering," *Journal of Nanoelectronics and Optoelectronics*, vol. 12, no. 6, pp. 598-601, 2017.



- [27] C.W. Ow-Yang, H.-y. Yeom, and D.C. Paine, "Fabrication of transparent conducting amorphous Zn-Sn-In-O thin films by direct current magnetron sputtering," *Thin Solid Films*, vol. 516, no. 10, pp. 3105-3111, 2008.
- [28] D.E. Proffit, S.P. Harvey, A. Klein, R. Schafraneck, J.D. Emery, D.B. Buchholz, R.P. Chang, M.J. Bedzyk, and T.O. Mason, "Surface studies of crystalline and amorphous Zn-In-Sn-O transparent conducting oxides," *Thin Solid Films*, vol. 520, no. 17, pp. 5633-5639, 2012.
- [29] Y.R. Denny, S. Seo, K. Lee, S.K. Oh, H.J. Kang, S. Heo, J.G. Chung, J.C. Lee, and S. Tougaard, "Effects of cation compositions on the electronic properties and optical dispersion of indium zinc tin oxide thin films by electron spectroscopy," *Materials Research Bulletin*, vol. 62, no. pp. 222-231, 2015.
- [30] H.C. Ma, F. Finanda, J.-J. Kim, and H.Y. Lee, "Effect of composition in transparent conducting indium Zinc Tin Oxide thin films deposited by RF magnetron sputtering," *Journal of nanoelectronics and optoelectronics*, vol. 7, no. 5, pp. 483-487, 2012.
- [31] M. Putri, C.Y. Koo, J.-A. Lee, J.-J. Kim, and H.Y. Lee, "Transparent conducting indium zinc tin oxide thin films with low indium content deposited by radio frequency magnetron sputtering," *Thin Solid Films*, vol. 559, no. pp. 44-48, 2014.
- [32] P. Janicek, M. Putri, K.H. Kim, H.J. Lee, M. Bouska, S. Šlang, and H.Y. Lee, "Spectroscopic Ellipsometry Characterization of As-Deposited and Annealed Non-Stoichiometric Indium Zinc Tin Oxide Thin Film," *Materials*, vol. 14, no. 3, pp. 578, 2021.
- [33] K.H. Kim, M. Putri, H.J. Lee, C.Y. Koo, J.-A. Lee, J.-J. Kim, and H.Y. Lee, "Non-Stoichiometric Indium Zinc Tin Oxide Thin Films Prepared by RF Magnetron Sputtering," *Journal of Nanoelectronics and Optoelectronics*, vol. 10, no. 4, pp. 541-545, 2015.
- [34] E.M. Kim, J.-P. Oh, T.-W. Ha, Y.-B. Kim, T.-W. Kim, and G.-S. Heo, "Physical stability against hydrogen plasma for ZnInSnO thin films deposited by combinatorial RF magnetron sputtering," *Japanese Journal of Applied Physics*, vol. 55, no. 12, pp. 125801, 2016.
- [35] D.E. Proffit, T. Philippe, J.D. Emery, Q. Ma, B.D. Buchholz, P.W. Voorhees, M.J. Bedzyk, R.P. Chang, and T.O. Mason, "Thermal stability of amorphous Zn-In-Sn-O films," *Journal of Electroceramics*, vol. 34, no. pp. 167-174, 2015.
- [36] G.-S. Heo, I.-G. Gim, H.-K. Lee, J.-H. Song, and T.-W. Kim, "Investigation of bending stability of amorphous Zn-In-Sn-O thin films on flexible poly (ether sulfone) substrates," *Japanese Journal of Applied Physics*, vol. 49, no. 3R, pp. 031104, 2010.
- [37] Y.S. Kim, W.J. Hwang, K.T. Eun, and S.-H. Choa, "Mechanical reliability of transparent conducting IZTO film electrodes for flexible panel displays," *Applied surface science*, vol. 257, no. 18, pp. 8134-8138, 2011.
- [38] Y.S. Kim, S.-I. Oh, and S.-H. Choa, "Mechanical integrity of flexible In-Zn-Sn-O film for flexible transparent electrode," *Japanese Journal of Applied Physics*, vol. 52, no. 5S1, pp. 05DA17, 2013.
- [39] J.Y. Choi, I.P. Park, and S.W. Heo, "Ultra-flexible organic solar cell based on indium-zinc-tin oxide transparent electrode for power source of wearable devices," *Nanomaterials*, vol. 11, no. 10, pp. 2633, 2021.
- [40] Y.S. Kim, E.K. Lee, K. Eun, and S.-H. Choa, "Electromechanical properties of amorphous In-Zn-Sn-O transparent conducting film deposited at various substrate temperatures on polyimide substrate," *Japanese Journal of Applied Physics*, vol. 54, no. 9, pp. 095501, 2015.
- [41] K.-D. Li, P.-W. Chen, and K.-S. Chang, "Low-temperature deposition of transparent conducting films applied to flexible electrochromic devices," *Materials*, vol. 14, no. 17, pp. 4959, 2021.
- [42] J.Y. Choi, I.P. Park, and S.W. Heo, "Ultra-flexible organic photovoltaics with low-temperature deposited IZTO on a cyclic polymer substrate having excellent mechanical properties," *ACS Applied Materials & Interfaces*, vol. 13, no. 43, pp. 51289-51296, 2021.
- [43] S. Biswas, Y. Lee, H. Jang, S. Han, and H. Kim, "Improved mechanical stability of indium zinc tin oxide based flexible transparent electrode through interlayer treatment," *Journal of Applied Polymer Science*, vol. 140, no. 1, pp. e53251, 2023.

- [44] X. Jiang, S. Long, G. Zhu, H. Xu, J. Song, X. Zhang, Y. Zhao, T. Wei, N. Guo, and Y. Gong, "Preparation and Properties of Izto Ceramic Target by Cold Sintering," *Available at SSRN 4255408*, vol., no.,
- [45] I. Saadeddin, H.S. Hilal, R. Decourt, G. Campet, and B. Pecquenard, "Indium oxide co-doped with tin and zinc: A simple route to highly conducting high density targets for TCO thin-film fabrication," *Solid state sciences*, vol. 14, no. 7, pp. 914-919, 2012.
- [46] G.-S. Heo, I.-G. Gim, J.-W. Park, K.-Y. Kim, and T.-W. Kim, "Effects of substrate temperature on properties of ITO-ZnO composition spread films fabricated by combinatorial RF magnetron sputtering," *Journal of Solid State Chemistry*, vol. 182, no. 10, pp. 2937-2940, 2009.
- [47] P.F. Ndione, A. Zakutayev, M. Kumar, C. Packard, J. Berry, J. Perkins, and D. Ginley, "Tuning the physical properties of amorphous In-Zn-Sn-O thin films using combinatorial sputtering," *MRS Communications*, vol. 6, no. 4, pp. 360-366, 2016.
- [48] H.A. Can, T. Öztürk, and H. Akyıldız, "A combinatorial study on ZnO-In<sub>2</sub>O<sub>3</sub>-SnO<sub>2</sub> system: The effects of different postgrowth annealing conditions on optical and electrical properties," *Journal of Alloys and Compounds*, vol. 924, no. pp. 166591, 2022.
- [49] H.A. Can, T. Öztürk, and H. Akyıldız, "Effect of deposition parameters on optical and electrical properties of ZnO-In<sub>2</sub>O<sub>3</sub>-SnO<sub>2</sub> thin films," *Materials Chemistry and Physics*, vol. 296, no. pp. 127256, 2023.
- [50] D. Sari, Z.C. Torunoglu, Y.E. Kalay, and T. Ozturk, "Preparation of La<sub>0.8</sub>Sr<sub>0.2</sub>CoO<sub>3-δ</sub> sputtering targets using a deformable compaction die," *Ceramics International*, vol. 43, no. 17, pp. 15185-15188, 2017.
- [51] B. Tönbul, H.A. Can, T. Öztürk, and H. Akyıldız, "Solution processed glass/fluorine-doped tin oxide/aluminum-doped zinc oxide double layer thin films for transparent heater and near-infrared reflecting applications," *Journal of Sol-Gel Science and Technology*, vol. 99, no. 3, pp. 482-496, 2021.
- [52] H.C. Ma, J.-J. Kim, and H.Y. Lee, "The electrical and optical properties of indium zinc tin oxide thin films with different Sn/Zn ratio," *Thin Solid Films*, vol. 520, no. 10, pp. 3741-3745, 2012.
- [53] T. Minami, T. Yamamoto, Y. Toda, and T. Miyata, "Transparent conducting zinc-co-doped ITO films prepared by magnetron sputtering," *Thin Solid Films*, vol. 373, no. 1-2, pp. 189-194, 2000.
- [54] H.A. Can, B. Tönbul, F. Pişkin, T. Öztürk, and H. Akyıldız, "Processing optimization of SiO<sub>2</sub>-capped aluminum-doped ZnO thin films for transparent heater and near-infrared reflecting applications," *Journal of Materials Science: Materials in Electronics*, vol. 32, no. pp. 5116-5137, 2021.
- [55] P. Pujar, S. Gandla, D. Gupta, S. Kim, and M.G. Kim, "Trends in low-temperature combustion derived thin films for solution-processed electronics," *Advanced Electronic Materials*, vol. 6, no. 10, pp. 2000464, 2020.
- [56] R. Khanal, D.B. Buchholz, R.P. Chang, and J.E. Medvedeva, "Composition-dependent structural and transport properties of amorphous transparent conducting oxides," *Physical Review B*, vol. 91, no. 20, pp. 205203, 2015.
- [57] A. Zhussupbekova, A. Kaisha, R.K. Vijayaraghavan, K. Fleischer, I.V. Shvets, and D. Caffrey, "Importance of Local Bond Order to Conduction in Amorphous, Transparent, Conducting Oxides: The Case of Amorphous ZnSnO<sub>y</sub>," *ACS applied materials & interfaces*, vol. 11, no. 47, pp. 44399-44405, 2019.
- [58] K.-D. Li and K.-S. Chang, "Effects of Zn ratio tuning on the structural and transport properties of amorphous indium zinc tin oxide thin films," *Journal of Electronic Materials*, vol. 49, no. 12, pp. 7336-7342, 2020.
- [59] P.-Y. Liao, T.-C. Chang, W.-C. Su, Y.-J. Chen, B.-W. Chen, T.-Y. Hsieh, C.-Y. Yang, Y.-Y. Huang, H.-M. Chang, and S.-C. Chiang, "Effect of mechanical-strain-induced defect generation on the performance of flexible amorphous In-Ga-Zn-O thin-film transistors," *Applied Physics Express*, vol. 9, no. 12, pp. 124101, 2016.

- [60] T. Kamiya, K. Nomura, and H. Hosono, "Origins of high mobility and low operation voltage of amorphous oxide TFTs: Electronic structure, electron transport, defects and doping," *Journal of display Technology*, vol. 5, no. 7, pp. 273-288, 2009.
- [61] J.E. Medvedeva, D.B. Buchholz, and R.P. Chang, "Recent advances in understanding the structure and properties of amorphous oxide semiconductors," *Advanced Electronic Materials*, vol. 3, no. 9, pp. 1700082, 2017.
- [62] L. Chen, N. Kumari, and Y. Hou, "Thermal resistances of crystalline and amorphous few-layer oxide thin films," *AIP Advances*, vol. 7, no. 11, 2017.
- [63] P. Nath and K. Chopra, "Thermal conductivity of amorphous vs crystalline Ge and GeTe films," *Japanese Journal of Applied Physics*, vol. 13, no. S1, pp. 781, 1974.
- [64] C. Baldasseroni, D. Queen, D.W. Cooke, K. Maize, A. Shakouri, and F. Hellman, "Heat transfer simulation and thermal measurements of microfabricated x-ray transparent heater stages," *Review of Scientific Instruments*, vol. 82, no. 9, 2011.
- [65] C. Hudaya, B.J. Jeon, and J.K. Lee, "High thermal performance of SnO<sub>2</sub>: F thin transparent heaters with scattered metal nanodots," *ACS Applied Materials & Interfaces*, vol. 7, no. 1, pp. 57-61, 2015.
- [66] B. Tönbul, H.A. Can, T. Öztürk, and H. Akyıldız, "Solution processed aluminum-doped ZnO thin films for transparent heater applications," *Materials Science in Semiconductor Processing*, vol. 127, no. pp. 105735, 2021.
- [67] Y.-R. Kim, J.-W. Park, S.-H. Park, and S.-J. Lee, "Radio-frequency and optically transparent radome de-icing materials: fluorine-doped tin oxide," *RSC Advances*, vol. 10, no. 59, pp. 35979-35987, 2020.



## DETERMINATION OF TRAFFIC IMPACT LEVEL IN URBAN CYCLING

<sup>1,\*</sup>Recep AYDAR , <sup>2</sup>Osman Nuri ÇELİK 

*Konya Technical University, Engineering and Natural Sciences Faculty, Civil Engineering Department, Konya,  
TÜRKİYE*



<sup>1</sup>[recepaydar@gmail.com](mailto:recepaydar@gmail.com), <sup>2</sup>[oncelik@ktun.edu.tr](mailto:oncelik@ktun.edu.tr)

### *Highlights*

- Traffic impact level (bikted and bikkted) has been developed for bicycle use in urban roads in Turkey.
- Traffic impact level in bicycle use is considered in two situations: corridor and intersection.
- A bicycle prototype was developed that enabled field data to be collected during the study methodology.
- Originally, for the first time in a bicycle model, the gap between vehicles, the amount of noise and the amount of vibration were taken into consideration.



## DETERMINATION OF TRAFFIC IMPACT LEVEL IN URBAN CYCLING

<sup>1,\*</sup>Recep AYDAR , <sup>2</sup>Osman Nuri ÇELİK 

*Konya Technical University, Engineering and Natural Sciences Faculty, Civil Engineering Department, Konya, TÜRKİYE*

<sup>1</sup>[recepaydar@gmail.com](mailto:recepaydar@gmail.com), <sup>2</sup>[oncelik@ktun.edu.tr](mailto:oncelik@ktun.edu.tr)

(Received: 02.09.2024; Accepted in Revised Form: 20.12.2024)

**ABSTRACT:** In recent years, the habit of cycling has been increasing. Particularly when active mobility is gaining prominence, there is a global emphasis on healthy living and natural sustainability. Although the current rate of bicycle use in Turkey is quite low, there is significant potential for cycling in metropolitan areas and districts. The concept of bikted (Traffic Impact Level in Bicycle Usage) has been developed to enhance bicycle usage in Turkey, address infrastructure deficiencies, and ensure more comfortable cycling. This method, which consists of parameters related to traffic infrastructure, environmental factors, and user behavior, was evaluated using eight parameters in corridors and five parameters at intersections. In corridors, assessments were made for separated bicycle paths, bicycle lanes, and roads without infrastructure; at intersections, evaluations were conducted for signalized intersections, modern roundabouts, and intersections with traffic markings. In corridors; slope, noise level, curbside parking, vertical marking, surface vibration amount, main road-side road intersection situations, speed limit and bicycle-vehicle gap distance were examined. In intersections; parking at the intersection, intersection visibility, intersection crossing distance, vertical marking presence and bicycle path presence were examined. Additionally, an experimental e-bicycle was developed to aid data collection for bikted. The scoring system in the model was designed using data obtained from field studies and previous literature. For the first time in a bicycle model study, noise intensity, gap distance measurement, slope and vibration were combined for corridor assessment. Slope accounts for approximately one-third of the scoring in corridor assessments for each infrastructure type, and corridors with high slopes cannot reach the "comfortable use" classification. The measurements may not be as reliable at intersections as the numerical data analysis conducted for corridors, but they still provide valuable insights for analyzing intersections. This study aims to contribute to the current state of bicycle corridors in Turkey's traffic infrastructure and future bicycle infrastructure projects, thereby promoting increased bicycle use. Furthermore, bikted is expected to raise awareness among local governments when planning and implementing bicycle-related projects.

**Keywords:** Cycleability, Cycling Safety, Traffic Stress Level, Cycling Infrastructure

### 1. INTRODUCTION

In recent years, countries worldwide have engaged in numerous social and technical efforts to promote bicycle use as part of active mobility initiatives. As urban traffic volumes in most countries have reached their maximum capacity, bicycles are increasingly being seen as an alternative, particularly for primary or multimodal transportation. This trend is especially noticeable in many European countries, where there is a marked shift away from private vehicle use toward bicycles, e-bikes, and scooters, all considered cleaner energy options [1].

In Turkey, the trend of bicycle usage has been increasing, especially since the global pandemic. However, despite the growing construction of bicycle paths in major cities, these efforts often lack comprehensive planning and integration into the broader transportation network. Furthermore, the existing bicycle paths (alongside roads and separate lanes) often fail to provide a well-planned network for cyclists. Insufficient infrastructure, a lack of adherence to cycling rules, and, most critically, errors by motor vehicle drivers hinder the widespread adoption of bicycles. In global cities, the utilization rates of

\*Corresponding Author: Recep AYDAR, [recepaydar@gmail.com](mailto:recepaydar@gmail.com)

bicycles have reached up to 45%, whereas in Konya, the city with the longest bicycle infrastructure in Turkey, the usage rate is only 2% [2]. Additionally, the impact of existing infrastructure on cyclists in Turkey has not been adequately studied, nor have these impacts been leveraged to promote cycling, which is a significant disadvantage. Globally, the bicycle has consistently maintained its place throughout history. Initially invented in the 1850s, bicycles were used mainly for recreation and transportation until the 1900s when the invention of motor vehicles led to a decline in their use [3].

In Turkish cities, the rate of bicycle use is closely linked to the level of investment in bicycle infrastructure, highlighting the importance of developing proper infrastructure. Turkey's longest bicycle path network is in Konya, which is 650 km, as shown in Figure 1. In 36% of Turkish metropolitan areas, the length of bicycle paths ranges from 26 to 100 km, while in 46%, it ranges from 1 to 25 km [4].



**Figure 1.** The length of bicycle paths in cities across Turkey

Considering the number of fatal and injury-causing traffic accidents in Turkey, the country suffers significant financial and emotional losses every year. The most important of these losses is the psychological impact on individuals who feel unsafe and stressed during their daily commute, which affects their overall well-being and productivity. For better traffic psychology, urban planning should be designed to increase people's health and productivity. Infrastructure design in almost all cities in Turkey is planned with vehicle traffic in mind. Parameters such as intersections, road alignments, pedestrian regulations, speed limits and parking areas create negative effects for cities that have started or are already using bicycles.

Turkey has a lower rate of bicycle use compared to European and other global countries, making all research and development efforts related to bicycles quite valuable. Bicycles in Turkey are mostly used in recreational areas, except for certain cities. The use of bicycles for transportation is minimal, almost non-existent. Although the concepts of micro-mobility and active transportation are increasing worldwide, their adoption in Turkey is increasing steadily, albeit more slowly. In this context, traditional bicycles and electric bicycles constitute the core of our study. In cities where the infrastructure is primarily designed for motor vehicles, this situation creates an unsafe user profile for cyclists. However, in order to encourage more active use of bicycle infrastructure and increase the number of cyclists, the concept of biked (Traffic Impact Level of Bicycle Use) is essential for Turkey. This concept has been studied as 'traffic stress level' and 'bikeability' in many countries and cities around the world, emphasizing its importance for Turkey.

The aim of the study is to encourage safe and more bicycle use and to make recommendations to improve the infrastructure. The difference of the study from the examples in the world is that a model is created by combining noise, surface vibration amount, vehicle-bicycle distance, slope and parking parameters. In addition, while the studies in the world only examine traffic stress in corridors, our study also evaluates intersections.

## 1.1. Literature studies on the relationship between bicycles, the environment, and infrastructure

### 1.1.1. General Studies

In recent years, infrastructure studies related to cycling have seen an increase. These studies have examined various parameters related to infrastructure, such as integrating bicycles with public transportation systems, which can influence route selection, traffic capacity, bicycle parking availability, and road gradients. Such analyses have been conducted to optimize cycling routes [5]. Other studies have emphasized the importance of dedicated bicycle lanes in traffic infrastructure [6]. For instance, a study on one of Turkey's leading micro-mobility organizations analyzed seasonal bicycle usage and various influencing factors in four cities offering bike-sharing services. A developed model predicted future trip numbers and their seasonal variations in these cities [7]. There are also studies on the status, planning, and implementation of bicycle use, particularly in Turkish cities like Konya and Antalya, where cycling is more prevalent [8],[9]. Several studies have been conducted at the city level to strengthen bicycle infrastructure to increase usage [10], [11].

Additionally, the impact of different types of bicycle infrastructure on usage has been examined [12], [13]. The strengths and weaknesses of bicycle infrastructure in Paris, France, have also been explored [14], [15]. To enhance cycling comfort, pavement analyses focusing on vibration have been conducted [16]. Some studies have compared comfort and safety parameters for better bicycle infrastructure design [17]. To understand the safety of bike lanes, the status of dedicated and shared bike lanes has been analyzed [18]. Additionally, some studies have evaluated safety from an accessibility perspective [19]. Naturalistic studies have analyzed near-miss situations using sensors to prevent bicycle accidents [20]. Another study comprehensively examined the impact of gradients, one of the most critical factors in bicycle use [21].

Another type of study focuses on cyclist behavior. These studies typically involve surveys that question users about their behavioral patterns, including hazard perception, evaluation of bike networks and facilities, the impact of traffic, the influence of road conditions, and factors that encourage or deter cycling [22], [23], [24], [25], [26].

For cyclists to comfortably use bicycles for transportation, environmental factors must also be conducive. Studies on environmental factors have highlighted noise levels, vibration, and bicycle path maintenance. For example, a study in Montreal, Australia, examined the impact of noise on cyclists [27], while another looked at the effect of noise levels on stress [28]. In Mumbai, India, the effects of vibration on cyclists were recorded along specific corridors [29]. Vehicle noise levels were measured and recorded in Thessaloniki, Greece, as environmental impacts [30]. An international study allowed for comparing noise levels in traffic in Copenhagen, Paris, and Montreal [31]. In Xi'an, China, the conditions caused by vibration were defined as dynamic cycling comfort, and measurements were conducted along corridors [32]. Some studies have measured vibration levels using various sensors placed on different parts of bicycles [33]. Another study explored the impact of different pavement types—such as asphalt, concrete, and pavers—on bicycle use by measuring and analyzing these surfaces [34]. Winter maintenance is also among the topics examined to ensure better bicycle use during winter [35].

Parking and passing distances, which significantly affect cyclists in bike lanes and mixed traffic, have been researched extensively in recent years [36], [37], [38]. Some studies specifically focus on a detailed analysis of all road types [39], while others attempt to correlate the impact of mixed traffic with passing distances [40].

As the use of electric bicycles has increased in recent years, some studies have examined the differences in riding and driving behaviors between conventional and electric bicycles [41]. Another study in Hangzhou, China, analyzed the behavior of e-bike riders at intersections using a survey method [42]. The e-bike program in the North Brabant province of the Netherlands has also provided benefits for promoting e-bike use [43].

Intersections are crucial structural elements for cyclists navigating through them. The literature on bicycle-intersection studies is limited. One study examined cyclists' tendencies to run red lights [44],

while another looked at cycling behaviors at different roundabouts [45]. A study analyzing cyclists' comfort, stress levels, and riding behaviors across three different intersection types identified the impact of intersection types on cycling [46]. Another experimental study explored the effects of bike lanes at signalized intersections [47]. Two studies evaluated both vehicle-cyclist interactions and the types of infrastructure where cyclists feel safest at unsignalized intersections [48], [49]. The visibility of intersections, which is rarely observed, was examined through field studies conducted at urban intersections in Madrid, Spain [50].

### 1.1.2. Traffic Stress Level for Cyclists

In recent years, active mobility in urban areas has gained global prominence regarding sustainable transportation. In this context, the concept of low-stress cycling and network connectivity, thoroughly explained by a group of researchers in the United States [51], was previously evaluated as an attempt to relate cyclists' perceptions of road types to specific geometric and traffic conditions under the concept of bicycle stress levels. The study's authors created a stress level rating from 1 to 5 by considering traffic variables such as volume, speed, and curb width. Additionally, a widely recognized model categorizes traffic stress levels into four distinct categories: LTS 1 (Low Traffic Stress Level 1) represents a level most children can tolerate; LTS 2 is suitable for the general adult population; LTS 3 is for the "enthusiastic and confident" cyclists; and LTS 4 is tolerated only by those characterized as "strong and fearless." The study examined various parameters: speed, annual average daily traffic, roadway classification, bike lane width, and parking conditions [52].

Another study analyzed LTS rankings by comparing parents' willingness to cycle with their willingness to allow their children to cycle [53]. Another study analyzed the relationship between bike network design and commuting mode shares in Franklin County, Ohio. Criteria for bicycle traffic stress levels were adopted to assess the bike network [54]. Another study classified bike network connectivity through two case studies to evaluate the adapted LTS system and demonstrate practical applications in infrastructure management [55]. Specifically, the study examined the levels of traffic stress for cyclists on street and trail networks in Toronto, Canada [56].

## 2. MATERIAL AND METHODS

Various methods have been developed to assess bikeability and traffic-induced stress levels. This study aims to build upon these existing models and methods by incorporating new elements and introducing a fresh perspective to develop a Traffic Impact Level Management System for Cycling (bikted). The study was conducted simultaneously: creating the bikted model and collecting data for bikted using an equipped experimental bicycle.

### 2.1. Material

As part of the study, a prototype bicycle was developed to collect field data. Volta A.Ş. and ISSD A.Ş supported this initiative. The hardware used in the field study includes an experimental bike equipped with various electrical components. A computer was used to record and store the data collected from the field and to conduct checks after each measurement. These components are essential for gathering and processing field data. The equipment was procured as part of the KTÜN BAP project. The bicycle and its components include one bicycle, one aluminum enclosed box for equipment storage, a mini panel, a regulator, a GPS module, a webcam, a mini P.C., 1 Micro SDXC 512 GB MicroSD card, a microcontroller, a sine inverter, temperature and acceleration sensors, ultrasonic and vibration sensors (Fig.2)



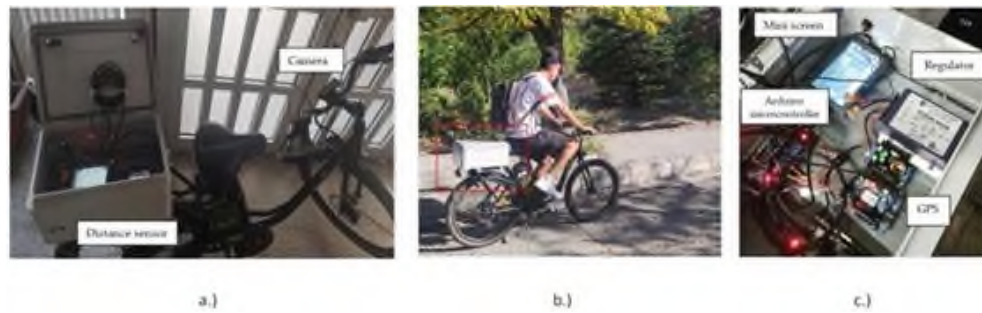


**Figure 2.** Experimental Bike a) Distance sensor and camera b) User collecting data in the field c) Display of main equipment components

The prototype consists of an electric bike with a bicycle equipment box mounted on the saddle, drawing power from the bike. The box contains all the necessary components for data analysis, including a mini PC, a power converter, an accelerometer, a GPS module, a camera capable of sound measurement, a sine inverter (useful for electrical conversion), a temperature sensor, ultrasonic sensors, a mini panel, and a vibration sensor. This setup enables comprehensive data collection and analysis directly in the field, providing valuable insights into the various parameters affecting cycling conditions.

## 2.2. BikTED Methodology

The bikted method was developed to classify and measure the impact of traffic on bicycle use in urban roads. Routes were examined in two categories: corridors and intersections (Fig.3).

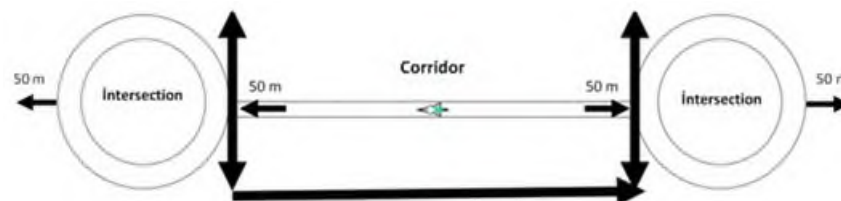


**Figure 3.** Illustration of corridors and intersections analyzed within the bikted model

For corridors, the physical conditions typically found in our country were considered: shared lanes next to vehicle lanes (bike lanes), mixed-use with vehicle lanes (shared lanes), and protected bike paths (separated bike paths). For intersections, classifications included signalized intersections, modern roundabouts, and traffic-sign-controlled intersections, encompassing various types of intersections. In the literature, traffic impact level has been discussed regarding traffic stress level and bikeability. Past studies have considered factors such as parking, vehicle speed, platform width, the presence of bike lanes, and bike lane width.

Unlike previous studies, this research evaluated corridors based on eight parameters: noise level, slope, rightmost lane parking, vertical signage, pavement surface vibration, side road intersections, speed limits, and vehicle spacing. Intersections were assessed using five parameters: parking, intersection visibility, crossing distance, vertical signage/signals for cyclists, and the presence of bike lanes. For separated bike paths, parameters like speed limits and vehicle spacing were not considered due to their physical separation from the roadway. Vertical signage for cyclists was not evaluated in mixed traffic as it does not typically exist.

The following indices were used in determining corridor and intersection parameters and determining (bikted) intervals.

Copenhagen Index; Established in Denmark, the Copenhagen Index provides the most comprehensive and holistic ranking of bicycle-friendly cities worldwide. Since 2011, it has evaluated cities based on categories like street scenery, culture, and passion, each rated on a scale of 1 to 4 points.

[57]. Munich Bicycle Availability Index; This index is used to identify areas of low bicycle accessibility across road networks with varying spatial extensions. Focusing on Munich, the index measures cycling capabilities by considering the presence and type of bike paths, speed limits, bicycle parking facilities, and the quality of bicycle intersection infrastructure. Parameters outside intersections are scored between 1 and 10 based on survey results, while intersections are examined in detail [58]. Bicycle Service Level; In the United States, a Bicycle Service Level was developed to measure the quality of service provided to cyclists traveling on urban road networks. The study found that road surface conditions and the presence of bike lanes are critical factors in determining the quality of service [59]. Bicycle Compatibility Index (BCI); The index was to identify and combine the key road and traffic variables that influence a cyclist's decision to cycle on a particular road [60].

By using the indexes mentioned above, as well as many demo studies conducted with experimental bikes in the field, the following scores and bikted impact levels were determined.

For corridors, separated bike paths, which are physically isolated from the roadway for safety, were scored out of 100 points. Bike lanes, which lose 20 points due to reduced infrastructure compared to separated paths, were scored out of 80. Cycling in mixed traffic without dedicated infrastructure, losing an additional 20 points for the lack of bike lanes, was scored out of 60 points. For intersections, signalized intersections were scored out of 100, modern roundabouts out of 90, and traffic-sign-controlled intersections out of 80. The scoring was entirely based on the author's review of past research, field experiences during the study, and technical expertise. In the bikted model, corridor or intersection evaluations are classified as bikted 1-6 for corridors and bikted 1-6 for intersections. A score of 1 represents very comfortable use or intersection crossing, while a score of 6 indicates that the corridor or intersection is unusable (Fig.4). Data collected using the prototype test bike should be averaged from at least two days of data collected during weekday rush hours in September-November or April-June to determine the level. For the method, 28 km of data collection was carried out in mixed traffic, roads with bicycle lanes and separated bicycle paths in Konya and Ankara cities.







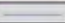
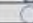


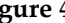

Corridor				Intersection			
Category	View	Point	Class	Category	View	Point	Class
bikTED-6		0-30	Not used	bikKTED-6		0-30	Not used
bikTED-5		30-50	bad use case	bikKTED-5		30-50	bad transition state
bikTED-4		50-60	Very uncomfortable to use	bikKTED-4		50-60	Very uncomfortable transition
bikTED-3		60-70	uncomfortable use	bikKTED-3		60-70	uncomfortable transition
bikTED-2		70-90	Comfortable use	bikKTED-2		70-90	comfortable transition
bikTED-1		90-100	Very comfortable use	bikKTED-1		90-100	Very easy transition

Figure 4. Classification and Symbolic Representation of the bikted Model

## 2.3. Parameters used in the methodology and methods of use

### 2.3.1. Parameters for corridor

Corridors are linear road segments extending from 50 meters before an intersection structure to 50 meters after the intersection approach. This study considered three types of bicycle infrastructure within corridors: separated bike paths, bike lanes, and mixed-traffic roads without specific bicycle infrastructure. According to the bicycle path regulations published by the Ministry of Environment and Urbanization in 2019, separated bike paths should have a minimum width of 190 cm, and bike lanes should be at least 175 cm wide [61]. In Turkey, especially in cities like Konya, Düzce, Istanbul, Eskişehir, and Sakarya, some compulsory adjustments were made irrespective of the regulations or due to zoning conditions. These adjustments resulted in separated bike paths narrower than 1.5 meters, bike lanes narrower than 1.2 meters, and sometimes without edge markings. Because of these factors, a thorough analysis was conducted. As shown in Table 1, since separated bike paths are far from the roadway, parameters like speed limit and vehicle clearance are not considered. Conversely, the vertical signage parameter is disregarded on roads without infrastructure (mixed traffic).

**Noise Intensity:** Studies on cycling across various countries have found noise levels between 45 and

85 dB. Numerous analyses indicate that a noise level of 65 dB or above is uncomfortable for cyclists [62], [63], [64], [65]. This study assesses noise intensity based on the average sound levels throughout a corridor. The basic noise levels are categorized as follows: 0-50 dB, 50-65 dB, and above 65 dB.

**Slope:** One of the most critical parameters in cycling is the slope, which has been examined in many studies, establishing specific criteria [66], [67]. The Dutch Bicycle Infrastructure Guide (2017), referenced in this study, adjusts slope values based on ride comfort. Accordingly, the criteria used in our study are +0-3% (unlimited), +3-5% (up to 222 meters), and above +5% (56-80 meters).

**Curbside Lane Parking:** Parking along the road is a negative condition for cyclists. Using roadside lanes as parking spaces, especially where legally prohibited, causes problems for cyclists. Various parking scenarios exist, such as perpendicular, angled, and parallel. In a survey, respondents were asked about physical cross-sections in areas with parking. A notable finding was that in areas with parking, a 3.5-meter-wide bike lane should have a 25 cm edge line, whereas a 2-meter-wide bike lane should maintain a 75 cm gap between the parked cars and the bike lane [13]. In our study, parking is expressed as a percentage of the road length along the entire corridor, with evaluations made at 0-10%, 10-30%, and 30-50% parking rates.

**Vertical Signage:** Vertical signage is essential for bicycle infrastructure, particularly for separated bike paths and roadside bike lanes. Vertical signage ensures cyclists feel safe in corridors and can approach, stop, and leave intersections more comfortably. These signs are necessary after every intersection and side road connection to increase driver awareness of cyclists. The study evaluated vertical signage using a 0-100% scale based on traffic signs and side road connections.

**Road Pavement Surface Vibration Effect:** The surface on which a bicycle is ridden is vital for safe and comfortable cycling. In Turkey, asphalt, concrete, and curb materials are generally used for bike paths, whereas asphalt is used for bike lanes and mixed traffic due to shared road use. On asphalt road platforms, minimal undulation, smoothness, and compatibility between the bicycle tire and the pavement enhance comfort. Poor pavement conditions can distract cyclists from environmental factors and require more effort. Some studies have explored different road types using experimental bicycles [33], [34]. In our study, bicycle comfort level was assessed based on the ISO-2631-1 standard, evaluating accelerations of 0-0.5 m/s<sup>2</sup>, 0.5-1 m/s<sup>2</sup>, 1-2.5 m/s<sup>2</sup>, and greater than 2.5 m/s<sup>2</sup>.

**Main Road-Secondary Road Intersection:** High intersections with side roads along a cyclist's route can compromise safety. Since separated bike paths are designed on sidewalks, intersections with side roads can pose obstacles due to height differences between the sidewalk and the road, hindering smooth cycling. The study classified side road intersections along a corridor as 0-2, 2-6, and more than six intersections.

**Speed Limit:** One of the most important factors for cyclists is the speed limit on the road. Speed limits vary according to road width and classification, and vehicle speeds must be considered to ensure cyclists feel safe. Speed has been particularly emphasized in past studies [51], [52], [59], [60]. Our study categorized speed into 0-30 km/h, 30-50 km/h, 50-82 km/h, and over 82 km/h.

**Vehicle Clearance Distance:** Another factor affecting cyclists, especially in bike lanes and mixed traffic, is the distance between them and passing vehicles. Although this distance varies with speed, anything below 100 cm is considered dangerously close, while 150 cm is considered more acceptable. This study assessed clearance distances in ranges of 0-50 cm, 50-100 cm, and 100-150 cm.

**Table 1.** Increasing efficiency according to the classification of bicycles in corridors

Parameters	Seperated Cycle Path	Bike Line	Mixed Traffic
Amount of Noise	●	●	●
Slope	●	●	●
Bicycle Path Parking	●	●	●
Vertical Sign	●	●	●
Coating Surface Vibration	●	●	●
Secondary Road	●	●	●
Intersection Status			
Speed Limit		●	●
Vehicle-Bicycle Distance		●	●

### 2.3.2. Parameters for intersection

Intersections are one of the two types of infrastructure examined in this study. In Turkey, intersections are mostly traffic-marked and signalized. In recent years, the number of modern roundabouts has increased globally and in Turkey, which has also been evaluated in this study. However, relatively few studies specifically investigate the impact of bicycle infrastructure at intersections worldwide. For example, the Munich Bicycle Usability Index [58] examines parameters such as vertical bicycle traffic lights and bicycle infrastructure.

As shown in Table 2, the study evaluates parking, intersection sight distance, intersection crossing distance, vertical bicycle signage/signaling, and the presence of bicycle infrastructure at signalized intersections, traffic-marked intersections, and modern roundabouts.

**Intersection Parking:** Parking within intersection areas is a condition that complicates cyclist crossings and creates safety risks. In Turkey, parking on approaches and within intersections is a major problem. Despite regulations under the Traffic Law stating that parking within intersections is not allowed, illegal parking is common in many cities. The approach and departure distance for intersections is taken as 50 meters. In this study, parking is expressed as a percentage of the road length throughout the intersection crossing distance, evaluated at 0-10%, 10-30%, and 30-50%.

**Intersection Sight Distance:** The sight distance and visibility at intersections are crucial for cyclists. Vertical curves, such as hills or valleys, or structures obstructing the view within the intersection pose a safety threat to cyclists approaching the intersection. While there have been no specific studies on intersection sight distance for cyclists, an urban intersection in Madrid, Spain, was evaluated for visibility from different angles, providing a reference for this study [50]. This study categorizes visibility as poor, normal, or good.

**Intersection Crossing Distance:** The intersection crossing distance is defined as the total distance a cyclist covers from a point 50 meters before entering the intersection to a point 50 meters after exiting it. Intersections with long crossing distances typically expose cyclists to greater danger due to vehicle traffic. Distances at modern and signalized intersections usually exceed 100 meters. Longer crossing distances imply more conflicts with other road users. Particularly in bike lanes and mixed traffic situations, these intersection and vehicle interactions can put cyclists in challenging positions. This study evaluated crossing distances as 0-50 meters, 50-100 meters, 100-150 meters, and over 150 meters.

**Vertical Signage or Signaling for Bicycles:** At modern roundabouts and traffic-marked intersections, vertical mini-traffic signs for bicycles should be installed to prevent cyclists' violations while crossing and alert drivers. At signalized intersections, bicycle-specific traffic signals are necessary to ensure that cyclists have their separate light system for safety, independent of vehicle signals. The Munich Bicycle Usability Index [58] considers the right-turn radius, bicycle-specific signals, horizontal markings, and designated areas for cyclists at intersections. In this study, the presence or absence of these parameters is evaluated.

**Presence of Bicycle Path:** A bicycle path at intersections is crucial for the controlled and safe crossing of cyclists, allowing them to stop and wait safely. In many instances, pedestrians and cyclists share the same crossing paths. Especially at traffic-marked and modern roundabouts, providing a dedicated bicycle path helps ensure that cyclists do not feel endangered by drivers. In this study, a bicycle path's presence is considered present or absent, depending on the infrastructure. A study mentions the importance of having separated bicycle lanes at intersections. A separated bicycle lane at an intersection has significantly reduced accidents in terms of visibility, attention, and ease of passage [68].

**Table 2.** Parameters scored according to bicycle infrastructure at intersections

Parameters	Signalized Intersection	Modern Roundabout	Intersection with Traffic Signs
Parking in the intersection	●	●	●
Sight at the intersection	●	●	●
Intersection passing distance	●	●	●
Bicycle Vertical Sign	●	●	●
Bicycle Path	●	●	●

### 3. RESULTS AND DISCUSSION

This study developed a method for bikted, which differs from previous studies by assigning weights and scores to each type of infrastructure to create a specific bikted class. This method allows for assessing how risky a particular urban road is for cycling, whether it has a dedicated bike lane, and how much of this risk can be tolerated by the user. In Turkey, there is still no standardization for urban road classification. Globally, recent studies have often referenced the Level of Traffic Stress (LTS) management system, focusing on road width and speed. Other model studies emphasize speed, curb lane volume, and width [51]. Additional models consider factors such as the type of bike lane, parking availability, and the percentage of heavy vehicles [59], [60].

The model developed in the study was examined in 2 categories. Corridors and intersections on the route where cyclists pass. Infrastructure conditions in corridors; roads without infrastructure, bicycle lanes or separated bicycle paths encountered in urban bicycle use in our country. In these 3 main road structures, different measurements were evaluated for each road structure type and parameters were determined. These are; noise, slope, parking, vertical marking, pavement vibration status, main road-secondary road junction status, speed limit and bicycle-vehicle distance status. Corridors were divided into three types according to their usage and safety status: dedicated bike lanes, shared bike lanes and protected bike paths. Dedicated bike paths were rated with 100 points (P), bike lanes with 80 points (P) and mixed traffic roads without dedicated bike infrastructure were rated with 60 points (P). Each parameter was weighted according to its impact on the infrastructure (Figure 5).

Infrastructure conditions in intersections were examined in 3 categories as signalized, modern roundabout and traffic marked. Here, different parameter evaluations were made for different types of intersections. These are; parking percentage, visibility of the intersection, distance of cyclists passing the intersection, presence of bicycle vertical markings and presence of bicycle path. Signalized intersections were rated the highest at 100 points (P) for intersections, as they are considered the safest design for cyclists in literature. Modern roundabouts, which lack a stopping system but provide a physical slowing effect, were rated at 90 points (P). In contrast, intersections regulated solely by traffic signs, without any physical slowing mechanisms, were rated at 80 points (P) (Fig. 6).

In addition, the most studied parameters in the literature for corridors in the world; parking, speed and slope were further developed in this model with field data, observations and extensive literature source studies sampling and a new model study was presented by combining road vibration status, vehicle-bicycle gap distance and sound level measurements in corridors. Similarly, although there are few studies examining the intersection crossing status of cyclists at field and model levels, in our study, the parameters of crossing distance, sight distance and parking at intersections were evaluated and the

concept of safety impact level was developed.

100			90			80		
Parameters	Separated Cycle Path		Parameters	Bike Lane		Parameters	Mixed Traffic	
	Point	Weight		Point	Weight		Point	Weight
Amount of Noise								
0-50 db	7		0-50 db	8		0-50 db	4	
50-65 db	4	7%	50-65 db	4	10%	50-65 db	2	7%
65 db and above	0		65 db and above	1		65 db and above	1	
Slope			Slope			Slope		
(+) 0-3 %	30		(+) 0-3 %	16		(+) 0-3 %	16	
(+) 3.5 % 0-222m (CROW)	10	30%	(+) 3.5 % 0-222m (CROW)	5	20%	(+) 3.5 % 0-222m (CROW)	7	27%
(+) 3% and above	1		(+) 3% and above	1		(+) 3% and above	2	
Bicycle Path Parking			Curbside Strip Parking			Curbside Strip Parking		
0<P<10%	7		0<P<10%	6		0<P<10%	8	
10<P<30%	5	7%	10<P<30%	4	7%	10<P<30%	4	13%
30<P<50%	1		30<P<50%	2		30<P<50%	2	
Vertical Sign			Vertical Sign			Coating Surface Vibration		
Traffic Sign / Secondary Road Intersection			Traffic Sign / Secondary Road Intersection			0-0.5 m/s <sup>2</sup>	9	
1	9		1	4		0.5-1 m/s <sup>2</sup>	6	15%
0.7	7	8%	0.7	3	5%	1-2.5 m/s <sup>2</sup>	3	
0.5	5		0.5	1		2.55 T m/s <sup>2</sup>	1	
0	1		0.3	0		Secondary Road Intersection Status		
Coating Surface Vibration			Coating Surface Vibration			0-2 K	6	
0-0.5 m/s <sup>2</sup>	15		0-0.5 m/s <sup>2</sup>	4		2-4 K	3	10%
0.5-1 m/s <sup>2</sup>	10	15%	0.5-1 m/s <sup>2</sup>	5		6-15 K	1	
1-2.5 m/s <sup>2</sup>	5		1-2.5 m/s <sup>2</sup>	3	10%	Speed limit		
2.55 T m/s <sup>2</sup>	1		2.55 T m/s <sup>2</sup>	1		0-30	9	
Secondary Road Intersection Status			Secondary Road Intersection Status			30-50	6	15%
0-2 K	12		0-2 K	8		50-82	3	
2-4 K	5	12%	2-4 K	3	10%	82-ve (over)	0	
6-15 K	1		6-15 K	1		Vehicle-Bicycle Distance		
			Speed limit			100-150 cm	8	
			0-30	6		50-100 cm	5	13%
			30-50	4		0-50 cm	2	
			50-82	1	7%			
			82-ve (over)	0				
			Vehicle-Bicycle Distance					
			100-150 cm	10				
			50-100 cm	4	13%			
			0-50 cm	2				

Figure 5. Bikted corridor Scoring a) Dedicated Bike Path b) Curbside Bike Lane c) Mixed Traffic (Without Bike Lane Infrastructure)

Parameters	100		90		80	
	Point	Weight	Point	Weight	Point	Weight
Parking at the intersection						
0<P<10%	20		20		18	
10<P<30%	12	20%	12	22%	10	20%
30<P<50%	6		6		4	
View at the intersection						
Poor Sight	6		6		4	
Normal Sight	16	26%	12	24%	12	24%
GoodSight	26		22		18	
Intersection Passing Distance						
0-50m	26		24		14	
50-100m	24		20		12	
100-150m	18	26%	16	27%	10	18%
150m and above	16		14		6	
Bicycle Vertical Sign						
Yes	12		10		14	
No	2	12%	2	11%	2	18%
Bicycle Path						
Yes	16		14		16	
No	2	16%	4	16%	2	20%

Figure 6. Intersection Parameters and Scoring for bikted a) Signalized Intersection b) Modern Roundabout c) Sign-Controlled Intersection

#### 4. CONCLUSIONS

In this study, a bicycle model that aims to increase bicycle use, make urban infrastructure bicycle-friendly or improve current conditions, and a bicycle specially equipped to collect data for the model were developed.

The following conclusions can be drawn regarding the Bikted model:

- The scoring system in the model was designed by the authors using data obtained from field studies and previous literature.
- For the first time in a bicycle model, corridor evaluation was performed by combining noise intensity, bicycle-vehicle gap, slope and vibration values, and the traffic impact status of the corridors at 6 levels was revealed.
- In the corridor evaluations of our study, the slope constitutes approximately one third of the score for each type of infrastructure, and corridors with high slopes cannot reach the "comfortable use" classification.
- In the corridor evaluations, separated (physical separation) bicycle paths can reach the "very

comfortable use" classification, bicycle lanes can reach the "comfortable use" classification, but corridors with mixed traffic (without bicycle infrastructure) are rated as "extremely uncomfortable use". This shows that roads without bicycle infrastructure are dangerous in terms of use.

- Measurements made with equipped bicycles may not be as reliable at intersections as the numerical data analysis presented for corridors, but still provide valuable insights for analyzing intersections.

- BikTED-3 and bikKTED-3 impact levels can be considered as acceptable levels for corridors and intersections in terms of safety, comfort and bicycle use on an urban road. However, situations below these levels are roads that need infrastructure development.

- The study may benefit municipalities, universities, provincial administrations and private institutions in terms of bicycle infrastructure investments and improvements.

This study presents a method for assessing traffic infrastructure and environmental factors in the context of urban bicycle use in Turkey. The method may require more reliable surveys or additional field studies to score infrastructure parameters. Future research should focus on collecting more user data that will contribute to the further development of the bicycle methodology.

### Declaration of Ethical Standards

Authors must follow all ethical guidelines, including authorship, citation, data reporting, and publishing original research.

### Credit Authorship Contribution Statement

**R.AYDAR:** Conceptualization, Methodology, Software, Validation, Formal analysis, Writing - Original Draft, Visualization, Prototype development

**O.N.ÇELİK:** Investigation, Resources, Writing - Review & Editing, Supervision, Project administration, FunXding acquisition

### Declaration of Competing Interest

Competing Interest is a set of conditions in which professional judgment concerning a primary interest, such as the validity of research, may be influenced by a secondary interest, such as financial gain.

### Funding / Acknowledgements

The authors were supported within the scope of the research by the Konya Technical University Scientific Research Projects Unit with Project No: 231104021.

### Data Availability

If you have made your research data available in a data repository, you can link your article directly to the dataset.

### REFERENCES

- [1] S. Eryiğit, "The place of the bicycle in the social dimension of sustainable transportation,".PhD Thesis, Selcuk University, Konya, Turkey, 2012.
- [2] Konya Sustainable Urban Mobility Plan n Project (KSHKP), Bank of Provinces, 2022.
- [3] A. Soni, K. Makde, K.Amrit, R. Vijay, R. Kumar. "Noise prediction and environmental noise capacity for urban traffic of Mumbai," Applied Acoustics,jan,p. 188, 2022.
- [4] Turkey Urban Bicycle Transportation Strategy Plan, WRI Turkey, S-41, 2022.

- [5] M. Saplıoğlu, and M.M. Aydın, "Choosing safe and suitable bicycle routes to integrate cycling and public transport system," *Journal of Transport & Health*, vol.10, pp.236-252, 2018.
- [6] V.E. Uz, and M. Karaşahin, "Bicycle in Urban Transportation," *Turkey Engineering News, Urban Transportation*, vol: 429, no.1, pp. 41-46, 2004.
- [7] S. Dündar, G. Günay, P.A. Gezginci, E. Soyer, and E. Mert, Modeling the demand for shared bicycle use. 14th Transportation Congress, İstanbul, Turkey, 2023.
- [8] K. Mert and E. V. Öcalır Akünel, "A comparison of the planning and application processes bicycle transportation in Konya," *Metu Journal of the Faculty of Architecture*, vol.27, no.1, pp.223-240, 2010.
- [9] S. Mansuroğlu, and V. Dağ, User Approaches to Bicycle Use and Bicycle Paths in Urban Transportation: Antalya Example, *City Academy*, vol.14, no 1, pp. 90-101. 2021.
- [10] L. Olmos, M. Tadeo, D. Vlachogiannis, F. Alhasoun, X. Alegre, C. Ochoa, F. Targa, and M. Gonzales, "A data science framework for planning the growth of bicycle Infrastructures," *Transportation Research Part C* 115,jun,pp.112,2020.
- [11] G. Barero, and A. Rodriguez-Valencia, "Asking the user: a perceptual approach for bicycle infrastructure design," *International Journal of Sustainable Transportation*, vol.16:3, no.1, pp. 246-257,2022.
- [12] N. Fournier, S. Bakhtiari,Valluru, N. Campbell, E. Christofa, S. Roberts, and M. Knodler, "Accounting for drivers' bicycling frequency and familiarity with bicycle infrastructure treatments when evaluating safety," *Accident Analysis and Prevention*,Feb.,pp. 137, 2020.
- [13] R. Stülpnagel, and N. Binnig, "How safe do you feel? A large-scale survey concerning the subjective safety associated with different kinds of cycling lanes," *Accident Analysis and Prevention*, Mar.,pp. 167, 2022.
- [14] C. Zhao, T. Carstensen, T. Nielsen, and T. Olafsson, "Bicycle-friendly infrastructure planning in Beijing and Copenhagen between adapting design solutions and learning local planning cultures," *Journal of Transport Geography*, vol. 68, no.1, pp. 149-159, 2018.
- [15] L. Wysling, and R. Purves, "Where to improve cycling infrastructure? Assessing bicycle suitability and bikeability with open data in the city of Paris," *Transportation Research Interdisciplinary Perspectives*, Feb, pp. 15, 2022.
- [16] B. Janssen, P. Schepers, H. Farah, and M. Hagenzieker, "Behaviour of cyclists and pedestrians near right angled, sloped and levelled kerb types: Do risks associated to height differences of kerbs weigh up against other factors?," *Ejtur*, vol.18, no.1, pp. 360-371, 2018.
- [17] O'Holleran C, and Hull A, "Bicycle infrastructure: can good design encourage cycling?," *Urban, Planning and Transport Research*, vol. 2, no.1, pp.369-406, 2014.
- [18] A. Knight, and S. Charlton, "Protected and unprotected cycle lanes' effects on cyclists' behaviour," *Accident Analysis and Prevention*, Jun, pp. 171, 2022.
- [19] P. Koh, and D. Wong, "Influence of infrastructural compatibility factors on walking and cycling route choices," *Journal of Environmental Psychology*, vol.36, no.2, pp. 202-213, 2013.
- [20] A. Karakaya, T. Ritter, F. Biessmann, and D. Bermbach, "CycleSense: Detecting near miss incidents in bicycle traffic from mobile motion sensors," *Pervasive and Mobile Computing*, Apr, pp. 90, 2023.
- [21] P. Furth, B. Sadeghinassr, and L. Moreno, "Slope stress criteria as a complement to traffic stress criteria, and impact on high comfort bicycle accessibility," *Journal of Transport Geography*, Elsevier, vol.112, 2023.
- [22] N. Kovacsova, W. Valkveld, J. Winter, and M. Hagenzieker "PC-based hazard



- anticipation training for experienced cyclists: Design and evaluation," *Safety Science*, Dec, pp.1-16, 2020.
- [23] G. Boisjoly, U. Lachapelle, and A. Geneidy, "Bicycle network performance: Assessing the directness of bicycle facilities through connectivity measures, a Montreal, Canada case study," *International Journal of Sustainable Transportation*, Apr, pp.1-15, 2019.
- [24] J. Bosen, H. Fuchte, and C. Scholten, "Cycling to work and making cycling work: What makes committed utility cyclists despite perceived risks of air pollution and traffic?," *Journal of Transport & Health*, vol. 28, no.1, pp.101519, 2023.
- [25] N. Ferencak, and W. Marshall, "Traffic safety for all road users: A paired comparison study of small & mid-sized U.S. cities with high/low bicycling rates," *Journal of Cycling and Micromobility Research*, vol. 2, no. 2, pp. 100010, 2024.
- [26] S. Useche, L. Montoro, J. Sanmartin, and F. Alonso, "Healthy but risky: A descriptive study on cyclists' encouraging and discouraging factors for using bicycles, habits and safety outcomes," *Transportation Research Part*, vol. 62, no. F, pp. 587–598. 2019.
- [27] P. Apparicio, M. Carrier, J. Gelb, A. Seguin, and S. Kingham, "Cyclists' exposure to air pollution and road traffic noise in central city neighbourhoods of Montreal," *Journal of Transport Geography*, vol. 57, pp. 63-69, 2016.
- [28] H. Ising, and B. Kruppa, "Health Effects caused by Noise: Evidence in the Literature from the Past 25 Years," *Noise- Health*, vol.6, no.22, pp. 5-13, 2004.
- [29] A. Soni, K. Makde, K. Amrit, R. Vijay, and R. Kumar "Noise prediction and environmental noise capacity for urban traffic of Mumbai," *Applied Acoustics*, vol. 188, no.3, pp. 108516, 2022.
- [30] P. Begou, P. Kassomenos, and A. Kelessis, "Dataset on the road traffic noise measurements in the municipality of Thessaloniki," *Data in brief*, vol.29, pp. 105214, 2020.
- [31] P. Apparicio, and J. Gelb, "Cyclists' Exposure to Road Traffic Noise: A Comparison of Three North American and European Cities," *Acoustics 2020*, vol. 2, pp. 73–86. 2020.
- [32] J. Gao, A. Sha, Y. Huang, L. Hu, Z. Tong, and W. Jiang, "Evaluating the cycling comfort on urban roads based on cyclists' perception of vibration," *Journal of Cleaner Production*, vol.192, pp. 531-541, 2018.
- [33] M. Olieman, R. Perianu, and M. Perianu, "Measurement of dynamic comfort in cycling using wireless acceleration sensors," *Procedia Engineering*, vol. 34, pp. 568-573, 2012.
- [34] H. Gomes, and D. Savionek, "Measurement and evaluation of human exposure to vibration transmitted to hand-arm system during leisure cyclist activity," *Brazilian Journal of Medical Engineering*, vol. 30, pp. 291-300, 2014.
- [35] A. Bergström, and R. Magnusson. "Potential of transferring car trips to bicycle during winter," *Transportation Research Part A*, vol. 37, no. 8, pp. 649–666, 2003.
- [36] J. Mackenzie, J. Dutschke, and G. Ponte, "An investigation of cyclist passing distances in the Australian Capital Territory," *Accident Analysis and Prevention*, May, 2021.
- [37] B.Beck,D.Chong,D.J.Olivier,J.Perkins,M.Tsay,A.Rushford,A.Li,L.Cameron,P.Fry,R.Johns on, "How much space do drivers provide when passing cyclists? Understanding the impact of motor vehicle and infrastructure characteristics on passing distance," *Accident Analysis and Prevention*, vol.128, pp. 253-260, 2019.
- [38] I. Walker, "Drivers overtaking bicyclists: Objective data on the effects of riding position, helmet use, vehicle type and apparent gender," *Accident Analysis and Prevention*, vol. 39, no.2, pp. 417–425, 2007.
- [39] R. Stülpnagel, R. Hologa, and N. Riachi, "Cars overtaking cyclists on different urban road types Expectations about passing safety are not aligned with observed passing distances," *Transportation Research Part F: Psychology and Behaviour*, vol. 89, pp. 334-346, 2022.

- [40] P. Apasnore, "Bicycle-Vehicle Interactions at Mid-Sections of Mixed Traffic Streets: Examining Passing Distance and Bicycle Comfort Perception", M.S. thesis, Carleton University, Carleton, Canada, 2016.
- [41] M. Moller, S. Useche, F. Siebert, and K. Janstrup, "What differentiates e-bike riders from conventional cyclists in Denmark? A user-based study," *Journal of Transport & Health*, vol. 34, 2024.
- [42] J. Xu, C. Ji, B. Li, P. Jiang, K. Qin, Z. Ni, X. Huang, R. Zhong, L. Fang, M. Zhao, "Riding practices of e-bike riders after the implementation of electric bike management regulations: An observational study in Hangzhou, China," *Heliyon*, Feb, 2024.
- [43] J. Kruijf, D. Lierop, D. Ettema, M. Kroesen, and M. Dijst, "E-cycling intention versus behavioral change: Investigating longitudinal changes in e-cycling intention and actual behavior change in daily commuting," *Journal of Cycling and Micromobility Research*, Dec, 2024.
- [44] L. Bai, and N. Sze, "Red light running behavior of bicyclists in urban area: Effects of bicycle type and bicycle group size," *Travel Behaviour and Society*, vol. 21, pp. 226–234, 2020.
- [45] P. Singleton, and N. Poudel "Bicycling comfort at roundabouts: Effects of design and situational factors," *Transportation Research Part F: Psychology and Behaviour*, vol. 94, pp. 227–242, 2023.
- [46] L. Deeter, D. Hurwitz, B. Russo, E. Smaglig, and S. Kothuri, "Assessing the impact of three intersection treatments on bicyclist safety using a bicycling simulator," *Accident Analysis and Prevention*, Jan, 2023.
- [47] S. Zangenehpour, J. Strauss, L. Moreno, and N. Saunier, "Are signalized intersections with cycle tracks safer? A case-control study based on automated surrogate safety analysis using video data Sohail," *Accident Analysis and Prevention*, vol. 86, pp. 161–172, 2016.
- [48] A. Mohammadi, G. Piccinini, and M. Dozza, "How do cyclists interact with motorized vehicles at unsignalized intersections? Modeling cyclists' yielding behavior using naturalistic data," *Accident Analysis and Prevention*, Sep, pp. 1-8, 2023.
- [49] A. Ng, A. Debnath, and K. Heesch, "Cyclist' safety perceptions of cycling in frastructure at un-signalised intersections: Cross-sectional survey of Queensland cyclists," *Journal of Transport&Health*, vol. 6, pp. 13–22, 2017.
- [50] K. Gomez, and M. Castro, "Analysis of sight distances at urban intersections from a vulnerable users' approach: A case study," *Transportation Research Procedia*, vol. 45, pp. 226–233, 2020.
- [51] A. Sorton and T. Walsh, "Cycling Stress Level as a Tool to Evaluate Urban and Suburban Cycling Compatibility," *Transportation Research Record*, vol. 1438, pp.17-24, 1994.
- [52] M. Mekuria, P. Furth, and H. Nixon "Low-Stress Bicycling and Network Connectivity," Report, pp. 11-19, Mineta Transportation Institute College of BusinessSan José State University, 2012.
- [53] L. Hagen, and K. Ralph, "Will parents let their children bike on "low stress" streets? Validating level of traffic stress for biking," *Transportation Research*, vol. 65, pp. 280–291, 2019.
- [54] K. Wang, G. Akar, K. Lee, and M. Sanders, "Commuting patterns and bicycle level of traffic stress (LTS): Insights from spatially aggregated data in Franklin County," *Journal of Transport Geography*, vol. 86, 2020.
- [55] C. Bearn, C. Mingus, and K. Watkins, "An adaption of the level of traffic stress based on evidence from the literature and widely available data," *Research in Transportation Business & Management*, vol. 29, pp. 50–62, 2018.

- [56] A. Imani, E. Miller, and S. Saxe, "Cycle accessibility and level of traffic stress: A case study of Toronto," *Journal of Transport Geography*, vol. 80, no.2, 2019.
- [57] Urban design consultancy based in Copenhagen, Brussels and Montréal."Copenhagenize Index 2019". Available:<https://copenhagenizeindex.eu/cities/copenhagen>. [Accessed: Nov. 12, 2019].
- [58] J. Querg, A. Keler, and G. Grigoropoulos, "The Munich Bikeability Index: A Practical Approach for Measuring Urban Bikeability", *Sustainability*, vol. 13, pp. 428, 2021.
- [59] B. Landis, V. Vattikuti, and M. Brannick "Real-Time Human Perceptions Toward a Bicycle Level of Service," *Transportation Research Record*, vol. 1578, pp.119-126, 1997.
- [60] D. Harkey, D. Reinfut, and M. Knuiman, "Development of the Bicycle Compatibility Index," *Transportation Research Record*, vol. 1636, pp. 13-20, 1998.
- [61] Ministry of Environment and Urbanization, *Bicycle Lanes Regulation*, vol. 30976, p.9, 12 Dec 2019.
- [62] J. Bosen, H. Fuchte, and C. Scholten, "Cycling to work and making cycling work: What makes committed utility cyclists despite perceived risks of air pollution and traffic?," *Journal of Transport & Health*, vol. 28, p. 101519, 2023.
- [63] P. Apparicio, M. Carrier, J. Gelb, A. Seguin, and S. Kingham, "Cyclists' exposure to air pollution and road traffic noise in central city neighbourhoods of Montreal," *Journal of Transport Geography*, vol. 57, pp. 63-69, 2016.
- [64] H. Ising, and B. Kruppa, "Health Effects caused by Noise: Evidence in the Literature from the Past 25 Years," *Noise- Health*, vol. 6, no. 22, pp. 5-13, 2004.
- [65] J. Gelb, and P. Appricio, "Cyclists' exposure to air and noise pollution, comparative approach in seven cities," *Transportation Research disciplinary Perspectives*, vol. 14, 2022.
- [66] P. Valenzuela, M. March, X. Muriel, M. Zabala, A. Lucia, J. Pallares, D. Barranco-Gil, "Road gradient and cycling power: An observational study in male professional cyclists," *Journal of Science and Medicine in Sport*, vol. 25, no. 12, pp. 1017-1022, 2022.
- [67] P. Furth, B. Sadeghinasr, and L. Moreno, "Slope stress criteria as a complement to traffic stress criteria, and impact on high comfort bicycle accessibility," *Journal of Transport Geography*, vol. 112, p.103708, 2023.
- [68] Morrisson, C., Thompson, J., Kondo, M., Beck, B. 2019, On-road bicycle lane types, roadway characteristics, and risks for bicycle crashes, *Accident Analysis and Prevention*, 123, 123-131.



## A COMPARATIVE STUDY OF DIVERSE AUTOENCODER MODELS IN LOCAL GEAR PITTING FAULT DIAGNOSIS

<sup>1,\*</sup>Mustafa YURTSEVER , <sup>2</sup>Rafet Can ÜMÜTLÜ , <sup>3</sup>Hasan ÖZTÜRK 

<sup>1</sup>İzmir Democracy University, Faculty of Economics and Administrative Sciences, Department of Management Information Systems, İzmir, TÜRKİYE

<sup>2</sup>TOFAŞ Turkish Automobile Factory Joint-Stock Company, Research & Development Center, Propulsion Systems, İzmir, TÜRKİYE

<sup>3</sup>Dokuz Eylül University, Faculty of Engineering, Department of Mechanical Engineering, İzmir, TÜRKİYE  
<sup>1</sup>[mustafa.yurtsever@idu.edu.tr](mailto:mustafa.yurtsever@idu.edu.tr), <sup>2</sup>[rafet.canumutlu@tofas.com.tr](mailto:rafet.canumutlu@tofas.com.tr), <sup>3</sup>[hasan.ozturk@deu.edu.tr](mailto:hasan.ozturk@deu.edu.tr)

### Highlights

- Gearbox pitting faults occur frequently in high-torque industrial systems.
- Vibration analysis is a common method for diagnosing gear pitting faults.
- Deep learning is increasingly used for gear pitting fault classification.
- Autoencoder models like CAE, SAE, and VAE extract gear pitting features.
- Sparse Autoencoder is efficient for diagnosing gear pitting using raw data.



## A COMPARATIVE STUDY OF DIVERSE AUTOENCODER MODELS IN LOCAL GEAR PITTING FAULT DIAGNOSIS

<sup>1,\*</sup>Mustafa YURTSEVER , <sup>2</sup>Rafet Can ÜMÜTLÜ , <sup>3</sup>Hasan ÖZTÜRK 

<sup>1</sup>İzmir Democracy University, Faculty of Economics and Administrative Sciences, Department of Management Information Systems, İzmir, TÜRKİYE

<sup>2</sup>TOFAŞ Turkish Automobile Factory Joint-Stock Company, Research & Development Center, Propulsion Systems, İzmir, TÜRKİYE

<sup>3</sup>Dokuz Eylül University, Faculty of Engineering, Department of Mechanical Engineering, İzmir, TÜRKİYE  
[1mustafa.yurtsever@idu.edu.tr](mailto:mustafa.yurtsever@idu.edu.tr), [2rafet.canumutlu@tofas.com.tr](mailto:rafet.canumutlu@tofas.com.tr), [3hasan.ozturk@deu.edu.tr](mailto:hasan.ozturk@deu.edu.tr)

(Received: 21.10.2024; Accepted in Revised Form: 20.12.2024)

**ABSTRACT:** Gearbox, which is one of the most important and frequently used components among mechanical power transmission systems, has often been observed to occur in gear surface pitting faults in industrial applications that require high torque. For the diagnosis of gear pitting faults, vibration analysis is one of the commonly utilized techniques. Recently, there has been an increasing interest in applying deep learning approaches for classification and learning feature representations. Deep learning provides an excellent opportunity to integrate vibration signals for gear pitting fault diagnosis. Therefore, in this study, autoencoder models Contractive Autoencoder (CAE), Sparse Autoencoder (SAE) and Variational Autoencoder (VAE) are used to extract deep feature representations of gear pitting data. Without using any additional feature extraction techniques, in this study uses the raw vibrational data directly to identify the local gear pitting faults. Experimental results have shown that Sparse Autoencoder is a viable and efficient feature extraction method and provides a new research method for gear pit fault diagnosis.

**Keywords:** Contractive Autoencoder, Sparse Autoencoder, Variational Autoencoder, Local Gear Pitting, Fault Diagnosis

### 1. INTRODUCTION

In terms of cost and downtime, mechanical system maintenance is critical for the industry, since unanticipated faults can result in significant losses of production, energy, and quality, as well as damage to machine parts, unscheduled downtimes, and higher expenses. The main advantage of a monitoring technique is that it makes it possible to detect escalating problems in the machine before they become serious. As a result, vibration analysis is a practical and frequently chosen technique for evaluating the conditions of a machine while it is in operation.

For industrial applications, mechanical power transmission systems in machine components are critical. Among mechanical power transmission systems, the gearbox is one of the most often utilized components. Gear systems are used to transfer rotation or power from one shaft to another at a predetermined rate. In the absence of any flaws in the gear system, these criteria may be accomplished effectively. Manufacturing flaws, beginning torques, overload, gear misalignment, lubrication debris, bearing failures, resonant vibrations, and other factors can all increase the magnitude of forces on a gearbox's tooth surface [1]. As a result of all these factors, some teeth may be subjected to a greater and more variable load than their capacity. Surface faults will develop after a specific number of working cycles if the surface tension of the teeth exceeds the fatigue limit of the gear material. Wear, cracks, pitting and tooth breakage are common surface problems in gears [2]. It has been frequently observed that pitting faults occur on the gear surface, especially in industrial applications that require high torque.

In predictive maintenance studies, data is collected by various methods and used in analysis. Infrared thermography [3], lubricant analysis [4], vibration analysis [5,6], acoustic emission [7,8], motor current signature analysis [9], and other condition monitoring techniques may all be used to identify faults in

\*Corresponding Author: Mustafa YURTSEVER, [mustafa.yurtsever@idu.edu.tr](mailto:mustafa.yurtsever@idu.edu.tr)

industrial systems. Among these techniques, vibration analysis is the most widely used for gearbox condition monitoring. The reason for this is that the failures on the teeth spoil the gear teeth surface and the unwanted forces that occur during meshing from these damaged areas cause vibration [10]. Based on this information, by measuring and analyzing the vibration of a gearbox, it is possible to determine the type of fault, which gear pair it is on in the gearbox, and the severity of the defect [11].

Extreme noise significantly impacts the vibration data collected from gearboxes, making it challenging to accurately interpret the signals. As a result, conventional vibration analysis methods, such as time domain and frequency domain analysis, become less effective in detecting faults within the gearbox. The presence of high levels of noise obscures the patterns that these methods rely on, complicating the identification of potential issues [12,13]. To handle fault detection difficulties, artificial neural networks (ANN) [6,14], support vector machines (SVM) [15], genetic algorithms (GA) [16], signal decomposition approaches [17], and support vector data descriptions [18] have all been developed recently. According to studies, using these approaches, it is feasible to interpret the machine's status. As a result, these categorization algorithms have become increasingly important in recent years.

In recent years, researchers have a high interest in deep learning in different fields. Deep learning uses multi-layer structures to extract hidden information from a dataset for classification or other purposes [19]. Deep learning excels at dealing with big data compared to traditional feature extraction methods. Signals collected in diagnostic problems are often affected by various forms of noise. The success of deep learning methods in noise removal and robust feature extraction increases the studies.

Chen, et al. proposed a fused-stacked AEs for planetary gear fault diagnosis method based on autoencoder methods [20]. The method is capable of learning features from raw data. Qu, et al. proposed a method for detecting gear pitting failures that incorporates dictionary learning in sparse coding into an autoencoder (AE) network [21]. This method is regarded as an adaptive feature extraction method for detecting machinery faults. Li, et al. presented a novel method for gear pitting fault diagnosis using stacked autoencoder and Gauss-Binary restricted Boltzmann machine (GBRBM) [22]. The GBRBM layer is used to process continuous time domain vibration signals. Li, et al. proposed a method for integrating vibration and acoustic emission signals using convolutional neural network (CNN) and gated recurrent unit (GRU) networks [23]. The results obtained using the presented method are more accurate than those obtained using the CNN or GRU network alone. The deep sparse autoencoder method is highly effective in diagnosing various pitting conditions in gear systems. It can also clearly illustrate trends in the severity of gear wear failures, offering valuable insights into the progression of damage. This method enables the detection and differentiation of fault levels with greater precision compared to traditional approaches [24]. Li, et al. presented a method for gear pitting fault diagnosis that integrated sparse autoencoder and deep belief network [25]. In the study the normalized frequency domain signals were used as the input.

Unsupervised learning algorithm, which is represented by deep learning method, especially AE, has a different structure from traditional neural networks. Deep learning can discover the hidden correlation between the data passed into the model. It can extract compressed features of input data without human intervention. Another diagnostic issue is the utilization of nonlinear and high-dimensional data. While having more data appears to be a benefit in terms of obtaining more information, it is challenging to put to good use. Dimensional reduction to create a smaller representation of higher-dimensional data which makes it easier to identify and store high-dimensional data is one technique of overcoming this difficulty. The autoencoder allows for greater data representation as well as reduced data [26].

The majority of the pitting diagnostic approaches listed above entail a feature extraction and feature selection process. For many years, vibration signals have been a key tool in diagnosing pitting faults in mechanical systems. Numerous signal processing and analysis methods have been developed and applied to extract valuable information from vibration data, allowing for the detection and monitoring of pitting-related issues in machinery like gearboxes and rotating equipment. These methods play an essential role in identifying fault patterns and assessing the condition of mechanical components. Recent advances in deep learning offer opportunities to use vibration signals raw. It eliminates the need for additional operations such as converting the time domain signals to the frequency domain.

Due to its higher performance when dealing with complicated, large-scale data, deep learning is a good choice for diagnostics. This paper proposes a method for diagnosis of local gear pitting based on stacked autoencoder models. In the proposed method, the input set created with various AE models. Three types of stacked network architectures are compared for gear pitting fault diagnosis. Such comparisons are rare in literature and can be extremely valuable to researchers and industry professionals. These comparisons can help us better understand the performance, efficiency and learning capacity of different stacked network structures, which can contribute to better design of future studies and applications.

## 2. MATERIAL AND METHODS

### 2.1. AutoEncoder

An autoencoder is a type of neural network designed to replicate the input data at the output layer. An autoencoder is a specialized neural network architecture used primarily for unsupervised learning. Its main purpose is to copy the input data and reproduce it at the output layer. The network consists of two parts: an encoder that compresses the input into a lower-dimensional representation, and a decoder that reconstructs the original input from this compressed form. By forcing the model to learn an efficient encoding, it can capture key features and patterns within the data, often useful for tasks like dimensionality reduction, feature extraction, and anomaly detection. At this point, the data output by the hidden layer units is the low-dimensional representation of the original data, containing all of the data's information. The autoencoder structure is shown in Figure 1.

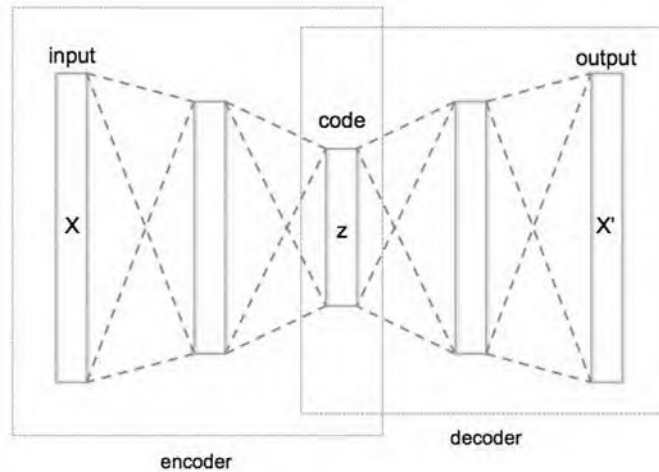


**Figure 1.** The Structure of an Autoencoder

The encoder network performs feature transformation on the input data. High-dimensional data is first compressed to extract its core features, then the decoder network uses this compressed data to generate an output similar to the original input. Assuming that there are  $n$  unlabeled training samples  $x = \{x_1, x_2, x_3, \dots, x_n\}$ . The encoder and decoder processes of AE are as follows:

$$h = f(Wx + b(1)) \quad (1)$$

$$x' = f(Wh + b(2)) \quad (2)$$

A conventional neural network with an activation function serves as the representation of the encoding network, in Eq. 1.  $H$  represents the latent dimension in Eq. 1.  $W$  is the weight matrices,  $b(1)$  and  $b(2)$  are the bias vectors, and  $f$  is the activation function. The decoding network can be represented similarly. It is expressed by varying weights, biases, and activation functions in Eq. 2.

## 2.2. Contractive AutoEncoder

CAE is a version of the classic AE that improves the resilience of the training set against noisy perturbations [27]. As a regularization term, a Frobenius norm of Jacobian is used. By adding a penalty to the Frobenius norm of the Jacobian matrix of the hidden features with respect to the inputs, the Contractive Autoencoder (CAE) encourages the model to learn more robust and stable representations. This regularization constrains how much the hidden features can change in response to small input variations, which helps the model capture the essential underlying factors in the data. As a result, CAE becomes a powerful tool for extracting meaningful, robust hidden features, making it particularly useful in tasks that require stable feature extraction under noisy or complex conditions [28].

CAE penalizes the sensitivity to input, which is measured by, in order to learn invariant and robust feature representation. A CAE is derived by augmenting the autoencoder's reconstruction loss with a regularization term. This term is computed as the Frobenius norm of the Jacobian matrix that captures the relationship between hidden layer activations and input variations, which is represented as

$$\|J_f(x)\|_F^2 = \sum_{i=1}^k \sum_{j=1}^e \left( \frac{\partial h_j(x)}{\partial x_i} \right)^2 \quad (3)$$

The total loss function can be stated numerically as:

$$L(x, x') + \lambda \|J_f(x)\|_F^2 \quad (4)$$

where  $\lambda$  is the penalty term parameter that regulates the penalty term's and reconstruction fault's relative relevance. The disturbance of the input in all directions can be decreased by adding the penalty term to the loss function, achieving the goal of anti-noise and therefore strengthening the robustness of the recovered features.

## 2.3. Sparse Autoencoder

A sparse autoencoder is a type of artificial neural network commonly used in the field of deep learning. Its primary objective is to represent and extract features from input data. An autoencoder typically consists of two main components: an encoder and a decoder. In the case of a sparse autoencoder, the concept of sparsity is introduced during the learning process, ensuring that the majority of activations in the model are close to zero. This encourages the model to learn more general and meaningful features, making it more resistant to noise. Sparsity aims to improve the feature extraction process, leading to more effective and learnable representations. One of the traditional methods, SAE penalizes the hidden unit biases in order to learn relatively sparse features [29]. The SAE emerges from augmenting the basic autoencoder's cost function with a sparsity penalty term. This modification enables the network to discover more abstract and meaningful compressed representations than what a standard autoencoder can achieve[30].

$$J_{\text{sparse}}(W, b) = J(W, b) + \beta \sum_{j=1}^{S_2} KL(p || \hat{p}_j) \quad (5)$$

The sparsity penalty term's weight is set by  $\beta$ . It is necessary to determine  $W$  and  $b$  ideal parameters during the coding procedure. Since  $W$  and  $b$  are directly related to the sparse cost function presented in Eq. (5), these two parameters can be obtained by solving the sparse cost function by minimizing  $J_{\text{sparse}}(W, b)$ .



### 2.4. Variational Autoencoder

As a powerful generative modeling tool in machine learning and deep learning, a VAE can learn the underlying distribution of data and generate new samples similar to the training data. VAEs are designed to learn a probabilistic representation of input data, particularly in the context of unsupervised learning. VAEs differentiate themselves from classical autoencoders by implementing a stochastic encoding process, where the latent space is characterized by probability distributions rather than deterministic encodings [31], often assuming a Gaussian distribution. This enables the generation of diverse and realistic samples during the decoding process. VAEs incorporate a loss function that not only measures the reconstruction error but also includes a term for the divergence between the learned latent distribution and a predefined prior distribution, usually a standard normal distribution. This dual-loss structure encourages the model to learn a compact and smooth representation of the data, making VAEs suitable for tasks like image generation, data synthesis, and latent space interpolation.

Real samples are encoded to latent vectors using the variational inference theory. As long as the vectors follow the Gaussian distribution, they effectively preserve the deep properties of the original data and transfer to the training dataset's distribution. The data that the decoder has deciphered will then make more sense and resemble the original data somewhat closely [32]. The most significant difference between a Variational Autoencoder (VAE) and a standard Autoencoder (AE) lies in the presence of a sampling layer. In a standard AE, there is no such sampling mechanism; the latent space is directly encoded from the input. In contrast, VAEs introduce a probabilistic approach by including a sampling layer, where latent variables are sampled from a distribution, typically a Gaussian. This enables VAEs to generate new data that closely resembles the original input. To achieve this, the VAE optimizes the marginal likelihood of the data, as demonstrated by the maximization of the marginal distribution, such as in Eq. 6. This probabilistic framework allows VAEs to generate more diverse and realistic data compared to standard AEs.

$$p_{\theta}(x) = \int p_{\theta}\left(\frac{x}{z}\right) p_{\theta}(z) dz \tag{6}$$

where  $p_{\theta}(z)$  denotes the previous distribution of hidden variables  $z$ , and  $p_{\theta}(x|z)$  reflects the reconstruction of the original data  $x$  through a hidden variable  $z$ . The variational autoencoder structure is shown in Figure 2.

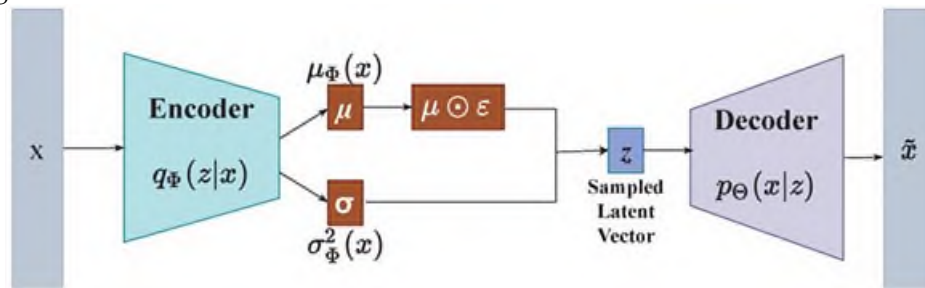


Figure 2. Variational autoencoder [33]

### 2.5. The General Procedure of the Proposed Method

A stacked autoencoder is constructed by connecting multiple autoencoders in sequence, one after the other. In this structure, the output of one encoder layer becomes the input for the next encoder layer. This process enables the network to learn progressively more abstract and higher-level feature representations of the input data at each layer. As each successive layer compresses the information further, stacked autoencoders are particularly useful for tasks that require deep feature extraction or hierarchical data representation. To acquire access to the optimum connection weights and bias values of the complete stacked auto-encoder network, the greedy layer-wise pre-training approach is utilized. The back-

propagation algorithm is mostly used in the network training section to alter the network's topology and hyper parameters. The optimization of weights and biases using the backpropagation algorithm can be significantly enhanced by employing a greedy layer-wise pre-training approach. This method involves initializing the network in a layer-by-layer manner, where each layer is trained independently before integrating it into the full network. Typically, unsupervised learning techniques like autoencoders are utilized during the pre-training phase to capture the hierarchical features in the data. Once pre-training is complete, the network undergoes fine-tuning using back propagation, which adjusts the weights and biases to minimize the overall loss function. This approach mitigates issues like vanishing gradients in deep networks, accelerates convergence, and improves generalization by providing a better starting point for the optimization process. The hyperparameters, such as the number of layers and neurons in each layer, were determined through a combination of domain knowledge and experimental validation. Initially, a range of configurations was explored based on commonly used heuristic values (e.g., powers of 2, such as 256 and 128 neurons). These configurations were evaluated using a separate validation dataset to identify the architecture that yielded the best performance. This iterative process ensured that the selected hyperparameters effectively balanced model complexity and generalization capability.

The purpose of the method used in the study is to classify the local gear pitting faults. The accelerometer sensor is utilized to gather the raw vibration signals of the gear in the initial data acquisition step. The complete set of collected vibration data is systematically divided into three subsets: the largest portion (60%) is allocated for training, while the remaining data is equally split between validation and testing (20% each). The collected data has been normalized for better training in the deep learning method. Test data is used to validate the model. The deep learning architecture has the capacity to turn several hidden layers into complicated nonlinear transformations. The effective deep features can be learned directly from the raw vibration signal using the layer-by-layer learning approach for deep features. The extracted deep features of each pit gear condition in each concealed layer are becoming more distinguishable. The gear pitting data set, which has 335 inputs, will be used in this instance. The encoder has 256 hidden neurons in its hidden layer, followed by 128 neurons in its center hidden layer. Because the model is symmetrical, the decoder also has an output layer with 335 neurons and a hidden layer with 256 neurons. As the number of hidden layers increases, stacked autoencoders are constructed. It implies that more than one input value will be compressed. We want to improve feature extraction performance by adjusting the stacked autoencoder's input value and hyperparameters. The deep model setup is finished after adding the last softmax layer. The structure of the proposed model is shown in Figure 3.

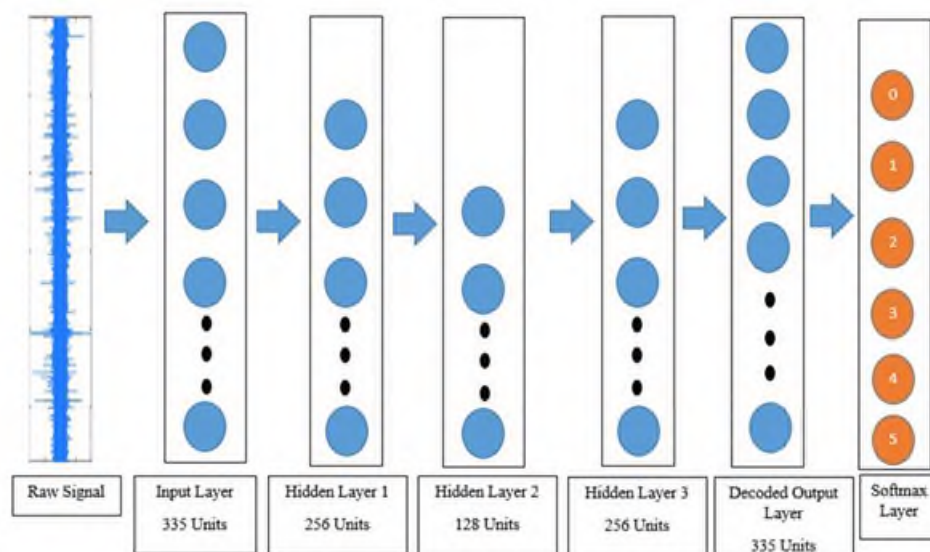


Figure 3. The Structure of Proposed Model

## 2.5. Experimental Setup

A two-stage industrial helical gearbox is employed in the experiment as illustrated in Figure 4. The whole set of helical gears is built from induction case-hardened steel. To avoid the negative impacts of misalignment, the alternating-current (AC) motor and direct-current (DC) generator are coupled via belt pulley contact mechanisms. The first-stage pinion gear has 29 teeth that mesh with a 40-tooth wheel. The second-stage pinion gear, which is driven directly by a 40-tooth wheel, has 13 teeth that mesh with a 33-tooth wheel. The 2.2 kW load capacity of the DC was substantially lower than the almost 8.1 kW load capacity of the gearbox employed, which was fed by a generator whose output was used to supply an adjustable resistor bank. For this reason, the face width of the pinion test gear was reduced from 12 mm to 4 mm, allowing it to be tested under reasonably high load conditions. This adjustment was made to ensure that the gear could endure the applied load without exceeding practical testing limits, enabling more accurate analysis of its performance under stress [34].

The vibration signals generated by the gears were measured using two [PCB 352A76] accelerometers, which are designed for vibration measurements within a frequency range of 5–16,000 Hz. These accelerometers were mounted mutually perpendicular to each other on the input shaft bearing housings to minimize the effects of the transmission path, as illustrated in Figure 4. A PCB 480C02 signal conditioner was employed to amplify the outputs from the accelerometers [34].

The position of the input shaft was monitored using a 5V DC ME4-S12L-PA inductive sensor, which generates a single pulse per revolution. All signals from the accelerometers and the positioning sensor were sampled at an appropriate rate and recorded using a National Instruments (NI DAQ Card 6036E) data acquisition system, with data collection and processing conducted through LabVIEW 7.0 software [34].

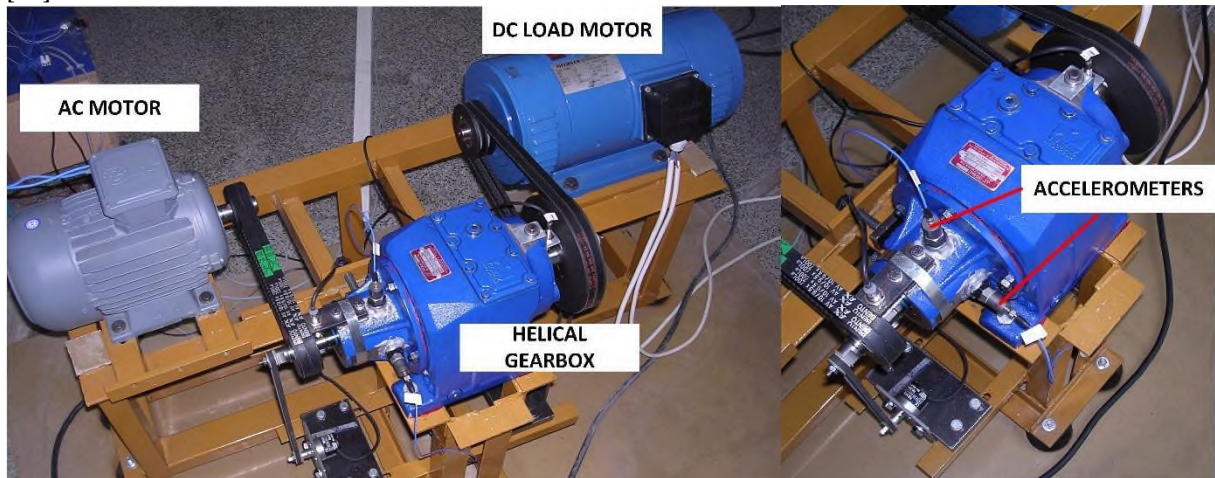


**Figure 4.** Experimental Setup With Helical Gearbox [34]

The operating settings of the experiments are given in Table 1. These settings were maintained throughout each test for all scenarios.

**Table 1.** Characteristics of the helical gearbox [34]

	First stage	Second stage
<b>Number of teeth</b>	29/40	13/33
<b>Normal module (mm)</b>	1.25	2.5
<b>Pressure angle (o)</b>	20	20
<b>Profile shift (pinion/wheel)</b>	+0.325/+0.259	+0.437/+0.340
<b>Helix angle (o)</b>	30	15

As a consequence of shock or cyclic load fluctuation, the specified gear load may be exceeded, and certain gear teeth may be subjected to a load greater than the gear's capacity. Pitting faults on the tooth

surfaces that are subjected to a greater load may develop over time in such instances. In the first stage, an electro-erosion machine was used to create a simulated surface defect resembling pitting on the 29th teeth of the pinion gear. These pitting faults occur as an initial fault and then recur on the teeth, increasing the severity of the failure. As illustrated in Figure 5b, a circular hole with a diameter and depth of roughly 0.7 mm and 0.1 mm was seeded into a single tooth surface. This gear tooth, called as the center tooth, was positioned so that it meshed with the pinion at about 270° pinion rotations. To represent the progression of the fault, the number of pits on the main tooth surface is raised to three, and its two neighbor teeth are pitted with one pit, as illustrated in Figure 5c. As illustrated in Figure 5d, the number of pits on main teeth is raised to five, and two pits are placed on both of the other two neighbor tooth surfaces in the third stage of fault simulation. The severity of the faults is doubled in the fourth step by increasing the number of pits on these teeth, as seen in Figure 5e. The number of pits was increased during the last stage of pitting development, and the surface of the center tooth is entirely covered by severe pitting markings, as illustrated in Figure 5f.

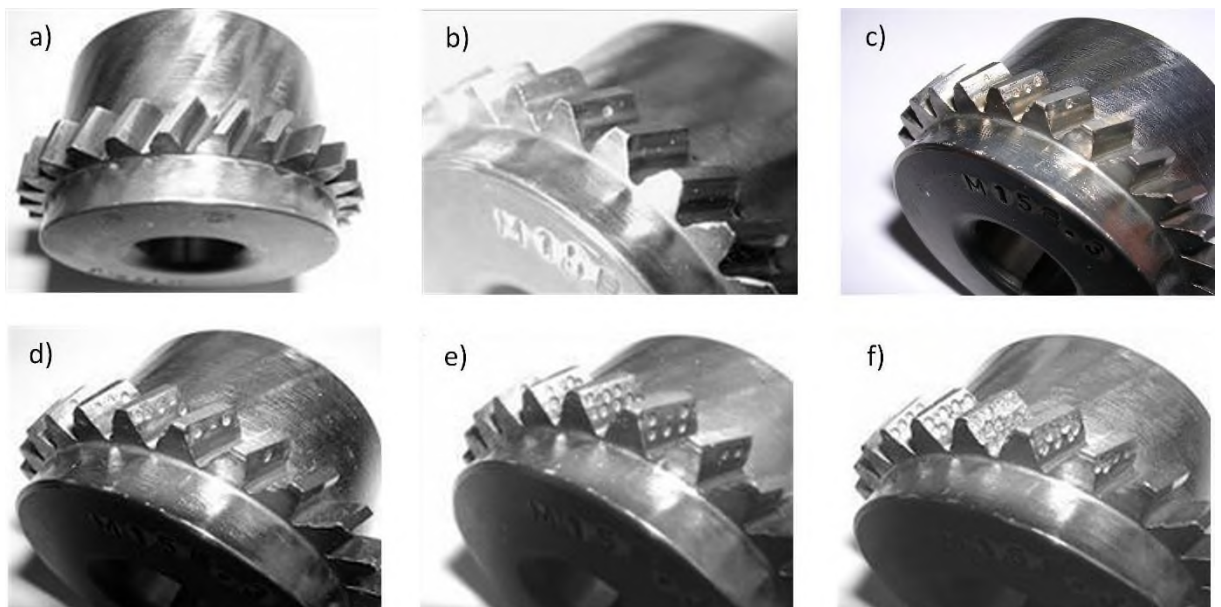


**Figure 5.** Fault stages used in the experiment: (a) healthy, (b) first fault, (c) second fault, (d) third fault, (e) fourth fault, and (f) fifth fault [34]

## 2.6. Analysis of Vibration Data in Time and Frequency Domain

The raw data were subjected to synchronous time averaging to highlight repeated characteristics and remove unnecessary noise. For every three turns of the input pinion gear, the averaged vibration signals are received. Figure 6 shows averaged signal of time domain gearbox vibration of vertical direction. It is seen that the gear vibration figures for healthy and each faulty condition are more or less similar to each other and no signs of fault progression are observed until the last fault stage. The frequency spectrum of each of the average helical gear vibrations is shown in Figure 7. The test pinion's speed is set at 2678 rpm during each testing, resulting in a fundamental tooth meshing frequency of 1294 Hz for the first stage and 420.7 Hz for the second stage. The computer-based recording and sampling of the vibration and location signals used a 15 kHz sample rate.

The spectra show a strong peak at 403 Hz, 1299 Hz and 2597 Hz, which correspond to the first gear mesh frequency for gearbox's second stage, first and second gear mesh frequencies for the gearbox's first stage. Except for Fault 5, the frequency spectra are quite similar. As in the time domain, the distortion in the last fault can be clearly observed in the frequency domain figures. Especially when the dominant frequencies and the amplitudes of these frequencies are considered, Fault 1 and Fault 2 are the most similar situations. As the fault progresses, the dominance of 5176 Hz, the fourth gear matching frequency of the

first stage, decreases. This is expected behavior due to high-frequency vibrations related to the growth of the fault.

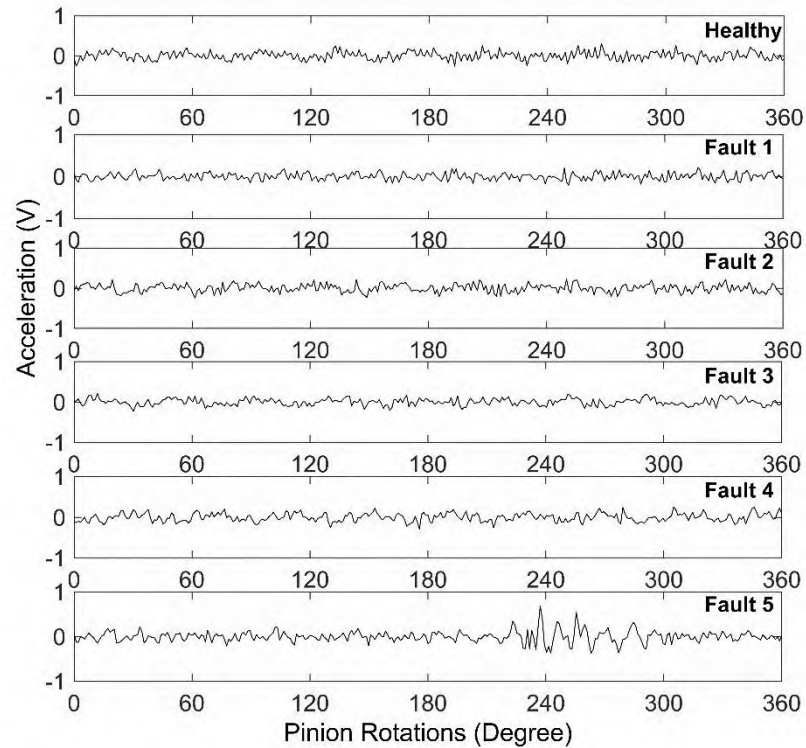


**Figure 6.** Averaged gear vibrations for one pinion rotation in time domain during the development of pitting fault.

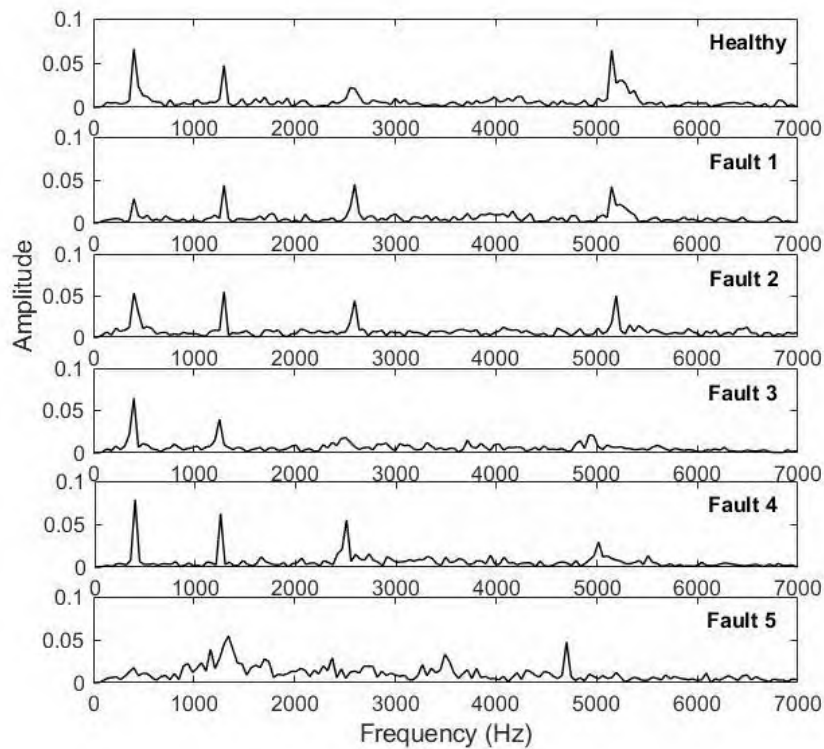


**Figure 7.** Averaged gear vibrations frequency domain during the development of pitting fault.

### 3. RESULTS AND DISCUSSION

A Local gear pitting dataset with five subsets was obtained for five different operating situations in this experiment. The total number of samples is 2670, with 445 samples for each condition. The number of input units in a deep neural network is governed by the sample length. As a result, sample length is a critical metric. On the one hand, a deep neural network with a small number of input units may not be capable enough. A deep neural network with a large number of input units, on the other hand, is likely to do better in diagnostics. However, it may result in a larger computing cost.

The vibration data, called sample consists of 335 sampling points because this data length is equal to one revolution of the drive pinion gear. The time synchronous average (TSA) method is applied to the raw data and each sample consists of three turns of the pinion gear. Indications of gear failure are caused by the vibrations of the gear surfaces that come into contact with each other, along with the rotation of the gears. Therefore, 335 vibration components related to faults tend to be periodic. Moreover, gear vibrations also contain many other undesirable components. The TSA method helps to remove unwanted components called noise from vibration data and makes the vibration signals caused by the rotation of the gearbox more pronounced. The model created with the training data was run with the test data to verify the effectiveness of the suggested method.

In this research, the raw vibration data to diagnose the local gear pitting faults without any signal preprocessing or manual feature extraction has been used. Raw signal data is reconstructed with CAE, SAE, VAE and used for fault classification. To begin, the sample length determines the input unit number. Second, the number of hidden layers and units in the proposed deep model should be large enough to support feature learning. Finally, the following hidden layer's unit number is lower than the preceding layer's, allowing feature learning to be viewed as a data compression process. The deep structure of the proposed approach is determined as 335-256-128-256-335 in the model. All of the tests were run on a Windows 10 computer with an Intel Core i5 processor and 8GB of RAM. Python3.6 is the compiler and language that was used to create and test these algorithms. The optimization parameters of the model are

given in Table 2.

**Table 2.** Optimization parameters

<b>Data set</b>	<b>Pitting Fault Data</b>
<b>Input Units</b>	335
<b>Output Units</b>	6
<b>Epoch</b>	100
<b>Batch size</b>	32

The model was tested using 534 samples. Table 3 shows the diagnostic recognition rates of test samples from various gear states. The test samples of each gear pitting condition have a high diagnostic recognition rate, as can be observed. Table 3 illustrates how the SAE model can accurately diagnose the various gear pitting defects, with an accuracy rate of more than 97%. The test set and the training set exhibit comparable accuracy levels, and no over-fitting phenomenon is evident.

**Table 3.** Diagnosis results

<b>Autoencoder Model</b>	<b>Training Set</b>	<b>Testing Set</b>
<b>CAE</b>	0,9101	0,9101
<b>SAE</b>	0.9757	0.9756
<b>VAE</b>	0,9082	0,9082

The confusion matrix shows each class's performance more clearly. This helps to evaluate the performance and verify the efficiency of the classifier. The multi-class confusion matrix displays all of the conditions' classification results in detail, including classification accuracy and misclassification fault. The confusion matrix's ordinate axis represents the actual classification label, while the horizontal axis predicts the classification label. As shown in Figure 8, the identification rate for healthy gear conditions, as well as for Fault 3 and Fault 5, is 100%. Additionally, the recognition rate for other gear pitting conditions is also very high, exceeding 98%. This demonstrates the effectiveness of the diagnostic method in accurately detecting and classifying various gear pitting faults. Fault 2 is misjudged as the gear of the Fault 1 and Fault 1 is misjudged as the gear of the Fault 2. This could be as a result of identical initial vibration signals caused by very close gear pitting. In Li's work [22], a combination of Sparse Autoencoder (SAE) and Gauss-Binary Restricted Boltzmann Machine (GBRBM) was used for fault diagnosis, effectively leveraging SAE's capabilities for feature compression and GBRBM's ability to handle continuous input data. In our study, SAE, along with CAE and VAE, was independently used to analyze raw vibration data without employing additional feature extraction methods, demonstrating the stand-alone capability of these autoencoders in learning deep feature representations directly from raw vibration signals.

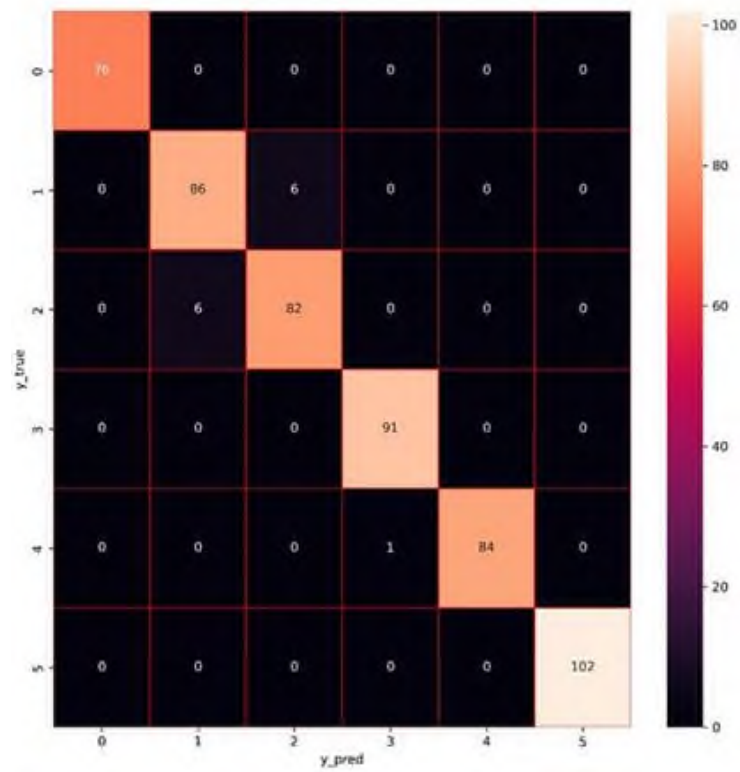


**Figure 8.** Multi-class confusion matrix of the SAE

As can be seen from Figure 9, the identification rate of condition healthy, Fault 3,4 and 5 are 100%. The recognition rate of the Fault 2 is also above 98%. Fault 1 is 0.50% misjudged as the gear of the Fault 2. Here, it seems that the CAE model fails to distinguish 2 faults with similar characteristics.

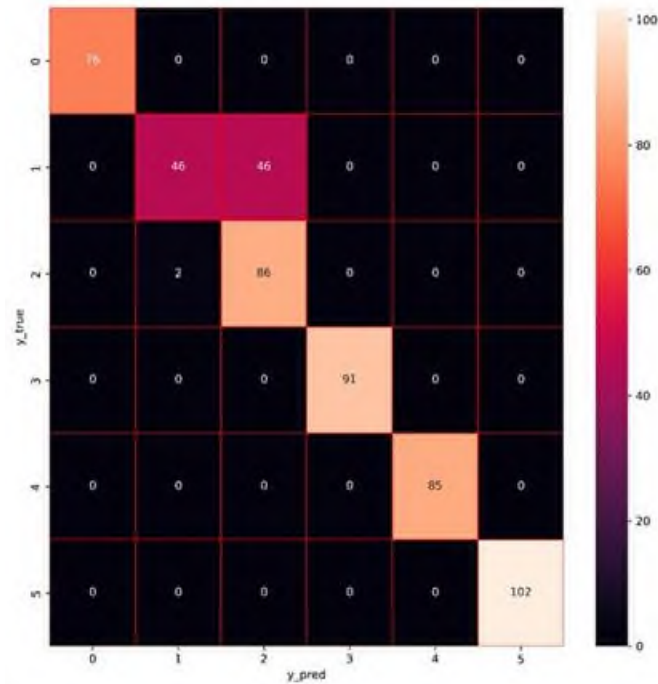


**Figure 9.** Multi-class confusion matrix of the CAE

As illustrated in Figure 10, the identification rate for condition Fault 5 is 100%. This indicates that the diagnostic method used was highly effective in accurately detecting and classifying this specific fault



without any errors. The recognition rate of faults 1,2 and 4 are close to 90%. Fault 4 is misjudged as the gear of the Fault 3 and Fault 3 is misjudged as the gear of the Fault 4. Also Fault 1 is misjudged as the gear of the Fault 2 and healthy. Fault 2 is misjudged as the gear of the Fault 1 and healthy. We can say that the variational autoencoder is not very successful in distinguishing faults with similar characteristics.

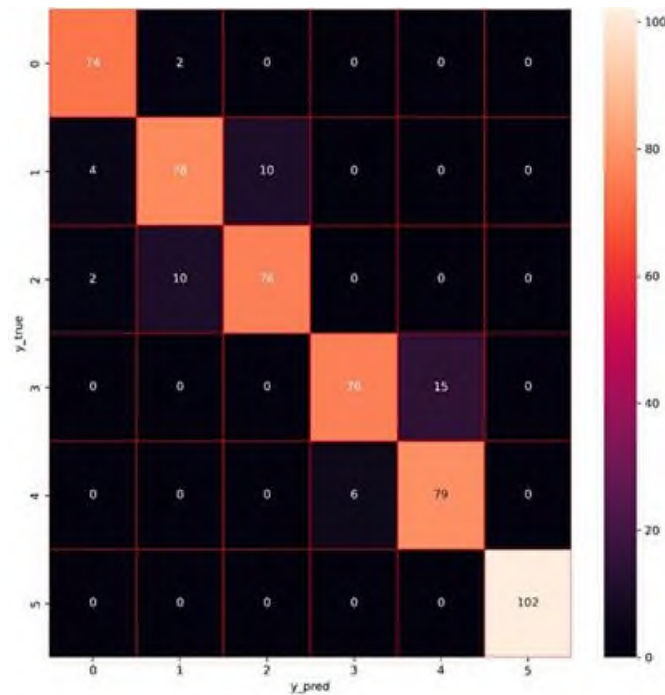


**Figure 10.** Multi-class confusion matrix of the VAE

To validate the feature extraction capability of the presented method, t-SNE was used to visualize the extracted features. t-SNE is a nonlinear dimensionality reduction technique that maps high-dimensional, interrelated data into a lower-dimensional space. By doing so, it preserves the local structure and relationships between the data points, allowing complex patterns in high-dimensional datasets to be visualized in 2 or 3 dimensions. The resulting reduced data provides an intuitive representation of the original data's structure, making it particularly useful for visualizing and interpreting clusters and patterns that may not be easily discernible in higher dimensions. Six different pitting faults can be clearly grouped, as shown in Figure 11. In this graph, we can see faults with similar characteristics more clearly. It can be seen that Fault 1 and Fault 2, which are the most similar to each other, overlap. We have seen in the confusion matrices above that these faults are the ones where AE models make the most mistakes.

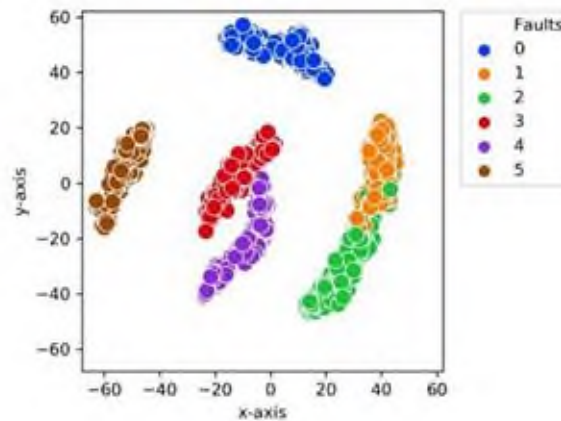


**Figure 11.** Two-dimensional features of gear pitting conditions

#### 4. CONCLUSIONS

In many industrial machines, gears are among the most important parts. Pitting is one of the most frequent gear problems and is typically hard to find. When the local gear pitting defect is not early detected, it can cause serious machine failures. This article compares the performance of different autoencoder models for the local pitting fault diagnosis method. The progressive learning process in deep learning architectures allows for the direct extraction of meaningful deep features from raw vibration signals. As more hidden layers are added, the ability to differentiate between the features corresponding to various gear states improves substantially. This makes deep learning a robust and efficient approach for deep feature extraction and gear fault diagnosis. AE can be seen as a way of transforming representation.

Through experiments, the methods' efficacy was evaluated. The gear pitting defect detection rate yielded findings that were higher than 90%. The SAE approach has the highest accuracy when compared to other auto encoder techniques, and it can satisfy the classification and detection needs for gears with various pitting conditions. Comparison between auto encoder models showed that the SAE model has better performance than the CAE and VAE models in automatically extracting adaptive features. This article provides automatic feature extraction, but network parameters such as the number of hidden layers, the number of neurons in each layer, and the learning rate depend on the human experience. Extending the developed approach to the identification of other mechanical component failures, such as bearing and motor failures, will be a focus of future research.

This study focused on the comparison of three autoencoder models (SAE, CAE, and VAE) for diagnosing gear pitting faults using raw vibration data. While these methods demonstrated strong performance, the application of traditional machine learning algorithms such as Random Forest or XGBoost was not explored. Given the well-separated nature of the dataset as seen in Figure 11, these methods could also achieve high accuracy. Future studies should include such algorithms to benchmark their performance against deep learning approaches, providing a broader perspective on fault diagnosis methodologies.

#### Declaration of Ethical Standards

The authors of this article state that the materials and methods employed in the study do not necessitate approval from an ethics committee or any specific legal permissions.

#### Credit Authorship Contribution Statement

1st Author, 2nd Author, and 3rd Author designed the study. 2nd Author and 3rd Author performed

the experiments and collected data. 1st Author derived the models and analyzed the data. 1st Author and 2nd Author wrote the manuscript in consultation with 3rd Author

### Declaration of Competing Interest

The authors declare that they have no known competing financial interests or personal relationships that could have appeared to influence the work reported in this paper.

### Data Availability

Data sharing not applicable

### REFERENCES

- [1] H. Öztürk, M. Sabuncu, and I. Yesilyurt, "Early detection of pitting damage in gears using mean frequency of scalogram," *J. Vib. Control*, vol. 14, 2008, pp. 469–484.
- [2] M. Amarnath and S. K. Lee, "Assessment of surface contact fatigue failure in a spur geared system based on the tribological and vibration parameter analysis," *Measurement*, vol. 76, 2015, pp. 32–44.
- [3] S. Bagavathiappan, B. B. Lahiri, T. Saravanan, et al., "Infrared thermography for condition monitoring – a review," *Infrared Phys. Technol.*, vol. 60, 2013, pp. 35–55.
- [4] Z. Peng, N. J. Kessissoglou, and M. Cox, "A study of the effect of contaminant particles in lubricants using wear debris and vibration condition monitoring techniques," *Wear*, vol. 258, 2005, pp. 1651–1662.
- [5] Y. E. Karabacak and N. G. Özmen, "Common spatial pattern-based feature extraction and worm gear fault detection through vibration and acoustic measurements," *Measurement*, vol. 187, 2022.
- [6] B. Hizarci, R. C. Ümütlü, H. Ozturk, and Z. Kiral, "Vibration region analysis for condition monitoring of gearboxes using image processing and neural networks," *Exp. Tech.*, vol. 43, no. 6, 2019, pp. 739–755.
- [7] T. Toutountzakis, K. T. Chee, and M. David, "Application of acoustic emission to seeded gear fault detection," *NDT E Int.*, vol. 38, no. 1, 2005, pp. 27–36.
- [8] K. Worden and J. M. Dulieu-Barton, "An overview of intelligent fault detection in systems and structures," *Struct. Health Monit.*, vol. 3, no. 1, 2004, pp. 85–98.
- [9] M. H. Benbouzid, "A review of induction motors signature analysis as a medium for faults detection," *IEEE Trans. Ind. Electron.*, vol. 47, no. 5, 2000, pp. 984–993.
- [10] S. Ebersbach and Z. Peng, "Expert system development for vibration analysis in machine condition monitoring," *Expert Syst. Appl.*, vol. 34, 2008, pp. 291–299.
- [11] F. P. G. Marquez, A. M. Tobias, J. M. P. Perez, and M. Papaalias, "Condition monitoring of wind turbines: Techniques and methods," *Renew. Energy*, vol. 46, 2012, pp. 169–178.
- [12] J. Zarei, M. A. Tajeddini, and H. R. Karimi, "Vibration analysis for bearing fault detection and classification using an intelligent filter," *Mechatronics*, vol. 24, 2014, pp. 151–157.
- [13] A. K. S. Jardine, D. Lin, and D. Banjevic, "A review on machinery diagnostics and prognostics implementing condition-based maintenance," *Mech. Syst. Signal Process.*, vol. 20, 2006, pp. 1483–1510.
- [14] R. C. Ümütlü, B. Hizarci, H. Ozturk, and Z. Kiral, "Classification of pitting fault levels in a worm gearbox using vibration visualization and ANN," *Sādhanā*, vol. 45, no. 1, 2020, pp. 1–13.
- [15] B. Samanta, "Gear fault detection using artificial neural networks and support vector machines with genetic algorithms," *Mech. Syst. Signal Process.*, vol. 18, 2004, pp. 625–644.
- [16] B. Samanta, K. R. Al-Balushi, and S. A. Al-Araimi, "Artificial neural networks and support vector machines with genetic algorithm for bearing fault detection," *Eng. Appl. Artif. Intell.*, vol. 16, no. 7, 2003, pp. 657–665.
- [17] W. Huang, H. Sun, Y. Liu, and W. Wang, "Feature extraction for rolling element bearing faults

- using resonance sparse signal decomposition," *Exp. Tech.*, vol. 41, 2017, pp. 251–265.
- [18] B. Zhang, H. Wang, Y. Tang, et al., "Residual useful life prediction for slewing bearing based on similarity under different working conditions," *Exp. Tech.*, vol. 42, 2018, pp. 279–289.
- [19] G. E. Hinton and R. R. Salakhutdinov, "Reducing the dimensionality of data with neural networks," *Science*, vol. 313, no. 5786, 2006, pp. 504–507.
- [20] X. Chen, A. Ji, and G. Cheng, "A novel deep feature learning method based on the fused-stacked AEs for planetary gear fault diagnosis," *Energies*, vol. 12, no. 23, 2019.
- [21] Y. Qu, M. He, J. Deutsch, and D. He, "Detection of pitting in gears using a deep sparse autoencoder," *Appl. Sci.*, vol. 7, no. 5, 2017.
- [22] J. Li, X. Li, D. He, and Y. Qu, "A novel method for early gear pitting fault diagnosis using stacked SAE and GBRBM," *Sensors*, vol. 19, no. 4, 2019.
- [23] X. Li, J. Li, Y. Qu, and D. He, "Gear pitting fault diagnosis using integrated CNN and GRU network with both vibration and acoustic emission signals," *Appl. Sci.*, vol. 9, no. 4, 2019.
- [24] X. Li, J. Li, Y. Qu, and D. He, "Semi-supervised gear fault diagnosis using raw vibration signal based on deep learning," *Chin. J. Aeronaut.*, vol. 33, no. 2, 2020, pp. 418–426.
- [25] J. Li, X. Li, D. He, and Y. Qu, "Unsupervised rotating machinery fault diagnosis method based on integrated SAE–DBN and a binary processor," *J. Intell. Manuf.*, vol. 31, 2020, pp. 1899–1916.
- [26] S. Khan and T. Yairi, "A review on the application of deep learning in system health management," *Mech. Syst. Signal Process.*, vol. 107, 2018, pp. 241–265.
- [27] S. Rifai, G. Mesnil, P. Vincent, et al., "Higher order contractive auto-encoder," in *Proc. Joint Eur. Conf. Mach. Learn. Knowl. Discov. Databases*, Berlin, Heidelberg, Sep. 2011, pp. 645–660, Springer.
- [28] C. Shen, Y. Qi, J. Wang, et al., "An automatic and robust features learning method for rotating machinery fault diagnosis based on contractive autoencoder," *Eng. Appl. Artif. Intell.*, vol. 76, 2018, pp. 170–184.
- [29] L. Wen, L. Gao, and X. Li, "A new deep transfer learning based on sparse auto-encoder for fault diagnosis," *IEEE Trans. Syst. Man Cybern. Syst.*, vol. 49, no. 1, 2017, pp. 136–144.
- [30] Y. Qi, C. Shen, D. Wang, J. Shi, X. Jiang, and Z. Zhu, "Stacked sparse autoencoder-based deep network for fault diagnosis of rotating machinery," *IEEE Access*, vol. 5, 2017, pp. 15066–15079.
- [31] A. He and X. Jin, "Deep variational autoencoder classifier for intelligent fault diagnosis adaptive to unseen fault categories," *IEEE Trans. Rel.*, vol. 70, no. 4, 2021, pp. 1581–1595.
- [32] S. Liu, H. Jiang, Z. Wu, and X. Li, "Rolling bearing fault diagnosis using variational autoencoding generative adversarial networks with deep regret analysis," *Measurement*, vol. 168, 2021, p. 108371.
- [33] D. Addo, S. Zhou, J. K. Jackson, G. U. Nneji, H. N. Monday, K. Sarpong, and C. A. Owusu-Agyei, "Evae-net: An ensemble variational autoencoder deep learning network for COVID-19 classification based on chest X-ray images," *Diagnostics*, vol. 12, no. 11, 2022, p. 2569.
- [34] H. Öztürk. Gearbox health monitoring and fault detection using vibration analysis. PhD Thesis, Graduate School of Natural and Applied Sciences of Dokuz Eylül University, Türkiye (2006)

## CHARACTERIZATION OF EPOXY RESIN AND SİLLE STONE POWDER BASED COMPOSITE MORTARS

<sup>1,\*</sup> Ahmet Cihat ARI , <sup>2</sup> Mustafa TOSUN 

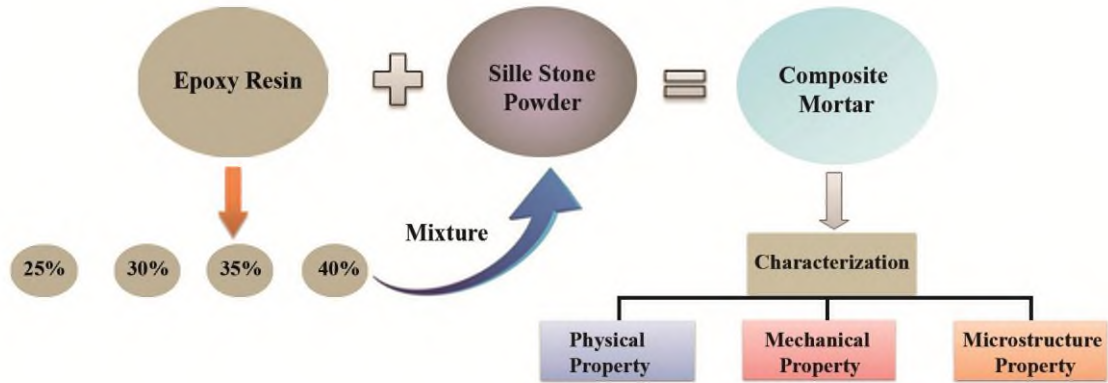
<sup>1</sup> Yozgat Bozok University, Akdagmadeni Vocational School, Architecture and Urban Planning Department, Yozgat, TÜRKİYE

<sup>2</sup> Konya Technical University, Architecture and Design Faculty, Architecture Department, Konya, TÜRKİYE  
<sup>1</sup> [a.cihat.ari@bozok.edu.tr](mailto:a.cihat.ari@bozok.edu.tr), <sup>2</sup> [mtosun@ktun.edu.tr](mailto:mtosun@ktun.edu.tr)

### Highlights

- Mechanical properties of epoxy resin and Sille stone powder based composite mortars.
- Development of new restoration mortars.
- Physical and microstructure properties of composite mortars.

### Graphical Abstract



Schematic illustration of production epoxy resin and Sille stone powder based composite mortars



## CHARACTERIZATION OF EPOXY RESIN AND SİLLE STONE POWDER BASED COMPOSITE MORTARS

<sup>1,\*</sup> Ahmet Cihat ARI , <sup>2</sup> Mustafa TOSUN 

<sup>1</sup> Yozgat Bozok University, Akdagmadeni Vocational School, Architecture and Urban Planning Department, Yozgat, TÜRKİYE

<sup>2</sup> Konya Technical University, Architecture and Design Faculty, Architecture Department, Konya, TÜRKİYE  
<sup>1</sup> [a.cihat.ari@bozok.edu.tr](mailto:a.cihat.ari@bozok.edu.tr), <sup>2</sup> [mtosun@ktun.edu.tr](mailto:mtosun@ktun.edu.tr)

(Received: 30.09.2024; Accepted in Revised Form: 07.01.2025)

**ABSTRACT:** Sille stone, extracted from the Sille region of Konya (Türkiye) province, is an andesitic stone used in the construction of historical buildings. Sille stone is subject to deterioration due to long-term natural and environmental factors. Repair mortars are used to prevent damage to the stones used in the construction of historical buildings. In this study, Epoxy resin (ER)/Sille stone powder (SSP) composite mortars were produced for the restoration of historical buildings and the properties of these composite mortars were investigated. In the production of composite mortars were prepared by contributing SSP into epoxy resin in varied ratios such as 60-75% wt.%. When 60% SSP filler was added to the ER matrix, the compressive strength of the resulting composite increased by approximately 66% compared to neat ER. Moreover, an increase in mechanical strength and a decrease in water absorption were observed in composite mortars due to the increase in SSP. In conclusion, the high strength, low water absorption rate and pore properties of epoxy matrix composite mortars provide great potential for restoration applications of historical buildings constructed from Sille stone.

**Keywords:** Characterization, Composite Mortar, Cultural Heritage, Sille Stone

### 1. INTRODUCTION

Repair mortars are used in the restoration of cracks or missing damaged areas in the material used in the construction of cultural assets. While the repair mortars are being developed, it is important to ensure the harmony between the material properties of the historical artifact in terms of preserving the historical properties of the building. For this reason, it is necessary to determine the properties of the components such as binder and aggregate in the repair mortar and to carry out restoration studies according to these properties. Additionally, knowing the properties of repair mortars ensures the durability of the historical artifact and the restoration compatibility of the building [1]. The use of repair mortars, similar to the material used in the construction of the historical monument, in the restoration works prevents new damages that may occur due to freezing-thawing events, and this is beneficial for the protection of cultural assets. The compatibility of the repair mortars with the original material in the design is important in terms of providing maximum protection with the principle of minimum intervention in the restoration of the building [2]. For this reason, the compatibility of repair mortars with the original material contributes to the development of the restoration intervention strategy of the building. Moreover, the development of repair mortars helps repair specialists to restore the building to its original form.

The stone used in the construction of cultural assets was preferred because of its strength and durability compared to other masonry materials. However, factors such as weathering of the stone material due to environmental conditions, physical changes of the structure, changes in temperature and humidity cause deterioration in the material [3]. Cultural assets built of Sille stone in Konya have been damaged due to climatic and environmental factors. In particular, the fact that Sille stone has been used both in Roman, Seljuk and Ottoman civilizations throughout the history in Konya and in the construction of today's buildings necessitates taking precautions against the deterioration problems that

\*Corresponding Author: Ahmet Cihat ARI, [a.cihat.ari@bozok.edu.tr](mailto:a.cihat.ari@bozok.edu.tr)

occur in these stones [4]. Many researchers have investigated the deterioration of Sille stone [4-9]. In the study conducted by Ozdemir [8], it was determined that cultural assets made of Sille stone in Konya are effective in the formation of moisture on the facade surfaces due to the porosity of the stone and the high amount of water absorption. In the study conducted by Fener and İnce [4] determined the mechanical and wear properties of freeze-thaw deterioration processes in Sille stone due to atmospheric effects. In the review made in the literature, the solution of the damages on the facade surfaces caused by the high water absorption amount in Sille stone was not mentioned. Additionally, no study has been published on the development of repair mortar to be used in the restoration of Sille stone.

Sille stone is cut to certain sizes before it is used in buildings and wastes are generated during this cutting process [10]. For this reason, the production of composite materials by evaluating waste products contributes to both the reduction of costs and the protection of the environment and nature. Regarding the production of composite materials from Sille stone powder, Öztürk, et al. [10] conducted a study on the use of floor tiles in their article. In the study, it has been concluded that Sille stone has a positive contribution to heat resistance and high strength floor tile products. Except for this study, no study has been found in the literature on the production of composite materials using Sille stone powder.

In the literature, studies have been carried out on the development of repair mortar, lime-based mortar [11], lime mortar with pozzolanic additives (brick powder) [12], organic-added lime mortar (brass) [13], industrial waste additive alkali active mortar (fly ash and blast furnace slag) [14] and polymer added mortar (epoxy) [15, 16]. Epoxy resins are used in the restoration of various stone materials due to their resistance to water, good adhesion to the substrate, and mechanical and abrasion resistance. For instance, Tesser, et al. [17], investigated the physicochemical properties of mortars produced with epoxy binders for use in the repair of marble and limestone. In the same study, it was determined that mortars produced with epoxy binders were resistant to biological deterioration in addition to providing structural stone reinforcement of monuments. In the research conducted by Alonso-Villar, et al. [18], the properties of mortars produced with and without the addition of micronized silica to epoxy and acrylic resins in the repair of historical buildings constructed from granite stone were investigated. It was determined that mortars produced by adding micronized silica significantly reduce the water absorption rate of the stone. In another study conducted by Roig-Salom, et al. [19], the properties of mortars produced with epoxy binders in the restoration of historical marble fountains were investigated. It was determined that mortars produced with epoxy binder are resistant to biological attacks and have similar mechanical behavior to natural marble. In all these studies, it was reported that mortars produced with epoxy binders have great potential in the restoration of historical buildings, in combining broken pieces of stones and in closing cracks and surface cavities. Additionally, it was stated in the literature that the properties of polymer-binding composite mortars should be examined before the restoration of historical buildings because stone types have different properties and different structural behaviors can occur as a result of the chemical reaction between the polymer material and the stone. To our knowledge, while the mechanical and physical properties of Sille stone are the subject of further research, no research has been conducted to date on the development of repair mortars for use in the restoration of historical buildings using Sille stone. This study investigates the properties of Sille stone powder and epoxy binder mortars for the restoration of historical buildings for the first time and fills the existing knowledge gap caused by the lack of sufficient number of studies in the literature on the use of polymer binder materials as repair mortars.

In this study, the development and characterization of Sille stone powder-epoxy matrix repair mortar was investigated for its usability in the restoration of cultural assets in Konya. Additionally, the physical and mechanical properties of Sille stone powder added epoxy matrix composite mortar were investigated. However, in the study, economical and high-strength composite mortar was produced by using Sille stone powder wastes for the restoration of cultural assets.

## 2. MATERIAL AND METHODS

In this chapter, the materials used in the study and their properties are explained. Additionally,

information is given about the methods applied in the characterization of composite sample samples produced from these materials.

## 2.1. Materials Used in Experiment Studies

Information about the materials used in the test studies, their locations and some properties of these materials are given below.

### 2.1.1. Sille Stone Powder (SSP)

The SSP used for the production of composite mortar was taken from a quarry in Sille region of Konya province. Since Sille stones were shaped in various sizes before being used as building materials, stone powders were collected from the quarry for experimental studies (Figure 1). Sieve analysis was performed for particle size distribution of SSP taken from the quarry. Stone powder was sieved using a sieve device (Retsch AS 200) and sieves of different sizes (63, 150, 250, 500, 1000, 2000 and 4000  $\mu\text{m}$ ). Each of the sieve set apparatus was placed with 100 gr SSP and then shaking was done for 10 minutes. At the end of this process, the powder remaining in each sieve was weighed and recorded. In the particle size distribution of SSP, approximately half of the particles are below 63  $\mu\text{m}$ , while less than 10% of the particles are larger than 500  $\mu\text{m}$  (Figure 2). Some features of the SSP used in the experimental study are given in Table 1. The chemical content of SSP is given in Table 2. It was determined that the chemical content of SSP was highest as  $\text{SiO}_2$  66.67% and  $\text{Al}_2\text{O}_3$  13.24%.



**Figure 1.** Photograph of the SSP used in the study



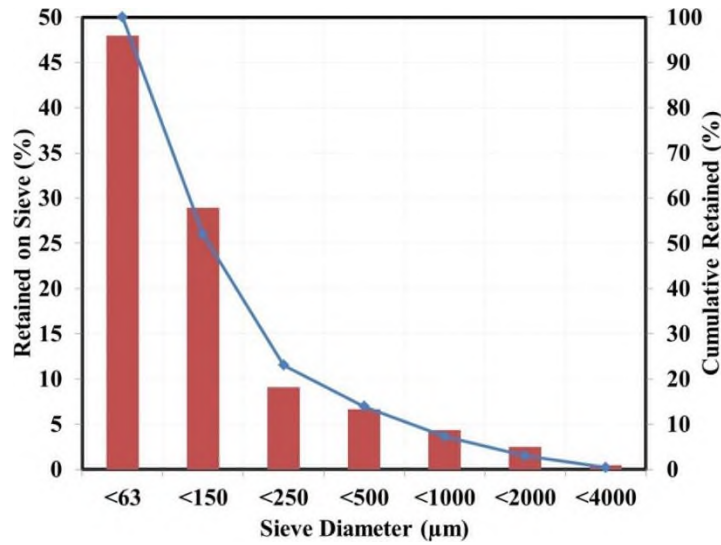


Figure 2. Particle size distribution of SSP [20]

Table 1. Some features of SSP used in this research [8, 21]

<b>Sille stone powder (SSP)</b>	Density (g.cm <sup>-3</sup> at 20 °C):	2.26 – 2.35
	Water absorption (% at 23 °C):	3.9
	Melting point (°C):	2000

Table 2. Chemical content of the SSP [22]

Content of the SSP	SiO <sub>2</sub>	Al <sub>2</sub> O <sub>3</sub>	K <sub>2</sub> O	Na <sub>2</sub> O	MgO	CaO	Fe <sub>2</sub> O <sub>3</sub>	TiO <sub>2</sub>	ZrO <sub>2</sub>
%	66.67	13.24	4.11	4.94	1.09	5.07	3.66	0.52	0.39

**2.1.2. Epoxy Resin (ER)**

The ER was used as the matrix material within the scope of the study. Bisphenol-A type epoxy resin and hardener, cycloaliphatic polyamine BRTR Kimya A.Ş. (Türkiye) was purchased from the company. Epoxy and hardener have transparent color, glossy appearance, the mixture is cured for 12 hours at 25°C, mechanical strength is completed in 7 days, and density of 1.10 g/cm<sup>3</sup>.

**2.2. Method**

The preparation method of the composite samples and the information about the tests performed on these samples are explained below.

**2.2.1. Preparation of Composite Sample**

Within the scope of this study, the SSP composite sample with neat epoxy resin and epoxy matrix was produced. Neat ER sample was obtained by adding a 5:3 wt. cycloaliphatic polyamine hardener to the neat ER, and the mixture was stirred for 3 minutes. For the production of SSP composite sample with epoxy matrix; each mixture in these composites was added to neat ER at 60 %, 65 %, 70% and 75% weight ratios and mixed for 3 minutes. Then, the cycloaliphatic polyamine hardener was added to the composite mixtures in a ratio of 5:3 by weight. Each of the obtained composite samples was mixed for 3 minutes (Table 3 and Figure 3). Composite samples were produced using the traditional hand lay-up

technique. Additionally, due to the high viscosity of the mixture, it was mixed manually without using a mechanical mixer. The reason for choosing this method is that it uses less equipment, does not require any heat treatment, and allows for fast and serial production under application conditions. The composite mortars that were mixed were cast in molds in accordance with ASTM standard and all the composite mortars produced were dried in these molds at room temperature for 24 hours.

**Table 3.** The abbreviations and ingredients of composite mortars

Composite mortars' abbreviations	Combination ratio of resin type/SSP
ER	100:0
ER/SSP-1	40:60
ER/SSP-2	35:65
ER/SSP-3	30:70
ER/SSP-4	25:75



**Figure 3.** (a) Photograph of the composite sample produced within the scope of the study, (b) Photograph of the Sille stone

### 2.2.2. Experiments on Composite Mortar

Within the scope of this study, experiments were carried out to determine the physical, chemical, mechanical and microstructural properties of the produced composite mortars. Compression tests were carried out to determine the strength and durability of composite mortars obtained from the epoxy resin mixture of SSP. Flexural test was also performed to determine the resistance of composite mortars against flexural under load. Since the adhesion force between the wall and the mortar causes mechanical tensile stresses in the mortars, tensile tests were carried out to determine the resistance of the composite mortars against mechanical tensile stresses. Depending on the increase in the SSP ratio in composite mortars, hardness tests were performed to determine the hardness and durability of the material. Water absorption test and void content were performed to determine the water resistance of composite mortars and the amount of water absorption of the material. SEM-EDS analysis was performed to determine the morphology of composite mortars and the changes that occur in the material due to increasing the SSP ratio in the composite material. FTIR analyses of composite mortars were performed to determine the properties of molecular bonds formed by the chemical interaction between epoxy resin and stone powder. All these experiments were carried out to evaluate whether the composite mortars produced within the scope of the study are suitable for use in restoration applications. One composite sample each was used for void content, SEM-EDS and FTIR analyses. Five composite samples each were used in the water absorption test, compression test, flexural test, tensile test and hardness test.

#### 2.2.2.1. Void Content

The amount of space and pore size of the repair mortar material used in the restoration of historical monuments affect the water absorption rate of the building. The presence of high water absorption causes freezing-thawing events in the material and causes damage to the structures. In order to prevent structural damage caused by atmospheric effects, it is necessary to determine the gap of the mortar

material used in the restoration of historical monuments. Within the scope of the research, the pore amount and size of the repair mortar material produced was determined by the pore size and the mercury porosimetry method (Micromeritics - Autopore 4) with the help of the formula in the ASTM-D2734 standard [23]. The mercury porosimetry method is used to determine the pore size and pore size distribution in the material. It is ensured that fine pores of mercury penetrate the material with sufficient pressure. In the measurement of the pore size of the material, it is calculated by decreasing the amount of mercury with the applied pressure [24].

#### **2.2.2.2. Water Absorption Test**

The amount of water absorbed by the samples was determined by the water absorption test. In the water absorption test, the dry weights of the samples were measured at room temperature (23°C) on a precision balance with an accuracy of 0.001 g, then the samples were placed in containers filled with pure distilled water. After the samples were kept for 24 hours, dry weight differences were determined on a precision balance with 0.001 g precision. The water absorption percentages of the samples were calculated using the formula given in the standard in ASTM-D570 [25].

#### **2.2.2.3. Flexural Test**

Flexural test was done with SHIMADZU AGS-X device and samples were prepared in 4x13x165 mm molds. Additionally, 5 samples were produced for each type of composite samples and a force of 0.2mm/min was applied to these samples. In this experiment, the sample was placed on the supports horizontally in the device and the force values formed as a result of the deflection value in the middle of the samples were recorded. In the flexural test, both the die dimensions in the preparation of the samples and the force values of the samples were calculated according to the ASTM-D790 standard [26]. Moreover, the standard deviation value in the force values of the 5 samples measured for the force values of each type of composite in the flexural test was calculated.

#### **2.2.2.4. Compression Test**

In the compression test, the samples were prepared in 20x20x20 mm molds. The preparation of these samples was made according to the ASTM-D695 standard. SHIMADZU AGS-X device was used in the compressive strength test and the force velocity value was applied to the samples at 0.5mm/min. Compressive strength values were calculated with the help of the formula given in the ASTM-D695 standard [27]. Additionally, 5 samples were produced for each type of composite sample during these tests and the standard deviation in the compression strength values of the samples was calculated.

#### **2.2.2.5. Tensile Test**

It was aimed to determine the strength of the composite mortar against mechanical tensile forces by performing the tensile test. For this purpose, samples for the test were prepared in 19x115x4 mm molds according to ASTM-D638 standard. Moreover, the tensile test was performed with the SHIMADZU AGS-X device and the tensile force of the device was applied to the samples at a speed of 0.2mm/min. The specimens were placed at the lower and upper points of the device, and the deformations of the specimens and the maximum force values at the moment of rupture were recorded against the force applied in these two directions. The calculations in these measurements were made with the help of the formulas specified in the ASTM-D638 standard [28]. Additionally, the standard deviation in the force values of the 5 samples measured for the force values of each type of composite in the tensile test was calculated.

### 2.2.2.6. Hardness Test

Since different amounts of stone powder were added to the samples and the strength properties of the samples changed according to this stone powder, the hardness test was carried out. Hardness measurements of composite samples were made according to Shore D hardness measuring device and ASTM-D2240 standard. The plunge tip in the hardness measuring device was immersed in the samples, and the amount of depth formed in the sample and the hardness values of the composites were calculated. Moreover, the immersion tip of the device was immersed into the hardness value of the composites five times for each sample type and measurements were made and the standard deviation in the hardness values of the samples was calculated accordingly. Calculation of the hardness values in this experiment was made using the formulas in the ASTM-D2240 standard [29].

### 2.2.2.7. Scanning Electron Microscope-Energy Dispersive X-Ray Spectroscopy (SEM-EDS)

The morphological features of the samples were determined by Hitachi-SU 1510 SEM-EDS device. With the SEM device, the deformations and structural changes that occurred due to the increase of Silice stone powder in the composites were determined by surface scanning. The elements in the samples were determined by EDS analysis.

### 2.2.2.8. Fourier Transform Infrared Spectroscopy (FTIR)

FTIR analysis was performed to determine the properties of molecular bonds in the samples. FTIR analysis Thermo Scientific – Nicolet iS20 device was used. Infrared rays were sent to the samples with the FTIR device. Then, the wave energies formed in the vibrations of the molecular bonds during the absorption of infrared light in the samples were determined. FTIR analysis has an important place in the design of new products and in ensuring the quality control of the material. For this reason, the microstructure properties of the material were determined by performing FTIR analysis of the composite mortar.

## 3. RESULTS AND DISCUSSION

### 3.1. Void Content

Void content of ER/SSP samples, test result data are given in Table 4, Figure 4 and Figure 5. The pore size distribution of the samples showed a multi-peak distribution, while the pore size ranged between 0.01-300  $\mu\text{m}$ . The density of the samples with pores was determined to be 0.005-0.25 mL/g. Additionally, the density of the samples with pores, the most significant peak was seen around 0.005 mL/g.

**Table 4.** Void determination test data of ER/SSP composites

Pore properties	ER/SSP-1	ER/SSP-2	ER/SSP-3	ER/SSP-4
Total Intrusion Volume (mL/g)	0.0409	0.0658	0.0488	0.0388
Total Pore Area (m <sup>2</sup> /g)	5.850	15.846	15.139	11.657
Median Pore Diameter (Volume) ( $\mu\text{m}$ )	17.1643	0.0186	0.0126	0.0125
Median Pore Diameter (Area) ( $\mu\text{m}$ )	0.0081	0.0093	0.0077	0.0076
Average Pore Diameter (4V/A) ( $\mu\text{m}$ )	0.0280	0.0166	0.0129	0.0133
Bulk Density at 0.55 psia (g/mL)	1.6171	1.5740	1.6659	1.7479
Apparent (skeletal) Density (g/mL)	1.7316	1.7560	1.8133	1.8751
Porosity (%)	6.6139	10.3617	8.1293	6.7863
Stem Volume Used (%)	5	7	6	6

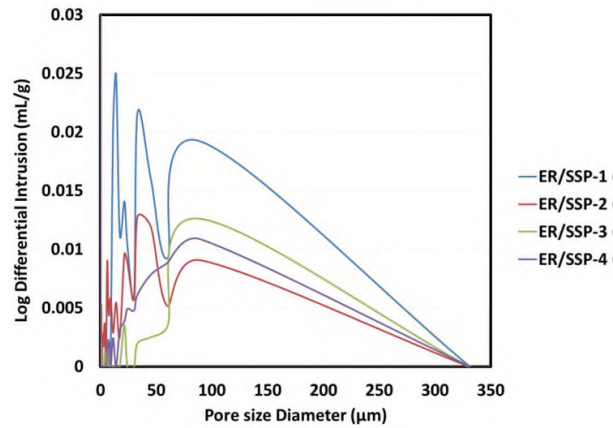


**Figure 4.** Void determination test result graph of ER/SSP composites

When the porosity ratios of ER/SSP composites are examined, the amount of voids decreases depending on the increase in the amount of SSP in all composites except ER/SSP-2 composite. According to the graph in Figure 5, it is seen that the porosity ratio of the ER/SSP-2 composite sample is higher than the porosity ratio of all other composites. The increase in the amount of voids in the material causes an increase in the water absorption rate. This situation causes deformations in the interior and exterior of the building such as humidity, blooming and rotting. The fact that the void ratio of the ER/SSP-4 sample developed within the scope of the study is the lowest, may help to reduce the damage caused by water absorption in the structure. Moreover, the use of this composite in the restoration of cultural assets may contribute to the long-term preservation of the structure.

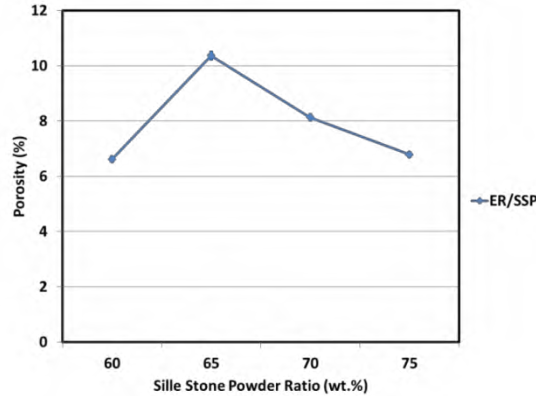


**Figure 5.** Graph of porosity (%) values of ER/SSP composites

In the study conducted by Lanas and Alvarez-Galindo [30] determined that the pore ratios of lime-based mortars ranged from 16.51% to 30.63%. In the study conducted by Török and Szemeray-Kiss [31] found that the pore ratios of limestones and portland pozzolanic cement repair mortars vary between 22.5% and 39.7%. In the study conducted by Zheng, et al. [32] showed in their study that the porosity ratios of epoxy resin-added cement-based mortar ranged from 5.19% to 14.46%. According to the studies in the literature, adding epoxy to the mortars reduces the pore rate. ER/SSP of composites the porosity varies between 6.61% and 10.36%, and a lower pore ratio than restoration mortars has been obtained in the literature. Additionally, this composite mortar gave a pore ratio comparable to epoxy resin-added mortars in the literature.

### 3.2. Water Absorption Test

The water absorption test of ER/SSP composites and Sille stone is given in Table 5 and the

comparison chart is given in Figure 6. According to the data in Table 5, it is seen that the water absorption rate of ER/SSP composites is lower than that of Sille stone. Moreover, in ER/SSP composites, the water absorption rate decreases due to the increase in the amount of Sille stone powder. It has been determined that the water absorption rate of the ER/SSP-4 composite has the lowest rate compared to all other composites. According to this test result, the fact that the composites are affected by water in the use of restoration repair mortar, and that it is less than Sille stone, prevents the deterioration of the structure caused by water. However, in the restoration of cultural assets, the low water absorption rate of the composite mortar prevents the damage caused during the freeze-thaw process due to atmospheric effects and the structure is preserved for a longer period of time.

**Table 5.** Water absorption test data of Sille stone and ER/SSP composites

Samples' ID	Composition Ratio (wt.%)	Water Absorption of Sille Stone and ER/SSP Composites (%)
ER/SSP-1	40:60	0.236
ER/SSP-2	35:65	0.181
ER/SSP-3	30:70	0.082
ER/SSP-4	25:75	0.070
Sille Stone	0:100	3.968

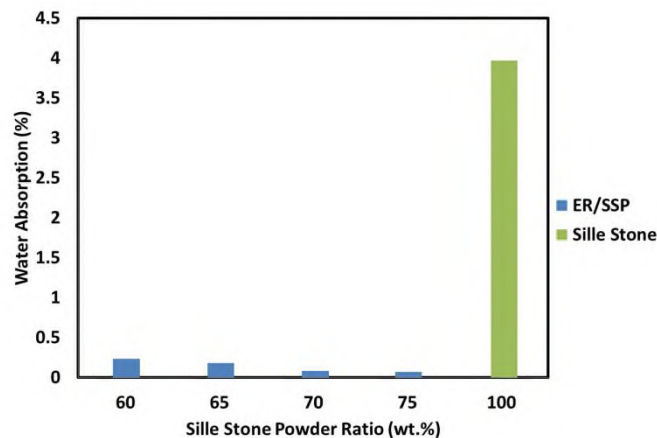


**Figure 6.** Graph of water absorption rate values of Sille stone and ER/SSP composites

In the study conducted by Korat, et al. [33] determined that the water absorption rate for tuff ranged from 8.0% to 8.3%, and the water absorption rate of mortars at atmospheric pressure ranged from 14.5% to 22.8%. In the study conducted by Alves, et al. [15] found that the water absorption data of epoxy polymer pozzolanic cement, white cement matrices and composites made with steatite rock powder vary between 0.27% and 13.72%. In the study conducted by Rahman and Islam [34] investigated the characterization of mortars made of epoxy resin and portland cement matrices with different proportions of sand. They observed that the water absorption rate of the epoxy matrix mortar was lower than the other matrix and the water absorption coefficient decreased due to the increase in the sand content. The ER/SSP composites have a water absorption rate between 0.07% and 0.236%, and this composite mortar has a lower water absorption rate than the restoration mortars in the literature. Moreover, the decrease in the water absorption coefficient of the composites due to the increase in stone powder shows that it is in good agreement with the literature.

### 3.3. Flexural Test

Flexural test results of ER/SSP composites are given in Table 6 and Figure 7. According to the data in Table 6, the flexural strength value of ER/SSP composites is between 20.11 MPa and 24.45 MPa. Moreover, it was determined that ER/SSP-4 composite had the highest strength value compared to other

composites. As seen in Figure 7, the reason for the decrease in the strength value of the composite from 60% to 65% by weight of SSP can be attributed to the agglomeration that occurs as a result of the interaction between the stone powder and the epoxy matrix. Agglomeration causes a decrease in the adherence between the epoxy matrix and the stone powder, and a decrease in the attraction force of the molecule in the stone powder. When these results are compared with the results of void determination; The fact that ER/SSP-2 composite has a higher porosity rate than other composites causes a decrease in strength. Moreover, the high amount of filling ensures that the void surface areas in the composite material are reduced. However, when the SSP is increased from 65% to 75% by weight, the strength value of the composite increases. Similar result is also seen in the study conducted by Rajput, et al. [35], in the flexural strength test of Kota stone powder as filler material in epoxy matrix. It was stated that there is an increase in flexural strength due to the higher surface hardness of stone particles compared to epoxy polymer. In the study conducted by Karthikeyan, et al. [36], in the flexural strength test of composites produced with marble powder and tamarind shell powder in epoxy matrix, it was found that the flexural strength increased due to the strengthening of the interface attraction in the composition when the ratio of epoxy resin was reduced. In the study conducted by Gomes, et al. [37], in the flexural strength test of composites produced with quarry powder (Brazil) and brick powder in the epoxy matrix, it was determined that the reduction of porosity in the composite material by homogeneously spreading the stone powder in the epoxy matrix increased the flexural strength. Therefore, as stated in literature studies, the decrease in porosity in the composite material by spreading the stone powder homogeneously in the epoxy matrix, the high surface hardness of the stone powder compared to the epoxy polymer and the strengthening of the interface attraction in its composition are the main reasons for the increase in the strength value of the composite.

**Table 6.** Flexural strength of ER/SSP composites

Samples' ID	Composition Ratio (wt.%)	Flexural Strength of ER/SSP Composites (MPa)
ER/SSP-1	40:60	21.12±1.38
ER/SSP-2	35:65	20.11±1.67
ER/SSP-3	30:70	23.28±2.02
ER/SSP-4	25:75	24.45±1.44

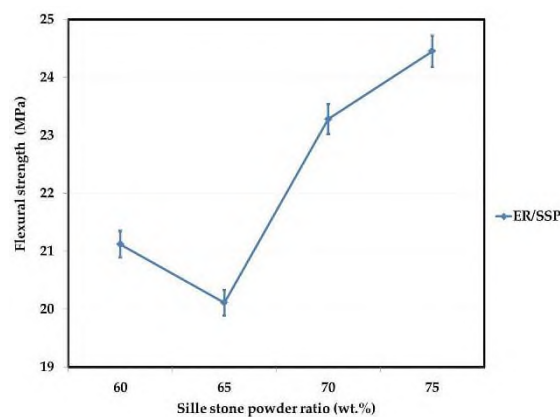


**Figure 7.** Flexural test result graph of ER/SSP composites

When the flexural test results of restoration mortars are examined in the literature, it varies between 0.07 MPa and 1.5 MPa in some studies [12, 30, 38, 39]. According to the studies in the literature, adding epoxy to the mortars increases the flexural strength [35, 40].

### 3.4. Compression Test

Compression test results of ER and ER/SSP composites are given in Table 7 and Figure 8. According to the data in Table 7, the strength value of ER/SSP composites is between 42.90 MPa and 52.36 MPa. Moreover, according to the compression test result, it was determined that the strength value of ER/SSP composites was higher than the strength value of neat ER (Figure 8). However, with the addition of 60% SSP filler to the ER matrix, its strength increased by 66% compared to neat ER. When the amount of SSP was increased from 60% to 70% by weight, the strength value of the composite decreased. The formation of agglomeration in the intermediate phase between the stone powder and the epoxy matrix causes a decrease in the adhesion strength of the matrix and a decrease in the strength of the composite. Nevertheless, when the amount of SSP was increased from 70% to 75% by weight, the stone powder was homogeneously dispersed in the epoxy matrix, and the decrease in the porosity ratio increased the strength value of the composite. When this result is compared with the flexural test result, the strength value of the composites gives similar results.

**Table 7.** Compressive strength of ER and ER/SSP composites

Samples' ID	Composition Ratio (wt.%)	Compressive Strength of ER/SSP Composites (MPa)
ER	100:0	28.31±2.34
ER/SSP-1	40:60	47.00±1.51
ER/SSP-2	35:65	45.11±0.47
ER/SSP-3	30:70	42.90±1.44
ER/SSP-4	25:75	52.36±1.78

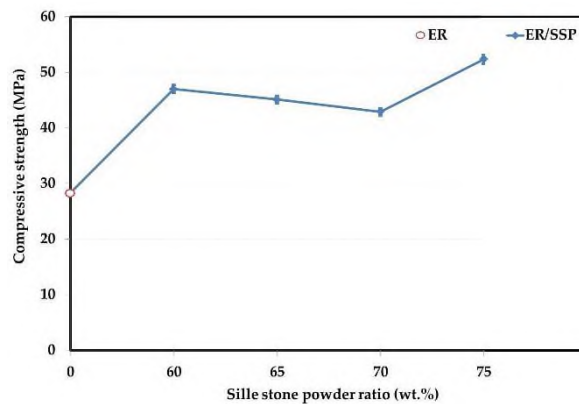


**Figure 8.** Compression test result graph of ER/SSP composites

When the compression test results related to the restoration mortars are examined in the literature, it varies between 0.3 MPa and 16 MPa in some studies [11, 12, 38, 39, 41]. In the study conducted by Kekeç [42] determined the compressive strength of Silite stone as 29.22 MPa. Moreover, in the literature, the addition of epoxy materials to improve the mechanical properties of repair mortars has contributed to the increase in the compressive strength of repair mortars [15, 34].

### 3.5. Tensile Test

The tensile test results of the ER/SSP composite are given in Table 8 and Figure 9. As shown in Table 8 and Figure 9, the tensile strength of ER/SSP composites is between 24.81 MPa and 27.30 MPa. Moreover, it was determined that ER/SSP-2 composite had the highest tensile value compared to other composites. When the amount of stone powder is increased from 60% to 65% by weight, an increase in tensile strength is observed, while a decrease in tensile strength is observed when the amount of stone



powder is increased from 65% to 70% by weight. While the filling loading strength of the composite material is increased to a certain extent, the filling loading causes a decrease in the adhesion force between the composite component when the ratio limit of the load is exceeded. Due to the non-homogeneous dispersed components of the composite in tensile strength, it leads to a decrease in its strength [40]. These results seem to be in agreement when compared with other results of mechanical property tests.

The ER/SSP-4 tensile test, which is another mixture obtained from the composite material, was carried out. These samples were prepared according to ASTM D638. ER/SSP-4 composite specimens could not be measured because they broke when their jaws were attached to the tensile testing machine. The main reasons for not measuring the ER/SSP-4 composite are the decrease in the bond strength between the stone powder and the epoxy matrix and the insufficient cure of the mixture during the production phase of the composite material [43, 44].

**Table 8.** Tensile strength of ER/SSP composites

Samples' ID	Composition Ratio (wt.%)	Tensile Strength of ER/SSP Composites (MPa)
ER/SSP-1	40:60	27.22±1.70
ER/SSP-2	35:65	27.30±1.45
ER/SSP-3	30:70	24.81±2.24

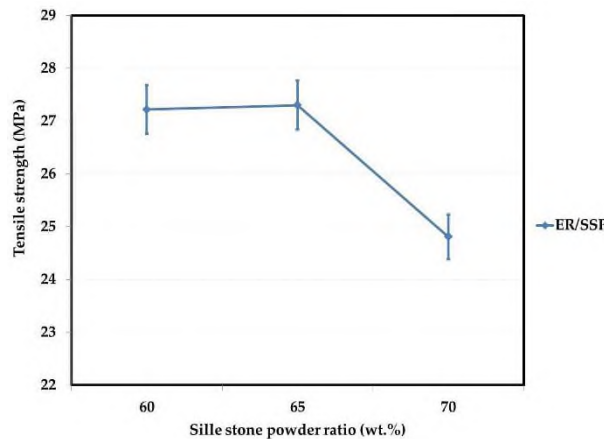


**Figure 9.** Tensile test result graph of ER/SSP composites

When the tensile test results of restoration mortars are examined in the literature, it varies between 2.5 MPa and 18 MPa in some studies [45-48]. According to the studies in the literature, adding epoxy to the mortars increases the tensile strength [45, 46, 48].

**3.6. Hardness Test**

The hardness test results of the ER/SSP composite are given in Table 9 and Figure 10. As seen in Table 9 and Figure 10, the hardness value of ER/SSP-4 composite is higher than the hardness value of all other composites. Moreover, an increase in the hardness value of the composite was observed when the amount of SSP was increased from 65% to 75% by weight. To explain the factor affecting this situation, the hardness of inorganic fillers can be attributed to the higher hardness of organic fillers [49]. Adding harder stone powder to the epoxy matrix can increase the hardness of the composite.

According to the data in Table 9 and Figure 10, it is seen that the hardness value of the ER/SSP-2 composite is lower than the other composites. It is seen that this result is compatible with the results of the void determination and other mechanical tests of the composite. As the void test result of ER/SSP-2 composite is explained, the fact that the porosity ratio is higher than the porosity ratio of other

composites causes a decrease in the hardness and strength of this composite. The increase in porosity and the amount of pores between the filler and the matrix creates agglomeration. This agglomeration leads to a decrease in the adhesion strength between the filler and the matrix, and a decrease in the strength of the composite material [50].

**Table 9.** Hardness test values of ER/SSP composites

Samples' ID	Composition Ratio (wt.%)	Shore-D Hardness Value of ER/SSP Composites
ER/SSP-1	40:60	81.4±0.5
ER/SSP-2	35:65	79.4±1.0
ER/SSP-3	30:70	81.2±1.0
ER/SSP-4	25:75	82.6±1.7

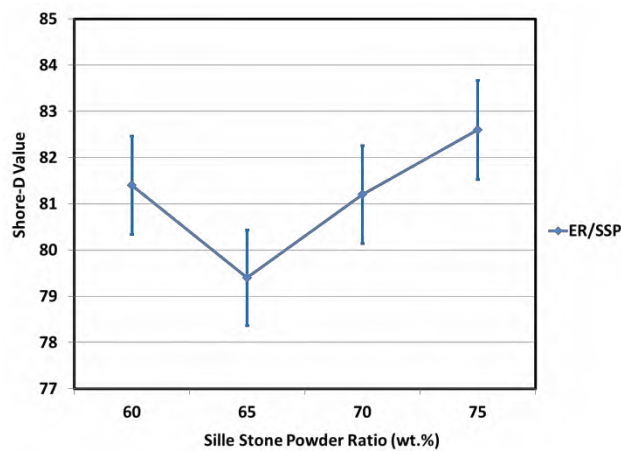


**Figure 10.** Shore-D hardness test result graph of ER/SSP composites

### 3.7. Scanning Electron Microscope-Energy Dispersive X-Ray Spectroscopy (SEM-EDS)

Figure 11 shows the SEM image of the ER/SSP composite taken at 500  $\mu\text{m}$  magnification. Figure 11a shows that neat epoxy has a smooth surface texture. However, adding the amount of SSP to the epoxy matrix causes the composite material to form a rough and hollow structure (Figure 11b-11e). This structural change contributes to the improvement of the strength of the composite material. The less porous structure of the ER/SSP-4 composite compared to other composites is effective in its high strength as observed in the mechanical test results (Figure 11b-11e). However, stone powder loading fills the fine voids in the composite material and reduces the porosity rate. This shows that the bond strength between the epoxy matrix and the stone powder is strong (Figure 11e).

In Figure 11b and Figure 11c, the SEM image of ER/SSP composites shows agglomeration between the epoxy matrix and the stone powder on the surface. This agglomeration causes a decrease in the strength of the composite, as observed in the mechanical test results of the composite material. Moreover, the agglomerations occurring in the composite material prevent the reduction of the bond strength between the matrix and the stone powder and the homogeneous distribution of the stone powder particles on the matrix surface. This shows that the bond strength of the epoxy matrix decreases and the bond strength between the epoxy matrix and the stone powder are weak.

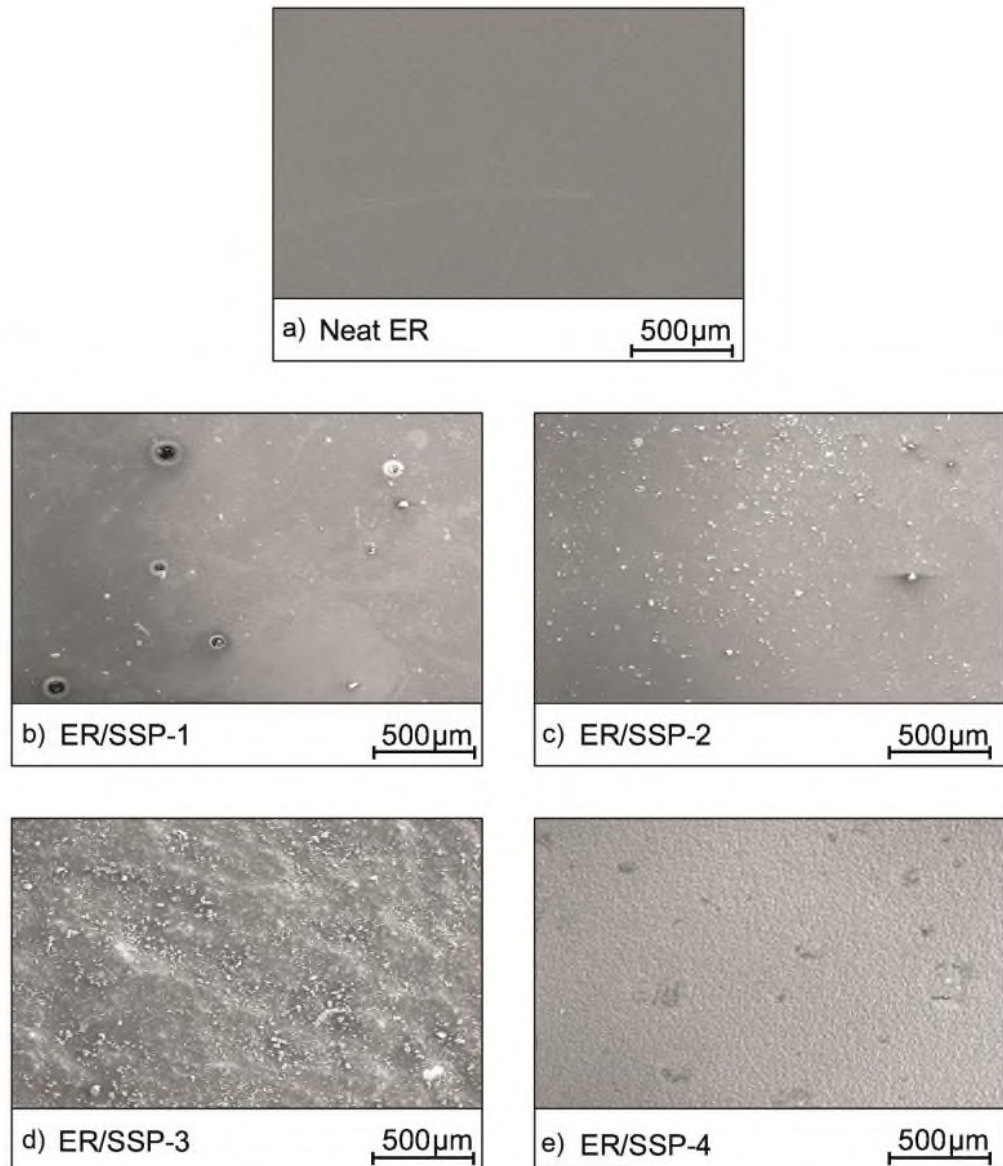


**Figure 11.** SEM image of ER/SSP composite

EDS analysis of ER/SSP-1 composite is given in Figure 12. When the map distribution of the elements in Figure 12 is examined, it is seen that it is the most dense carbon element. Moreover, the densities and distribution map of other elements in the ER/SSP-1 composite are oxygen, silicon, aluminum, potassium, iron, calcium, sodium and magnesium, respectively (Figure 12b-12j). It shows that the carbon and oxygen elements belong to the epoxy matrix. However, due to the carbonation of some of the compounds in Sille stone, the carbon element is also found in the stone powder. Oxygen and other elements are also present in the compounds of stone powder. According to the result of the EDS analysis of the ER/SSP-1 composite, it is observed that the epoxy matrix covers all the stone powder, and the stone powder is homogeneously dispersed into the epoxy matrix (Figure 12a-12k).

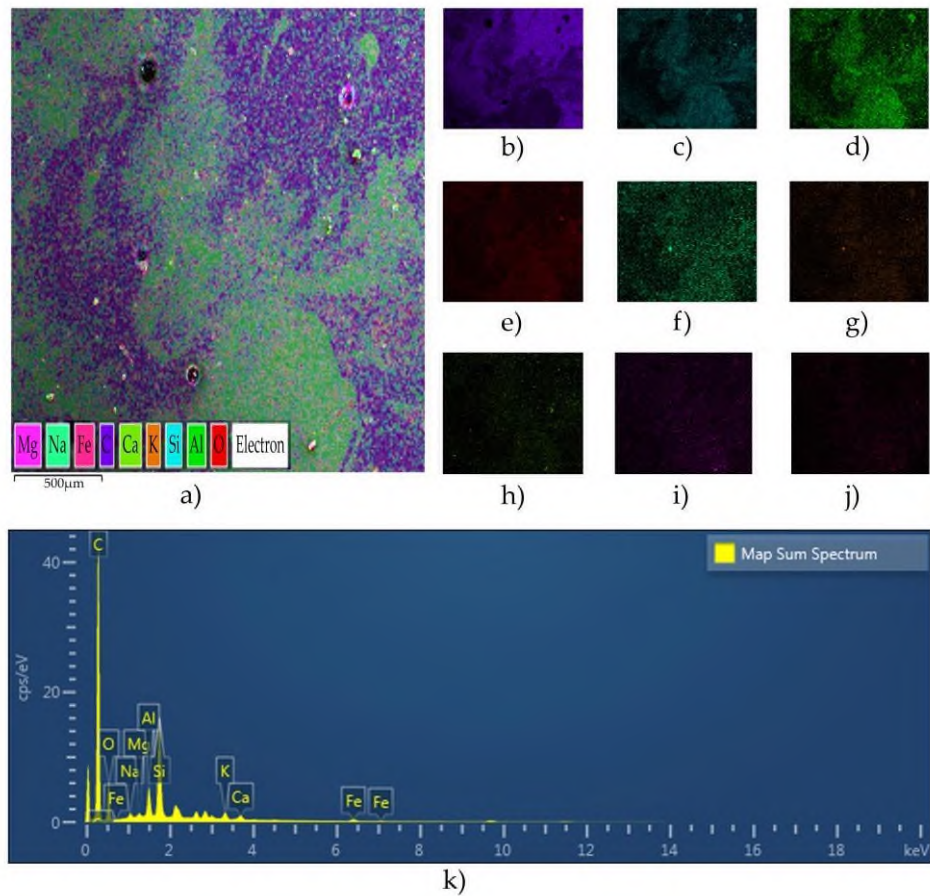


**Figure 12.** a) Elemental analysis and distribution map of ER/SSP-1 composite, b) Distribution of carbon element in ER/SSP-1 composite, c) Distribution of silicon element in ER/SSP-1 composite, d) Distribution of aluminum element in ER/SSP-1, e) Distribution of oxygen element in ER/SSP-1 composite, f) Distribution of sodium element in ER/SSP-1 composite, g) Distribution of potassium element in ER/SSP-1 composite, h) Distribution of calcium element in ER/SSP-1 composite, i) Distribution of magnesium element in ER/SSP-1 composite, j) Distribution of iron element in ER/SSP-1 composite, k) EDS analysis in ER/SSP-1 composite

EDS analysis of ER/SSP-2 composite is given in Figure 13. When the map distribution of the elements in Figure 13 is examined, it is seen that it is the most dense carbon element. Moreover, the densities and distribution map of the other elements in the ER/SSP-2 composite are oxygen, silicon, aluminum, potassium, iron, calcium, sodium and magnesium, respectively (Figure 13b-13j). It shows that the carbon and oxygen elements belong to the epoxy matrix. However, due to the carbonation of some of the compounds in Sille stone, the carbon element is also found in the stone powder. Oxygen and other elements are also present in the compounds of stone powder. ER/SSP-2 composite shows an increase in silicon element compared to ER/SSP-1. However, the oxygen element in ER/SSP-2 composite decreases compared to ER/SSP-1. This is due to an increase in the amount of stone powder and a decrease in the epoxy matrix. According to the result of the EDS analysis of the ER/SSP-2 composite, it prevents the homogeneous distribution of the elements due to the agglomeration that occurs between the epoxy matrix and the stone powder (Figure 13a-13k).

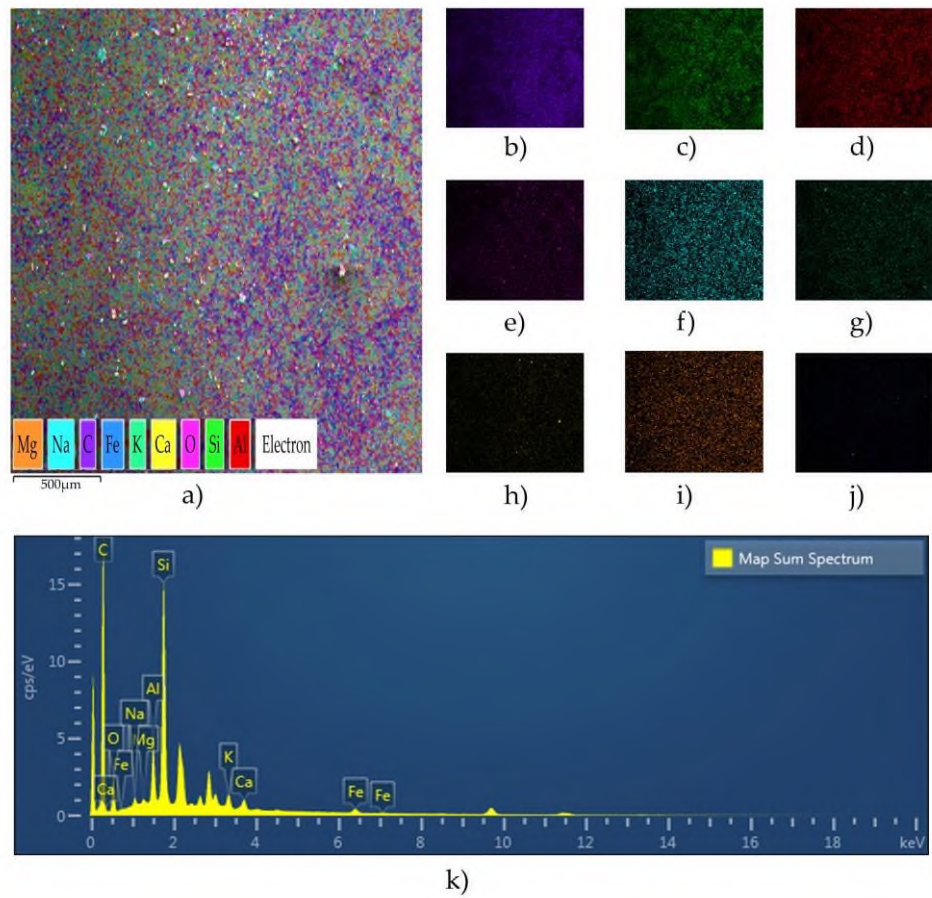


**Figure 13.** a) Elemental analysis and distribution map of ER/SSP-2 composite, b) Distribution of carbon element in ER/SSP-2 composite, c) Distribution of silicon element in ER/SSP-2 composite, d) Distribution of aluminum element in ER/SSP-2 composite, e) Distribution of oxygen element in ER/SSP-2 composite, f) Distribution of sodium element in ER/SSP-2 composite, g) Distribution of potassium element in ER/SSP-2 composite, h) Distribution of calcium element in ER/SSP-2 composite, i) Distribution of magnesium element in ER/SSP-2 composite, j) Distribution of iron element in ER/SSP-2 composite, k) EDS analysis in ER/SSP-2 composite

EDS analysis of ER/SSP-3 composite is given in Figure 14. When the map distribution of the elements in Figure 14 is examined, it is seen that it is the most dense carbon element. Moreover, the densities and distribution map of the other elements in the ER/SSP-3 composite are oxygen, silicon, aluminum, potassium, iron, calcium, sodium and magnesium, respectively (Figure 14b-14j). It shows that the carbon and oxygen elements belong to the epoxy matrix. However, due to the carbonation of some of the compounds in Silice stone, the carbon element is also found in the stone powder. Oxygen and other elements are also present in the compounds of stone powder. Silicon and oxygen element in ER/SSP-3 composite show an increase compared to ER/SSP-1 and ER/SSP-2. This is due to the decrease in the epoxy matrix due to the increase in the amount of stone powder. According to the results of the EDS analysis of the ER/SSP-3 composite, the agglomeration between the epoxy matrix and the stone powder prevents the homogeneous distribution of the elements. Moreover, this agglomeration causes the formation of pores in the composite material, since it cannot cover the stone powder to the epoxy matrix over the entire area (Figure 14a-14k).

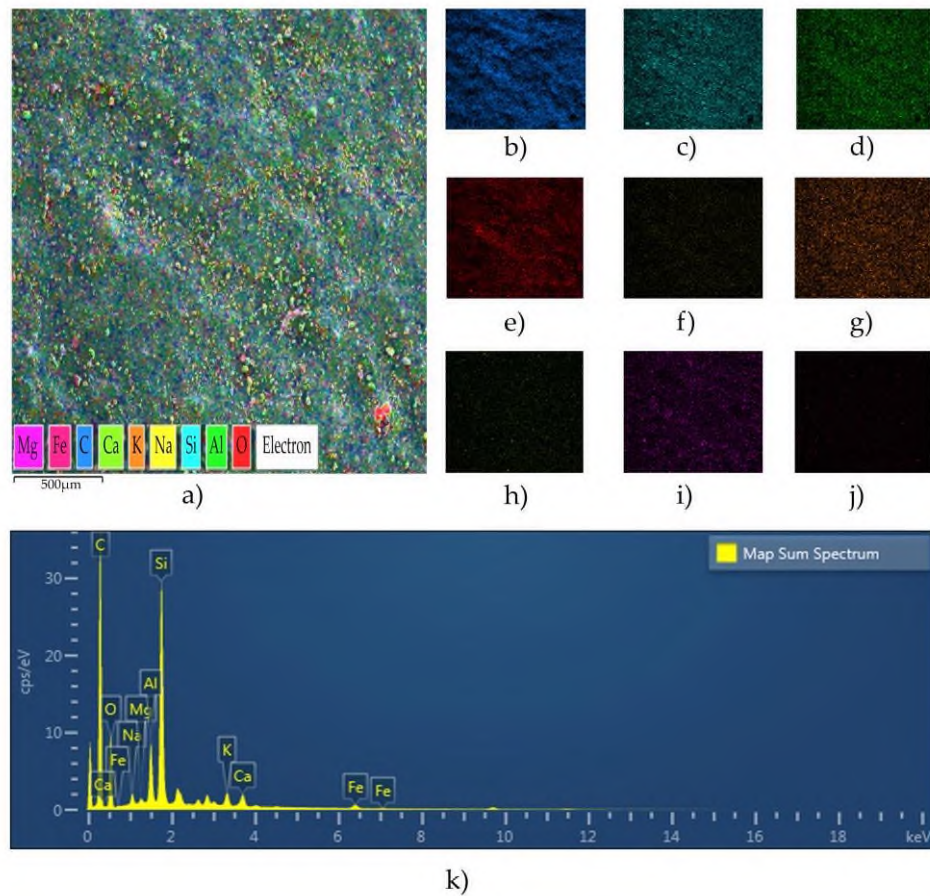


**Figure 14.** a) Elemental analysis and distribution map of ER/SSP-3 composite, b) Distribution of carbon element in ER/SSP-3 composite, c) Distribution of silicon element in ER/SSP-3 composite, d) Distribution of aluminum element in ER/SSP-3, e) Distribution of oxygen element in ER/SSP-3 composite, f) Distribution of sodium element in ER/SSP-3 composite, g) Distribution of potassium element in ER/SSP-3 composite, h) Distribution of calcium element in ER/SSP-3 composite, i) Distribution of magnesium element in ER/SSP-3 composite, j) Distribution of iron element in ER/SSP-3 composite, k) EDS analysis in ER/SSP-3 composite

EDS analysis of ER/SSP-4 composite is given in Figure 15. When the map distribution of the elements in Figure 15 is examined, it is seen that it is the most dense carbon element. Moreover, the densities and distribution map of the other elements in the ER/SSP-4 composite are oxygen, silicon, aluminum, potassium, iron, calcium, sodium and magnesium, respectively (Figure 15b-15j). It shows that the carbon and oxygen elements belong to the epoxy matrix. However, due to the carbonation of some of the compounds in Sille stone, the carbon element is also found in the stone powder. Oxygen and other elements are also present in the compounds of stone powder. According to the results of the EDS analysis of the ER/SSP-4 composite, the element distribution is more homogeneous than the other composites. Additionally, since the stone powder covers the entire area in the epoxy matrix in the ER/SSP-4 composite, it has been observed that the pores and porosities are less than the other composite types (Figure 15a-15k).

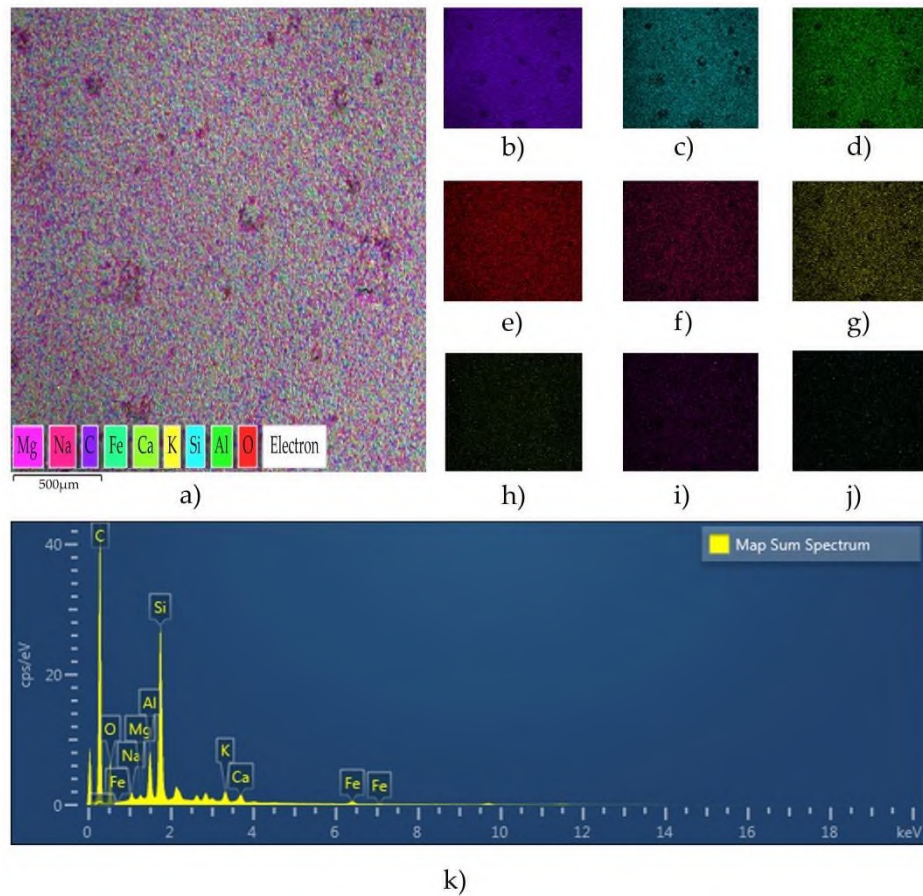


**Figure 15.** a) Elemental analysis and distribution map of ER/SSP-4 composite, b) Distribution of carbon element in ER/SSP-4 composite, c) Distribution of silicon element in ER/SSP-4 composite, d) Distribution of aluminum element in ER/SSP-4, e) Distribution of oxygen element in ER/SSP-4 composite, f) Distribution of sodium element in ER/SSP-4 composite, g) Distribution of potassium element in ER/SSP-4 composite, h) Distribution of calcium element in ER/SSP-4 composite, i) Distribution of magnesium element in ER/SSP-4 composite, j) Distribution of iron element in ER/SSP-4 composite, k) EDS analysis in ER/SSP-4 composite

### 3.8. Fourier Transform Infrared Spectroscopy (FTIR)

Infrared electromagnetic waves of ER and ER/SSP composites were made between 4000 and 500  $\text{cm}^{-1}$ . Additionally, in the FTIR analysis of the samples, it was applied starting from the 100% transmittance rate from 4000  $\text{cm}^{-1}$  wave number to 500  $\text{cm}^{-1}$  wave number. While examining the FTIR analysis of the samples, it was observed that the transmittance ratios decreased in the wave number value. The types of bonds corresponding to the vibrations or rotations between the atoms in the sample were determined [51, 52].

FTIR analysis result of ER and ER/SSP composites are given in Table 10 and Figure 16. As can be seen in Table 10 and Figure 16, the peak values at which the transmittance value of ER and ER/SSP composites decreased vary between 3345  $\text{cm}^{-1}$  and 554  $\text{cm}^{-1}$ . According to the results given in Table 10 shows the O–H stretching the bond type corresponding to the wavenumber peak value at 3345  $\text{cm}^{-1}$ , the aliphatic C–H stretching the bond type corresponding to the wavenumber peak value at 2920  $\text{cm}^{-1}$ , the C=O strong stretching the bond type corresponding to the wavenumber peak value at 1735  $\text{cm}^{-1}$ . Moreover, It also expresses aromatic ring C=C stretching the bond type corresponding to the wavenumber peak value at 1606  $\text{cm}^{-1}$ , aromatic C–C stretching the bond type corresponding to the wavenumber peak value at 1541  $\text{cm}^{-1}$ ,  $\text{CH}_3$  in the radical group C–H asymmetrical bending the bond

type corresponding to the wavenumber peak value at  $1457\text{ cm}^{-1}$ . Additionally, It have also been detected C–O bonds stretching the bond type corresponding to the wavenumber peak value at  $1235\text{ cm}^{-1}$ , Ar–O–R asymmetrical bending the bond type corresponding to the wavenumber peak value at  $1180\text{ cm}^{-1}$ , C–O–C of ethers stretching the bond type corresponding to the wavenumber peak value at  $1032\text{ cm}^{-1}$ , C–O–C of oxirane group stretching the bond type corresponding to the wavenumber peak value at  $825\text{ cm}^{-1}$  [53, 54].

The C–H aromatic ring bending shows the bond type corresponding to the wavenumber peak value at  $728\text{ cm}^{-1}$  and  $696\text{ cm}^{-1}$ , and C–H, N–H bending the bond type corresponding to the wavenumber peak value at  $554\text{ cm}^{-1}$  [55]. While these results were seen in all samples, a different peak value was determined at  $1090\text{ cm}^{-1}$  wave number, unlike the ER samples of ER/SSP composites. It expresses the C–N of ethers aromatic stretching the bond type corresponding to the wavenumber peak value at  $1090\text{ cm}^{-1}$  [56]. As a result of the FTIR analysis of the ER/SSP composite samples, the peak value at a wavelength of  $1090\text{ cm}^{-1}$  emerged due to the strong C–N bonds between the epoxy matrix and the stone powder.

**Table 10.** Type of bonds formed between corresponding atoms according to wave numbers of ER and ER/SSP composites

Wavenumber ( $\text{cm}^{-1}$ )	Bond Type
3345	O–H stretching
2920	Aliphatic C–H stretching
1735	C=O strong stretching
1606	Aromatic Ring C=C stretching
1541	Aromatic C–C stretching
1457	CH <sub>3</sub> in the radikal group C–H asymmetrical bending
1235	C–O bonds stretching
1180	Ar–O–R asymmetrical bending
1090	C–N aromatic stretching
1032	C–O–C of ethers bonds stretching
825	C–O–C of oxirane group bonds stretching
728	C–H aromatic ring bending
696	C–H aromatic ring bending
554	C–H, N–H bending



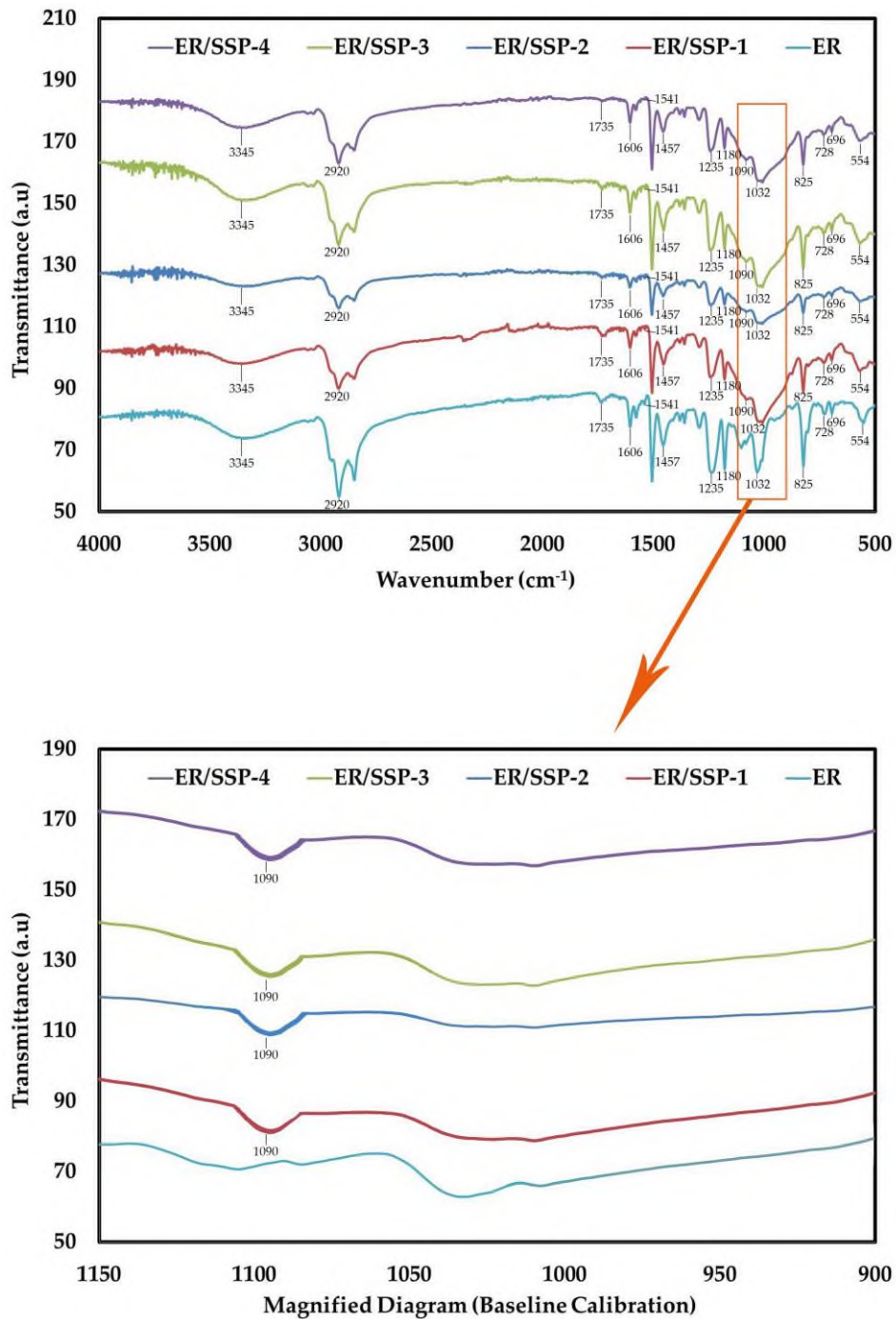


Figure 16. FTIR analysis result graph of ER and ER/SSP composites

#### 4. CONCLUSIONS

In this study, the mechanical, physical and microstructural properties of SSP repair mortar with epoxy matrix were demonstrated. Based on the test results conducted in the study, the following conclusions can be drawn:

- According to the void determination and water absorption test results, it has been determined that the composite mortar has a lower water absorption rate and porosity than Silice stone. The low water absorption rate and pore numbers of the composite material reduce the damage caused by decay in the structure. Moreover, the low water absorption rate of repair mortars in the restoration of cultural assets is beneficial for the protection of the structure.

- Due to the porous structure and high water absorption rate of Sille stone, it causes deterioration and damage in structures such as humidity and flowering.
- According to the test results performed to determine the mechanical properties of the repair mortar, the strength of the ER/SSP-4 composite was found to be higher than the other composite types. Additionally, the use of high levels of SSP in the production of this composite contributes to both the economy of the material and the protection of natural resources and the environment.
- The agglomeration between the ER/SSP-2 and ER/SSP-3 epoxy matrix and the stone powder increased the number of voids and pores in the composites. This reduced the strength of the agglomeration composites.
- According to SEM images, increasing the amount of SSP in ER/SSP composites creates rough surfaces and pores in the material. Moreover, it has been observed that the bond strength between the epoxy matrix and the stone powder has an effect on the loading of stone powder on the composite and the homogeneous distribution of the epoxy matrix.
- SEM-EDS and FTIR analyzes of ER/SSP composites were shown to be compatible with the mechanical test results.

As a result, the high strength, low water absorption rate and pore properties of epoxy matrix composite mortars provide great potential for the restoration applications of historical buildings constructed from Sille stone. Moreover, the color of the epoxy matrix composite mortars being compatible with the color of the sille stone contributes to the preservation of the original forms in the restoration of historical buildings.

#### **Declaration of Ethical Standards**

The authors declare that the study complies with all applicable laws and regulations and meets ethical standards.

#### **Credit Authorship Contribution Statement**

**A.C.A:** Investigation, Experimental Section, Data Curation, Methodology, Investigation, Writing – original draft. **M.T:** Validation, Writing -review & editing, Supervision.

#### **Declaration of Competing Interest**

The authors declare that they have no known competing financial interests or personal relationships that could have appeared to influence the work reported in this paper.

#### **Funding / Acknowledgements**

This study was prepared from the first author's PH.D. thesis. This thesis study was supported by the Scientific Research Projects Commission of the Konya Technical University within the scope of Ph.D. (Project number: 211120045). The authors are grateful for the support provided by Konya Technical University (Türkiye). Experimental studies of this research were carried out in laboratories of the Science and Technology Research and Application Center (BITAM) at Necmettin Erbakan University. We would like to thank the staff of BITAM for their assistance as well.

#### **Data Availability**

The data that support the findings of this study are available from the corresponding author upon reasonable request.

## REFERENCES

- [1] A. Isebaert, L. Van Parys, and V. Cnudde, "Composition and compatibility requirements of mineral repair mortars for stone—A review," *Construction and Building Materials*, vol. 59, pp. 39-50, 2014.
- [2] L. Schueremans, Ö. Cizer, E. Janssens, G. Serré, and K. Van Balen, "Characterization of repair mortars for the assessment of their compatibility in restoration projects: Research and practice," *Construction and building materials*, vol. 25, no. 12, pp. 4338-4350, 2011.
- [3] J.-D. Mertz, M. Guiavarc'h, and P. Pagnin, "Dilation behaviour of lime mortars for restoration work: application to the compatibility of cracked stone reassembling," *European Journal of Environmental and Civil Engineering*, vol. 16, no. 5, pp. 527-542, 2012.
- [4] M. Fener and İ. İnce, "Effects of the freeze–thaw (F–T) cycle on the andesitic rocks (Sille-Konya/Turkey) used in construction building," *Journal of African Earth Sciences*, vol. 109, pp. 96-106, 2015.
- [5] M. E. Hatır, "Determining the weathering classification of stone cultural heritage via the analytic hierarchy process and fuzzy inference system," *Journal of Cultural Heritage*, vol. 44, pp. 120-134, 2020.
- [6] M. E. Hatır, M. Barstuğan, and İ. İnce, "Deep learning-based weathering type recognition in historical stone monuments," *Journal of Cultural Heritage*, vol. 45, pp. 193-203, 2020.
- [7] M. Korkanç *et al.*, "Interpreting sulfated crusts on natural building stones using sulfur contour maps and infrared thermography," *Environmental Earth Sciences*, vol. 78, pp. 378, 2019.
- [8] A. Ozdemir, "Capillary water absorption potential of some building materials," *Geological Engineering*, vol. 26, no. 1, pp. 19-32, 2002.
- [9] V. Zedef, K. Kocak, A. Doyen, H. Ozsen, and B. Kekec, "Effect of salt crystallization on stones of historical buildings and monuments, Konya, Central Turkey," *Building and Environment*, vol. 42, no. 3, pp. 1453-1457, 2007.
- [10] Ç. Öztürk, S. Akpınar, and M. Tarhan, "Investigation of the usability of Siliceous stone as additive in floor tiles," *Journal of the Australian Ceramic Society*, vol. 57, pp. 567-577, 2021.
- [11] J. Lanás, J. P. Bernal, M. Bello, and J. A. Galindo, "Mechanical properties of natural hydraulic lime-based mortars," *Cement and concrete research*, vol. 34, no. 12, pp. 2191-2201, 2004.
- [12] E. Navrátilová and P. Rovnaníková, "Pozzolanic properties of brick powders and their effect on the properties of modified lime mortars," *Construction and Building Materials*, vol. 120, pp. 530-539, 2016.
- [13] Y. Zeng, B. Zhang, and X. Liang, "A case study and mechanism investigation of typical mortars used on ancient architecture in China," *Thermochimica Acta*, vol. 473, no. 1-2, pp. 1-6, 2008.
- [14] G. F. Huseien and K. W. Shah, "Performance evaluation of alkali-activated mortars containing industrial wastes as surface repair materials," *Journal of Building Engineering*, vol. 30, p. 101234, 2020.
- [15] R. A. Alves, K. Strecker, R. B. Pereira, and T. H. Panzera, "Mixture design applied to the development of composites for steatite historical monuments restoration," *Journal of Cultural Heritage*, vol. 45, pp. 152-159, 2020.
- [16] B. Dębska and L. Lichołai, "A study of the effect of corrosive solutions on selected physical properties of modified epoxy mortars," *Construction and Building Materials*, vol. 65, pp. 604-611, 2014.
- [17] E. Tesser, L. Lazzarini, and S. Bracci, "Investigation on the chemical structure and ageing transformations of the cycloaliphatic epoxy resin EP2101 used as stone consolidant," *Journal of Cultural Heritage*, vol. 31, pp. 72-82, 2018.
- [18] E. M. Alonso-Villar, T. Rivas, and J. S. Pozo-Antonio, "Adhesives applied to granite cultural heritage: effectiveness, harmful effects and reversibility," *Construction and Building Materials*, vol. 223, pp. 951-964, 2019.

- [19] J.-L. Roig-Salom, M.-T. Doménech-Carbó, J. de la Cruz-Cañizares, F. Bolívar-Galiano, M.-J. Pelufo-Carbonell, and Y. Peraza-Zurita, "SEM/EDX and vis spectrophotometry study of the stability of resin-bound mortars used for casting replicas and filling missing parts of historic stone fountains," *Analytical and bioanalytical chemistry*, vol. 375, pp. 1176-1181, 2003.
- [20] A. C. Ari, M. Tosun, and Y. R. Eker, "Polymer matrix and stone powder based composite mortar for the restoration of siliceous stone structures," *Studies in Conservation*, vol. 69, no. 1, pp. 50-57, 2024.
- [21] F. Güyer *et al.*, "Konya İli Çevre Jeolojisi ve Doğal Kaynaklar," *MTA Rap*, no. 42149, 1998.
- [22] A. C. Ari, M. Tosun, İ. Oral, and Y. R. Eker, "Ultrasonic characterization of polymer based siliceous stone powder composite mortars," *Turkish Journal of Civil Engineering*, vol. 35, no. 3, pp. 21-46, 2024.
- [23] ASTM-D2734, *Standard test method for void content of reinforced plastics*, 2009.
- [24] URL1. (19.07.2022). Available: <https://www.erbakan.edu.tr/bitam/sayfa/3297>.
- [25] ASTM-D570, *Standard test method for water absorption of plastics*, 2005.
- [26] ASTM-D790, *Standard test methods for flexural properties of unreinforced and reinforced plastics and electrical insulating materials*, 2000.
- [27] ASTM-D695, *Standard test method for compressive properties of polymer matrix composite materials*, 2010.
- [28] ASTM-D638, *Standard test method for tensile properties of plastic*, 2005.
- [29] ASTM-D2240, *Standard test method for rubber property-durometer hardness*, 2010.
- [30] J. Lanas and J. I. Alvarez-Galindo, "Masonry repair lime-based mortars: factors affecting the mechanical behavior," *Cement and concrete research*, vol. 33, no. 11, pp. 1867-1876, 2003.
- [31] Á. Török and B. Szemerey-Kiss, "Freeze-thaw durability of repair mortars and porous limestone: compatibility issues," *Progress in Earth and Planetary Science*, vol. 6, pp. 42, 2019.
- [32] Z. Zheng, Y. Li, X. Ma, X. Zhu, and S. Li, "High density and high strength cement-based mortar by modification with epoxy resin emulsion," *Construction and Building Materials*, vol. 197, pp. 319-330, 2019.
- [33] L. Korat, B. Mirtič, A. Mladenović, A. M. Pranjic, and S. Kramar, "Formulation and microstructural evaluation of tuff repair mortar," *Journal of Cultural Heritage*, vol. 16, no. 5, pp. 705-711, 2015.
- [34] M. M. Rahman and M. A. Islam, "Effect of epoxy resin on the intrinsic properties of masonry mortars," *Iranian Polymer Journal*, vol. 21, pp. 621-629, 2012.
- [35] V. Rajput, S. K. Somani, A. Agrawal, and V. S. Pagey, "Mechanical properties of epoxy composites filled with micro-sized kota stone dust," *Materials Today: Proceedings*, vol. 47, pp. 2673-2676, 2021.
- [36] R. Karthikeyan, R. Girimurugan, G. Sahoo, P. Maheskumar, and A. Ramesh, "Experimental investigations on tensile and flexural properties of epoxy resin matrix waste marble dust and tamarind shell particles reinforced bio-composites," *Materials Today: Proceedings*, vol. 68, pp. 2215-2219, 2022.
- [37] M. L. P. Gomes, E. A. Carvalho, L. N. Sobrinho, S. N. Monteiro, R. J. Rodriguez, and C. M. F. Vieira, "Production and characterization of a novel artificial stone using brick residue and quarry dust in epoxy matrix," *Journal of materials research and technology*, vol. 7, no. 4, pp. 492-498, 2018.
- [38] K. A. Gour, R. Ramadoss, and T. Selvaraj, "Revamping the traditional air lime mortar using the natural polymer-Areca nut for restoration application," *Construction and Building Materials*, vol. 164, pp. 255-264, 2018.
- [39] F. Iucolano, B. Liguori, and C. Colella, "Fibre-reinforced lime-based mortars: A possible resource for ancient masonry restoration," *Construction and Building Materials*, vol. 38, pp. 785-789, 2013.
- [40] J. A. V. Gonçalves, D. A. T. Campos, G. d. J. Oliveira, M. d. L. d. S. Rosa, and M. A. Macêdo, "Mechanical properties of epoxy resin based on granite stone powder from the Sergipe fold-and-thrust belt composites," *Materials Research*, vol. 17, no. 4, pp. 878-887, 2014.

- [41] M. L. Santarelli, F. Sbardella, M. Zuena, J. Tirillò, and F. Sarasini, "Basalt fiber reinforced natural hydraulic lime mortars: A potential bio-based material for restoration," *Materials & Design*, vol. 63, pp. 398-406, 2014.
- [42] B. Kekeç, "Investigation of the texture, physical and mechanical properties of the rocks used as building stone," Seljuk University Graduate School of Natural Sciences, MS Thesis, Konya, 2005.
- [43] C. Borsellino, L. Calabrese, and G. Di Bella, "Effects of powder concentration and type of resin on the performance of marble composite structures," *Construction and Building Materials*, vol. 23, no. 5, pp. 1915-1921, 2009.
- [44] D. Olmos, A. Aznar, and J. González-Benito, "Kinetic study of the epoxy curing at the silica particles/epoxy interface using the fluorescence of pyrene label," *Polymer testing*, vol. 24, no. 3, pp. 275-283, 2005.
- [45] M. A. R. Bhutta, "Effects of polymer-cement ratio and accelerated curing on flexural behavior of hardener-free epoxy-modified mortar panels," *Materials and structures*, vol. 43, pp. 429-439, 2010.
- [46] K. Hassan, P. Robery, and L. Al-Alawi, "Effect of hot-dry curing environment on the intrinsic properties of repair materials," *Cement and Concrete Composites*, vol. 22, no. 6, pp. 453-458, 2000.
- [47] A. Mallat and A. Alliche, "Mechanical investigation of two fiber-reinforced repair mortars and the repaired system," *Construction and building materials*, vol. 25, no. 4, pp. 1587-1595, 2011.
- [48] M. Medeiros, P. Helene, and S. Selmo, "Influence of EVA and acrylate polymers on some mechanical properties of cementitious repair mortars," *Construction and building materials*, vol. 23, no. 7, pp. 2527-2533, 2009.
- [49] S.-Y. Fu, X.-Q. Feng, B. Lauke, and Y.-W. Mai, "Effects of particle size, particle/matrix interface adhesion and particle loading on mechanical properties of particulate-polymer composites," *Composites Part B: Engineering*, vol. 39, no. 6, pp. 933-961, 2008.
- [50] T. T. L. Doan, H. M. Brodowsky, U. Gohs, and E. Mäder, "Re-use of marble stone powders in producing unsaturated polyester composites," *Advanced Engineering Materials*, vol. 20, no. 7, p. 1701061, 2018.
- [51] S. Ramesh, K. H. Leen, K. Kumutha, and A. Arof, "FTIR studies of PVC/PMMA blend based polymer electrolytes," *Spectrochimica Acta Part A: Molecular and Biomolecular Spectroscopy*, vol. 66, no. 4-5, pp. 1237-1242, 2007.
- [52] M. R. Reddy, A. Subrahmanyam, M. M. Reddy, J. S. Kumar, V. Kamalaker, and M. J. Reddy, "X-RD, SEM, FT-IR, DSC Studies of Polymer Blend Films of PMMA and PEO," *Materials Today: Proceedings*, vol. 3, no. 10, pp. 3713-3718, 2016.
- [53] M. R. M. Hafiezal, A. Khalina, Z. A. Zurina, M. D. M. Azaman, and Z. M. Hanafee, "Thermal and flammability characteristics of blended jatropha bio-epoxy as matrix in carbon fiber-reinforced polymer," *Journal of Composites Science*, vol. 3, no. 1, pp. 6, 2019.
- [54] F. Kasim, M. Mahdi, J. Hassan, S. Al-Ani, and S. Kasim, "Preparation and optical properties of CdS/Epoxy nanocomposites," *International Journal of Nanoelectronics and Materials*, vol. 5, pp. 57-66, 2012.
- [55] G. Nikolic, S. Zlatkovic, M. Cakic, S. Cakic, C. Lacnjevac, and Z. Rajic, "Fast fourier transform IR characterization of epoxy GY systems crosslinked with aliphatic and cycloaliphatic EH polyamine adducts," *Sensors*, vol. 10, no. 1, pp. 684-696, 2010.
- [56] A. Carrillo-Castillo and J. G. Osuna-Alarcón, "Preparation and characterization of hybrid materials of epoxy resin type bisphenol a with silicon and titanium oxides by sol gel process," *Journal of the Mexican Chemical Society*, vol. 55, no. 4, pp. 233-237, 2011.



## AN ADAPTIVE AND HYBRID STATE OF CHARGE ESTIMATION METHOD INTEGRATING SEQUENCE-TO-POINT LEARNING AND COULOMB COUNTING FOR LI-ION BASED ENERGY STORAGE SYSTEMS

\* Halil ÇİMEN 

*Konya Technical University, Engineering and Natural Sciences Faculty, Electrical-Electronics Engineering Department, Konya, TÜRKİYE*  
[hcimen@ktun.edu.tr](mailto:hcimen@ktun.edu.tr)

### *Highlights*

- An adaptive and hybrid model has been proposed to achieve high-accuracy SOC estimation
- The estimation process has been improved by integrating sequence-to-point learning with the coulomb counting method, leading to more precise estimations
- Multi-scale CNN-based sequence-to-point learning is used to obtain initial SOC values
- The estimation weights have been adaptively adjusted to optimize estimation performance under various operating conditions, ensuring robust and reliable outcomes



## AN ADAPTIVE AND HYBRID STATE OF CHARGE ESTIMATION METHOD INTEGRATING SEQUENCE-TO-POINT LEARNING AND COULOMB COUNTING FOR LI-ION BASED ENERGY STORAGE SYSTEMS

\* Halil ÇİMEN 

*Konya Technical University, Engineering and Natural Sciences Faculty, Electrical-Electronics Engineering Department, Konya, TÜRKİYE*  
[hcimen@ktun.edu.tr](mailto:hcimen@ktun.edu.tr)

(Received: 23.09.2024; Accepted in Revised Form: 09.01.2025)

**ABSTRACT:** For safe and long-lasting operation of Li-ion batteries used in electric vehicles and electric grid applications, the State of Charge (SOC) of the battery cell must be estimated with high accuracy. However, due to the uncertainty in environmental conditions and the complex nature of battery chemistry, SOC estimation still presents a significant challenge. In this study, an adaptive and hybrid method for SOC estimation of a Li-ion battery cell is proposed. Convolutional Neural Network (CNN) based Sequence-to-point learning architecture is used to estimate the initial SOC values at specific time intervals. In order to increase the estimation accuracy, a multi-scale CNN architecture is designed, and useful features are captured. The obtained estimation values are integrated with the partial coulomb counting method to increase the accuracy. In addition, the proposed model adaptively updates the estimation weights with the help of the estimation error data obtained during the full charging of the batteries. The proposed model is tested on the LG 18650HG2 dataset. The results prove that the proposed model is 23% more accurate than benchmark models at 25°C and 55.5% more accurate at 0°C.

**Keywords:** *Convolutional Neural Networks, Coulomb Counting, Deep Learning, Li-Ion Batteries, Sequence-to-Point Learning, State of Charge*

### 1. INTRODUCTION

Today, there is a major revolution in the energy sector due to global warming, the rapid depletion of underground resources, and the increasing share of new energy sources in production. The most important components of this revolution are undoubtedly renewable energy sources and energy storage elements. While cleaner and cheaper electrical energy can be produced with renewable energy sources, the excess energy produced can be stored as a reserve power source. Although there are many different energy storage systems, lithium-ion batteries are the most preferred storage element in power grid applications [1].

Li-ion batteries are preferred in many applications due to their high gravimetric and volumetric energy density, higher cell voltage compared to other batteries, long cycle and calendar lifetime, and low self-discharge. Although batteries have a chemical structure, they are analyzed by modeling them electrically. The characteristics of the battery are modeled using passive circuit elements and detailed information about battery performance is obtained. Parameters such as internal resistance and SOC of the battery are estimated using voltage, current, and temperature measurements, which can be measured by sensors. SOC indicates the instantaneous state of charge of the battery and defines the remaining capacity within the battery cell in percentage terms. Since it cannot be measured directly, it is estimated by various methods. The first of these estimation methods is the Coulomb Counting method. The current drawn (or injected) from the battery cell is measured with a certain sampling frequency and the measured values are accumulated to determine the amount of capacity drawn (or injected) from the battery. However, in order to use this method, the initial SOC value of the battery must be known. However, this value is not always known accurately. In addition, the accuracy of this method is insufficient due to the need to know the coulombic efficiency and the need for recalibration [2]. The second estimation method is the look-up table.

\*Corresponding Author: Halil ÇİMEN, [hcimen@ktun.edu.tr](mailto:hcimen@ktun.edu.tr)

Here, a table is created by determining the open circuit voltage value of the battery against the SOC value with the help of experiments. The SOC value corresponding to the voltage value measured during operation is selected from the table. However, the open circuit voltage of the battery can only be measured after a long relaxation time. For this reason, the SOC value cannot be determined accurately. In addition, the open circuit voltage-SOC table may change due to effects such as temperature and aging. The most important disadvantage of the method is that the SOC curve has a flat structure for some battery chemistries, which significantly reduces the estimation accuracy [3]. Model-based and model-free methods are used to overcome the disadvantages of the above-mentioned methods. Model-based methods such as Kalman filter [4], Adaptive Lyapunov observer [5], Fractional-order observer [6] use a battery model and create a closed-loop system for SOC estimation. In this way, the estimation accuracy is increased with feedback. However, this model relies on high model accuracy. The estimation accuracy may decrease due to incorrect determination of model parameters and changes in parameters due to aging. Model-free methods are used to eliminate the need for models in model-based methods. Machine learning and deep learning are the most used model-free SOC estimation methods [7, 8]. Artificial Neural Networks [9], Recurrent Neural Networks (RNNs) [10], CNNs [11] are the most commonly used SOC estimation methods. [12] presents a self-attention assisted Long Short-Term Memory model that can analyze batteries under different operating conditions and aging levels. This allows the model to capture the dependencies in the sequence in more detail. In [13], a CNN-based multi-task learning mechanism is designed to predict the SOC, state of energy and Future temperature of a lithium-ion battery. In [14], it is aimed to increase the SOC estimation accuracy by extracting more features with 2-D time–frequency domain spectrogram analysis. The generalization performance of the estimations is increased with a CNN-based model. The advantage of neural network-based methods is that there is no need for any battery model. Networks are trained using battery cell data obtained as a result of experiments conducted at different temperatures in the laboratory environment. The models trained with voltage, current, and temperature data predict SOC with the data obtained during operation. However, the biggest disadvantage of deep learning is the generalization capacity of the models. Generalization is defined as the accuracy of deep learning models when tested with data not used during training. The distribution of training data and test data may be different. In addition, data distribution shifts may occur due to the aging of the battery cell over time. Due to these factors, the estimations made by deep learning models can be significantly inaccurate.

This paper presents an adaptive and hybrid SOC prediction model that mitigates the disadvantages of the above-mentioned methods. The model is developed by integrating deep learning and coulomb counting methods. Using a CNN-based sequence-to-point learning approach, an initial SOC estimation is performed using voltage, current, and temperature data measured from the cell. This estimate value is processed with the coulomb counting method to obtain a final estimate. The estimates obtained by coulomb counting and sequence-to-point learning are made adaptive by the weighted average method. Main contributions of the paper:

- An adaptive and hybrid model has been proposed to achieve high-accuracy SOC estimation.
- Multi-scale CNN-based sequence-to-point learning is used to obtain highly accurate initial SOC values.
- The estimation process has been improved by integrating sequence-to-point learning with the coulomb counting method, leading to more precise estimations.
- The estimation weights have been adaptively adjusted to optimize estimation performance under various operating conditions, ensuring robust and reliable outcomes.

## 2. METHODOLOGY

### 2.1. Problem Formulation

The SOC value of Li-ion batteries cannot be measured directly and must be estimated. Especially in applications such as electric vehicles where the remaining range is important, it is vital to accurately



determine the SOC. It can be formulated as follows using the measurable values of voltage, current and temperature of the battery:

$$SOC(t) = f(v(t), i(t), T(t)) \quad (1)$$

where  $v$  is voltage,  $i$  is current and  $T$  is battery surface temperature. Since SOC is an unmeasurable quantity, it is estimated. Therefore, the estimation value can be expressed by the formula  $\widehat{SOC}(t) = f(v(t), i(t), T(t)) + \epsilon$ . Different approaches such as coulomb counting, look-up tables, neural networks can be used for the function  $f$  here. The coulomb counting method uses only the value of  $i(t)$  for prediction, while the look-up table method uses the value of  $v(t)$ .

## 2.2. Sequence to Point Learning

Deep learning models have the capacity to model time dependencies such as time series. Time dependencies in data divided into sequences with sliding windows can be detected with different deep-learning architectures. Modified versions of RNNs such as Long-short Term Memory (LSTM) [15] and Gated Recurrent Units [16] have the capacity to analyze long-time series. In addition, Temporal CNN [11] architectures have the capacity to capture long-term dependencies and make better predictions. When performing time series analysis, data can be organized in two different ways. The first is when the input and output are sequential. This approach is called Sequence-to-Sequence (seq2seq).

The seq2seq approach considers a sequence of length  $w$ ,  $X(t:t+w-1)$  as input and estimates  $Y(t:t+w-1)$  corresponding to the same time period or a future time period sequence  $Y(t+w:t+2w)$  as output. Here  $X$  represents input data and  $Y$  represents output data. A neural network that maps input data to output data can be defined as  $f_N(X(t:t+w-1))=Y(t:t+w-1)$ . In this approach, multiple predictions are made for each output, and the final prediction is obtained as the average of all predictions. Forecasting by averaging affects the success of the forecasting results as it causes smoothing of the edges. Another disadvantage is that while more accurate predictions can be made for the nodes in the middle of the sequence (midpoint), the predictions for the nodes in the corners may be less accurate. This is because the midpoint output prediction can be predicted with more information using both past and future data [17]. Sequence-to-Point (seq2point) approach is used to overcome this problem. The seq2point accepts a sequence of length  $w$ ,  $X(t:t+w-1)$  as input and predicts a single point  $Y(t+w/2)$  corresponding to the midpoint of the same time period as output. The neural network can be defined as  $f_N(X(t:t+w-1))=Y(t+w/2)$ . In this way, there is no need for averaging, and more accurate predictions can be made with a non-causal approach. The seq2seq and seq2point architectures are visualized in Figure 1.

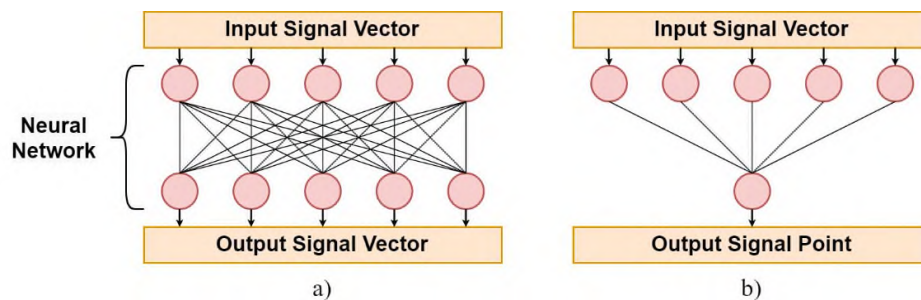


**Figure 1.** Different types of learning schemes, a) Sequence-to-sequence learning, b) Sequence-to-point learning

## 2.3. Coulomb Counting

The other name of this method is Ampere-hour counting method. It is a method used to estimate the SOC of a battery cell. By integrating the current injected or withdrawn from the battery over time, it tries to determine the current capacity of the battery with the following formula:

$$SOC_{Coulomb}(t) = SOC(t_0) + \frac{1}{Q_{total}} \int_{t_0}^t i(\tau) \cdot \eta \cdot d\tau \quad (2)$$

where  $Q_{total}$  is the total capacity of the battery cell,  $i$  is the battery current,  $\eta$  is the coulombic efficiency of the battery. Since the computational power required is small, it is often preferred in practical applications. As can be seen from (1), the initial SOC value and  $\eta$  value must be known. In addition, the estimates need to be calibrated due to the measurement error of the current sensor. The constant current-constant voltage (CC-CV) curve during charging can be used for calibration.

### 3. PROPOSED SYSTEM

#### 3.1. System Definition

The architecture of the adaptive and hybrid SOC estimation model proposed in this study is shown in Figure 2.

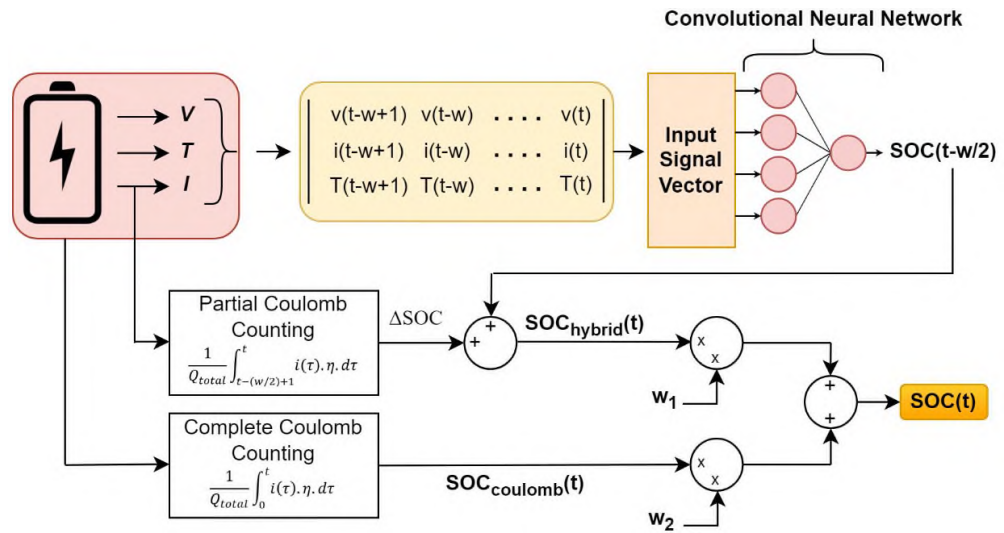


Figure 2. Proposed SOC estimation architecture

Two different forecasts are realized in the model. The first one is the  $SOC_{hybrid}(t)$  estimation obtained with the hybrid approach. In the hybrid structure, it is first aimed to accurately determine the initial SOC value required for the coulomb counting method with the help of CNN-based seq2point learning. The seq2point method estimates the midpoint SOC value  $SOC(t-w/2)$  against the input data  $X(t-w+1:t)$ . However, SOC estimation should be done for time  $t$ . For this purpose, the  $SOC_{hybrid}(t)$  value was obtained by summing the estimation value obtained from the seq2point method for time  $(t-w/2)$  with the SOC value calculated by partial coulomb counting. The hybrid SOC estimate can be formulated as follows:

$$SOC_{hybrid}(t) = f_{CNN}(v, i, T(t-w+1:t)) + \frac{1}{Q_{total}} \int_{t-\frac{w}{2}+1}^t i(\tau) \cdot \eta \cdot d\tau \quad (3)$$

where  $f_{CNN}$  represents a CNN-based deep learning model. This model uses data windows of length  $w$  as input. These windows are obtained with sliding windows. The CNN model uses voltage, current and temperature data from time  $t-w+1$  to time  $t$  to estimate the point  $t-w/2$ . The partial coulomb counting method obtains a  $\Delta SOC$  value by summing the current data read from point  $t-(w/2)+1$  to point  $t$ . By summing the obtained SOC values, the  $SOC_{hybrid}(t)$  value at  $t$  is determined. The estimated value can be used as the final SOC value. However, it should be kept in mind that the deep learning model cannot

always make accurate predictions. If the prediction made by CNN is inaccurate, the final  $SOC(t)$  estimation will also be inaccurate. For this reason, a parallel estimation method is added to the hybrid estimation.

The second estimation method is complete coulomb counting. In this method, the initial SOC value is set to 1 when the full charge condition defined by the manufacturer is reached during charging. From this moment on, the  $SOC_{coulomb}(t)$  value is calculated by calculating the Ah value withdrawn/injected from the battery with the traditional coulomb counting method. Each time the battery is fully charged, the initial SOC value is set to 1 again.

Using the values obtained with both estimation methods, the final SOC value is calculated as weighted average as follows:

$$SOC(t) = w_1 \cdot SOC_{hybrid}(t) + w_2 \cdot SOC_{coulomb}(t) \quad (4)$$

where  $w_1$  and  $w_2$  are weighting factors that weight two different estimations and allow the proposed system to be adaptive. The estimation accuracy of the two estimation methods mentioned above may vary depending on factors such as noise of current sensors, operating conditions, ambient temperature, etc. For this reason, considering the variable conditions, giving more weight to the method with higher estimation accuracy and lower error rate will increase the success of the final SOC estimation. Adaptivity is based on continuously updating the weights. These weights are updated based on the error rate of the two different estimations methods. Therefore, the weight value of the method with low error rate will be higher and the weight value of the method with high error rate will be lower. The process of updating the weights is explained in detail below.

In electric vehicle applications, batteries can be charged up to 100% SOC with the CC-CV method. During charging, CC is used until the battery voltage is equal to the charging cut-off voltage, and after equality is achieved, CV is used until the charging current reaches a certain level. The CC-CV charging curve obtained under 25°C temperature from the LG 18650HG2 dataset shared by MacMaster University in 2020 is shown in Figure 3 [18].

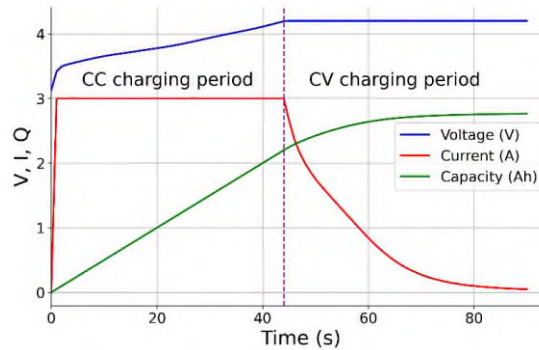


**Figure 3.** CC-CV charging characteristic

As seen in Figure 3, the capacity curve (green) shows a linear change during CC and a non-linear change during CV. In this study, the capacity increase curve during charging is used to determine the True SOC value. To determine the True SOC value, the battery must be fully charged. The  $TrueSOC(t_{plug-in})$  value at the time the battery is plugged in can be determined by the time until the battery is fully charged. The True SOC value is calculated mathematically by converting the linear/non-linear variation of the CC-CV charging periods into a function with the curve fitting method. According to the obtained  $TrueSOC(t_{plug-in})$  value, the weights  $w_1$  and  $w_2$  are updated as follows:

$$w_h = \frac{1}{\left|1 - \frac{SOC_{hybrid}(t_{plug-in})}{TrueSOC(t_{plug-in})}\right|}, \quad w_c = \frac{1}{\left|1 - \frac{SOC_{coulomb}(t_{plug-in})}{TrueSOC(t_{plug-in})}\right|} \quad (5)$$

$$w_1 = \frac{\alpha \cdot w_h}{\alpha \cdot w_h + w_c}, \quad w_2 = \frac{w_c}{\alpha \cdot w_h + w_c} \quad (6)$$

where  $\alpha$  is a coefficient greater than 1. The coefficient  $\alpha$  acts as a balancing parameter between the two approaches. If  $\alpha$  is increased, the weight of the Hybrid method becomes larger and the weight of the Coulomb method decreases accordingly. Adjusting the  $\alpha$  coefficient helps to optimize the performance of the model under different operating conditions.

### 3.2. CNN Model Definition

CNNs are a deep learning model frequently used in areas such as image recognition and segmentation [19]. In this study, a CNN-based multi-scale deep learning model is used to implement seq2point learning. Multi-scale is an approach that processes sequence inputs at different scales to extract different features from the same data. Deep learning models such as U-Net [20] can extract different features from different layers by combining low-layer features with high-layer features with skip-connections. In addition, different filter sizes and different dilation rates are used for multi-scale [21]. In this study, it is aimed to extract more features and capture different dependencies over time by using different dilation rates. The developed model is shown in Figure 4.

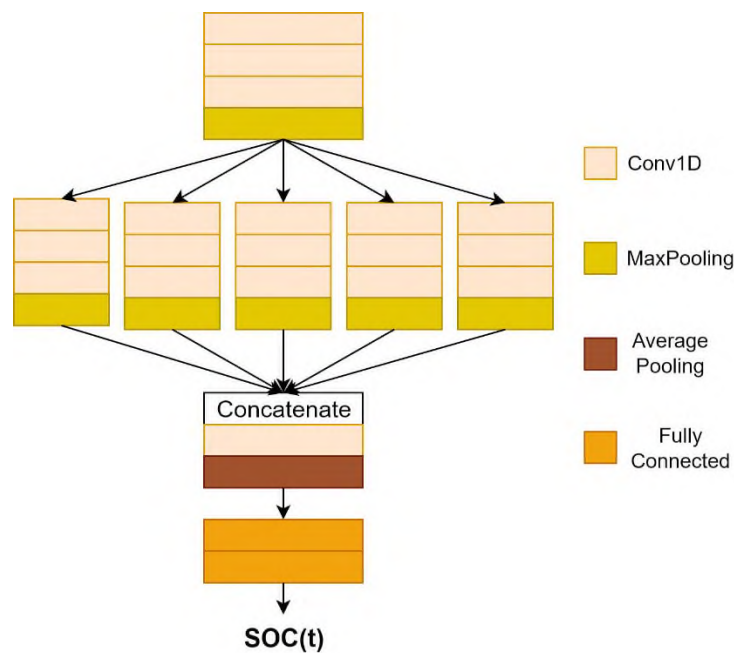


**Figure 4.** Proposed sequence-to-point CNN architecture

First, low-level features are extracted using three convolution layers and one maxpooling layer. Then, the model was divided into five parallel branches. In each arm, multi-scale feature extraction was performed using different dilation rates. The features collected from these branches were then concatenated and passed through a convolution and average pooling layer. In order to perform SOC estimation, the last two layers of the model are chosen to be fully connected.

## 4. RESULTS AND ANALYSIS

### 4.1. Implementation Details

*Dataset:* This study used the LG 18650HG2 (Nickel Manganese Cobalt-NMC) dataset shared by MacMaster University in 2020 [18]. The most important reason for choosing this dataset is that the open access datasets created by Dr. Phillip Kollmeyer are frequently used in SOC estimation publications shared in the literature [10, 11, 22-24]. Li-ion battery cells were tested at six different temperatures and different values of the battery were recorded. Data from the tests performed at temperatures between  $-20^{\circ}\text{C}$  and  $40^{\circ}\text{C}$  were collected with a sampling frequency of 10Hz. The CC-CV method was used for the full charge of the battery. For discharge, four different drive cycles and eight drive cycles consisting of a mixture of these drive cycles, 12 different drive cycles in total, were used. During discharge, voltage, current, cell surface temperature and capacity data were recorded.

*CNN Model Details:* Since the main objective of this study is to demonstrate the success of the designed adaptive and hybrid SOC prediction system, the hyperparameter selections of the deep learning model are adapted from [17]. In the designed deep learning model, the number of filters in the first three convolution layers are 30, 30 and 40, and the filter sizes are 10, 8 and 6, respectively. After the convolution layer, a maxpooling layer with a pool value of 3 was used to increase the learning capacity of the network and reduce the risk of overfitting. The number of filters of each convolution layer in parallel branches was set to 50, the filter size was set to 10, and the pool value of each maxpooling layer was set to 3. In order to perform multi-scale feature extraction, dilation rates of 1, 2, 4, 6 and 8 were used in parallel arms respectively. After the concatenate process, a convolution layer with a filter number of 64 and a filter size of 1 was used. The pool size of the averagepooling layer was set to 3. The number of nodes of the last two fully connected layers were chosen as 512 and 1, respectively. ReLU function was used as activation function in all layers. Experiments were performed with sliding windows by selecting the window size  $w$  512 for splitting the data. The data were normalized with z-score and the models were trained with Adam optimizer. Mean squared error function was used as the loss function during training. The models were created using the Tensorflow-Keras library and were run on Google Colab.

For the hybrid approach, the SOC estimator was updated every five minutes using the outputs from the seq2point model. The coulombic efficiency of the battery cell was set as 0.998 based on the values in the dataset. The SOC estimation weights are updated when the battery is fully charged. In the final SOC estimation, the  $\alpha$  value was set to 3.

### 4.2. Experimental Results

The experimental results will be evaluated in two different ways. First, the results obtained with CNN-based seq2point learning are shared.

The LG 18650HG2 dataset contains experimental data under temperatures of  $-20^{\circ}\text{C}$ ,  $-10^{\circ}\text{C}$ ,  $0^{\circ}\text{C}$ ,  $10^{\circ}\text{C}$  and  $25^{\circ}\text{C}$ . The proposed CNN model is trained and tested first for positive temperatures and then for all temperatures. US06, HWFET, Mixed1-8 drive cycle data were used for training and LA92 and UDDS drive cycle data were used for testing. 20% of the training data was reserved as a validation set. The values obtained for positive temperatures are shown in Tables 1 and 2. LSTM [25] and CNN [22] models were used as benchmark models. For comparison purposes, the model is designed to predict last point instead of midpoint with the proposed model and the results are compared in the tables. Mean absolute error (MAE) and mean squared error (MSE) metrics were used to evaluate the results. MAE is used to assess the error magnitude of a model by measuring the mean absolute difference between predicted values and true values. The most important advantage is that it is easy to interpret as the unit is the same as the unit of the predicted value. MSE squares the errors between predicted and true values and calculates their average. This metric is an important indicator for detecting noise in the predictions. Noise increases the variance of errors in the time series forecasts, which leads to a higher MSE.

**Table 1.** MAE results obtained for positive temperatures

	0°C		10°C		25°C		Average	
	LA92	UDDS	LA92	UDDS	LA92	UDDS	LA92	UDDS
LSTM [25]	1,3362	1,6929	1,2725	1,0898	0,874	1,0577	1,1609	1,2801
CNN [22]	1,444	1,0745	1,6666	1,3205	0,9832	1,209	1,3646	1,2013
Seq2last	0,7951	<b>1,0017</b>	1,2312	1,0474	0,6161	0,7411	0,8808	0,9301
Proposed	<b>0,6288</b>	1,0589	<b>1,1737</b>	<b>0,9938</b>	<b>0,5305</b>	<b>0,656</b>	<b>0,7777</b>	<b>0,9029</b>

**Table 2.** MSE results obtained for positive temperatures

	0°C		10°C		25°C	
	LA92	UDDS	LA92	UDDS	LA92	UDDS
LSTM [25]	0,0293	0,044	0,0255	0,0199	0,0137	0,0193
CNN [22]	0,0324	0,0211	0,0385	0,0268	0,0152	0,0225
Seq2last	0,0113	<b>0,0192</b>	0,0209	0,0169	0,0062	0,0094
Proposed	<b>0,0077</b>	0,0212	<b>0,0183</b>	<b>0,0159</b>	<b>0,0049</b>	<b>0,0073</b>

When the results obtained are analyzed, the proposed model achieves more accurate estimations than the benchmark models. Comparable results are obtained for the 0°C test data for the UDDS drive cycle. The average MAE values of the predictions are shared in the last column of Table 1. According to these values, the proposed model is 33% more accurate for LA92 and 29% more accurate for UDDS than LSTM. When the MSE results in Table 2 are analyzed, it is observed that the proposed model makes less noisy predictions than the benchmark models.

Secondly, the results obtained using the adaptive and hybrid SOC prediction model are analyzed. Three different scenarios are created considering different measurement errors of the current sensor, and they are listed in Table 3.

**Table 3.** List of scenarios

	Measurement Error	Sensor Bias (A)	Mean of Sensor Noise (A)	Standard Deviation of Sensor Noise (A)
Scenario 1	×	×	×	×
Scenario 2	✓	+0.1	0	0.01
Scenario 3	✓	+0.2	0	0.1

*Scenario 1–Error-Free Measurement:* In this scenario, although it is not possible in real-world applications, the analysis will be performed assuming that the current sensor measurements are accurate and error-free. The obtained results are shown in Figure 5, where the performance of the proposed model and two different deep learning models, LSTM and CNN, are visually compared. Figures 5.a and 5.b show the SOC values obtained using the LA92 driving cycle at 0°C and 25°C respectively. When the obtained results are analyzed, it is seen that the proposed model significantly outperforms the deep learning models and makes more accurate predictions. This is an expected situation, and the reason is quite clear. Because the proposed model makes adaptive predictions using both deep learning and current sensor data. Since the values read from the current sensor are error-free, the model significantly increases the prediction success by increasing the value of the  $w_2$  weight. Coulomb counting is undoubtedly a practical and useful method if the data read from the sensor is accurate. Since the problem of not knowing the initial SOC value, which is the biggest disadvantage of the Coulomb counting method, is solved with the sequence to point learning approach, the predictions are quite successful. If the predictions visualized in Figure 5 are evaluated with numerical metrics, the MAE value obtained by the proposed model for the LA92 driving cycle at 0°C is 0.1266. The minimum MAE value achieved by the LSTM model is 1.3364 and the CNN model is 2.5115. The MAE values obtained by the proposed model, LSTM and CNN for the LA92 drive cycle at 25°C are 0.3198, 0.8738 and 1.4743, respectively. Since MAE is a metric that indicates the prediction error, it can be said that the model with the lowest value performs the most successful predictions. Therefore, the proposed model made more accurate predictions compared to the benchmark models.

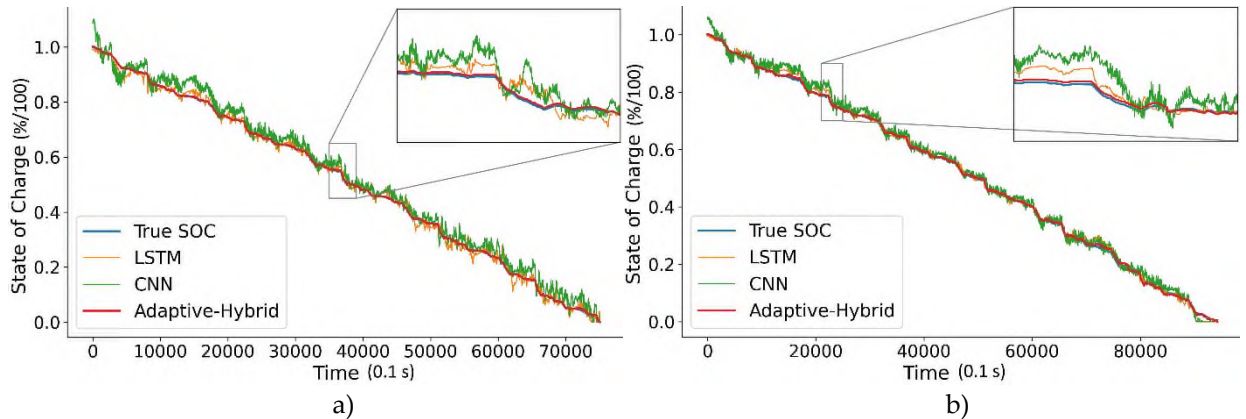


**Figure 5.** SOC estimation results for Scenario 1, a) 0°C-LA92 drive cycle, b) 25°C-LA92 drive cycle

*Scenario 2—Measurement with bias=0.1 and std=0.01:* In this scenario, it is assumed that the current sensor makes both noisy and biased measurements. The bias value of the current sensor is determined as +0.1A. The noise is added to the current signal with a mean value of 0 and a standard deviation of 0.01. The SOC estimation is performed using the obtained erroneous measurements. The obtained results are shown in Figure 6, where the performance of the proposed model and benchmark models are visually compared. Figures 6.a and 6.b show the SOC values obtained using the LA92 driving cycle at 0°C and 25°C respectively. It is observed that the accuracy of SOC estimation decreases due to inaccurate measurements of the current sensor used in SOC estimation. However, the proposed model adaptively detects the sensor error during charging and increases the value of the weight  $w_1$  and decreases the value of  $w_2$  to achieve better prediction accuracy. The proposed model automatically and adaptively updated the weights using the error rate it determined during charging. The  $w_1$  weight was calculated as 0.9396 and the  $w_2$  weight as 0.0604. The MAE value obtained by the proposed model for the LA92 drive cycle at 25°C is 0.735, 0.8092 for LSTM, and 1.2889 for CNN. The MAE value obtained by the proposed model for the LA92 drive cycle at 0°C is 0.5491, for LSTM it is 1.401, and for CNN it is 2.0612. According to the results obtained, in the experiments at 25°C, the proposed model performed 11.2% more successful predictions than the LSTM model and 43% more successful predictions than the CNN model, respectively. In the experiments at 0°C, the proposed model performed 61% and 73.4% more successful predictions than the LSTM and CNN models, respectively.

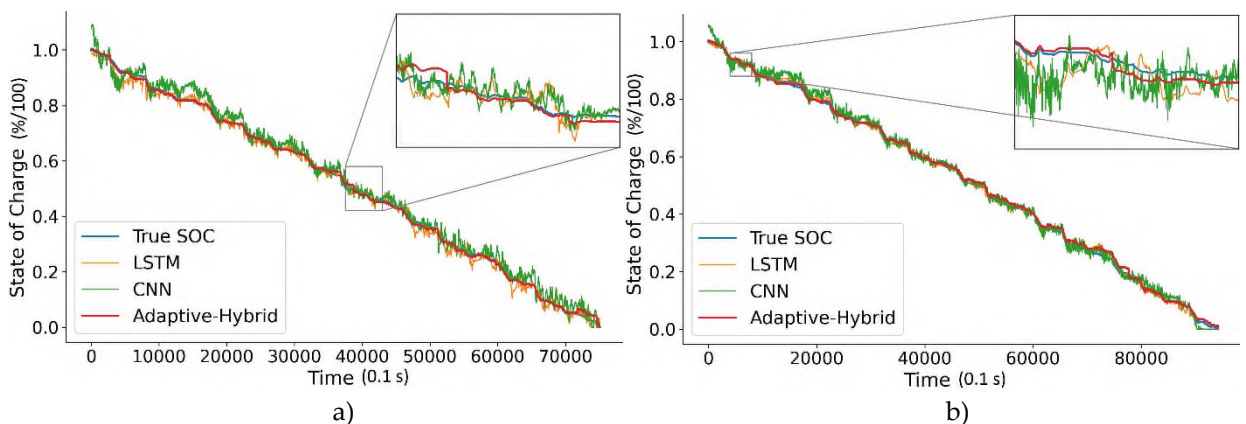


**Figure 6.** SOC estimation results for Scenario 2, a) 0°C-LA92 drive cycle, b) 25°C-LA92 drive cycle

*Scenario 3—Measurement with bias=0.2 and std=0.1:* In this scenario, the bias value of the current sensor is determined as +0.2A. The noise is added to the current signal with a mean value of 0 and a standard deviation of 0.1. The SOC estimation is performed using the obtained erroneous measurements. Figure 6

illustrates the results, providing a visual comparison between the proposed model and the benchmark models. Specifically, Figures 6.a and 6.b display the SOC estimations under the LA92 driving cycle at temperatures of 0°C and 25°C, respectively. It is evident that inaccuracies in the current sensor's measurements negatively impact the SOC estimation accuracy. Nevertheless, the proposed model effectively adapts by detecting sensor errors during charging phases, dynamically adjusting the weights – by increasing  $w_1$  and reducing  $w_2$  to enhance prediction accuracy. The proposed model adaptively updated the weights using the error rate determined during charging. The  $w_1$  weight is calculated as 0.9674 and the  $w_2$  weight is calculated as 0.0326. The MAE value obtained by the proposed model for the LA92 drive cycle at 0°C is 0.7601, 1.6525 for LSTM, and 1.7586 for CNN. The MAE value obtained by the proposed model for the LA92 drive cycle at 25°C is 0.773, for LSTM it is 0.8799, and for CNN it is 1.1782. According to the results obtained, in the experiments at 25°C, the proposed model performed 12.2% more successful predictions than the LSTM model and 34.4% more successful predictions than the CNN model, respectively. In the experiments at 0°C, the proposed model performed 54% and 56.8% more successful predictions than the LSTM and CNN models, respectively.

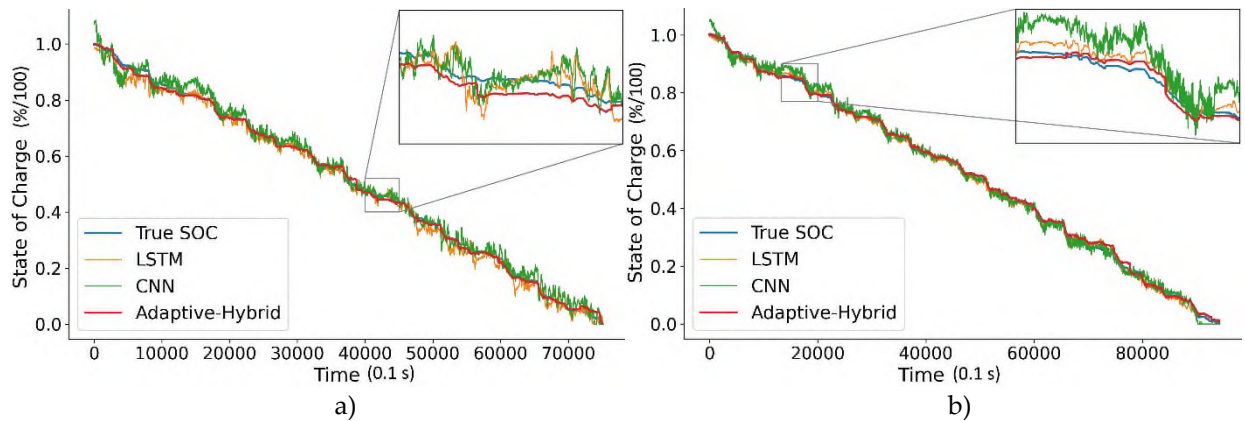


**Figure 7.** SOC estimation results for Scenario 3, a) 0°C-LA92 drive cycle, b) 25°C-LA92 drive cycle

## 5. CONCLUSIONS

In this study, an adaptive and hybrid SOC estimation system for Li-ion battery cells is proposed. A hybrid model is created using CNN-based seq2point learning and coulomb counting methods. Less noisy and more accurate estimations are achieved with seq2point learning. Instantaneous SOC estimation is made by performing forward partial ampere counting from midpoint with coulomb counting. In addition, an adaptive approach is proposed by updating the weights based on the estimation error during charging. Experiments are carried out for battery cells operated at different temperatures. In addition, simulation studies are carried out considering different current sensor errors. The proposed model has achieved more accurate SOC estimation by outperforming deep learning models such as LSTM and CNN. Apart from this, the estimation noise is significantly reduced. For the scenario with the highest current sensor error, 12.2% more accurate estimations are obtained compared to LSTM, 34.4% more accurate estimations are obtained compared to CNN at 25°C, 54% more accurate estimations are obtained compared to LSTM and 56.8% more accurate estimations are obtained compared to CNN at 0°C.

### Declaration of Ethical Standards

The author declares that the materials and methods used in this study do not require ethical committee permission and/or legal-special permission.



### Credit Authorship Contribution Statement

Author - Conceived and designed the study, analyzed data and interpreted results, drafted and revised the manuscript.

### Declaration of Competing Interest

The author declares that they have no known competing financial interests or personal relationships that could have appeared to influence the work reported in this paper.

### Funding / Acknowledgements

The authors have not disclosed any funding.

### Data Availability

The datasets analyzed during the current study are available in <https://data.mendeley.com/datasets/b5mj79w5w9/2>

## 6. REFERENCES

- [1] International Renewable Energy Agency, *Innovation landscape brief: Utility-scale batteries*, IRENA, Abu Dhabi, 2019.
- [2] Y. Ko, K. Cho, M. Kim, and W. Choi, "A Novel Capacity Estimation Method for the Lithium Batteries Using the Enhanced Coulomb Counting Method With Kalman Filtering," *Ieee Access*, vol. 10, pp. 38793-38801, 2022, doi: 10.1109/ACCESS.2022.3165639.
- [3] X. Lin, "Theoretical Analysis of Battery SOC Estimation Errors Under Sensor Bias and Variance," *IEEE Transactions on Industrial Electronics*, vol. 65, no. 9, pp. 7138-7148, 2018, doi: 10.1109/TIE.2018.2795521.
- [4] W. Hou, Q. Shi, Y. Liu, L. Guo, X. Zhang, and J. Wu, "State of Charge Estimation for Lithium-Ion Batteries at Various Temperatures by Extreme Gradient Boosting and Adaptive Cubature Kalman Filter," *IEEE Transactions on Instrumentation and Measurement*, vol. 73, pp. 1-11, 2024, doi: 10.1109/TIM.2023.3346509.
- [5] G. Sethia, S. K. Nayak, and S. Majhi, "An Approach to Estimate Lithium-Ion Battery State of Charge Based on Adaptive Lyapunov Super Twisting Observer," *IEEE Transactions on Circuits and Systems I: Regular Papers*, vol. 68, no. 3, pp. 1319-1329, 2021, doi: 10.1109/TCSI.2020.3044560.
- [6] R. Guo, Y. Xu, C. Hu, and W. Shen, "Self-Adaptive Neural Network-Based Fractional-Order Nonlinear Observer Design for State of Charge Estimation of Lithium-Ion Batteries," *IEEE/ASME Transactions on Mechatronics*, vol. 29, no. 3, pp. 1761-1772, 2024, doi: 10.1109/TMECH.2023.3321719.
- [7] V. Chandran, C. K. Patil, A. Karthick, D. Ganeshaperumal, R. Rahim, and A. Ghosh, "State of Charge Estimation of Lithium-Ion Battery for Electric Vehicles Using Machine Learning Algorithms," *World Electric Vehicle Journal*, vol. 12, no. 1, 2021, doi: 10.3390/wevj12010038.
- [8] J. Tian, C. Chen, W. Shen, F. Sun, and R. Xiong, "Deep Learning Framework for Lithium-ion Battery State of Charge Estimation: Recent Advances and Future Perspectives," *Energy Storage Materials*, vol. 61, p. 102883, 2023, doi: <https://doi.org/10.1016/j.ensm.2023.102883>.
- [9] V. Q. Dao *et al.*, "Design of an Effective State of Charge Estimation Method for a Lithium-Ion Battery Pack Using Extended Kalman Filter and Artificial Neural Network," *Energies*, vol. 14, no. 9, 2021, doi: 10.3390/en14092634.
- [10] C. Vidal, P. Malysz, M. Naguib, A. Emadi, and P. J. Kollmeyer, "Estimating battery state of charge using recurrent and non-recurrent neural networks," *J Energy Storage*, vol. 47, p. 103660, 2022, doi: <https://doi.org/10.1016/j.est.2021.103660>.

- [11] Y. Liu, J. Li, G. Zhang, B. Hua, and N. Xiong, "State of Charge Estimation of Lithium-Ion Batteries Based on Temporal Convolutional Network and Transfer Learning," *Ieee Access*, vol. 9, pp. 34177-34187, 2021, doi: 10.1109/Access.2021.3057371.
- [12] G. Chen, W. Peng, and F. Yang, "An LSTM-SA model for SOC estimation of lithium-ion batteries under various temperatures and aging levels," *J Energy Storage*, vol. 84, 2024, doi: 10.1016/j.est.2024.110906.
- [13] Y. Che *et al.*, "Battery States Monitoring for Electric Vehicles Based on Transferred Multi-Task Learning," *Ieee T Veh Technol*, vol. 72, no. 8, pp. 10037-10047, 2023, doi: 10.1109/TVT.2023.3260466.
- [14] K. H. Kim, K. H. Oh, H. S. Ahn, and H. D. Choi, "Time-Frequency Domain Deep Convolutional Neural Network for Li-Ion Battery SoC Estimation," *Ieee T Power Electr*, vol. 39, no. 1, pp. 125-134, 2024, doi: 10.1109/TPEL.2023.3309934.
- [15] K. Jia, Z. Gao, R. Ma, H. Chai, and S. Sun, "An Adaptive Optimization Algorithm in LSTM for SOC Estimation Based on Improved Borges Derivative," *IEEE Transactions on Industrial Informatics*, vol. 20, no. 2, pp. 1907-1919, 2024, doi: 10.1109/TII.2023.3280340.
- [16] F. Wu, S. Wang, D. Liu, W. Cao, C. Fernandez, and Q. Huang, "An improved convolutional neural network-bidirectional gated recurrent unit algorithm for robust state of charge and state of energy estimation of new energy vehicles of lithium-ion batteries," *J Energy Storage*, vol. 82, 2024, doi: 10.1016/j.est.2024.110574.
- [17] C. Zhang, M. Zhong, Z.-H. Wang, N. H. Goddard, and C. Sutton, "Sequence-to-point learning with neural networks for nonintrusive load monitoring," in Proc. 32nd AAAI Conf. Artif. Intell. (AAAI-18), 2018, pp. 2604-2611.
- [18] P. Kollmeyer, C. Vidal, M. Naguib, and M. Skells, "LG 18650HG2 Li-ion battery data and example deep neural network xEV SOC estimator script," *Mendeley Data*, vol. 2, 2020, doi: 10.17632/cp3473x7xv.3.
- [19] S. Minaee, Y. Boykov, F. Porikli, A. Plaza, N. Kehtarnavaz, and D. Terzopoulos, "Image Segmentation Using Deep Learning: A Survey," *IEEE Transactions on Pattern Analysis and Machine Intelligence*, vol. 44, no. 7, pp. 3523-3542, 2022, doi: 10.1109/TPAMI.2021.3059968.
- [20] O. Ronneberger, P. Fischer, and T. Brox, "U-Net: Convolutional Networks for Biomedical Image Segmentation," in Medical Image Computing and Computer-Assisted Intervention – MICCAI 2015, 2015, pp. 234-241.
- [21] Y. Li, Y. Chen, N. Wang, and Z. Zhang, "Scale-Aware Trident Networks for Object Detection," 2019 IEEE/CVF International Conference on Computer Vision (ICCV), 2019, pp. 6053-6062.
- [22] A. Bhattacharjee, A. Verma, S. Mishra, and T. K. Saha, "Estimating State of Charge for xEV Batteries Using 1D Convolutional Neural Networks and Transfer Learning," *Ieee T Veh Technol*, vol. 70, no. 4, pp. 3123-3135, Apr 2021, doi: 10.1109/Tvt.2021.3064287.
- [23] C. Bian, H. He, and S. Yang, "Stacked bidirectional long short-term memory networks for state-of-charge estimation of lithium-ion batteries," *Energy*, vol. 191, 2020, doi: 10.1016/j.energy.2019.116538.
- [24] M. A. Hannan *et al.*, "SOC Estimation of Li-ion Batteries With Learning Rate-Optimized Deep Fully Convolutional Network," *Ieee T Power Electr*, vol. 36, no. 7, pp. 7349-7353, 2021, doi: 10.1109/Tpel.2020.3041876.
- [25] Z. Du, L. Zuo, J. Li, Y. Liu, and H. T. Shen, "Data-Driven Estimation of Remaining Useful Lifetime and State of Charge for Lithium-Ion Battery," *Ieee T Transp Electr*, vol. 8, no. 1, pp. 356-367, Mar 2022, doi: 10.1109/Tte.2021.3109636.



**ONE-STATION, DOUBLE-STATION AND ARRAY ANALYSIS OF RAYLEIGH SURFACE WAVES  
APPLIED TO A COMMON-SHOT GATHER: A PROGRAMMED TECHNIQUE DESCRIBED  
THROUGH SYNTHETIC SEISMOGRAMS IN NEAR-SURFACE**

\* Özcan ÇAKIR 

<sup>1</sup> Süleyman Demirel University, Engineering and Natural Sciences Faculty, Geophysics Department, Isparta,  
TÜRKİYE  
[ozcancakir@sdu.edu.tr](mailto:ozcancakir@sdu.edu.tr)

**Highlights**

- Rayleigh surface waves are effective to resolve the near-surface shear-wave velocity structure
- Shear-wave velocity structure is inverted using three methods in coordination
- One-dimensional solutions are combined to build two-dimensional structure of the subsurface



## ONE-STATION, DOUBLE-STATION AND ARRAY ANALYSIS OF RAYLEIGH SURFACE WAVES APPLIED TO A COMMON-SHOT GATHER: A PROGRAMMED TECHNIQUE DESCRIBED THROUGH SYNTHETIC SEISMOGRAMS IN NEAR-SURFACE

\* Özcan ÇAKIR 

<sup>1</sup> Süleyman Demirel University, Engineering and Natural Sciences Faculty, Geophysics Department, Isparta, TÜRKİYE

[ozcancakir@sdu.edu.tr](mailto:ozcancakir@sdu.edu.tr)

(Received: 22.09.2024; Accepted in Revised Form: 16.01.2025)

**ABSTRACT:** The knowledge of near-surface shear-vibration speed (i.e.,  $V_{S30}$ ) is crucial to properly define the dynamic characteristic of shallow subsurface in the earthquake mitigation efforts. In this respect, we propose a programmed technique in which the Rayleigh surface vibrations are solved for the determination of two-dimensional (2D) speed structure (vertically polarized shear-vibration –  $V_{SV}$ ) in terms of fundamental mode (FM) dispersal curves (both group and phase speeds). The synthetic seismograms are calculated to simulate the real Earth and then the three data processing procedures, i.e., the weighted preconditioned linear radon transform (WPLRT), one-station (OS) approach and double-station (DS) approach, are sequentially applied to these synthetics. The common-shot gather (CSG) is assumed as data collection geometry. The WPLRT is first used to produce a phase speed dispersal curve from which the one-dimensional (1D)  $V_{SV}$  structure corresponding to the average structure underneath the CSG is inverted. The average 1D  $V_{SV}$  structure between the source and receiver is next inverted using the OS group speed dispersal curve where the number of OS curves is proportional to the number of geophones. In the third step, the average 1D  $V_{SV}$  structure corresponding to the DS pathway is inverted utilizing the group and phase speed curves where the number of DS curves is proportional to the number of inter-station pathways. Hundreds of dispersal curves (both group and phase speeds) take place in each step of the proposed technique. To select the associated dispersal curve, a programmed scheme is established. The studied area is described in terms of grid points and then the OS and DS dispersal curves are transferred into unique dispersal curves at these grid points for which a set of linear systems defined through travel times are solved. A pseudo 2D cross-section beneath the studied area is eventually established by merging the 1D  $V_{SV}$  structures found by the inversion of dispersal curves at grid points.

**Keywords:** Inversion, Radon Transform, Rayleigh Surface Waves, One-Station, Double-Station

### 1. INTRODUCTION

Geophysical, geological, and geotechnical engineers are eager to learn about the physical conditions of the subsurface material in the Earth for which geophysical engineering offers non-invasive techniques [1, 2, 3]. There exist several diverse reasons triggering this interest in the subsurface structure. Seismic hazards (e.g., liquefaction and landslides) [4], exploration for underground resources (e.g., rare earth elements) [5], need for long-term endurance of the geotechnical structures (e.g., subways, excavations and dams) [6] and environmental concerns (e.g., underground pollution) [7] are some of these main reasons. The geophysical engineering employs different methods (i.e., seismic, electrical, gravity and magnetics) [8] to image the subsurface structure where different physical parameters (e.g., seismic speed, density, electrical resistivity, and magnetic susceptibility) are measured. The seismic method employing the elastic vibrations (i.e., compressional, shear and surface waves) [9] provide effective tools to characterize the distribution of subsurface seismic speeds in multi-dimensions. Several seismic sources (i.e., earthquakes, explosions, impact sources, vibrators, and ambient noise) initiate elastic vibrations in the subsurface and then a set of receivers (i.e., geophones, hydrophones, seismometers, and

\*Corresponding Author: Özcan ÇAKIR, [ozcancakir@sdu.edu.tr](mailto:ozcancakir@sdu.edu.tr)

accelerometers) located at certain distance from the source is used to record the incoming vibrations. One-dimensional (linear) or two-dimensional (circular, triangular, orthogonal grid or custom) receiver array distributions are commonly employed in the field. Elastic vibrations generated by multiple sources are recorded by each receiver in the array creating tomographic ray paths between sources and receivers. The compressional (P) and shear (S) speeds and group and phase speeds of surface waves (Rayleigh and Love) are measured along each ray path from which tomographic speed images are generated corresponding to the subsurface beneath the region of interest [10].

In real world applications, it is desirable to jointly consider data from diverse backgrounds (i.e., geophysical, geological, and geotechnical) for better interpretation of the studied area. For instance, lithological data from geological observations and standard penetration tests performed during geotechnical engineering practices should be considered together with the geophysical data to prevent misinterpretations. It is desirable to consider these different geophysical methods (i.e., seismic, electrical, gravity and magnetics) together so that the observed data volume can be significantly increased in a way that the subsurface is measured using different physical parameters (i.e., seismic, electrical, gravity and magnetics). The latter should make the modelling efforts more sensitive to the underground structure. However, the geophysical field survey is typically restricted by several factors, e.g., survey budget, geophysics equipment available for data collection and field conditions. In case of the seismic method, the field survey may include both body waves (compressional and shear) and surface waves (Rayleigh and Love) or may be limited to just body waves or surface waves. Herein we study the fundamental mode Rayleigh surface waves propagating in the shallow underground. The MASW (Multi-channel Analysis of Surface Waves) is a well-known acronym for shallow surface waves analysis [11, 12, 13]. The surface wave methods mostly employ active sources (i.e., sledgehammer, explosion, impact source and vibrator) as well as earthquakes, but recent applications utilize ambient noise (passive source) to extract surface waves embedded in noise recordings [14, 15, 16]. The REMI (Refraction Microtremor) [17, 18] and SPAC (Spatial Autocorrelation) originally proposed by Aki (1957) [19] are two methods applied to noise recordings.

The seismic surface waves acquired through either active source or passive source are frequently utilized to predict the shear-wave speeds in the subsurface [20, 21, 22, 23]. The passive data processing with the SPAC method calculates dispersion curves by comparing observed SPAC traces (cross-correlation functions between two stations) and theoretical Bessel functions [24] while the active data processing with the MASW method employs an integral transformation to the frequency-domain waveforms to compute the phase velocities between stations in the linear station array [11, 25]. The one-dimensional (1D) MASW surveying involves a common-shot gather (CSG) where a set of receivers aligned along a (pseudo) linear line records the surface waves emanating away from the source. The shear-wave velocity-depth profile representing the average structure beneath the receiver array is solved through the 1D MASW. In the two-dimensional (2D) MASW, the CSG geometry is laterally shifted to the right or left so that the 2D variations of the subsurface is measured along extended straight lines. In the present work, we employ one-station (group speeds), double-station (group and phase speeds) and array (phase speeds) analysis of geophone recordings in a CSG. These three analysis methods are commonly employed in global seismology [26, 27] and are currently adapted for shallow seismic applications. To the best of our knowledge, the proposed algorithm jointly considering multiple sets of active Rayleigh surface wave data in terms of both group and phase speeds is the first time reported for the respective literature.

We evaluate the performance of the proposed data processing technique by selecting a model structure to represent the near-surface ( $\leq 40$ -m depth) speed variation in which the synthetic seismograms of Rayleigh surface waves in the vertical component are computed to simulate the wave propagation. The one-station approach results in a group speed dispersal curve representing the average structure between the source and receiver. The double-station approach works on the cross-correlogram computed from two stations in the geophone spread, which yields both group and phase speed dispersal curves representative of the average structure between the two receivers. The array analysis of

the geophone spread is performed based on the weighted preconditioned linear radon transform, which results a phase speed dispersal curve standing for the average structure underneath the geophone spread. All these dispersal curves are combined to invert the 2D shear-wave velocity structure underneath the CSG.

## 2. MATERIAL AND METHODS

### 2.1. Model Structure

It is essential that geophysical numerical methods suggested for the data processing are assessed for performance before they are applied to real-world data collections. In the case of seismic methods, synthetic seismograms are ideal candidates to perform the necessary test processes. We aim to solve the  $V_{SV}$  (vertically polarized shear-vibration) structure in the near surface ( $\leq 40$ -m depth) for which we consider a representative model structure as listed in Table 1. The model structure is one-dimensional with multiple depth sections where each depth section is represented by compressional ( $V_p$ ) and vertically polarized shear ( $V_{SV}$ ) speeds, density ( $d$ ) and compressional ( $Q_p$ ) and shear ( $Q_s$ ) quality factors. In Table 1, based on the seismic speeds, each depth section is characterized according to its stiffness as soft, softer, hard, and harder above the half space corresponding to the basement rocks.

**Table 1:** Model structure with a low-speed zone (LSZ) in the middle depth section. The depth sections are considered Poisson solid, i.e.,  $V_p = \sqrt{3}V_{SV}$ . The density is computed from  $d = 0.32V_p + 0.77$  [28]. The shear-vibration quality factor is set to  $Q_s = Q_p/2$ .

Depth sections (m)	$V_p$ (m/s)	$V_{SV}$ (m/s)	$d$ (gr/cm <sup>3</sup> )	$Q_p$	Stiffness
2	693	400	1.00	200	Softer near surface
2	1039	600	1.10	200	
2	1386	800	1.21	300	
2	1559	900	1.27	400	Hard middle layers
6	1732	1000	1.32	400	
6	1386	800	1.21	300	LSZ
6	1472	850	1.24	300	
2	1732	1000	1.32	500	Hard lower layers
2	1905	1100	1.38	500	
10	1992-2061	1150-1190	1.41-1.43	500	Harder transition
$\infty$	2078	1200	1.44	500	Basement rocks

Figure 1 shows the data collection geometry (i.e., common-shot gather – CSG) as well as the data processing schemes consistent with the one-station, double-station, and array analysis. Each geophone (solid triangle) in the array records the seismic energy arrivals created by the source at the shot point to the right. A vertical source (e.g., accelerated weight drop) and vertical geophones are considered. The geophone recordings are processed to extract the Rayleigh surface vibration dispersal curves (phase and group speed). The recordings are processed either alone for the one-station group speeds (*i*), together for the double-station phase and group speeds (*ii*) or all together for the array analysis of phase speeds (*iii*). The grid points (solid circles) refer to the intervals between geophones. The first grid point (indexed zero in Figure 1) corresponds to the distance range in the near offset. A linear system processing the Rayleigh surface vibration in terms of the group and phase arrival times is utilized to determine the 1D speed-depth profile corresponding to each grid point. The 1D solutions are then combined to attain the 2D speed structure underneath the CSG.

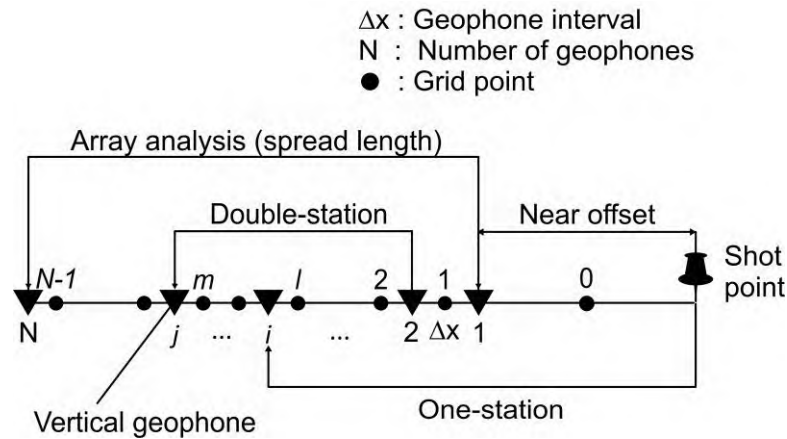


**Figure 1:** Spread configuration for the common-shot gather – CSG. The shot point is a P-vibration generator, and the vertical geophones record vertical (V) component displacement. Both shot point and geophones are placed at the surface. One-station geometry between source and geophone, double-station geometry between geophone pairs, and array geometry including all geophones are indicated.

## 2.2. Synthetic Seismograms

There are certain parameters that we need to set up for the CSG before the synthetic seismograms are computed. The near offset measuring the distance between the shot point and the first geophone in the geophone array is set to 30 m. With increasing offset the surface vibration energy reaches greater depth of penetration, and the fundamental mode (FM) separates better from the overtones. However, if the offset gets longer, then sending the surface vibration energy to greater distances becomes increasingly difficult because of anelastic attenuation. Therefore, the near offset (see Figure 1) should be chosen to meet the requirements of the respective field surveying. The geophone interval ( $\Delta x$ ) in the array is set to 2 m. The horizontal resolution of the CSG is proportional to  $\Delta x$ , i.e., better horizontal resolution is obtained with smaller  $\Delta x$ . The number of geophones is set to  $N=60$ , which determines the spread length. The distance to the last geophone (i.e.,  $N$ ) in the array establishes the maximum possible depth of penetration. An even deeper depth of penetration is possible if  $N$  is further increased to, for instance,  $N=120$ , but then a stronger seismic source (double strength) should be preferred to deliver the seismic energy to such greater distances. The sample interval of the computed seismograms is  $\Delta t = 0.25$  ms while the record length is set to 1 s, which is a time length good enough to include all the seismic energy arrivals at current geophone locations. A vertical impact source with a parabolic pulse shape of base  $4\Delta t$  is assumed to produce the seismic vibrations.

For the current numerical calculations, we mostly employ the software package by Herrmann (2002) [29]. Figure 2 displays the synthetic shot-record corresponding to the model structure in Table 1. The display gains are adjusted according to the maximum amplitudes at each receiver location so that the designated space for each trace is optimized in the shot window. The Rayleigh surface vibrations show complex pattern of amplitude highs and lows with travel time indicating both normal and reverse dispersals due to vertically heterogeneous subsurface and interference from higher modes. In addition, the waveforms spread in time with increasing geophone distance (see orange color lines).

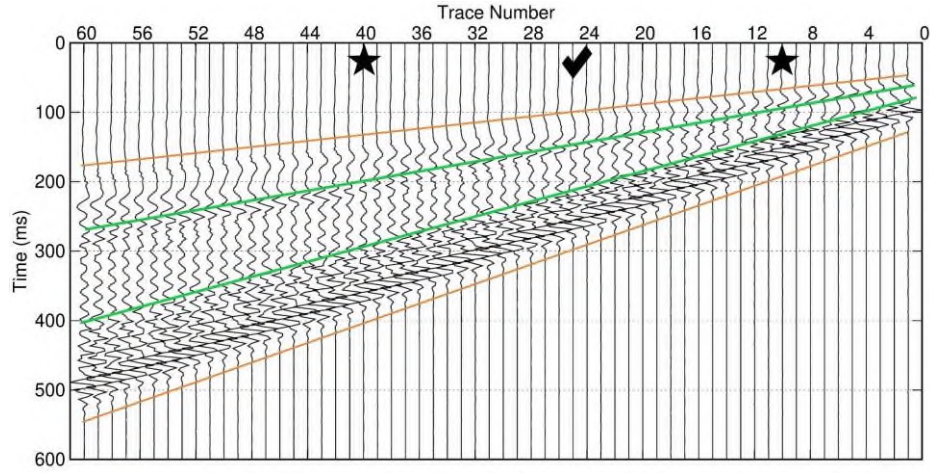


**Figure 2:** Vertical component Rayleigh synthetic seismograms are shown. Source is a vertical impact (see Figure 1). Stars indicate geophone locations (#10 and #40) used to demonstrate sample calculations of double-station (DS) approach. Tick mark stands for geophone location (#25) used for sample calculations of one-station (OS) approach.

### 2.3. Array Analysis of Seismograms

We employ the weighted preconditioned linear radon transform (WPLRT) to compute the phase speeds corresponding to the subsurface beneath the geophone spread. The LRT considers the plane-wave decomposition of the wavefield through the following relation [30].

$$\mathbf{d} = \mathbf{L}\mathbf{m} \quad (1)$$

where  $\mathbf{d}$  and  $\mathbf{m}$  represent the CSG and radon panel, respectively, which are connected by the forward operator  $\mathbf{L}$  defined by complex exponential  $\mathbf{L} = e^{jkx}$ . The operator  $\mathbf{L}$  employs the travel distance  $x$  and wavenumber  $k = \omega/c$  where  $\omega$  is the angular frequency (rad/s) and  $c$  is the phase speed (m/s). The following linear system is used to solve the radon panel  $\mathbf{m}$ .

$$(\mathbf{W}_m^{-T} \mathbf{L}^T \mathbf{W}_d^T \mathbf{W}_d \mathbf{L} \mathbf{W}_m^{-1} + \lambda \mathbf{I}) \mathbf{W}_m \mathbf{m} = \mathbf{W}_m^{-T} \mathbf{L}^T \mathbf{W}_d^T \mathbf{W}_d \mathbf{d} \quad (2)$$

Herein  $\mathbf{W}_m$  is the matrix defining model weights,  $\mathbf{W}_d$  is the matrix for data weights,  $\mathbf{I}$  is the identity matrix,  $\lambda$  is the operator condition number and  $-T$  stands for the transpose of inverse matrix. We solve Equation (2) by utilizing the conjugate gradient algorithm [15]. The radon panel  $\mathbf{m}$  is a complex valued function of frequency ( $f$ ) and phase speed ( $c$ ). We build an ( $f, c$ ) diagram using the spectral amplitudes  $|\mathbf{m}|$  from which we pick the phase speed dispersal curves corresponding to the maximum amplitudes on the diagram.

### 2.4. One-Station Approach

The Rayleigh surface vibration data is collected through the CSG where the number of receivers is set to  $N=60$ . We apply the Multiple Filter Technique (MFT) to the Fourier transformed seismogram  $S(\omega)$  at each receiver (geophone) location from which the (observed) fundamental mode ( $n=0$ ) group speed curve is constructed. In the frequency ( $f$ ) domain, the MFT utilizes the Gaussian filter ( $\exp[-\alpha(f - f_c)^2/f_c^2]$ ) where  $f_c$  (Hz) is the filter center frequency at which point the one-station (OS) group speed is sought [29, 31]. The parameter  $\alpha$  determines the resolution in the time and frequency domains. A higher (lower)  $\alpha$  value corresponds to the higher (lower) resolution in the frequency domain



while the resolution inversely gets lower (higher) in the time domain. Therefore, there is a tradeoff between time and frequency domain resolutions. Different  $\alpha$  values should be experimented to achieve better resolution of the observed dispersal curve throughout the MFT.

### 2.4.1. Linear system for one-station approach

The lateral extent covered by the CSG is discretized via some grid points (see Figure 1). At each grid point, the slowness is defined by  $S = \Delta s + S_{ave}$  where  $\Delta s$  is the unknown slowness perturbation to the average slowness (i.e.,  $S_{ave}$ ), which is valid for both group (OS and/or DS) and phase (DS) arrival times. In this respect, we set up a linear system to solve the OS group arrival times as follows.

$${}^{OS}\mathbf{C} \gamma \mathbf{q} = {}^{OS}\mathbf{d} \quad (3)$$

where  $\gamma = G$  representing the group speed and the system matrix  ${}^{OS}\mathbf{C}_{N_1 \times N}$  ( $N_1 = {}^{OS}N_a$ ) is defined by the following matrix.

$${}^{OS}\mathbf{C} = \begin{bmatrix} x_0 & 0 & \dots & 0 \\ x_0 & \Delta x & \dots & 0 \\ \vdots & \vdots & \ddots & \vdots \\ x_0 & \Delta x & \dots & \Delta x \end{bmatrix} \quad (4)$$

Herein  ${}^{OS}N_a = N$ . The column vector  $\gamma \mathbf{q}_{N \times 1}$  (unknown group slowness vector) in Equation (4) is given as follows.

$$\gamma \mathbf{q} = \begin{bmatrix} G_{\Delta s^{(0)}} \\ G_{\Delta s^{(1)}} \\ \vdots \\ G_{\Delta s^{(N-1)}} \end{bmatrix} \quad (5)$$

The elements of the column vector  ${}^{OS}\mathbf{d}_{N_1 \times 1}$  (known group travel time vector) in Equation (4) have the following combined form.

$${}^{OS}d_i = [x_0 + (i-1)\Delta x] {}^{OS}S_{obs}^{(i)} - x_0 {}^{OS}S_{ave}^{(0)} - \Delta x \sum_{j=1}^{i-1} {}^{OS}S_{ave}^{(j)} \quad i = 1, 2, \dots, N \quad (6)$$

where the  ${}^{OS}S_{ave}^{(i)}$  is calculated from the observed slowness ( ${}^{OS}S_{obs}^{(i)}$ ) by the application of the succeeding expression.

$${}^{OS}S_{ave}^{(k)} = \frac{1}{N-k} \sum_{j=k+1}^N {}^{OS}S_{obs}^{(j)} \quad k = 0, 1, \dots, N-1 \quad (7)$$

The following equation is used to compute the group travel times of OS Rayleigh surface vibrations.

$${}^{OS}t^{(i)} = x_0 (\Delta s^{(0)} + {}^{OS}S_{ave}^{(0)}) + \sum_{k=1}^{i-1} \Delta x (\Delta s^{(k)} + {}^{OS}S_{ave}^{(k)}) \quad i = 1, 2, \dots, N \quad (8)$$

### 2.5. Double-Station Approach

The cross-correlation process measures the similarity between two signals. We utilize this property to quantify the phase speed  $c(\omega)$  and group speed  $u(\omega)$  between two stations [ $A_1(\omega) = |A_1(\omega)|e^{-j\varphi_1(\omega)}$  and  $A_2(\omega) = |A_2(\omega)|e^{-j\varphi_2(\omega)}$ ] in the receiver array. In the frequency domain, the cross-correlogram  $A(\omega)$  is defined as follows.

$$A(\omega) = |A(\omega)|e^{-j\varphi(\omega)} \quad (9)$$

where  $|A(\omega)| = |A_1(\omega)||A_2(\omega)|$  is the amplitude spectrum,  $\varphi(\omega) = \varphi_2(\omega) - \varphi_1(\omega)$  is the phase

spectrum,  $j = \sqrt{-1}$  and  $\omega = 2\pi f$ . The MFT is applied to the cross-correlogram  $A(\omega)$  to resolve the double-station (DS) group speed  $u(\omega)$ . The phase spectrum  $\varphi(\omega)$  is utilized to compute the DS phase speed  $c(\omega)$  as follows.

$$c(\omega) = \omega x / [\varphi(\omega) + 2n\pi] \quad n = \dots, -2, -1, 0, 1, 2, \dots \quad (10)$$

Herein  $x$  describes the distance between two stations. There exists some ambiguity (or cycle skipping) in the phase speed measurement, which is quantified by the term  $2n\pi$  in Equation 10. This issue of ambiguity is fixed by applying a method described in Çakır and Kutlu (2023) [32].

### 2.5.1. Linear system for double-station approach

We set up two linear systems to solve the DS data, i.e., one linear system for the phase arrival times and another one for the group arrival times. The respective system can be outlined as follows.

$${}^{DS}\mathbf{C} \gamma \mathbf{q} = {}^{DS}\mathbf{d} \quad (11)$$

where  $\gamma = P$  (i.e., phase speed) or  $\gamma = G$  (i.e., group speed). The system matrix  ${}^{DS}\mathbf{C}_{N_2 \times N}$  ( $N_2 = {}^{DS}N_a$ ) is defined by the following expression.

$${}^{DS}C_{ij} = \begin{bmatrix} {}^{DS}y_{ij}^{(0)} \\ {}^{DS}y_{ij}^{(1)} \\ \vdots \\ {}^{DS}y_{ij}^{(N_d-1)} \end{bmatrix} \quad i = 1, 2, \dots, N_d(N_d + 1)/2, \quad j = 1, 2, \dots, N - 1 \quad (12)$$

where

$${}^{DS}y_{ij}^{(m)} = \begin{cases} \Delta x & i = 1, \dots, N_d - m, \quad j = m + 1, \dots, m + N_c + i - 1 \\ 0 & \text{otherwise} \end{cases} \quad m = 0, 1, \dots, N_d - 1 \quad (13)$$

$${}^{DS}N_a = N_d(N_d + 1)/2 \quad (14)$$

$$N_d = N - N_c \quad (15)$$

Herein  $N_c = 30$  defines the minimum number of geophone intervals between two stations. The column vector  $\gamma \mathbf{q}_{N_2 \times 1}$  (unknown phase or group slowness vector) in Equation (11) is given as follows.

$${}^{P,G}\mathbf{q} = \begin{bmatrix} {}^{P,G}\Delta S^{(1)} \\ {}^{P,G}\Delta S^{(2)} \\ \vdots \\ {}^{P,G}\Delta S^{(N-1)} \end{bmatrix} \quad (16)$$

The column vector  ${}^{DS}\mathbf{d}_{N_2 \times 1}$  (known phase or group travel time vector) in Equation (11) has the following composite form.

$${}^{DS}d_i = (j - 1)\Delta x {}^{DS}S_{obs}^{(i,j)} - \Delta x \sum_{j=1}^{i-1} {}^{DS}S_{ave}^{(j)} \quad i = 1, 2, \dots, N_d, \quad j = N_c + i, \dots, N \quad (17)$$

The observed phase or group slowness denoted by the  ${}^{DS}S_{obs}^{(i)}$  is utilized to calculate the average phase or group slowness  ${}^{DS}S_{ave}^{(i)}$  via the subsequent expressions.

$$DS_{ave}^{(k)} = \frac{1}{k[N_d - (k-1)/2]} \sum_{i=1}^k \sum_{j=N_c+i}^N DS_{obs}^{(i,j)} \quad k = 1, 2, \dots, N_d \quad (18)$$

$$DS_{ave}^{(k)} = DS_{ave}^{(N-N_c)} \quad k = N_d + 1, \dots, N \quad (19)$$

The phase or group travel times of DS Rayleigh surface vibrations are determined by the application of the below expression.

$$DS_{t_i}^{(j)} = \sum_{k=i}^j \Delta x (\Delta S^{(k)} + DS_{ave}^{(k)}) \quad i = 1, 2, \dots, N_d, \quad j = N_c + i, \dots, N \quad (20)$$

### 3. NUMERICAL RESULTS

#### 3.1. Application of Array Analysis

The WPLRT is applied to the model structure and Figure 3a shows the result. The theoretical phase speed curves for the fundamental plus higher modes are demonstrated by the blue lines. The spectral amplitudes  $|\mathbf{m}|$  characterized by the red color distinctly exhibit the fundamental mode ( $n=0$ ), which is prevalent on the recordings. The higher modes ( $n=3, 4 \dots$ ) are represented by weak amplitudes on the seismograms and are absent on the  $(f, c)$  diagram. On the other hand, the higher modes ( $n=1, 2$ ) are represented by some spectral amplitudes  $|\mathbf{m}|$  as shown by the black color arrow. The mode mingling [33, 34] prevents us from separating these modes from each other and therefore we did not consider this part of the phase speed spectrum in the structural inversion. The black dots showing the locations of the maximum  $|\mathbf{m}|$  values at each frequency (Hz) correspond to the fundamental mode (FM). As indicated by the purple color arrows, at low frequencies ( $< 20$  Hz) these black dots show some scattering around the true values (i.e., blue line). The actual surface vibrations are guided by cylindrical wavefronts and therefore our plane-wave decomposition is not exact. The latter case called near field effect [35] is particularly eminent on the low frequency surface vibrations. To increase the near offset (see Figure 1) should be helpful to alleviate this disturbance on the (observed) phase speed curve.

In Figure 3b, we show the inversion result of the (observed) phase speed curve (black color symbols – FM attained from the WPLRT approach in Figure 3a), which aims to resolve the average 1D speed-depth distribution underneath the geophone array. A linearized inversion method [36, 37, 38, 39] initially starting with a half-space model (blue line in Figure 3b) is employed. Figure 3c displays the resulting phase speed fit after the inversion. In Figures 3b and 3c, the inverted (theoretical) 1D model and phase speed curves are shown by the red (green) color. The purple color arrows in Figure 3c indicate that the longer period phase speeds ( $c$ ) are poorly resolved in the inversion. Moreover, the underground speed jumps as indicated by the cyan color arrows in Figure 3b are determined as more like speed gradients.

#### 3.2 Group Speeds

In surface wave dispersion analysis, meddling (or interference) between the fundamental mode and higher modes (i.e., different modes crossing and touching each other) may occur. Therefore, one needs to be careful against the mode mixing events, e.g., apply some filtering and time windowing before the dispersal analysis. In Figure 4, we show the fundamental ( $n=0$ ) and higher mode ( $n=1, 2, 3 \dots$ ) group speed ( $u$ ) dispersal curves calculated for the theoretical model in Table 1. The group speed curves exhibit some mixing between higher modes ( $n=1, 2$  – indicated by orange color arrow) for frequencies around 45 Hz and then the mode mixing event becomes worse at higher frequencies ( $> 55$  Hz) among other higher modes ( $n=2, 3, 4$  as pointed out by blue color arrow). On the other hand, the fundamental mode ( $n=0$ ) made of both normal and reverse dispersal is free of any interference from the higher modes for the full frequency range 6-100 Hz.

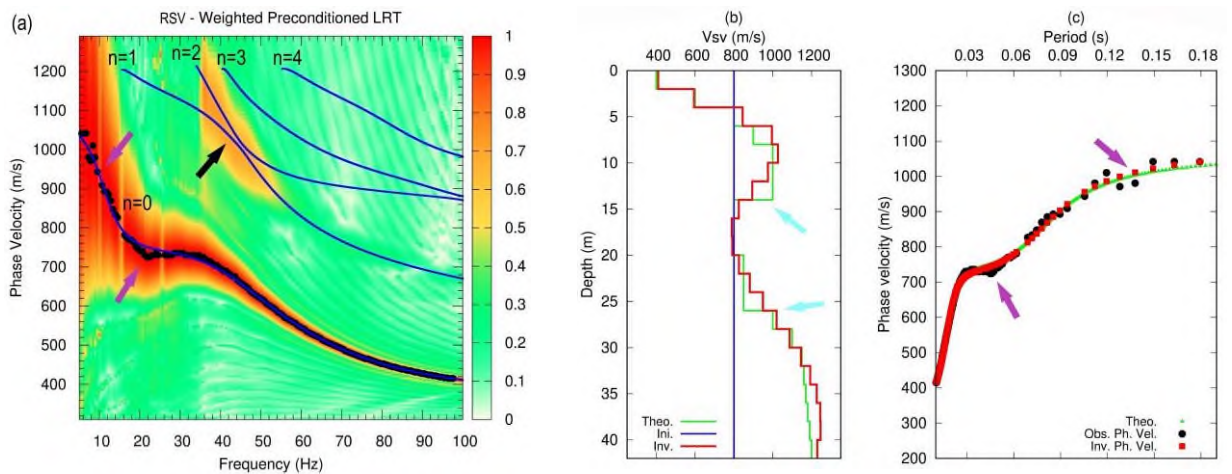


**Figure 3:** (a) The result of weighted preconditioned linear radon transform (WPLRT) is shown where the blue lines show the theoretical phase speed curves for the fundamental ( $n=0$ ) plus higher modes ( $n=1, 2, 3 \dots$ ). The fundamental mode (FM) selected from the WPLRT amplitudes represented by the black dots is inverted. (b) The inverted 1D speed structure represented by the red color line is shown where the initial model (blue line) and the theoretical model (green line) are also shown. (c) The inverted (red color), observed (black color) and theoretical (green color) dispersal curves are illustrated.

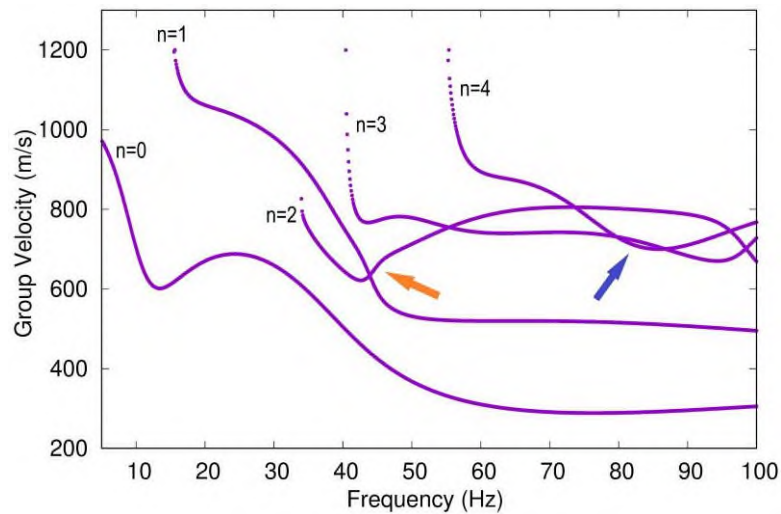


**Figure 4:** Theoretical group speed dispersal curves computed for the model structure in Table 1 are shown. Fundamental mode ( $n=0$ ) and higher modes ( $n=1, 2, 3 \dots$ ) are indicated. The orange and blue color arrows point to the higher mode group velocity curves crossing each other.

### 3.3. Application of One-Station Approach

The model structure (Table 1) includes velocity highs and lows changing with depth, which results Rayleigh surface waveforms showing complex pattern of amplitude highs and lows varying with time (see green lines in Figure 2). To manage such a complex amplitude pattern in the MFT analysis, we employ  $\alpha$  values changing with period. For longer periods ( $> 0.1$  s), we employ a smaller  $\alpha$  value set to  $\alpha = 12$ , which means that we have lower resolution in the frequency domain but higher resolution in the time domain. The  $\alpha$  value is increased to  $\alpha = 40$  for shorter periods ( $\leq 0.1$  s) so that a higher resolution in the frequency domain is attained. The latter means that we sacrifice some time domain resolution. Figure 5 shows the MFT results realized for geophone location #25, which is offset by 78 m (see Figure 2). Figure 5a displays the MFT result obtained by  $\alpha = 40$  and Figure 5b by  $\alpha = 12$  where color coding is

used in the MFT amplitudes. The highest resolution of the group speeds is achieved on the  $(f,u)$  diagram represented by the red color and then a gradual loss in the resolution occurs as indicated by the MFT amplitudes from orange to green color. The Rayleigh surface wave seismogram is provided on the right in each panel. The OS group speed curve representing the geophone location #25 is constructed by combining the two parts indicated by these white color circles in Figures 5a and 5b. The black color arrow in Figure 5b exhibits that the group speed curve is disrupted when  $\alpha = 12$ , but this disruption is alleviated when  $\alpha = 40$  (Figure 5a). The cyan color arrow in Figure 5a shows that the lower frequency (or longer period) group speeds are slightly incorrect when  $\alpha = 40$ , but gets better when  $\alpha = 12$  (Figure 5b).

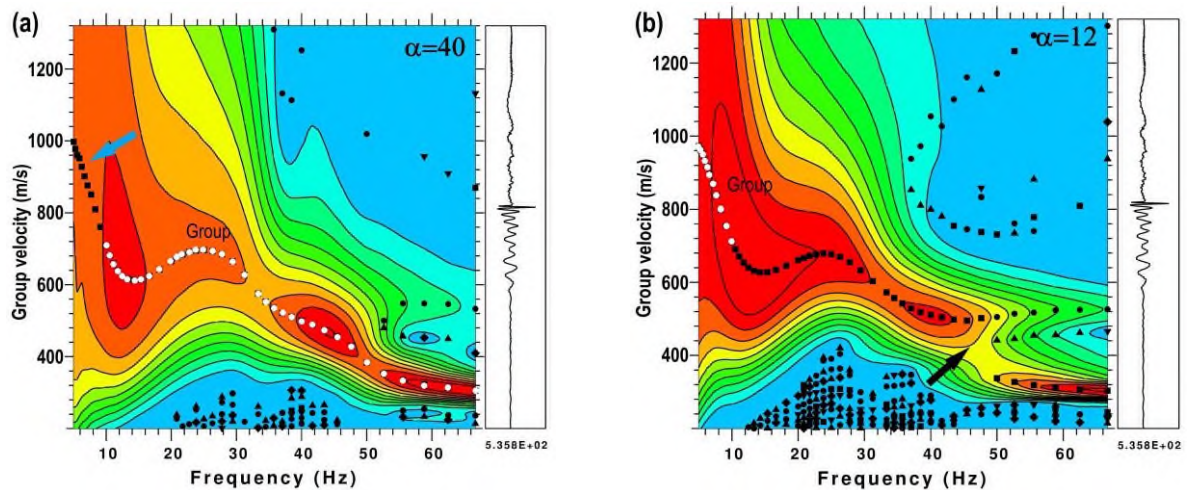


**Figure 5:** One-station (OS) approach applied to the model structure is shown at geophone location #25 indicated by a tick mark in Figure 2. Results of MFT at two different  $\alpha$  values are shown. a)  $\alpha = 40$  and b)  $\alpha = 12$ .

Figure 6a shows the (observed) group speed curve (blue color symbols) constructed by combining the two parts in Figures 5a and 5b (i.e., maximum MFT amplitudes denoted by white color symbols). This curve is inverted to reveal the average 1D speed-depth distribution beneath the distance range between the source and geophone location #25 (Figure 6b). A linearized inversion technique such as applied in Figure 3 is also utilized for this inversion, but this time the initial model (blue line in Figure 6b) is obtained from the inversion in Figure 3b (red line). Figure 6c shows the group speed fit reached after the inversion. The inverted (theoretical) 1D model is depicted by the red (green) color in Figure 6b.

The inverted (observed) group speed curve is displayed in the red (black) color in Figure 6c. Like Figure 3, the cyan color arrows in Figure 6b specify that the underground speed jumps are inverted as more like speed gradients. Moreover, the black color arrow in Figure 6a indicates that the shorter period ( $< 0.035$  s) group speeds are acquired with some error ( $< 40$  m/s), which causes the group speed mismatch between the observed and inverted, which is pointed out by the black color arrow in Figure 6c.

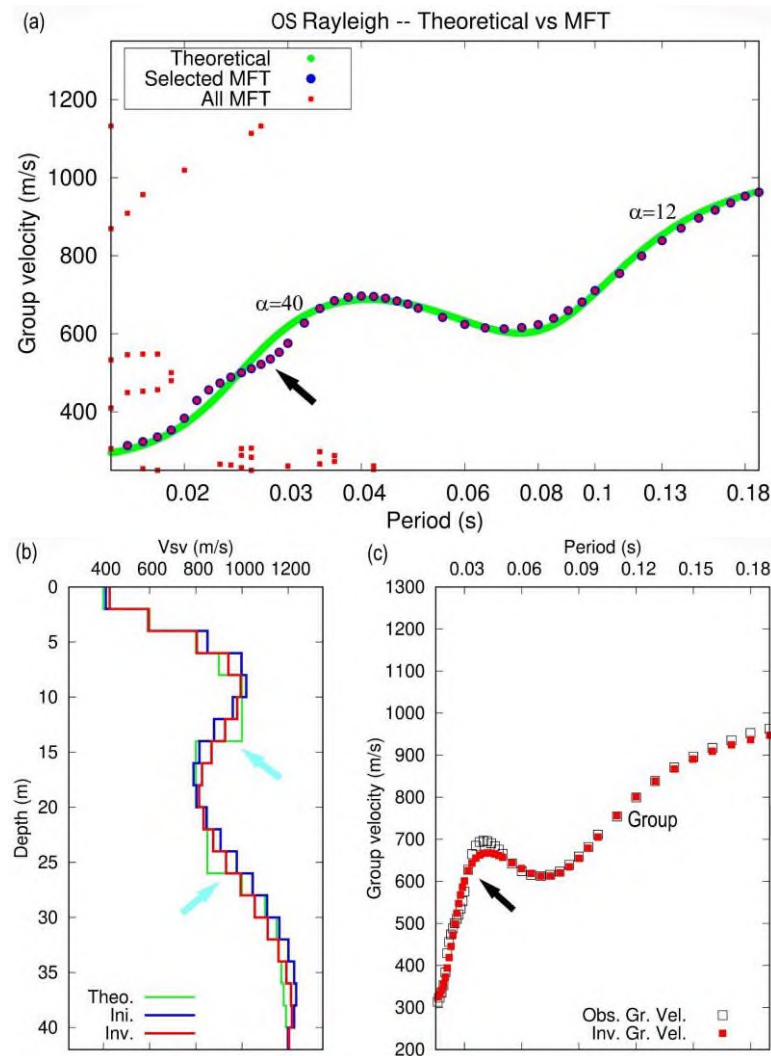


**Figure 6:** a) The fundamental mode (FM) group speed dispersal curve obtained from the combination of white dots in Figures 5a and 5b is shown where the theoretical group speed (green color), selected MFT group speed (blue color), and all computed MFT group speed (red color) are indicated. The FM group speed curve is inverted. (b) The inverted 1D speed structure (red color), initial model (blue color) and theoretical model (green color) are illustrated. (c) The observed (black color) and inverted (red color) group dispersal curves are shown.

### 3.3.1. Group speed result of one-station approach

We repeat the one-station (OS) approach presented in Figure 5 for every other geophone location in the receiver array, which yields FM group speed curves totaling to  ${}^{OS}N_a = 60$ . The corresponding MFT amplitudes illustrated by purple color solid circles are superimposed in Figure 7. We have computed the group speed curve using the inverted model in Figure 3, which is illustrated by the green color curve. The latter curve is utilized to produce the upper (cyan color) and lower (orange color) boundary curves. The interval width between these boundary curves increases from short to longer period, i.e., the width

is 160 m/s at 0.02-s period and increases to 310 m/s at 0.18-s period. This interval is employed as a selection range to bracket the OS group speed curves at all geophone locations. These MFT amplitudes corresponding to the FM staying outside the respective interval as pointed out by the yellow color arrow in Figure 7 are discarded during the process of dispersal curve selection.

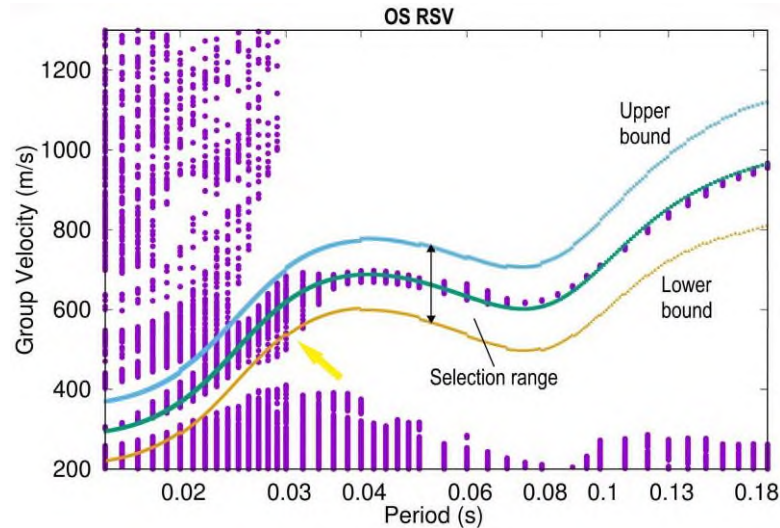


**Figure 7:** Purple color symbols correspond to the one-station (OS) MFT results. All the results at multiple geophone locations are shown superimposed. Rayleigh surface vibration (RSV) group speeds are chosen when staying between the upper (cyan color) and lower (orange color) boundaries.

### 3.4. Application of Double-Station Approach

We employ two seismogram records at geophone locations #10 (offset by 48 m) and #40 (offset by 108 m) for the DS approach. The corresponding cross-correlogram is calculated by the correlation of respective seismograms. Figure 8 illustrates the resulting group and phase speed diagrams. The MFT results, which are color coded changing from highest (red color) to lowest resolution (green color), are shown in two parts, i.e., the first part (Figure 8a) is attained by setting the  $\alpha$  value to  $\alpha = 40$  and the second part (Figure 8b) to  $\alpha = 12$ . In Figures 8a and 8b, the cross-correlogram is demonstrated on the right. The DS group speed curve  $u(\omega)$  representing the inter-station distance between the two geophones (#10 and #40) is built by merging the two parts specified by these white color circles in Figures 8a and 8b. The group speed (FM) resolution tends to be interrupted when  $\alpha = 12$  as pointed out by the black color arrow in Figure 8b. The latter resolution improves when  $\alpha = 40$  (Figure 8a). The longer period (or lower frequency) group speeds are inaccurate when  $\alpha = 40$  as pointed out by the brown color arrow in Figure 8a. The corresponding group speeds improve when  $\alpha = 12$  (Figure 5b). The result of DS phase speed  $c(\omega)$  analysis is provided in Figure 8c. The black color symbols represent these branches resulting from different  $n$  values in  $2n\pi$  where the FM phase speed curve  $c(\omega)$  is depicted by the red color symbols.

In Figure 9a, we illustrate the (observed) group speed curve (blue color symbols) versus period assembled by joining the two parts in Figures 8a and 8b (i.e., white color symbols). As pointed out by the orange color arrows (Figure 9a), some shorter period group speeds are excluded since they stay outside the selection range (see Figure 10). On the other hand, Figure 9b displays the (observed) phase speed curve (blue color symbols) versus period converted from Figure 8c. By utilizing the linearized inversion technique like applied in Figure 6, we invert the latter group and phase speed curves to determine the 1D  $V_{SV}$  structure (Figure 9c). This joint inversion of  $u(\omega)$  and  $c(\omega)$  represents the average speed structure between the two geophones (#10 and #40) considered in the DS analysis and the subsequent dispersal

curve fits are shown in Figure 9d. The red (green) color depicts the inverted (theoretical) 1D model in Figure 9c while the red (black) color displays the inverted (observed) group and phase speed curves in Figure 9d. Like Figures 3 and 6, the underground speed jumps are inverted as more like speed gradients (see cyan color arrows in Figure 9c). Moreover, the black color arrow in Figure 9a indicates that the group speeds around 0.045 s period exhibit some error ( $< 30$  m/s), which causes relative group speed mismatch between the inverted and observed (see black color arrow in Figure 9d).

### 3.4.1. Phase and group speed results of double-station approach

Multiple inter-station pathways exist in the DS approach. For the minimum path length, we enforce a restriction described by  $\Delta l = N_c \Delta x = 60$  m where  $\Delta x$  is the geophone interval (set to 2 m) and  $N_c$  is the minimum number of geophone intervals between two stations (set to 30). The expression  ${}^{DS}N_a = N_d(N_d + 1)/2$  defines the total number of DS pathways where  $N_d = N - N_c$ . We utilize  $N = 60$  which produces  ${}^{DS}N_a = 465$ . The expression  $[L = (N - 1)\Delta x]$  defines the maximum inter-station distance where the inter-station distances change in the range 60-118 m. The process explained in Figure 9 is repeated for all occurrences of the DS approach. All the DS group (Figure 10a), and phase (Figure 10b) speed results (purple color solid circles) are assembled to show them superimposed. The inverted model in Figure 3b (red color) is employed to calculate the group and phase speed curves shown by the green color curves in each panel. The selection range for the DS group and phase speeds is created by the upper (cyan color) and lower (orange color) boundary curves. This range has variable width changing with period, which is 160 m/s at a shorter period (i.e., 0.02 s) and then increases to 310 m/s at a longer period (i.e., 0.18 s). For all inter-station distances, these intervals, which are the same for both group and phase speeds, are employed as the selection ranges to bracket the DS dispersal data.



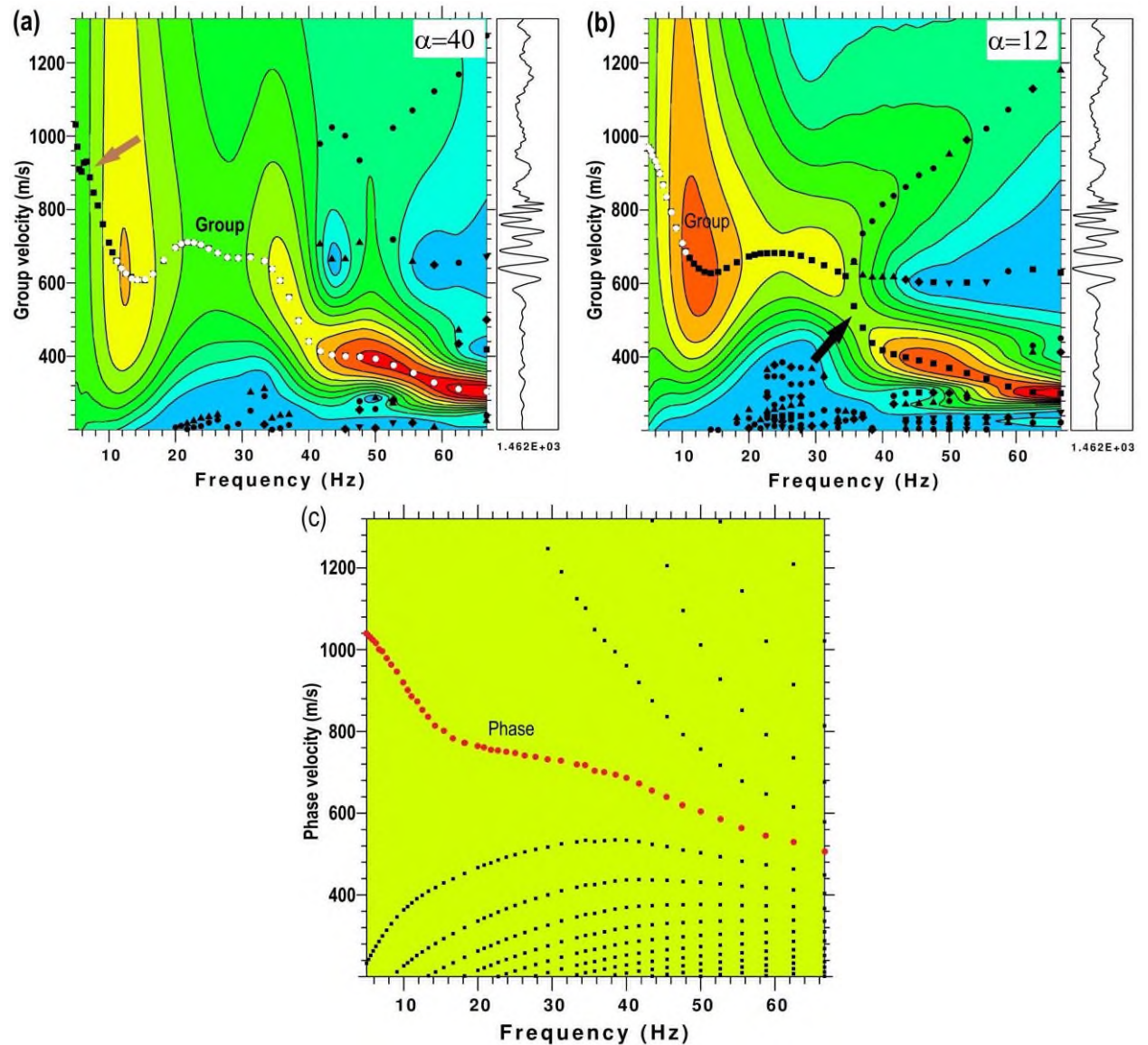


**Figure 8:** Rayleigh surface wave propagation between geophone locations #10 and #40 indicated by two stars in Figure 2 is shown using the double-station (DS) approach applied to the model structure. The DS MFT results employing two different  $\alpha$  values are illustrated. a)  $\alpha = 40$  and b)  $\alpha = 12$ . The phase speed cycles are displayed in (c). The fundamental model (FM) phase speed curve is indicated by the red color.

Both OS group speeds (see yellow arrow in Figure 7) and DS group and phase speeds (see yellow arrows in Figure 10) develop some uncertainties at specifically shorter periods ( $< 0.04$  s), i.e., the inconsistency surrounding the green color dispersal curve. To attain more accurate group and phase speed results one may need to choose a smaller time sampling (e.g.,  $\Delta t = 0.1$  ms instead of current  $\Delta t = 0.25$  ms). In addition, one may work on the  $\alpha$  parameter for fine tuning, i.e., various  $\alpha$  values other than  $\alpha = 42$ , which is currently preferred, could be evaluated to see if any improvement is gained. The MFT is a sizable procedure to complete, which has overall time complexity of  $O(N^2 \log N)$  at numerous geophone positions ( ${}^{\text{OS}}N_a$ ) and inter-station spaces ( ${}^{\text{DS}}N_a$ ). We were not able to trail the calculations using finer parameters (i.e.,  $\Delta t$  and  $\alpha$ ) since we have limited computational power in terms of memory – RAM and processor – CPU. Therefore, we stay with the existing parameters.

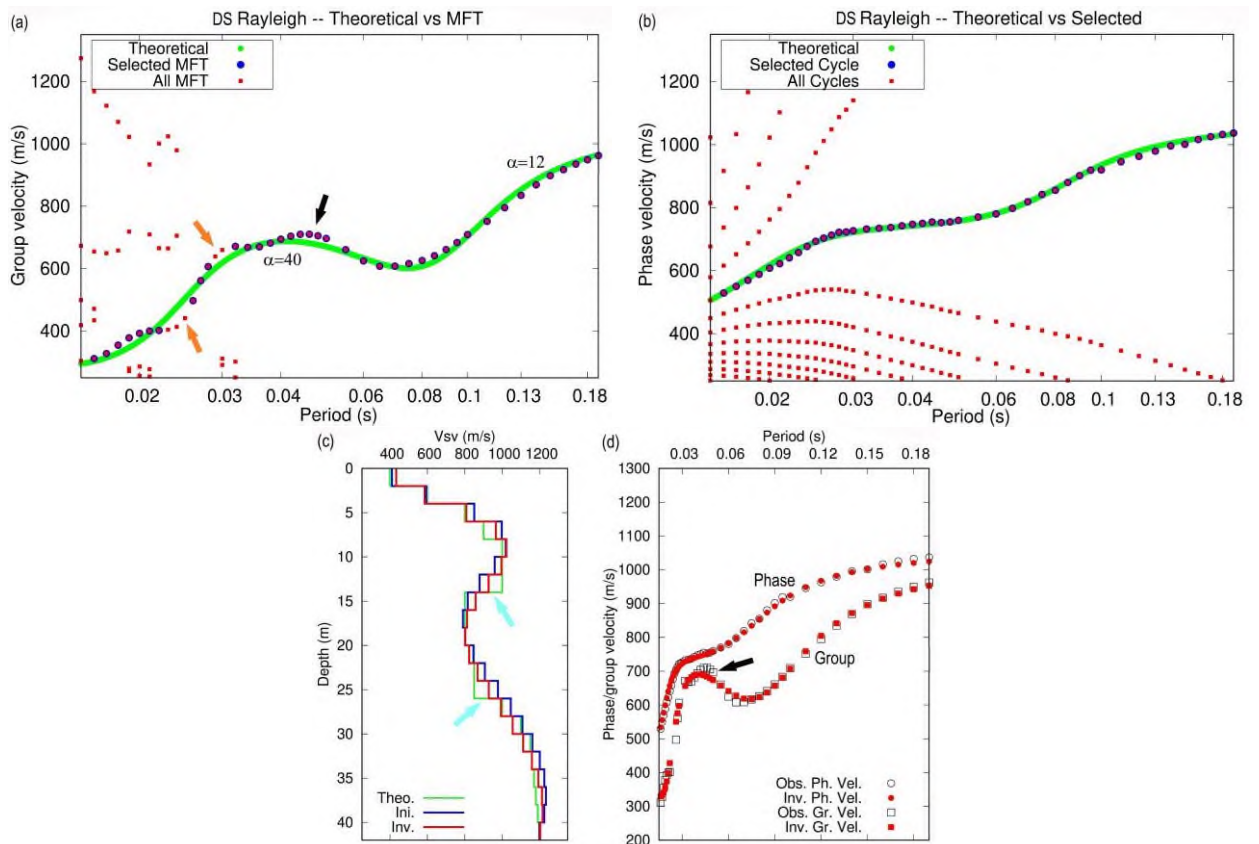


**Figure 9:** a) The white dots in Figures 8a and 8b are combined to get the fundamental mode (FM) group speed dispersal curve where the theoretical group speed (green color), selected MFT group speed (blue color), and all computed MFT group speed (red color) are specified. The phase speed cycles are displayed in (b) where the theoretical phase speed (green color), selected cycle (blue color), and all computed cycles (red color) are indicated. The FM group and phase speed curves are jointly inverted. (c) The inverted 1D speed structure (red color), initial model (blue color) and theoretical model (green color) are displayed. (d) The observed (black color) and inverted (red color) group and phase dispersal curves are illustrated.

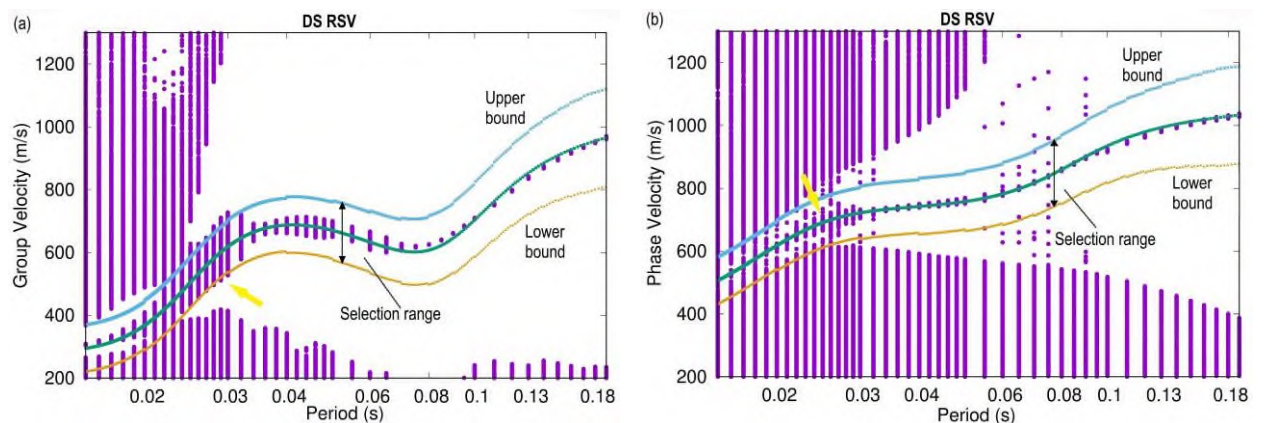


**Figure 10:** Double-station (DS) results (purple color symbols) are shown superimposed for multiple inter-station distances. (a) DS MFT results and (b) DS phase speed cycles. The upper (cyan color) and lower (orange color) boundaries specify the selection range of group and phase speeds of Rayleigh surface vibration (RSV) in (a) and (b).

One should note that we have considered seismograms without noise and yet the dispersal analysis still shows some disturbances (Figures 7 and 10). In actual measurements, the noise effect caused by three-dimensional (3D) scattering, multipathing and mode interferences [40, 41, 42, 43] might further create disturbances on the observed dispersal data. The selection ranges employed for the speed bracketing processes (Figures 7 and 10) should help resolve the disturbance issues persistent on the observed dispersal curves so that smoother inversions of the subsurface are achieved.

### 3.5. 2D Vertical Cross-Section Under Common-Shot Gather

There exist three linear systems to solve, i.e., one for the OS group arrival times and two for the DS group and phase arrival times. We chain all these three systems together to jointly solve the phase and group speed data to recover the 2D  $V_{SV}$  structure underneath the common-shot gather (CSG). First, the DS phase arrival times are solved through the respective linear system to find the phase slowness values at grid points (see Figure 1). Second, we merge the two linear systems consistent with the OS and DS group arrival times to resolve the group slowness values at the same grid points. The damped least squares method is employed for the solution of each linear system [29, 44, 45]. At each grid point, the phase and group speed dispersal curves are separately constructed by repetitively solving the above linear systems for each discrete frequency (Hz) value. To find the 1D  $V_{SV}$  structure beneath a grid point, the corresponding dispersal curves (phase and group speeds) are jointly inverted for which the inversion strategy used in Figure 9 is followed. The 2D  $V_{SV}$  cross-section corresponding to the structure underneath the CSG is finally built by combining all the 1D  $V_{SV}$  solutions together [46].

In Figure 11, we demonstrate the subsequent 2D cross-section where the speed changes with depth are shown. In the near surface from 0-m to 4-m depth, the speed structure is represented by two layers each with 2-m thickness where the  $V_{SV}$  speed increases from 400 m/s to 600 m/s. This two-layer structure is correctly resolved by the inverted speeds. The depth range from 4-m to 8-m includes two layers in which the  $V_{SV}$  speed rises from 800 m/s to 900 m/s, which is properly characterized by the inverted speeds but there exists slight resolution loss for this two-layer structure. Below this depth range the  $V_{SV}$  speed increments to 1000 m/s creating a high-speed zone (HSZ), which is suitably represented by the inverted speeds. There exists a speed reversal (i.e., low speed zone – LSZ) at 14-m depth in which the  $V_{SV}$  speed drops to 800 m/s, which is represented by the 2D cross-section (Figure 11). From 20-m to 30-m depth, the  $V_{SV}$  speed constantly increases from 850 m/s to 1100 m/s (i.e., a 250-m/s speed increment), which is presented by the color change from green to yellow in the cross-section. The  $V_{SV}$  speeds steadily increase from 1100 m/s to 1200 m/s in the depth range 30-40 m for which the inverted speeds show a structure more like a one-layer, which is depicted by the red color in the color scale. Such deeper structures are solved by the longer period Rayleigh surface waves (FM), which exhibit lower resolution power in the vertical direction.

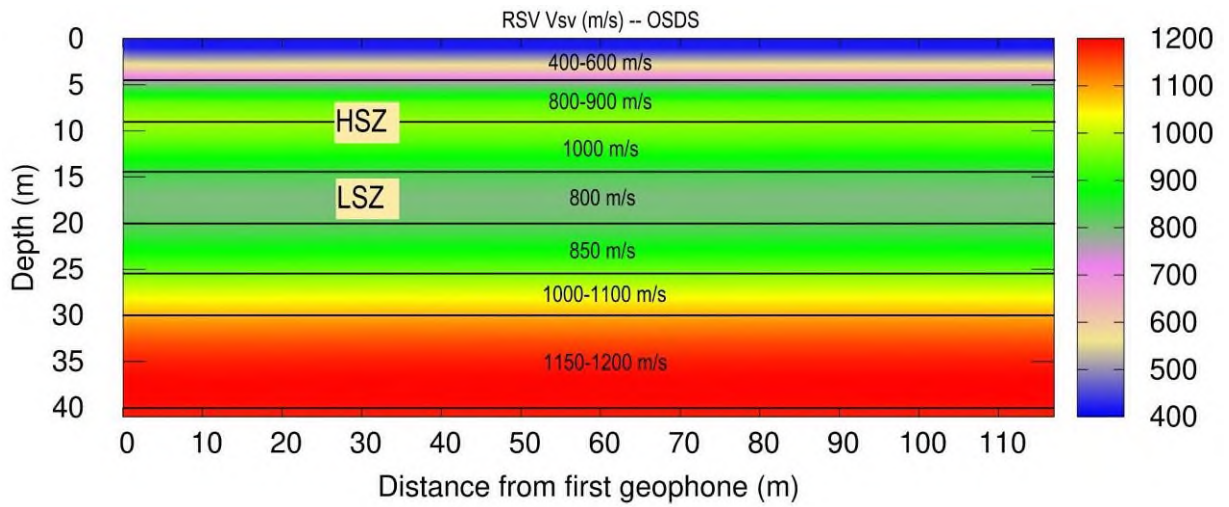


**Figure 11:** Two-dimensional (2D) vertical cut corresponding to the shear-wave ( $V_{SV}$ ) speeds obtained by the inversion of group and phase speed dispersion curves is shown. The one-station (OS) and double-station (DS) approaches are joined.

#### 4. DISCUSSION AND CONCLUSIONS

We mathematically replicate the Rayleigh surface waves in a multilayered subsurface. The vertical component synthetic seismograms are calculated to characterize the wave propagation. These synthetic calculations are utilized to evaluate the performance of the programmed technique proposed for the determination of the seismic speed structure above 40-m depth. The data collection geometry is assumed as the CSG, which employs multiple stations aligned along a linear line to record the Rayleigh surface vibrations. The CSG is employed to estimate the 2D variation of vertically polarized shear-vibration ( $V_{SV}$ ) speeds with depth. In the programmed approach, we first estimate the average structure beneath the geophone spread for which the weighted preconditioned linear radon transform (WPLRT) is employed to solve the phase speeds. Secondly, the OS group speeds are realized by applying the multiple filter technique (MFT) to each geophone recording. In the third step, we calculate the cross-correlations between two stations in the CSG. Herein, the cross-correlograms, which are free of the source phase, are employed to acquire the DS group and phase speeds. The WPLRT approach utilizing the phase speeds provides an initial model, which effectively represents the 1D  $V_{SV}$  speeds under the CSG, which is discretized using a set of grid points (Figure 1). This initial model is then used to invert the OS (group speeds) and DS (phase and group speeds) data. In this way, the subsurface beneath each grid point is represented by an individual 1D  $V_{SV}$  depth profile and then these profiles are joined to build the 2D vertical cut under the CSG.

In Table 2, we compare the current algorithm with similar studies, i.e., CMP-CC MASW [47, 48, 49, 50, 51] and CMP-CC SPAC [52, 53, 54, 55, 56] where CMP stands for Common Midpoint and CC for Cross-Correlation. The CMP-CC [57] is a procedure utilized to maximize the spatial resolution of MASW or SPAC. The CMP-CC MASW involves multi-channel and multi-shot surface waves [57] in which continuous distance profiling is performed to collect horizontally extended surface wave data. There exist common midpoints between pairs of receivers in a common shot gather for which cross-correlations are computed. The latter procedure is repeated for multi-shot surface waves. Those correlation signals sharing the same CMP and receiver spacing are stacked from which CMP-CC gathers are eventually constructed. The conventional MASW method [11] is applied to the CMP-CC gathers to compute the phase velocities, which are then inverted to attain a pseudo 2D  $V_{SV}$  structure underneath the studied area [57]. The CMP-CC SPAC, which is a multi-channel passive surface wave method, works in an analogous way to that in the CMP-CC MASW. Several minutes of ambient noise is recorded for spatial autocorrelation (SPAC) analysis. The 2D receiver array is divided into several blocks and for each

receiver pair in each block, SPAC traces (i.e., coherencies) are computed [24]. In the frequency domain, computed coherencies over all blocks are averaged and those coherencies sharing the same common midpoint are grouped as CMP-SPAC gathers. The observed coherencies are compared with the theoretical Bessel function to calculate the phase velocities, which are finally inverted to reconstruct a pseudo 2D/3D  $V_{SV}$  model underneath the region of interest [58].

**Table 2:** Brief comparison of the current algorithm with the CMP-CC MASW and CMP-CC SPAC methods.

Properties	Current study	CMP-CC MASW	CMP-CC SPAC
Active/Passive Source	Active	Active	Passive
Dispersion curves	Phase and Group Velocity	Commonly Phase Velocity	Commonly Phase Velocity
Resolution depth (m)	Shallow (< 50 m)	Shallow (< 50 m)	Deep (> 50 m)
2D/3D Tomographic imaging	Yes	Yes	Yes

#### *Concluding remarks*

- The phase velocities are computed from the phase spectrum of surface waves while the amplitude spectrum is utilized to calculate the group velocities. We jointly invert group and phase velocities to predict the near-surface shear-wave velocities ( $V_{SV}$ ).
- The current algorithm involves hundreds of dispersion curves (both phase and group velocity). To hand-pick this much dispersion curve can be quickly overwhelming. We select these dispersion curves by employing a programmed scheme like the one reported in Çakır and Kutlu (2023) [32].
- The phase velocities at low frequencies are determined by using a long receiver array for which a strong seismic source (e.g., a shaker or vibrator) is needed to deliver the surface wave energy up to the end of profile.
- The parameter  $N_c = 30$ , which is the minimum number of geophone intervals between two stations can be set to 20 or 10, which will help increase the number of DS dispersion data along with an increment in the lateral resolution.
- An observed dispersion curve is converted into a dispersion curve defined at a grid point for which a linear system regularized around a reference slowness computed from the average of the observed slowness is solved along with a damping parameter.
- Like the CMP-CC MASW and CMP-CC SPAC methods, the current algorithm can predict the 2D variation of  $V_{SV}$  underneath the 2D continuous-profiling and this coverage can be extended into a 3D tomographic study along with the 2D cross-profiling.

#### **Declaration of Ethical Standards**

The authors of this article declare that the materials and methods used in this study do not require ethical committee permission and/or legal-special permission.

#### **Credit Authorship Contribution Statement**

CRedit (Contributor Roles Taxonomy) was introduced with the intention of recognizing individual author contributions, reducing authorship disputes, and facilitating collaboration.

#### **Declaration of Competing Interest**

The authors declare that they have no known competing financial interests or personal relationships that could have appeared to influence the work reported in this paper.

### Funding / Acknowledgements

We are grateful to the anonymous reviewers for critically reviewing the manuscript.

### Data Availability

There is not any data from a data repository.

### 5. REFERENCES

- [1] D.A. Robinson, A. Binley, N. Crook, F.D. Day-Lewis, T.P.A. Ferre, V.J.S. Grauch, R. Knight, M. Knoll, V. Lakshmi, R. Miller, J. Nyquist, L. Pelleri, K. Singha, and L. Slater, "Advancing process-based watershed hydrological research using near-surface geophysics: a vision for, and review of, electrical and magnetic geophysical methods," *Hydrological Processes*, vol. 22, pp. 3604–3635, 2008.
- [2] L.V. Socco, and C. Strobbia, "Surface-wave method for near-surface characterization: a tutorial," *Near Surface Geophysics*, vol. 2, pp. 165–185, 2004.
- [3] V. Pérez-Gracia, J.O. Caselles, J. Clapes, R. Osorio, G. Martínez, and J.A. Canas, "Integrated near-surface geophysical survey of the Cathedral of Mallorca," *Journal of Archaeological Science*, vol. 36, pp. 1289–1299, 2009.
- [4] Y. Huang, and M. Yu, *Hazard analysis of seismic soil liquefaction*. Springer, Singapore, 2017.
- [5] V. Balaram, "Rare earth elements: a review of applications, occurrence, exploration, analysis, recycling, and environmental impact," *Geoscience Frontiers*, vol. 10, pp. 1285–1303, 2019.
- [6] C. Lin, X. Wang, L. Nie, H. Sun, Z. Xu, Y. Du, and L. Liu, "Comprehensive geophysical investigation and analysis of lining leakage for water-rich rock tunnels: a case study of Kaiyuan Tunnel, Jinan, China," *Geotechnical and Geological Engineering*, vol. 38, pp. 3449–3468, 2020.
- [7] E.A. Ayolabi, A.F. Folorunso, and O.T. Kayode, "Integrated methods for environmental Assessment of municipal dumpsite system," *International Journal of Geosciences*, vol. 4, pp. 850–862, 2013.
- [8] M. Everett, *Near-surface applied geophysics*. Cambridge University Press, 2013.
- [9] A. Turesson, "A comparison of methods for the analysis of compressional, shear, and surface wave seismic data, and determination of the shear modulus," *Journal of Applied Geophysics*, vol. 61, pp. 83–91, 2007.
- [10] K. Luxbacher, E. Westman, P. Swanson, and M. Karfakis, "Three-dimensional time-lapse velocity tomography of an underground longwall panel," *International Journal of Rock Mechanics and Mining Sciences*, vol. 45, pp. 478–485, 2008.
- [11] C.B. Park, R.D. Miller, and J. Xia, "Multichannel analysis of surface waves," *Geophysics*, vol. 64, pp. 800808, 1999.
- [12] A. Ali, M. Ullah, A. Barkat, W.A. Raza, and A. Qadir, "Multi-channel analysis of surface waves (MASW) using dispersion and iterative inversion techniques: implications for cavity detection and geotechnical site investigation," *Bulletin of Engineering Geology and the Environment*, vol. 80, pp. 9217–9235, 2021.
- [13] G. Dal Moro, "MASW? A critical perspective on problems and opportunities in surface-wave analysis from active and passive data (with few legal considerations)," *Physics and Chemistry of the Earth*, vol. 130, pp. 103369, 2023.
- [14] H. Nakahara, K. Emoto, and T. Nishimura, "Extending the formulation of the spatial autocorrelation (SPAC) method to strain, rotation and tilt," *Geophysical Journal International*, vol. 227, pp. 287–302, 2021.
- [15] C. Feng, K. Yamaoka, R. Ikuta, T. Watanabe, and S. Tsuji, "Surface wave monitoring using ambient noise for detecting temporal variations in underground structures in landslide area," *Engineering Geology*, vol. 341, pp. 107706, 2024.
- [16] Q. Liu, L. Lu, K. Wang, L. Chang, and Y. Zhu, "Rayleigh Wave Phase Velocity Maps at Regional Scale Inferring from SPAC of Ambient Noise at a Dense Array: A Case Study in Northeastern

- Tibetan Plateau," *Pure and Applied Geophysics*, vol. 180, pp. 1973–1988, 2023.
- [17] S. Coccia, V. Del Gaudio, N. Venisti, and J. Wasowski, "Application of Refraction Microtremor (ReMi) technique for determination of 1-D shear wave velocity in a landslide area," *Journal of Applied Geophysics*, vol. 71, pp. 71–89, 2010.
- [18] J.N. Louie, A. Pancha, and B. Kissane, "Guidelines and pitfalls of refraction microtremor surveys," *Journal of Seismology*, vol. 26, pp. 567–582, 2022.
- [19] K. Aki, "Space and time spectra of stationary stochastic waves, with special reference to microseisms," *Bulletin of the Earthquake Research Institute*, vol. 35, pp. 415–456, 1957.
- [20] T.F. Abdallatif, A.A. Khozma, and A.A. Ghandour, "Determination of Seismic Site Class and Potential Geologic Hazards using Multi-Channel Analysis of Surface Waves (MASW) at the Industrial City of Abu Dhabi, UAE," *Journal of Astronomy and Geophysics*, vol. 11, pp. 193–209, 2022.
- [21] B. Mi, J. Xia, J.H. Bradford, and C. Shen, "Estimating Near-Surface Shear-Wave-Velocity Structures Via Multichannel Analysis of Rayleigh and Love Waves: An Experiment at the Boise Hydrogeophysical Research Site," *Surveys in Geophysics*, vol. 41, pp. 323–341, 2020.
- [22] K. Zheng, W. Hou, J. Li, J. Yang, Y. Yang, F. Xiao, and Y. Chen, "Imaging urban near-surface structure with passive surface waves method: A case study in Guangzhou, southern China," *Journal of Applied Geophysics*, vol. 215, pp. 105089, 2023.
- [23] M. Asten, A. Askan, and S. Karimzadeh, "Blind study site assessment of shear-wave velocity at Kumamoto City, Japan, using direct-fitting SPAC methods," *Earth, Planets and Space*, vol. 75, pp. 40, 2023.
- [24] Q. Liu, L. Lu, T. Qin, and L. Chang, "Determination of surface-wave phase velocities by zeros of Aki's spectrum of active-source records. Application to the dense array in Tongzhou, China," *Earthquake Science*, vol. 38, pp. 1–16, 2024.
- [25] K. Abdelrahman, A.B. Saadon, and S. Qaysi, "Estimating shear wave velocity and site characterization of western Riyadh City, Saudi Arabia based on multichannel analysis of surface waves," *Frontiers in Earth Science*, vol. 12, pp. 1395431, 2024.
- [26] A. Kaviani, A. Paul, A. Moradi, P.M. Mai, S. Pilia, L. Boschi, G. Rumpker, Y. Lu, Z. Tang, and E. Sandvol, "Crustal and uppermost mantle shear wave velocity structure beneath the Middle East from surface wave tomography," *Geophysical Journal International*, vol. 221, pp. 1349–1365, 2020.
- [27] Z. Zhang, H. Yao, and Y. Yang, "Shear wave velocity structure of the crust and upper mantle in Southeastern Tibet and its geodynamic implications," *Science China Earth Sciences*, vol. 63, pp. 1278–1293, 2020.
- [28] K.A. Berteussen, "Moho depth determinations based on spectral analysis of NORSAR long period P waves," *Physics of the Earth and Planetary Interiors*, vol. 15, pp. 13–27, 1977.
- [29] R.B. Herrmann, *Computer programs in seismology, version 3.30*. St. Louis University, Missouri, United States, 2002.
- [30] Y. Luo, J. Xia, R.D. Miller, Y. Xu, J. Liu, and Q. Liu, "Rayleigh-wave mode separation by high-resolution linear radon transform," *Geophysical Journal International*, vol. 179, pp. 254–264, 2009.
- [31] A. Dziewonski, S. Bloch, and M. Landisman, "A technique for the analysis of transient seismic signals," *Bulletin of Seismological Society of America*, vol. 59, pp. 427–444, 1969.
- [32] Ö. Çakır, and Y.A. Kutlu, "A New Method for Selecting the Phase and Group Velocity Dispersion Curves of Rayleigh and Love Surface Waves: Real Data Case of Central Anatolia, Turkey (Türkiye)," *Indonesian Journal of Earth Sciences*, vol. 3, pp. 795, 2023.
- [33] L. Gao, J. Xia, Y. Pan, and Y. Xu, "Reason and Condition for Mode Kissing in MASW Method," *Pure and Applied Geophysics*, vol. 173, pp. 1627–1638, 2016.
- [34] Ö. Çakır, and N. Coşkun, "Theoretical Issues with Rayleigh Surface Waves and Geoelectrical Method Used for the Inversion of Near Surface Geophysical Structure," *Journal of Human, Earth, Future*, vol. 2, pp. 183–199, 2021.
- [35] D.J. Zywicki, and G.J. Rix, "Mitigation of Near-Field Effects for Seismic Surface Wave Velocity Estimation with Cylindrical Beamformers," *Journal of Geotechnical and Geoenvironmental Engineering*,


- vol. 131, pp. 970–977, 2005.
- [36] A. Tarantola, "Linearized inversion of seismic reflection data," *Geophysical Prospecting*, vol. 32, pp. 998–10115, 1984.
- [37] R.J. Geller, and T. Hara, "Two efficient algorithms for iterative linearized inversion of seismic waveform data," *Geophysical Journal International*, vol. 115, pp. 699–710, 1993.
- [38] Ö. Çakır, "Seismic crust structure beneath the Aegean region in southwest Turkey from radial anisotropic inversion of Rayleigh and Love surface waves," *Acta Geophysica*, vol. 66, pp. 1303–1340, 2018.
- [39] Ö. Çakır, "Love and Rayleigh Waves Inverted for Vertical Transverse Isotropic Crust Structure beneath the Biga Peninsula and the surrounding area in NW TURKEY," *Geophysical Journal International*, vol. 216, pp. 2081–2105, 2019.
- [40] Ö. Çakır, "The multilevel fast multipole method for forward modelling the multiply scattered seismic surface waves," *Geophysical Journal International*, vol. 167, pp. 663–678, 2006.
- [41] I.B. Morozov, and M. Din, "Use of receiver functions in wide-angle controlled-source crustal data sets," *Geophysical Journal International*, vol. 173, pp. 299–308, 2008.
- [42] V. Maupin, "Upper-mantle structure in southern Norway from beamforming of Rayleigh wave data presenting multipathing," *Geophysical Journal International*, vol. 185, pp. 985–1002, 2011.
- [43] Ö. Çakır, "A multilevel fast multipole method to compute propagation of multiply scattered 2.5-D teleseismic surface waves underneath a linear or quasi-linear seismic station array," *International Journal of Physical Sciences*, vol. 7, pp. 5687–5700, 2012.
- [44] J. Julià, C.J. Ammon, R.B. Herrmann, and A.M. Correig, "Joint inversion of receiver function and surface wave dispersion observations," *Geophysical Journal International*, vol. 143, pp. 99–112, 2000.
- [45] Ö. Çakır, and N. Coşkun, "Love Surface Waves and Electrical Resistivity Used to Delineate the Near Surface Geophysical Structure: Theoretical Considerations," *Earth Sciences Malaysia*, vol. 5, pp. 104–113, 2021.
- [46] Ö. Çakır, and N. Coşkun, "Dispersion of Rayleigh Surface Waves and Electrical Resistivities Utilized to Invert Near Surface Structural Heterogeneities," *Journal of Human, Earth, Future*, vol. 3, pp. 1–16, 2022.
- [47] P.P. Kruiver, M. Pefkos, E. Meijles, G. Aalbersberg, X. Campman, W. van der Veen, A. Martin, K. Ooms-Asshoff, J. J. Bommer, A. Rodriguez-Marek, R. Pinho, H. Crowley, F. Cavalieri, A.A. Correia, and J. van Elk, "Incorporating dwelling mounds into induced seismic risk analysis for the Groningen gas field in the Netherlands," *Bulletin of Earthquake Engineering*, vol. 20, pp. 255–285, 2022.
- [48] K. Leontarakis, C. Orfanos, and G. Apostolopoulos, "Common-midpoint cross-correlation stacking tomography: A 3D approach for frequency-dependent mapping of Rayleigh waves, group and phase velocity throughout an active seismic network," *Near Surface Geophysics*, vol. 21, pp. 39–64, 2023.
- [49] I. Barone, J. Boaga, A. Carrera, A. Flores-Orozco, and G. Cassiani, "Tackling Lateral Variability Using Surface Waves: A Tomography-Like Approach," *Surveys in Geophysics*, vol. 42, pp. 317–338, 2021.
- [50] F. Cheng, J. Xia, C. Shen, Y. Hu, Z. Xu, and B. Mi, "Imposing Active Sources during High-Frequency Passive Surface-Wave Measurement," *Engineering*, vol. 4, pp. 685–693, 2018.
- [51] B. Mi, J. Xia, J.H. Bradford, and C. Shen, "Estimating Near-Surface Shear-Wave-Velocity Structures Via Multichannel Analysis of Rayleigh and Love Waves: An Experiment at the Boise Hydrogeophysical Research Site," *Surveys in Geophysics*, vol. 41, pp. 323–341, 2020.
- [52] M.S. Craig, K. Hayashi, and Ö. Kozacı, "Active and passive seismic surface wave methods for levee assessment in the Sacramento–San Joaquin Delta, California, USA," *Near Surface Geophysics*, vol. 19, pp. 141–154, 2021.
- [53] J. Pang, J. Xia, C. Zhou, X. Chen, F. Cheng, and H. Xing, "Common-midpoint two-station analysis of estimating phase velocity using high-frequency ambient noise," *Soil Dynamics and Earthquake*



- Engineering*, vol. 159, pp. 107356, 2022.
- [54] K. Hayashi, M.W. Asten, W.J. Stephenson, C. Cornou, M. Hobiger, M. Pilz, and H. Yamanaka, "Microtremor array method using spatial autocorrelation analysis of Rayleigh-wave data," *Journal of Seismology*, vol. 26, pp. 601–627, 2022.
- [55] F.J. Chávez-García, M.V. Manakou, F. Hollender, and D.G. Raptakis, "Site effects using methods based on lateral homogeneity and laterally heterogeneous media: An impossible marriage?," *Bulletin of Earthquake Engineering*, vol. 16, pp. 2729–2756, 2018.
- [56] F. Cheng, J. Xia, Z. Xu, Y. Hu, and B. Mi, "Frequency–Wavenumber (FK)-Based Data Selection in High-Frequency Passive Surface Wave Survey," *Surveys in Geophysics*, vol. 39, pp. 661–682, 2018.
- [57] K. Hayashi, and H. Suzuki, "CMP cross-correlation analysis of multi-channel surface-wave data," *Exploration Geophysics*, vol. 35, pp. 7–13, 2004.
- [58] K. Hayashi, J.M. Lorenzo, and A. Gostic, "Application of 2D ambient noise tomography to levee safety assessment in New Orleans," *The Leading Edge*, vol. 37, pp. 740–745, 2018.



## LAND ADMINISTRATION AND ITS DIGITAL SHIFT IN BANGLADESH AND TÜRKİYE: A COMPARATIVE ANALYSIS

\*Md Moynul AHSAN 


*Ankara University, Faculty of Applied Sciences, Real Estate Development and Management Department, Ankara,  
TÜRKİYE*  
[moynulurp01@gmail.com](mailto:moynulurp01@gmail.com)

### *Highlights*

- Bangladesh is making progress on land management, but desired progress is not satisfactory whereas Türkiye is making significant progress on its land management and its economy.
- Digital land management practices of Türkiye are now in reality whereas Bangladesh is a way of reality and seems very challenging.
- A robust governance system is vital for both countries.



## LAND ADMINISTRATION AND ITS DIGITAL SHIFT IN BANGLADESH AND TÜRKİYE: A COMPARATIVE ANALYSIS

\*Md Moynul AHSAN 

Ankara University, Faculty of Applied Sciences, Real Estate Development and Management Department, Ankara,  
TÜRKİYE  
[moynulurp01@gmail.com](mailto:moynulurp01@gmail.com)

(Received: 04.07.2024; Accepted in Revised Form: 21.01.2025)

**ABSTRACT:** This study has focused on the land administration practices in Bangladesh and Türkiye, covering existing state, institutional structure and relevant policies followed in the past two decades. A major focus has been given to the shift from manual to digital land administration practices in both countries. By using an explanatory qualitative analysis through secondary based data and information, it has found that the governments of Bangladesh and Türkiye are aiming to make the country's land management system fully digitalised and bring land services to the doorsteps of people to ensure proper land utilisation/entitlement as per targets of Sustainable Development Goals. It has found that Bangladesh is achieving progress, but the desired progress is not satisfactory, whereas Türkiye is achieving successive progress and now considered is one of the best practised countries in the world. The country is making significant contribution in its economy through land management practices. Digital land administration practices of Türkiye are now in reality while Bangladesh is a way of reality and seems very challenging as it requires robust administration and sufficient human resource mobilisation. Bangladesh also needs a centralised administrative system, more user friendly one stop services, capacity building activities, and modern technology-based practices. Finally, a robust governance system by ensuring land crime prevention and redress is a vital need for both countries.

**Keywords:** Land Administration, Land Planning, Digitalisation, Land Governance, Bangladesh, Türkiye

### 1. INTRODUCTION

"Land - a natural asset" encompasses all physical elements, to a specific area or piece of property, identity etc. (Mahalaya, 2010). It is a scarce resource and consider as a primary factor of production. The scarcity of land, increasing demand, and resulting high prices poses important implications for the prospect of industrialization and development of a country (Raihan et al., 2020). The existing urbanization trends, future demographic demands, environmental and climatic change, green transition effort, value creation, availability and use of open data etc. all creates a significant demand for digital transition (FAO, UNECE and FIG. 2022). Land requires sustainable planning, use and management in order to meet the present and future needs (Uisso et al., 2022). Its sustainable practices with a data and knowledge-driven and modern technology-based procedure can meet the rising development demand of the people in the planet. Its administration and management is a profound issue for every developing country in the world. Considering its importance, the United Nations has put emphasis on land in its Sustainable Development Goals (SDGs) (UN, 2020), as a major concern for development of a country. It has estimated that more than 70% of the targets are related to geospatial technologies and land administration (Ercan, 2022). The SDG 15 regarding "Life on Land" has explicitly discussed on land and land related issues. Among the 17 SDG goals eight of them are directly and indirectly discussed on land and its management, administration and related issues. Land tenure or land right is explicitly linked to poverty eradication (SDG1), food security (SDG2), and gender equality and women's empowerment (SDG5) and some goals have implicit links to land-related outcomes (Heider & Connelly, 2016), and therefore, countries should perform explicit role on land administration and planning for their sustainable development.

The land issues are extremely complex and can be relieved by deploying "digitalised" based practices.

\*Corresponding Author: Md Moynul AHSAN, [moynulurp01@gmail.com](mailto:moynulurp01@gmail.com)

Globally, land offices in many countries are still noticeable due to traditional analog service methods. Countries could not perform precise role on land related issues for their sustainable development. The automation of services is one method for solving these traditions. However, all land services must be automated through coordination with related services provided by other ministries and stakeholders using top-notch, interoperable software and apps. A digitalised system could ease monitoring and evaluation of various major activities on land administration, including land registration and transfer, title deeds etc. It could represent highly effective in the market-based economies and could ensure good governance by curbing corruption, ensuring transparency and accountability, maintaining rule of law.

Being a developing country, Bangladesh is characterised one of the densely populated countries in the world with 1301 people per square kilometers (sq.km) in 2021 in its 147,570 sq.km of land mass (World Bank, 2024c). The country occupies around 0.03% of the world's land area but it supports slightly over 2% of the world's population. On the other hand, Türkiye is also a developing country located around 97% in Western Asia comprising around 90% of the country's population, and the remaining 3% portion located in the European part comprising around 10% of the country's total population. The country is characterised as a less densely populated country in the world with 109.3 people per sq.km in its 783,600 sq.km of land mass (World Bank, 2024c), which represents around 12 times less than Bangladesh. The following table 1 shows a brief comparison of general characteristics in Bangladesh and Türkiye.

**Table 1.** General characteristics in Bangladesh and Türkiye.

Characteristics	Bangladesh	Türkiye	Remarks
Area (sq. km)	147,570	783,600	Türkiye is 5.04 times bigger than Bangladesh
Population (in million)	165.2	84.98	Bangladesh population is around 2 times bigger than Türkiye
Urban population (% of total population)	31.66	77	Still more than two-third of the population of Bangladesh are living in rural area
Land Parcels	No exact data received	Approximately 59 million	Around 45 million land record available in Bangladesh
Province/district	64	81	District and Province are interchangeable
Upazila	495	973	Upazila and District are interchangeable
Villages	90,049	18,253	Only 6.8% people live in villages in Türkiye

Source: World Bank, 2024a; TURKSTAT, 2022; BBS, 2024

From the above characteristics, including data and information, it has found that Türkiye's land-man ratio is about 5 times bigger than Bangladesh, but Bangladesh's population is more than 2 times bigger than Türkiye. Therefore, land management, its planning and administrative actions are much more challenging for Bangladesh. In Türkiye, a major proportion of people are living in urban areas whereas Bangladesh's population are living predominantly in rural areas. Around 86.51% land area is considered as rural and the remaining 13.49% is urban in Bangladesh (BBS, 2024). As per World Bank (2024a), the Urban population (% of total population) in Türkiye is 77% whereas only 6.8% people live in villages in Türkiye (TURKSTAT, 2022), and the remaining 93.2% population are living in urban areas.

Considering the importance of land administration, the Bangladesh government has identified 'land' as one of the priority development areas of intervention in its various long-term development plans such as Perspective Planning 2021-41, Delta plan 2100 etc. The Article 42(1) of the Constitution of Bangladesh has provided land rights to the individual. It states that "Subject to any restrictions imposed by law, every citizen shall have the right to acquire, hold, transfer or otherwise dispose of property, and no property shall be

*compulsorily acquired, nationalised or requisitioned save by authority of law*" (Ministry of Law, Justice and Parliamentary Affairs, 2019).

On the other hand, Türkiye government is giving importance of land administration and planning (more specifically digital land administration) as per of its development policies and activities. The country has poses land rights to the individual. The Article 35 of the Constitution of the People's Republic of Türkiye has been stated that *"Everyone has the right to own and inherit property. These rights may be limited by law only in view of public interest. The exercise of the right to own property may not be in contravention of the public interest"* (Department of Laws and Resolutions, 2019).

Türkiye now, is practicing land management issues through its digitalized administration systems whereas Bangladesh government aims to digitalize its land administration system and making some progress from the last decade. As per the World Bank, Türkiye is one of the best practising land management and administrative countries in the world (World Bank, 2020) and is making significant contribution through its digitalise land management system at the national and international level.

As the world is moving towards a digitalised system, which contributes all aspects of our life, where land issues are vital. In this conjunction, countries also urge to improve their land administration services, better decision making, better security, minimise dispute, fairer taxation, good governance in both urban and rural areas (FAO, UNECE and FIG. 2022). Therefore, comparing countries in land administration practices and its digital effort from the past decades could make beneficial role for the development of a country. Both Bangladesh and Türkiye pose a long history of land laws and policies from ancient periods, and their digital movement could be visible from the past two decades, therefore focusing these countries on land administration and management can contribute the administrative and managerial practices more efficient and further effective action. Considering this background, Bangladesh and Türkiye case has been considered in this study, and outlined to find out the existing state, challenges and opportunities for land administration and management practices in both countries.

## 2. MATERIAL AND METHODS

In this study, an explanatory qualitative analysis through secondary based data and information conducted in order to gain the insights relying on the findings gained. Content analysis was applied to gather data based on secondary based research such as government published reports from Bangladesh Bureau of Statistics (BBS), Turkish Statistical Institute (TURKSTAT), General Directorate of Land Registry and Cadastre (GDLRC); non-government reports, peer-reviewed articles, books etc. to understand the land administration practices in Bangladesh and Türkiye. There are many crosscutting issues that could be considered in land administration and management but this study is mainly focused on several priority areas of development such as: land registration, administration and digital transition in both countries. The following table 2 outlined to express methodological correlation in this study:

The land administration in Bangladesh has a long history that dates back to systems developed by the Ayra, Hindu, and Muslim rulers of ancient India (Raihan et al., 2020); later on, British colonial and Pakistan period, and presently the Republic of Bangladesh. On the other hand, Türkiye also poses a long history of land administration that dates back to the Ottoman period and the present Republic of Türkiye. Though both countries are posing long history of land, laws, planning and policies dates back to the ancient period but this study has focused on the governmental action after 2000; more specifically, Bangladesh former Prime Minister Sheikh Hasina's came to power in 2009 and Turkish President Recep Tayyip Erdoğan's came to power in 2002, as both government has expressed their urgency of shift in land management practices from manual to digital.

**Table 2.** Methodological correlation of the study

	<b>Contents</b>	<b>Technique</b>
<b>Research questions and objectives</b>	<ul style="list-style-type: none"> <li>• What existing land administration practices available in Bangladesh and Türkiye?</li> <li>• Are the existing practices, more especially digital transition sufficient to overcome land administrative problems?</li> <li>• Are Turkish land administration practices applicable in Bangladesh and vice versa?</li> <li>• What necessary actions needed to overcome the challenges?</li> </ul>	Insights of providing the state of land, existing institutional structure, governmental intervention in digital perspectives and insights,
<b>Data collection</b>	Secondary based	Reliable sources of gray literature, peer-reviewed article, book etc.; data and reports
<b>Data analysis</b>	Content analysis	Land, land distribution, institutions, existing structure, digitalization efforts, and challenges
<b>Verification of results</b>	Analytical generalizability of land administration and digital issues	Manual to digital practices, performance

### 3. FINDINGS AND ANALYSIS

#### 3.1. State of Land

Bangladesh is primarily a low-lying country. The human interaction on land is very high especially in land transfer and conversion. The country is rapidly losing arable land due to growing industrialization, economic development, urbanisation, urban sprawl-based development, lack of proper planning and plan implementation (Ahsan & Rahman, 2013). Land speculation, grabbing, disputes all are frequent events in Bangladesh (GED, 2020). The private investors, real estate developers intensify the exploration of availability of land in the city periphery areas or remote areas to set up factories or housing projects (Mahmood & Ahsan, 2019) leads to a hike of residential, commercial/industrial or even agricultural land. The scenario could be visible in all big cities in the country. A consequence of farmland depletion is creating another dimension of involuntary relocation and migration (Mahmood & Ahsan, 2019) in Bangladesh. In addition, the increasing climate change impacts on land are aggravating development concerns in Bangladesh (Ahsan, 2019). It creates increasing pressure on land and resulting various impacts such as drought, desertification, degradation, loosing land-based ecosystems and so on.

In addition, the countries land-man ratio is one of the lowest in the world, estimating around 0.06 hectares per person (World Bank, 2022). The arable land (hectares per person) was 0.16 in 1961, showing a downward trend over the years and in 2021 it reached only 0.05 (World Bank, 2024a). Due to governmental interventions, the agricultural land (% of land area) has increased from 70.1% in 2011 to 77.3% in 2021 (World Bank, 2024b). The following table 3 shows the size-wise distribution (% share in number of total farm holdings) of farm holdings in Bangladesh.

**Table 3.** Distribution of farm holdings by size in Bangladesh

		Small (in acre )			Medium (in acre )	Large (in acre )	Total
0.05-0.49	0.50-0.99	1.00-1.49	1.50-2.49	<b>Total</b>	2.50-7.49	7.50+	<b>Total farm holdings</b>
%28.0	%23.8	%16.4	%16.3	%84.4	%14.1	%1.5.0	%100.0

Source: BBS, 2018

On the other hand, Türkiye represents a flat alluvial plain of land with almost 29.4% classified as forest land (OGM, 2020). Like Bangladesh, here human interaction on land is high especially in land transfer, selling and conversion. Though the situation is not similar to Bangladesh, but the country is also losing arable land due to growing industrialization, economic development, gentrification, urban sprawl-based development, climate change impact etc. (Ahsan, 2022). More specifically, private and cooperative investors' investment in the land and real estate sector are making intense speculation of residential, agricultural, commercial and industrial land.

The agricultural land (% of land area) of Türkiye has reduced slightly in proportion to Bangladesh from 49.7% in 2011 to 49.5% in 2021 (World Bank, 2024b). The land-man ratio is 0.23 hectares per person, which is around 5 times bigger than Bangladesh. Unlike Bangladesh, the arable land (hectares per person) poses a downward trend from the past, in 1961 it was 0.81 and in 2021 it became only 0.24 (World Bank, 2024a) (Table 4).

**Table 4.** Farm size distribution in Turkish agriculture (in % of total farms)

Farm size (in ha)	Year (% of total farms)	
	1991	2001
0-2	35.8	33.4
2-5	31.0	31.5
5-10	17.8	18.5
10-20	9.8	10.8
20-50	4.6	5.1
Above 50	0.9	0.7

Source: EC, 2006 (No updated data received)

According to a study by Ercan (2024), a significant 98.2% of holdings consist of land areas ranging from 5 to 499 hectares, with 77.5% falling within the 20-to-499-hectare range. On average, each agricultural holding contains 5.9 parcels of land, and the average parcel size for agricultural land is 12.9 decares (Ercan, 2024).

### 3.2. Institutional structure

Bangladesh's current land administration and management system includes three main components: settlement, registration, and record keeping (GED, 2022). The Ministry of Land (MoL), the Ministry of Law, Justice and Parliamentary Affairs (MLJPA), the Ministry of Public Administration (MoPA), and the Ministry of Housing and Public Works (MoHPW) are the four Ministries in Bangladesh that carry out this land management and administration. However, MLJPA and MoL continue to carry out the fundamental duties of land administration. The Ministry of Land (MoL) is responsible for land administration through its various divisions such as Land Record and Survey Department (LRSD), Land Reform Board (LRB), Land Appeal Board (LAB) and Land Administration Training Centre (LATC); and the Directorate of Registration under the Ministry of Law, Justice and Parliamentary affairs (MLJPA) is responsible for changes in ownership and taxation (MoL, 2023). The MoL performs most land-related activities including land record surveys, collection of land development tax, and arbitration process, the MLJPA mainly performs records land mutation and transfers. Considering the case of digital land management in Bangladesh, the Land Record and Survey Department (LRSD) is the major responsible organisation performing with its 3 wings: Administration, Land Records and Survey. There is no notary system. Like GDLRC in Türkiye, there is no Research Planning and Coordination Department or Information

Technology Department or Inspection board or internal audit department. The land management system in Bangladesh still largely conventional and old-fashioned, marked by inefficiencies and a lack of implementation of modern policies (Masum, 2017; Raihan et al., 2024). Efforts to better management of land sector are ongoing, but insufficient progress due to entrenched interests and institutional complexities (Raihan et al., 2024).

However, the land administration system in Türkiye is characterised by a structured approach involving planning, cadastre, and real estate valuation, supported by digitalization efforts (Sürmeneli, 2024; Ercan, 2024). The country is following a centralised administration system through General Directorate of Land Registry and Cadastre (GDLRC) (*Tapu ve Kadastro Genel Müdürlüğü*- TKGM) under the Ministry of Environment, Urbanisation and Climate Change so that they can plan, execute and ensure the renewal and updating cadastral work of immovable property as well as to create land register, ensuring the archiving and protection, mapping, to determine production standards and to ensure archiving (GDLRC, 2010). The GDLRC is the main government body of land registry and cadastre. Land registry and cadastre are managed and carried out by one organisation i.e., centralised management. There are 1,101 Units in the Central and Provincial Organization with 19,404 staff. Around 9 million transactions are happening per year. It approximately served 25 million citizens and the annual revenue is around 2 billion USD (Adlı, 2019). There were no provisions of the notary system in the past but from 2023 Notary Public could also receive the applications.. As part of the changing and developing conditions, it has transformed the Research Planning and Coordination Department into the Information Technologies Department, and it strengthened its organisational structure by establishing the Land Valuation Department in 2019.

### 3.3. Government Intervention: A Shift from Manual to Digital Land Administration and Planning

The human interaction on land in Bangladesh and Türkiye is very high. Digitalisation reduces human interaction, so it represents itself as a tool for successive development of a country. However, proper digital transformation requires a holistic approach. As it should incorporate all relevant stakeholders and align with national policy agendas (FAO, UNECE and FIG, 2022). Both Bangladesh and Türkiye are practising digital land management to reduce the harassment, delays, complexities, and other related problems as well as ensure proper governance and planning of land related activities. In this study, digital shifts have focused on new digital practices or movements that are staying on the innovation and ensuring proper land administration.

#### 3.3.1. Bangladesh Case

The Bangladesh government now is transitioning from a paper-based system to a cloud-based multi-channel approach, focusing on user-friendly web and mobile applications to streamline land administration and reduce fraud (Pereira et al., 2018; Talukder et al., 2014). In this connection, the government of Bangladesh approved a Tk 3.37 billion (397,895,144 USD) project in 2020 to prepare a digital database for ensuring a transparent land administration system in the country. The Law Commission of Bangladesh has published a draft legislation called 'Bangladesh Land Act 2020' with an aim to bring uniformity in land management and land administration in Bangladesh. Major reforms focus on computerization of land records, simplification of land transactions and land registration etc. as land registration is considered as a revenue generator as it applies various fees, charges during its transactions to make the process more transparent. In 2021, the government has adopted the 'Land Crime Prevention and Redress Act, 2023' was enacted to prevent land fraud and miscellaneous crimes relating to illegal possession and title of land. The previous laws on land reforms and land development tax reformulated as the Land Reforms Act, 2023 and the Land Development Tax Act, 2023 to delineate the provisions on land ceiling, banning anonymous transactions; distribution of government lands for landless, sharecropping and taxes. Government has also adopted 'Land Use Act 2021' to ensure planned use of land. These laws will help to protect agricultural land/farmland, ensure food security, and reduce the



negative impacts of climate change. Again, the Land Development Tax Act, 2023 will help to provide free online land rent for harassment where citizens can be able to pay directly with a National Identity Card.

Through the inclusion of four pillars (Smart Citizen, Smart Society, Smart Economy, and Smart Governance), the government hopes to fully automate the land management system in the country and deliver land services to residents' doorsteps as part of Smart Bangladesh Vision-2041. The government of Bangladesh is implementing several initiatives like Smart Land Map, Smart Land Records, Smart Land Pedia, Smart Land Service Center, and Modern Land Offices at 400 upazilas nationwide.

As part of the digitalization move, the Bangladesh government established a task force to digitize the land registry and management sector in 2008. The Sheikh Hasina government of Bangladesh started digitization of land services in 2009. A thorough concept paper was prepared in 2016, and the digitalization was initiated in stages under different projects both centrally and locally at district and upazila (sub-district) level. In 2018, the Ministry of Lands introduced an *e-Namzari (e-mutation)* system. The outline for digitising the land service was prepared in 2021, and as a result the digitization of the entire land service (*Bhoomiseba*) system and administration started centrally. The land services digitization program involves more than just switching to an electronic system and maintaining the manual service delivery process. The Ministry of Land began action to finish the first phase of the process of continuing the sustainable reform of the asymmetric land service system by 2026 that dates back hundreds of years. In 2020 the government of Bangladesh started to prepare a digital database for the country. In June 2024, the Ministry of Land started using government funds exclusively to carry out the plot-based and *mouza*<sup>1</sup>-based nationwide digital land zoning project. In total 64 districts across the nation, the project will encompass around 56,348 mouzas under 4,562 unions of 493 upazilas (Khan, 2020). It indeed needs to be used judiciously and the management system of Bangladesh's land should be maintained in a planned way. On March 9, 2022, The Ministry of Land released a tender for 'Land Management Automation Project' and 'Capacity Development of Land Records and Surveys to Perform Digital Survey Project' in 2021.

When a piece of land is bought, sold, or transferred, the *Khotian*<sup>2</sup> or Pamphlet is one of the most crucial documents proving ownership. It is getting harder to keep the records in the record rooms because they are so old and worn out. The existing records are so feeble that they cannot be captured or tricked, especially given the age of the Cadastral Survey (CS) records, which is causing harm to them (Khan, 2020).

In 2020, the government launched the Digital Land Records (*e-Porcha*) system; nearly 4.5 crore ledgers have been digitalised. Therefore, citizens can now access and retrieve their land records online, provided they have paid the required fees, from any location in the world (Khan, 2020).

In the past, land tenure security is often undermined by complex registration systems in Bangladesh, which could lead to disputes and hinder agricultural productivity. The present land record digitization process follows a decentralised system where digitalisation will be available in three nodal offices: land registration, Assistant Commissioner of land and Deputy Commissioner of districts. This will ensure easy access of data and quicker disposal of land disputes. Plot wise of this digitalisation with clear and accurate records will provide an efficient and transparent result for ownership authentication or inheritance including all previous transactions. The government also inaugurated the Second Generation Khotian Continuity Chain/Tree System. This *Khotian* tree has been added to the Porcha system with the aim of saving digital information of all surveys, adding history of all surveys in one *Khotian*, determining real ownership by settling cases in a short time. It has been predicted that human suffering will be decreased by connecting e-Mutation with national e-Registration, consequently, there will be decreased lawsuits and forgeries.

With the aim of enriching citizens with land information, the Ministry of Land has launched artificial intelligence, so called *land-pedia*. Citizens will be able to get all types of legal information and advice related to land from this single digital platform. The main objective of artificial intelligence i.e., *Bhumi*

---

<sup>1</sup> It is a map is used to maintain the record of land measurement.

<sup>2</sup> It is an accounting journal as a physical object, or a record in which commercial accounts are recorded.

*Pedia* (In English: *Land pedia*) is to establish a strong 'knowledge network' by bridging the knowledge gap between land service providers and land service aspirants. From this platform, citizens will get answers and suggestions for all questions related to land by typing the keyword voyage. It also has a chatbot facility with artificial intelligence. This system will gradually become a virtual advisor by constantly extracting knowledge from various media. *Bhumi Pedia* will have a blog and forum facility, one can find solutions from one another to solve land related problems.

In future the *Bhoomiseba* policy will be governed by 60-30-10 principle i.e., 60% citizens of the land services by digital mode, 30% by professional agent and remaining 10% from land offices directly. The main goal of the government is to ensure that most of the land services are done at home, including bringing down border disputes, land robbery to zero through automation software for land management, i.e. no one needs to come to the land office.

### 3.3.2. Türkiye Case

Over the last two decades, Türkiye is improving the efficiency and accuracy of land registry and administration processes. As of April 20, 2024 in Türkiye, it has calculated that the total number of cadastral parcels is 58,245,747 and approximately 21.8 million individual units are available (GDLRC, 2024). Around 11,087,897 cadastral parcels were produced within 3 years (Ercan, 2020). Generally, the accuracy and consistency are very challenging in cadastral maps, including various errors in digitalisation and registry process (Meral and Ahsan, 2021). Outdated maps in many localities' do not correspond with the exact parcel areas or location is a serious issue. The GDLRC performed a two ways approach: Applying new technologies in areas where there were no cadastral works and renewing problematic or graphic or outdated cadastral parcels. Since 2005, land registry activities have been carried out in the computer environment through the Land Registry and Cadastre Information System (*Tapu ve Kadastro Bilgi Sistemi-TAKBİS*). The primary and auxiliary registers that constitute the land register are managed through this TAKBİS system. It is one of the most significant and fundamental e-government initiatives that aims to ensure inquiry based on spatial data maps and transfer various property information to computers nationwide (GDLRC, 2024). It analyses within the logic of GIS and LIS to determine problems and find solutions including Land registry and cadastre modernization project (TKMP) (GDLRC, 2024). The GDLRC has built Continuously Operating Reference Stations (CORS-TR), completed rural area cadastre throughout the country, renewed rural cadastre for about 14 million of 23 million parcels (Ercan, 2023), started 3D map production projects, and cooperated with the General Directorate of Forestry for establishing forest cadastre and supported the establishment of forest cadre. The Cadastral data were digitised and presented to the use of citizens and companies through the Spatial Property System (Mekânsal Gayrimenkul Sistemi - MEGSİS) using the parcel query mobile application for informative purposes without taking legal responsibility. The GDLRC has become a data provider in terms of providing registry and cadastral data. Figure 1 shows the Integrated Information System of cadastral system in Türkiye. It is calculated that if the GDLRC continued to make cadastre using traditional methods; it would need around 31.5 years to release the entire country cadastre instead of 3 years (Ercan, 2020).

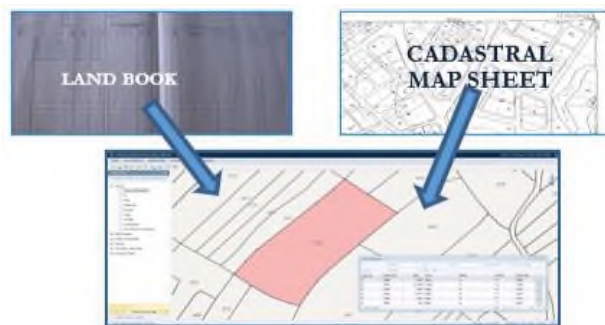


**Figure 1.** Integrated Land Information System of Türkiye

The cadastral data were digitised and presented to the parcel query mobile application for informative purposes without taking legal responsibility. The GDLRC has become a data provider in terms of providing registry and cadastral data. The GDLRC have transformed to an electronic system and deliver the following electronic transactions: E- taxes, duties and charges (*E-Tahsilat*), E-Appointment (*E-Randevu*), E- announcement (*E-İlan*), Digital Archive (*E-Arşiv*), E- Seizer (*E-Haciz*), E-Cancellation (*E-Terkin*), E-mortgage (*E-İpotek*), WEB land registry (*Web Tapu*), Application Query (*Başvuru Sorgu*), Parcel Query (*Parsel Sorgu*), Clearing room (*Tapu Takas*), Digital Land Registry Archive System (*Tapu Arşiv Bilgi Sistemi-TARBİS*), Land Registry and Cadastre Information System (*Tapu ve Kadastro Bilgi Sistemi-TAKBİS*), Spatial Property System (*Mekânsal Gayrimenkul Sistemi-MEGSİS*). The 3D city models and cadastre projects were planned in 2019 to lasted three years aiming to create 3D models of individual units (apartments) in buildings and provide visual representations of these individual units with legal information. Turkish National Permanent GNSS Network- Active (*Türkiye Ulusal Sabit GPS Ağı – Aktif* or *TUSAGA-Aktif*), started to establish in 2006 and fully operational since 2009. It has 158 stations entire country and provides cm-level accuracy position information in real time with Real-time kinematic positioning (RTK) GPS (Global Positioning System) network, its datum transformation between ED50-ITRFxx, it has no GCP needed for surveying and cadastral works. In Türkiye, it saves around \$50 million USD annually, which translates to a 30% reduction in all surveying and GIS projects (Ercan, 2019; Olmez, 2009).

Through these electronic systems the data offered by GDLRC in the first half of 2017 can be analysed with statistic given below;

- i. 65,540,247 WMS inquiries in average per month,
- ii. 4,336,810 WFS inquiries in average per month,
- iii. 4,006,553 inquiries in average per month over e-government,
- iv. 30,858,447 inquiries on average per month over the parcel inquiry application by national and international users. (Ercan, 2020)

There are over 21.8 million registered individual units, and in 2019, municipalities received 100,000 OP applications annually for new buildings (GDLRC, 2020).

### 3.3.3. Comparison between two countries

In the past, land management experiences included broker violence, document forgeries, and traditional analog service methods in the land offices of Bangladesh. Despite ongoing digitization efforts, there are still a lot of gaps in governance and loopholes in countries' various land administration sectors (Akter, 2022; TIB, 2015). Additionally, all of these tasks and sectors face many administrative and governmental obstacles. However, Türkiye's ongoing digitization efforts reduces gaps in governance challenges and loopholes in the country (World Bank, 2020).

Türkiye has also experienced lack of governance due to its traditional analog service methods in the past (Hülya & Ahsan, 2021). The land-man ratio, farmland etc. are decreasing, and therefore the government's movement to fully digitise the system will ensure opportunities for development of the country. The Government of Bangladesh also started the digitalisation process around a decade before, but the government started employing digital technology in various aspects of land services such as online *Khotian* collection, inheritance calculators and online databases just a few years before. To counter this, Türkiye already has reached a certain level of digitalisation by maintaining institutional framework and resource mobilisation properly. Reviewing both countries, it has found that both countries have taken numbers of digitalised or web-based actions where the Turkish government's effort is much more comprehensive by following a number of digitalised applications. The following table 5 shows the digitalisation activities in both countries.

**Table 5.** Digitalisation activities on land management in Bangladesh and Türkiye

Türkiye	Bangladesh
E-state	Land service ( <i>Bhumi seba</i> ), Mobile app
E- taxes, duties and charges	Online Land development tax
E-Appointment	E-Appointment
E- Announcement	-
E- Seizer	-
E-Cancellation	-
E-mortgage	-
WEB land registry	<i>Bhoomi seba</i>
Application Query	
Parcel Query	E- <i>Khotian (porcha)</i>
Clearing room	-
Digital Land Registry Archive System	E-mutation (naming), Digital Record Room Online Hearing
Land Registry and Cadastre Information System	E-mutation (naming), Digital Record Room
Spatial Property System	-
The 3D city models and cadastre projects	-
Turkish National Permanent GNSS Network- Active	-
Service can be received by SMS/hotline service	Service can be received by SMS/e-mail/hotline

Türkiye is making successive progress on land registry and cadastre systems over the recent years. Türkiye now consider one of the best practises land management and administrative countries (World Bank, 2020). It is making significant contribution on digitised land administration system at international level, including integrating its national standards with international standards. For instance, its National Geographic Information System, so called TUCBS, an e-government project where geographic data themes are compatible with International Organization for Standardization Open Geospatial Consortium (OGC) and Infrastructure for Spatial Information in the European Community (INSPIRE) (Gürsoy Sürmeneli and Alkan, 2021). It has been standardised to implement the semantic interoperability of national geographic data effectively.

The following Table 5 shows the state of land administration performance in Türkiye, Bangladesh and OECD countries covering different indicators highlighted by doing business report of World Bank.

**Table 5.** Land administration performance in Türkiye and Bangladesh

Indicator	Türkiye	Europe & Central Asia	OECD High Income	Best Regulatory Performance	Bangladesh (World Bank 2019)
Procedures (number)	6	5.5	4.7	1(5 Economies)	Not Available (-)
Time (days)	4.5	20.8	23.6	1(2 Economies)	270.8
Cost (% of property value)	3.0	2.7	4.2	0.0(Saudi Arabia)	7.2
Quality of land administration index (0-30)	27.0	20.4	23.2	None in 2018/19	6.5
Reliability of infrastructure index(0-8)	8.0	-	-	-	-
Transparency of information index (0–6)	4.0	-	-	-	-
Geographic coverage index (0–8)	8.0	-	-	-	-
Land dispute resolution index (0–8)	7.0	-	-	-	-
Equal access to property rights index (-2–0)	0.0	-	-	-	-

Note: The rankings for all economies are benchmarked to May 2019. The World Bank discontinued publishing the Doing Business report from 2021.

Source: World Bank, 2020, World Bank, 2019

According to World Bank's Doing Business 2020 Report, the Quality of land administration index<sup>3</sup> (0-30) ranked 27, scoring 81.6 (World Bank 2020), represents that Türkiye is following effective approaches

<sup>3</sup> The quality of the land administration index is measured by considering the reliability of infrastructure, transparency of information, geographic coverage, land dispute resolution, and equal access to property rights (World Bank, 2020).

in registering property. Reliability of infrastructure index (0-8), Türkiye scored 8.0; Transparency of information index (0-6) scored 4.0; Geographic coverage index (0-8) scored 8.0; Land dispute resolution index (0-8) scored 7.0; Even by comparison with OECD countries Türkiye stood 4th in sharing property data following United States, Sweden and Denmark. Türkiye reduced the cost of property registration temporarily by lowering the mortar charges associated with property transfers, and also expedited the process by shortening the time required to receive a tax assessment. However, as per World Bank's Doing Business 2019 Report, the Quality of land administration index (0-30), Bangladesh scored only 6.5. again, in terms of score for registering property (0-100) Bangladesh scored only 28.91 and ranked 183 which is very low. Though Bangladesh government has introduced Grievance Redress System (GRS) system aiming to address the challenges of corruption, lack of accountability, and poor service delivery. The government wants to make hassle free services and expected to make the Automated Land Administration and Management System (ALAMS) Program 2022-2026 functional by 2026 though the project was originally scheduled to complete by 2025. With the goal of increasing land ownership transparency, the government initiated around 102 million USD project introduced the Digital Land Surveying System (DLSS). Unfortunately, the projects' current progress is unsatisfactory; three and a half years after 2020, the project's progress is still only 0.28%, which has led the authorities to consider abandoning it midway through (dhakatribune.com). The dismal performance raises concerns about weaknesses in planning of the project, which was undertaken without a feasibility study. Again, a severe shortage of human resources in the Department of Land Record and Survey is one of the major causes behind these (dhakatribune.com). In addition, the Planning Commission officials also stated that under the project, the target was to install 260,369 geodetic control pillars in 470 upazilas across 61 districts whereas Türkiye is following Turkish National Permanent GNSS Network- Active which provides cm-level accuracy position information in real time with RTK GPS network.

#### 4. CONCLUSION AND RECOMMENDATIONS

The world has been changing at a speedy rate, and technology has been leading the digital transformation. Digitalization now has already deeply affected all aspects of social, economic and business life, and new spatial technologies have been becoming a part and parcel in our daily lives. The land administration practices in Bangladesh and Türkiye exhibit significant differences, influenced by the integration of digital technologies. Türkiye has made strides in adopting modern digital solutions that enhance efficiency and transparency in land administration. However, Bangladesh struggles with an outdated and inefficient land management system, with many loopholes and managerial deficits in different sectors of land governance.

As more than 70% of the SDG's targets are related to geospatial technologies and land administration, thus, it is not possible to achieve land related SDG goals unless issues related to land ownership, use, value and development are resolved on the common ground of a Spatial Data Infrastructure (SDI) and its proper planning and management. Bangladesh is now achieving progress in land and cadastre systems whereas Türkiye is making progressive success on digitalised land registry and cadastre systems without delaying any steps of digitalisation or automation system. The following recommendations have been proposed in this study:

##### i. Centralised management

The land administration system in Bangladesh still mostly paper-based though government planned to govern by 60-30-10 principle i.e., 60% citizens of *Bhoomiseva* will be able to receive services by themselves through digital mode. For 30% of land service, citizens will take the help of a professional agent by paying a fixed fee. And in case of 10% land service only citizens will go to land office (Sultana, 2023). But in practice, it seems challenging due to lack of infrastructure and decentralised management. Again, land records are kept in different offices, which create duplication and a lack of coherence. On the other hand, GDLRC in Türkiye under the Ministry of Public Works and Settlement is the central organisation plays a comprehensive role in land management, registry, cadastre and survey. The Bangladesh government could manage its land management, record and services activities through a

single organisation like GDLRC to remove loopholes and governance problems and make a better economic contribution for the country. These centralised land management could provide a strong structure within an organisation. It can develop a uniform information-sharing procedure, can increase efficiency, reduce costs, and make property management easier than ever.

ii. From paperwork to robust digitalisation movement

The digital transformation of land, i.e., integration of spatial data, data analytics, and real-time operations all are highly needed for the advancement of a country. Its data-driven approach also increase administrative performance in different aspects related to transactions, customer interactions, maintenance and so on. Türkiye started its TAKBIS project in 2002 but it could finish in 2012, exhibits a decade required for the project The progress of Bangladesh is not satisfactory so it needs to expedite land registry and cadastre to complete the digitalisation process otherwise it may take decades of time. Again, every land office or cadastre office must ensure efficient digital infrastructure with utilisation of ICT tools properly.

iii. User friendly one stop service

Integrated management is required for the quick and user friendly one stop service. It will enhance service delivery quickly, improve transparency and good governance. Though the Bangladesh government has launched a hotline service (call no.16122) but it requires an active and proper implementation. Bangladesh Government has prepared Citizen Charter for every ministry and its departments/directorates to ensure an efficient, effective and high-quality service which is fruitful for Türkiye also. However, there needs to be an effective Monitoring and Evaluation system.

iv. Planned judiciary and management system

The management of land, digitalisation is very challenging as it requires robust land governance and modern technology-based practices to solve the problems. The Bangladesh government has adopted an act on land crime prevention and redress but there needs proper implementation. Türkiye is also tackling governance challenges though the e-government system is providing benefits to the citizens, but it also requires a robust governance system.

v. Capacity building project

It has been identified that the digital land administration system is not performing well in Bangladesh due to lack of skilled human capital. Therefore, the government should ensure qualified personnel by recruiting or by increasing qualification of the existing personnel by providing adequate training programs. In this respect, the government should organise capacity building programs/projects to the existing personnel. Though *Bhumi Seba* digitization activities are taking place, still many practices are needed.

vi. Alternative projects

Serious or immediate attention can be taken to the need for alternative strategies which will promote efficiency in land management. For instance, the government is targeting to install 260,369 geodetic control pillars in 470 upazilas across the country. But in Türkiye, Turkish National Permanent GNSS Network-Active has reduced time and money that could be an alternative project for Bangladesh.

Both countries need new disruptive based technology-based projects on Artificial Intelligence, Blockchain, Internet of Things, Big Data, Cloud Computing, Visual Reality and Augmented Reality in order to ensure more effective services in land administration, management and planning for the future.

Finally, it can be stated that the land surveying and cadastre, land record with best-practised countries' experience like Türkiye is beneficial for the improvement of land administration like Bangladesh.

Again, it can be stated here that this study has proposed some future research:

- One of the key components of the Turkish success story of land administration is private sector involvement. Considering the extent of the study, private sector issues have not focused on this study which could be performed in further research.
- Further research could answer the efficiency and effectiveness of land registry and cadastre services and digitalisation performance in both countries.
- As both countries have a long history of land laws and policies from ancient periods therefore

analysing past experience could provide a glimpse of land management and administration practices.

### Declaration of Ethical Standards

Author declares that this study is completely original by adhering to all ethical rules including authorship, citation, and data reporting.

### Declaration of Competing Interest

Author declares that there is no conflict of interest.

### Funding/Acknowledgements

Author received no financial support for the research.

### REFERENCES





- [1] M. Z. Adli, Land Administration in Türkiye. Accessed: 1 October 2023. [Online]. Available: <https://www.clge.eu/wp-content/uploads/2019/04/clge-istanbul-2019-EN.pdf>
- [2] M.M. Ahsan, and M.H. Rahman, "Environmental Impact of Rapid Urban Growth in Dhaka Megacity: A Case Study of Bhatara Union". In *Dhaka Metropolitan Development Area and Its Planning Problems, Issues and Policies*, Sarwar Jahan & A K M Abul Kalam. Bangladesh Institute of Planners, pp. 99-109.
- [3] M.M Ahsan, Environmentally Induced Migration on Selected Coastal Areas in Bangladesh and United States of America, Department of Political Sciences and Public Administration, Ankara University, Ankara, Türkiye.
- [4] M.M. Ahsan, "Urban Governance in Turkish Global Competitive Cities: A Study on Right to the City Perspective", *Journal of Civilization Studies*, vol. 7, no. 2, pp.14-27. 2022. DOI: 10.52539/mad.1161732
- [5] M. Akter, "Digitalization in the Land Service Delivery: Comparison between Bangladesh and Indonesia", *Southeast Asia: A Multidisciplinary Journal*, vol. 22 No. 1, pp.79-91. 2022. <https://doi.org/10.1108/SEAMJ-01-2022-B1006>
- [6] BBS- Bangladesh Bureau of Statistics. Population and Housing Census 202, National report Vol. 1. [https://bbs.portal.gov.bd/sites/default/files/files/bbs.portal.gov.bd/page/b343a8b4\\_956b\\_45ca\\_872f\\_4cf9b2f1a6e0/2024-01-31-15-51-b53c55dd692233ae401ba013060b9cbb.pdf](https://bbs.portal.gov.bd/sites/default/files/files/bbs.portal.gov.bd/page/b343a8b4_956b_45ca_872f_4cf9b2f1a6e0/2024-01-31-15-51-b53c55dd692233ae401ba013060b9cbb.pdf)
- [7] A. Barkat, and P. Roy, "Political Economy of Land Litigation in Bangladesh: A Case of Colossal National Wastage." Dhaka: ALRD & Nijera Kori, 2004.
- [8] Department of Laws and Resolutions, Constitution of the Republic of Türkiye. Available: [https://www5.tbmm.gov.tr/yayinlar/2021/TC\\_Anayasasi\\_ve\\_TBMM\\_Ic\\_Tuzugu\\_Ingilizce.pdf](https://www5.tbmm.gov.tr/yayinlar/2021/TC_Anayasasi_ve_TBMM_Ic_Tuzugu_Ingilizce.pdf), 2019.
- [9] EC – European Commission., *Screening report Türkiye. Chapter 11 – Agriculture and Rural Development*. Available: [http://ec.europa.eu/agriculture/enlargement/countries/Türkiye/index\\_en.htm](http://ec.europa.eu/agriculture/enlargement/countries/Türkiye/index_en.htm) (2008-08-04), 2006.
- [10] O. Ercan, "Improvement of Current Cadastral System and Recent Developments in Türkiye". [PowerPoint slides]. Accessed: 5 February 2024. [Online]. Available: [http://fig.netwww.fig.net/resources/proceedings/2019/08\\_com7/0808\\_1\\_Türkiye.pdf](http://fig.netwww.fig.net/resources/proceedings/2019/08_com7/0808_1_Türkiye.pdf), 2019
- [11] O. Ercan, "A closer look at Turkish cadastre and its successful completion", *Land Use Policy*, vol. 110. 2020.
- [12] O. Ercan, "Land Management Paradigm: Global Agenda and the Case in Türkiye", *Konya Journal of Engineering Sciences*, vol.10, no.3, pp.793–806. 2022. doi: 10.36306/konjes.1143000.

- [13] O. Ercan, "Agricultural land-based functional model for effective rural land management in Türkiye", *Journal of Agricultural Sciences*, 2024.
- [14] O. Ercan, "Evolution of the cadastre renewal understanding in Türkiye: A fit-for-purpose renewal model proposal", *Land Use Policy*, vol. 131., 2023.
- [15] GED- General Economics Division., Eighth Five Year Plan (July 2020-June 2025). Accessed: 17 August 2022. [online]. Available: <https://oldweb.lged.gov.bd/UploadedDocument/UnitPublication/1/1166/8FYP.pdf>.
- [16] GDLRC- General Directorate of Land Registry and Survey, Law on Organisation and Duties of the Directorate General of Land and Cadastre. 2010. <https://www.tkgm.gov.tr/node/4231> [Accessed: 1 March 2019].
- [17] GDLRC., *Annual Report*. Accessed: 13 April 2020. [online]. Available: [https://www.tkgm.gov.tr/sites/default/files/icerik\\_ekleri/btdb\\_2019\\_faliyet\\_raporu\\_0.pdf](https://www.tkgm.gov.tr/sites/default/files/icerik_ekleri/btdb_2019_faliyet_raporu_0.pdf). 2019.
- [18] GDLRC., Land Registry and Cadastre Information System (TAKBIS), Accessed: 20 April 2024. [Online]. Available: <https://www.tkgm.gov.tr/en/land-registry-and-cadastre-information-system-takbis> 2024.
- [19] C. Heider, and A. Connelly, Why Land Administration Matters for Development. Available: <https://ieg.worldbankgroup.org/blog/why-land-administration-matters-development>, 2016
- [20] M. Hülya and M.M. Ahsan. "Share Errors of Land Registry in Türkiye". *Turkish Journal of Land Management*, Vol. 3, No. 2, pp.66-78.
- [21] S. Khan, Digital land management on the cards. The Financial Express. October 30, 2020. Available: <https://thefinancialexpress.com.bd/views/digital-land-management-on-the-cards-1601738172>.
- [22] Landbrugsrådet., Agriculture in Denmark: Facts and Figures 2008. Danish Agriculture and Danish Agricultural Council. 2008.
- [23] S. Mahalaya, Impact evaluation of agriculture research in Papua, Indonesia using the sustainable livelihood framework. Doctoral dissertation, The University of Adelaide, Australia.
- [24] S.M. Mahmood and M.M. Ahsan, Involuntary Relocation Process of Local People due to Private Land Development Projects: A Study of Eastern Fringe Area of Dhaka City. In *ISBS 2019* Arzuhan Gültekin (Ed.), pp.337-348. London: IntechOpen. DOI: 10.5772/intechopen.87812
- [25] F. Masum, "Rural land management in Bangladesh: problems and prospects", *Geomatics, Land management and Landscape*, Vol. 4, pp. 79–93, 2017.
- [26] Mol-Ministry of Land., An Overview of Present Land Administration and Management in Bangladesh. Accessed: 1 November 2023. Available: <http://minland.gov.bd/site/page/6d032730-5948-4022-91a4-da20d2caa520/এক-নজরে-বর্তমান-ভূমি-প্রশাসন-ও-ব্যবস্থাপনা>, 2023.
- [27] Ministry of Law, Justice and Parliamentary Affairs, The Constitution of the People's Republic of Bangladesh. Accessed: 26 March 2023, <http://bdlaws.minlaw.gov.bd/act-367/section-24590.html#:~:text=Rights%20to%20property-,42.,save%20by%20authority%20of%20law>, 2019.
- [28] M. Moniruzzaman, "Digitizing Land Administration and Standards in Bangladesh". [PowerPoint slides]. Accessed: 12 November 2023. Available: [https://geospatialworldforum.org/speaker/presentations2022/land-administration/Digitizing-and-administration-and-standards-in-bangladesh-Mohd\\_Moniruzzaman.pdf](https://geospatialworldforum.org/speaker/presentations2022/land-administration/Digitizing-and-administration-and-standards-in-bangladesh-Mohd_Moniruzzaman.pdf), 2022.
- [29] OGM-Orman Genel Mudurluğu., 2020 Türkiye Orman Varlığı. Accessed: 1 November 2023. <https://www.ogm.gov.tr/tr/ormanlarimiz-sitesi/TurkiyeOrmanVarligi/Yayinlar/2020%20T%C3%BCrkiye%20Orman%20Varl%C4%B1%C4%9F%C4%B1.pdf>
- [30] A. Olmez, Turkish national spatial data infrastructure project & related projects. Accessed: 12 November 2023. <https://www.unoosa.org/documents/pdf/psa/activities/2009/azerbaijan/presentations/34.pdf>, 2009
- [31] S. Raihan, M. J.E. Jalal, E. Sharmin and M. A., Eusuf, *Chapter 9: Institutional challenges in land administration and management in Bangladesh*. Accessed: 8 June, 2022. Available:



- [https://edi.opml.co.uk/wpcms/wp-content/uploads/2020/05/09-Land\\_21052020-edited-v2.pdf](https://edi.opml.co.uk/wpcms/wp-content/uploads/2020/05/09-Land_21052020-edited-v2.pdf). 2020.
- [32] R. Sultana, Smart Land Services. Accessed: 1 April 2024, Available: [https://pressinform.portal.gov.bd/sites/default/files/files/pressinform.portal.gov.bd/page/50aa82ee\\_7a92\\_4aa7\\_817b\\_bb323c098833/2024-02-29-03-37-21fe8f67b0e8e9db041d99b618745278.pdf](https://pressinform.portal.gov.bd/sites/default/files/files/pressinform.portal.gov.bd/page/50aa82ee_7a92_4aa7_817b_bb323c098833/2024-02-29-03-37-21fe8f67b0e8e9db041d99b618745278.pdf), 2024.
- [33] TIB- Transparency International Bangladesh., Land Management and Services in Bangladesh: Governance Challenges and Way-forward. TIB, Dhaka, Bangladesh. 2015
- [34] R. D. Tirumala and P. Tiwari, "Importance of Land in SDG Policy Instruments: A Study of ASEAN Developing Countries", *Land*, vol. 11 no.2, 2022. <https://doi.org/10.3390/land11020218>
- [35] TURKSTAT- Türkiye Statistical Institution, Adrese Dayalı Nüfus Kayıt Sistemi Sonuçları, Accessed 1 June, 2023, <https://data.tuik.gov.tr/Bulten/Index?p=49685>, 2022
- [36] A.M. Uisso, Y., Tanrıvermiş, M. M. Ahsan, and H. Tanrıvermiş, Revisiting land distribution policies among land-based sectors in Tanzania, *African Journal on Land Policy and Geospatial Sciences*, vol. 5, no.4, pp. 735-752, 2022. DOI: <https://doi.org/10.48346/IMIST.PRSM/ajlp-gs.v5i4.33875>.
- [37] UN- United Nations. *SDG indicator metadata*. Accessed: 6 June 2020. Available: <https://unstats.un.org/sdgs/metadata/files/Metadata-01-04-02.pdf>, 2020.
- [38] World Bank. *Doing Business 2019*. Accessed: 16 May 2021, Available: [https://www.worldbank.org/content/dam/doingBusiness/media/Annual-Reports/English/DB2019-report\\_web-version.pdf](https://www.worldbank.org/content/dam/doingBusiness/media/Annual-Reports/English/DB2019-report_web-version.pdf). 2019.
- [39] World Bank. *Ease of Doing Business in Türkiye*, Accessed: 16 May 2021, Available: [https://www.doingbusiness.org/en/data/exploreconomies/Türkiye#DB\\_rp](https://www.doingbusiness.org/en/data/exploreconomies/Türkiye#DB_rp), 2020.
- [40] World Bank, *Arable land (hectares per person)*. Accessed: 2 April 2024. Available: <https://data.worldbank.org/indicator/AG.LND.ARBL.HA.PC?locations=TR>, 2024a.
- [41] World Bank, *Agricultural land (% of land area)*, Accessed: 2 April 2024, Available: <https://data.worldbank.org/indicator/AG.LND.ARBL.HA.PC?locations=TR>, 2024b.
- [42] World Bank, *World Development Indicators*, Accessed: 11 November 2024, Available: <https://databank.worldbank.org/reports.aspx?source=2&country=bgd>
- [43] H. G. Sürmeneli and M. Alkan, "Towards standardisation of Turkish cadastral system using LADM with 3D cadastre", *Survey Review*, 53, pp. 543–58. <https://doi.org/10.1080/00396265.2020.1855700>
- [44] H. G. Sürmeneli, "Comparative Performance Analysis of Türkiye's Land Management System Using SWOT Analysis Method", Vol. 7 No. 1, 7th International Conference of Contemporary Affairs in Architecture and Urbanism, 2024
- [45] M. Hülya and M M Ahsan. "Türkiye'de Tapu Sicilinde Hisse Hataları", *Türkiye Arazi Yönetimi Dergisi*, Vol. 3 issue. 2, pp. 66-78. 2021
- [46] FAO, UNECE and FIG. "Digital transformation and land administration – Sustainable practices from the UNECE region and beyond". FIG Publication No. 80. Rome. 88 pp. FAO, UNECE and FIG. <https://doi.org/10.4060/cc1908en>.

## ANALYZING THE IMPACT OF THE 2023 GENERAL ELECTIONS ON LAND PRICES USING MACHINE LEARNING: A CASE STUDY IN ÇANAKKALE, TURKEY

<sup>1</sup> Simge DOĞAN , <sup>2,\*</sup> Levent GENÇ , <sup>3</sup> Sait Can YÜCEBAŞ , <sup>4</sup> Şükran YALPIR 

<sup>1</sup> Çanakkale Onsekiz Mart University, Graduate School of Education, Real Estate Development Department, Computer Agriculture Environmental Planning, Çanakkale, TÜRKİYE

<sup>2</sup> Çanakkale Onsekiz Mart University, Architecture and Design Faculty, Urban and Regional Planning Department, Computer Agriculture Environmental Planning, Çanakkale, TÜRKİYE

<sup>3</sup> Çanakkale Onsekiz Mart University, Engineering Faculty, Computer Engineering Department, Çanakkale, TÜRKİYE

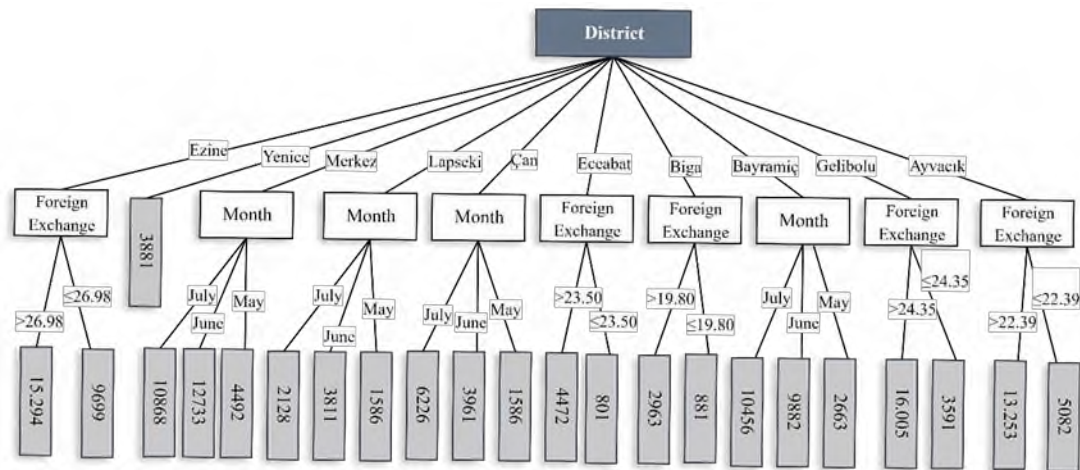
<sup>4</sup> Konya Technical University, Engineering and Natural Sciences Faculty, Geomatics Department, Konya, TÜRKİYE

<sup>1</sup> [simgedogan1988@gmail.com](mailto:simgedogan1988@gmail.com), <sup>2</sup> [leventgc@comu.edu.tr](mailto:leventgc@comu.edu.tr), <sup>3</sup> [can@comu.edu.tr](mailto:can@comu.edu.tr), <sup>4</sup> [syalpir@ktun.edu.tr](mailto:syalpir@ktun.edu.tr)

### Highlights





- This study analyses the impact of the 2023 Turkish elections on Çanakkale land prices.
- The 'Regression Tree' model, one of the machine learning models, is used to estimate land unit prices.
- Changes in foreign exchange and gold values during the election period affected land unit prices.
- According to the machine learning price prediction model, changes in exchange rates after the elections increased land unit prices.
- Regression trees show how district, gold and exchange rates affect prices.
- Regression tree model, one of the machine learning methods, performs better than linear regression in price prediction.

### Graphical Abstract





## ANALYZING THE IMPACT OF THE 2023 GENERAL ELECTIONS ON LAND PRICES USING MACHINE LEARNING: A CASE STUDY IN ÇANAKKALE, TURKEY

<sup>1</sup> Simge DOĞAN , <sup>2,\*</sup> Levent GENÇ , <sup>3</sup> Sait Can YÜCEBAŞ , <sup>4</sup> Şükran YALPIR 

<sup>1</sup> Çanakkale Onsekiz Mart University, Graduate School of Education, Real Estate Development Department, Computer Agriculture Environmental Planning, Çanakkale, TÜRKİYE

<sup>2</sup> Çanakkale Onsekiz Mart University, Architecture and Design Faculty, Urban and Regional Planning Department, Computer Agriculture Environmental Planning, Çanakkale, TÜRKİYE

<sup>3</sup> Çanakkale Onsekiz Mart University, Engineering Faculty, Computer Engineering Department, Çanakkale, TÜRKİYE

<sup>4</sup> Konya Technical University, Engineering and Natural Sciences Faculty, Geomatics Department, Konya, TÜRKİYE

<sup>1</sup> [simgedogan1988@gmail.com](mailto:simgedogan1988@gmail.com), <sup>2</sup> [leventgc@comu.edu.tr](mailto:leventgc@comu.edu.tr), <sup>3</sup> [can@comu.edu.tr](mailto:can@comu.edu.tr), <sup>4</sup> [syalpir@ktun.edu.tr](mailto:syalpir@ktun.edu.tr)

(Received: 05.11.2024; Accepted in Revised Form: 21.01.2025)

**ABSTRACT:** This study analyses the impact of the general elections to be held on 14 May 2023 on the real estate market in Turkey. The aim of the study is to develop a model to predict land unit prices (₺/m<sup>2</sup>) by analysing land prices, exchange rates and gold values observed before (February-March-April) and after (May-June-July) elections for Ayvacık, Bayramiç, Biga, Çan, Eceabat, Ezine, Gelibolu, Lapseki, Merkez and Yenice districts of Çanakkale province. Daily fluctuations in foreign exchange and gold values, which are the main economic parameters in the study, were recorded during the election period. The findings of this research, which predicts price movements in the property market using machine learning methods such as regression trees, reveal that unit prices of land generally tend to increase with increases in exchange rates, but in some districts where gold prices increase, the unit price shows a reverse trend. This is attributed to the fact that investors prefer gold as a safer asset in times of economic uncertainty. The results obtained can help investors and buyers to predict future trends in property prices, as well as contribute to the development of economic policies by experts to stabilise fluctuations in investment instruments.

**Keywords:** Election, Sustainability Land Price, Economic Parameters, Regression Tree, Machine Learning

### 1. INTRODUCTION

Real estates, which make a great contribution to the country's economy, are at the forefront of today's study topics. The type, characteristics and method searches of real estates are on the agenda of many different professional disciplines in the literature. In real estate valuation, methods and principles should be applied by taking into account current market values. Current market values are also important in sales or construction, mortgages and taxation. Real estate market values are shaped by supply and demand in free market conditions. For this reason, it is difficult to determine current market values. Different methods and techniques are used for this. These techniques have developed with the increase in artificial intelligence applications in today's conditions. Another element as effective as methods in estimating the value of real estates is the type of real estate and the factors (features) affecting its value according to its type. These features vary according to location or lifestyle. They are grouped according to the purpose of use as locational, local, physical, legal and structural [1]. In addition, affecting current market values; It is known that the existence of micro and macroeconomic variables, political events and current force majeure (unexpected sudden events such as earthquakes, disease outbreaks, etc.) also affect the real estate market.

The valuation approach should be expected to be in line with economic theory and to be prone to producing reliable predicts for transaction prices. The valuation process should be in line with economic

\*Corresponding Author: Levent GENÇ, [leventgc@comu.edu.tr](mailto:leventgc@comu.edu.tr)

theory and should produce values that are good predicts of observed transaction prices (market value). In general, the approaches used to predict real estate value (comparative, income and cost methods) are not sufficient to predict market value. Determining whether the real estate features affecting the value are actually effective or the degree of effect is one of the primary operations for a real estate valuation system to be created. In general, it has been observed that in the studies conducted in the literature, the local characteristics of real estate are addressed and used in the value predict model [2]. It has been determined that the studies conducted on economic and political effects are more limited. Therefore, the purpose of the article is designed to determine how real estates are affected by economic factors and political events using machine learning methods.

Elections, which are political events that are on the country's agenda and repeated at certain periods of time, play a crucial role in selecting administrators who represent diverse viewpoints within a community [3],[4]. These important decision-making events directly relate to social and economic dynamics and affect various sectors that impact the living conditions of the community. Economic uncertainties related to election processes can influence preferences and prices for real estate investments in developing countries, with noticeable variations in preferences for types of real estate such as housing, parcels, and land before and after elections. It has been observed that studies in the literature generally focus on the effect of changes in housing prices during election periods. It has been concluded that the effect of the election on the market values of houses is generally negative due to the uncertainty involved [5], [6], [7], [8]. In other words, it is understood that citizens are cautious for a management situation whose outcome can change at any time. In studies, it is generally seen that statistical methods (logistic regression, two-way fixed effects, Difference-Difference) are preferred in order to understand the correlation relationship in the pre-election and post-election market comparison [9], [5], [10], [11].

Aizenman [12], also examined the relationship between economic parameters and real estate prices in 20 international countries using a panel data regression model. They found that international economic indicators such as Gross Domestic Product (GDP), interest rates, inflation rates and exchange rates played a determinant role on real estate prices. In another study, the effects of macroeconomic variables on housing prices in Turkey for the period 1990-2006 were analyzed using Johansen Cointegration and Granger Causality Test. They found that house prices had a bidirectional causality with interest rates and exchange rates, while GDP had a unidirectional relationship with house prices [13]. Two studies conducted in South Africa and Lithuania showed that inflation, interest rates GDP and political risk have both short-term and long-term effects on housing prices. In South Africa, political risks were associated with a long-term decrease in housing prices, while high interest rates and inflation were associated with an increase in housing prices. In Lithuania, they concluded that inflation and interest rates do not affect housing prices, and GDP depends on housing prices [14],[15].

The effect of the exchange rate on the value of housing built in China, Japan and Taiwan has been examined [16], [17]. According to the studies, it has been concluded that the increase in housing prices led to a decrease in the exchange rate. When Komşuoğlu [18], analyzed the exchange rates and gold prices between 2013 and 2019 in Turkey with housing sales, it was determined that there was no causality between gold and exchange rates. In another study, it was found that housing prices interacted with exchange rates and caused price changes [19].

It is understood that the effect of exchange rates on housing prices is generally accepted. In the studies conducted, as the exchange rate increases, housing sales prices also increase [20], [21], [22],[23]. Unlike these methods, [24], investigated the effect of economic parameters on real estate investments in Kenya using the Arbitrage Pricing Theory (APT). Accordingly, they found that a one percent increase in the exchange rate led to a 1.995 percent decrease in real estate prices, while a 1 percent increase in inflation led to a 2.248 percent increase in housing prices.

There are many different methods to determine the effect of economic factors on the value of real estate. In recent years, with the developing technological applications, it is seen that machine learning techniques are used in the studies conducted on this subject in the literature. The results of the studies have concluded that machine learning techniques are effective in developing accurate prediction models

by analyzing large data sets [25], [26], [27], [28]. It is also predicted that the inclusion of such economic factors, especially exchange rates, in machine learning-based real estate price prediction models can increase predict accuracy and market predicts [29].

This study was conducted to examine the impact of political events on real estate values. The 2023 Turkish Presidential election was held on May 14, 2023. The changes in the purchase and sale values of lands were examined according to the expectations and economy of the country's administration that changed according to this date. According to the data of the Turkish Statistical Institute (TUIK), while the pre-election GDP increased by 4.0% compared to the same quarter of the previous year, it is seen that real estate activities had a share of 1.4% in this rate. After the election, the GDP increased by 3.8% compared to the same quarter of the previous year, and when the components constituting the GDP were taken into account, it was determined that real estate activities increased by 3.2% [30]. These values explain the uncertainty effect of the election on real estate values. It is understood that citizens are cautious about the changes that will occur in the administration, and therefore they are hesitant to enter into real estate purchase and sale.

There is also a strong relationship between exchange rates and GDP. The economic size of a country determines exchange rates by affecting the value of its currency in international markets. It is known that exchange rates fluctuate during election periods. It is thought that the increase in exchange rates due to these fluctuations may affect real estate prices. High exchange rates attract foreign investors, which causes an increase in demand and real estate prices in the real estate market. Depending on the economic structure and cultural perspective of the country before and after the election, economic indicators may cause excessive increases or decreases in land and housing prices as a result of imbalances in purchasing preferences.

Economic parameters often fluctuate, particularly as election periods approach. Addressing these fluctuations is crucial for creating resilient societies and economies, as emphasized by the 11th United Nations Sustainable Development Goal (UN-SDG). Election-induced hikes in land prices can undermine sustainable urban development. Notably, there have been no studies using machine learning decision tree algorithms to predict land prices before and after election periods. This study aims to develop a model for predicting land unit prices (₺/m<sup>2</sup>) by analyzing observed land prices, exchange rates, and gold values for the districts of Ayvacık, Bayramiç, Biga, Çan, Eceabat, Ezine, Gelibolu, Lapseki, Merkez, and Yenice in Çanakkale province, both before (February-March-April) and after (May-June-July) the elections. The goal is to predict future land prices during election periods, providing valuable insights for investors and buyers at both local and national levels.

## 2. MATERIAL AND METHODS

### 2.1. Study Area

Çanakkale province has witnessed significant changes in terms of economic and social dynamics. In particular, the opening of the 1915 Çanakkale Bridge to traffic on 18 March 2022 strengthened Çanakkale's transport infrastructure and made the region attractive for investors. This led to an increase in the demand for land for sale. In addition, fluctuations occurred in economic parameters across the country due to the general elections held in 2023. These fluctuations caused differences in the intensity of real estate purchases and sales and in the supply-demand balance of land stocks. Çanakkale offers an important area of investigation to analyse the effects of both the strategic importance it gained with the opening of the 1915 Çanakkale Bridge and the economic parameters during the election period on land prices.

The province of Çanakkale is situated in the northwestern region of Turkey, positioned at coordinates 40.073°N latitude and 26.6225°E longitude, and spans the two coastlines that separate the continents of Europe and Asia (Figure 1).

The surface area of the province is 9995 km<sup>2</sup>. Its neighboring provinces are Balıkesir, Tekirdağ and Edirne. The population is 559,383, and it is a province with 12 districts and 576 neighborhoods [31]. The districts of Çanakkale are Ayvacık, Bayramiç, Biga, Bozcaada, Çan, Eceabat, Ezine, Gelibolu, Gökçeada,

Lapseki, Merkez and Yenice. These districts, Biga has the largest surface area of 1,354 km<sup>2</sup>, while the district with the largest population is Merkez (Central) district [32].

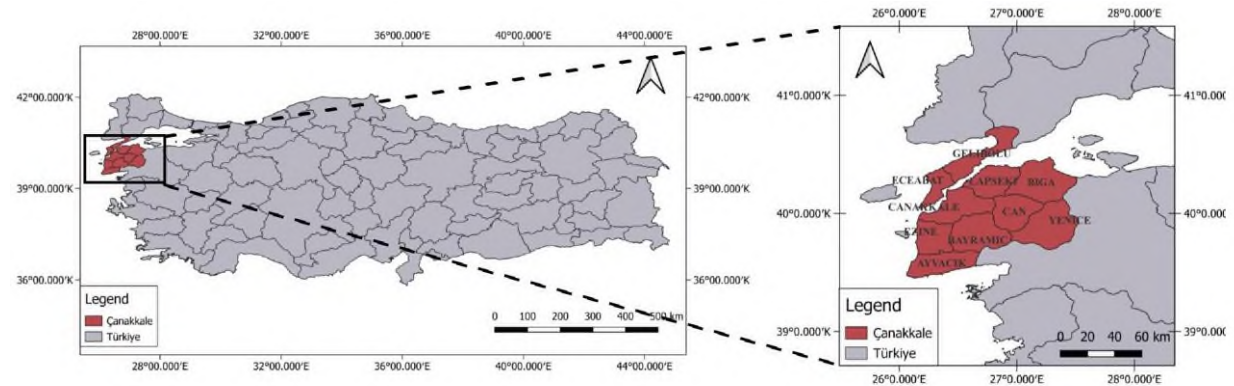


Figure 1. Location of the workspace.

## 2.2. Materials

To construct a price predicting model, data on land sales in various districts of Çanakkale (Ayvack, Bayramiç, Biga, Çan, Eceabat, Ezine, Gelibolu, Lapseki, Merkez and Yenice) excluding Bozcaada and Gökçeada were collected from the open access website [www.hepsiimlak.com](http://www.hepsiimlak.com) using a web scraper developed using the Python Scrapy library. The land data in these districts were created through two separate datasets: pre-election (February-March-April 2023) and post-election (May-June-July 2023). There were 474 land sales data in the pre-election dataset and 424 land sales data in the post-election dataset. Each land sale data had 7 variables. These variables and data types are given in Table 1.

Table 1. Variables and data types

Variables	Data Type
Unit Price (₺)	Numeric
Foreign Exchange Rate	Numeric
Gold	Numeric
Neighborhood	Categorical
Month	Categorical
District	Categorical
Area Size (m <sup>2</sup> )	Categorical

Two different data types were used in the related study. In these data types, unit price, foreign exchange rate and gold values were used as numerical data types, while district, neighborhood, area size and month data types were used as categorical data types in the model. Although the area size (m<sup>2</sup>) is a numerical variable, it was transformed into a categorical variable in order not to cause too much branching in the decision tree. Accordingly, area size (m<sup>2</sup>) was categorized into 3 classes as 'High, Medium and Low'. Standard deviation ( $\sigma$ ), mean ( $\bar{x}$ ), and minimum and maximum area sizes were used for the value ranges in these classes (Eq. 1,2,3), [33].

$$\text{Low} = [\text{MinUnit\_Price}, \text{MinUnit\_Price} + \sigma] \quad (1)$$

$$\text{Medium} = [\text{MinUnit\_Price} + \sigma + 1, \bar{x} + \sigma] \quad (2)$$

$$\text{High} = [\bar{x} + \sigma + 1, \text{MaxUnit\_Price}] \quad (3)$$

After the transformation, the dataset for the pre-election period (February-March-April) consisted of 342 areas with low size, 75 areas with medium size, and 57 areas with high size. Similarly, the post-election

dataset (May-June-July) comprised 295 low-sized areas, 59 medium-sized areas, and 70 high-sized areas. The daily values of gold and foreign exchange rates on the dates when the lands were advertised for sale on the real estate website were recorded and included in the dataset.

The minimum exchange value (\$) in the dataset before the election was 18.74₺ and the maximum exchange value was 19.46₺. The minimum gold value (gr) before the election was 1103.57₺ and the maximum gold value was 1273.78₺. After the election, the minimum foreign exchange (\$) value was 19.21₺ and the maximum foreign exchange value was 26.99₺. After the election, the minimum gold (gr) value was 1219.64₺ and the maximum gold value was 1724.27₺.

In the dataset created for the pre-election and post-election periods, area size (m<sup>2</sup>) was determined in the districts of Çanakkale. In February, the highest average unit price was 4924₺ in Ayvacık and the lowest was 1409₺ in Biga (Figure 2). In March, the highest average unit price was 954₺ in Merkez district and the lowest was 129₺ in Biga. In April, the highest average unit price was 2777₺ in Ezine and the lowest was 511₺ in Eceabat.

In May, the highest average unit price was 7698₺ in Ezine and the lowest was 205₺ in Eceabat (Figure 2). In June, the highest average unit price was 8731₺ in Merkez district and the lowest was 1560₺ in Eceabat. In July, the highest average unit price was 8519₺ in Ezine and the lowest was 2065₺ in Biga.

Accordingly, while the pre-election value averages were low in March and April, in May (election time), mobilisations are observed in real estate prices in the districts. It is understood that there is an increase in values in the market in June and July after the elections. The highest land value change is observed in Ezine, Merkez and Ayvacık districts after the elections (Figure 2).

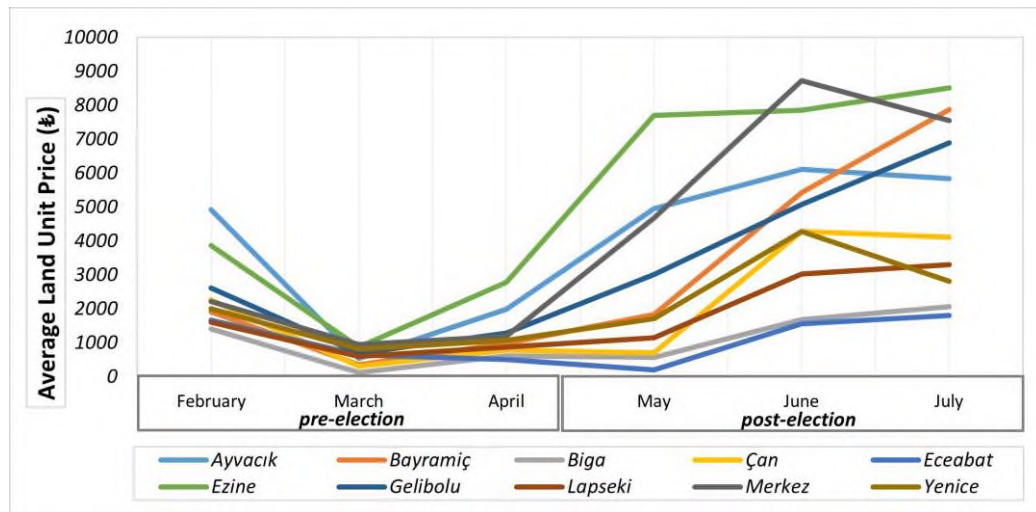
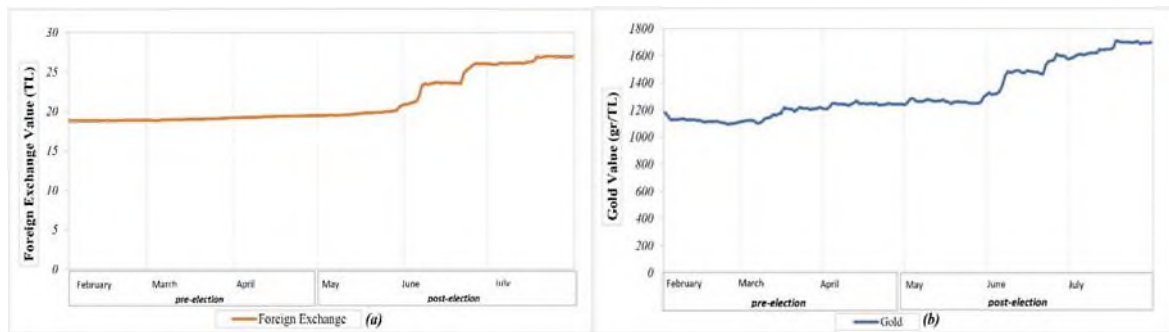


Figure 2. Average land unit price (₺) in pre-election and post-election districts.

In the dataset created for the pre-election and post-election periods, daily foreign exchange and gold values were entered according to the announcement dates on the relevant website of the land data obtained with the Python Scrapy Library. Among the economic variables, gold and foreign exchange rates were included in the model as descriptive variables. The main reason for choosing these variables is that they have daily data and thus provide time compatibility according to the announcement dates. Other economic variables, especially those with monthly or longer-term data, were not included in the model.

Figure 3a illustrates the fluctuations in exchange rates (\$) during the 2023 election period in Turkey. There was a significant increase in the exchange rates from May to July following the election period. Therefore, it demonstrates that the real estate sector was also affected by this increase in exchange rates (\$) (Figure 3a, Figure 3b). The relationship between real estate prices and exchange rates has been an important topic frequently discussed in the literature [34]. The rate of change in the value of gold in Turkey increased between February 2023 and July 2023 (Figure 3b). During this six-month period, there were notable fluctuations in gold values, especially following the elections and more prominently after May

2023.



**Figure 3.** (a) Foreign exchange (1\$) versus ₺ and (b) gold (gr) versus ₺ values in the election period in Turkey.

### 2.3. Method

In the study, regression trees, one of the machine learning methods and multiple linear regression methods, were used to predict the unit price of land before and after the elections and to determine the features affecting this price. The regional effects of these features determined within the scope of the study and their impact paths on the decision-making mechanism were determined. It was aimed to compare both model performances and to find the impact rates of economic and political features by comparing the situation before and after the election with the multiple linear regression method.

#### 2.3.1 Multiple Linear Regression (MLR)

Multiple Linear Regression is the most basic labelled learning method among machine learning methods. It basically works with the logic of the least squares method. It is used to determine the connection between variables. In this method, it consists of 2 different variables as dependent and independent variable. In Formula 1,  $y_i$  is the dependent variable in the dataset (the value we predict), the  $x_i$  variable is the features in the dataset,  $i$  independent variables,  $\beta_1$  is the effect coefficients of the features,  $j$  is the number of features, and  $n$  is the number of rows [35], (Eq. 4,5). In the linear regression used to compare the performance values in this study, the minimum tolerance interval was set as 0.05. The ridge value, which prevents the complexity of the model, was set as 1.0E-8.

$$y_i = \beta_0 + \beta_1 x_{1i} + \dots + \beta_n x_{ni} + \varepsilon_i, \quad i = 1.. \quad (4)$$

$$y = \begin{pmatrix} y_1 \\ y_2 \\ y_3 \\ \vdots \\ y_n \end{pmatrix}, \quad X = \begin{pmatrix} x_{11}^T \\ x_{21}^T \\ x_{31}^T \\ \vdots \\ x_{n1}^T \end{pmatrix} = \begin{pmatrix} 1 & x_{11} & \dots & x_{1l} \\ \vdots & x_{21} & \vdots & \vdots \\ 1 & x_{n1} & \dots & x_{nl} \end{pmatrix}, \quad \beta = \begin{pmatrix} \beta_0 \\ \beta_1 \\ \vdots \\ \beta_n \end{pmatrix}, \quad \varepsilon = \begin{pmatrix} \varepsilon_1 \\ \varepsilon_2 \\ \varepsilon_3 \\ \vdots \\ \varepsilon_n \end{pmatrix} \quad (5)$$

#### 2.3.2 Regression Tree

The most widely used algorithm among machine learning methods is decision trees [36]. However, decision trees are used for classification. Regression trees, which are similar to decision trees, are preferred as a more appropriate method for this study because they predict numerical variables. In this study, regression decision tree is used to analyse the land prices in Çanakkale districts before and after the elections. The main advantage of regression trees is that they can model complex and non-linear relationships. It is preferred because it is visually more descriptive and easier to interpret. This algorithm



uses measures such as variance reduction to split the data set and thus improve prediction accuracy [37]. The splitting is done in such a way as to minimise the variance of the target variable, and at each leaf node the prediction value is calculated as the average of the data at that node. In this model, each internal node represents a decision about a variable, each branch represents the outcome of a decision, and leaf nodes represent classes. [38]. The variable  $\mu$  in the formula indicates the mean of the features,  $n$  indicates the number of data in the features, and  $c$  indicates the different values that the relevant feature will take (Eq. 6,7,8). The regression tree is constructed by first calculating the standard deviation of the datasets. Then, binary standard deviation is calculated for each feature in the dataset. Standard deviation reduction is obtained by subtracting the binary standard deviation value for each feature from the obtained standard deviation values. The feature with the largest standard deviation reduction is selected as the first branch. The process continues until all leaves are obtained [35]. The formulas containing these stages are as in 6,7 and 8.

$$S = \sqrt{\frac{\sum(x-\mu)^2}{n}} \quad (6)$$

$$S(T, X) = \sum_{C \in X} S(T) - S(T, X) \quad (7)$$

$$SDR(T, X) = S(T) - S(T, X) \quad (8)$$

The purpose of the regression tree is to predict the continuous dependent variable (target variable) by utilizing continuous and categorical independent variables [39]. It helps predict the results based on an existing dataset.

The decision tree starts branching out according to the least square prediction variable. To develop the prediction model, 0.60 of the dataset was used as a training set for the learning phase of the algorithm. In this study, the maximum depth for the decision tree was set as 4 and pre-pruning was applied. The minimum gain variable for pre-pruning was 0.01. The minimum number of data for a leaf was set as 2.

The dataset includes numerical and categorical data. Among the numerical data, the 'Field Curvature' feature increases the branching in decision trees, making it difficult to read the tree. Therefore, this data feature was converted to categorical data type. The other numerical data were left as numerical data since they are the main factors in predicting the numerical unit price.

### 2.3.3 Performance Metrics

Root Mean Square Error (RMSE) is used to measure the predictive ability of a model. RMSE is calculated as the square root of the mean square of the difference between the predicted value and the true value. According to Formula 9,  $n$  is the number of observations,  $y_i$  is the true value, and  $\hat{y}_i$  is the predicted value.

$$RMSE = \sqrt{\frac{1}{n} \sum_{i=1}^n (y_i - \hat{y}_i)^2} \quad (9)$$

The fit of the regression equation to the model is indicated by the coefficient of determination ( $R^2$ ). It shows how well the predictions of the model match the actual data [40]. According to Formula 10,  $\hat{y}_i$  is the predicted value for observation  $i$ ,  $\bar{y}$  is the mean value of the dependent variable,  $y_i$  is the true value of the observation, and  $n$  is the number of observations in the data set.

$$R^2 = 1 - \frac{\sum_{i=1}^n (\hat{y}_i - y_i)^2}{\sum_{i=1}^n (\hat{y}_i - \bar{y})^2} \quad (10)$$

### 3. RESULTS AND DISCUSSION

#### 3.1 Multiple Linear Regression (MLR) Modelling

In the study, the effects of variables on unit price in the pre- and post-election periods are analysed using the MLR model. In the pre-election period, area size ( $\beta = -0.394$ ) and foreign exchange value ( $\beta = -0.247$ ) have a negative effect on unit price, while gold ( $\beta = 0.113$ ) and district ( $\beta = 0.329$ ) variables have a positive effect on unit price. In the post-election period, the negative effect of area size ( $\beta = -0.455$ ) on unit price continues, but the effects of gold ( $\beta = 0.052$ ), foreign exchange ( $\beta = 0.178$ ) and district ( $\beta = 0.23$ ) variables change positively (Table 2).

**Table 2.** Results of Multiple linear regression model

	Intercept	Coefficient	Std. Error	Std. Coefficient
<b>Pre-Election</b>	Area Size	-0.394	0.042	-0.364
	Gold	0.113	0.032	0.141
	Foregin Exchange	-0.247	0.177	-0.053
	District	0.329	0.036	0.371
<b>Post- Election</b>	Area Size	-0.455	0.033	-0.548
	Gold	0.052	0.128	0.082
	Foregin Exchange	0.178	0.147	0.245
	District	0.230	0.037	0.240

When the pre- and post-election periods are compared, it is observed that the effect of district, gold value and area size on unit price decreased in the post-election period. In particular, while the foreign exchange value had a negative effect on the unit price in the pre-election period, it was found that this effect changed positively in the post-election period. This shows that the effect of foreign currency value on unit price tends to increase in the post-election period.

Although a large change in land values was observed in regional terms after the elections (Figure 2), there was a decrease in the change in value of the region according to MLR after the elections. When looked at in general, it is seen in Figure 3 that there was an increase in the foreign exchange and gold values after the elections compared to before the election. Although the change in the country's economy is in the direction of increase, it is revealed by modeling that these have different effects on the purchase and sale values of the lands (Table 2).

#### 3.2 Regression Tree Modelling

In this section, decision tree models constructed with the pre-election (a) and post-election (b) data using gold and foreign exchange values are presented (Figure 4-Figure 10.) Due to the large size of the decision trees, the sub-branches of the trees are shown separately.

The regression trees indicated that the initial branching for both pre-election and post-election periods was based on the area size (Figure 4). In both trees, if the area size is small, the district factor becomes crucial in determining the unit price of the land. For medium and large areas, the foreign exchange rate is more significant in determining the land unit price. However, after the elections, the gold value becomes more important than the foreign exchange rate for medium-sized areas.



Figure 4. First branch of the decision tree (a: Pre-election b: Post-election).

For land plots with small pre-election area sizes, the regression tree shows that the district characteristic is the most important variable in price determination, as it appears at the root of the tree (Figure 5). This district characteristic branches out differently for the 10 districts in Çanakkale. For Ayvacık district, if the gold value is less than 1217₺, the unit price of land is 2456₺. If the gold value is greater than 1217₺, foreign exchange values gain importance, and the land unit price becomes 4747₺. For Gelibolu district, if the gold value is less than 1128, the land unit price is 2332₺, and if it is greater than 1128, the land unit price is 5273₺. In Bayramiç district, the most important feature in determining the land unit price is the gold value, as in Gelibolu and Ayvacık. If the gold value is less than 1135, it is predicted as 1235₺; if it is greater than 1135, it is predicted as 573₺. In Eceabat district, the foreign currency value stands out in determining the land unit prices; if the foreign exchange value is less than 18.82₺, the unit price of the land is 653₺, and if it is higher, it is 2088₺. In Çan, the month feature stands out in determining the unit price of land. It is 745₺ in February, 1991₺ in March, and 873 ₺ in April. In Biga, if the gold value is less than 1150, it is 281₺, and if it is greater than 1150, it is 769₺. Gold value is important in determining land prices in Lapseki. If the gold value is less than 1157, the final price of the land is 949₺, and if the gold value is greater than 1157, it is 3078₺. Similarly, gold value is important in Merkez district. If the gold value is less than 1121, it is predicted as 6542₺, and if it is greater than 1121, it is predicted as 3571₺. In Yenice, foreign exchange value is important in determining the unit price of land. If the foreign exchange value is less than 18.84, the unit price of land in the district is 1893₺, and if it is greater than 18.84, it is 4472₺. In Ezine district, as in Ayvacık, Gelibolu, Bayramiç, Biga, Merkez, Lapseki districts, the most important feature in determining the land unit price is the gold value. If the gold value is less than 1268, the land unit price is 2974₺, and if it is greater than 1268, the land price is predicted as 7917₺ (Figure 5).

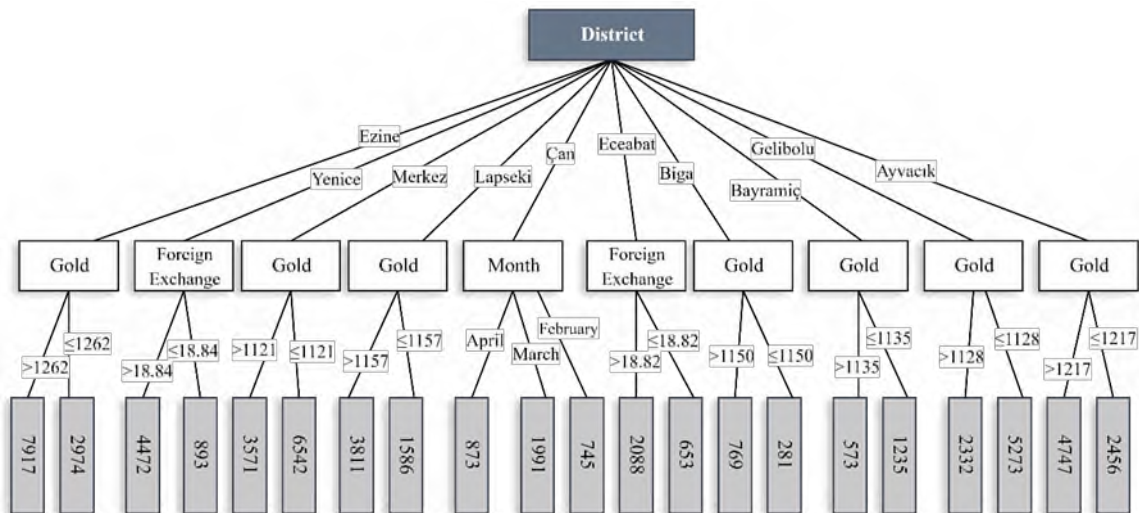


Figure 5. Regression tree for land with low pre-election area size.

In the context of low post-election area size, the district feature is the most important feature in price determination according to the regression tree, as it is located at the root of the tree (Figure 6). The district attribute branches out differently within the 10 districts in Çanakkale, as shown in Figure 8 from the

regression trees formed before the elections. For Ayvaci district, the most important feature in determining the post-election price is the foreign exchange value. If the foreign exchange value is less than 22.39, the land unit price is predicted as 5082₺, and if the foreign exchange value is greater than 22.39, the land unit price is predicted as 13,253₺. The most important feature for Gelibolu district is the foreign exchange value. If the foreign exchange value is less than 24.35, the unit price is 3591₺, and if it is greater than 24.35, it is 16.005₺. In Bayramiç district, the most important feature in determining the unit price of land is the month feature at the first level. According to the regression tree, the unit prices in May, June and July are 2663 ₺, 9882 ₺ and 10.456 ₺, respectively. In Biga and Eceabat districts, the foreign exchange value at the first level of the tree gains importance in determining the price. If the foreign exchange value is less than 19.80, the unit price in Biga district is 881₺, and if it is greater than 19.80, it is 2963₺. If the foreign exchange value is less than 23.50, the unit price of land in Eceabat district is 801₺, and if it is greater than 23.50, it is 4472₺. In Yenice district, the post-election land unit price is predicted as 3881₺. According to the regression tree, the post-election month feature stands out in the land unit price predict of Merkez, Çan and Lapseki districts. In Lapseki district, the land unit price predict is 1586₺ in May, 3961₺ in June, and 6226₺ in July. In Çan, it is 844₺ in May, 3961₺ in June, and 6226₺ in July. In Merkez district, according to the decision tree model, the unit price of land is predicted as 4492₺ in May, 15,733₺ in June, and 10,868₺ in July. Finally, in Ezine district, the foreign exchange value gains importance in determining the price. If the foreign exchange value is less than 26.98, the land unit price is 9699₺, and if it is greater than 26.98, it is 16,294₺ (Figure 6).

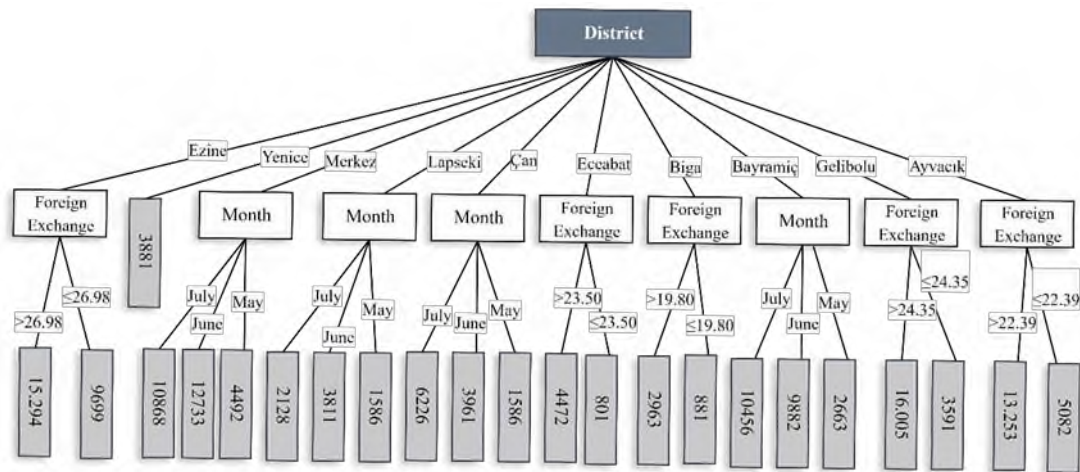


Figure 6. Regression tree for land with post election low area size.

For pre-election medium-sized plots, the foreign exchange value is the most important feature as it is at the root of the tree. When the foreign exchange value is greater than 19.38, the unit price for a medium-sized plot is set at 992₺. If the foreign exchange value is less than 19.38, the foreign exchange value becomes important again. When the foreign exchange value is less than 18.85, the pre-election land unit price for a medium-sized plot is 108₺, and when it is greater than 18.85, it is predicted to be 192₺ (Figure 7).

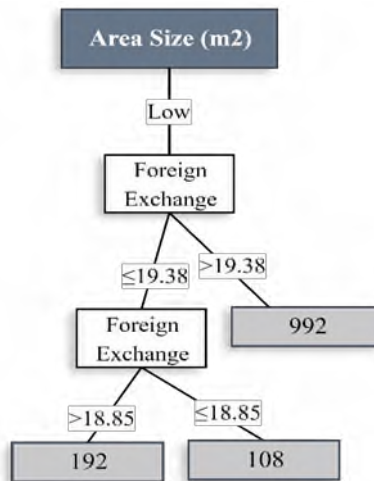


Figure 7. Regression tree for land with pre-election medium area size.

The most important determinant of unit price for medium-sized land after the elections is the gold value (Figure 8). If the gold value is less than 1489, the foreign exchange value becomes important. If the foreign exchange value is less than 19.54, the unit price is 86₺, and if it is greater than 19.54, the projected unit price is 263₺. If the gold value is greater than 1489, the foreign exchange value becomes important again. If the foreign exchange value is less than 25.83, the unit price of the land is 1056₺, and if it is greater than 25.83, the unit price is 573₺ (Figure 8).

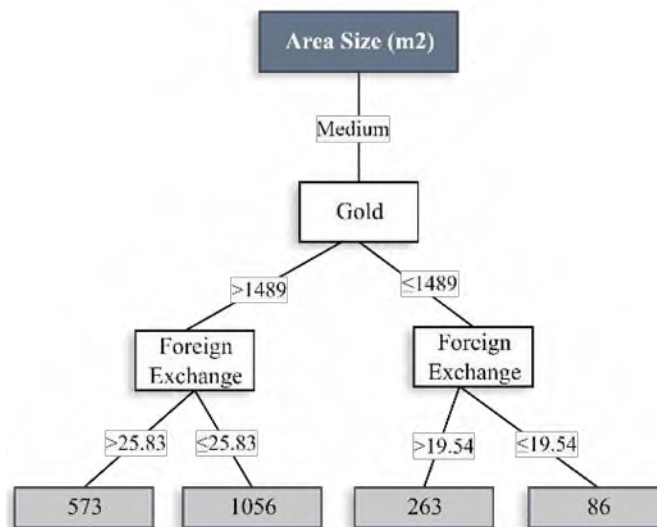


Figure 8. Regression tree for land with post election medium area size.

Before the election, the most important feature in the regression tree for land with high area size is the change value (Figure 9). If the value of foreign exchange is less than 19.27, the month feature gains importance in determining the unit price. Before the election, the unit price for land with high area size was 94₺ in February, 106₺ in March, and 45₺ in April. If the foreign exchange value is greater than 19.27, the gold value gains importance. If the gold value is less than 1250₺, the unit price of the plot is 205₺, and if it is greater than 1250₺, it is 340₺ (Figure 9).

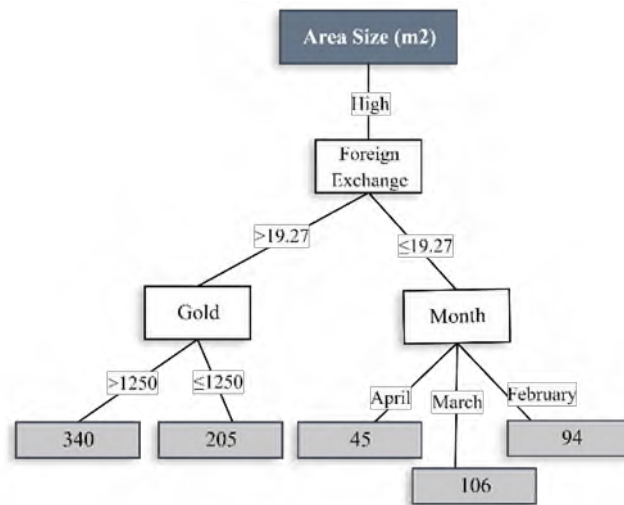


Figure 9. Regression tree for land with pre-election high area size.

When there is a high post-election area size, according to the model, the foreign exchange value gains importance in unit price estimation (Figure 10). If the foreign exchange value is less than 26.07, the gold value gains importance, and if the foreign exchange value is greater than 26.07, the foreign exchange value is considered again.

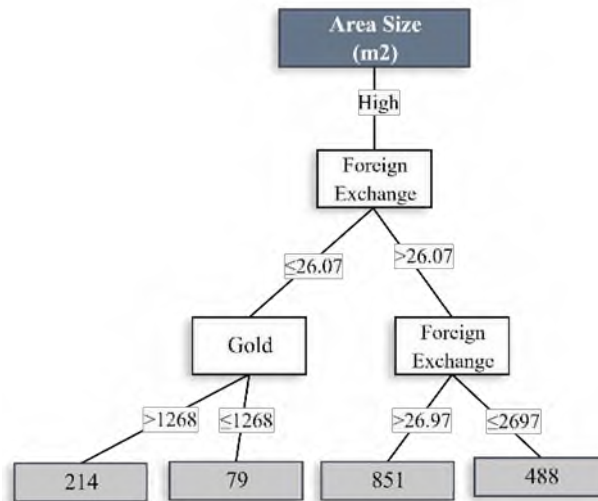


Figure 10. Regression tree for land with post election high area size.

### 3.3 Evaluation of Regression Tree Models

Regression trees, a machine learning technique, are employed to predict unit prices of land based on various characteristics including pre- and post-election periods, foreign exchange rates, and gold prices. As the size of the area changes, the characteristics that determine the unit price also change. The features that become important in determining the price in each tree model are given in Figure 11. The importance of the attributes decreases from the root to the lower levels. According to the regression tree, before the elections, district and foreign exchange values were the most important features in determining the price as they were at the root of the tree. After the elections, district, gold, and foreign exchange values were the most important characteristics affecting the price. The pre- and post-election branching of the tree according to district characteristics enabled the estimation of unit prices of land in Çanakkale. Thus, land unit prices for the districts in Çanakkale (excluding Bozcaada and Gökçeada) were predicted based on

daily changes in gold and foreign exchange values. Before the elections, gold value was generally important in determining prices (Figure 5), whereas after the elections, foreign exchange values (Figure 6) became important in determining prices (Figure 11). According to the regression trees constructed before the elections, an increase in gold values led to an increase in prices in certain districts, while a decrease in gold values led to a decrease in prices in certain districts. However, this was not the case in Gelibolu, Bayramiç, Merkez and Çan districts. In these districts, land unit prices decreased with the increase in the value of foreign exchange and land unit prices increased with the decrease in the value of foreign exchange values (Figure 5). According to the regression trees for the pre-election period, unlike the other districts, the month feature was important in determining the price in Çan district of Çanakkale (Figure 5). It was observed that the unit price of land increased in March compared to February and April.

According to the regression trees for the post-election period, currency value was more effective in determining the unit price of land (Figure 9). When the low-sized land was evaluated according to district characteristics, it was observed that foreign exchange values and month characteristics were important. While an increase in foreign exchange values increases the unit price of land, a decrease in foreign exchange values decreases the unit price of land (Figure 6). According to the regression tree model, the most expensive lands after the elections were located in Gelibolu, Merkez, Ezine and Ayvacık districts of Çanakkale. In the branching of low-sized land by month, the unit price of land increased after the elections, especially in June, in Merkez, Bayramiç, Lapseki and Çan districts of Çanakkale (Figure 6). This confirms the post-election increase in land prices.

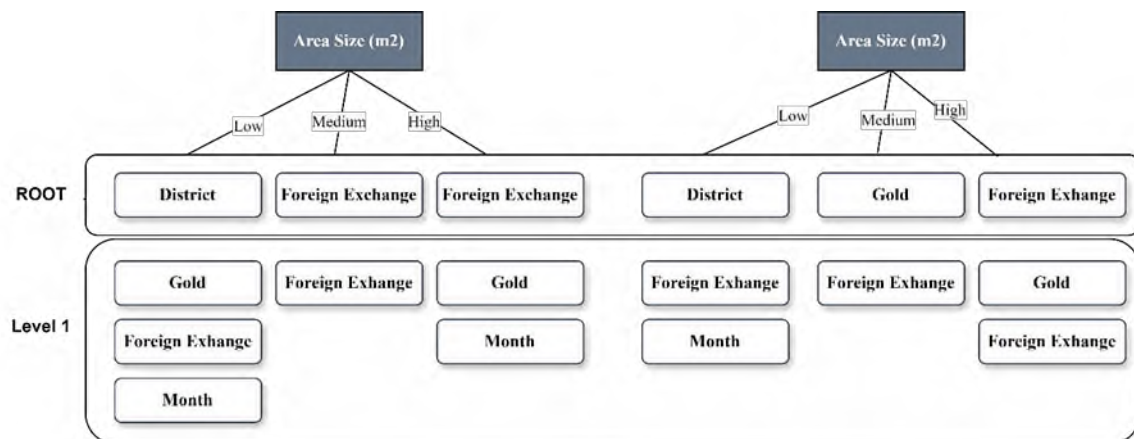


Figure 11. General representation of branching in regression trees.

### 3.4 Performance Evaluation of the Models

Root mean square and  $R^2$  deviation is used to compare the performance of regression tree and MLR models used for land unit price predicting. These performance values were compared separately for pre-election and post-election price predicts (Table 3).

The datasets used to determine the performance of the two models were the same. For the MLR model, the RMSE value was 2118 for the pre-election dataset and 5343 for the post-election dataset. According to the regression tree model, it was 4984 before the election and 1863 after the election. In this case, the error rate was higher in the linear regression model. The unit price prediction performance of the regression tree model was more successful.

When the  $R^2$  values of the models are analysed, the pre-election  $R^2$  value of the MLR model is 0.326 and the post-election  $R^2$  value is 0.389. The pre-election  $R^2$  value of the regression tree model is 0.326 and the post-election  $R^2$  value is 0.183. In this model, the  $R^2$  values range between 0.326 and 0.389, which indicate an acceptable level of explanatory power considering the dataset and the nature of the problem studied.

In the post-election period, the RMSE value of the Multiple Linear Regression model decreased to 4300

and the  $R^2$  value increased to 0.389. This shows that the fit of the model has improved significantly. In the post-election period, the RMSE of the Regression Tree model decreased to 1863, which is lower than the RMSE of the Multiple Linear Regression model (4300). This indicates that the Regression Tree model provides better accuracy in unit price predicting. Since RMSE measures the prediction errors of the model, a lower RMSE value indicates a better prediction performance.

**Table 3.** Performance values of the models.

Models	Performance Metrics	Pre-Election	Post- Election
Multiple Linear Regression	RMSE	1739	4300
	$R^2$	0.326	0.389
Regression Tree	RMSE	4984	1863
	$R^2$	0.326	0.183

### 3.5 Discussion

Elections affect political, economic, and social life in a country. Economic parameters change with the changes in economic policies at the time of elections, and the real estate market is also affected by this situation. Changes in economic parameters such as foreign exchange and gold also affect real estate investment demands and prices. In Turkey, elections took place in the first round on May 14, 2023, followed by the second round on May 28, 2023. During this election period, foreign exchange rates exhibited a stable trajectory from February to May but surged post-May. Conversely, gold values experienced a modest rise in March, escalating further in May. Inflation, which is another parameter, showed a balanced decrease until the election period and an increase after the election. No study was found in Turkey that analyses the real estate price change with these changing economic parameters during the election period. According to this study, the change in land unit prices before and after the elections in 10 districts of Çanakkale (excluding the islands) was predicted using gold and foreign exchange values through a regression tree from machine learning models. The regression tree model was employed to analyze the pre-election and post-election land unit price predictions, along with the influential features affecting the price. Additionally, multiple linear regression was utilized to assess and compare the performance of the model. The Regression Tree model has a lower RMSE value in the post-election and pre-election periods, indicating that the machine learning method is better at predicting unit prices. One of the main objectives of the study is to predict the unit prices of land. Although post-election  $R^2$  values are higher in the multiple linear regression model, RMSE values evaluating the accuracy of unit price predicts show that the regression tree model gives more accurate results after the election. Accordingly, in the post-election period, the regression tree model predicts comparative land unit prices more accurately than the linear regression model. Regression tree models were created to predict the unit prices of land with economic parameters such as gold and foreign exchange before and after the elections and to find the features that affect the price. Upon reviewing various studies in the literature, it is apparent that research on housing values predominantly employs financial methods rather than machine learning techniques [5], [9], [10], [11], [14], [41]. According to the regression tree model, the first branching in predicting the unit price of land before and after the elections was shaped according to the area size feature. This can be explained by the fact that the change in area size directly affects the unit price. Afterwards, district, foreign exchange and gold characteristics came to the fore. The fact that the district feature was effective in land unit price estimation enabled the district-based change to be analysed according to gold and foreign exchange values. According to the regression tree model, it was determined that the unit prices of land increased in Ayvacık, Biga, Eceabat, Ezine, Lapseki, Yenice districts with the increase in gold values before the election. The increase in gold values can be explained in relation to the socioeconomic status of the districts in Çanakkale. Especially Biga and Lapseki districts have become attractive regions for investors due to their proximity to the 1915 Çanakkale Bridge, which opened on 18



March 2022. This suggests that the increase in gold values may have affected land prices in Biga and Lapseki districts more than other regions. On the other hand, Ayvacık district stands out as one of the regions with high tourism potential in Çanakkale. The fact that the increase in gold values resulted in an increase in land prices in Ayvacık, a touristic region, supports this relationship. However, in contrast to this situation, in Bayramiç and Merkez districts, the land unit prices decreased with the increase in gold prices, and the unit prices increased with the decrease in gold prices. Bayramiç district can be considered as a region with lower attractiveness in terms of the real estate market compared to Biga and Lapseki districts, whose popularity increased with the opening of the 1915 Çanakkale Bridge. This may have caused investors to turn to alternative investment instruments instead of real estate. In this case, with the increase in gold prices, investors turned to gold, which is considered to be safe. In other words, investors preferred the investment tool with the highest return.

In this case, it reduced the demand for land and caused the unit price of land to decrease. When gold prices fall, investors turn to alternative investment tools. The reverse is also the case. The decline in gold prices increases the demand for real estate, which is one of the investment tools, and increases land prices. According to the regression tree, there was a significant increase in the unit price of land in Çan district, especially in March. This increase can be interpreted as a result of the impact of the earthquakes centered in Kahramanmaraş on 6 February. According to the regression tree, there was a significant increase in the unit price of land in Çan, especially in March. The decline in gold prices increases the demand for real estate, which is one of the investment instruments, and increases land prices. According to the regression tree, there was a significant increase in the unit price of land in Çan, especially in March. This increase can be interpreted as a result of the impact of the Kahramanmaraş-based earthquakes that occurred on 6 February 2023. Due to the safety concerns caused by the Kahramanmaraş earthquakes, a migration trend from big cities or high-risk areas to safer and rural areas also supported this increase. This may have increased the demand for land in safe areas by raising awareness of the earthquake risk and thus contributed to the price increase. It is also an indication that this earthquake affected not only the regional properties but also the property prices in Turkey as a whole.

According to the post-election regression tree model, the most important feature affecting the unit price of land is the foreign exchange value. As the foreign exchange value increased, the land unit prices increased, and as the foreign exchange value decreased, the land unit prices decreased. The districts with the highest land unit prices are Gelibolu, Ayvacık, Merkez and Ezine. These districts support this claim, as they are among the districts with the highest buying and selling density in Çanakkale [42].

In addition, in some districts, the month feature also came to the fore in determining the unit price of land. The increased significance of the month factor in influencing prices during the post-election period can be attributed to the gradual manifestation of changes in economic, political, and market conditions. Notably, May, June, and July emerge as critical months in determining unit prices. The summer period is traditionally characterized by heightened real estate activity. This seasonal surge in demand, along with an influx of foreign investors during the summer months, exerts upward pressure on land prices. The model corroborates the finding that May, June, and July significantly impact unit prices. According to the model, Lapseki, Bayramiç and Çan districts, which are predicted to have high land unit prices in June, also support the fact that prices increased in these districts after the elections. In addition, the intensification of real estate sales in Lapseki district with the construction of the 1915 Çanakkale Bridge and its opening to vehicle traffic [42], [43]. confirms that prices have also increased with the increase in demand for the region.

#### 4. CONCLUSIONS

This study, which covers 10 districts in Çanakkale province, is a pioneering study that demonstrates that machine learning can be used successfully in determining price predicts for pre- and post-election periods and determining the economic characteristics that affect them. In this study, not only the effect of the elections but also economic parameters such as gold and foreign exchange, which change before and after the election, were used to predict the unit price of land. Obtaining district-specific results in the model

allows predicting the change in real estate prices during periods of important events such as future elections. It can demonstrate important results for those who would like to invest in real estate in a region. While helping investors and buyers make decisions, it can also increase confidence in the real estate market. It can also help control real estate price increases by shaping the economic policies of governments. In addition, real estate prices are not in constant increase with economic parameters such as foreign currency and gold. Events that are important for a country or region affect changes in real estate prices. In order to see the general situation in a country, larger datasets can be used to predict the unit price of land. In parallel with the increasing data size, studies have also started to be modeled with different machine learning methods. Thus, it is possible to obtain different results in different regions.

### Declaration of Ethical Standards

The authors conducted this study in accordance with all ethical standards.

### Credit Authorship Contribution Statement

**Author 1:** Played a key role in developing the research design, performing the analysis, drafting the manuscript. Actively participated in the discussion of the results and contributed significantly to the final version.

**Author 2:** Formulated the main idea, contributed significantly to its development and helped to write the manuscript while finalising the overall concept.

**Author 3:** Focused on contributing to the description of the analyses, editing the manuscript and interpreting the results.

**Author 4:** Performed the analyses, revised the manuscript and contributed to the final version by actively participating in the discussion of the results.

### Declaration of Competing Interest

The authors declare that they have no known competing financial interests or personal relationships that could have appeared to influence the work reported in this paper.

### Funding / Acknowledgements

No funding is available for this research.

### Data Availability

No funding is available for this research.

## 5. REFERENCES


- [1] S. Yalpir, S. Sisman, A. U. Akar, and F. B. Unel, "Feature selection applications and model validation for mass real estate valuation systems," *Land Use Policy*, vol. 108, no. 105539, 2021, doi.org/10.1016/j.landusepol.2021.105539.
- [2] W. Coleman, B. Johann, N. Pasternak, J. Vellayan, N. Foutz, and H. Shakeri, "Using machine learning to evaluate real estate prices using location big data," In Proc. Systems and Information Engineering Design Symp. (SIEDS), 2022, pp. 168-172.
- [3] C. Haydaroğlu and G. Çevik, "Türkiye'de seçim sistemlerinin demokrasi ve ekonomi ilişkisi çerçevesinde incelenmesi," *Uluslararası Politik Araştırmalar*, vol. 2, no. 1, pp. 51-63, 2016, doi: 10.25272/j.2149-8539.2016.2.1.05.
- [4] H. S. Türk, "Seçim, seçim sistemleri ve anayasal tercih," *Anayasa Yargısı*, vol. 22, no. 1, pp. 75-113, 2006.

- [5] C. Y. Choi, D. Quigley, and X. Wang, "The impacts of local housing markets on US presidential elections: Via the collateral channel," *SSRN*, 2023, doi: 10.2139/ssrn.4544008.
- [6] M. Zimmer, "Home prices and the 2008 presidential election: Evidence from state level data," *The Social Science Journal*, vol. 47, no. 2, pp. 439-446, 2010, doi: 10.1016/j.soscij.2009.11.004.
- [7] B. Aha, D. Higgins, and T. Lee, "UK political cycle and the effect on national house prices: An exploratory study," In Proc. European Real Estate Society 25th Annu. Conference, 27-30 June, 2018.
- [8] V. Nguyen and C. Vergara-Alert, "Political uncertainty and housing markets," *Journal of Housing Economics*, vol. 61, p. 101952, 2023, doi: 10.1016/j.jhe.2023.101952.
- [9] E. Cifci, A. Tidwell, J. S. Clements, and A. Jauregui, "Housing performance and the electorate," *Journal of Real Estate Research*, vol. 45, no. 4, pp. 462-484, 2023, doi: 10.2765/87943.
- [10] B. Aha, D. Higgins, and T. Lee, "United Kingdom general elections and the impact on house prices," *International Journal of Housing Markets and Analysis*, vol. 16, no. 1, pp. 206-217, 2023, doi: 10.1108/IJHMA-04-2020-0047.
- [11] S. Monfared and A. Pavlov, "Political risk affects real estate markets," *Journal of Real Estate Finance Economics*, vol. 58, pp. 1-20, 2019, doi: 10.1007/s11146-017-9619-y.
- [12] J. Aizenman and Y. Jinjark, "Current account patterns and national real estate markets," *Journal of Urban Economics*, vol. 66, no. 2, pp. 75-89, 2009, doi: 10.1016/j.jue.2009.05.002.
- [13] İ. Ö. Badurlar, "Türkiye'de konut fiyatları ile makro ekonomik değişkenler arasındaki ilişkinin araştırılması," *Anadolu University Journal of Social Sciences*, vol. 8, no. 1, pp. 223-228, 2008
- [14] T. Habanabakize and Z. Dickason, "Political risk and macroeconomic effect of housing prices in South Africa," *Cogent Economics and Finance*, vol. 10, no. 1, p. 2054525, 2022, doi: 10.1080/23322039.2022.2054525.
- [15] V. Cohen and L. Karpavičiūtė, "The analysis of the determinants of housing prices," *Independent Journal of Management & Production*, vol. 8, no. 1, pp. 49-63, 2017, doi: 10.14807/ijmp.v8i1.521.
- [16] L. I. U. Yang and H. U. Zhiqiang, "On correlation between RMB exchange rate and real estate price based on financial engineering," *Systems Engineering Procedia*, vol. 3, pp. 146-152, 2012, doi: 10.1016/j.sepro.2011.11.020.
- [17] Xiuzhi, Z. and Xiaoguang, W., "The analysis: The influence of RMB exchange rate fluctuation on real estate price in China," In Proc. XXIII FIG Congress, Munich, Germany, 2006, pp. 1-9.
- [18] N. K. Yılmaz, "Investigation of the relationship between gold, dollar, euro exchange rates and housing sales: A study with Granger causality analysis," *Florya Chronicles of Political Economy*, vol. 7, no. 2, pp. 169-193, 2021.
- [19] M. Bahmani-Oskooee and T. P. Wu, "Housing prices and real effective exchange rates in 18 OECD countries: A bootstrap multivariate panel Granger causality," *Economic Analysis and Policy*, vol. 60, pp. 119-126, 2018, doi: 10.1016/j.eap.2018.09.005.
- [20] E. Benson, J. Hansen, A. Schwartz, and G. Smersh, "Canadian/US exchange rates and nonresident investors: Their influence on residential property values," *Journal of Real Estate Research*, vol. 18, no. 3, pp. 433-461, 1999, doi: 10.1080/10835547.1999.12091005.
- [21] N. Miller, M. Sklarz, and N. Real, "Japanese purchases, exchange rates and speculation in residential real estate markets," *Journal of Real Estate Research*, vol. 3, no. 3, pp. 39-49, 1988.
- [22] J. Lipscomb, J. Harvey, and H. Hunt, "Exchange-rate risk mitigation with price-level-adjusting mortgages: The case of the Mexican UDI," *Journal of Real Estate Research*, vol. 25, no. 1, pp. 23-42, 2003, doi: 10.1080/10835547.2003.12091103.
- [23] H. A. Karadaş and E. Salihoğlu, "Seçili makroekonomik değişkenlerin konut fiyatlarına etkisi: Türkiye örneği," *Ekonomik ve Sosyal Araştırmalar Dergisi*, vol. 16, no. 1, pp. 63-80, 2020.
- [24] O. A. Odhiambo and B. Ombok, "Analysis of inflation, interest rate, exchange rate and real estate residential property prices, Kenya," *The International Journal of Business & Management*, vol. 10, no. 11, 2022, doi: 10.24940/theijbm/2022/v10/i11/BM2211-007.

- [25] A. Derdouri and Y. Murayama, "A comparative study of land price estimation and mapping using regression kriging and machine learning algorithms across Fukushima Prefecture, Japan," *Journal of Geographical Sciences*, vol. 30, pp. 794-822, 2020, doi: 10.1007/s11442-020-1756-1.
- [26] A. Louati, R. Lahyani, A. Aldaej, A. Aldumaykhi, and S. Otai, "Price forecasting for real estate using machine learning: A case study on Riyadh City," *Concurrency and Computation: Practice and Experience*, vol. 34, no. 6, 2022, doi: 10.1002/cpe.6748.
- [27] W. K. Ho, B. S. Tang, and S. W. Wong, "Predicting property prices with machine learning algorithms," *Journal of Property Research*, vol. 38, no. 1, pp. 48-70, 2021, doi: 10.1080/09599916.2020.1832558.
- [28] J. Kim, J. Won, H. Kim, and J. Heo, "Machine-learning-based prediction of land prices in Seoul, South Korea," *Sustainability*, vol. 13, no. 23, p. 13088, 2021, doi: 10.3390/su132313088.
- [29] A. S. Ravikumar, "Real estate price prediction using machine learning," Ph.D. dissertation, National College of Ireland, Dublin, 2017.
- [30] Türkiye İstatistik Kurumu (TÜİK), "Gayri safi yurt içi hasıla," 2023. [Online]. Available: <https://data.tuik.gov.tr/>. [Accessed: 12-Oct-2023].
- [31] Türkiye İstatistik Kurumu (TÜİK), "Adrese dayalı nüfus kayıt sistemi," 2023. [Online]. Available: <https://data.tuik.gov.tr/>. [Accessed: 05-Sep-2023].
- [32] S. K. Sümer, S. M. Say, and G. Çiçek, "Determining the residue and energy potential of field crops in Çanakkale," *Anadolu Tarım Bilimleri Dergisi*, vol. 31, no. 2, pp. 240-247, 2016. doi: 10.7161/omuanajas.260980.
- [33] S. Yücebaş, M. Doğan, and L. Genç, "A C4.5-CART decision tree model for real estate price prediction and the analysis of the underlying features," *Konya Journal of Engineering Sciences*, vol. 10, no. 1, pp. 147-161, 2022. doi: 10.36306/konjes.1013833.
- [34] J. K. A. Jack, F. Okyere, and E. K. Amoah, "Effects of exchange rate volatility on real estate prices in developing economies: A case of Ghana," *Advances in Social Sciences Research Journal*, vol. 6, no. 11, pp. 268-287, 2019. doi: 10.14738/assrj.611.7392.
- [35] F. K. Gülağız and E. Ekinci, "Farklı regresyon analizi yöntemleri kullanılarak ev fiyatlarının tahmini," In Proceedings of the International Symposium on Industry, vol. 4, pp. 203-207, 2017.
- [36] X. Wu, V. Kumar, J. R. Quinlan, J. Ghosh, Q. Yang, H. Motoda, and D. Steinberg, "Top 10 algorithms in data mining," *Knowledge and Information Systems*, vol. 14, pp. 1-37, 2008. doi: 10.1007/s10115-007-0114-2.
- [37] W. Y. Loh, "Classification and regression trees," *Data Mining and Knowledge Discovery*, vol. 1, no. 1, pp. 14-23, 2011. doi: 10.1002/widm.8.
- [38] R.P. Liu, "Research of decision tree classification algorithm in data mining," *Journal of East China Institute of Technology*, vol. 9, no. 5, pp. 1-8, 2010.
- [39] M. Doğruel and S. Ü. Fırat, "Veri madenciliği karar ağaçları kullanarak ülkelerin inovasyon değerlerinin tahmini ve doğrusal regresyon modeli ile karşılaştırmalı bir uygulama," *Istanbul Business Research*, vol. 50, no. 2, pp. 465-493, 2021. doi: 10.26650/ibr.2021.50.015019.
- [40] N. J. Nagelkerke, "A note on a general definition of the coefficient of determination," *Biometrika*, vol. 78, no. 3, pp. 691-692, 1991.
- [41] C. Wang, "Can RMB exchange rate expectations explain the fluctuations of China's housing prices?," *Journal of Applied Finance Banking*, vol. 10, no. 5, pp. 211-233, 2020. doi: 10.47260/jafb/10512.
- [42] Tapu Kadastro Genel Müdürlüğü, "Parsel sorgu uygulaması, alım satım yoğunluğu," 2023. [Online]. Available: <https://parselsorgu.tkgm.gov.tr/>. [Accessed: 24-Jan-2024].
- [43] Tapu Kadastro Genel Müdürlüğü, "Parsel sorgu uygulaması, alım satım yoğunluğu," 2022. [Online]. Available: <https://parselsorgu.tkgm.gov.tr/>. [Accessed: 24-Jan-2024].



## IMPACT ANALYSIS OF PLUG-IN ELECTRIC VEHICLES ON THE REAL RESIDENTIAL DISTRIBUTION NETWORK

\* Muhammed Sait AYDIN 

*Siirt University, Engineering Faculty, Electrical and Electronic Engineering Department, Siirt, TÜRKİYE*  
[saitaydin@siirt.edu.tr](mailto:saitaydin@siirt.edu.tr), [saitaydin1@gmail.com](mailto:saitaydin1@gmail.com)

### *Highlights*

- A generic and comprehensive impact analysis framework is proposed to be applied to low-voltage networks to investigate an evaluation of the integration of small-scale renewable energy systems and/or new forms of demand such as electric vehicles.
- The influence of the transformer loading on secondary substations as well as the effects on low voltage customers, feeders and energy losses are analyzed separately for different cases whilst assessing the corresponding dependencies – crucial for a realistic quantification.
- It demonstrates the effectiveness of the proposed indicators with a UK case study that considers real Low Voltage Networks (typically, 0.4 kV), as well as realistic time-varying residential demand and Electric Vehicle Profiles.
- The discussion section is also presented with the corresponding caveats and suggestions.



## IMPACT ANALYSIS OF PLUG-IN ELECTRIC VEHICLES ON THE REAL RESIDENTIAL DISTRIBUTION NETWORK

\* Muhammed Sait AYDIN

*Siirt University, Engineering Faculty, Electrical and Electronic Engineering Department, Siirt, TÜRKİYE*  
[saitaydin@siirt.edu.tr](mailto:saitaydin@siirt.edu.tr), [saitaydin1@gmail.com](mailto:saitaydin1@gmail.com)

(Received: 17.10.2024; Accepted in Revised Form: 05.02.2025)

**ABSTRACT:** The growing share of Electric Vehicles (EVs) in the personal automobile market is expected to accelerate in the years to come. With increased demand at a household level, technical problems such as transformer and feeder overloading are likely to emerge. Therefore, this highlights the need for a comprehensive impact analysis framework for EVs to overcome the challenges ahead. A smoother transition, exploiting scalable performance indicators, to Low Voltage (LV) networks with this new form of demand could be achieved as imminent problems can be computed in a realistic manner. To this end, the impact analysis framework is proposed and the corresponding performance indicators are formulated to be used by researchers and/or Distribution Network Operators (DNOs) for different purposes. Under different scenarios, the impacts of EVs on the real underground unbalanced three-phase network are comprehensively explored considering household voltage profiles, transformer-loading, utilization of feeders, and daily total energy losses. For the summer and winter seasons, three cases covering all possible circumstances are investigated: without EVs, with EVs, and a worst-case scenario where all EVs connect at the same time. From the study, it can be deduced that the impact of EVs on the network and household voltage could reach unacceptable levels, and diversifying the connection times of EVs is vital to coping with potential problems posed by residential-level participation in EVs.

**Keywords:** *Plug-in Electric Vehicles, Low Voltage Network, Impact Analysis, Thermal Overloading, Performance Indicators*

### 1. INTRODUCTION

The concerns associated with reducing reliance on fossil fuels and decarbonizing the personal automobile market, together with the falling prices of electric vehicles and government incentives, have paved the way for the boom of electric vehicle uptake in recent years. Consequently, investment in EVs and their batteries increased 19 times more in 2019 compared to 2018 in the European Union alone [1]. Some countries have already reached a significant share/penetration of vehicles running on electricity. For instance, the proportion of EVs in the personal automobile market in 2019 was 56%, 25.5%, and 15% in Norway, Iceland, and the Netherlands, respectively [2]. Despite global car sales declining by 16% due to the pandemic-related worldwide downturn, electric car registrations grew by 41% in 2020 [3]. However, this opportunity is likely to result in some technical issues (such as voltage drop and thermal overloading), as residential peak demand is expected to coincide with the new form of demand posed by EVs [4–7].

Given that traditional distribution networks are not designed to deal with these new forms of demands, some technical problems might eventually emerge due to significant peak demand hours [8]. Since householders with EVs are likely to charge their automobiles at home, the corresponding infrastructures are highly likely to be the first place affected (in particular, European-style LV networks on which hundreds of customers are connected to the grid). It is, consequently, essential to quantify the impact of the adoption of EVs on customers and the network-level to propose efficient and scalable solutions through which greater the hosting capacity of the network is gained.

In general, the impact analysis and various solutions in the literature have been documented. These can be categorized under three main headings: optimization-based solutions, control-based methods, and

\*Corresponding Author: Muhammed Sait AYDIN, [saitaydin@siirt.edu.tr](mailto:saitaydin@siirt.edu.tr), [saitaydin1@gmail.com](mailto:saitaydin1@gmail.com)

deterministic or probabilistic impact analysis studies at the residential and/or network level.

The first group aims to provide impact analysis and solutions with various advanced optimization techniques [9–11]. These analyses typically require charge status, extensive information, visibility and communication technologies, and real-time pricing [12–14]. However, this does not yet fully correspond with real-world conditions, as acquiring all this information is not cost-effective and, therefore, is not readily available in a straightforward manner.

The second method, control-based solutions, typically aim at voltage or congestion mitigation (conductor and transformer levels) [15–18]. For voltage impact analysis, the primary objective is to reduce the voltage magnitude per unit, while current reduction or utilization reduction is employed to address thermal overloading. However, achieving this requires both data from the network and a communication system for remote control. Therefore, similar to the optimization-based solutions, in the absence of real-time data, corresponding communication channels and interoperability issues make these approaches challenging to be viable. The control actions can also be achieved through Machine Learning approaches (e.g., employing nodal voltage and its sensitivity to the design controller) [19]. Furthermore, some methods might require additional specific control elements such as phase-shifting ability [20].

The third common method is to perform a deterministic or probabilistic (DoP) impact analysis [21–24]. Most of the studies documented in the literature focus on DoP. The majority of these studies are on assessing/mitigating thermal overloading on the transformer, lines, and customer voltage profiles [25–28]. However, for utilities, especially in terms of voltage, the penalties are given based on the existing voltage standards of the relevant countries. Therefore, related studies should be evaluated in this context. In addition, thermal overloading poses a risk to the corresponding assets. Moreover, these analyses are to be generic, in turn, they must be expressed mathematically. Thus, it can be adapted in other countries with minor setting modifications. In addition, most studies have not examined low-voltage networks, where the effects are expected to emerge first [29]. This is likely to create hesitation in terms of the applicability of the relevant solutions. Also, some studies using simplified models may not disclose their particularities [5].

However, none of the aforementioned studies address mathematically expressed dynamic voltage calculation as performed in real life scenarios. Furthermore, none of the studies conduct a comprehensive analysis that simultaneously examines both customer and network-level technical issues.

### 1.1. Contributions

In this paper, a generic and comprehensive impact analysis framework is proposed to be applied to low-voltage networks to evaluate the integration of EVs. In addition, this framework could be applied to quantify the impact of battery energy storage systems, small-scale renewable energy systems, and new forms of demand, such as electric heat pumps. This framework allows Distribution Network Operators (DNOs) to identify the networks with technical problems in advance, providing them with sufficient time to implement potential solutions.

This impact analysis framework includes the realistic dynamic voltage calculation according to European standards (EN 50160). Furthermore, simpler and applicable calculations for network energy losses are mathematically expressed for the planning stage. Consequently, the impact analysis combines the utilization of feeders and the transformer, voltage issue (voltage drop), and network energy losses which in turn, is able to realistically quantify network and customer-level technical issues.

For the case studies, therefore, this study aims to mimic real-life applications by considering a fully modeled three-phase four-line real LV network, generating realistic high resolution (1-min) plug-in electric vehicle profiles and obtaining 1-min demand profiles.

The remainder of the paper is organized as follows: An overview of the proposed methodology is presented in section 2. Modelling and analysis considerations, together with performance indicators, are provided. In section 3, the results and discussion are presented for the case study. Finally, section 4 concludes the study.

## 2. MATERIAL AND METHODS

The methodological framework proposed comprises three stages and is illustrated in Fig.1. In the first stage, a fully modeled LV network and household demand profiles are needed. Once EVs are considered for the analysis, corresponding EV profiles are taken into account. Given uncertainties surrounding the usage of demand and EV profiles, the analysis needs to be tailored to each household. For illustrative purposes, the worst-case scenario may include only one EV profile. While this might not accurately reflect real-life conditions, the objective is to provide insights into potential outcomes when all customers behave in a similar manner.

In stage two, three-phase four-wire power flow analyses are carried out. In stage three, performance indicators are obtained and compared against the explored cases.

A generic synthetic LV network model is given in Fig.2, where the measurement points are in place to allow the capturing/computing of the aforementioned indicators.

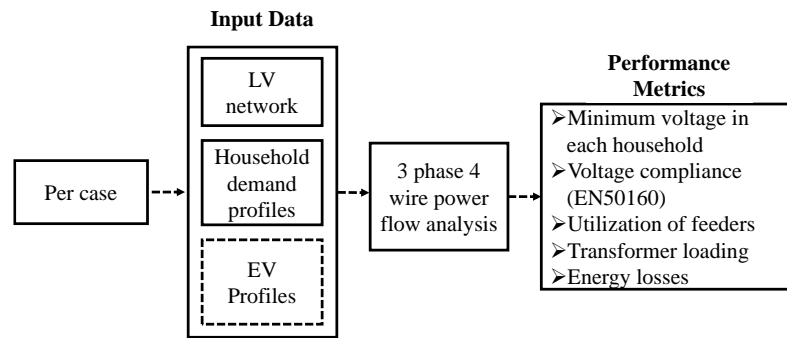


**Figure 1.** Flow chart for the performance assessment framework

The measurement point at the secondary side of the transformer provides active ( $P^{tr_{sec},\phi}$ ) and reactive ( $Q^{tr_{sec},\phi}$ ) power, and current drawn by each feeder ( $i_t^{F_{head},\phi}$ ).

Furthermore, measurements at household connection points provide corresponding daily voltage profiles ( $Vh_N^\phi$ ). This enables the calculation of the corresponding performance indicator.

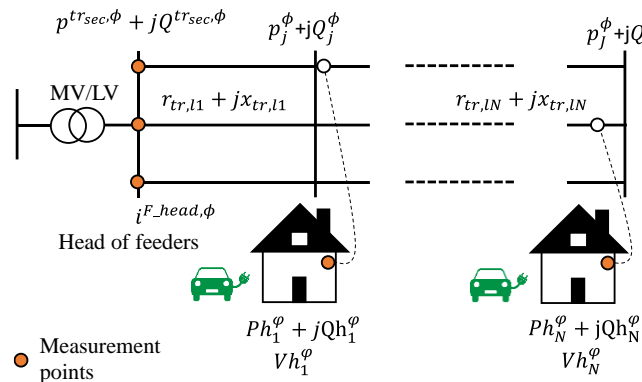


**Figure 2.** Layout of synthetic LV network

### 2.1. EV modeling considerations

For EV impact analysis, typically real data is employed. By means of long-term charge measurements for EV cars, starting charging time and energy demanded during a connection are typically captured. Along with these, considering the constant charging rate and the battery capacity, EV profiles can be modeled accordingly. For this study, the detail of the modeling is provided in section 3.



## 2.2. Performance indicators

To assess the performance of EVs on the network, voltage, utilization of feeders, transformer loading, and energy losses are analyzed. This approach aims to provide a thorough analysis of each component within the studied network.

One of the striking features in the transition to LV networks with emerging technologies such as EVs is voltage instability. Voltage rise or drop may exceed the statutory limits. Given that EV and household demand profiles are analyzed on the network, it is essential to apply a voltage drop equation.

For an exemplary two-bus system demonstrated in Fig.3, voltage drop from  $Bus_j$  to  $Bus_{j+1}$ , for the phases (i.e.,  $\varphi$ ), is shown as  $\vec{V}_j^\varphi - \vec{V}_{j+1}^\varphi$ , which can be expressed by power flow between buses as in (1).

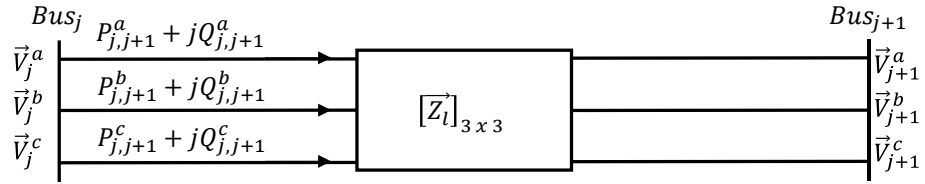


Figure 3. Exemplary two-bus system

$$\begin{bmatrix} \vec{V}_j^a \\ \vec{V}_j^b \\ \vec{V}_j^c \end{bmatrix} - \begin{bmatrix} \vec{V}_{j+1}^a \\ \vec{V}_{j+1}^b \\ \vec{V}_{j+1}^c \end{bmatrix} = \begin{bmatrix} (P_{j,j+1}^a + jQ_{j,j+1}^a)/\vec{V}_j^a \\ (P_{j,j+1}^b + jQ_{j,j+1}^b)/\vec{V}_j^b \\ (P_{j,j+1}^c + jQ_{j,j+1}^c)/\vec{V}_j^c \end{bmatrix}^* \times [\vec{Z}_l]_{3 \times 3} \quad (1)$$

For each phase, this three-by-three matrix equation can be transformed into the form in which only the corresponding current and impedance could be utilized as in (2).

$$\vec{V}_j - \vec{V}_{j+1} = \left[ \frac{(P_{j,j+1}^a + jQ_{j,j+1}^a)}{\vec{V}_j \angle \theta_j} \right]^* \times \vec{Z}_l = \vec{I}_{j,j+1} \times \vec{Z}_l \quad (2)$$

It is crucial to compute voltage drop (or rise) more realistically, as DNOs are legally obliged to keep their end users' voltage profile within the statutory limits (e.g., according to BS EN50160). According to regulation, 95% of the measured supply voltage (10-min average r.m.s. value) must be within 1.1 p.u. and 0.9 p.u. of nominal voltage. In addition, all measured supply voltage must never breach 1.1 p.u. and 0.85 p.u. of nominal voltage.

To comply with statutory obligations, the following three steps proposed in [30] are adopted. In the first stage, a 10-min average of household demand profile-based decisions are made (e.g., 144 decisions for 1440-min resolution). Due to the fact that day-long analysis is adopted, in this study, the corresponding regulation is adapted as daily. As such, in each time of  $t$  (time of measurement), a 10-min average of voltage profile (i.e.,  $av(Hd_t)$ ) a day is greater than 1.1 p.u. or less than 0.9 p.u., then, the associated time (i.e.,  $i$ ) is flagged as 1 (i.e., problem arisen), if not,  $i$  is defined as 0. This is mathematically expressed in (3).

Considering all-day-long analysis, for each 10-min average a value is assigned, in turn, a set of binary decisions (i.e.,  $TP_i^{Daily}$ ) is given, for a certain customer.

$$TP_i^{Daily} = \begin{cases} 1, & \text{if } av(Hd_t) \geq 1.1pu \vee \text{if } av(Hd_t) \leq 0.9pu \\ 0, & \text{else} \end{cases} \quad (3)$$

$\forall t \in T$

In stage two, the final daily decision is made for a given customer. In accordance with EN50160, in the first stage, if any 10-min average of voltage profile (i.e.,  $av(Hd_t)$ ) is higher than 1.1 p.u. or lower than 0.85

p.u., the customer is identified as a customer with a voltage problem.

When all 10-min average voltage profile decisions ( $\sum_i TP_i^{Daily}$ ) is greater than five percent of the duration of household demand resolution ( $D^{HDR}$ ), then, a voltage problem is identified, otherwise, no voltage problem is considered for a given customer.

Considering all customers for the given network, the recurrent process in stages 1 and 2, is carried out for all customers ( $\sum H_n$ ) on the network, in stage three as in (4).

$$H_n = \begin{cases} 1, & \sum_i TP_i^{Daily} > 0.05 \times D^{HDR} \\ 1, & \text{if any, } av(Hd_t) \geq 1.1pu \vee av(Hd_t) \leq 0.85 pu \\ 0, & \sum_i TP_i^{Daily} < 0.05 \times D^{HDR} \end{cases} \quad (4)$$

Finally, the percentage of the total customer number ( $T_{cus}^{per}$ ) with voltage problems are identified. This process can also be adopted to feeder-by-feeder calculation in (5).

$$T_{cus}^{per} = \frac{\sum H_n}{N \times 10^{-2}}, \forall n \in N \quad (5)$$

Given that thermal overloading might affect the first feeders more than the corresponding transformer, it is crucial to calculate the utilization of feeders. Therefore, for a given time period (t), the average current drawn by the head of each feeder (i.e., considering all phases,  $\phi$ ) is captured and divided by ampacity, and the percentage value is calculated as given in (6). This provides the daily percentage of feeder utilization ( $F_{ut}^{D,per}$ ).

$$F_t^{per} = \frac{av(i_t^{total,F\_head,\phi})}{FA \times 10^{-2}}, \forall t \in T \quad (6)$$

A set of feeder utilization is obtained, the maximum one is the feeder utilization.

This is one of the important indicators as it is well known that EVs have an adverse effect on the utilization of feeders, hence, it provides insight into DNOs' understanding as to when their feeders are expected to be reinforced.

Due to the fact that EVs have the potential to increase transformer loading, it is essential to measure this according to profiles' resolution to cater for time-varying impact. Therefore, in each predefined resolution time (t), considering all phases ( $\phi$ ) at the secondary side of the transformer, the total active ( $P_t^{trsec,total,\phi}$ ) and reactive power ( $Q_t^{trsec,total,\phi}$ ) is measured and transformed to complex power and divided by transformer capacity ( $TR^{cap}$ ) so that the corresponding transformer capacity percentage ( $TR^{cap,per}$ ) computed for a given penetration level. The mathematical expression is provided in (7).

$$TR^{cap,per} = \frac{\sum_{t=1}^T ((P_t^{trsec,total,\phi})^2 + (Q_t^{trsec,total,\phi})^2)^{1/2}}{TR^{cap} \times 10^{-2}}, \forall t \in T \quad (7)$$

As a result, the impact of EVs on the transformer loading based on resolution is captured. This allows DNOs to be aware of the usage of a transformer for a given LV network and take precautionary measures, if necessary.

Energy losses on the network are expected to increase due to the power drawn by EVs, therefore, the impact of EVs on energy losses could be considered another indicator to be taken into account.

For a given two-bus system in Fig.2, power injection at  $Bus_i$  (i.e.,  $P_{j,j+1}^\varphi$  and  $Q_{j,j+1}^\varphi$ ) is computed by power balance equations. Since the household demand (e.g., customer number one exists in place) is known (i.e.,  $Ph_1^\varphi$  and  $Qh_1^\varphi$ ), the active ( $P_{j,j+1}^{losses,\varphi}$ ) and reactive power ( $Q_{j,j+1}^{losses,\varphi}$ ) losses can be calculated in a straightforward manner (as given in 8 and 9).

$$P_{j,j+1}^{losses,\varphi} = \left( \frac{P_{j,j+1}^\varphi}{\bar{V}_j} \right)^2 r_{j,j+1} = P_{j,j+1}^\varphi - Ph_1^\varphi \quad (8)$$

$$Q_{j,j+1}^{losses,\varphi} = \left( \frac{Q_{j,j+1}^\varphi}{\bar{V}_j} \right)^2 x_{j,j+1} = Q_{j,j+1}^\varphi - Qh_1^\varphi \quad (9)$$

$\forall \varphi \in \phi$   
 $\forall \varphi \in \phi$

For a network with numerous buses and customers, a simpler method for quantification is needed.

Unlike voltage, utilization, and transformer loading equations in which time is essential for accurate quantification, only the total daily amount is sufficient for calculating energy losses.

Therefore, total daily active and reactive energy losses (i.e.,  $P_{sum}^{losses,\varphi}$  and  $Q_{sum}^{losses,\varphi}$ ) are quantified as shown in (10) and (11) where  $\sum_{n \in N} Ph_n^\varphi$  and  $\sum_{n \in N} Qh_n^\varphi$  denote the total daily active and reactive demands of all households, respectively.  $P^{tr_{sec,total,\varphi}}$  and  $Q^{tr_{sec,total,\varphi}}$  represent total daily active and reactive power at the secondary side of the transformer, respectively.

$$P_{sum}^{losses,\varphi} = P^{tr_{sec,total,\varphi}} - \sum_{n \in N} Ph_n^\varphi, \forall \varphi \in \phi, n \in N \quad (10)$$

$$Q_{sum}^{losses,\varphi} = Q^{tr_{sec,total,\varphi}} - \sum_{n \in N} Qh_n^\varphi \quad (11)$$

$\forall \varphi \in \phi, n \in N$

### 3. RESULTS AND DISCUSSION

In this section, the demand profiles, EV profiles, and network employed to assess the impact of EVs on the network is introduced. The tool developed by the Centre for Renewable Energy Systems Technology (CREST) in [31] is utilized for modeling the domestic profiles (one-minute resolution). Each load of individual dwelling is realistically modeled by considering factors such as the number of occupants, the type of day, seasonality, and the corresponding usage of electrical appliances.

For the considered network, the number of occupants per household aligns with UK statistics [32], i.e., the percentage of houses with 1, 2, 3, and more than 4 person/people are 29, 35, 16, and 20%, respectively. Two seasons (summer and winter) are investigated, therefore, for each season, a pool of 1,000-weekday customer profiles (1-min resolution) is created to be employed. For each season (July and February), the average of the created pool is normalized and demonstrated in Fig.3. As the EV statistics (for Nissan leaf brand EV cars) are publicly available in [33], where probability distribution function for daily EV energy requirement and probability distribution function of EC connection times during the field trials are provided. The corresponding figures are provided in Fig.4 and Fig.5. This data is employed to generate a pool of 1000 profiles (1-min resolution). The average of the created pool is normalized and demonstrated in Fig.6. In this study, EV profiles are considered to operate at the unity power factor. The battery capacity is 24kWh [34]. Since EVs are connected to the grid at home, only slow charging mode is considered, with a constant charging rate of 3kW. Furthermore, generated EV profiles are randomly allocated between customers to cater for uncertainty.

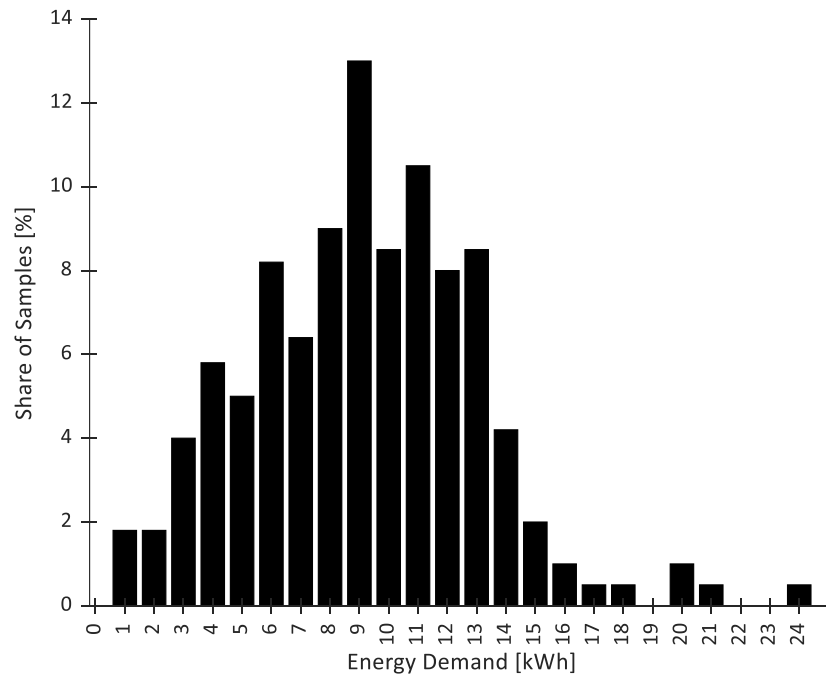


**Figure 4.** The probability distribution function for daily EV energy requirement.

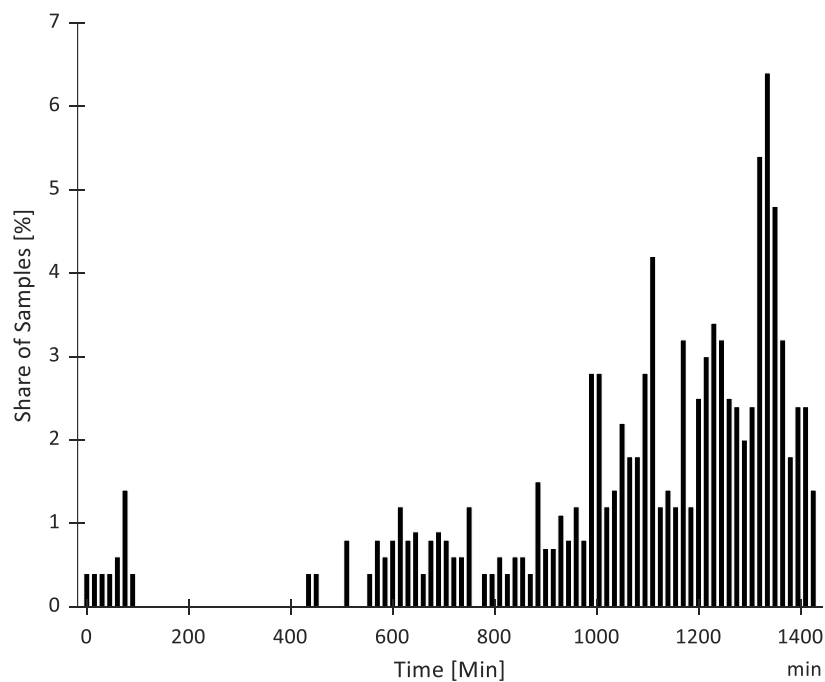


**Figure 5.** The probability distribution function of EC connection times.

In order to coincide the maximum EV profile with the corresponding seasonal demand profiles, the time of connection is shifted to one and four hours for summer and winter, respectively. Therefore, the effect of EV connection on voltage profiles can be observed. For the worst-case scenario (also referred to as Dumb Charging), the same EV profile is chosen to be able to connect at the same hours, which also coincides with peak demands. Although it is highly unlikely to observe Dumb Charging under normal conditions throughout the year, it may happen in exceptional cases (e.g., after a sports event, etc.)

In this section, the real underground residential UK LV network (feeder by feeder) from the North West of England, part of the Low Carbon Networks Fund Project 'LV Network Solutions', is used [35]. It is modified as an LV network to assess the network-based impact analysis shown in Fig.7. The network consists of six LV feeders (three-phase four-wire), each of which is shown with different colors. A total of 351 customers are connected to feeders through single-phase connections.

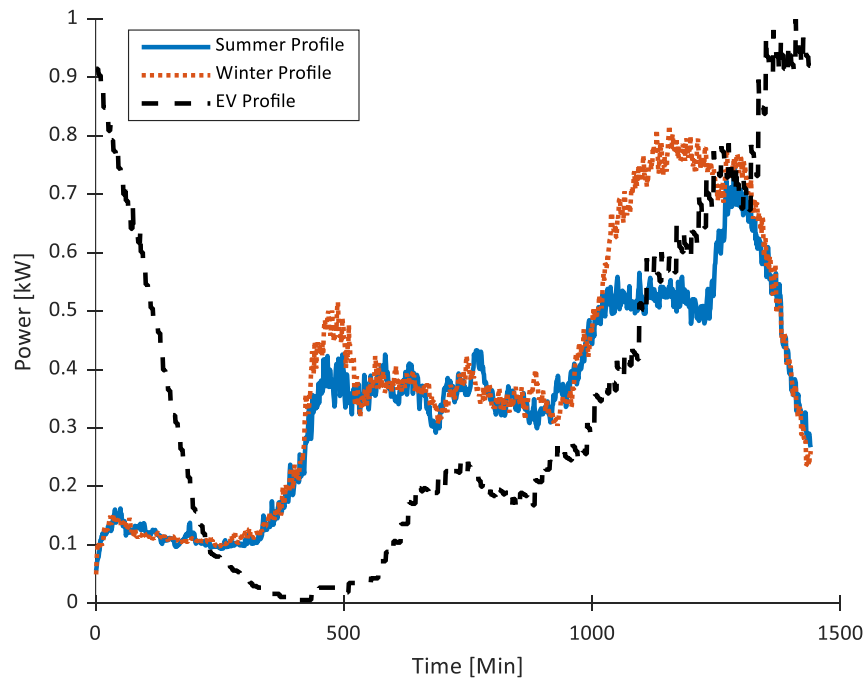


**Figure 6.** Normalized average of EV, summer, and winter demand profiles.

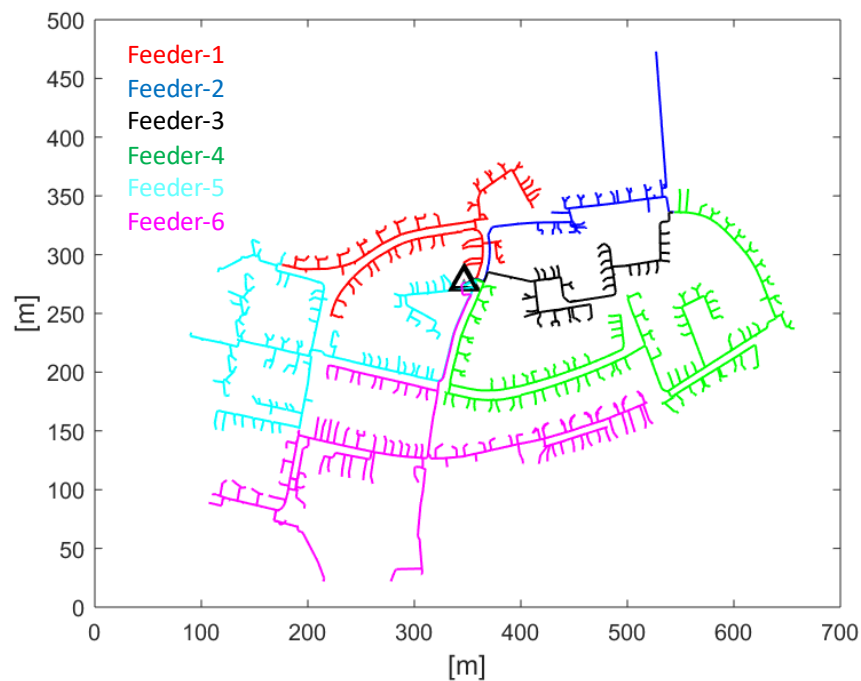


**Figure 7.** Studied real LV network on which feeders are shown in different colors and the secondary substation is represented by a triangle.

The corresponding transformers (illustrated in the triangle) have a voltage ratio of 11 kV to 0.433 kV (8.7% offload tap boost), which is typical in the UK [36]. The capacity of the transformer is 500 kVA. For simplicity purposes, the voltage at the primary side of the transformer is considered fixed at 1 pu.

### 3.1. Results

In this section, a realistic three-phase four-line time series unbalanced power flow analysis is carried out through OpenDSS to assess the impact of EVs on the network along with customer voltage profile considering different scenarios. The results and corresponding discussions are provided.

In order to assess the impact of EVs on the voltage, the analysis of with and without EVs, and the worst-case scenario is carried out for summer and winter. For the without EVs cases, only demand profile impacts on the network and the customers are quantified considering seasons. For the 'with EV' and 'worst-case' scenarios, each dwelling has an EV connected in a certain time period of the day (the worst-case scenario considers the same connection time of EVs).

The minimum voltages of households throughout the day for each case are captured and compared against each other to provide insight into how EV profiles' effects are on the voltages shown in Fig.8.

The results show that the reduction in minimum voltages for all feeders analyzed varies according to the location of households (a total of 351 customers). The more demand drawn from households indicates the lower voltages.

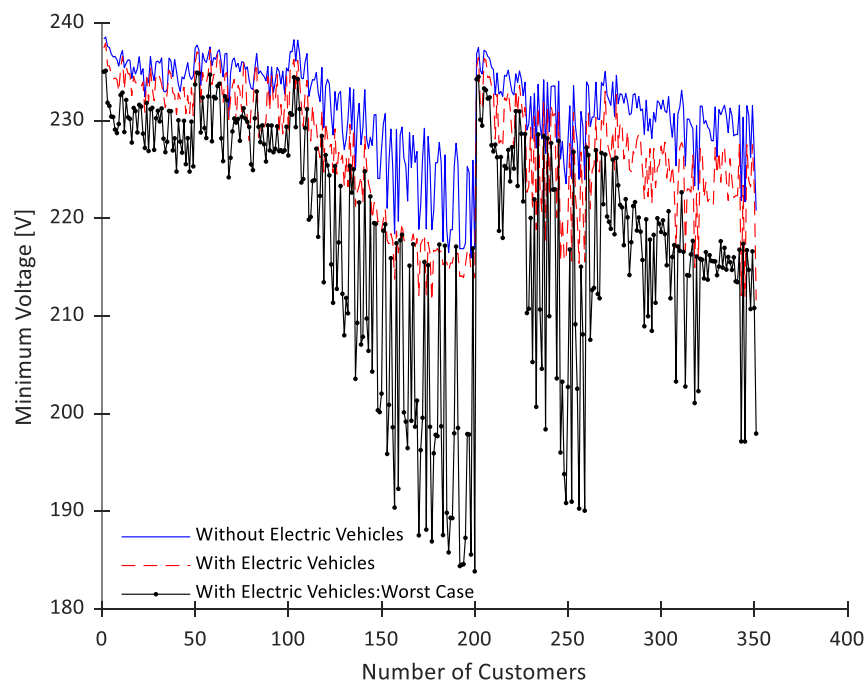


**Figure 8.** The minimum voltage at each household on the network for without, with, and worst-case study.

Due to the nature of EVs, the current drawn by dwellings is expected to increase. Therefore, voltage profiles along the feeders are to be affected. The change in voltage profile along with the feeders with EVs in winter is, for Feeder-4, demonstrated in a time series manner in Fig.9.

It is evident that the change in voltage profiles of households from the transformer to the end of the feeder increases. It is a fact that customers with the largest distance from the transformer are expected to be the most challenging dwelling in terms of voltage (i.e., relatively large voltage drop). Crucially, voltage drops are primarily observed at late hours when most EVs are connected. It is noteworthy that, according to EN50160, none of the customers experience voltage problems in the case of employing without EVs and different EV profiles for summer and winter. Whereas, in the worst-case scenario, a total of 44 and 51

customers are affected by voltage problems (i.e., breaching the statutory limits) for summer and winter, respectively.

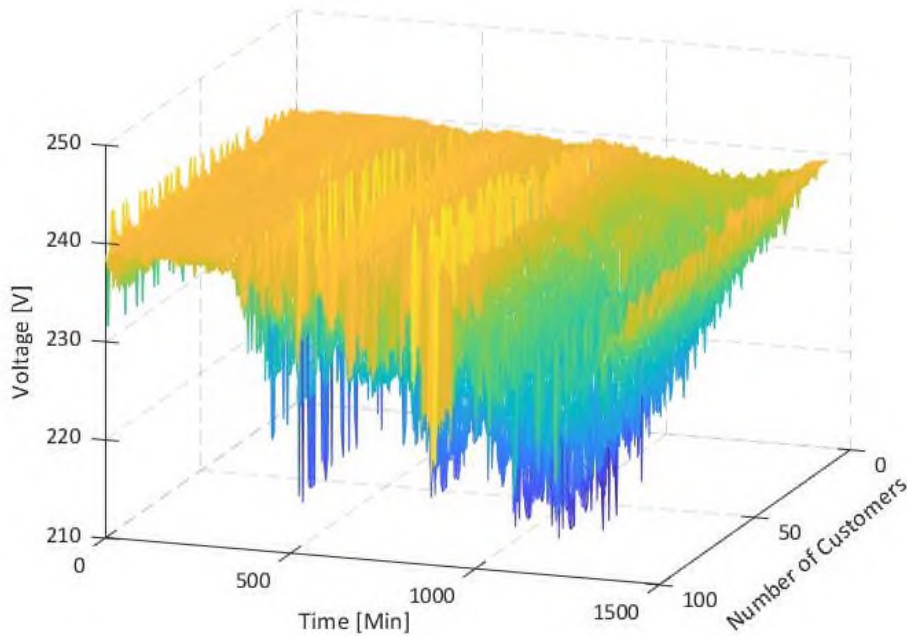


**Figure 9.** Daily min-by-min voltage profiles of households from the transformer (customer number is labeled as 0) to the end of Feeder-4 (labeled as 100).

The hourly utilization of each feeder considering the seasons and various scenarios is shown in Fig.10. Once feeder utilization exceeds one hundred percent, thermal overloading occurs in the feeder. Note that the utilization percentage of each feeder increases with the adoption of EVs as the currents drawn by households increase. For the worst-case analysis, Feeders from 4 to 6 pose thermal overloading. From the seasonal perspective, the utilization of feeders increases slightly in response to the growth in demand.

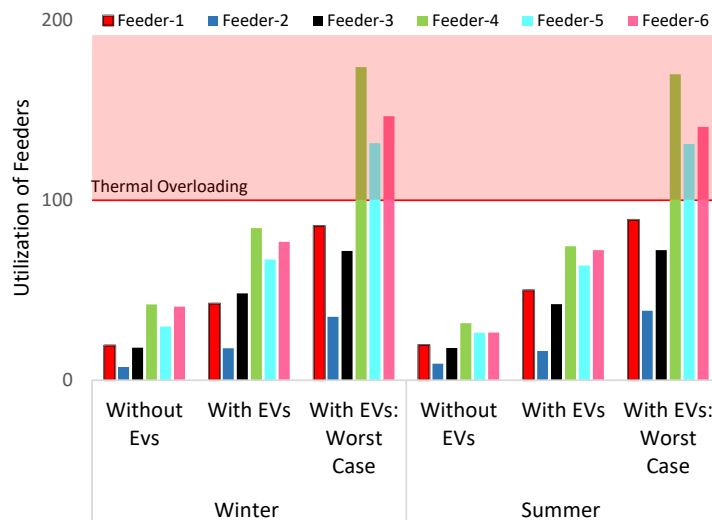


**Figure 10.** Utilization of feeders for different cases in two seasons.

From utilization feeder impacts, it is obvious that currents drawn by households increase to a great

extent with the adoption of EVs. This is, in turn, expected to result in amplification in transformer loading. For the analyzed three cases in each season, the transformer loading percentage is given in Fig.11. It can be seen from the figure that EVs augment transformer loading due to the growth in demand profiles. In the case of the worst-case scenario, thermal overloading exceeds its limit (i.e., 100%), which indicates no headroom is left to host EVs. Furthermore, from utilization impact, only feeders from 4 to 6 are overloaded, yet, the room provided by other feeders is not sufficient for the transformer to overcome overloading.

Another indicator considered is energy loss as it can be expected to increase with greater demand (EVs). Daily total energy losses for the studied network are given in Fig.12. With larger demand (considering EVs and seasonality), daily energy losses are increased, as expected.

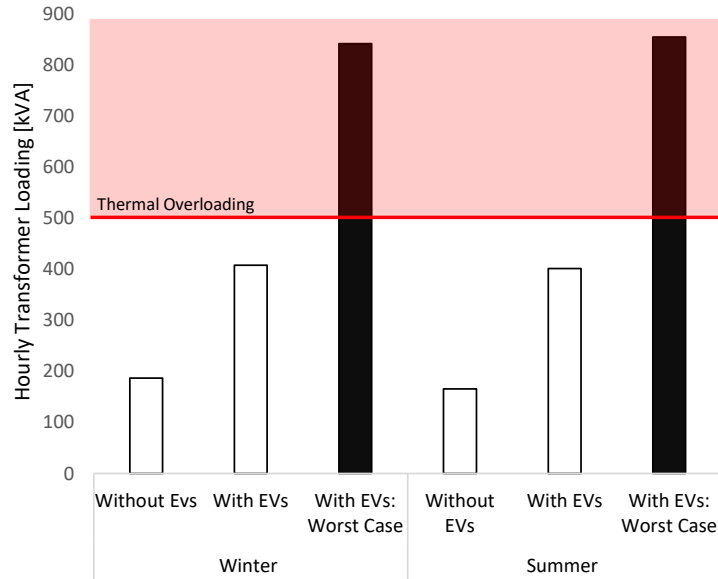


Figure 11. Hourly transformer loading for different cases in two seasons.

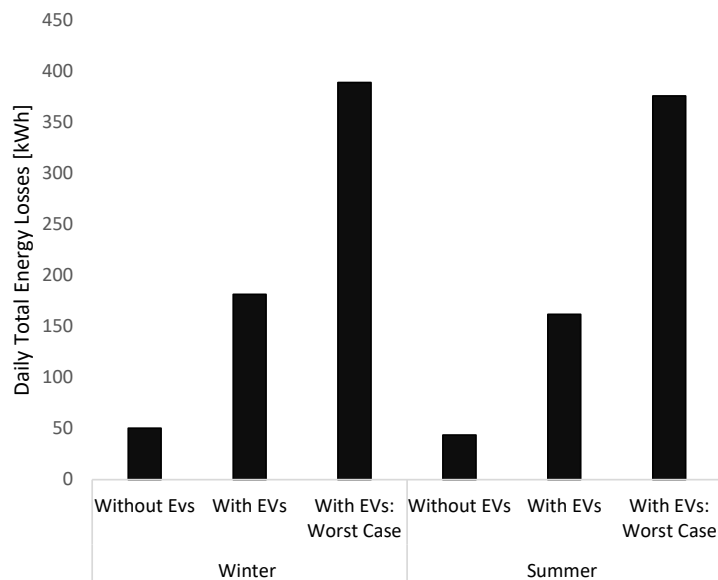


Figure 12. Daily energy losses for different cases in two seasons.

It is noteworthy to highlight that total daily energy losses are to be significantly low compared to total energy drawn by households.



### 3.2. Discussion

As demonstrated by the results, the impact of EVs on the households and network level depends on seasonality and instances in which how EVs are engaged in the network.

Although impact analysis may be computed from different perspectives, the proposed methodology and formulated performance indicators could be used to assess the impact in a more realistic manner by adopting timely analysis, real-time control of networks and EVs, etc. The resolution of profiles is also key to computing performance indicators, as the realistic manner of calculating voltage issues depends on the average 10-min voltage profile according to BS EN50160.

From a planning/operational perspective, the methodology considers the extent to which feeders are prone to voltage/utilization problems and when the solution could be required to cope with eminent technical problems.

Despite most DNOs currently having little or no measurements from the customers and/or network points, publicly available or generated high-resolution demand profiles can be used to conduct this analysis.

The identical connection time case (worst-case scenario) poses technical problems such as voltage problems, utilization of feeders, and thermal overloading of the transformer. Therefore, DNOs are to be ready for this case even if no technical problem is posed by their networks currently. While this scenario is highly unlikely to occur under normal circumstances, it remains a possibility to occur under some circumstances (e.g., in the aftermath of sports activities in some neighborhoods). This could pave the way for greater investment in charging stations at workplaces and malls. Another topic that deserves to be discussed is the interoperability of EVs with other technologies, such as energy storage systems, to diminish the potential reverse impact on the network.

Additionally, the methodologies developed to enhance hosting capacity in low-voltage (LV) networks with photovoltaic (PV) systems can be extended to the domain of LV networks with electric vehicles (EVs). These include network reconfiguration, the deployment of battery energy storage systems (BESS) to support LV feeders hosting both PVs and EVs, and the implementation of demand response strategies [37–41].

## 4. CONCLUSION

In this study, the participation of EVs in the real LV network is studied. A pool of EV profiles is generated from real-world statistics. Under three different scenarios, the impact of EVs on the LV networks is investigated in a comprehensive manner considering household voltage profile, the network transformer loading, utilization feeders, and daily total energy losses. Without EVs, with EVs and worst-case scenarios for summer and winter are considered to cover all possible circumstances.

For scalability purposes, all performance indicators are formulated to be used in a straightforward/practical manner by researchers and/or DNOs. Taking into account that the share of electric vehicles will increase in the years to come, the formulated performance indicators promote a smoother transition to this new form of demand at a residential level as imminent problems can be computed and the corresponding solution could be put in place.

The presented case study exemplifies the computation of the formulated performance indicators that could be adopted to any network. The study suggests that diversifying the connection times of EVs is vital to coping with potential problems posed by residential-level EV participation. Therefore, incentivizing householders to shift the connection time of their EVs into the grid could be a potential solution.

### Declaration of Ethical Standards

The author followed all ethical guidelines including authorship, citation, data reporting, and publishing original research.

### Credit Authorship Contribution Statement

The author is responsible for conceptualization, methodology, software, formal analysis, discussion of the results, writing, reviewing, and editing of the manuscript.

### Declaration of Competing Interest

The author declares no conflict of interest.

### Funding / Acknowledgements

The author declares no funding or research grants received in the course of study, research, or assembly of the manuscript.

### 5. REFERENCES

- [1] S. Lopez, "Record €60bn investment in electric cars and batteries in Europe secured last year," T&E. Accessed: Apr. 19, 2024. [Online]. Available: <https://www.transportenvironment.org>
- [2] D. Hall, S. Wappelhorst, P. Mock, and N. Lutsey, "European Electric Vehicle Factbook 2019/2020," *The International Council On Clean Transportation*, p. 19, 2020.
- [3] International Energy Agency, "Global EV Outlook 2021 - Accelerating ambitions despite the pandemic," *Global EV Outlook 2021*. [Online]. Available: <https://iea.blob.core.windows.net/assets/ed5f4484-f556-4110-8c5c-4ede8bcba637/GlobalEVOutlook2021.pdf>
- [4] L. Pieltain Fernández, T. Gómez San Román, R. Cossent, C. Mateo Domingo, and P. Frías, "Assessment of the impact of plug-in electric vehicles on distribution networks," *IEEE Transactions on Power Systems*, vol. 26, no. 1, pp. 206–213, 2011, doi: 10.1109/TPWRS.2010.2049133.
- [5] M. A. Awadallah, B. N. Singh, and B. Venkatesh, "Impact of EV Charger Load on Distribution Network Capacity: A Case Study in Toronto," *Canadian Journal of Electrical and Computer Engineering*, vol. 39, no. 4, pp. 268–273, 2016, doi: 10.1109/CJECE.2016.2545925.
- [6] H. Sun *et al.*, "Review of Challenges and Research Opportunities for Voltage Control in Smart Grids," *IEEE Transactions on Power Systems*, vol. 34, no. 4, pp. 2790–2801, 2019, doi: 10.1109/TPWRS.2019.2897948.
- [7] W. J. Nacmanson, J. Zhu, and L. F. Ochoa, "Assessing the unmanaged EV hosting capacity of Australian rural and urban distribution networks," *IET Conference Proceedings*, vol. 2022, no. 3, pp. 681–685, Jun. 2022, doi: 10.1049/icp.2022.0795.
- [8] S. Cuddihy and B. Hatton, "UK power networks engineering design standard eds 08-0136: LV network design," *UK Power Networks*, 2015.
- [9] M. Liu and M. Sahraei-Ardakani, "Chance-Constrained Shrunken-Primal-Dual Subgradient (CC-SPDS) Approach for Decentralized Electric Vehicle Charging Control," *2019 IEEE PES Innovative Smart Grid Technologies Asia, ISGT 2019*, pp. 1520–1525, 2019, doi: 10.1109/ISGT-Asia.2019.8881381.
- [10] X. Zhang, Z. Wang, and Z. Lu, "Multi-objective load dispatch for microgrid with electric vehicles using modified gravitational search and particle swarm optimization algorithm," *Appl Energy*, vol. 306, no. PA, p. 118018, 2022, doi: 10.1016/j.apenergy.2021.118018.
- [11] M. Lotfi, T. Almeida, M. S. Javadi, G. J. Osório, C. Monteiro, and J. P. S. Catalão, "Coordinating energy management systems in smart cities with electric vehicles," *Appl Energy*, vol. 307, no. October 2021, p. 118241, 2022, doi: 10.1016/j.apenergy.2021.118241.
- [12] J. Zhao, J. Wang, Z. Xu, C. Wang, C. Wan, and C. Chen, "Distribution Network Electric Vehicle Hosting Capacity Maximization: A Chargeable Region Optimization Model," *IEEE Transactions on Power Systems*, vol. 32, no. 5, pp. 4119–4130, 2017, doi: 10.1109/TPWRS.2017.2652485.

- [13] O. Hafez and K. Bhattacharya, "Optimal PHEV charging in coordination with distributed generation operation in distribution systems," *IEEE Power and Energy Society General Meeting*, 2012, doi: 10.1109/PESGM.2012.6345320.
- [14] P. Wang, S. Zou, and Z. Ma, "A partial augmented lagrangian method for decentralized electric vehicle charging in capacity-constrained distribution networks," *IEEE Access*, vol. 7, pp. 118229–118238, 2019, doi: 10.1109/ACCESS.2019.2935020.
- [15] W. Qi, Z. Xu, Z. J. M. Shen, Z. Hu, and Y. Song, "Hierarchical coordinated control of plug-in electric vehicles charging in multifamily dwellings," *IEEE Trans Smart Grid*, vol. 5, no. 3, pp. 1465–1474, 2014, doi: 10.1109/TSG.2014.2308217.
- [16] M. Liu, P. K. Phanivong, Y. Shi, and D. S. Callaway, "Decentralized charging control of electric vehicles in residential distribution networks," *IEEE Transactions on Control Systems Technology*, vol. 27, no. 1, pp. 266–281, 2019, doi: 10.1109/TCST.2017.2771307.
- [17] C. G. Veloso, K. Rauma, J. Fernández, and C. Rehtanz, "Real-time control of plug-in electric vehicles for congestion management of radial lv networks: A comparison of implementations," *Energies (Basel)*, vol. 13, no. 6, pp. 1–19, 2020, doi: 10.3390/en13164227.
- [18] J. Quiros-Tortos, L. F. Ochoa, S. W. Alnaser, and T. Butler, "Control of EV Charging Points for Thermal and Voltage Management of LV Networks," *IEEE Transactions on Power Systems*, vol. 31, no. 4, pp. 3028–3039, Jul. 2016, doi: 10.1109/TPWRS.2015.2468062.
- [19] S. Shafiq, B. Khan, P. Raussi, and A. T. Al-Awami, "A novel communication-free charge controller for electric vehicles using machine learning," *IET Smart Grid*, vol. 4, no. 3, pp. 334–345, 2021, doi: 10.1049/stg2.12032.
- [20] E. Vega-Fuentes and M. Denai, "Enhanced Electric Vehicle Integration in the UK Low-Voltage Networks With Distributed Phase Shifting Control," *IEEE Access*, vol. 7, pp. 46796–46807, 2019, doi: 10.1109/ACCESS.2019.2909990.
- [21] J. Pablo Carvallo *et al.*, "A framework to measure the technical, economic, and rate impacts of distributed solar, electric vehicles, and storage," *Appl Energy*, vol. 297, no. April, p. 117160, 2021, doi: 10.1016/j.apenergy.2021.117160.
- [22] M. Muratori, "Impact of uncoordinated plug-in electric vehicle charging on residential power demand," *Nat Energy*, vol. 3, no. 3, pp. 193–201, 2018, doi: 10.1038/s41560-017-0074-z.
- [23] P. Rodríguez-Pajarón, A. Hernández, and J. V. Milanović, "Probabilistic assessment of the impact of electric vehicles and nonlinear loads on power quality in residential networks," *International Journal of Electrical Power and Energy Systems*, vol. 129, 2021, doi: 10.1016/j.ijepes.2021.106807.
- [24] R. C. Leou, C. L. Su, and C. N. Lu, "Stochastic analyses of electric vehicle charging impacts on distribution network," *IEEE Transactions on Power Systems*, vol. 29, no. 3, pp. 1055–1063, 2014, doi: 10.1109/TPWRS.2013.2291556.
- [25] Y. Mu, J. Wu, N. Jenkins, H. Jia, and C. Wang, "A Spatial-Temporal model for grid impact analysis of plug-in electric vehicles," *Appl Energy*, vol. 114, pp. 456–465, 2014, doi: 10.1016/j.apenergy.2013.10.006.
- [26] C. Dimas, G. Ramos, L. Caro, and A. C. Luna, "Parallel Computing and Multicore Platform to Assess Electric Vehicle Hosting Capacity," *IEEE Trans Ind Appl*, vol. 56, no. 5, pp. 4709–4717, 2020, doi: 10.1109/TIA.2020.3004287.
- [27] M. M. Rahman, E. A. Al-Ammar, H. S. Das, and W. Ko, "Comprehensive impact analysis of electric vehicle charging scheduling on load-duration curve," *Computers and Electrical Engineering*, vol. 85, 2020, doi: 10.1016/j.compeleceng.2020.106673.
- [28] M. S. Aydin, S. Alnaser, and S. Althaher, "Using OLTC-Fitted Distribution Transformer to Increase Residential PV Hosting Capacity: Decentralized Voltage Management Approach," *Energies (Basel)*, vol. 15, no. 13, p. 4836, Jul. 2022, doi: 10.3390/en15134836.
- [29] K. Qian, C. Zhou, M. Allan, and Y. Yuan, "Modeling of load demand due to EV battery charging in distribution systems," *IEEE Transactions on Power Systems*, vol. 26, no. 2, pp. 802–810, 2011, doi: 10.1109/TPWRS.2010.2057456.

- [30] M. S. Aydin, "Strategies for increasing hosting capacity in PV-rich LV feeders via radiality-imposed reconfiguration," *Sustainable Energy, Grids and Networks*, vol. 38, p. 101288, Jun. 2024, doi: 10.1016/j.segan.2024.101288.
- [31] I. Richardson and M. Thomson, "Integrated simulation of photovoltaic micro-generation and domestic electricity demand: a one-minute resolution open-source model," *Proceedings of the Institution of Mechanical Engineers, Part A: Journal of Power and Energy*, vol. 227, no. 1, pp. 73–81, Aug. 2012, doi: 10.1177/0957650912454989.
- [32] Office for National Statistic, "Statistical bulletin families and households , 2013," Office for National Statistic,UK.
- [33] P. Richardson, M. Moran, J. Taylor, A. Maitra, and A. Keane, "Impact of electric vehicle charging on residential distribution networks: An Irish demonstration initiative," in *22nd International Conference and Exhibition on Electricity Distribution (CIRED 2013)*, Institution of Engineering and Technology, 2013, pp. 0674–0674. doi: 10.1049/cp.2013.0873.
- [34] Nissan, "Nissan LEAF." Accessed: Feb. 18, 2024. [Online]. Available: <https://www.nissan.co.uk/vehicles/new-vehicles/leaf.html>
- [35] A. Navarro-Espinosa and L. F. Ochoa, "Probabilistic Impact Assessment of Low Carbon Technologies in LV Distribution Systems," *IEEE Transactions on Power Systems*, pp. 1–12, 2015. doi: 10.1109/TPWRS.2015.2448663.
- [36] P. Leather, "Distribution System Design Low Voltage Network," *Electricity North West Limited*, no. 6, 2015.
- [37] M. S. Aydin and S. Çiftçi, "Alçak gerilim şebekelerinde PV kaynaklı gerilim artışlarına karşı BESS kullanımının yerel ve merkezi kontrolörler aracılığıyla değerlendirilmesi," *Pamukkale University Journal of Engineering Sciences*, 2024, doi: 10.5505/pajes.2024.06432.
- [38] M. S. Aydin, "Investigating the Adoption of Ring Operation in LV Networks with PV Systems," Thesis, The University of Manchester, 2017. Accessed: Feb. 10, 2024. [Online]. Available: <https://www.escholar.manchester.ac.uk/uk-ac-man-scw:312239>
- [39] N. Shabbir *et al.*, "Enhancing PV hosting capacity and mitigating congestion in distribution networks with deep learning based PV forecasting and battery management," *Appl Energy*, vol. 372, p. 123770, Oct. 2024, doi: 10.1016/j.apenergy.2024.123770.
- [40] F. Ahmed, A. Arshad, A. U. Rehman, M. H. Alqahtani, and K. Mahmoud, "Effective incentive based demand response with voltage support capability via reinforcement learning based multi-agent framework," *Energy Reports*, vol. 12, pp. 568–578, Dec. 2024, doi: 10.1016/j.egy.2024.06.036.
- [41] U. Azhar, M. Rizwan, W. Shen, and M. Korke, "Performance Analysis of a Low Voltage Distribution Network in Pakistan under High Penetration of Rooftop Solar PV Systems," in *2022 IEEE PES 14th Asia-Pacific Power and Energy Engineering Conference (APPEEC)*, IEEE, Nov. 2022, pp. 1–6. doi: 10.1109/APPEEC53445.2022.10072154.



## OPTIMIZATION OF SHEAR AND PEEL STRESSES IN DOUBLE-L-BRACKET JOINTS USING RESPONSE SURFACE METHODOLOGY

\* Bertan BEYLERGİL 

*Alanya Alaaddin Keykubat University, Engineering Faculty, Mechanical Engineering Department, Alanya,  
TÜRKİYE*

[bertan.beylergil@alanya.edu.tr](mailto:bertan.beylergil@alanya.edu.tr)

### *Highlights*

- Optimized shear and peel stresses in double-L-bracket joints using RSM.
- Key factors: joint height, arm lengths, adhesive thickness, shear, and peel forces.
- Reduced L2 and increased Tg minimized both shear and peel stresses effectively.
- Box-Behnken Design generated predictive models with high accuracy (99.8% variance).
- Findings offer design insights for stronger adhesive joints.



## OPTIMIZATION OF SHEAR AND PEEL STRESSES IN DOUBLE-L-BRACKET JOINTS USING RESPONSE SURFACE METHODOLOGY

\* Bertan BEYLERGİL

*Alanya Alaaddin Keykubat University, Engineering Faculty, Mechanical Engineering Department,  
Alanya, TÜRKİYE*  
[bertan.beylergil@alanya.edu.tr](mailto:bertan.beylergil@alanya.edu.tr)

(Received: 17.10.2024; Accepted in Revised Form: 07.02.2025)

**ABSTRACT:** This study aims to optimize the design parameters of a double-L-bracket joint using an analytical approach combined with Response Surface Methodology (RSM). The focus is on minimizing the joint's shear and peel stresses, which are critical for adhesive joint integrity. A Bigwood & Crocombe analytical model was employed to simulate the stress distributions in the joint under various geometrical configurations and loading conditions. Six factors, including joint height (H), vertical arm length (L1), horizontal arm length (L2), adhesive thickness (Tg), shear force (Fx), and peel force (Fz), were analyzed. A Box-Behnken Design (BBD) was used to generate 54 configurations, and the resulting stress responses were modeled through quadratic regression models. The analysis reveals that horizontal arm length (L2), adhesive thickness (Tg), and applied forces (Fx and Fz) significantly influence the stress levels in the joint. The optimization results indicate that reducing L2 and increasing Tg can effectively minimize both shear and peel stresses. The optimized configuration achieves a peel stress of 1.450 MPa and a shear stress of 2.120 MPa, both of which align closely with analytical predictions. The close agreement between RSM-based predictions and analytical calculations validates the robustness of the model. This optimization provides valuable insights for improving the structural performance of adhesive joints in practical applications.

**Keywords:** *Response Surface Methodology (RSM), Box-Behnken Design (BBD), Adhesive Joint Optimization, Double-L-Bracket Joint*

### 1. INTRODUCTION

The adhesive bonding technique, a cornerstone of modern engineering, presents enormous advantages in such ways that it can join dissimilar materials, distribute loads in a more uniform manner than that of mechanical fasteners, reducing stress concentration. However, complexity, especially its inherent susceptibility to peel and shear stresses, demands great understanding and optimization of the joints to ensure structural integrity and longevity. With the demands on lightweight and high-performance structures in aerospace, automotive, and civil engineering applications, there is an increasing need for optimization of adhesive bonding [1-3].

In the process of optimizing and evaluating adhesive bonding, statistical methodologies have proved to be very important tools for engineers to investigate complex design spaces while highlighting the most feasible bonding configuration. While these methods improve mechanical performance in adhesive joints, they also have a tendency to give highly reduced material consumption and manufacturing costs, hence being greatly advantageous in both academic research and industrial applications. These approaches permit the determination of the bonding conditions which minimize the risk of failure, by systematically exploring a number of design factors such as adhesive thickness and overlap length, including material properties.

\*Corresponding Author: Bertan BEYLERGİL, [bertan.beylergil@alanya.edu.tr](mailto:bertan.beylergil@alanya.edu.tr)

For example, da Silva et al. [4] took a statistical approach by using the Taguchi method to investigate adhesive type and thickness on lap shear strength in single-lap joints. The authors could quantify the relative importance of these variables by testing three adhesives with distinct levels of ductility and three different bondline thicknesses: 0.2 mm, 0.5 mm, and 1 mm. The ANOVA test showed adhesive thickness and toughness to be the most influencing factors on joint strength, with adhesive thickness having a slightly higher effect. The statistical approach yielded a predictive model for lap shear strength based on the properties of adhesives. In a similar vein, Kim et al. [5] coupled the mixed-mode continuum damage model with the Taguchi method and Response Surface Methodology (RSM) to investigate the failure characteristics of functionally graded adhesive bonded joints. Their analysis identified the adhesive shear strength as the most influential factor on failure load, and RSM was used in developing a predictive model that determines the optimal parameters to enhance joint load-bearing capacity.

In another research, Vieira et al. [6] employed the Taguchi method for optimizing tensile performance in adhesively bonded rod-tube joints. The study investigated geometric factors such as overlap length, tube thickness, rod diameter, and adhesive fillet angle, and also investigated adhesive type. ANOVA described overlap length and adhesive type as the most important variables affecting performance. The Taguchi method reduced the number of experiments, and this research is far more effective in analyzing each factor's effect on joint strength, arriving at an optimum design for structural applications. Similarly, Mandolino et al. [7] applied RSM combined with a Face-centered Central Composite Design to investigate the optimization of adhesive bonding in pulsed laser-treated CFRP composites. The statistical methodology pursued the best parameters for laser treatment concerning power, pitch, and lateral overlap affecting the TSS of adhesive joints. Using ANOVA, the significance of each factor and their interactions was tested, after which statistical models useful in the prediction of joint performance against parameter combinations that have not been previously tested were developed, hence optimizing the process at reduced energy consumption.

The effect that adhesive thickness has on the mechanical performance and reliability of structural adhesive joints was studied by Arenas et al. [8] using statistical techniques based on the Weibull distribution. The tensile shear strength they analyzed with respect to different thicknesses of adhesives indicated that thinner adhesives, in general, may develop a higher strength due to fewer defects. In another study, Wang and Zeng [9] utilized RSM with the Box-Behnken design in the optimization of particle-reinforced adhesive joints. ANOVA was done to check parameters like the size of the particles, thickness of the adhesive layer, and mass fraction in respect of failure load and energy absorption. The results indicated that the particle size had the most significant impact on failure loading, while mass fraction represented the most influencing factor with regard to energy absorption. It is statistically analyzed in order to develop predictive models for the optimization of joint performance..

Ariaee et al. [10] applied RSM and Central Composite Rotatable Design (CCRD) to optimize the mechanical performance of the composite-steel single-lap joints. In their case study, curing time and temperature were the selected key factors, while the authors developed mathematical models for the prediction of the shear strength and elongation. ANOVA confirmed curing temperature was indeed the most important variable that dictates joint strength, a methodology which allowed optimizing the adhesive bonding process, and experimental validation proved the accuracy of the predicted values. Besides, Kraisornkachit et al. [11] have introduced active learning and machine learning-based multi-objective optimization approach to optimize the adhesive joint strength and elastic modulus in epoxy adhesives. Their study adopted a methodology of training the machine learning model with 32 experimental conditions, which validated the accuracy using K-fold cross-validation and

statistical analysis mainly by Bayesian optimization to study the trade-off involving adhesive strength and modulus.

Optimum failure load, production time, and mass in adhesively bonded 3D-printed single lap joints were investigated by Ozturk [12] using the RSM method. It was found that OL had the most dominant factor in failure load, and AT had a great influence on the production of time and mass. To this end, ANOVA and CCD were further carried out to optimize the performances of the joints with the least production time and utilization of materials. In a related vein, Gorgun [13] applied the BB design in addition to ANOVA in order to obtain the optimum bonding conditions for thermoplastic adhesive joints. The study examined variables such as the mixing ratio, curing time, and primer application, and obtained a quadratic model that can make an accurate prediction of bond performance. Validity was further supported by the high values of the R-squared and the significant F-values..

Sutherland et al. [14] utilized statistical experimental design procedures such as ANOVA to determine the strength of adhesively bonded T-joints commonly used in marine composite structures. They studied the influence of the level of surface preparation, cleaning methods, and types of adhesives on joint strength. The statistical analysis showed that there were large interactions among these factors. The complex relationships of the factors in interaction plots were presented in a useful way, enabling the derivation of practical recommendations for real adhesive joint optimization in marine applications. Finally, the work by Haddou et al. [15], applied full factorial DOE to optimize the strength of notched single-lap adhesive joints. The authors documented that the adhesive thickness was the most influential factor on joint strength with the largest contribution ratio of 58.81% to its overall performance. The notch depth and extension also played an important role, and a quadratic regression model was developed to predict the optimum joint strength.

Cetin and Fossi [16] introduced the optimization of hygrothermal mechanical strength of adhesively bonded 3D-printed joints with the Taguchi method, in this work, the effects of surface patterns, adhesive types, and aging durations on lap shear strength were evaluated with a Taguchi L16 orthogonal array. From the ANOVA analysis, adhesive type was found as the most effective factor with 60.76%, followed by the aging duration factor with 23.62%. Regression analysis confirmed the experimental results and proved that the Taguchi method was efficient in optimizing adhesive joint performance under environmental stressors.

Analytical models play a crucial role in understanding stress distributions within the adhesive layer, with the Bigwood and Crocombe model [17] being widely recognized for its ability to predict shear and peel stresses accurately in various joint configurations. Abbasi et al. [18] investigated the effectiveness of the backface strain (BFS) method in detecting damage initiation and propagation in composite single-lap joints (SLJs). They utilized the Bigwood and Crocombe analytical model to explain the presence of the zero strain point (ZSP) on the backface of the joint and correlated the experimental findings with the analytical predictions. Their results demonstrated the capability of this model to predict stress distributions under varying adhesive types and joint dimensions. Similarly, Abbasi et al. [19] analyzed the effect of bonding area dimensions on the mechanical behavior of SLJs, employing the Bigwood and Crocombe model to estimate shear and peel stress distributions. Their findings highlighted the model's utility in assessing the influence of joint width, overlap length, and adherend thickness on load capacity and failure mechanisms. Goglio et al. [20] conducted an experimental study on the impact rupture of adhesively bonded joints under different stress combinations, incorporating the Bigwood and Crocombe model to evaluate the shear and peel stresses under dynamic loading conditions. Their work demonstrated the model's robustness in predicting failure under combined loading scenarios.

Weißgraeber et al. [21] proposed a general sandwich-type analytical model for adhesive joints with composite adherends, extending the Bigwood and Crocombe model by



incorporating First Order Shear Deformation Theory (FSDT) to account for shear deformations in fiber-reinforced plastic (FRP) adherends. Their study provided a more comprehensive understanding of stress distributions in various joint configurations. Domínguez et al. [22] focused on hybrid joints between fiber-reinforced plastic (FRP) and steel panels reinforced with tubular structures. They applied the Bigwood and Crocombe model to estimate interlaminar stresses and validate the analytical predictions against finite element analysis (FEA) results. Momm and Fleming [23] employed the Bigwood and Crocombe model to investigate adhesive degradation effects in real-life bonded joints exposed to environmental conditions. Their study incorporated adhesive plasticity and aging effects into the model, providing a comprehensive approach to stress analysis under non-pristine conditions. Methfessel and Becker [24] applied the Bigwood and Crocombe model in a higher-order displacement approach for thick adhesive joints. The model was used to estimate stress distributions across the adhesive thickness, showing improved accuracy compared to traditional thin-layer assumptions. Wang et al. [25] adopted the Bigwood and Crocombe model to analyze adhesive joint strength with adherend yielding effects. They modified the model to accommodate nonlinear adherend behavior, allowing for better predictions of joint performance under high-load conditions.

da Silva et al. [26] compared elastic and nonlinear adhesives using the Bigwood and Crocombe model. The research demonstrated that the model could be extended to nonlinear adhesives and effectively capture the impact of different adhesive thicknesses on stress distribution. Additionally, the study assessed the computational efficiency of the model, highlighting its advantages in terms of preparation and solution time compared to more complex numerical methods. In another study, da Silva et al. [27] conducted a comprehensive review of analytical models for adhesively bonded joints, with a particular focus on the Bigwood and Crocombe model. The study evaluated the model's applicability under various adhesive types and loading conditions. The Bigwood and Crocombe model was found to be effective in predicting stress distributions by considering the combined effects of axial loads and bending moments. The study provided valuable insights into the practical application of the model in the design process of adhesive joints.

This study makes a significant contribution by integrating the Bigwood and Crocombe analytical model with Response Surface Methodology (RSM) to optimize the performance of double-L-bracket adhesive joints, specifically by minimizing shear and peel stresses. While extensive research has been conducted on stress distribution in adhesive joints, the novelty of this work lies in the application of RSM alongside an analytical model tailored to this specific joint configuration. This study presents a comprehensive regression model that not only predicts stress responses but also identifies optimal design configurations by systematically analyzing key parameters, including joint height, vertical and horizontal arm lengths, adhesive thickness, and applied loads. RSM provides a robust framework for simultaneously evaluating multiple design factors and developing quadratic regression models, which effectively capture the interactions between these parameters in influencing shear and peel stresses. Notably, the methodology highlights horizontal arm length as the most critical factor affecting joint performance, offering practical design guidelines that engineers can adopt to enhance structural integrity. The proposed optimization approach has been validated through a strong correlation between RSM predictions and analytical calculations, reinforcing its reliability and practical applicability.

Beyond enhancing joint performance, the proposed approach delivers substantial industrial benefits by providing a systematic method to optimize material usage, reduce production costs, and extend the service life of bonded structures under varying environmental conditions. This study supports the development of lightweight, high-strength adhesive structures that align with the growing industry demands for sustainability and efficiency in manufacturing processes. Furthermore, the insights gained from this research can be directly

implemented in real-world applications, empowering engineers to make informed decisions in design and production, ultimately resulting in safer and more reliable engineering solutions across various sectors, including aerospace, automotive, and civil engineering.

## 2. PROBLEM DEFINITION

The objective of this study is to optimize the design parameters of a double-L-bracket joint through an analytical approach, with a particular focus on minimizing the joint's shear and peel stresses. The shear and peel stress values were calculated using the CalcBond software [28], which employs the Bigwood-Crocombe analytical model to determine stress distributions through theoretical formulations. Providing an efficient computational framework, CalcBond facilitates accurate predictions by considering key parameters such as adhesive thickness, material properties, and loading conditions. Its capability to generate detailed stress distribution profiles enables a comprehensive understanding of joint behavior, significantly contributing to the optimization process and allowing for further analysis of the effects of various design parameters on joint performance [28]. By leveraging the Response Surface Methodology (RSM), the effects of various geometric parameters and loading conditions on the stress distribution in the joint are thoroughly investigated.

Figure 1 provides a detailed schematic of the double-L-bracket joint configuration used in this study. The total height of the joint ( $H$ ) is defined as the distance from the bottom of the vertical arm to the top of the horizontal arm, and is varied between 70 mm, 80 mm, and 90 mm. The lengths of the vertical arm ( $L1$ ) and the horizontal arm ( $L2$ ) are also varied, with each parameter taking values of 10 mm, 20 mm, and 30 mm. The thickness of the adhesive layer ( $Tg$ ) between the two brackets is another critical parameter, with values of 0.1 mm, 0.2 mm, and 0.3 mm analyzed. The forces applied to the lower arm—namely the shear force ( $F_x$ ) and the peel force ( $F_z$ )—are varied at 50 N, 75 N, and 100 N. The upper arm of the joint remains fixed, while these forces are applied to the lower arm to simulate realistic loading conditions.

Table 1 outlines the mechanical properties of the materials used in the joint. The adherends are made of aluminum with a thickness of 3 mm, an elastic modulus of 70 GPa, and a Poisson's ratio of 0.3. The adhesive used to bond the brackets is Araldite 2014-2, which has an elastic modulus of 3200 MPa, a shear modulus of 0.56 GPa, and a Poisson's ratio of 0.32.

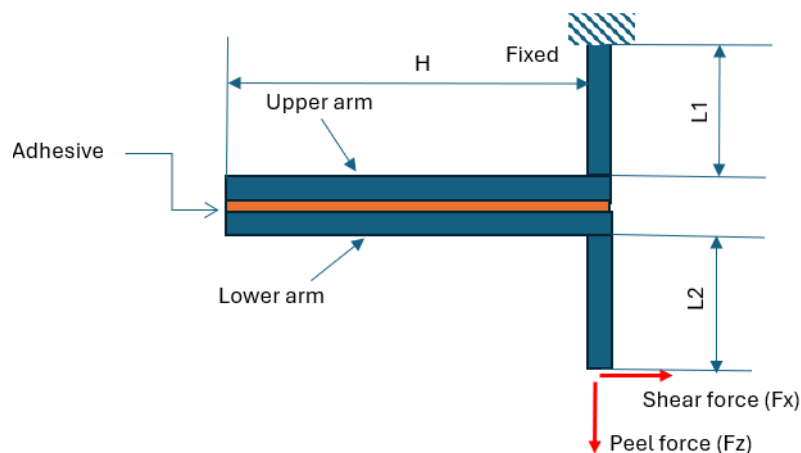


**Figure 1.** The configuration of double-L-bracket joint

**Table 1.** Mechanical properties [29, 30]

	Unit	Adherend	Adhesive
		Aluminum	Araldite 2014-2
Elastic modulus (E, GPa)	GPa	70	3.2
Shear Modulus ( $G_a$ )	GPa	25	0.56
Poisson's ratio ( $\nu$ .-)	-	0.3	0.32

### 3. RESPONSE SURFACE METHODOLOGY (RSM) DESIGN

In the context of this study, Response Surface Methodology (RSM) is employed as a powerful statistical and mathematical tool to optimize the design parameters of a double-L-bracket joint. The primary objective is to identify the optimal combination of design variables that minimize both shear and peel stresses, which are critical failure modes in adhesive joints. To systematically investigate the effects of various design parameters on stress responses, a Box-Behnken Design (BBD) is selected as the experimental design framework. BBD is a popular form of RSM, specifically chosen for its efficiency in exploring quadratic response surfaces. It provides an effective means of conducting experiments or simulations when the aim is to build a second-order polynomial model. Unlike other design methods such as central composite design (CCD), BBD does not require experiments to be run at extreme levels (corners) of the design space, which makes it particularly suitable for cases where such conditions may be impractical or unsafe.

The design includes 54 experimental runs (Table 2), each experimental run corresponds to a specific combination of the six factors, and for each run, the shear and peel stresses are calculated using the Bigwood Crocombe analytical model. These calculated stresses are then used as response variables in the subsequent regression analysis, which aims to develop a predictive model for both shear and peel stresses. For example, in Run 7, a configuration with  $H = 80$  mm,  $L1 = 30$  mm,  $L2 = 30$  mm,  $Tg = 0.2$  mm,  $Fx = 100$  N, and  $Fz = 75$  N results in a shear stress of 13.4 MPa and a peel stress of 2.7 MPa.

**Table 2.** Design of Experiments (DOE) for Shear and Peel Stress Evaluation

DOE	H	L1	L2	Adhesive thickness	Fx	Fz	Shear stress	Peel stress
1	80	10	20	0.2	50	50	4.5	1.6
2	80	20	10	0.1	75	50	5.0	2.5
3	90	30	20	0.3	75	75	5.5	2.1
4	80	10	30	0.2	50	75	6.7	2
5	70	30	20	0.1	75	75	9.6	3
6	90	10	20	0.3	75	75	5.5	2.1
7	80	30	30	0.2	100	75	13.4	2.7
8	80	10	10	0.2	50	75	2.3	2.1
9	80	30	10	0.2	50	75	2.3	2.1
10	70	20	20	0.3	100	75	7.3	2.4
11	70	10	20	0.3	75	75	5.5	2.1
12	90	20	30	0.2	75	100	10.1	2.8
13	70	20	10	0.2	75	100	3.5	2.8
14	80	20	30	0.1	75	50	14.3	2.4
15	90	20	30	0.2	75	50	10.1	1.9
16	80	20	20	0.2	75	75	6.8	2.4
17	80	10	20	0.2	50	100	4.5	2.5
18	80	30	30	0.2	50	75	6.7	2
19	80	30	10	0.2	100	75	4.7	2.7
20	70	20	20	0.1	50	75	6.4	2.5

21	80	20	20	0.2	75	75	6.8	2.4
22	80	30	20	0.2	50	100	4.5	2.5
23	90	20	20	0.3	50	75	3.7	1.8
24	70	20	10	0.2	75	50	3.5	1.9
25	80	30	20	0.2	100	50	9.0	2.3
26	70	20	30	0.2	75	50	10	1.9
27	80	20	10	0.3	75	50	2.9	1.7
28	80	10	20	0.2	100	50	9.0	2.3
29	90	20	20	0.3	100	75	7.4	2.4
30	70	20	30	0.2	75	100	10	2.8
31	80	20	20	0.2	75	75	6.8	2.4
32	80	10	20	0.2	100	100	9.0	3.2
33	80	20	30	0.3	75	100	8.2	2.5
34	80	20	20	0.2	75	75	6.8	2.4
35	70	20	20	0.1	100	75	12.8	3.4
36	90	20	10	0.2	75	100	3.5	2.8
37	80	20	20	0.2	75	75	6.8	2.4
38	80	20	30	0.3	75	50	8.2	1.7
39	90	20	10	0.2	75	50	3.5	1.9
40	80	10	10	0.2	100	75	4.7	2.7
41	80	20	10	0.3	75	100	2.9	2.5
42	70	20	20	0.3	50	75	3.7	1.8
43	80	30	20	0.2	50	50	4.5	1.6
44	90	20	20	0.1	100	75	12.9	3.5
45	70	10	20	0.1	75	75	9.6	3
46	80	20	20	0.2	75	75	6.8	2.4
47	90	20	20	0.1	50	75	6.4	2.6
48	90	10	20	0.1	75	75	9.7	3
49	70	30	20	0.3	75	75	5.5	2.1
50	80	20	10	0.1	75	100	5.0	3.6
51	90	30	20	0.1	75	75	9.7	3
52	80	20	30	0.1	75	100	14.3	3.5
53	80	10	30	0.2	100	75	13.4	2.7
54	80	30	20	0.2	100	100	9.0	3.2

The model generated from the BBD data is evaluated based on multiple statistical metrics, including R-squared, adjusted R-squared, and predicted R-squared values, as well as the significance of individual model terms (linear, interaction, and quadratic). The ANOVA (Analysis of Variance) results are also used to assess the model's overall fit and the significance of each design factor. The use of BBD in conjunction with RSM enables the identification of key design variables that have the most significant effects on shear and peel stresses. This insight allows for targeted optimization, reducing the likelihood of failure in the joint due to excessive stresses.

## 4. RESULTS and DISCUSSION

### 4.1. Analysis of Variance (ANOVA) Results for Shear and Peel Stress

#### 4.1.1. Shear stress ANOVA

Supplementary Table 1 shows the ANOVA results for shear stress, revealing that the model explains 99.79% of the total variance in the response. This exceptionally high  $R^2$  value demonstrates the robustness of the model in capturing the behavior of shear stress in the joint. The linear terms contribute significantly to the model, with L2 (horizontal arm length), Fx (shear

force), and adhesive thickness (Tg) standing out as the most important factors. The F-values for these terms are extremely high, particularly for L2 (6407.20), Tg (2348.24), and Fx (3060.88), indicating that these parameters have a pronounced effect on the shear stress response. The P-values for these factors are 0.000, underscoring their statistical significance in the model. In terms of interactions, the results also highlight significant two-way interactions between L2 and Tg ( $F = 184.75$ ,  $P = 0.000$ ) and Tg and Fx ( $F = 90.53$ ,  $P = 0.000$ ). These interactions suggest that while increasing L2 raises the shear stress, the effect can be moderated by increasing adhesive thickness, which distributes the stress more effectively. Similarly, the interaction between Tg and Fx shows that a thicker adhesive layer reduces the stress concentrations caused by higher shear forces. These interaction effects emphasize the complex, non-linear relationships between design parameters and stress responses in the joint. The lack-of-fit test indicates no significant lack of fit ( $P = 0.21$ ), confirming that the model accurately represents the data and does not miss any critical trends. The small error term (0.21%) further enhances confidence in the model's predictive capability.

#### 4.1.2 Peel Stress ANOVA

Supplementary Table 2 presents the ANOVA results for peel stress, showing that the model explains 99.83% of the total variance. Similar to the shear stress model, the peel stress model exhibits a high level of statistical reliability, with an  $R^2$  value indicating that nearly all of the variability in peel stress is captured by the model. The linear effects of Fz (peel force), Tg (adhesive thickness), and L2 (horizontal arm length) are the most significant contributors to the peel stress response. The F-values for Fz (5825.93), Tg (5616.00), and L2 (7.70) indicate the strength of their influence on peel stress, with P-values of 0.000, affirming their importance. Peel force (Fz) is the dominant factor in the model, as expected, given that peel stress directly arises from forces applied perpendicular to the adhesive bond. The large F-value and corresponding low P-value underscore that any increase in Fz leads to a substantial rise in peel stress. The adhesive thickness (Tg) also plays a critical role, with a large negative coefficient indicating that increasing the thickness of the adhesive layer effectively reduces peel stress by distributing the applied forces more evenly. The interaction effects for peel stress, while not as pronounced as those for shear stress, still show significant relationships. For example, the interaction between L2 and Tg ( $F = 5.78$ ,  $P = 0.024$ ) demonstrates that reducing horizontal arm length can help mitigate peel stress, particularly when combined with a thicker adhesive layer. Moreover, the interaction between Tg and Fx ( $F = 52.00$ ,  $P = 0.000$ ) suggests that a thicker adhesive layer can offset the increase in peel stress caused by higher shear forces, although the primary influence on peel stress remains Fz. The model also passes the lack-of-fit test ( $P = 0.17$ ), confirming that it provides an accurate fit to the experimental data. The residual error is minimal, accounting for only 0.17% of the total variation, further supporting the model's reliability in predicting peel stress in double-L-bracket joints.

## 4.2. Regression Models for Shear and Peel Stress

### 4.2.1. Shear Stress Regression Model

The regression model for shear stress was developed using Response Surface Methodology (RSM), with six factors (H, L1, L2, Tg, Fx, Fz) included as predictors. The model was constructed to predict the shear stress response as a function of these parameters, and its statistical performance was evaluated through various metrics, including the significance of individual terms, model fit, and residual analysis. The regression equation for shear stress is provided in the supplementary document as Eq. (1).

The coded coefficients from the regression model, presented in Supplementary Table 3, highlight the key factors influencing shear stress. Notably, the most significant term is the horizontal arm length (L2), with a large positive coefficient (3.4000) and a highly significant T-value (80.04). This indicates that increasing L2 has a strong positive effect on shear stress. Physically, this can be explained by the fact that a longer horizontal arm amplifies the moment arm for the applied forces, increasing the torque and thus the shear stress at the adhesive interface. This result is consistent with mechanical theory and reinforces the importance of carefully controlling L2 to prevent excessive shear forces in the joint.

Adhesive thickness (Tg) also plays a critical role in the model, with a substantial negative coefficient (-2.0583) and a T-value of -48.46. This negative sign indicates that increasing Tg reduces shear stress, which is a reflection of the adhesive's ability to absorb and distribute the applied forces more effectively as its thickness increases. A thicker adhesive layer allows for more elastic deformation, spreading the shear load over a larger area and reducing peak stress concentrations. This finding aligns with expectations from adhesive joint theory, where thicker bond lines are often associated with improved stress distribution and lower localized stresses.

The applied shear force (Fx) is another significant factor, with a positive coefficient (2.3500) and a T-value of 55.33. As expected, increasing Fx directly raises the shear stress in the joint, as the magnitude of the applied force determines the load borne by the adhesive layer. This result is particularly important for design applications where shear forces cannot be easily reduced, emphasizing the need for compensatory design strategies, such as increasing Tg or reducing L2, to offset the rise in stress caused by high shear forces.

In addition to the main effects, the regression model also includes interaction and quadratic terms to capture more complex relationships between the factors. For example, the interaction between L2 and Tg, with a coefficient of -1.0000 and a T-value of -13.59, indicates that the effect of L2 on shear stress is moderated by the adhesive thickness. This interaction suggests that while increasing L2 raises the shear stress, this effect is less pronounced when Tg is large. In other words, the detrimental impact of long horizontal arms can be mitigated by using thicker adhesive layers, which helps distribute the shear forces more evenly.

**Table 3.** Model Summary: Shear Stress and Peel Stress Regression Statistics

<b>Shear stress</b>						
S	R-sq	R-sq(adj)	PRESS	R-sq(pred)	AICc	BIC
0.208090	99.79%	99.58%	5.88190	98.92%	74.74	59.92
<b>Peel stress</b>						
S	R-sq	R-sq(adj)	PRESS	R-sq(pred)	AICc	BIC
0.0294174	99.83%	99.66%	0.117551	99.12%	-136.55	-151.37

Table 3 presents the model summary. The model fit is excellent, with an R-squared value of 99.79%, indicating that nearly all the variability in shear stress is explained by the model. The adjusted R-squared (99.58%) and predicted R-squared (98.92%) are similarly high, confirming that the model performs well both in fitting the training data and predicting new, unseen data. The low standard error (S = 0.208090) and the results from the analysis of variance (ANOVA) further support the model's reliability.

#### 4.2.2. Peel Stress Regression Model

Similar to the shear stress model, the peel stress regression model was developed using RSM and incorporates the same six factors (H, L1, L2, Tg, Fx, Fz). Peel stress, which arises when forces act perpendicular to the adhesive layer, is a key factor in joint failure modes, as adhesive bonds are typically weaker in tension than in shear. Thus, understanding the factors that

influence peel stress is critical for designing robust joints. The regression equation for shear stress is provided in the supplementary document as Eq. (2).

Supplementary Table 4 presents the coded coefficients for the peel stress regression model, with the peel force ( $F_z$ ) emerging as the most significant factor. The coefficient for  $F_z$  is positive (0.45833) and highly significant (T-value of 76.33), indicating that increasing  $F_z$  directly raises peel stress. This result is consistent with the physics of peel stress, where forces applied perpendicular to the bond line concentrate stress at the edges of the adhesive layer, making the joint susceptible to peeling or delamination. The strong influence of  $F_z$  suggests that minimizing peel forces in applications where peeling is a concern should be a primary design objective.

Adhesive thickness ( $T_g$ ) also plays a critical role in the peel stress model, with a large negative coefficient (-0.45000) and a highly significant T-value (-74.94). As in the shear stress model, increasing  $T_g$  reduces peel stress by allowing the adhesive to better absorb and distribute the applied forces. Thicker adhesive layers reduce the concentration of peel stresses at the edges of the bond line, where failures are most likely to initiate. This finding underscores the importance of optimizing  $T_g$  in applications where peel forces are expected, as it provides a straightforward method for reducing stress and enhancing joint durability. Interestingly, the horizontal arm length ( $L_2$ ) has a smaller, but still significant, negative effect on peel stress, with a coefficient of -0.01667 and a T-value of -2.78. This indicates that reducing  $L_2$  can help mitigate peel stress, although its impact is less pronounced than  $T_g$  or  $F_z$ . The physical interpretation of this result is that shorter horizontal arms reduce the leverage applied to the adhesive bond, thereby decreasing the tendency for the joint to peel under applied forces.

Quadratic terms and interactions are also included in the model to capture non-linear effects and the combined influence of multiple parameters. For example, the interaction between  $T_g$  and  $F_x$  has a significant negative coefficient (-0.0750), indicating that the effect of  $F_x$  on peel stress is moderated by the adhesive thickness. When  $T_g$  is large, the peel stress induced by  $F_x$  is less severe, reflecting the adhesive's improved ability to distribute the applied forces across a thicker bond line. This interaction highlights the complex nature of peel stress in multi-parameter systems and the need for a holistic approach to joint design.

The peel stress model also shows an excellent fit to the data (Table 3), with an R-squared value of 99.83% and similarly high adjusted and predicted R-squared values (99.66% and 99.12%, respectively). The low standard error ( $S = 0.0294174$ ) indicates that the model provides precise predictions of peel stress, while the results from the ANOVA confirm the statistical significance of the model as a whole.

The high significance of most terms in the model, as reflected by their low P-values and high T-values, indicates that the relationships between the input factors and peel stress are well-captured by the regression model. The model can be used to accurately predict peel stress under a wide range of joint configurations and offers valuable insights into the design strategies that can be employed to minimize peel stress.

### 4.3. Graphical Analysis and Visualization of Stress Responses

#### 4.3.1. Residual Analysis

Residual analysis is a fundamental tool in statistical modeling, used to validate the accuracy and reliability of regression models. The residuals represent the differences between observed values and the predicted values from the model. Proper residual analysis ensures that the model is unbiased, and it helps detect any systematic errors or patterns that may indicate a misfit.

In Figure 2 (a), the residual plot for shear stress shows a random distribution of residuals around zero, which is a key indicator that the regression model provides an unbiased and accurate prediction of the data. This randomness suggests that no patterns are present in the residuals, meaning that the model has successfully captured the relationship between the input parameters and the shear stress response. The absence of any clear trend, such as a funnel-shaped distribution or clustering of points, further indicates that the model does not suffer from heteroscedasticity, where the variance of the residuals would depend on the magnitude of the predicted values. This is critical for the validity of the model, as heteroscedasticity can lead to biased estimates and affect the confidence intervals of the regression coefficients. Additionally, the spread of the residuals in Figure 2 (a) appears consistent across the range of predicted shear stress values, supporting the assumption of homoscedasticity. Homoscedasticity implies that the variance of the residuals is constant, reinforcing the reliability of the regression model. This property ensures that the model is equally effective in predicting shear stress across both lower and higher ranges, thereby improving the generalizability of the findings.

Similarly, the residual plot for peel stress in Figure 2 (b) displays a random scatter of residuals around zero, further validating the model's predictive accuracy for peel stress. The plot shows no discernible patterns or trends, confirming that the regression model is well-suited for predicting peel stress under varying configurations. The consistency in the spread of residuals also indicates that the model handles both small and large peel stress values equally well, with no indication of bias or distortion.

Residual analysis also aids in identifying potential outliers or influential data points that may disproportionately affect the regression model. In this study, there are no significant outliers present in either the shear or peel stress residual plots, further enhancing confidence in the robustness of the model. The lack of unusual residuals suggests that the dataset is well-behaved, and that the regression models are not unduly influenced by any extreme or erroneous observations. This conclusion is critical, as outliers can distort the regression coefficients and lead to incorrect conclusions.

Overall, the residual analysis confirms that the models for both shear and peel stress are reliable, unbiased, and appropriate for the given dataset. The lack of heteroscedasticity, combined with the random distribution of residuals, reinforces the statistical soundness of the regression models and supports their use for stress prediction in the double-L-bracket joint design.

#### 4.3.2. Pareto Charts of Standardized Effects

Pareto charts are an essential graphical tool for identifying the most influential factors in a regression model. By ranking the standardized effects of each factor, these charts provide a clear visualization of the relative importance of each design parameter in affecting the response variable. In this study, the Pareto charts for shear and peel stress highlight the key factors driving stress concentrations in the double-L-bracket joint.

Figure 3 (a) presents the Pareto chart for shear stress, which clearly demonstrates that the horizontal arm length ( $L_2$ ), adhesive thickness ( $T_g$ ), and shear force ( $F_x$ ) are the most significant contributors to shear stress. The bar corresponding to  $L_2$  is the tallest, indicating that it has the largest standardized effect on shear stress. This result is consistent with the theoretical expectation that longer horizontal arms increase the moment arm, thereby amplifying the shear forces acting on the adhesive layer. The high significance of  $L_2$  in the model underscores the need for careful control of this parameter in joint design to prevent excessive shear stress concentrations. The next most significant factor is adhesive thickness ( $T_g$ ), which has a substantial negative effect on shear stress. The negative coefficient indicates that increasing  $T_g$  reduces shear stress, likely due to the adhesive's ability to absorb and distribute forces more effectively as its thickness increases. This finding reinforces the role of adhesive thickness as a



key parameter in mitigating stress and improving the joint's load-bearing capacity. The Pareto chart shows that, while L2 increases stress, Tg can counteract this effect by providing better stress distribution. The shear force (Fx) also has a major positive influence on shear stress, as expected. The higher the applied shear force, the greater the stress acting on the adhesive layer. This result emphasizes the importance of limiting Fx in applications where high shear stress is a concern. The Pareto chart indicates that the interaction between Fx and L2 should be closely monitored, as these two factors together can lead to critical stress concentrations if not properly managed. The smaller bars on the Pareto chart, representing parameters such as joint height (H), vertical arm length (L1), and peel force (Fz), indicate that these factors have relatively minor impacts on shear stress. However, it is important to note that while their individual effects may be small, their interactions with more significant factors (such as L2 and Tg) could still play a role in stress distribution. Understanding these interactions is critical for optimizing the overall joint performance.

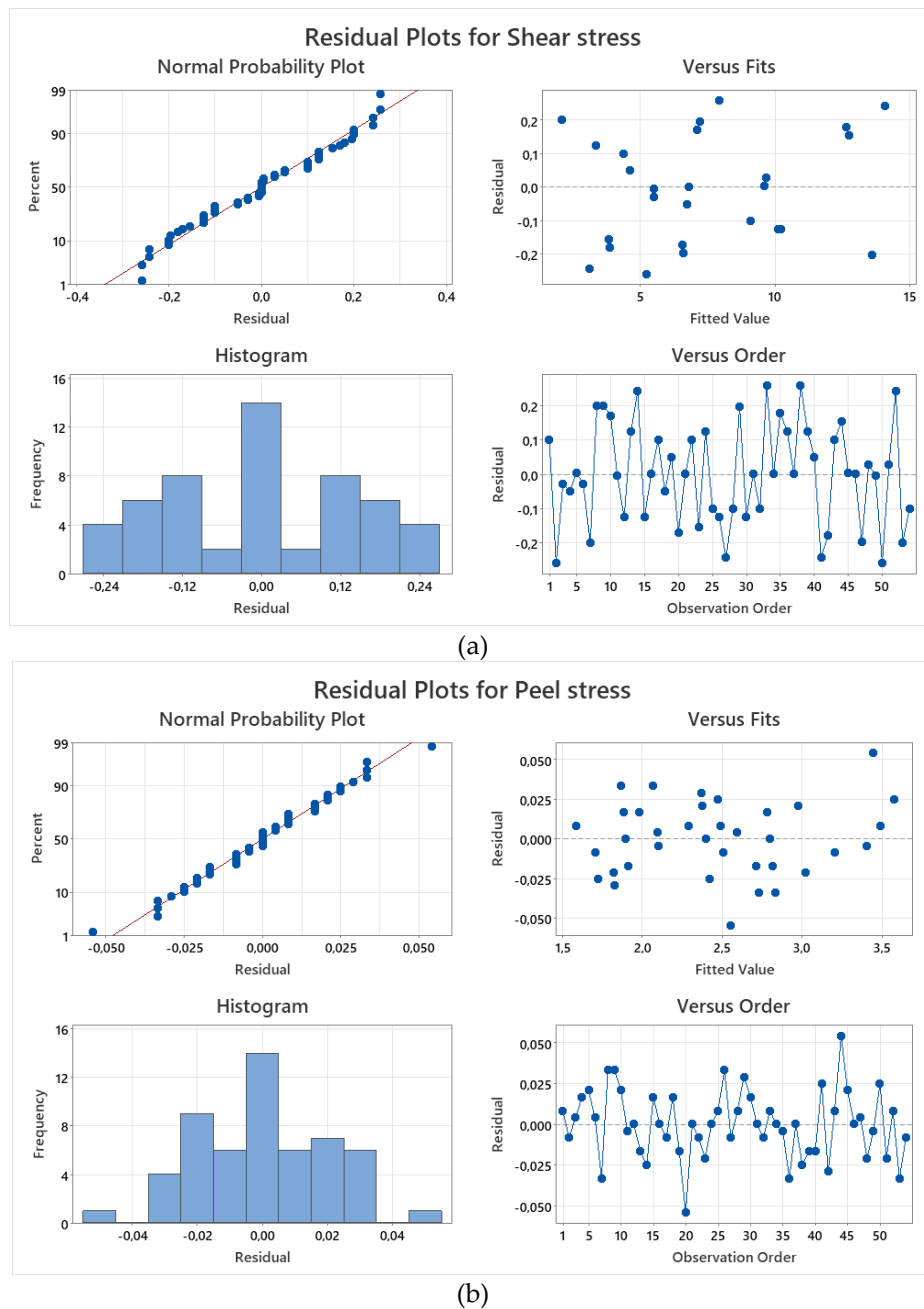


Figure 2. Residual Plots for (a) Shear and (b) Peel stress

In Figure 3 (b), the Pareto chart for peel stress highlights the dominant role of peel force ( $F_z$ ) and adhesive thickness ( $T_g$ ). The tallest bar corresponds to  $F_z$ , confirming that peel force is the most significant driver of peel stress. This is consistent with the physical nature of peel stress, which is directly induced by forces acting perpendicular to the adhesive layer. The high importance of  $F_z$  suggests that managing peel forces is critical for minimizing stress concentrations and preventing adhesive failure. Adhesive thickness ( $T_g$ ) again emerges as a key factor, with a significant negative effect on peel stress. The negative coefficient indicates that increasing  $T_g$  reduces peel stress, likely by allowing the adhesive to better distribute the applied forces and reduce peak stress concentrations at the edges of the joint. This finding is consistent with the contour and surface plots, which show that  $T_g$  plays a crucial role in stress mitigation for both shear and peel forces. The horizontal arm length ( $L_2$ ) also has a notable, though smaller, negative effect on peel stress. This result suggests that reducing  $L_2$  can help to mitigate peel

stress, which may be beneficial in certain applications. However, the primary focus for controlling peel stress should be on managing  $F_z$  and optimizing  $T_g$ , as these are the most significant factors driving the stress response.

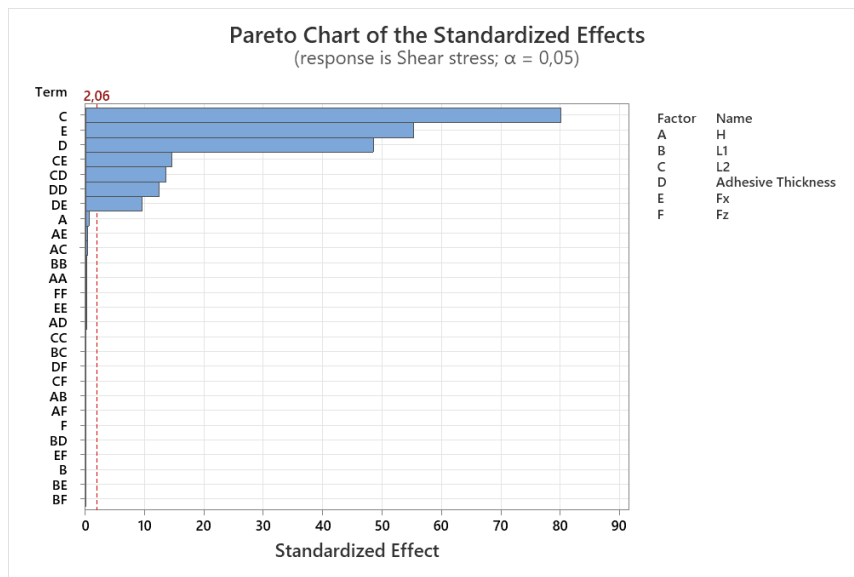
Overall, the Pareto charts provide valuable insights into the relative importance of different design parameters in influencing shear and peel stresses. The charts make it clear that  $L_2$ ,  $T_g$ , and  $F_x$  are the primary factors for controlling shear stress, while  $F_z$  and  $T_g$  dominate the peel stress response. These findings inform the optimization process by identifying the key parameters that should be targeted for stress minimization, offering practical guidance for improving joint design.

#### 4.4. Visualization of Interaction Effects

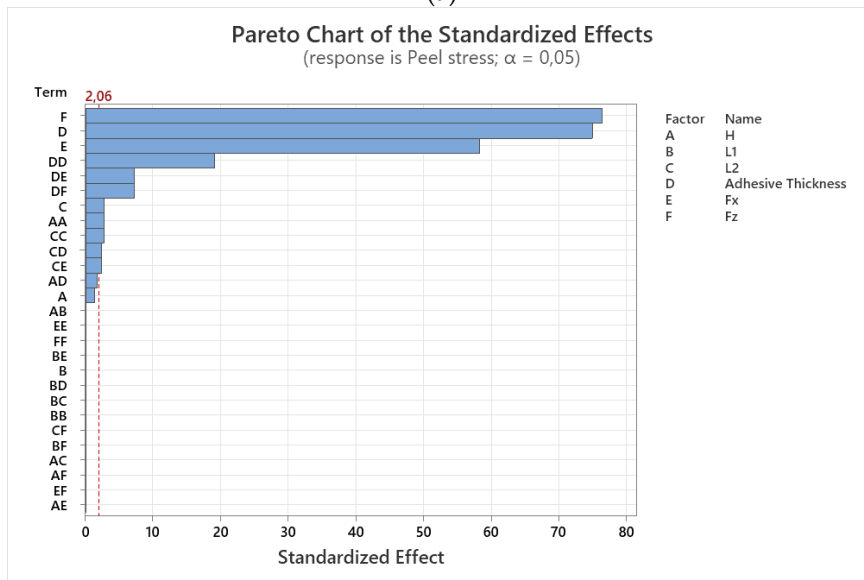
##### 4.4.1. Contour Plots for Shear and Peel Stress

Contour plots are a crucial tool in visualizing the relationship between two input parameters and their combined effect on a response variable, in this case, shear and peel stress. By holding other factors constant, these plots provide insight into how variations in specific parameter pairs influence the stress distribution within the joint.

Supplementary Figure 1 (a) presents the contour plots of shear stress, illustrating the complex interplay between key design parameters such as joint height ( $H$ ), horizontal arm length ( $L_2$ ), vertical arm length ( $L_1$ ), adhesive thickness ( $T_g$ ), and applied forces ( $F_x$  and  $F_z$ ). The contour plots provide a visual representation of shear stress distribution across various combinations of these parameters, offering critical insights into their influence on joint performance. From the plots, it is evident that shear stress is highly dependent on the horizontal arm length ( $L_2$ ) and adhesive thickness ( $T_g$ ), as indicated by the steep gradient transitions observed in the respective contour regions. A larger  $L_2$  generally results in lower shear stress values, contributing to a more uniform stress distribution and reducing the likelihood of stress concentration near the adhesive-substrate interface. Conversely, when  $L_2$  is reduced, shear stress becomes more localized, which may lead to premature failure due to excessive stress accumulation. Additionally, the adhesive thickness ( $T_g$ ) plays a crucial role in shear stress mitigation; increasing  $T_g$  tends to reduce peak stress values and distribute loads more effectively. However, beyond a certain limit, the benefits of increased adhesive thickness may plateau, emphasizing the need for an optimized balance between material usage and joint performance. Furthermore, the applied force  $F_x$  significantly influences shear stress patterns, with higher force values leading to greater shear stress magnitudes, underscoring the importance of selecting appropriate load conditions for the intended application. The contour plots also highlight interaction effects between adhesive thickness and loading parameters, which must be carefully considered during the design process to ensure optimal joint performance and durability.



(a)



(b)

**Figure 3.** Pareto Chart of the Standardized Effects (a) Shear and (b) Peel stress

Supplementary Figure 1 (b) provides contour plots illustrating the distribution of peel stress in the double-L-bracket adhesive joint. Peel stress is a critical factor in bonded joints, as it contributes significantly to delamination and failure propagation at the adhesive-adherent interface. The contour plots reveal that peel stress is most influenced by vertical arm length (L1) and the applied peel force (Fz), with variations in these parameters leading to distinct stress distribution patterns. A longer L1 generally reduces peel stress concentrations, allowing for better load transfer and enhancing joint longevity. However, shorter vertical arm lengths result in higher localized peel stress, which can lead to adhesive failure under cyclic or sustained loading. Additionally, adhesive thickness (Tg) has a notable effect on peel stress distribution; increasing Tg tends to lower peel stress levels by improving the adhesive's load-bearing capability and energy absorption properties. Nevertheless, an excessively thick adhesive layer may introduce flexibility-related issues, which could adversely affect joint stiffness and load distribution efficiency. The contour plots also indicate that the interaction between peel force (Fz) and adhesive thickness (Tg) is crucial in determining the joint's overall performance, as

higher peel forces tend to exacerbate stress concentrations, especially in joints with thinner adhesive layers. The insights provided by these contour plots are invaluable in guiding the selection of optimal design parameters to minimize peel stress and extend the service life of the joint.

Overall, Supplementary Figures 1(a) and 1(b) provide a comprehensive understanding of how key design parameters influence shear and peel stress distributions in double-L-bracket adhesive joints. These visual representations facilitate the identification of critical stress regions and offer practical design recommendations for optimizing joint performance. The findings underscore the importance of selecting appropriate values for adhesive thickness, joint dimensions, and applied forces to achieve an optimal balance between structural integrity and material efficiency. By leveraging the insights gained from these contour plots, engineers can make informed design decisions to enhance joint reliability, reduce material consumption, and extend operational lifespan in applications across industries such as aerospace, automotive, and civil engineering.

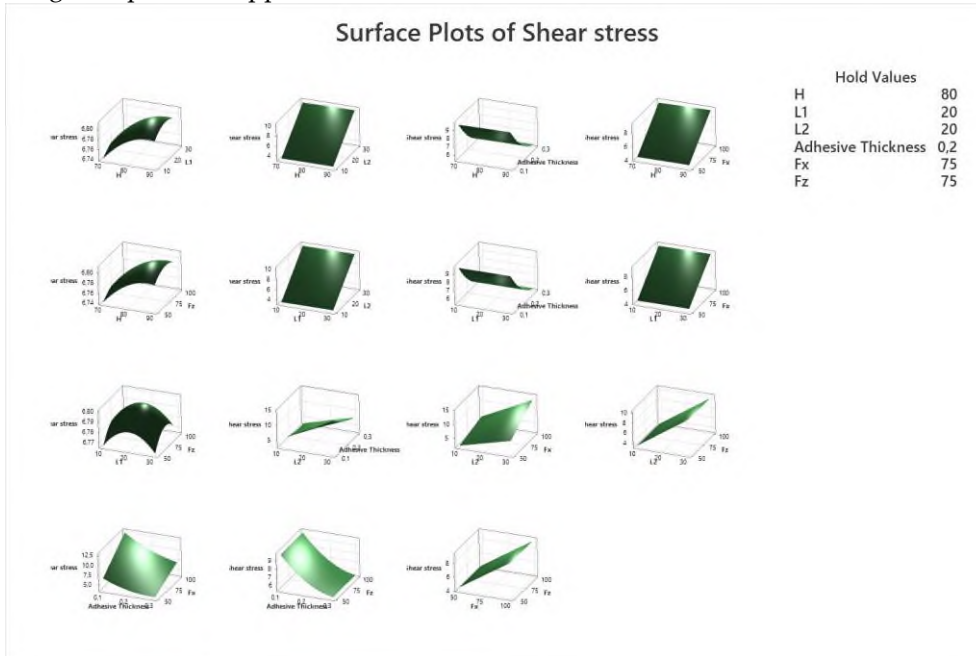
#### 4.4.2. Surface Plots for Shear and Peel Stress

While contour plots offer two-dimensional views of parameter interactions, surface plots provide a more comprehensive, three-dimensional visualization of how two factors simultaneously affect stress responses. Surface plots not only reveal the magnitude of the stresses but also depict the curvature of the response surface, providing insights into the non-linear interactions between variables.

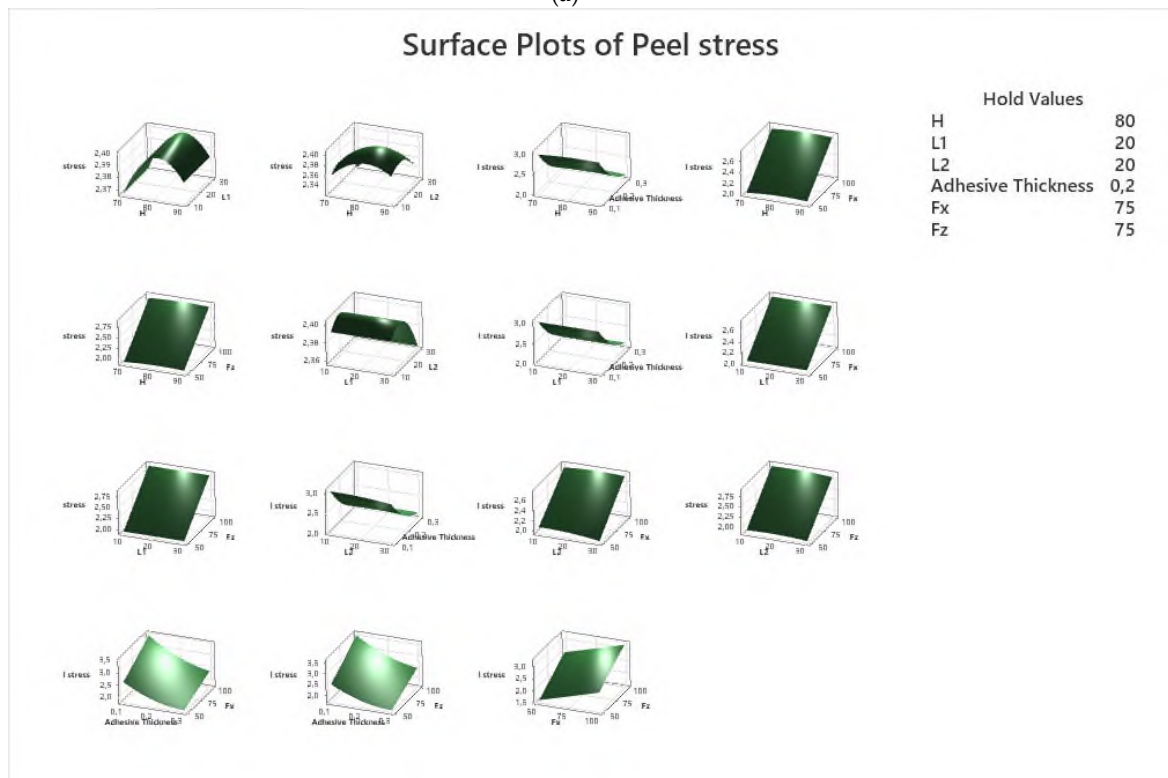
In Figure 4(a), the surface plot for shear stress illustrates the interaction between  $L_2$  and  $T_g$ . The plot shows a pronounced increase in shear stress as  $L_2$  increases, particularly when  $T_g$  is small. The steep gradient of the surface at low  $T_g$  values indicates that small changes in  $L_2$  or  $T_g$  can lead to large changes in shear stress, especially when both parameters are at their extreme values (large  $L_2$  and thin  $T_g$ ). As  $T_g$  increases, the surface flattens, indicating that the adhesive layer absorbs and distributes the applied forces more effectively, reducing the overall stress. The surface plot clearly demonstrates the non-linear relationship between  $L_2$  and  $T_g$ , with  $T_g$  acting as a critical factor in controlling shear stress under high  $L_2$  conditions. This three-dimensional visualization also highlights the diminishing returns of increasing  $T_g$  beyond a certain point. While increasing  $T_g$  significantly reduces shear stress for large  $L_2$  values, the stress reduction becomes less pronounced at very high  $T_g$  levels, suggesting an optimal adhesive thickness that balances stress mitigation and material usage. This insight is valuable for practical applications where increasing  $T_g$  too much could result in excessive material costs or manufacturing difficulties.

Figure 4b presents the surface plot for peel stress, depicting the interaction between peel force ( $F_z$ ) and adhesive thickness ( $T_g$ ). Similar to the shear stress surface plot, the peel stress increases steeply with increasing  $F_z$ , particularly when  $T_g$  is small. The steep slopes at low  $T_g$  values indicate that the joint is highly sensitive to peel forces when the adhesive layer is thin, leading to higher stress concentrations. As  $T_g$  increases, the surface flattens, showing that the adhesive layer is better able to distribute the peel forces, reducing the peak stresses. The surface plot also reveals the non-linear nature of the interaction between  $F_z$  and  $T_g$ . While increasing  $T_g$  significantly reduces peel stress for high  $F_z$  values, the benefits of thicker adhesive layers become less pronounced beyond a certain point. This suggests that there is an optimal  $T_g$  value, beyond which further increases in thickness do not yield substantial stress reduction. Designers must therefore carefully balance the thickness of the adhesive layer with the expected peel forces to achieve the desired performance without overusing material. Both surface plots provide critical insights into the non-linear interactions between the input parameters. They emphasize the importance of balancing the horizontal arm length ( $L_2$ ) and peel force ( $F_z$ ) with

the adhesive thickness (Tg) to minimize both shear and peel stresses. The three-dimensional nature of these plots allows for a more nuanced understanding of how small changes in design parameters can lead to significant stress variations, offering valuable guidance for optimizing joint designs in practical applications.



(a)



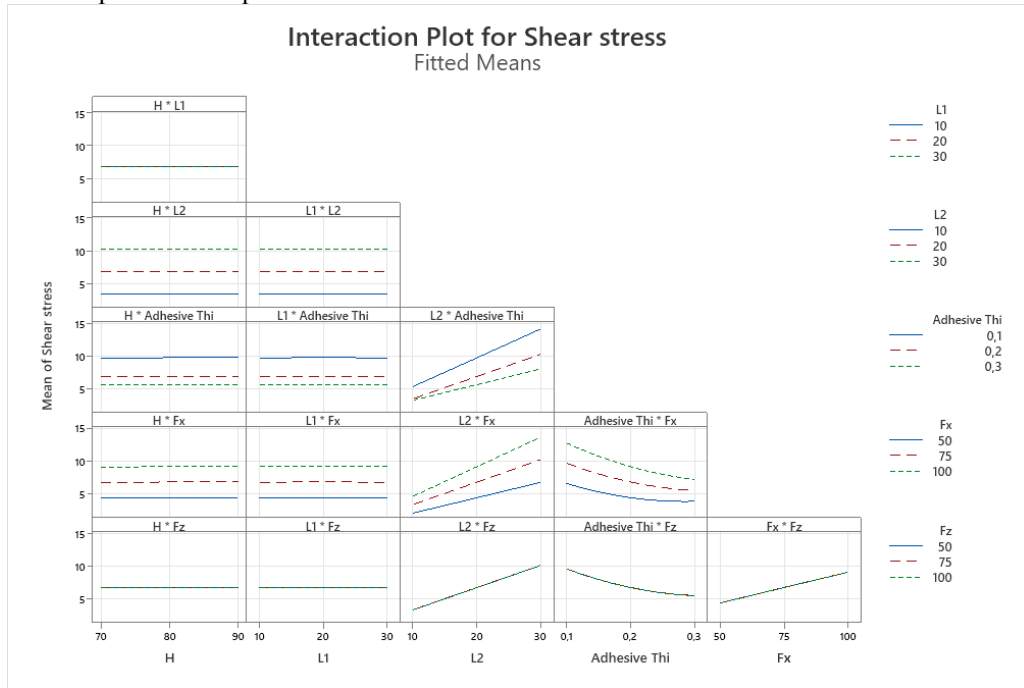
(b)

**Figure 4.** Surface Plots of (a) Shear and (b) Peel stress

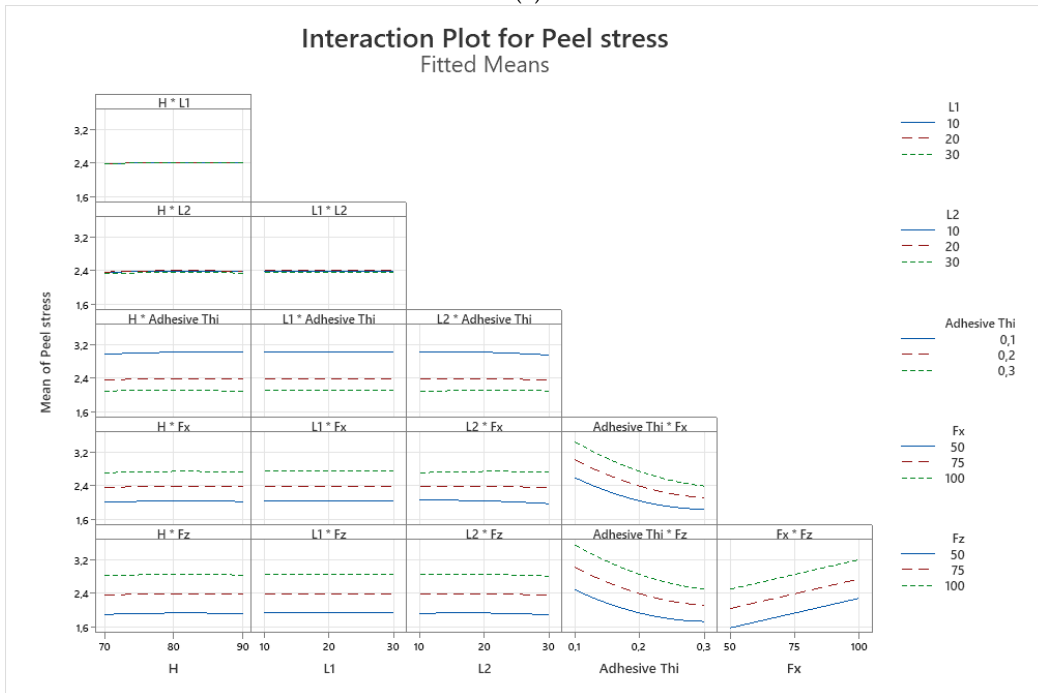
### 4.5. Optimization and Interaction Effects

#### 4.5.1 Interaction Plots for Stress Minimization

A thorough understanding of the interactions between design parameters is essential to minimize shear and peel stresses in the double-L-bracket joint. Interaction plots help visualize the combined effects of different variables on stress levels, revealing important trends that guide the optimization process.



(a)



(b)

**Figure 5.** Interaction Plots for (a) Shear and (b) Peel stress

In Figure 5(a), the interaction between horizontal arm length ( $L_2$ ) and applied shear force ( $F_x$ ) shows that as both parameters increase, shear stress rises significantly. This effect is expected because a longer  $L_2$  increases the moment arm for the applied force  $F_x$ , leading to greater shear forces concentrated at the adhesive interface. Simultaneously, higher  $F_x$  directly increases the stress applied to the joint. This interaction highlights the need for careful management of  $L_2$  and  $F_x$  to prevent excessive shear stress, particularly in designs requiring extended horizontal arms. However, the interaction between adhesive thickness ( $T_g$ ) and  $F_x$  shows a different behavior. As  $T_g$  increases, the shear stress decreases, even with an increase in  $F_x$ . This suggests that a thicker adhesive layer improves the stress distribution, mitigating localized stress concentrations. The increased thickness allows for more elastic deformation of the adhesive, which absorbs and dissipates the applied shear forces more effectively. Therefore,  $T_g$  serves as a critical parameter to control when aiming to reduce shear stress in configurations that involve high shear forces.

The peel stress interaction plots, shown in Figure 5(b), reveal similar trends. As the peel force ( $F_z$ ) increases, the peel stress increases substantially, especially when the adhesive thickness ( $T_g$ ) is thin. This is due to the inability of thin adhesive layers to adequately distribute the peel forces, resulting in concentrated stresses at the edges of the joint. In contrast, increasing  $T_g$  mitigates peel stress, as the thicker adhesive layer can flex and distribute the force more evenly across the bond line. Interestingly, the interaction between joint height ( $H$ ) and  $F_z$  has a less pronounced effect on peel stress. Although variations in  $H$  have a measurable impact, the dominant factor remains  $F_z$ . Therefore, the optimization of  $F_z$  and  $T_g$  is crucial for minimizing peel stress, while the height ( $H$ ) plays a secondary role in the stress distribution.

These interaction plots underscore the importance of controlling the parameters that influence shear and peel stresses the most. For example, while increasing  $L_2$  and  $F_x$  exacerbates shear stress, the detrimental effects can be countered by increasing  $T_g$ . Similarly, optimizing  $T_g$  and managing  $F_z$  are critical to reducing peel stress. These findings demonstrate the complex interplay between design parameters and highlight the need for a multi-response optimization approach to ensure a balanced design.

#### 4.5.2 Response Optimization and Comparison with Analytical Calculations

The multi-response optimization of the joint design is performed using a desirability function, which balances the minimization of both shear and peel stresses. The optimization aims to find a configuration that reduces both stresses simultaneously, while also taking into account the interactions between parameters. The results of the optimization are shown in Figure 6, which presents the optimal settings for each parameter: joint height ( $H$ ) of 90 mm, vertical arm length ( $L_1$ ) of 30 mm, horizontal arm length ( $L_2$ ) of 10 mm, adhesive thickness ( $T_g$ ) of 0.2616 mm, and applied forces  $F_x$  and  $F_z$  of 50 N each. The optimization yields a peel stress of 1.450 MPa and a shear stress of 2.120 MPa, both of which are significantly lower than the other configurations tested in the design of experiments. The composite desirability score of 1.000 indicates that this solution represents the optimal balance between minimizing both shear and peel stresses. Figure 6 also shows the sensitivity of each parameter to the stress responses. For instance, the steep slopes of the  $F_x$  and  $L_2$  curves indicate their strong influence on shear stress. Conversely, the  $T_g$  curve shows a more moderate, yet consistent, reduction in stress as adhesive thickness increases. The peel stress plot reveals similar sensitivities, with  $T_g$  playing a crucial role in lowering stress as its value approaches the upper limit.





**Figure 6.** Optimization Plot for Shear and Peel Stress Minimization Using Composite Desirability

**Table 4.** Comparison of Optimized and Analytical Stress Predictions for Double-L-Bracket Joint

Variable	Setting			
H	90			
L1	30			
L2	10			
Adhesive Thickness	0.261616			
Fx	50			
Fz	50			
Response	Fit	SE Fit	95% CI	95% PI
Peel stress	1.4502	0.0391	(1.3698; 1.5305)	(1.3496; 1.5507)
Shear stress	2.120	0.276	(1.552; 2.688)	(1.409; 2.831)
Analytical				
Peel stress (MPa)	1.5			
Shear stress (MPa)	2.0			

A comparison of the optimized results with the analytical calculations derived from the Bigwood and Crocombe model, as shown in Table 4, validates the RSM optimization. The analytically calculated peel stress is 1.5 MPa, while the shear stress is 2.0 MPa—both values are in close agreement with the RSM-predicted results of 1.450 MPa for peel stress and 2.120 MPa for shear stress. The small discrepancies, amounting to 3.33% for peel stress and 6% for shear stress, are well within acceptable error margins for such calculations. These slight differences are attributable to the inherent approximations in the regression model used by RSM but are not significant enough to undermine the reliability of the optimization process.

The optimization also highlights the critical role of adhesive thickness in minimizing both shear and peel stresses. A Tg value of 0.2616 mm was found to be optimal, as it provides a balance between reducing stress concentrations and maintaining the adhesive's structural

integrity. Although thicker adhesive layers generally perform better at reducing stress, practical limitations such as manufacturing constraints and material costs necessitate a compromise. The selected thickness offers the best trade-off between performance and feasibility.

Another key finding from the optimization is the influence of L2 on shear stress. The optimal configuration involves reducing L2 to 10 mm, which significantly reduces the shear stress by minimizing the moment arm created by  $F_x$ . However, to maintain overall joint stability and load-bearing capacity, the optimization compensates by selecting a larger joint height (H) and vertical arm length (L1), ensuring that the design remains structurally sound. The desirability function used in this optimization process allows for a comprehensive evaluation of the trade-offs between different design objectives. The final configuration achieves the best possible balance between minimizing shear and peel stresses while taking into account practical constraints such as adhesive thickness, arm lengths, and applied forces. The composite desirability score of 1.000 confirms that this solution is optimal for the given design requirements.

In conclusion, the optimization process has successfully minimized both shear and peel stresses in the double-L-bracket joint. The close agreement between the RSM-based predictions and analytical calculations further validates the robustness of the optimization approach. The selected configuration provides a practical and efficient solution for real-world joint designs, where stress minimization is critical for ensuring long-term performance and reliability.

## 5. CONCLUDING REMARKS

This study successfully applied Response Surface Methodology (RSM) to optimize the shear and peel stresses in a double-L-bracket joint. By employing a Bigwood & Crocombe analytical model and using a Box-Behnken Design (BBD), the key factors affecting stress—horizontal arm length (L2), adhesive thickness (Tg), and applied forces ( $F_x$  and  $F_z$ )—were systematically analyzed. The optimization results showed that reducing L2 and increasing Tg can effectively minimize both shear and peel stresses, with the optimal configuration achieving stress levels closely aligned with analytical predictions. The findings provide valuable insights into the design of adhesive joints, offering practical guidelines for minimizing stress concentrations and improving structural durability in various engineering applications. This approach demonstrates the utility of RSM in complex joint design problems, providing a robust framework for optimizing multi-parameter systems.

### Declaration of Ethical Standards

The author declares that the research was conducted in accordance with ethical standards. No human or animal subjects were involved in this study, and all ethical guidelines pertinent to the field have been followed.

### Credit Authorship Contribution Statement

This work was solely conducted by Bertan Beylergil, who was responsible for the conception, design, data collection, analysis, and interpretation, as well as drafting the manuscript and approving the final version for submission.

### Declaration of Competing Interest

The author declares that there are no conflicts of interest or competing interests regarding the publication of this article.

## Funding / Acknowledgements

The author gratefully acknowledge financial support from the Scientific and Technological Research Council of Turkey (TÜBİTAK) with project number 218M710.

## Data Availability

The author confirms that the data supporting the findings of this study are available within the article. Additional data, if required, can be provided by the author upon reasonable request.

## REFERENCES

- [1] R. D. Adams, Ed., *Adhesive Bonding: Science, Technology and Applications*, 2nd ed. Elsevier, 2021. doi: 10.1016/C2019-0-00395-0.
- [2] L. F. M. da Silva, P. J. C. Neves, R. D. Adams, and J. K. Spelt, "Analytical models of adhesively bonded joints—Part I: Literature survey," *International Journal of Adhesion and Adhesives*, vol. 29, no. 3, pp. 319–330, 2009.
- [3] C. Yildirim, H. Ulus, B. Beylergil, A. Al-Nadhari, S. Topal, and M. Yildiz, "Tailoring adherend surfaces for enhanced bonding in CF/PEKK composites: Comparative analysis of atmospheric plasma activation and conventional treatments," *Composites Part A: Applied Science and Manufacturing*, vol. 180, 2024, Art. no. 108101.
- [4] L. F. M. da Silva, T. N. S. S. Rodrigues, M. A. V. Figueiredo, M. F. S. F. de Moura, and J. A. G. Chousal, "Effect of adhesive type and thickness on the lap shear strength," *The Journal of Adhesion*, vol. 82, no. 11, pp. 1091–1115, 2006.
- [5] M. H. Kim, H. S. Hong, and Y. C. Kim, "Determination of failure envelope of functionally graded adhesive bonded joints by using mixed mode continuum damage model and response surface method," *International Journal of Adhesion and Adhesives*, vol. 106, 2021, Art. no. 102815.
- [6] A. J. A. Vieira, R. D. S. G. Campilho, and K. Madani, "Statistical analysis of adhesive rod-tube joints under tensile stress for structural applications," *Journal of the Brazilian Society of Mechanical Sciences and Engineering*, vol. 46, no. 574, 2024.
- [7] C. Mandolino, L. Cassettari, M. Pizzorni, S. Saccaro, and E. Lertora, "A Response Surface Methodology approach to improve adhesive bonding of pulsed laser treated CFRP composites," *Polymers*, vol. 15, no. 1, 2023, Art. no. 121.
- [8] J. M. Arenas, J. J. Narbon, and C. Alia, "Optimum adhesive thickness in structural adhesive joints using statistical techniques based on Weibull distribution," *International Journal of Adhesion and Adhesives*, vol. 31, no. 4, pp. 265–270, 2010.
- [9] Y. Wang and K. Zeng, "Parameter optimization of particle-reinforced adhesive bonded joints based on the response surface method," *Journal of Adhesion Science and Technology*, vol. 37, no. 8, pp. 1311–1325, 2023.
- [10] S. Ariaee, A. Tutunchi, A. Kianvash, and A. A. Entezami, "Modeling and optimization of mechanical behavior of bonded composite–steel single lap joints by response surface methodology," *International Journal of Adhesion and Adhesives*, vol. 54, pp. 30–39, 2014.
- [11] P. Kraisornkachit, M. Naito, C. Kang, and C. Sato, "Multi-objective optimization of adhesive joint strength and elastic modulus of adhesive epoxy with active learning," *Materials*, vol. 17, no. 12, 2024, Art. no. 2866.
- [12] F. H. Öztürk, "Optimization of adherend thickness and overlap length on failure load of bonded 3D printed PETG parts using response surface method," *Rapid Prototyping Journal*, vol. 30, no. 8, pp. 1579–1591, 2024.

- [13] E. Gorgun, "Ultrasonic testing and surface conditioning techniques for enhanced thermoplastic adhesive bonds," *Journal of Mechanical Science and Technology*, vol. 38, no. 3, pp. 1227–1236, 2024.
- [14] L. S. Sutherland, C. Amado, and C. Guedes Soares, "Statistical experimental design techniques to investigate the strength of adhesively bonded T-joints," *Composite Structures*, vol. 159, pp. 445–454, 2017.
- [15] Y. M. Haddou, M. Salem, A. Amiri, R. Amiri, and S. Abid, "Numerical analysis and optimization of adhesively-bonded single lap joints by adherend notching using a full factorial design of experiment," *International Journal of Adhesion and Adhesives*, vol. 126, 2023, Art. no. 103482.
- [16] E. Cetin and C. T. Fossi, "Experimental investigation on mechanical strength of adhesively bonded 3D-printed joints under hygrothermal conditions using Taguchi method," *International Journal of Adhesion and Adhesives*, vol. 126, 2023, Art. no. 103472.
- [17] A. D. Crocombe and D. A. Bigwood, "Non-linear adhesive bonded joint design analyses," *International Journal of Adhesion and Adhesives*, vol. 10, pp. 31–41, 1990.
- [18] M. Abbasi, R. Ciardiello, and L. Goglio, "Backface strain as an index to detect damage initiation in composite single-lap bonded joints: Effects of adhesive type and joint dimensions," *International Journal of Adhesion and Adhesives*, vol. 134, 2024, Art. no. 103791.
- [19] M. Abbasi, R. Ciardiello, and L. Goglio, "Experimental study on the effect of bonding area dimensions on the mechanical behavior of composite single-lap joint with epoxy and polyurethane adhesives," *Applied Sciences*, vol. 13, no. 7683, 2023.
- [20] L. Goglio and M. Rossetto, "Impact rupture of structural adhesive joints under different stress combinations," *International Journal of Impact Engineering*, vol. 35, pp. 635–643, 2008.
- [21] P. Weißgraeber, N. Stein, and W. Becker, "A general sandwich-type model for adhesive joints with composite adherends," *International Journal of Adhesion and Adhesives*, vol. 55, pp. 56–63, 2014.
- [22] F. Domínguez and L. Carral, "The hybrid joints between an FRP panel and a steel panel through tubular reinforcements: A methodology for interlaminar stress calculations," *Applied Sciences*, vol. 10, no. 3962, 2020.
- [23] G. G. Momm and D. Fleming, "Analytical models for stress analysis of real-life bonded joints," *The Journal of Adhesion*, vol. 98, no. 14, pp. 2253–2276, 2022.
- [24] T. S. Methfessel and W. Becker, "A generalized model for predicting stress distributions in thick adhesive joints using a higher-order displacement approach," *Composite Structures*, vol. 291, 2022, Art. no. 115556.
- [25] R. X. Wang, J. Cui, A. N. Sinclair, and J. K. Spelt, "Strength of adhesive joints with adherend yielding: I. Analytical model," *The Journal of Adhesion*, vol. 79, no. 1, pp. 23–48, 2003.
- [26] L. F. M. da Silva, P. J. C. das Neves, R. D. Adams, and J. K. Spelt, "Analytical models of adhesively bonded joints—Part I: Literature survey," *International Journal of Adhesion and Adhesives*, vol. 29, 2009, pp. 319–330.
- [27] L. F. M. da Silva, P. J. C. das Neves, R. D. Adams, and J. K. Spelt, "Analytical models of adhesively bonded joints—Part II: Comparative study," *International Journal of Adhesion and Adhesives*, vol. 29, 2009, pp. 331–341.
- [28] CalcBond, "Adhesive joint calculation software," [Online]. Available: <https://app.calcbond.com/calcbond/index/>. Accessed: 21-01-2025.
- [29] N. F. Doğan, M. V. Çakır, and Ö. Özbek, "Bonding performance of nano boron nitride filled epoxy adhesive," *Journal of the Brazilian Society of Mechanical Sciences and Engineering*, vol. 46, 2024, Art. no. 240.

- [30] M. V. Çakır, "The synergistic effect of hybrid nano-silica and GNP additives on the flexural strength and toughening mechanisms of adhesively bonded joints," *International Journal of Adhesion and Adhesives*, vol. 122, 2023, Art. no. 103333.



## INDUCED STRESSES & DISPLACEMENTS CAUSED BY SINKHOLE DEVELOPMENT

<sup>1</sup>Mehmet Kemal GOKAY , <sup>2,\*</sup>Mehmet MESUTOĞLU 

*Konya Technical University, Engineering and Natural Sciences Faculty, Mining Engineering Department,  
Konya, TÜRKİYE*

<sup>1</sup>[mkgokay@ktun.edu.tr](mailto:mkgokay@ktun.edu.tr), <sup>2</sup>[mmesutoglu@ktun.edu.tr](mailto:mmesutoglu@ktun.edu.tr)

### *Highlights*

- Analyzes of induced stresses and displacements in underground cavities.
- Examining the impact of groundwater on rock mass stability and sinkhole risk.
- Understanding the mechanics of progressive rock failures in overburden layers.
- Providing engineering implications for sinkhole mitigation in subsurface environments.



## INDUCED STRESSES & DISPLACEMENTS CAUSED BY SINKHOLE DEVELOPMENT

<sup>1</sup>Mehmet Kemal GOKAY , <sup>2,\*</sup>Mehmet MESUTOĞLU 

*Konya Technical University, Engineering and Natural Sciences Faculty, Mining Engineering Department,  
Konya, TÜRKİYE*

<sup>1</sup>[mkgokay@ktun.edu.tr](mailto:mkgokay@ktun.edu.tr), <sup>2</sup>[mmesutoglu@ktun.edu.tr](mailto:mmesutoglu@ktun.edu.tr)

(Received: 30.10.2024; Accepted in Revised Form: 10.02.2025)

**ABSTRACT:** Induced stress-strain conditions around underground spaces which could be excavated or naturally formed have their destructive influences on the surrounding rock masses. Roof and sidewall rocks surrounding these spaces are strained due to 3D induced stress fields formed just after their introductions. Cavities/excavated underground spaces have their stability difficulties due to surrounding rock masses' strength/discontinuity features. Stable rocks around these spaces including stable pillars are candidates which supply deformations in time due to their long-term strength characteristics. Collapsing of the rock masses surrounding the underground spaces causes caving effects through the rock masses above the spaces. If the collapsed rock masses cannot support the above overburden dead-loads as fragmented rock fills in the caved spaces, progressive failures are continued upward directions to form further subsidence deformations. Underground water circulations at the caved spaces provide different circumstances including the transportations and/or solution of the caved rocks in time. These processes eventually provide progressive subsidence/sinkhole in time due to elimination of submerged caved/fragmented rocks. The procedures causing progressive roof failures were analysed here for hypothetical rock mass conditions to understand the procedures' governing factors. Evaluating these factors supply hints about what could be the engineering manners to decrease the risk of sinkhole developments.

**Keywords:** *Ground Displacements, Sinkholes, Subsidence, Ground Surface Deformations, Underground Spaces*

### 1. INTRODUCTION

Earth has numerous solid, liquid and gas form elements and it has a crust cover consisting of different types of rock masses. Rocks with their mineral contents and structural configurations have their mechanical properties which are differentiated through their water contents (saturations), void ratios, discontinuity contents, etc. Uncertainties in the determination of representative values for these properties have supplied their complexities in engineering decision circumstances. Since the values characterising the strength or mechanical behaviours of the earth crust materials/masses, which are mainly rocks, cannot be provided through referenced value intervals. Field and laboratory tests performed to characterise rock/soil materials or masses should be repeated through test specimens which should be sampled in regular intervals to reach meaningful averaged values for the selected rock mass locations (in/on the earth crust). Actually, all these efforts cannot eliminate influences of uncertain factors influencing the mechanical behaviours of the rocks/soils. Rock engineering context has the basic explanations related to these uncertainties and International Society of Rock Mechanics, ISRM, has gradually suggested rock testing methods for rock materials/masses to help engineers via the standardisations. Similar complex decision environments are encountered by engineers to supply decisions for the different aspects related to the rock mass cavities. The rock masses can be massive and uniform in their characteristic structures (it is very rare to come across such rocks), but even these intact rocks have their porosities influencing their mechanical behaviours besides their permeability values. Liquids and gasses occupying the rocks' pore volumes have their effects on the rock masses' mechanical properties. Saturated rock masses can be influenced through pressurised groundwater, oil, and natural gasses at shallow/deep rock reservoirs conditions. Pressurised medium (water, oil, and gas types) in

\*Corresponding Author: Mehmet MESUTOĞLU, [mmesutoglu@ktun.edu.tr](mailto:mmesutoglu@ktun.edu.tr)

rock porosities have their relations with induced stresses-strains around the pores, cavities. Possibilities of any change in pore pressure in rock masses then have their stress-strain redistributions around the pores. Pumping out the groundwater, oil and natural gasses for different purposes then result in changes at rock pore pressures. Thus, change in pore dimensions due to overstressed peripheries of pores are then expected results at oil, natural gas fields, and groundwater discharging pump locations. In addition, earthquake vibrations, subsidence due to man-made cavities, man-made vibrations (machine or blast originated ones), etc. are the other external influences on pore pressure-oriented rock mass deformations. When the voids or cavities are in concern, the rock masses' reservoir dimensions, porosities & permeability properties of the rock masses direct the available open space volumes in the rock masses. Encapsulating with impermeable rock masses, certain rock masses have their potential to have liquids, gasses, or liquids+gasses in their micro-cavities. Underground water, oil, and gas reservoirs have their individual characteristics but at the beginning the conditions started through proper reservoir bedrocks which have huge amounts of void spaces in it.

Natural voids, cavities have surrounding rock masses which have their tendency to resource fractures, and their propagations. These fractures (discontinuities) either belong to the surrounding rock masses or they are initiated due to these rock pores, voids, which are controlled by induced stress and pore pressure relations (conditions). In addition, surrounding rock masses' mechanical properties are also governing factors in rock fracturing procedures. When the rock pores, voids, turn into small cavities and then to the caves, and cave-network, it is important to concentrate the types of host rock masses which are most probably karstic rock types.

Rock masses mechanical behaviours, especially at the roof layers of rock voids, cavities or caves are important for the cases of vertical upward enhancement of these underground spaces. These layers either inherit their upward extensions (caving) due to their higher strength characteristics (Fig.1a) or they supply pathways to these extensions due to their fractures and weakness zone directions. Fissures, joints and sets of discontinuities, even the fault zones, are the common instability causes directing the collapses of overburden rock masses (layers) into the existing underground spaces. Actually, collapsed rock masses always have higher volumes, (due to fragmentation), when their original volumes are taken as reference values. Thus, caved rock masses into the existing underground spaces eventually filled all the empty spaces created during the caving evolvments (Fig.1b). Caved roof rock zones have more open spaces among their blocked & fragmented rocks. These caved rocks have then possibly been compacted firmly by induced 3D stresses. It is very rare to visualise such situation but the shallow coal seam which had been mined with underground mining methods and were then excavated with open pit mining operations to mine-out the remaining coals left as coal pillars of abandoned coal mine supplied such opportunity, (Fig. 1), [1, 2, and 3]. Caves are like other underground spaces have their instability circumstances and they progressively approach their collapsing phases due to the induced fractures initiated&propagated in their surrounding rock masses. Fractures elongating at the middle of the roof strata of the caves, galleries, etc. are examples of induced stress fracturing (Fig. 1c). In some occasions, fracturing and caving processes of the caves' roof rocks have reached to the ground surface to form sinkhole type failures (Fig, 1d). Failure of roof rocks above caves could be slow and in progressive manner or it can also be sudden events like especially for their caprock collapses. It can also be expected to be a combined-event which consists of these two caving behaviours in the same sinkhole development. The procedures are depended on the type of rock masses surrounding the underground spaces which initiate roof rock caving steps.

Caving of the overburden rock masses have purposely been engineered in certain mining method steps, (procedures), to handle safety of works & workplaces. For instance, low grade ore reserves are forced to be caved in controlled manner towards the underlying ore collection shuts for their loading and hauling operations (sublevel caving method, and block caving method). Rock masses over the ore bodies in these operations are also caved. These mining methods form large scale crater-like ground surface subsidence features in time. In some coal mining operations, mine-out panels of the coal seams cannot be kept open. Thus, they are forced to be collapsed like the case at underground long-wall



mining method applications. This is necessary to protect the underground coal mines from “coal-gas explosions”, and “coal mine fire” dangers. In these caving operations underground mine spaces’ volume which are forced to be collapsed are the main governing factors directing caving advancing upward over these spaces. Types and mechanical properties of the overburden rock masses in these cases are also important factors on subsidence influences. Sublevel caving and block caving mining methods on the other hand have their orebody caving actions in their main mining procedures. Mechanical properties of overburden rock masses and their discontinuity contents govern the caving procedures advancing upwards towards the ground surface. In some cases, underground spaces supply progressive roof rock failures due to induced 3D stress concentrations. In these circumstances, dimensions of underground empty spaces are getting changed with extra progressive roof collapses. Then vertical chimney type underground spaces could possibly be formed. When these roof failures are approached to the ground surface, caprock parts of the overburden layers then collapse to form sinkhole type features, [6].

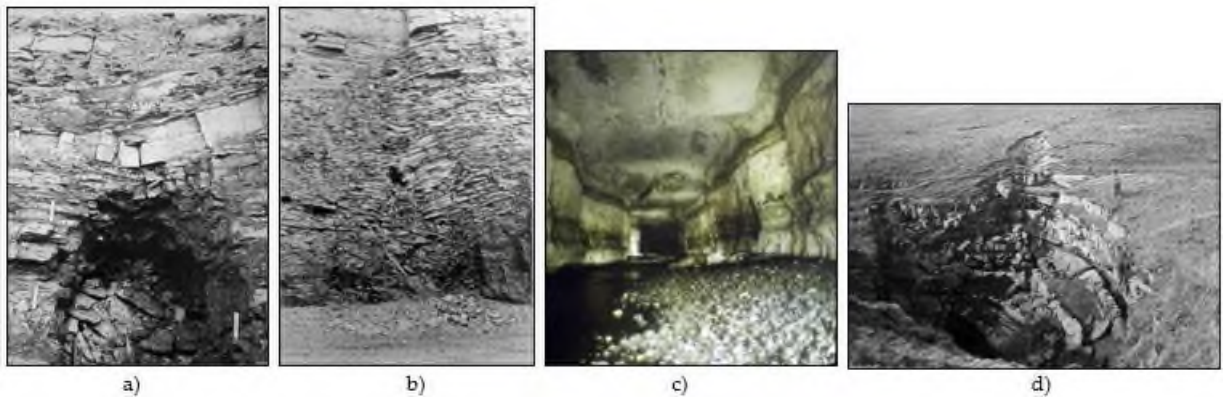


**Figure 1.** a) Roof collapse at an abandoned coal gallery inherited with thick overlying strata [2 & 3], b) Abandoned coal mine gallery which had been totally filled with caved overburden roof rocks [2 & 3]; c) Fracturing roof strata at Sof-Omar cave (Ethiopia), [4], d) Sinkhole formed at Yorkshire (England) due to collapse of roof layers at a limestone cave, [5].

## 2. UNDERGROUND SPACES AND THEIR ROOF FAILURES

There are different types of volumetric spaces used by human civilisations since the beginning of human history. Surface structures have been supplied by different types of volumetric living, working and other civil purpose spaces on the earth crust. Underground structures on the other hand provide structures at subterranean spaces. Actually, caves as underground spaces had been the earlier urbanisation locations before man-made underground excavations, and surface structures. There are many types of underground spaces in rock masses which are naturally formed or excavated. They are used for different human requirements. *The Commission of Artificial Cavities of the Italian Speleological Society*” supplied classification for this complex usage of underground spaces. Galeazzi, [7], wrote about this classification which include 7 main branches: a) Hydraulic underground works, (1. Water level control, drainage-ways; 2. Underground stream interception structures; 3. Underground water ducts, aqueducts; 4. Cisterns, water reservoirs; 5. Wells; 6. Hydraulic distribution works; 7. Sewer; 8. Ship, boat canals; 9. Ice wells, snow-houses, 10. Tunnels or ducts with unknown function), b) Hypogean Civilian dwellings, (1. Permanent dwellings; 2. Temporary shelters; 3. Underground plants, factories; 4. Warehouses stores, cellars; 5. Underground silos; 6. Stables for any kind of animals; 7. Pigeon houses; 8. Any other kind of civilian settlements), c) Religious cult, (1. Nymphaeum, Mithraea temples, sacred wells, shrines, monasteries, churches, and chapels, etc. 2. Burial places), d) Military & war works, (1. Defensive works, 2. Galleries and connecting passages, 3. Mine and counter mine tunnels, 4. Firing stations, 5. Deposits, 6. Sheltered accommodation and soldiers, 7. War shelters for civilians), e) Mining works, (1. Aggregate quarries, 2. Metal mines, 3. Mines and quarries of other materials, (non-metallic), 4. Non-specific mining surveys, 5. Underground spaces to grow vegetables), f) Transit underground

works, (1. *Tunnels for vehicles, pedestrians or horses*, 2. *Transit works, not military*, 3. *Railway tunnels, tramways or funicular (out of use)*, 4. *Non-hydraulic wells, shafts etc.*), g) Other works. Underground spaces naturally exist as micro voids, pores, (porosity properties of rock masses), cavities (formed due to rock forming circumstances, and enlargements of micro voids through chemical weathering, and further fracturing & crushing), caves, and cave networks in karstic rock masses are all have their instability problems which have tendency to form ground surface vertical deformations as subsidence or sinkholes. At this point, it should be noted also the vertical deformations of a large-scale surface area due to pumping out of groundwater, oil, and natural gasses through underground voids.

If there is a space in the earth crust, there are induced stresses around them. Therefore, if the surrounding rock masses cannot bear these 3D stresses, they are deformed and supply new fractures or they provide fracture propagations for their existing fracture networks. Thus, due to gravity, tectonic stresses, and earthquake vibrations underground spaces which have instable roof and siderocks have eventually collapsed. Existing spaces in earth crust are also potential candidates for further collapsing events. Actually, when the induced stress distributions around underground spaces are considered by evaluating available research: rock-load height calculation criteria and dead-load concerns are common explanations. Due to the complexity of the earth crust content, rocks cannot be considered massive material. They are inhomogeneous and they have different mechanical characters in different parts of their mass bodies. Induced stresses influencing vertical and horizontal peripheries of the underground spaces cannot be transferred through these empty spaces without available load-bearing solid pillars. Therefore, these stresses are redistributed around the spaces by supplying bridge type load transfer features over empty spaces. Rock-load height concept (rock mass classification procedure) supplied by Terzaghi, (Fig 2a), [8], is then based on the estimation of this height which is different for different rock mass characteristics. Basically, massive rocks have lower rock-load height with respect to the rock masses having discontinuities [8]. When the rock-load height is getting higher consequently dead-loads calculated for certain sections of the underground spaces (roof area= roof span x length of the selected section of the space) are getting higher. Shape and dimension of the spaces (which have direct influences on the spaces' roof spans) are then the important design features besides several other factors like surrounding rock mass mechanical behaviours for stable man-made underground openings in mining and civil engineering context. Kirsch, [9], for instance, supply estimation for the induced tangential and radial stresses formed around a circular opening in a homogeneous & uniform medium which is loaded under a 2D stress field. Consideration of rock masses as homogeneous and uniform (massive) in condition is hypothetical but, applying Kirsch solutions for circular underground spaces supply also valuable information for further rock mechanics analysis. In this content, work supplied by Li et al. [10] covered information how the shape and positioning of the selected underground space are also influencing factors on induced stresses, (Fig. 2b and 2c). They presented induced tangential stress concentrations around elliptical holes which were considered that they were under uniaxial compressions and they had different inclination angles.

It is obvious that vertical stresses above the underground spaces are bridging around the empty spaces which consequently increase the tangential induced stresses according to the spaces' span values. Same shape and size of the underground spaces illustrated in Fig. 2b and 2c cause different induced tangential stresses which were calculated by Li et al. [10] as 5P for horizontally positioned elliptical holes, and 2P for vertically positioned elliptical holes. Vertical elliptical holes have more advantage in stability circumstances with respect to the horizontally positioned elliptical holes. Actually, existing stable caves, natural conduits, and cavities have their clues of their stability characteristics, (Fig. 3), like; Arch shaped roofs, inclined and nearly vertical elliptical conduit cross-sections, reinforced roof and sidewall rocks at caves, (including their fractured inner bodies and caves' inner peripheries), with precipitated carbonates, pillar type roof supports at caves through developed stalactite & stalagmite, relatively good strength quality rock masses surrounding the caves, comparatively small size cave with no nearby openings, and relatively low induced stress locations in the rock masses, etc. These are the common features of stable caves & cavities around the world. Caves which had not gotten opportunities to have these kinds of

shapes, dimensions, field stresses & induced stresses, rock strengths, earth crust positioning conditions had gradually collapsed. Their overburden rocks had been gradually caved into their empty spaces. Some of them have delivered examples of ground subsidence, sinkholes, or deep valleys according to their caving procedures in geological times.

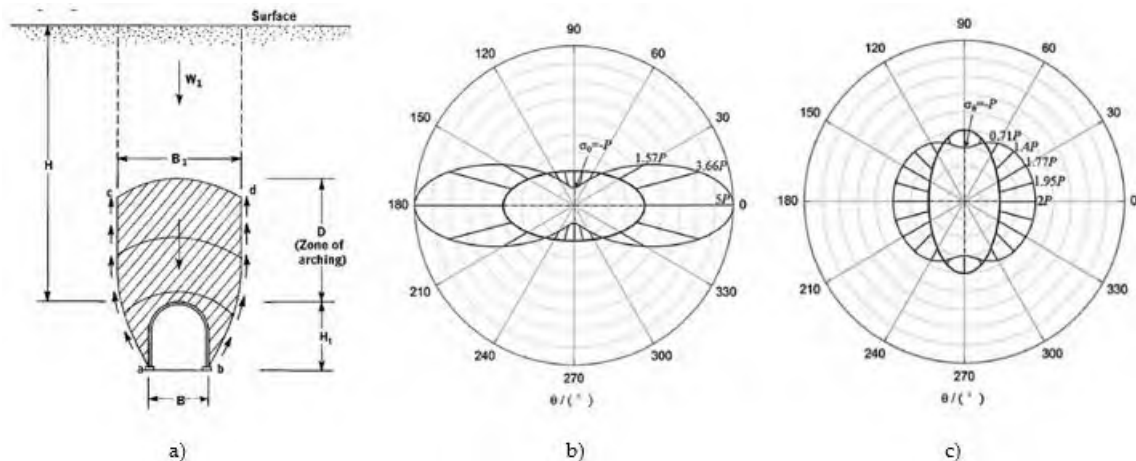


**Figure 2.** a) Rock-load height concept supplied by Terzaghi, [8], b) Induced tangential stresses around elliptical (long axis length=12mm, short axis length=10mm) holes with (b) horizontal ( $0^\circ$ ) and, (c) vertical ( $90^\circ$ ) inclination angle under uniaxial compression ( $P$ ), [10].

### 3. UNDERGROUND SPACE COLLAPSE AND SUBSIDENCE

Since the natural underground spaces in earth crust in micro and macro scale are one of the reasons why the humans can manage to continue their civilisations. Man-made underground spaces for mineral, groundwater, and energy gaining purposes through engineering procedures have left underground spaces at the back in micro and macro scales. These spaces have a tendency to collapse to start rock mass caving events. Earth crust has many examples of underground space collapses & related overburden rock mass cavings explored and recorded by the researchers. The rock mass caving conditions illustrated in Fig. 1, and basic subsidence features & results illustrated in Fig.3 and Fig.4 provide the cases illustrate the influences of rock masses' mechanical characteristic on the ongoing procedures of the downward deformations, (caving), of the rock masses. Caving which has been progressed (slowly or quickly) in the overburden rock masses depends on their mechanical properties and behaviours. Mining activities performed in history have abandoned numerous open underground spaces which have their potential for their caving activities in time to form subsidence or sinkhole type failures. Types of overburden rock masses affect the angle of influence zones. Fracturing and bending of the horizontal rock layers, homogeneous deformations through other rock types, etc, have influenced the downward movements of them through their fracturing & fragmentation procedures. If the abandoned underground mine openings are located in shallow depth ranges, their collapses form egg-voile types surface morphology (with many holes of depressions, Fig. 4a). Similarly, abandoned underground spaces have gradually formed stability risk for the surface urban structures. The situation presented by Pellicani, et al. [15] in Fig. 4b illustrates the surface areas which have higher failure risks due to abandoned underground spaces. Mining history includes excavation of coal and building stones through shallow underground mines which were mainly handled with room & pillar mining methods. Their abandoned rooms are the main sources of subsidence which influences the current urban and agricultural lands. These spaces have been analysed to predict their risks on the surface/underground structures, (Fig. 4c). Subsidence over coal mines had dramatic influences in urban areas. Therefore, countries which have abandoned coal mines have also their individual experiences of subsidence, and sinkholes. Singh & Dhar, [17], worked on subsidence types over coal mines, and they illustrated chimney type (steep-sided, Fig. 5c) subsidence

migration, (there are also shallow-sided sinkholes which have volumetric upside-down conical geometries at their ground surface intersections over their steep-sided sinkhole layers). When the caving started in the overlying rock strata of coal rooms; these authors wrote that, “*caving migrates through the overlying strata until the fracture zone intercepts the unconsolidated overburden*”, (Fig. 5a). The weak rock layers over the underground rooms, (spaces), collapse due to their tensile and shear behaviours, [18]. Caving of the roof layers migrates towards the ground surface by the effects of induced stresses and it can only be decelerated by rock strata which have higher strength values or “*bulking of roof debris*”, [17], (Fig 5b). Subsidence influences over coal seam mining operation have studied by several researchers and their works have been handled through the subsidence and sinkhole risk evaluation literature related to underground mines and natural cavities. Heritage, [19] for instance presented numerical analyses results provided through FLAC 2D analyses to be used in the evaluations of subsidence over coal seam panels. Researchers in this field analysed; the mode of failures, vertical displacements, cumulative & incremental subsidence, rock failure modes, hydraulic conductivity differentiations for overburden rock masses through their 2D modelling procedures. Figure 6 illustrates one of the results related to rock mass hydraulic conductivity differentiation over the extracted coal panels of the coal field at Southern Coalfields of NSW, Australia, [19]. The rock masses’ fracturing & their migrations over the coal seam resembles with the hydraulic conductivity increases. Heritage, [19], wrote that the vertical conductivity model here supplied output, (Fig. 6), which has “*a distinct high conductivity zone in the 60m above the seam*”.

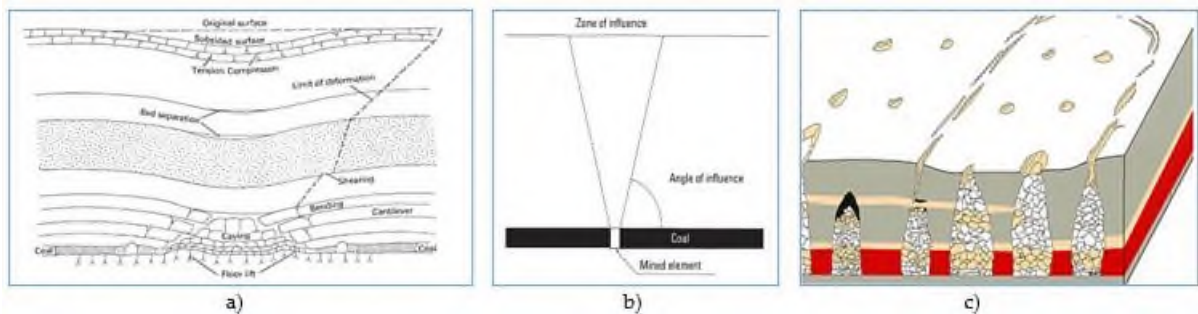


**Figure 3.** Subsidence influences, a) Deformations (caving) of overburden rock masses due to coal seam mining [11, modified from 12], b) Influence zone above coal seam galleries (or panels) which have tendency of caving (schematic illustration), [13], c) Collapses of over layer rock masses governed by induced stress conditions and rock mass discontinuities, [14].

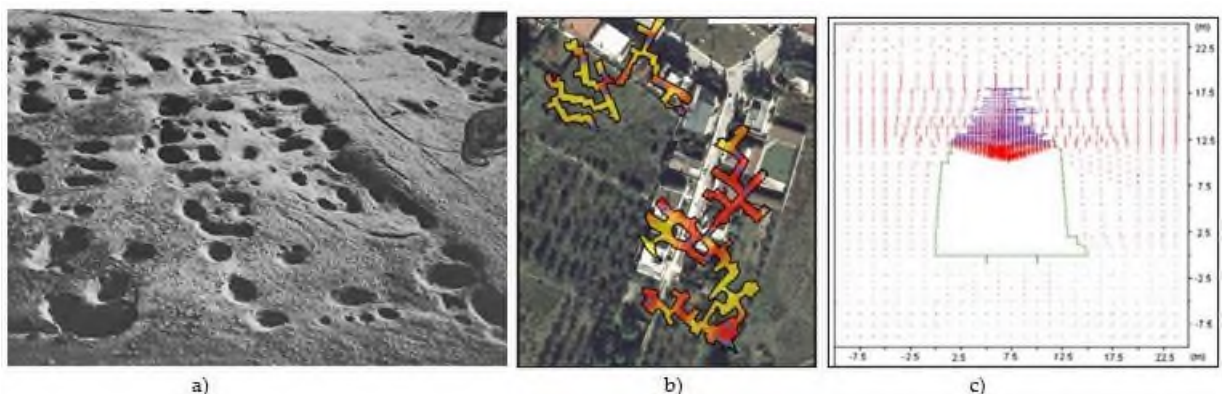


**Figure 4.** a) Ground surface deformations due to coal mine subsidence holes, troughs, and cracks above a coal mine at the Western Powder River Basin, Wyoming, US, (Photo-graph; C.R. Dunrud), [11], b) Location of instability evidences, (Barcelona Street, Altamura, Italy), [15], c) Example of numerical (distinct element method) analysis which helps to understand failure conditions around the underground mined out spaces at Castellana, Italy, [16].

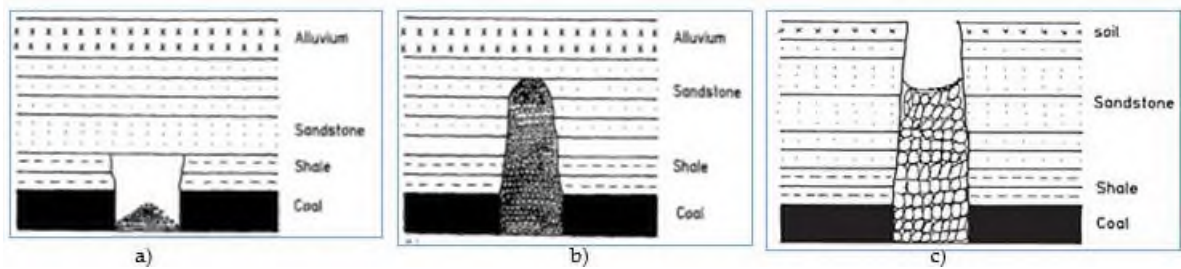


**Figure 5.** Rock mass collapse migration through overburden layers, [17].

Numerical model studies have obstacles about their material behaviour models, approaches, (*rock mass behaviours, for instance, have not totally modelled, there are only criteria to evaluate these behaviours*). Uncertainties in input data form also unclearness for 3D rock mass property distributions. These natural features of rock masses cannot be eliminated but available approaches for rock mass mechanical behaviours, and developments in rock engineering research area push the numerical analyses to supply more reliable outputs for real-world rock engineering problems. However, Zhou, et al., [20] studied hard rock failures around underground spaces and they presented the complexity of the parameters in their failure analyses. Uncertainties in rock properties and their distributions in the rock masses have formed main unclearness in the results of the analyses in which engineers must supply a bunch of decisions to direct their engineering related works in the underground space operations (which covers dangerous conditions for work & work-place safety concerns). Thus, different approaches have then been handled to deal with these uncertainties including statistical analyses and/or expert decision support systems. The results supplied through them, (like rock failure criteria, rock mass classification systems, etc.) are valuable sources of engineering resources to be evaluated in engineering decisions. For instance, when the failures of roof layers of underground spaces are in consideration, (where there is a tendency of caving procedures), the work supplied by Park, [21], for hard-soils & soft-rocks (Fig. 8) can also be considered to understand mechanical failure mechanism of the “early phases of cavity formation” at the roof layers of underground spaces, (conduits, tunnels, etc.). Modelling rock masses above collapsed mine openings or natural cavities provides assistance during the evaluation of their influences and risks of failures. These considerations are valuable assets in our populated world which subsidence & sinkholes could possibly cause unprecedented damages to urban, industrial, agricultural land parcels. Therefore, evaluations & predictions of failure risks due to subsidence&sinkholes for these parcels are important. These works then should be realised by national and local governments to supply stable land parcels for different human activities. Numerical models therefore have their values especially in rock mechanic analyses to supply induced stress-strain cases for such subsidence influenced local areas. Numerical analyses performed for homogeneous massive metals which have uniform mechanical behaviours could supply more reliable results when compared with the heterogeneous solid materials. Rock masses have their numerous types and compositions with indefinite numbers of discontinuity contents. That means uncertainty of measured test data (laboratory or field data sets) cannot be put aside when the rock mechanics are under analyses & evaluations for their characteristics. When the decisions required to be supplied for the sinkhole risks for a specific land parcel, overburden rock masses above any underground spaces (natural or man-made excavations) should be analysed for their caving (subsidence) characteristics. However, contents covered undefined 3D rock characteristics and behaviours are comprehensive and complex in characteristics. Therefore, they are preferred to be considered with expertises like the cases of “rock mass classification rating systems”. Shiau et al., [22], for instance supply idealised sinkhole analyses for their supplied course procedures. These authors assumed that the cross-sectional shape of the sinkhole cavity is round at the beginning. Then it can be enlarged to have conical cross-sectional shape, (when it is advancing towards the ground surface). The whole volumetric geometry of the sinkhole can also be defined like the cases described for Fig. 5 cases. The results obtained by Shiau et al., [22], through their idealised numerical models including limitations

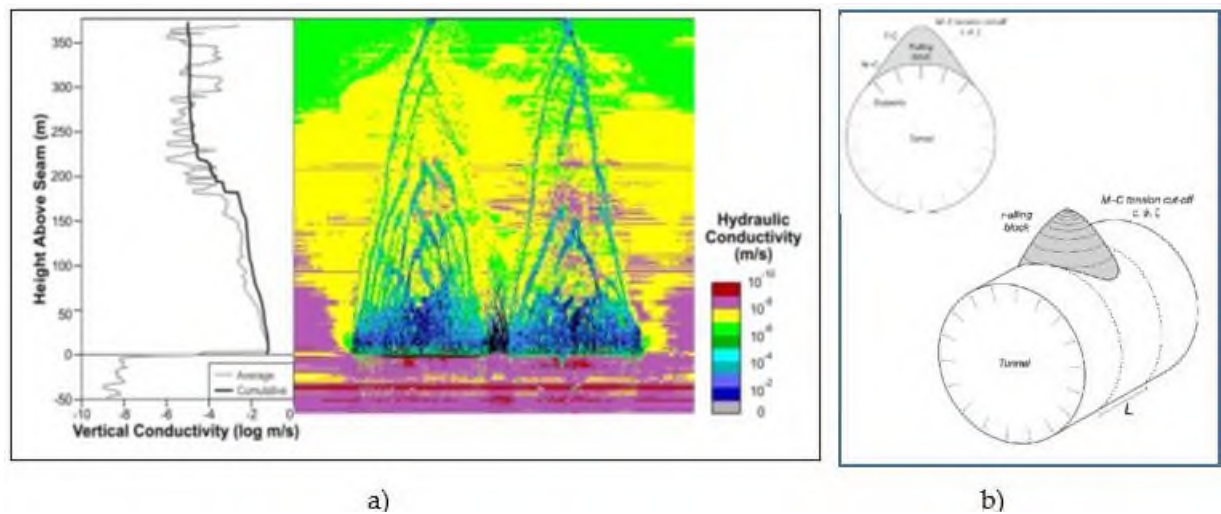


**Figure 6.** a) Rock masses hydraulic conductivity differentiation in modelled coal-seam overburden rock mass, [19], b) Triangular arch-shaped cavity considerations through Mohr-Coulomb (M-C) envelope & Tension-cut off (T-C), [21].

in, “the depth ratio ( $h/w$ ), the width ratio ( $l/w$ ), the soil strength ratio ( $c/\gamma w$ ), and the angle of internal friction ( $\phi$ )”, (Fig.7). When the caving procedures of sinkholes & subsidence, especially the chimney types of cavings are under considerations, the studies provided through field sinkhole observations, and numerical solutions offered for their failure considerations. These information and knowledge have been reviewed here to deliver reasonable explanations for the sinkholes and their induced stresses&strains at Karapinar (Konya, Turkey). Like the overlaying materials considered in Park analyses, [21], which were hard-soil / soft-rock, overburden rock masses above the sinkhole are layered low strength rocks. Sinkholes located in this region have their long-known history. As Dogan & Yilmaz, [23], stated that pumping (discharge) of groundwater for increased requirements of irrigation have decreased the groundwater level in the region. Gutierrez, [24], stated that the developments of sinkholes in this region have been related to the, “*Late-Quaternary lacustrine deposits of the Konya pluvial lake underlain by Pliocene limestone*”. Dogan & Yilmaz also wrote that the lacustrine formation related to sinkholes near Konya was “*Insuyu-formation*” and it had been formed “*as a result of an extension regime during the Upper Miocene–Pliocene*”, [25]. The types of rock masses in Insuyu-formation were listed as; “*thick limestone in the upper section, limestone, marl, clay, tuff and silt intercalation in the lower section*”, [26, 27]. After supplied this information, Dogan&Yilmaz, [24], mentioned also about “*the thickness of fractured lacustrine limestone, suitable for karstification*”. It has a thickness over 200m, [28]. Central region of Turkey is an elevated Plato, (850-1000m) and it is a hydro geologically closed region. Therefore, it has its own groundwater circulation circumstances, [24]. Main groundwater flowing direction towards the lowest ground surface area at the elevation of 902m at “*Tuzgolu*” Salt Lake, (Konya, Turkey). Groundwater paths and their numerous branches in the rock masses are then expected to form water circulation conduits which have formed micro & macro cavities (karstification). When these underground water circulation paths have come across weakness zones, these conduits may have interrupted with roof collapses. Rock materials solubility and fragmentation properties have then been governing factors in material removal away from the collapsed underground spaces’ locations. Collapsed parts of the underground conduit spaces which have groundwater or not are then form additional small scale underground cavities at the roof of these conduits. As the induced stress with/without groundwater influences continue to affect stabilities of these conduits and cavities, it is natural to expect further roof & sidewall collapses as the strength of the surrounding rock masses have been overwhelmed by these influences. Thus, even the small-scale cavity which might be formed at the roof of the underground conduits are important factors to initiate sinkhole type caving actions at the overburden rock masses. If the surrounding rock masses of underground spaces are weaker in strength, and cannot increase their 3D load-bearing characteristics,

(solid material precipitation like calcination effects at the fractures and inner surfaces of the conduits due to groundwater circulations), they collapse according to their 3D rock failure conditions. Earthquake vibrations, changing the induced stresses and groundwater conditions, and pore pressure differentiation due to changes in rock gasses & groundwater reservoir conditions have influenced these collapses and their rate of occurrences in geological time periods.

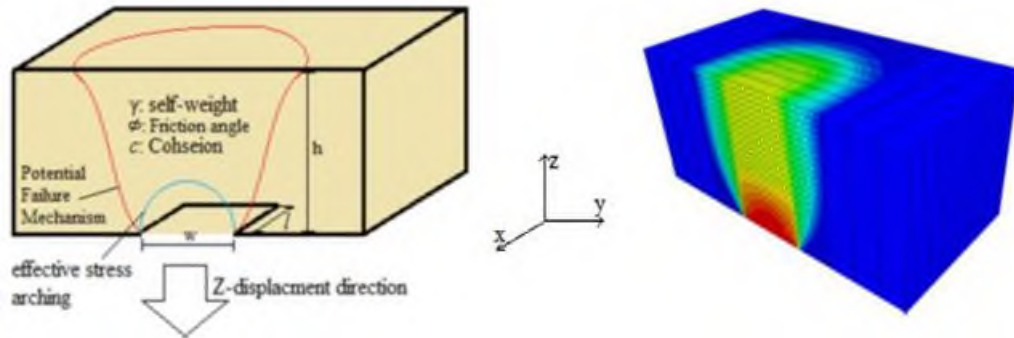


**Figure 7.** Subsidence (sinkhole cavity) model idealised for numerical FLAC 3D analyses and resultant velocity contours obtained (for the case of;  $h/w=2$ ,  $w/l=2$ ,  $c_u/\gamma D=1.05$ ), [22].

#### 4. ANALYSIS OF STRESS-STRAIN CONDITIONS AROUND A HYPOTHETICAL SINKHOLE

Underground spaces (in micro/macro scales) are widespread in earth crust. Their occurrences are vital for the creatures living on earth. Groundwater and other liquids and gasses occupy the pores & cavities of earth crust for their reservoir locations. Their time-dependent chemical and physical processes (under high overburden earth pressure) have continued there according to the depth of deposition as well. Initiation of micro scale cavities through rock fractures, and rock property alterations after their chemical weatherings are expected features for all celestial planetary rock crust which have their gravitational force. As far as there is no human activities around subsidence & sinkhole areas, these cavity collapses related to ground surface morphologic differentiations might be accepted as normal features. However, human urbanisation areas, crop fields, forests, etc. have required stable ground dynamics. Displacements even in the micro-scale which were realised at the base of them have caused damages on their structural conditions in time. For instance, the ground surface at Konya Plato (Turkey) has developed flat landforms at the centre of the region. The rock masses and related rock formation units have formed according to the conditions of geological eras and the regional morphology has shaped with ongoing volcanic, tectonic, and sedimentation activities. Types of rock masses and; their thicknesses, angular settlements, layers, fractures, cavities, weakness zones, etc. are all related to those activities and climatic conditions (differentiations) in geological eras. The resultant rock masses are reported through research [24; 26, 27] with related “rock-formations” and their geological eras as stratigraphic columns. Ulu reported that Insuyu-formation which is Miocene-Pliocene era rock consist of sinkholes in Konya region [25, 26, 27] has *conglomerate, sandstone, siltstone, claystone, marl, limestone, platy limestone, tuff, ignimbrite, and chert rocks*. The stratigraphic section obtained for the Karapinar (Konya) region was supplied by Törk et al., [29; 30] as well. Miocene aged Insuyu rock formation contented rocks are listed here as; *red conglomerate, sandstone, mudstone, chert, limestone, dolomitic limestone, micritic, marl, platy limestone, claystone, conglomerate, Ignimbrite, tuff, claystone, mudstone, and lacustrine limestone*. The other rock formations over the Insuyu-formation were listed (with their rock contents) as follows, [30]; Insuyu-formation had first been over-layered with Pliocene aged Karacadag-formation (*agglomerate, andesite, basalt, dacite, riolite*). Then, Kilavuztepe-formation (Pliocene) had formed over them with its *basalt* rocks. Incesu-formation has a transition time between Pliocene and Pleistocene era, and it consists of *conglomerate, sandstone, claystone, mudstone, lacustrine limestone*. Pleistocene era rock formations were formed over Incesu-formation one over the other as follows: Akviran-formation (*conglomerate*); Karapinar-formation (*pyroclastics of maar, basalt, stag*); Divanlar-formation (*gravel, sand&mud*); Tuzgolu-

formation (*gravel-sand, silt-clay, clay with gypsum, clay with limey, sand&silt, clay&sand with organic soil*); Koymatyayla-formation (*gravel&sand, silt with carbonate, silt&marl with sand*); Hotamis-formation formed during Pleistocene and Holocene era. Its Pleistocene aged rocks are listed as; (*gravel&sand, sand with gravel, silt, clay, lignite, sand&gravel, silt&clay with carbonate, gravel&sand*), Hotamis-formation's Holocene era rocks are listed as; *clay with organic soil or soft clay*. Other Holocene era rock formations are Taburici-formation (*wind sand-dunes*), and Traverten-formation (*travertine*). The rock types at *debris rocks, alluvium, alluvial fans* are the latest rock types listed by Törk et al., [30]. The rock type images near the ground surface can also be observed at sinkhole photos which were taken at Konya, Turkey. As it is seen from the photographs (Fig. 8), the rock masses below the ground surface at the sinkhole region of Konya are layered rocks and their stratifications were listed through the works performed by Törk et al., [30]. Groundwater levels can also be observed at some of the sinkholes collapsed in Karapinar, (Konya) region (Fig. 8c).

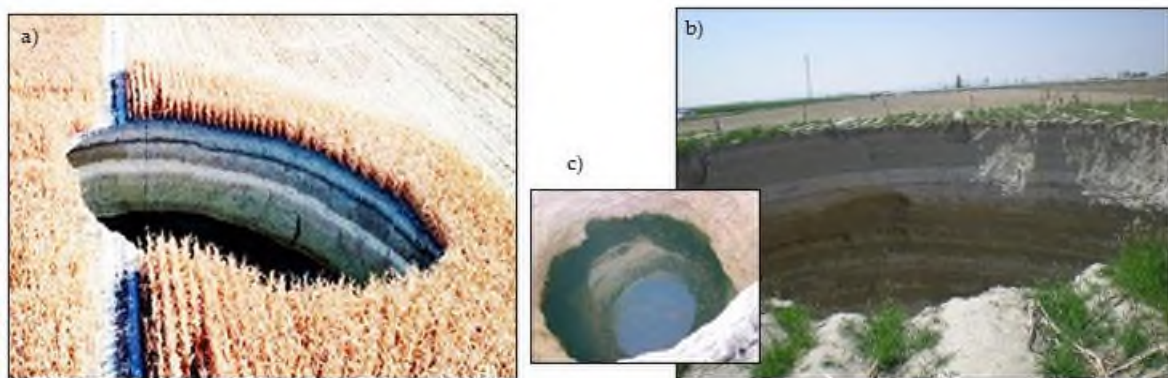


**Figure 8.** a) Rock layers just below the ground surface at a sinkhole formed at a cornfield in Sep.2018 (Konya), [31]. b) Rock layers at Yarimoglu sinkhole, collapsed in Dec. 2008 at Karapinar-Konya, [32], c) Groundwater level observed at the bottom of the Yarimoglu sinkhole (in May 2009), [32].

Rock mechanics behaviours of the layered rocks listed through stratigraphic sections require complex & comprehensive research. Underground conduits/spaces which groundwater can be deposited or flow through could be in different sizes and shapes. Underground water reservoirs, passage routes, conduits might also come across faults, fracture zones, weakness zones, etc. to initiate upward caving procedures to form overburden caving activity described like in Fig. 5, [17] and Fig. 6b, [21]. Possible chimney type sinkhole progress could happen step by step in time as it is illustrated in Fig. 9. This figure presents hypothetical sinkhole development phases that occurred due to mechanical property deterioration which could be directed by induced stresses, rock masses' property differentiation and groundwater influences. In order to visualize the mechanical property influences and groundwater effects together with cavity size variation, in this preliminary education targeted study, two types of hypothetical material models (two scenarios) were handled through numerical FLAC 3D v6.0, [33], solutions. In the first scenario, one type of low strength, uniform, homogeneous rock mass around the small sized cavity which tends to provide chimney type sinkhole was modelled as a massive rock material which deforms according to Mohr-Coulomb failure criteria. Input data facilitated for this step of the analysis are supplied for 40x40x40m cubic volume, (64000m<sup>3</sup>), which the calculation mesh was arranged to simulate deep sinkhole cases' (>40m), observed at Karapinar, (Konya), region like Yarimoglu sinkhole. Most of the sinkholes observed at Karapinar region have their depths, [29], less than 40m. Dursun wrote that 7 out of 52 sinkholes have their depths more than 40m, [29]. In this preliminary hypothetical study, numerical modeling techniques used were conducted to simulate sinkhole formation and assess its effects on surrounding rock mass deformation and stress fields through two scenarios. For the first scenario, soil and limestone units were layered above a defined water table at a depth of 30 meters. Sequential cavings happened at these layers simulate sinkhole progression in the hypothetical model in the first scenario. In the second scenario, additional horizontal



rock layers were introduced within the same geometric framework, enabling a comparative analysis of displacements and stresses under varying multi-layered rock mass conditions. In these models, each rock material type, unit, (i.e.: soil, limestone, silty clay, and sandstone, etc.) was assigned a Mohr-Coulomb failure criterion, with specific mechanical properties, (such as: density, elastic modulus, Poisson's ratio, friction angle, cohesion, and tensile strength), informed for low strength rock properties in general, [34, 35]. Fluid properties were activated by using the "fluid" module in FLAC 3D, assigning permeability and porosity for each rock type to reflect natural fluid behavior. Boundary conditions were applied to restrain normal displacement velocities along the side surfaces, with zero-velocity conditions at the top and bottom surfaces to stabilize the model. The water table was represented by a fluid plane defined at 30m depth of the model (which has 40x40x40m dimension) with a normal vector (0, 0, -1), establishing an underground water source with pore pressure conditions allocated to layers below this plane. Pore pressure and saturation were initialized to handle modelling of the hydrostatic effect at this depth. Through stepwise excavation and monitoring, sinkhole evolution was simulated in both scenarios, with outputs captured to analyze the stress and deformation patterns resulting from sinkhole formation. The results of numerical models by using FLAC 3D software are obtained for hypothetical sinkhole cases which simulate deep sinkhole cases are illustrated in Fig.10-14. Induced displacement levels are presented for the vertical directions of the models in Fig. 10. In similar manner, induced stress levels differentiations in vertical axis are also presented in Fig. 11. The second scenario of the hypothetical sinkhole model analysis included 3D rock layer modelling which has horizontal rock layers (massive & uniform) in the model, (Fig. 12). The resultant vertical displacement (Fig. 13) and vertical stress differentiations (Fig. 14) are then plotted to evaluate the differences with respect to 1<sup>st</sup> scenario results. Hypothetical models which are used in this study are actually an engineering attitude to model the complex rock mass structures observed at Karapinar regions. As the general stratigraphic sections supplied by Ulu [26, 27] and Törk et al., [30] illustrated that rock masses in the Karapinar (Konya) region have their layered characteristics with their different values of thicknesses. In order to approach more realistic 3D rock mass modelling for the Karapinar region, inclusive studies should then be scheduled to obtain mechanical properties of each rock mass encountered through the unique rock-formations belonging to this region. The research most probably will include several drill-holes to collect enough rock carot samples to determine rock masses' thicknesses, depths, mechanical properties, porosities, permeability, etc. for observed stratigraphic rock masses.

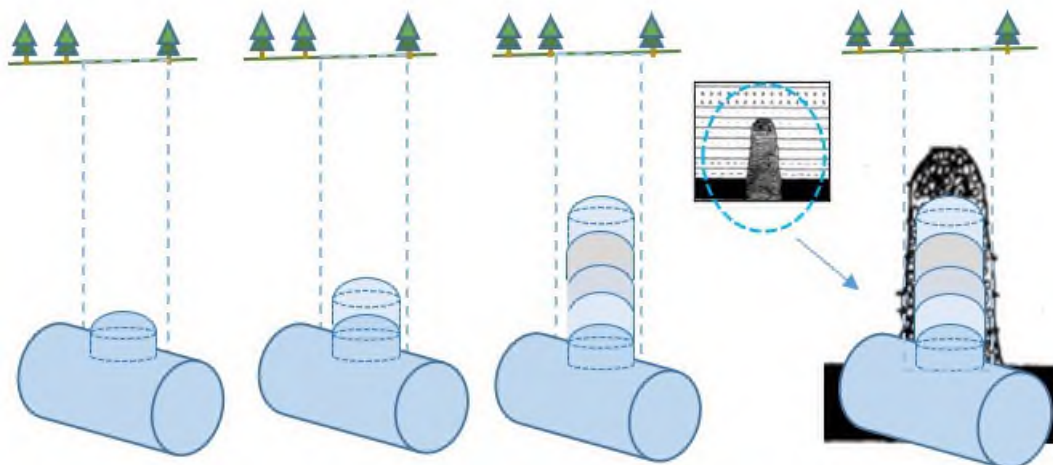


**Figure 9.** Hypothetical considerations for chimney type sinkhole development. Caving procedures have taken place in time step by step in upward direction where the rock masses are fractured according to induced 3D stresses-strains conditions.

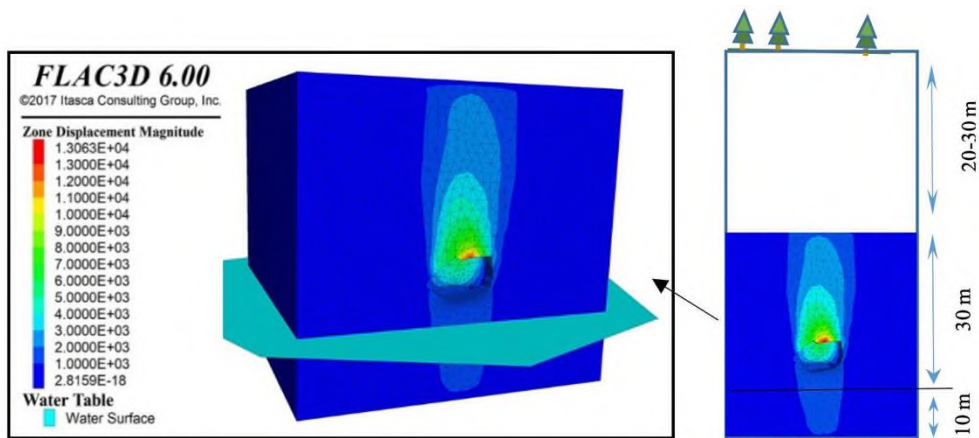


Figure 10. Induced displacement zone values (in mm) for the 1<sup>st</sup> case scenario modelled through FLAC 3D for hypothetical small scale roof cavity of groundwater conduit tending to develop sinkhole.

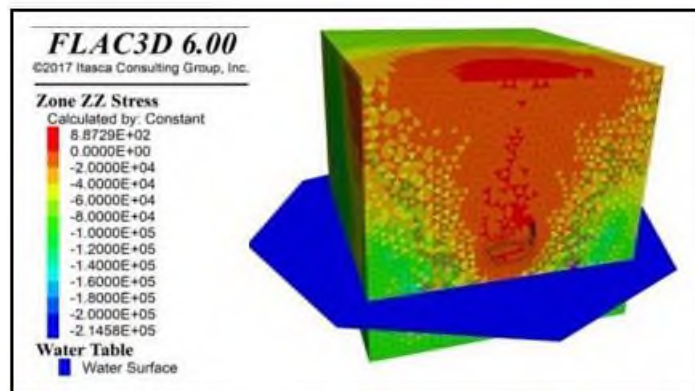


Figure 11. Induced vertical stress (in Pa) distributions for the 1<sup>st</sup> case scenario at the modelled hypothetical sinkhole development through FLAC 3D start from small scale roof cavity of groundwater conduit tending to chimney type sinkhole.

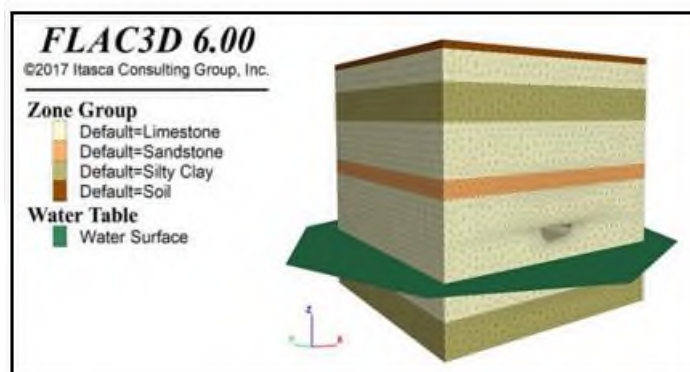
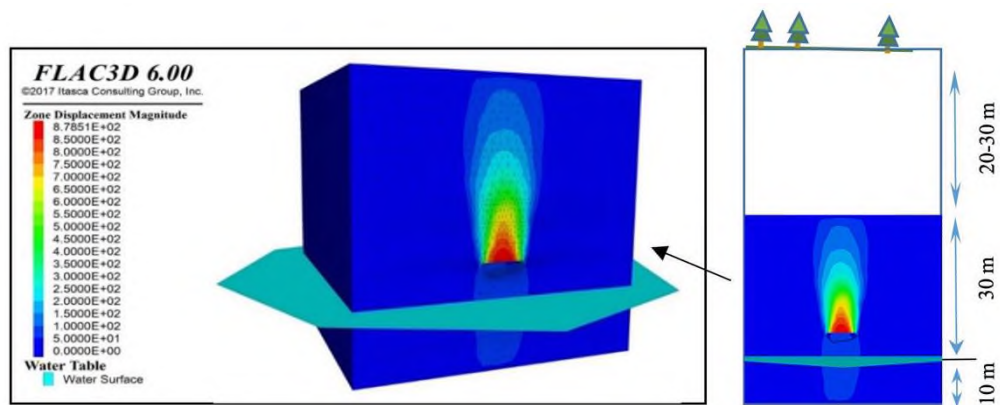
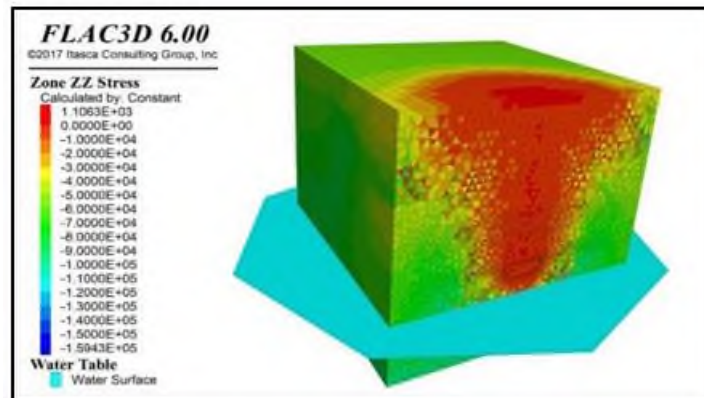


Figure 12. Hypothetical layered rock mass modelling example for the analysis of 2<sup>nd</sup> scenario through FLAC 3D analyses.



**Figure 13.** Induced displacement zone values (in mm) for the 2<sup>nd</sup> case scenario modelled through FLAC 3D for hypothetical small-scale roof cavity of groundwater conduit tending to develop sinkhole.



**Figure 14.** Induced vertical stress (in Pa) distributions for the 2<sup>nd</sup> case scenario at the modelled hypothetical sinkhole development through FLAC 3D start from small scale roof cavity of underground groundwater conduit tending to chimney type sinkhole.

## 5. CONCLUSION

Underground spaces micro and macro scale in dimensions are widespread in earth crust. Their stabilities concerns are not only related to their structural healths and safety but also the stabilities of overburden layers which have potential danger of caving due to their collapses. Underground mining spaces, natural rock pores, voids, cavities, caves, all types of civil subterranean spaces etc. have their potential to initiate subsidence & sinkholes. Mechanical behaviours of the rock masses in the fields are difficult to estimate due to their scales, and uncertainties encountered. Laboratory rock material test results and their evaluations supply valuable data but they have their limitations for the real-world rock mass cases. When the problem encountered by engineers is sinkhole collapse and its development, sinkhole occurrences and their developments for certain regions are required to be analysed through rock mass mechanical behaviours. Roof failure analyses supplied for underground spaces are the starting point in these kinds of analyses. Rock fracturing, fracture initiations and propagations according to induced stresses around the cavities are directing research fields to be followed. Numerical analyses supply also data & results for engineering decision circumstances. Preliminary numerical analyses handled here to understand the stress and displacement distributions around sinkhole cavities. Massive rock mass consideration was enhanced here with massive horizontal rock mass layer additions to the hypothetical sinkhole models to visualise the stress and deformation differentiation. Engineers should follow rock mechanics procedures to evaluate subsidence and sinkhole developments and their dangers on economic assets (urban areas, crop-fields, forests, etc.). Comprehensive researchers including drill-holes to obtain carrot samples from each geologically named rock-formation below the targeted land

parcels could be required for further rock mechanic analyses to handle more representative input data for numerical analyses. Decreasing the uncertain features of the rock strength properties and rock discontinuity set related parameters, provide more realistic results in conceptual and numerical analyses. Thus, collecting representative input data and modelling the sinkhole host rock masses in a more realistic manner helps to evaluate sinkhole occurrences at Karapınar (Konya) region as well.

### **Declaration of Ethical Standards**

The authors declare that the study complies with all applicable laws and regulations and meets ethical standards.

### **Credit Authorship Contribution Statement**

M.Kemal GOKAY: Methodology, Conceptualization, Resources, Investigation, Writing, Review & Editing, Supervision.

Mehmet MESUTOGLU: Methodology, Conceptualization, Resources, Investigation, Writing.

### **Declaration of Competing Interest**

The authors declare that they have no known competing financial interests or personal relationships that could have appeared to influence the work reported in this paper.

### **Funding / Acknowledgements**

The authors have not disclosed any funding

### **Data Availability**

Data will be made available on request.

### **REFERENCES**

- [1] M.K. Gokay, "Yeraltında bulunan doğal (obruk, mağara) ve yapay (galeri, depo, şehir) boşlukların stabilitesi", Seminar notu #2, (*Stability of natural (sinkhole, caves) and man-made (galleries, depots, subterranean city spaces) underground spaces*), Seminar-notes #2. (in Turkish), Departmental Seminar, Feb. 2<sup>nd</sup> 2011, Selcuk University, Mining Engineering Department, Konya, Turkey, p125, 2011.
- [2] R.K. Taylor, "Characteristics of shallow coal mine workings and their implications in urban redevelopment areas", (Section 7 in; *Site investigations in area of mining subsidence*, Bell,F.D. ed.), Newnes & Butterworths Publication, London, UK,1975.
- [3] F.G. Bell, "Site investigations in area of mining subsidence", Newnes & Butterworths Publication, London, UK, 1975.
- [4] A.B. Klimchouk, D.C. Ford, A.N. Palmer, and W. Dreybrodt, (eds.) "Speleogenesis, Evolution of Karst Aquifers", Jan.2000 Edition, National Speleogenesis Society Inc. Alabama, US.
- [5] B.N. Whittaker and D.J. Reddish, "Subsidence, Occurance, Prediction and Control". Elsevier Publication, London, UK., 1989.
- [6] T. Waltham, "Rock failkure n collapse and caprock sinkholes, Rock failure under imposed load over caves", Chapter (3 &7) in; *Sinkholes and Subsidence : Karst and cavernous rocks in engineering and construction* (Eds: T. Waltham, F. Bell, and M. Clshaw), Springer Publ. Berlin, and Praxis Publ. Chichester, 2005.
- [7] C. Galeazzi, "The typological tree of artificial cavities: A contribution by the Commission of the Italian Speleological Society", (*Proceedings of the international workshop on speleology in*

- artificial cavities, "Classification of the typologies of artificial cavities in the world", 18-20 may 2012, Torino, Italy), *Opera Ipogea*, 1, pp11-20, 2013.
- [8] K. Terzaghi, "Rock defects and loads on tunnel supports. In: Rock tunneling with steel supports", (Eds: R.V. Proctor and T.L. White), Youngstown, OH: Commercial Shearing and Stamping Company, 1, pp17-99, 1946.
- [9] E.G. Kirsch, "Die Theorie der Elastizität und die Bedürfnisse der Festigkeitslehre". *Zeitschrift des Vereines deutscher Ingenieure*, 42, pp797-807, 1898.
- [10] D. Li, Q. Zhu, Z. Zhou, X. Li, and P.G. Ranjith, "Fracture analysis of marble specimens with a hole under uniaxial compression by digital image correlation". *Engineering fracture mechanics*, 183, pp109-124, 2017.
- [11] F.T. Lee, and J.F. Abel, Jr, "Subsidence from underground mining: Environmental analysis and planning considerations", Geological Survey Circular: 876, US Department of Interior, p28, 1983.
- [12] C.H. Shadbolt, "Mining subsidence-historical review and state of the art", in Geddes, J. D., ed., Conference on large ground movements and structures: Cardiff, Wales, July 4-7, 1977, Proceedings, pp705-748, 1978.
- [13] D.L. Galloway, G.W. Bawden, S.A. Leake, and D.G. Honegger, "Land subsidence hazards", (Chapter in Landslides and land subsidence hazards to pipelines, Open-File Report 2008-1164, US. Department of Interior, US Geological Survey, pp40-106, 2008.
- [14] J.E. Turney, A. Amundson, C. Greenman, and B.K. Stover, "P-26 Subsidence above inactive coal mines: Information for the Homeowner. Special Publication". Denver, CO: Colorado Geological Survey, Department of Natural Resource and the Colorado Division of Reclamation, Mining & Safety, CGS Publications, 1985, 2009.
- [15] R. Pellicani, G. Spilotro, and F. Gutiérrez, "Susceptibility mapping of instability related to shallow mining cavities in a built-up environment", *Eng. geology*, 217, pp81-88, 2017.
- [16] M. Parise, and P. Lollino, "A preliminary analysis of failure mechanisms in karst and man-made underground caves in Southern Italy", *Geomorphology*, 134, pp132-143, 2011.
- [17] K.B. Singh and B.B. Dhar, "Sinkhole subsidence due to mining", *Geotechnical and Geological Engineering*, 15, pp327-341, 1997.
- [18] M.G. Karfakis, "Chimney subsidence over abandoned coal mines", *International Journal of Mining and Geological Engineering*, (Short communication), 5, pp131-141, 1987.
- [19] Y. Heritage, "Validation of subsidence prediction approach of combined modelling and empirical methods", *Proceedings of the 10<sup>th</sup> Triennial conference on mine subsidence*, Pokolbin, NSW, Australia, pp193-205, 2017.
- [20] J. Zhou, Y. Zhang, C. Li, H. He, and X. Li, "Rockburst prediction and prevention n underground space excavation", *Underground space*, 14, pp70-98, 2024.
- [21] D. Park, "Roof stability analysis of cylindrical tunnels in hard soil/soft rock with reduced tension strength", *Computers and geotechnics*, 164, 105838, 2023.
- [22] J. Shiau, B. Lamb, and M. Sams, "The use of sinkhole models in advanced geotechnical engineering teaching", *Int. J. of geomate*, 10, 2, pp1718-1724, 2016
- [23] U. Dogan, and M. Yilmaz, "Natural and induced sinkholes of the Obruk plateau and Karapınar-Hotamis plain, Turkey". *Journal of Asian earth sciences*, 40, pp496-508, 2011.
- [24] F. Gutierrez, "Sinkhole hazards", Oxford Research Encyclopedias, natural hazard science, 20126, p86, Retrieved in Oct. 2024. Doi: 10.1093/acrefore/9780199389407.013.40.
- [25] A. Kocuyigit, "The Denizli graben-horst system and the eastern limit of western Anatolia continental extension: Basin fill, structure, deformational mode, throw amount and episodic evolutionary history SW Turkey". *Geodinamica Acta*, 18, 3-4, pp167-208, 2005.
- [26] U. Ulu, "Geological Maps of Turkey Karaman-M30 Sheet". *General Directorate of Mineral Research and Exploration*, Ankara (in Turkish), 2009a.
- [27] U. Ulu, "Geological Maps of Turkey Karaman-M31 Sheet". *General Directorate of Mineral Research and Exploration*, Ankara (in Turkish), 2009b.

- [28] B. Canik and I. Corekcioglu, "The formation of sinkholes (Obruk) between Karapınar and Kızoren-Konya. In: *Karst Water Resources*", *Proceedings of Ankara-Antalya Symposium, July 1985*. IAHS Publ., 161, pp193-205, 1986.
- [29] A.E. Dursun, "Risk analysis of natural sinkholes hazards in Karapınar basin (Konya, Turkey)", *Arabian J. of geosciences*, 15, 279, 2022, doi:10.1007/s12517-022-09564-8.
- [30] K. Törk, B. Erduran, P. Yılmaz, S. Sülükçü, I.N. Güner, S. Ates, G. Mutlu, S. Keles, A. Cınar, S. Demirbas, N. Sertel, C. Ozerk, A. Bulut, L. Yeleser, K. Avcı, A. Ayva, and A.T. Toksoy, "Determination of karstic subsidence areas and hazard assessment in Konya closed basin". *General Directorate of Mineral Research and Exploration of Turkey, Research Project Report*, No: 11605, Ankara, Turkey, (in Turkish), p320, 2013.
- [31] O. Orhan, T. Oliver-Cabrera, S. Wdowinski, S. Yalvac, M. Yakar, "Land subsidence and its relations with sinkhole activity in Karapınar region, Turkey: A multi-sensor InSAR time series study", *Sensors*, 21, 774, 2021, Doi: 10.3390/s21030774.
- [32] K. Dogan, and M.K. Gokay, "Konya-Karapınar'da oluşan obruklar; Yarımoglu örnek incelemesi, (Sinkhole at Konya-Karapınar: Works on Yarımoglu sinkhole example)", Selcuk University, BAP research project, Konya, p55, 2014.
- [33] Itasca, "Fast Lagrangian analysis of continua (FLAC) 3D", Itasca Consulting Group Inc., Minneapolis, Minn., 2005.
- [34] M. Caudron, F. Emeriault, R. Kastner, M. Al-Heib, "Sinkhole and soil-structure interactions: Development of an experimental model." International Conference on Physical Modelling in Geotechnics 2006, Hong-Kong, China. pp1261-1267, 2006.
- [35] Z. Zhang and Z. Chen, "Numerical simulation of bedrock sagging sinkholes in strain-softening rock induced by embankment construction" *Hindawi Advances in Civil Engineering*, Article ID 9426029, p19, 2019, Doi: 10.1155/2019/9426029.



## REAL-TIME DETECTION OF TRAFFIC SIGNS WITH YOLO ALGORITHMS

\* Abdil KARAKAN 

*Afyon Kocatepe University, Dazkırı Vocational Scholl, Electrical Department, Afyonkarahisar, TÜRKİYE*  
[akarakan@aku.edu.tr](mailto:akarakan@aku.edu.tr)

### *Highlights*

- Customized Turkish Traffic Signs dataset consisting of 78895 images
- Preprocessing methods have been added to increase the efficiency of the model.
- The accuracy of the proposed YOLOv8 model is 99.60%.
- Detection was made in different weather conditions and at different speeds.



## REAL-TIME DETECTION OF TRAFFIC SIGNS WITH YOLO ALGORITHMS

\* Abdil KARAKAN 

*Afyon Kocatepe University, Dazkırı Vocational Scholl, Electrical Department, Afyonkarahisar, TÜRKİYE*  
[akarakan@aku.edu.tr](mailto:akarakan@aku.edu.tr)

(Received: 10.08.2024; Accepted in Revised Form: 10.02.2025)

**ABSTRACT:** The number of electric vehicles is increasing day by day. The biggest reason for the increase in electric vehicles is their autonomous or semi-autonomous use feature. Autonomous or semi-autonomous driving; It is the movement of the vehicle with the data coming from the sensors, cameras, and sensors around the vehicle. The majority of traffic accidents are caused by driver errors. The most important of these mistakes is not obeying traffic rules. Autonomous or semi-autonomous driving largely prevents driver-related traffic accidents. The biggest problem of autonomous vehicles is the difficulties in detecting traffic signs in real-time. The locations, shapes, and scales of traffic signs are very different. Traffic signs are difficult to detect in real-world conditions due to their similarity to other objects. The study carried out real-time detection of traffic signs. For this purpose, images were taken from the camera placed inside the vehicle. A data set was created with these images. The more real environment images the data set consists of, the more accurate the real-time detection process increases. In this study, 8931 traffic sign images were taken from real environments. These images were taken from different locations, different lighting levels, and different distances. In addition, the number of data was increased to 78895 by adding grayscale, adding slope, blurring, adding variability, adding noise, changing image brightness, changing colour vividness, changing perspective, resizing, and positioning the images. With this study, the data set was adapted to the real environment. The created data set was used in 3 different versions of YOLOv5 architecture, YOLOv6, YOLOv7 and YOLOv8 architectures. As a result of the study, the highest accuracy was found to be 99.60%, F1-Score was 0.962 and mAP@.5 value was 0.993 in YOLOv8 architecture.

**Keywords:** *Deep Learning, Real-Time Detection, Traffic Signs, YOLO*

### 1. INTRODUCTION

As a result of increasing air and environmental pollution, approximately 90% of the world's population breathes polluted air. More than five million people die due to air and environmental pollution every year. Our fossil fuel-powered private cars, which are used extensively in our daily lives, also have a large share in this pollution. In addition to air pollution, exhaust gas emissions also cause climate change. When we look at today's energy consumption, fossil fuels are used as the primary source and to the greatest extent. However, the amount of fuel used in transportation and transportation accounts for an average of 14% of the greenhouse gases and 23% of the CO<sub>2</sub> emissions worldwide [1-3].

It is predicted that electric vehicles can help reduce pollution caused by fossil fuel vehicles. However, considering that autonomous vehicles will both reduce air pollution and contribute to traffic safety, it has also focused on this area.

The idea of giving vehicles autonomous features dates back to the 1920s. In 1939, as a result of the joint research and development activities of General Motors and the American Sarnoff Laboratory, the idea of autonomous vehicles was presented to the public for the first time at the New York World's Fair. The autonomous vehicle idea exhibited also included a highway system that would assist the vehicle. In 1958, testing of this type of vehicle was carried out for the first time, and a self-driving autonomous car was tested. Later, much work was done to develop autonomous buses, trucks, super smart vehicle systems, and driving video image processing [4].

The biggest problem for autonomous vehicles is the detection of traffic signs. Traffic signs must be

\*Corresponding Author: Abdil KARAKAN, [akarakan@aku.edu.tr](mailto:akarakan@aku.edu.tr)



identified so that vehicles can move or direct their movement. For this, traffic signs must be detected with high accuracy in all kinds of environments. Many methods are applied to detect traffic signs and markers. These detection structures have many variants with different data structures, training methods, and detection functions. One approach uses colour and shape, two important physical characteristics of traffic signs. Colour-based detection method uses blue, red, and yellow colours present in traffic signs and markers and intensity detection technique. With this method, the image is separated into colour channels. The largest area of these separated colour pixels is created to be connected to each other. Intensity information is obtained by converting the image into colour space. In shape-based detection, triangles, circles, quadrilaterals, and octagons are used as common standard shapes of traffic signs. In shape-based detection, detection is made by highlighting these features. For these features, border lines, structures and textures, and key points of standard shapes are used. The Hough transform is usually applied to detect these features. In its most basic sense, the Hough transform is used to define lines in the image. In recent years, significant developments have been experienced in machine learning, and machine learning-based detection methods have been developed. Machine learning methods such as AdaBoost, Support Vector Machine (SVM), and Neural Networks (NN) are used to detect traffic signs and markers. These methods have different training methods and different detection processes. In these detection processes, there are many input derivatives with different properties. AdaBoost and Cascade-based detection structures have been successful in many object identification problems, such as face recognition, vehicle recognition, and license plate identification. This structure has also been successfully applied to detect traffic signs and markers [5-8].

Ortataş used the Haar cascade algorithm to identify traffic signs and markers. Although there are examples of this structure in the literature for face recognition, pedestrian recognition, and license plate recognition, there is no application for plate recognition. In this context, firstly, a data set consisting of traffic signs and markers was prepared. Then, machine learning was performed on this data set with the Haarcascade algorithm. A simulation environment has been prepared to prove the accuracy of this learning. With the Vector Zero Roadrunner program, a road with traffic signs, and markers was defined on a three-dimensional track. Possible signs that a driver may encounter in traffic flow and which are learned with the Haarcascade structure have been placed in the simulation environment. This created track was added to the Unreal Engine platform, and an autonomous vehicle with a camera that can use this track was defined. Optimization studies were also carried out according to simulation outputs [9].

Convolutional Neural Network (CNN)-based detection methods learn features through a convolutional network. With the development of deep learning methods, CNN was used to detect traffic signs and markers. A CNN classifier is used to identify these objects. Most CNN-based detection networks are quite slow to detect objects. Among these networks, You Only Look One (YOLO) has very fast performance [10]. YOLO neural network basically starts by extracting a single image from a video. It resizes this image extracted in the second step. These images represent entry into the YOLO network. The YOLO network consists of layers. There are different structures in each layer. YOLO network takes an image as input. Then, it gets the coordinate information by drawing a boundary box. Evaluates the probability of there being an object inside the box. Finally, it checks whether the objects in the box belong to any class [11].

In the study conducted by Shao et al., the Faster R-CNN model was used for traffic sign detection. The recognition speed was increased by including Gabor wavelets in the detection process. They especially worked on the detection of small targets. For this, it made changes to the layers of the VGG16 architecture. It used Chinese and German traffic sign datasets as data sets. In experimental results, it achieved high detection, especially on small targets. As a result of the study, a high accuracy of 99.01% was achieved with the proposed method [12]. Zhang used YOLOv2 architecture for traffic sign detection. It used the Chinese traffic sign dataset as the data set. This data set contains 9176 samples from 25 different classifications. It divides the input entry images into grids to detect small traffic signs. As a result of the experimental study, it achieved an accuracy rate of 89.7% [13]. In their study, Lui and his colleagues worked on detecting small traffic signs. The data set used the Chinese traffic sign data set. As a result of

their study, they achieved a 6% increase in performance in detecting small traffic signs [14]. Belghaoui and his colleagues used the Ghost-YOLO architecture, a lightweight model, to detect traffic signs. With this model, they focused on features for detecting small signals. In the experimental study, it was determined that mAP50 was 92.71%. It shows that the number of parameters and calculations of the study decreased to 91.4% and 50.29% of the original, respectively [15]. Tabernik and Skocaj used the MASK R-CNN algorithm in their study. In their studies, they worked on data sets. They have improved the overall performance of the datasets. He applied his studies to the detection of 200 traffic sign categories. With the proposed approach, they found an error rate below 3%, which is sufficient for distribution in practical applications of traffic sign inventory management [16]. Stallkamp and his colleagues used Convolutional Neural Networks to recognize traffic signs using CNN. In their study, they used a dataset containing images of more than 50,000 German road signs from 43 different classes. As a result of their experimental studies, a high classification accuracy of 99.46% was achieved [17]. Kim and Lee used the Consensus (RANSAC) algorithm and CNN networks for lane tracking. In their study, they achieved superior performance compared to other lane detection algorithms by combining RANSAC with CNN [18]. Qian used the CNN method for traffic sign detection to achieve high performance in terms of traffic sign detection speed and recognition accuracy. Chinese traffic signs and GTSDDB dataset were used in their study. They worked on detecting 96 different traffic signs. As a result of their studies, an average accuracy rate of 97.56% was obtained [19]. Acros and his colleagues used the comparative analysis method to detect traffic signs. They used the German traffic signs dataset as the data set. They worked with different architectures. It achieved the highest accuracy of 95.77% in the Resnet V2 architecture, and 95.15% in the Resnet 101 architecture. The difficulties in detecting small traffic signs were noted in their models and it was determined that MobileNet-based models were suitable for mobile and embedded devices [20]. Hussian used Fast Branch architecture from CNN models to recognize traffic signs. They achieved a high accuracy rate of 98.52% in their study [21].

When the literature studies are examined, most of them use ready-made data sets. Experimental studies give good results in studies using ready-made data sets. When experimental results are applied in real life, traffic signs are either not detected or detected very little. The biggest reason for this is that in real life, traffic signs are located in different locations, at different lighting levels and the surrounding objects make it difficult to detect the event. In the study, photographs of real traffic signs were taken with the camera placed in the vehicle. This was done from different positions, different distances, different lighting conditions, and levels to ensure adaptation to the real environment. The resulting data set was used in 3 different algorithms in the YOLO5 architecture. As a result of the study, the highest accuracy was 98.80% in the YOLOV5 architecture, F1-Score was 0.950, and mAP@.5 value was 0.981.

## 2. MATERIAL AND METHODS

Real-time detection of traffic lights with the YOLO algorithm was carried out in three steps. In the first step, sub-processes related to the preparation of the data set were carried out. These transactions; include data preparation, pre-processing, training data, and test data processes. The second step is to create and adjust the convolutional neural network to be used for deep learning. These transactions; Creating a deep learning neural network model, adjusting deep learning neural network parameters, and uploading training and test data to the system. The last step is to run the system. In this step; training the model, retraining the system based on the results, and finally getting the results. Figure 1 shows the general working principle of real-time detection of traffic lights with the YOLO algorithm.

### 2.1. Data Set

Traffic signs differ in shape and size. At the same time, the places where traffic signs are placed are different. Especially the surroundings of the places where traffic signs are used are very different. For these reasons, it is difficult to detect traffic signs. To overcome these difficulties, the photographs that make up the data set must be very similar to the real environment. To achieve this, the data set was created

from images obtained with a camera placed in the vehicle. In this way, images very close to the real environment were obtained.

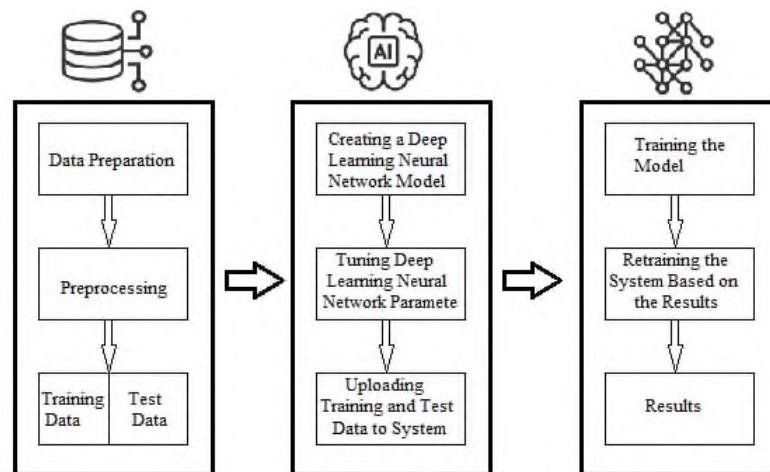


**Figure 1.** General working principle of real-time detection of traffic lights with the YOLO algorithm.

Some issues were taken into consideration when creating the data set. The first of these is the height of traffic signs. Not all traffic signs are equal in height. For this purpose, photographs of traffic signs at different heights were taken and added to the data set. Traffic signs are not always on one side of the road. For this purpose, photographs of the traffic signs on the right and left of the road were taken. Vehicles move at all hours of the day. In this case, traffic signs are encountered at different illumination levels. To minimize error, photographs of traffic signs in different lighting conditions and levels were added to the data set. Traffic lights do not always approach at the same distance. Especially at traffic lights on winding roads, the approach distance can be very short. To prevent this, images of traffic signs were taken from different distances and added to the data set. Figure 2 shows 9 different examples that make up the data set.

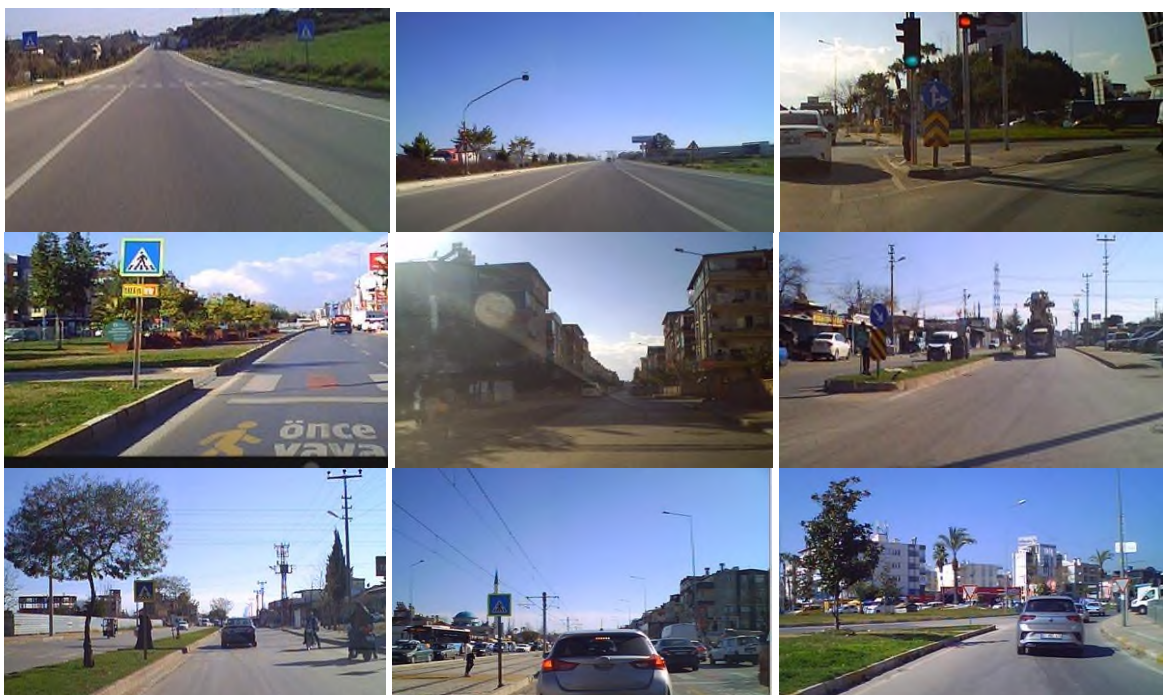


**Figure 2.** Some sample photos from the dataset

The weather is not always nice. Sometimes there is wind, rain and snow. In the study, photographs of

traffic signs taken in different weather conditions were added. In this way, the study was adapted to real life. Figure 3 shows traffic signs taken in three different weather conditions.



**Figure 3.** Traffic signs taken in three different weather conditions.

25 of them were used in traffic signs in the data set. Table 1 shows the names and sampling numbers of the traffic signs used in the data set.

**Table 1.** The names and sampling numbers of the traffic signs used in the data set are shown.

Traffic Sign	Number of Samples	Traffic Sign	Number of Samples
Traffic Lamp	305	50km/h	400
Stop	700	60 Km/h	105
Park	251	70 Km/h	500
Left Turn Prohibited	378	80 Km/h	435
Turn Right	450	Main Road	409
No entry	378	Risk of Ice	201
Parking Prohibited	402	No Turn Right	178
Road Closed to Traffic	301	No Turn Left	202
Forced Direction Forward Left	205	Stop Giving Way	329
Forward Right Forced Direction	322	No Parking	394
Red light	708	School Crossing	217
Green Light	725	Level Crossing with Gate	221
30 Km/h	215		

Many changes to the images that make up the dataset. With these changes, two important features were added to the data set. Firstly, the data set must be very large for real-time detection. With these operations performed on the data set, the size of the data set was increased. A second important feature minimizes errors that may occur from cameras in real-time detection. In real-time detection, cameras do not always capture proper images. The distortions that these images will be exposed to make the detection process difficult. With this process, the photographs in the data set are introduced to the model in advance. Thus, higher efficiency is achieved in real-time detection operations.

With these changes made from the photographs that make up the data set, the error rate in real-time traffic sign detection has been minimized. A camera is placed inside the vehicle for real-time detection. The detection process was carried out using the images taken from this camera. Distortions occur in the photos taken due to camera and vehicle movement. The changes made to the data set and the errors that occurred during the detection process were downloaded.

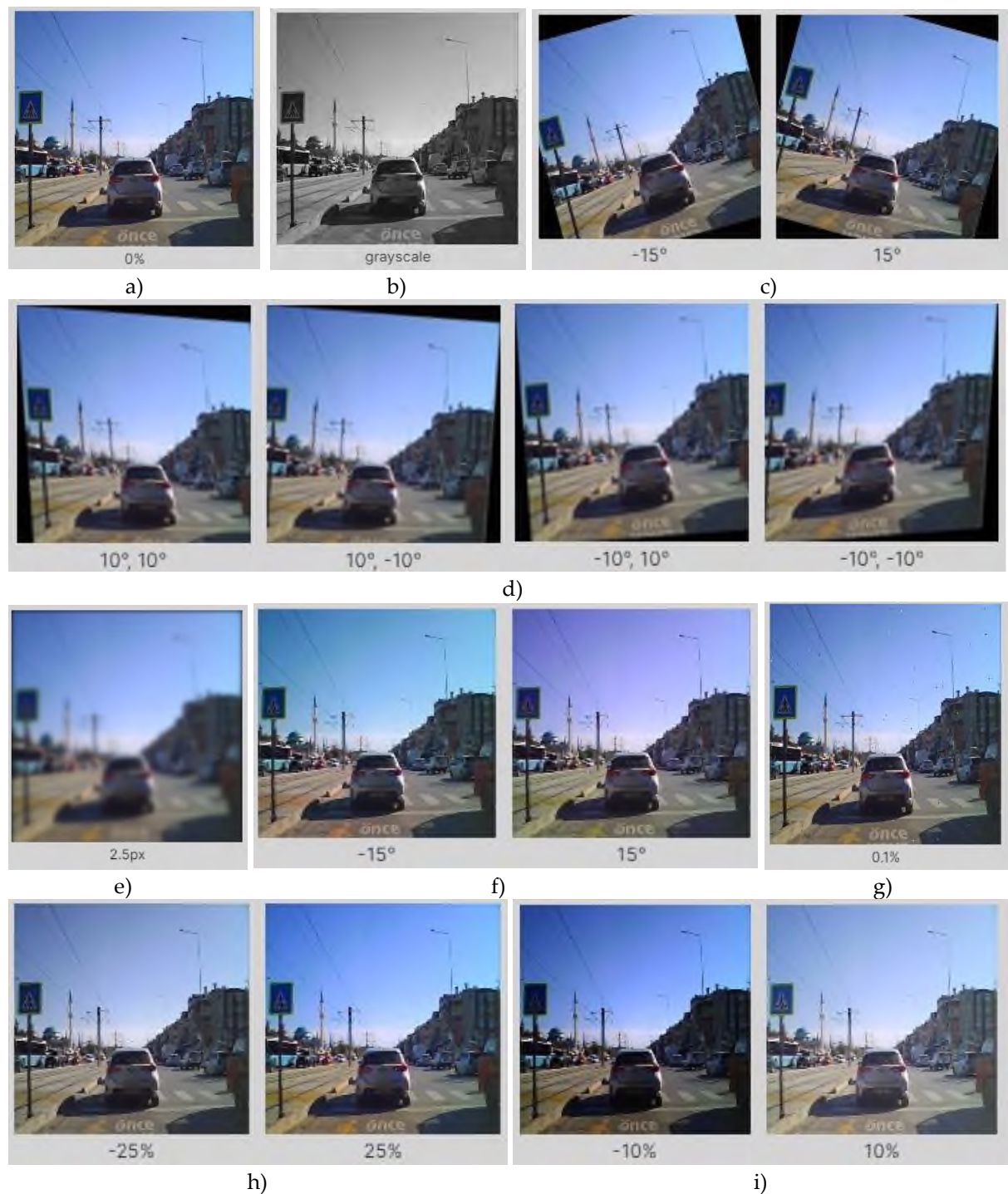


**Figure 4** a) Sizing and position change, b) Grayscale, c) Adding slope, d) Blurring, e) Adding variability, f) Adding noise, g) Image brightness change, h) Colour vividness change, i) Perspective change.

## 2.2. YOLO Algorithm

YOLO architecture was introduced by Joseph Redmon in 2015. YOLO is used for real-time object detection. This algorithm detects box-shaped objects in the image with forward propagation. The YOLO algorithm operates extremely quickly. It sees the entire image during the training and testing of the data set. Thus, it encodes information about classes and their views. YOLO learns generalizable representations of objects. Thus, the algorithm performs better when trained and tested on natural images. Figure 5 shows the YOLO architecture.

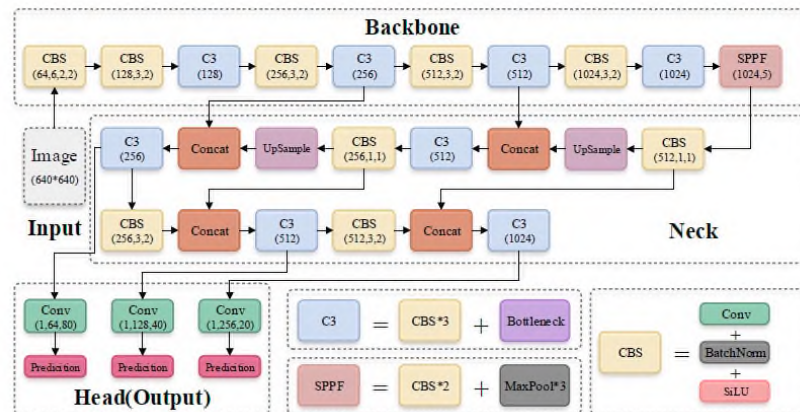


Figure 5. YOLO architecture [22].

### 2.2.1 YOLOv5

YOLOv5 is a model in the You Only Look Only (YOLO) family of computer vision models. YOLOv5 is widely used to detect objects. YOLOv5 comes in four main versions: small (s), medium (m), large (l), and extra-large (x), each offering increasingly higher accuracy rates. Each variant also takes a different amount of time to train. In the graph, the goal is to create a very performance object detection model (Y-axis) based on extraction time (X-axis). Preliminary results show that YOLOv5 performs very well compared to other state-of-the-art techniques for this purpose. Figure 6 shows the features of four different YOLOv5 architectures.

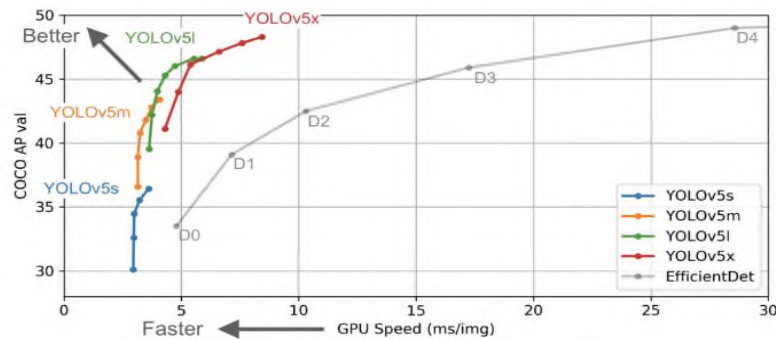


Figure 6. YOLOv5 architecture [23].

There are four algorithms in the YOLOv5 architecture: YOLOv5x, YOLOv5l, YOLOv5m, and YOLOv5s. The highest accuracy rate in these algorithms is realized in the YOLOv5x algorithm. The lowest accuracy rate is in the YOLOv5s algorithm. There is a contrast between accuracy rates and detection times. In the study conducted, both the high accuracy rate and the detection speed should be very low.

### 2.2.2 YOLOv6

The main goal of YOLOv6 is to provide superior performance, especially in real-time applications, by operating at high speed and low latency. The architecture of the model includes various improvements and optimizations to achieve better overall accuracy. These improvements include optimized convolutional layers for more effective feature extraction, new activation functions for better overall performance, and advanced data augmentation techniques. YOLOv6 has also managed to create lighter structures by reducing model sizes, thus becoming a system that can run efficiently even on low-power hardware. This model is quite successful in detecting objects of different sizes and scenes with various levels of complexity. The basis of this success is the large datasets and optimized loss functions used in

the training process of the model. With its multi-scale detection capabilities, YOLOv6 can effectively detect both small and large objects, and thus can be used in a wide range of applications. For example, it can be used effectively in tasks such as pedestrian detection, other vehicles, and traffic signs in autonomous vehicles, in recognizing suspicious objects or people in security systems, and in tasks such as shelf tracking and inventory management in the retail sector. In addition, thanks to its versions optimized for mobile devices, fast and accurate object detection is also possible on portable devices. YOLOv6 is open to continuous development and optimization thanks to its open source and wide community support. At the same time, it can be adapted to different needs by offering a customizable structure for different datasets and application scenarios. The high accuracy, low latency, and optimized performance offered by YOLOv6 are important models that make it stand out in today's computer vision applications that require speed and accuracy. Figure 7 shows the features of four different YOLOv6 architectures.

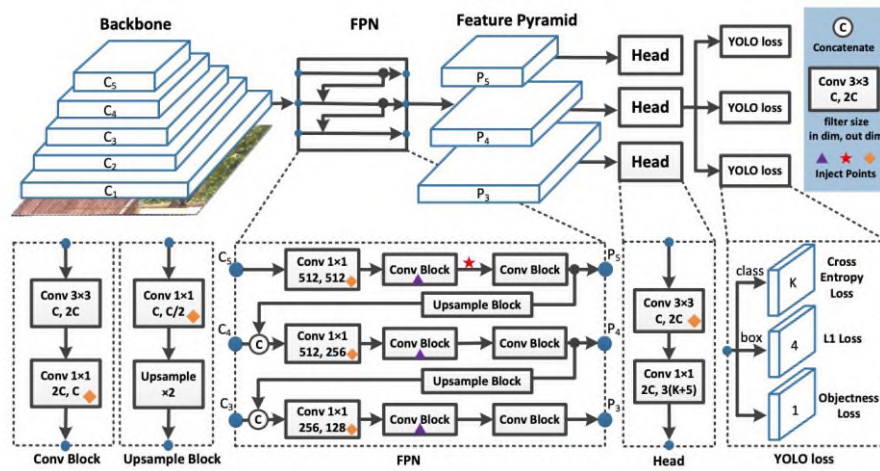


Figure 6. YOLOv6 architecture [24].

### 2.2.3 YOLOv7

YOLOv7 has made significant progress in the field of object detection, improving the strengths of previous versions while also introducing innovations that increase performance and efficiency. Unlike previous versions, YOLOv7 is equipped with optimized architectural changes and new training techniques. This provides superior performance in terms of both accuracy and speed. One of the most significant improvements of the model is its ability to strike a perfect balance between computational efficiency and detection accuracy. This feature makes YOLOv7 ideal for both high-performance servers and devices with limited hardware resources. The model uses advanced model scaling strategies that offer flexible scalability depending on the hardware. In this way, it can run on different platforms without losing quality. In addition, thanks to its improved feature extraction mechanisms and attention modules, it can detect objects of different sizes and complexity with high accuracy even in challenging environments. One of the most striking features of YOLOv7 is its high performance in real-time applications. The fact that it does not compromise on accuracy while maintaining high frame rates provides a great advantage, especially in areas where fast and precise object recognition is critical, such as autonomous driving. In addition, it can be effectively used in various fields such as security systems, robotic applications, and augmented reality. YOLOv7 integrates new techniques for better generalization on different datasets, providing consistent performance despite the variability in the input data. The flexibility of the model allows it to adapt to a wide range of deployment environments, from cloud-based infrastructures to endpoint devices such as mobile devices and embedded systems. The open-source nature of YOLOv7 provides a foundation for continuous development and community-supported improvements. The model supports advanced training optimizations such as dynamic label assignment and adaptive loss functions, resulting in faster training times and higher overall performance. Figure 8 shows the features of four different YOLOv7 architectures.

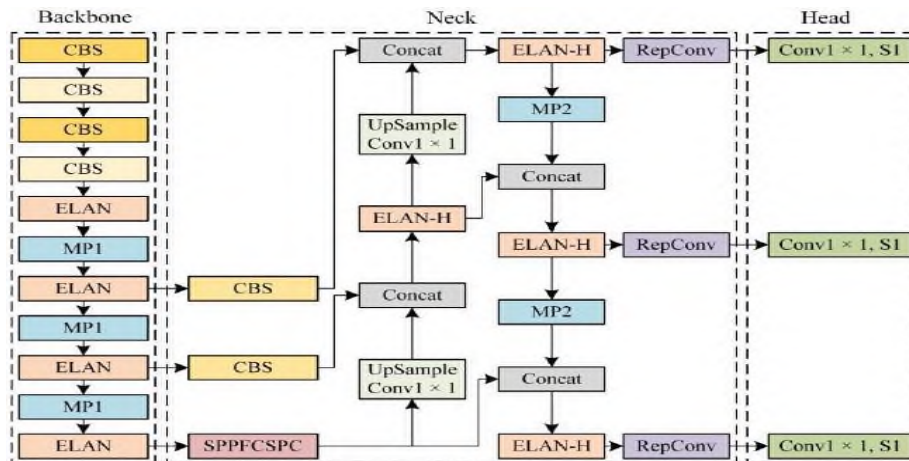


Figure 8. YOLOv7 architecture [25].

2.2.4 YOLOv8

YOLOv8 presents a lighter and more powerful structure thanks to the radical changes made in terms of architecture and advanced training techniques. YOLOv8 draws attention with the new layer arrangements and parameter optimizations developed to increase the efficiency of the model. These improvements allow faster and more accurate results to be obtained, while providing high performance even on low-power devices. The model's attention mechanisms and advanced feature extraction layers help it detect objects of different sizes and difficulty levels more precisely. In this way, YOLOv8 can detect and classify a large number of objects with high accuracy even in complex scenes. Another important innovation is the versatility of YOLOv8. The model is designed to be used in different computer vision tasks, such as not only object detection but also image segmentation and pose estimation. This makes it usable in a wide range of applications, from autonomous driving to security systems, from the healthcare sector to robotics. YOLOv8's improved training processes are supported by techniques such as dynamic label assignment and adaptive loss functions. This enabled the model to reach higher accuracy rates in a shorter time. YOLOv8's modular structure and flexible architecture allow users to customize it according to their own datasets and specific needs. YOLOv8's comprehensive documentation and user-friendly interface provide an easy integration process for both beginners and advanced users. The model's high accuracy, low latency, and optimized computational efficiency make it one of the most advanced solutions in object detection and computer vision. Figure 9 shows the features of four different YOLOv8 architectures.

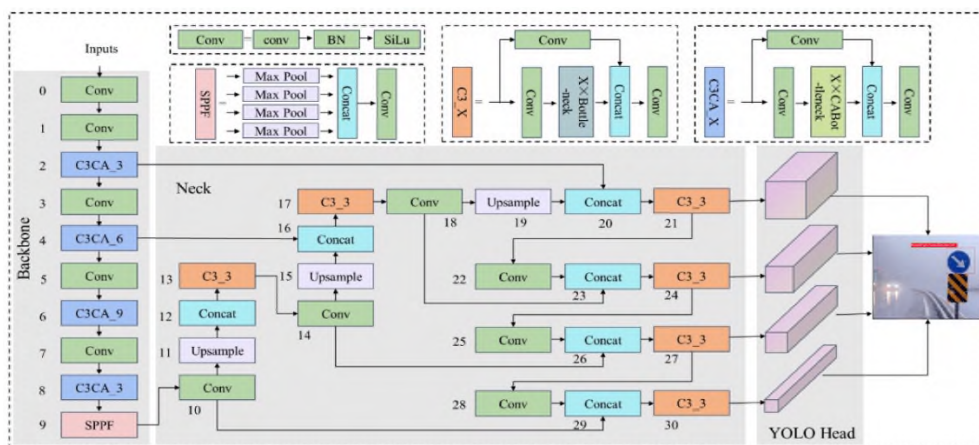


Figure 9. YOLOv8 architecture [26].



### 3. RESULTS AND DISCUSSION

In the study, traffic signs were detected in real time. For this purpose, a camera is placed inside the vehicle. Detection is carried out using images taken from the in-car camera. Figure 10 shows the working algorithm prepared for the operation of the system.

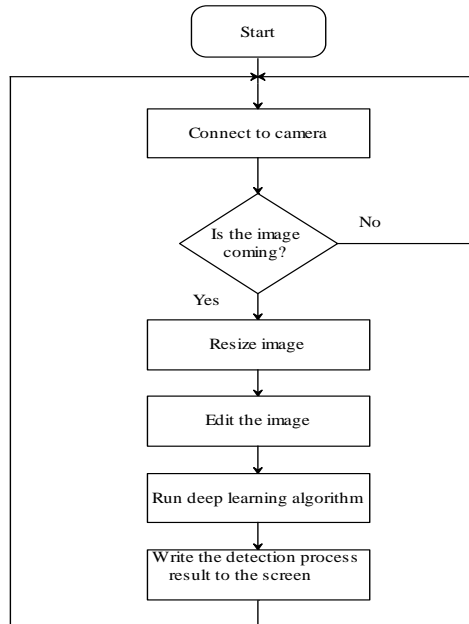


Figure 10. Operating algorithm of the system

The study was used in YOLOv5x, YOLOv6, YOLOv7, and YOLOv8 models. The same data set was used in each architecture. In this way, errors that may occur due to the data set are minimized. In the YOLOv5x model, the confusion matrix achieved a success rate of 97.20%. In the study, F1-Score was 0.98. Figure 11 shows the results after training on the YOLOv5x architecture.

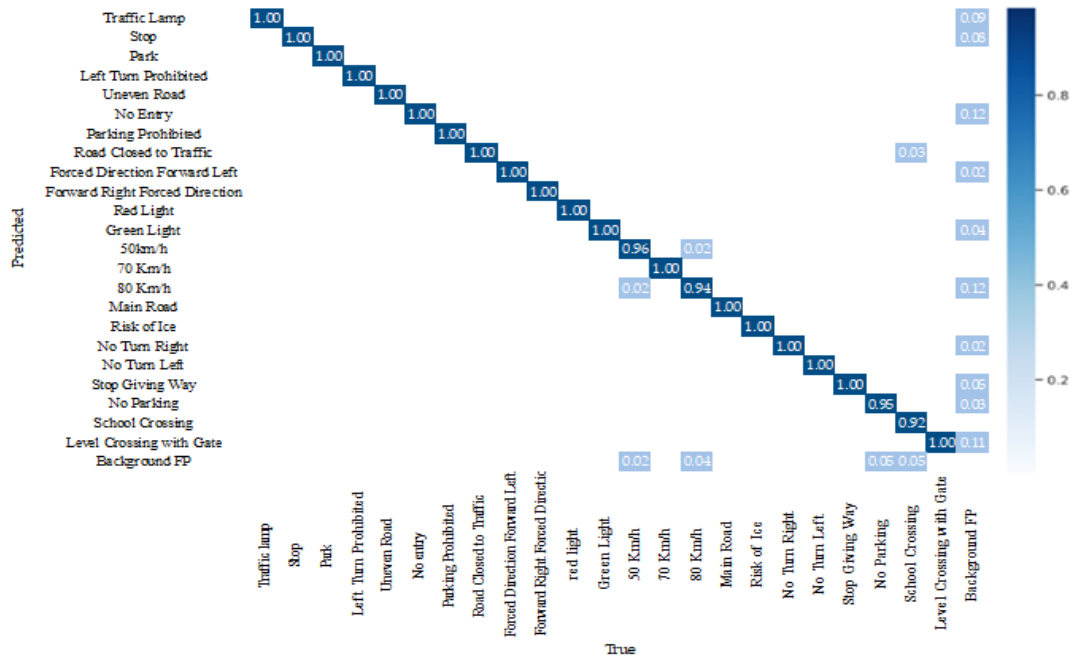


Figure 11. Results after training on YOLOv5x architecture.

The YOLOv6 model has a less complex structure. In the YOLOv6 model, the confusion matrix achieved a success rate of 99.1%. In the study, F1-Score was 0.95. Figure 12 shows the results after training on the YOLOv6 architecture.

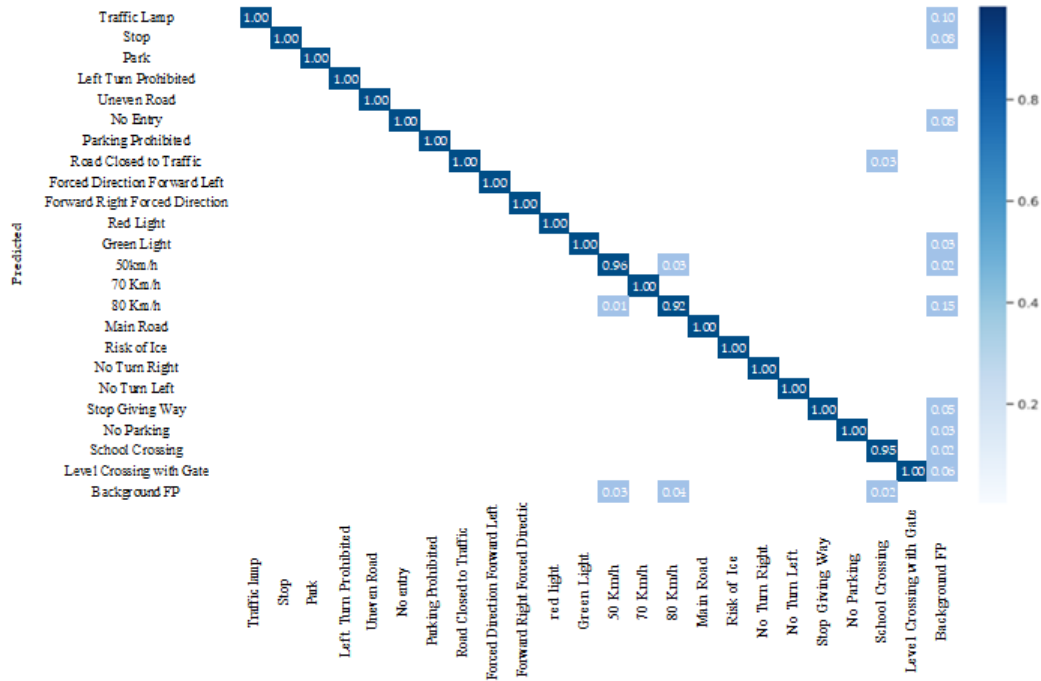


Figure 12. Results after training on YOLOv6 architecture.

In the YOLOv7 model, the confusion matrix achieved a success rate of 99.50%. In the study, F1-Score was 0.99. Figure 13 shows the results after training on the YOLOv7 architecture.

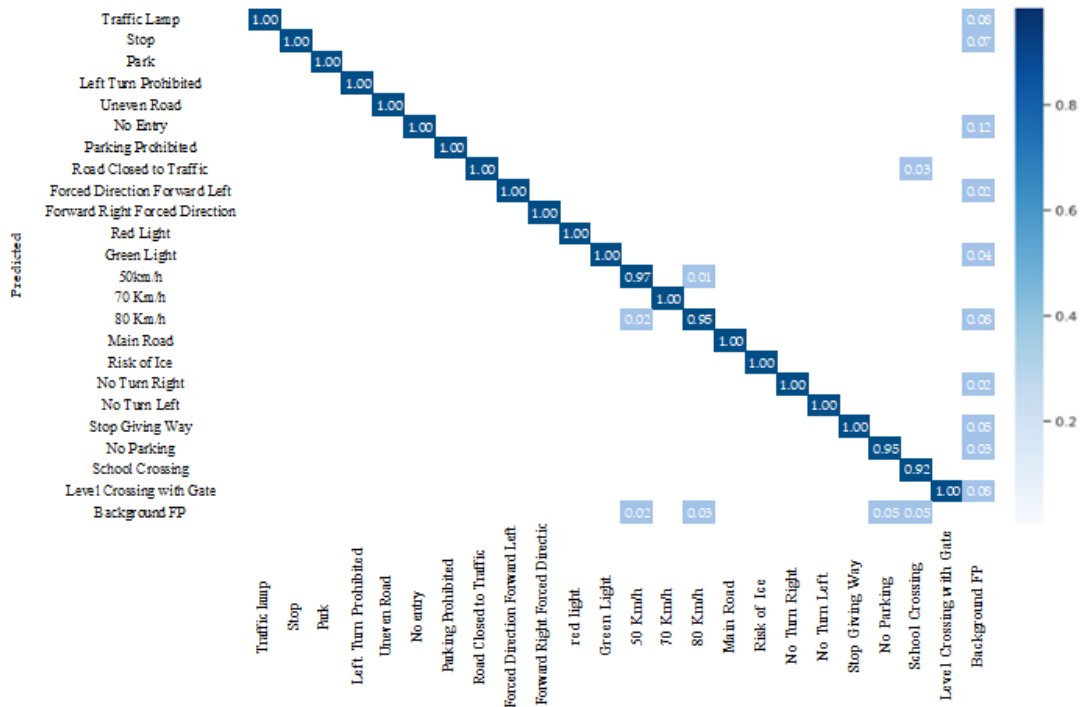


Figure 13. Results after training on YOLOv7 architecture.

In the YOLOv8 model, the confusion matrix achieved a success rate of 99.60%. In the study, F1-Score

was 0.99. Figure 14 shows the results after training on the YOLOv8 architecture.

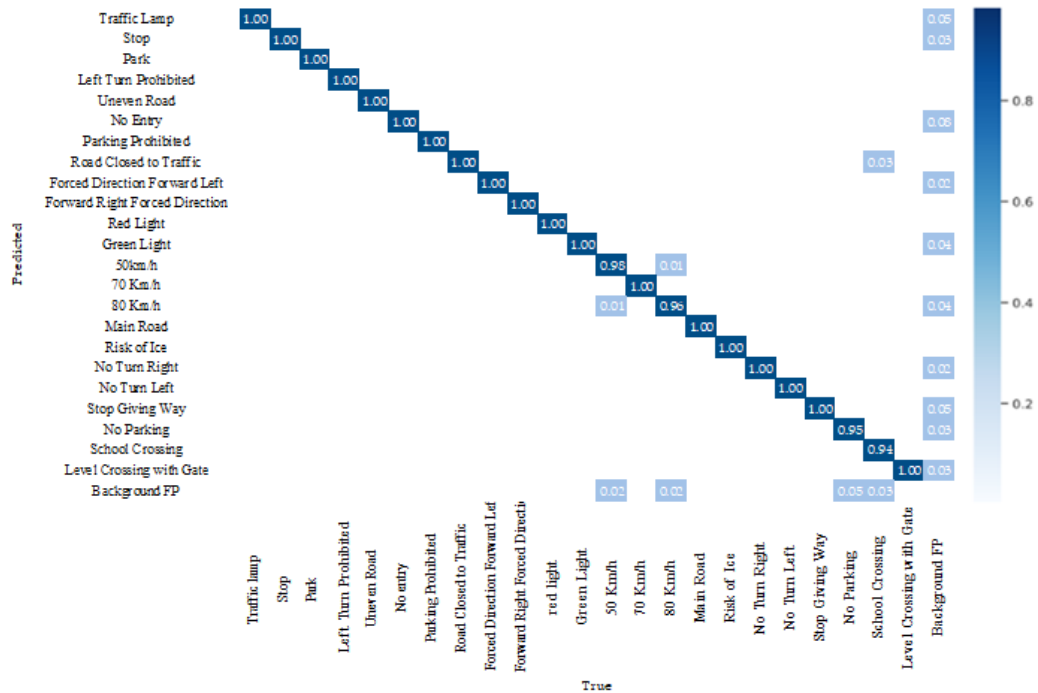


Figure 14. Results after training on YOLOv8 architecture.

In the study, 25 traffic signs were identified. For this, YOLOv5m, YOLOv5s, YOLOv5x, YOLOv6, YOLOv7, and YOLOv8 architectures were used. The internal structure of each architecture is different. For this reason, different results occur. Table 2 shows the average values of the YOLOv5m, YOLOv5s, YOLOv5x, YOLOv6, YOLOv7, and YOLOv8 models.

Table 2. Average values of YOLOv5m, YOLOv5s and YOLOv5x models shown.

Architectural Name	Precision	Recall	mAP50
YOLOv5m	0.985	0.926	0.974
YOLOv5s	0.988	0.945	0.981
YOLOv5x	0.994	0.939	0.969
YOLOv6	0.991	0.951	0.985
YOLOv7	0.995	0.955	0.991
YOLOv8	0.996	0.962	0.993

When the training results of YOLOv5m, YOLOv5s, YOLOv5x, YOLOv6, YOLOv7 and YOLOv8 models are examined, the model with the highest accuracy rate is the YOLOv8 model. The model with the lowest accuracy rate is the YOLOv5m model with 98.50%. When the mAP50 results of the models are examined, the highest YOLOv8 model is calculated as 0.993 and the lowest YOLOv5x model is calculated as 0.969.

In real-time traffic sign detection, the selection is not made only based on the highest accuracy rate. The frames per second (FPS) of the architecture to be selected, the weight file size of the architecture, training, and detection time were taken into consideration. It was chosen among six different architectures, taking into account the results of YOLO. YOLOv8's architecture showed better performance in real-time traffic sign detection.

Raspberry Pi4B 4GB and Raspberry Pi4B 8GB models were used in the study. In the study, different sizes such as 1024 × 1024, 800 × 600, 600 × 360, 416 × 416 and 320 × 320 were used. The best performance was at 320 × 320. In the study conducted with Raspberry Pi4B 4GB and photo size 320 × 320, a speed of 0.6 FPS was achieved. In the study conducted with Raspberry Pi4B 8GB and photo size 320 × 320, a speed of

2,5 FPS was achieved.

Real-time traffic sign detection was tested at 4 different speeds. Testing was carried out at speeds of 30 km/h, 40 km/h, 50 km/h and 60 km/h, taking into account the city speed limits. Table 3 shows the number of traffic signs and signals and different speed limits read by the model from a moving vehicle during the testing process.

**Table 3.** The rate of detecting traffic signs of the system at different speed

Traffic Sign	60 km/h		50 km/h		40 km/h		30 km/h	
	Sign	Read Sign	Sign	Read Sign	Sign	Read Sign	Sign	Read Sign
Stop	60	51	60	53	60	54	60	55
Green Light	57	50	57	51	57	53	57	53
Red Light	50	45	50	45	50	46	50	47
Crosswalk	35	31	35	31	35	33	35	33
Turn Right	33	29	33	30	33	30	33	31
Total Sign	235	206	235	210	235	216	235	219
Total Rate	% 87.65		% 89.36		% 91.91		% 93.19	

An accuracy of 87.65% was achieved in real-time traffic sign detection at a vehicle speed of 60 km/h. The second highest accuracy was achieved at a speed of 50 km/h with 89.36% and then at a speed of 40 km/h with an accuracy rate of 91.91%. The best result was achieved with an accuracy rate of 93.19% at a speed of 30 km/h. The main reasons for this are due to the processing speeds of the camera and graphics card used.

When we look at the literature studies, many studies have been done on traffic signs. Ready-made data sets were used in most of their studies. High accuracy rates were achieved in these studies. However, in real-time detection applications, traffic signs were detected at a very low rate or not at all. Table 4 shows literature studies.

**Table 4.** Literature studies.

Authors	Data Set	Architectural	Precision
Zhu et al. [27]	Custom	YOLOv5	0.97
Wan et al. [28]	GTSDDB	TSYOLO	0.83
Lu et al. [29]	Custom	YOLOv5	0.88
Yi et al. [30]	TT100K	YOLOv4	0.92
Jiang et al. [31]	TT100K	YOLOv5	0.87
Aggar et al. [32]	IQTSDB	YOLOv5	0.90
Çınarel et al. [33]	GTDRB	YOLOv5	0.99
Azimjanov et al. [34]	own data set	YOLO	0.95
Rodriguez et al. [35]	own data set	YOLOv3	0.95
Ren et al. [36]	TT100K	YOLOv7	0.92
Hsieh et al. [37]	OCR	YOLOv7	0.97
Kuppusamy et al. [38]	GTSRB	YOLOv7	0.98
Yu et al. [39]	KITTI	YOLOv7-Tiny	0.96
Zhao et al. [40]	TT100K	YOLO-MAM	0.84
Ji et al. [41]	TT100K	YOLOv8	0.98
Zhang et al. [42]	TT100K	TST-DETR	0.99
Yaamini et al. [43]	own data set	YOLOv8	0.90
Han et al. [44]	GTSRB	EDN-YOLO	0.93
Mercoldo et al. [45]	own data set	YOLO	0.97
Sun et al. [46]	TT100K	ERF-YOLO	0.84

The majority of literature studies have been conducted experimentally. It has not been implemented

in a real environment. The study was carried out both experimentally and practically. A very high level of accuracy has been achieved in experimental studies. Such high accuracy has not been achieved in real applications. Detection studies were carried out at different speeds in real applications. Thus, the accuracy rates of the study at different speeds were compared. Accuracy rates were high at low speeds. As speed increased, accuracy rates decreased. There are two important reasons for this. Firstly; The frame per second rate (FPS) of the work is not high enough. The higher the FPS speed, the higher the detection rate of traffic signs at high speeds. Since the FPS rate is sufficient at low speeds, the detection rate has increased to high levels. The second important reason is the speed of the computer used. Raspberry Pi4B 8GB was used in the study. Increasing the graphics card and processor speed of the computer used will affect the accuracy rate in the studies. Figure 11 shows the traffic signs detected in the study.



Figure 11. Traffic signs identified in the study.

#### 4. CONCLUSIONS

In the study, real-time detection of traffic signs was achieved. A camera is placed inside the vehicle for this process. The data set was prepared with images taken from the real environment. Grayscale, tilt, blurring, variability, noise, image brightness change, colour vividness change, perspective change, sizing, and position change were made on the photographs that make up the data set, to ensure their harmony with the real environment. The dataset was used in 3 different versions of the YOLOv5 architecture and YOLOv6, YOLOv7 and YOLOv8 architectures. As a result of the study, 99.60% accuracy was achieved in the YOLOv8 architecture. The study was implemented in a real environment. For the application, the car was detected at speeds of 60, 50, 40, and 30 km/h. An accuracy of 87.65% was achieved in real-time traffic sign detection at a vehicle speed of 60 km/h. The second highest accuracy was achieved at a speed of 50 km/h with 89.36% and then at a speed of 40 km/h with an accuracy rate of 91.91%. The best result was achieved with an accuracy rate of 93.19% at a speed of 30 km/h. The main reasons for this are due to the processing speeds of the camera and graphics card used.

#### Declaration of Ethical Standards

As the author of this study, he declares that he complies with all ethical standards.

#### Declaration of Competing Interest

The authors declared that they have no conflict of interest.

#### Funding / Acknowledgements

No funding is available for this research.

#### Data Availability

Data available on request from the author.

#### REFERENCES

- [1] J. Webb, C. Wilson, and T. Kularatne, "Will people accept shared autonomous electric vehicles. A survey before and after receipt of the costs and benefits," *Economic Analysis and Policy*, vol. 61, pp. 118–135, 2019. <https://doi.org/10.1016/j.eap.2018.12.004>.
- [2] A. Moorthy, R. De Kleine, G. Keoleian, J. Good, and G. Lewis, "Shared autonomous vehicles as a sustainable solution to the last mile problem: A case study of Ann Arbor-Detroit area," *SAE International Journal of Passenger Cars-Electronic and Electrical Systems*, vol. 10(2), 2017. <https://doi.org/10.4271/2017-01-1276>.
- [3] A. Faisal, T. Yigitcanlar, G. Currie, S. Journal, and L. Use, "Understanding autonomous vehicles Linked references are available on JSTOR for this article: Understanding autonomous vehicles: A systematic literature re- view on capability, impact, planning and policy," *Journal of Transport and Land Use*, vol. 12(1), pp. 45–72, 2019. <https://doi.org/10.5198/jtlu.2019.1405>
- [4] H. Fleyeh, "Color detection and segmentation for road and traffic signs," *IEEE Conference on Cybernetics and Intelligent Systems*, vol. 2, pp. 809-814, 2004. <https://doi.org/0000-0002-1429-2345>.
- [5] S. Houben, J. Stallkamp, J. Salmen, M. Schlipsing, and C. Igel, "Detection of traffic signs in realworld images: The German traffic sign detection benchmark," *The 2013 International Joint Conference on Neural Networks*, pp. 1-8, 2013. <https://doi.org/10.3390/app11073061>.
- [6] J. Liu, and X. Wang, "Tomato diseases and pests detection based on improved Yolov3 convolutional neural network," *Frontiers in Plant Science*, vol. 11, pp. 898, 2020. <https://doi.org/10.3389/fpls.2020.00898>.



- [7] S. Tan, G. Lu, Z. Jiang, and L. Huang, "Improved Yolov5 network model and application in safety helmet detection," *2021 IEEE International Conference on Intelligence and Safety for Robotics*, pp. 330-333, 2021. <https://doi.org/10.1109/ISR50024.2021.9419561>
- [8] F. Zhou, H. Zhao, and Z. Nie, "Safety helmet detection based on Yolov5," *IEEE International Conference on Power Electronics Computer Applications*, pp. 6-11, 2021. <https://doi.org/10.3390/s22249843>.
- [9] F. N. Ortataş, and E. Çetin, "Traffic Sign Recognition and the Application of Simulation Using Machine Learning in Electric and Autonomous Vehicles," *El-Cezerî Journal of Science and Engineering*, vol. 8 (3), pp. 1081-1092, 2021. <https://doi.org/10.31202/ecjse.867733>.
- [10] F. Mehdi, and G. Sedigheh, "Traffic Road Sign and Classification," *Majlesi Journal of Electrical Engineering*, vol. 4 (23), pp. 54- 62, 2021.
- [11] L. Zeng, B. Sun, and D. Zhu, "Underwater target detection based on Faster R-CNN and adversarial occlusion network," *Engineering Applications of Artificial Intelligence*, vol. 100, pp. 104190, 2021. <https://doi.org/10.1016/j.engappai.2021.104190>
- [12] F. Shao, X. Wang, F. Meng, J. Zhu, D. Wang, and J. Dai, "Improved faster R-CNN traffic sign detection based on a second region of interest and highly possible regions proposal network," *Sensors*, vol. 19 (10), pp. 2288, 2019. <https://doi.org/10.3390/s19102288>.
- [13] J. Zhang, M. Huang, X. Jin, and X. Li, "A real-time Chinese traffic sign detection algorithm based on modified Yolov2," *Algorithms*, vol. 10 (4), pp. 127, 2017. <https://doi.org/10.3390/a10040127>.
- [14] C. Liu, S. Li, F. Chang, and Y. Wang, "Machine Vision Based Traffic Sign Detection Methods: Review," *Analyses and Perspectives, IEEE Access*, vol. 7(1), pp. 86578-86596, 2019. <https://doi.org/10.1109/Access.2019.2924947>
- [15] O. Belghaouti, W. Handouzi, and M. Tabaa, "Improved traffic sign recognition using deep ConvNet architecture," *Procedia Computer Science*, vol. 177, pp. 468-473, 2020. <https://doi.org/10.1016/j.procs.2020.10.064>
- [16] D. Tabernik, and D. Skočaj, "Deep learning for large-scale traffic-sign detection and recognition," *IEEE transactions on intelligent transportation systems*, vol. 21 (4), pp. 1427-1440, 2019. <https://doi.org/10.1109/TITS.2019.2913588>
- [17] J. Stallkamp, M. Schlipsing, J. Salmen, and C. Igel, "Man vs. computer: Benchmarking machine learning algorithms for traffic sign recognition," *Neural networks*, vol. 32, pp. 323-332, 2022. <https://doi.org/10.1016/j.neunet.2012.02.016>.
- [18] J. Kim, and M. Lee, "Robust Lane Detection Based On Convolutional Neural Network and Random Sample Consensus," *Neural Information Processing*. 2014. [https://doi.org/10.1007/978-3-319-12637-1\\_3](https://doi.org/10.1007/978-3-319-12637-1_3).
- [19] R. Qian, B. Zhang, Y. Yue, Z. Wang, an F. Coenen, "Robust Chinese traffic sign detection and recognition with deep convolutional neural network," *11th International Conference on Natural Computation*, pp. 791-796, 2015. <https://doi.org/10.1109/ICNC.2015.7378104>.
- [20] A. Arcos-Garcia, J. A. Alvarez-Garcia, and L. M. Soria-Morillo, "Evaluation of deep neural networks for traffic sign detection systems," *Neurocomputing*, vol. 316, pp. 332-344, 2018. <https://doi.org/10.1016/j.neucom.2018.07.072>.
- [21] S. Hussain, M. Abualkibash, and S. Tout, "A survey of traffic sign recognition systems based on convolutional neural networks," *IEEE International Conference on Electro/Information Technology*, pp. 0570-0573, 2018. <https://doi.org/10.1109/EIT.2018.8399772>.
- [22] M. E. I. Malaainine, H. Lechgar, H. Rhinane, "YOLOv2 Deep Learning Model and GIS Based Algorithms for Vehicle Tracking," *Journal of Geographic Information System*, vol. 13, pp. 395-409, 2021. <https://doi.org/0.4236/jgis.2021.134022>.
- [23] D. Dlužnevskij, P. Stefanovic, S. Ramanauskaite, "Investigation of YOLOv5 Efficiency in iPhone Supported Systems," *Baltic J. Modern Computing*, vol. 9, pp. 333-344, 2021. <https://doi.org/10.22364/bjmc.2021.9.3.07>

- [24] B. R. Chang, H. Tsai, C. Hsieh, "Accelerating the Response of Self-Driving Control by Using Rapid Object Detection and Steering Angle Prediction," *Electronics*, vol. 12, pp. 2161, 2023. <https://doi.org/10.3390/electronics12102161>
- [25] H. Herfandi, O. S. Sitanggang, M. R. A. Nasution, H. N, Y. M. Jang, "Real-Time Patient Indoor Health Monitoring and Location Tracking with Optical Camera Communications on the Internet of Medical Things," *Appl. Sci.* vol. 14, pp. 1153, 2024. <https://doi.org/10.3390/app14031153>
- [26] B. Xing, W. Wang, J. Qian, C. Pan, Q. Le, "A Lightweight Model for Real-Time Monitoring of Ships," *Electronics*, vol. 12, pp. 3804, 2023. <https://doi.org/10.3390/electronics12183804>.
- [27] Y. Zhu, and W. Yan, "Traffic sign recognition based on deep learning," *Multimedia Tools and Applications*, vol. 81(13), pp. 17779-17791, 2022. <https://doi.org/10.1007/s11042-022-12163-0>
- [28] H. Wan, L. Gao, M. Su, Q. You, H. Qu, and Q. Sun, "A novel neural network model for traffic sign detection and recognition under extreme conditions," *Journal of Sensors*, 2021. <https://doi.org/10.1155/2021/9984787>.
- [29] E. Lu, H. C. M. Gozdzikiewicz, K. H. Chang, and J. M. Ciou, "A hierarchical approach for traffic sign recognition based on shape detection and image classification," *Sensors*, vol. 22 (13), pp. 4768, 2022. <https://doi.org/10.3390/s22134768>.
- [30] L. Yi, L. Jinguo, Z. Yongjie, and M. Ping, "Detection of self-explosive insulators in aerial images based on improved Yolov4," *In Journal of Physics: Conference Series*, vol. 2320 (1), pp. 012025, 2022. <https://doi.org/10.1088/1742-6596/2320/1/012025>
- [31] L. Jiang, H. Liu, H. Zhu, and G. Zhang, "Improved Yolov5 with balanced feature pyramid and attention module for traffic sign detection," *MATEC Web of Conferences*, pp. 355, 2022. <https://doi.org/10.1051/mateconf/202235503023>
- [32] A. Aggar, M. Zaiter, "Iraqi traffic signs detection based on Yolov5," *International Conference on Advanced Computer Applications*, pp. 5-9, 2021. [https://doi.org/10.2991/978-94-6463-034-3\\_72](https://doi.org/10.2991/978-94-6463-034-3_72)
- [33] G. Çınarer, "Deep Learning Based Traffic Sign Recognition Using YOLO Algorithm," *Düzce University Journal of Science & Technology*, vol. 12, pp. 219-229, 2022. <https://doi.org/10.29130/dubited.1214901>.
- [34] A. Jahongir, and Ö. A. Ahmet, "A real-time vehicle detection and a novel vehicle tracking systems for estimating and monitoring traffic flow on highways," *Advanced Engineering Informatics*, vol. 50, pp. 101393, 2021. <https://doi.org/10.1016/j.aei.2021.101393> ,
- [35] R. B. Rodriguez, C. M. Carlos, O. O. V. Villegas, V. G. C. Sanchez, and H. J. O. Dominguez, "Mexican traffic sign detection and classification using deep learning," *Expert Systems With Applications*, vol. 202, pp. 117247, 2022. <https://doi.org/10.1016/j.eswa.2022.117247>.
- [36] B. Ren, J. Zhang, T. Wang "A Hybrid Feature Fusion Traffic Sign Detection Algorithm Based on YOLOv7," *Computer, Materials and Continua*, vol. 80, pp. 1425-1440, 2024. <https://doi.org/10.32604/cmc.2024.052667>
- [37] C. Hsieh, C. Hsu, W. Huang, "A two-stage road design detection and text recognition system based on YOLOv7," *Internet of Things*, vol. 27, pp. 101330, 2024. <https://doi.org/10.1016/j.iot.2024.101330>
- [38] P. Kappusamy, M. Sanjay, P. V. Deepshree, C. Iwendi, "Traffic Sign Reorganization for Autonomous Vehicle Using Optimized YOLOv7 and Convolutional Block Attention Module," *Computer, Materials and Continua*, vol. 77, pp. 445-466, 2023. <https://doi.org/10.32604/cmc.2023.042675>
- [39] Q. Yu, X. Xu, P. Xia, S. Xu, H. Wang, A. Rodic, P. B. Petrovic, "YOLOv7-Tiny road target detection algorithm based on attention mechanism," *Procedia Computer Science*, vol. 250, pp. 95-110, 2024. <https://doi.org/10.1016/j.procs.2024.11.014>
- [40] R. Zhao, S. H. Tang, J. Shen, E. E. B. Supeni, S. A. Rahim "Enhancing autonomous driving safety: A robust traffic sign detection and recognition model TSD-YOLO," *Signal Processing*, vol. 225, pp. 109619, 2024. <https://doi.org/10.1016/j.sigpro.2024.109619>
- [41] B. Ji, J. Xu, Y. Liu, P. Fan, M. Wang, "Improved YOLOv8 for small traffic sign detection under complex environmental conditions," *Franklin Open*, vol. 8, pp. 100167, 2024. <https://doi.org/10.1016/j.fraope.2024.100167>



- [42] L. Zhang, K. Yang, Y. Han, J. Li, W. Wei, H. Tan, P. Yu, K. Zhang, X. Yang, "TSD-EDR: A lightweight real-time detection transformer of traffic sign detection for long-range perception of autonomous driving," *Engineering Applications of Artificial Intelligence*, vol. 139, pp. 109536, 2025. <https://doi.org/10.1016/j.engappai.2024.109536>
- [43] H. S. G. Yaamini, K. J. Swathi, N. Manohar, G. A. Kumar, "Lane and traffic sign detection for autonomous vehicle: addressing challenges on Indian road conditions," *MethodsX*, vol. 14, pp. 103178, 2025. <https://doi.org/10.1016/j.mex.2025.103178>
- [44] Y. Han, F. Wang, W. Wang, X. Zhang, X. Li, "EDN-YOLO: Multi-scale traffic sign detection method in complex scenes," *Digital Signal Processing*, vol. 153, pp. 104615, 2024. <https://doi.org/10.1016/j.dsp.2024.104615>
- [45] F. Mercaldea, F. Martinellib, A. Santonea, "Real-Time Road Sign Localisation through Object Detection," *Procedia Computer Science*, vol. 246, pp. 30–37. <https://doi.org/10.1016/j.procs.2024.09.225>
- [46] Y. Sun, X. Li, D. Zhao, Q. Wang, "Evolving traffic sign detection via multi-scale feature enhancement, reconstruction and fusion," *Digital Signal Processing*, vol. 160, pp. 105028, 2025. <https://doi.org/10.1016/j.dsp.2025.105028>

## IMAGE ENHANCEMENT IN INDUSTRIAL WELDING ENVIRONMENT WITH IMAGE PROCESSING TECHNIQUES

<sup>1</sup>Levent CİVCİK , <sup>2,\*</sup>Muhammed Alperen AKSİN 

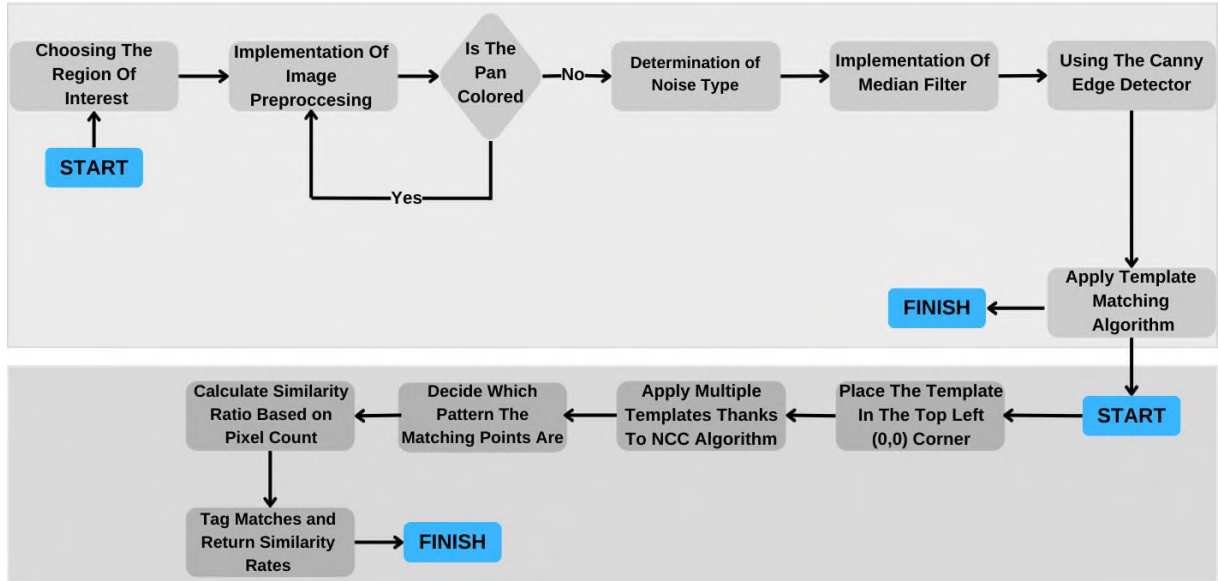
Konya Technical University, Technical Sciences Vocational School, Computer Technologies Department, Konya  
TÜRKİYE

<sup>1</sup>lcivcik@ktun.edu.tr, <sup>2</sup>alperenaksin@gmail.com

### Highlights

- The importance of filtering and preprocessing stages in images
- Using template matching algorithm
- Applying NCC Template Matching Algorithm to Images
- Industrial Welding Processes


### Graphical Abstract



Template Matching Algorithm in Welding Robots



## IMAGE ENHANCEMENT IN INDUSTRIAL WELDING ENVIRONMENT WITH IMAGE PROCESSING TECHNIQUES

<sup>1</sup>Levent CİVCİK , <sup>2,\*</sup>Muhammed Alperen AKSİN 

*Konya Technical University, Technical Sciences Vocational School, Computer Technologies Department, Konya  
TÜRKİYE*

<sup>1</sup>lcivcik@ktun.edu.tr, <sup>2</sup>alperenaksin@gmail.com

(Received: 10.02.2024; Accepted in Revised Form: 11.02.2025)

**ABSTRACT:** With the increase and acceleration of production capacity, computer-based control mechanisms are becoming increasingly common in industrial applications. The use of intelligent welding robots in the welding industry is increasing due to their instant decision-making and application capabilities. For this reason, computer vision systems and image processing algorithms are increasingly used. Although visual limitations in sensors and industrial environmental conditions (arc, noise, dust, etc.) cause problems in robotic welding applications, computer-controlled systems achieve much more efficient results than operator-controlled systems.

One of the most important points here is the applicability and stability of the algorithm to the system. In this study, considering the computational load of image processing algorithms and the negative effects of this computational load in moving environments, a more stable and efficient image feature extraction algorithm was tried to be created for robotic welding applications. After the welding process, object recognition was performed by performing object feature matching with the help of samples taken from the weld images. A new algorithm was created to recognize welding processes that differ from each other in some aspects with multiple samples and even to detect different types of welds. This algorithm reduces the images to gray level and performs a pre-processing step to remove noise with a filtering process, then detects the weld points with the help of predetermined templates and decides how accurately these points are made. Thanks to the NCC Template Matching method used in the algorithm, the running time of the algorithm is accelerated and more accurate results are obtained by introducing more than one template

Experimental method aimed both to calculate the accuracy rate in case the same type of weld operations are different from each other and to recognize the operations performed with different types of welds. While the detection level was around 60% in images without image preprocessing, the detection rate exceeded 70% in images with image preprocessing. In the experiments conducted on the images taken with the Template Matching algorithm, it was observed that the detection rate increased to around 75% at different threshold values. In addition, with the region of interest selection and NCC method, the running time of the algorithm was reduced to 190 ms on average.

Considering the results obtained in the experiments, the algorithm significantly improved the accuracy rates of spot welding and the differentiation of different weld types. By using sufficient light welds and correct experimental equipment, the success rate of the Template Matching algorithm has been increased and the processing load has been alleviated. The effect of external environmental conditions, which is considered the biggest disadvantage of the algorithm, is minimized with lighting elements.

**Keywords:** *Object Recognition Based Template Matching, Image Filters, Full Frame Method, Pattern Matching Method, Industrial Welding Process*

### 1. INTRODUCTION

With the rapid development of the modern manufacturing industry, more and more welding robots are being applied in automated production processes. Welding robots are used in many fields thanks to their high productivity, consistency of quality and uninterrupted operation even under adverse working

**\*Corresponding Author:** Muhammed Alperen AKSİN, [alperenaksin@gmail.com](mailto:alperenaksin@gmail.com)

conditions [1]. Welding robots, which are widely preferred in areas such as the automotive industry and shipbuilding processes, play an important role in compensating for operator-induced errors. They can also provide more autonomous and flexible working conditions. They are supported by computer-based applications to provide this flexibility and autonomous operation. Today, operators are replaced by computerized vision systems. In order to integrate these vision systems, some results must first be obtained and these results must be transferred to the hardware. For this reason, most welding robots are teach-and-operate robots. Parameters can be taught to the computer using previously obtained test results and the weld can be evaluated as a result of this learning. But during the welding process, radiation, heat propagation paths, gap variations, stepped edges, etc. often cause distortion of the seam position [1]. If this seam position change is not corrected, it reduces the weld forming quality. These factors negatively affect robots that are programmed as teach-and-play. Therefore, to solve this problem, the use of image sensors and dynamic programming with instantaneous feedback is proposed. The purpose of this feedbacks are to imitate the movements of the human welder in order to develop smart robot welding. Three basic technical steps are required to perform automatic welding by imitating a human welder. The first is to acquire and perceive information about the dynamic welding process, such as how it is acquired by human sensory organs, to detect internal and external welding conditions. The second is to extract the characteristics of the welding assembly, i.e. model the dynamic welding process; the third is to develop a human brain-like controller to manage the process to determine control methods. Seam tracking is a major problem in intelligent robotic welding, and visual sensing technology is an effective way to deal with it. With the help of image-based seam tracking technology, traditional teach-and-play robots can overcome challenging conditions during welding application and fulfill high-quality welding requirements [2]. These detection processes are provided by cameras and software. At this point, the images from the cameras need to be processed quickly and accurately. In order for images to be processed quickly, image quality and resolution must be good. Here, vision sensors are supported in a variety of ways to ensure good visibility. These supports can be lighting elements, laser strips, etc. Vision perception technology can be divided into passive vision and active vision. Passive vision uses the arc as a light weld, and its images contain rich information. Active vision is the method that uses an external light weld. One of the most popular non-optical detection methods is arc detection [3-5]. The difference between passive and active methods is based on the use of an optional light weld. Active vision uses a camera device and a light weld while passive vision uses two camera devices that are not light welds. In passive vision, due to the complex nature of the weld environments, a wide variety of methods have been proposed by the researchers. Two different types of information can be obtained using a passive vision system; alternatively, the seam profile (1) obtained using active vision and the weld pool profile (2) obtained by passive vision only.

Unlike active vision, which provides only one point at a time, passive vision systems can be used holistically to achieve the stitch path. Numerous techniques have been proposed for image pretreatment, seam profiling and weld pool profiling of the passive vision system. In the active vision system, triangulation is applied to find the geometric features of the seam. The detected points are accepted as peaks in certain regions and triangular shaped areas are found and coordinates are calculated according to this triangle. It uses a camera and light weld device to capture the image of the weld seam.

There are several methods commonly used for positioning in the second and third stages of welding robots. Some of these methods include teaching and playing, visual perception, offline programming, and coordinates. The method of teach-operate is used only for teaching and positioning, but the efficiency and autonomous control of this method are low. In such systems, visual detection methods can be used to detect weld seam for teaching [4]. However, most welding robots are teaching and operating robots. Parameters can be taught to the computer using the test results obtained earlier and the weld to be made as a result of this learning can be evaluated. Offline programming requires a lot of preparatory work, and the location of the robot and its welding parts in the virtual environment should be the same as in the real environment. There may be some discrepancies between preliminary studies on these parameters and in practice. A serious preparation process is necessary to resolve such situations.

With the increase and acceleration of production capacity, computer-based control mechanisms are becoming increasingly common in industrial applications in order to prevent loss of time in this preliminary preparation process. In the welding industry, the use of intelligent welding robots is becoming widespread due to instant decision making and application. For this reason, computer vision systems and image processing algorithms are increasingly being used. Visual limitations in sensors and industrial environment conditions (arc, noise, dust, etc.) cause negativity in robotic welding applications. Despite these disadvantages, computer-controlled systems achieve much more efficient results than operator-controlled systems.

Based on these disadvantages, it has been shown that each method of various template matching algorithms has its own different application areas, advantages and disadvantages. The NCC method is used in high-speed industrial applications and is a very suitable method for finding multiple patterns simultaneously. However, this method may fail due to brightness changes and object displacement. On the other hand, it is a very effective method for searching and finding templates through took images. Another disadvantage about this algorithm is that it is slow. That is why we used NCC Template Matching. But NCC have some problem about industrial environment. It is proposed to solve the problem of NCC being affected very quickly and badly by brightness and complex background by trying different methods. Although this method is widely used in object tracking and outdoor applications, it requires optimization to precisely determine pixel coordinates [6, 7]. The results obtained here show that the NCC algorithm can also be used in this study. In this study, the NCC template matching method was chosen because it can scan more than one template at the same time.

Thanks to this experimental study that we made, the low performance of the Template Matching algorithm, which is easily affected by such conditions, has been improved in harsh industrial environments. Thus, the disadvantages of computer-controlled systems are tried to be eliminated. This is achieved by identifying multiple templates, making different pairings at the same time, and using the right lighting patterns.

After the region of interest of the strip was obtained, segmentation and edge detection algorithms were used. After detecting the edges of the weld strip, a detection algorithm based on the intensity distribution of pixels and neighborhood search is proposed. Another method used to find the edge features of the pool is histogram values. The histogram gives us edge information based on pixel density. During the application, difficulties were encountered such as rotation of the laser strip and too much reflection of the laser. The algorithm failed in the case of rotation, but gave positive results against laser reflection. Additionally, the average image processing time for 1200x1600 resolution images is 300 ms. Welding operations are carried out at an average speed of 0.1 m/sec. For welding, which is generally a very slow process, processing three images in one second is practically sufficient [8]. IN this experimental study, the processes defined on average around 250-320 ms have been reduced to 180-200 ms thanks to image preprocessing and NCC Template Matching method applications. In this way, welding robots, which are usually programmed offline in teach-play format, can be used with instant feedback. Considering other studies in the literature, this study tried to provide a more optimum light weld and lighting conditions since the template matching algorithm is affected by light and background parameters. In addition, healthier templates were selected for the NCC method, thus affecting the speed and robustness of the algorithm less. The algorithm applied to the weld points gave good results despite the high threshold rates against light reflection. Although high threshold values were determined in the preprocessed images, it managed to detect three of the four points.

In another study, CCD image sensor, line laser and optical lenses were used to monitor the weld seam. The optical system of the sensor enables reasonable selection of laser sensor light weld and filter band for arc characteristics; this solves the problem that the laser power of the sensor differs greatly from the arc intensity in the arc welding. It enables the image detection system to obtain an ideal laser stripe image. The purpose of calibration for the imaging system is to find the transformation relationship between the pixel coordinates of the image and the three-dimensional coordinates of the objective world. The mathematical description of the parameters of this transformation relationship is determined by the

imaging model of the visual system. After this model is determined, line correction operations are applied with image processing models. In this study, stitch tracking was performed using fast image segmentation and convolutional neural networks. However, since there is a lot of arc flash and spatter, the sensor calibration, robot processing module and seam tracking system need to be developed [9].

The experimental set used in this experiment was avoided from being complex. In addition, external light welds were used to directly process camera images without the need for different visual perception devices. In this way, the experimental set was simplified and extra expenses were avoided.

As a result, with this experimental study;

- The usability of the Template Matching technique in the industrial environment has been increased.
- By increasing the algorithm speed, instant workability with welding robots has been ensured.
- The processability of the images was ensured with noise and filtering steps.
- It has been shown that weld detection of colored pans can be done with edge detection algorithms.
- It has been shown that both the same type of welds can be classified and different types of welds can be detected with a single algorithm.

## 2. METHODOLOGY

There are many types of welding seams in real industrial production. The seam lift method based on morphological image processing is always designed for a specific weld seam. To perform different types of welding processes, the property extraction algorithm must be evaluated according to the shape characteristics of different welding seams. Therefore, the flexibility of the algorithm is relatively poor. Meanwhile, when many images are faced with the morphological processing step, the real-time performance of the stitch tracking will be affected [1].

The type of seam in the images used in this study distinguishes the template matching algorithm from other image processing algorithms. Because the similarity of the weld points can be easily detected by the template matching algorithm. The template should contain the features in the images. The similarity of such weld played an important role in determining the algorithm selection as Template Matching. In the experimental setup, a KUKA brand robot arm was used as the welding robot, as seen in Figure 1. This robot used in the experimental study uses a KR C5 processor. It consists of 6 axes. These axes are controlled by angular positioning. This robot performs welding operations at an average speed of 0.1 m/s. It has a load carrying capacity of 10 kg. It has an average accessibility range of 1500 mm. This welding robot is used to weld aluminum-nickel alloy pans used in the food industry for cake production. Welding is the process of welding the pan-shaped material into which the cake dough will enter the mold. These molds are made by attaching them to the pan from its four corners. These welding operations must be welded by properly centering in order to produce correct cakes. Therefore, an experimental study was carried out to determine whether the welding points were made correctly.

The images used in the study were processed using the OpenCV V4.5.3 library in the Python 3.9 version environment with the Template Matching algorithm.

Figure 2 shows what the welded pans look like. As mentioned before, the molds welded to the pan from its four corners are welded by centering them. Since some of the weld points are displaced, these faulty pans can become unusable. For this reason, in order to prevent this situation, the images taken with the camera are processed with image processing and the aim is to minimize errors.



**Figure 1.** Robot Used In The Welding Process



**Figure 2.** Image of Welded Cake Pan

The images were subjected to morphological processing. These operations are performed matrically. When applying the necessary signal processing methods to images, the image is treated as a two-dimensional matrix. A digital image with  $M$  rows and  $N$  columns is displayed in the form of  $f(x,y)$ . This is because the values in their coordinates  $(x,y)$  become discrete values. This makes it easy to specify image pixels. Thus, the values at the origin  $(x,y)$  of the coordinates are represented as  $(0,0)$ . In Equation 1, an image with rows  $M$  and columns  $N$  is represented in coordinates.  $f(x,y)$  represents a pixel for each element; and so on; and so on; and so on; and so on; and so on; and so on; and so on; an image with  $M$  rows and  $N$  columns has  $M \times N$  pixels. Expressing rows and columns in this way makes it easier to apply algorithms to the image and express how they are applied. Thus, the positions of the detected weld points are more easily expressed. The distance to the reference point of the weld to the robot can be provided as feedback.

$$f(x,y) = \begin{bmatrix} f(0,0), f(0,1), \dots, f(0,N-1) \\ f(1,0), f(1,1), \dots, f(1,N-1) \\ \vdots \\ \vdots \\ f(M-1,0), f(M-1,1), \dots, f(M-1,N-1) \end{bmatrix} \quad (1)$$

The steps of our work are given below, step by step.

### a. Image Development

Basically, the aim is to make some improvements to the image, better detect the features of interest, and thus create a better input to the image processing algorithm to be implemented [9]. The main purpose of image enhancement is to create an image that is more suitable for the observer by highlighting the characteristics of the image.



**Figure 3.** a) Original Image b) Enhanced Image

Figure 3 shows an image enhanced by the image enhancement method. Here, better input images were obtained using various filtering tools. Because the type of noise in the image was salt and pepper noise, the type of filter was chosen as a median filter.

### b. Object Recognition

The process of finding the object to look for in a picture. For any object in an image, there are multiple points that can be removed from the object to identify its properties. These points, which are extracted from the object and provide rich information about the object, are used in images where the object to be detected is in the same frame as more than one object, they help to recognize and detect the object [10]. Algorithms such as template mapping can also perform object recognition by comparing pixels sequentially.





**Figure 4.** a) Original Image b) Recognized Object Image

Figure 4 shows the input image of the algorithm and the image of the detected object. Templates set as examples for the detection of weld points are defined. As all the weld points are similar to each other, detection is not difficult thanks to the taught template. However, since the coordinates of the weld points are different, it can interfere with the detection process. This intervention can be done with threshold determination or image preprocessing. In this case, both the noise in the template image and the weld image must be removed. It is aimed to detect the weld made on different colored patterns pre-treated with Canny edge detection algorithm by applying the template matching algorithm.

Again, to more easily detect the weld points scattered across various regions of the image, the ROI region is selected from the image and the part where the weld point is to be detected is narrowed. Thus, the parts where other welding points are located can be more easily detected by ignoring. In this study, thanks to the ROI, instead of focusing on the whole cake pan, each of the cake molds is individually focused, reducing both the algorithm time and the processor's processing load. In different applications, ROI has been used for different purposes. For example, in the spot welding seam, the continuous welding seam detection is made as follows:

1) ROI Selection: Before removing the property, it is necessary to select two ROI zones, including laser strips and welding seams, respectively. If the image selected as a template contains only the weld type, it can be very useful in selecting ROI. Thus, only the welded region in the image can focus faster. As we can see in equation 2:

$$\begin{cases} x = \frac{x_0}{4} \\ y = y_0 + \frac{h}{2} + w \\ w = x_0 + 2 \\ H = 2 * w \end{cases} \quad (2)$$

$(x, y)$  welding seam is the image coordinates of the upper left corner,  $(x_0, y_0)$  is the image coordinates of the upper left corner of the ROI of the laser strip,  $(w, h)$  is the width and height of the area of the weld seam, the,  $h$  and  $w$  are the ROI height and width of the weld.

2) In the removal of the welding seam edges, the average gray value of the image is calculated before the edge is removed. The gray level values of the pixels are then compared to a threshold value set by the user or using a function called Otsu. If the gray value of the pixels is smaller than the threshold, logarithmic conversion and normalization are used to improve the original image.

3) In the determination of edge fitting equations, the gradients of the points on the two sides are opposite. They can therefore be easily distinguished. Using the Canny edge detection algorithm, the edges are identified by detecting high frequency transitions in the image. Since the gradients of these transitions are opposite to each other, it is concluded that the regions involved contain edges. Points that meet the

edge criteria can be maintained as absolute edge points. Similarly, hysteresis thresholds are used to filter false edge points [2].



Figure 5. a) Welded Cake Pan b) ROI Area

Figure 5 shows the region selection where the points of weld are identified using ROI. The pixels of these images are reduced to gray level. This step was applied to perform thresholding on the images.

### 2.1. Image Preprocessing

There are several methods used to remove noise from the resulting images and keep the data of interest intact. In this way, it is ensured that the algorithm to be used gives healthy results. By applying various filter operations to the noisy image, the noise is eliminated so that the algorithm can provide more accurate results. In the filtering step, unnecessary details are removed by removing salt and pepper noise in the image. These filters also improved the data quality by making contrast changes more pronounced and sharpening the edge information in the image.

There are various types of noise as different factors cause noise generation. A good image filtering algorithm is expected to give good results when applied to different types of noise. Noisy image is defined as in Equation 3:

$$f(i, j) = g(i, j) + n(i, j) \quad (3)$$

Where  $f(i, j)$  is the intensity value of the image,  $n(i, j)$  is the gray level value of the noise and  $g(i, j)$  is the intensity value of the pixel without noise. There are many filter methods to reduce noise in images. One of them, spatial plane image filters, is divided into linear and nonlinear. In general, in the nonlinear method, the filtered image is determined by the intensity values of the pixels in the filter mask with the help of ordinal statistical methods. In linear methods, filtering is done by applying the filter mask to all pixels individually.

A filter type was chosen according to the type of noise detected in the weld images. The purpose of using the median filter is to remove unwanted data and emphasize the data of interest. The median filter can also retain detailed information such as edge segments and sharp seam angles. In median filtering, the input intensity is replaced by the median of the intensities present in its neighboring pixels. The size of the filter used depends on the welding application and the configuration of the welding system [12]. For salt and pepper noise, the use of a linear filter such as a mean or Gaussian filter reduces the effect of the noise on the processed pixel but distorts the information in the noise-free pixels. For this reason, linear filters are not preferred and nonlinear filters are used to remove salt and pepper noise. Because outliers

can be easily removed in non-linear filters. The minimum filter, which assigns the smallest intensity value of the pixels in the region within the filter window to the processed pixel, gives good results for images containing salt noise. The maximum filter, which assigns the highest intensity value from the intensity values in the filter mask to the processed pixel, gives good results in removing pepper noise. However, the maximum filter does not work well with salt noise and the minimum filter does not work well with pepper noise. Since salt and pepper noise were detected in the images used in this study, median filtering, one of the nonlinear method filters, was proposed. Median filter is one of the most commonly used nonlinear filters to reduce salt and pepper noise. The median filter is expressed using the equation 4:

$$y(i, j) = \text{median}\{x(m, n), (m, n) \in w\} \quad (4)$$

Where  $w$  refers to the neighboring pixels depending on the kernel size, and this size can be varied according to the application. Since the intensity values of the pixels in the neighborhood of the processed pixel in the median filter are ordered from small to large and the median value is the intensity value of the processed pixel, values close to the maximum and minimum values are successfully eliminated. Intensity values with extreme values are eliminated because values close to the maximum and minimum, i.e. noisy pixels, will be found at the beginning or end of the row and the mean value will form the filtering result. Therefore, the median filter is highly effective in removing salt and pepper noise or impulse noise. Another benefit of the median filter is that it preserves the details in the image by reducing the distortion caused by filtering [11].



**Figure 6.** Image Reduced to Gray Level



**Figure 7.** Image filtered using the median filter

Noise is removed by superimposing it on the kernel image.  $K$  is the kernel matrix used for filtering in  $N \times N$  dimensions,  $I_R$  is the matrix of the color image from the camera, and  $I_R^i$  is the new image matrix at the end of filtering. Equation 5 provides the formula for calculating the new values for each pixel.

$$temp = \frac{N}{2}$$

$$I_R^i(x, y) = \frac{1}{N \times N} \sum_{i=1}^N \sum_{j=1}^N K(i, j) * I_R(x + i - temp, y + i - temp) \quad (5)$$

It is desirable to use negative values in the  $I_R$  matrix during the filtering process. In this case, the value in the index closest to the relevant indexes is used. For example,  $I_R^i(0, 0)$  multiplied by the closest value in the  $K(0, 0)$  matrix for  $I_R(-1, -1)$ ,  $I_R(0, 0)$  was used in the calculation. Since the image has three channels and was captured in RGB (Red, Green, Blue) color space, the values of the three colors in the  $I_R$  image matrix are updated using equation 5. After the image is reduced to gray level, the filtering step comes next. For example, when calculating  $K(0,0) * I_R(-1, -1)$  for  $I_R^i(0, 0)$ , the closest value in the matrix  $I_R(0, 0)$  is used.

The median filter provided a simpler image after the image was reduced to gray level. This makes it easier to extract edge points with the Canny edge detection algorithm. As a result of these preprocessing processes, it is aimed to obtain similarities between the template and the image more easily, to shorten CPU operations and to prevent the similarity ratio from decreasing due to unnecessary data. The results of the applied median filter are shown in Figure 6 and Figure 7. The differences created by this filtering process to remove noise are clearly shown. As shown in Equation 6, the size of the kernel matrix of the median filter was determined as  $5 \times 5$  as a result of noise measurements. This kernel size was determined by analyzing the noise on the images.

$$K = \begin{vmatrix} 1 & 1 & 1 & 1 & 1 \\ 1 & 1 & 1 & 1 & 1 \\ 1 & 1 & 1 & 1 & 1 \\ 1 & 1 & 1 & 1 & 1 \\ 1 & 1 & 1 & 1 & 1 \end{vmatrix} \quad (6)$$

## 2.2 Template Matching

After removing noise from the image, image processing algorithms were applied. In image processing, there are multiple approaches and methods to evaluate a fragment independently from the whole image from which it was extracted and to identify the object in its content. One of the main methods of object detection is Template Matching. This algorithm uses a sliding window method to overlay a template on the weld image and detect similar points on the this image. The template is overlaid on the weld image at coordinates (0,0), all pixels are individually shifted and matched, a similarity ratio is generated according to the similarity method used, and if the template is combined with the existing part of the image, it returns those pixels as a result. Based on the similarity ratios of the pixels and by choosing a threshold value for these ratios, objects in the image can be identified. The threshold helps to ignore pixel similarity that holds redundant information and find the results accurately [13].

This method is a technique in digital image processing for finding small parts of an image that match the template image. It can be used in manufacturing as part of quality control, as a way to navigate a mobile robot, or as a way to detect edges in images. Although the accuracy of this method is high, the computational load is quite high. In fact, with today's hardware, it is very difficult to implement without using acceleration techniques. When it comes to tracking an object, the processing needs to be done in real time. This requires very fast hardware and algorithms. In computer vision applications, it is very difficult to track an object in nature in real time [14]. Object tracking involves estimating the trajectory of an object moving in consecutive frames. Dynamic variables such as the features that denote objects, the motion and temporal changes of objects, or the exact addition of the tracked object need to be considered in tracking [15]. This monograph describes methods and systems for object tracking systems, as well as object tracking system structure and the development of new trends in proposed systems. In another study on weld tracking, although images in nature are 3-dimensional, the resulting images are 2-dimensional, there is

noise in the image, and there are complete object overlaps, the presence of complex object shapes, the presence of irregular or fragmented objects, and the disadvantages of object tracking because the movements of the objects can be complex and partial has been investigated [16, 17]. Changes in image brightness, real-time application needs, and shadows from moving objects make object tracking complex [18]. These complexities make it difficult to dynamically track objects. Template matching is less affected by the above disadvantages than most algorithms. The main challenges in this algorithm are: occlusion, detection of non-strict transformations, illumination, background changes, background clutter and scale changes. In this study, the shape matching algorithm is used to extract various weld seam features. In the algorithm, firstly, a filter is applied to the gray level images and Canny algorithm is used to identify the points of weld where edges are found. With Template Matching, these points are compared with the features in the target image to determine the types of welds or the extent to which spot welds are made correctly. With template matching, it is aimed to make the decision-making mechanism faster and more accurate while the robot is working.

Although it is difficult to recognize the welding environment, we are only interested in the starting position of the weld seam. Searching only for the position of interest is a practical method. Template matching is the process of comparing the position in an image and the intensity values in the template with the corresponding values in the image to determine its presence at that point and place the template in an appropriate position. This principle meets the requirements of initial weld location recognition, which avoids complex recognition of the entire environment of weld. In fact, an exact match of intensity values is rare. A measure of difference between the intensity values of the template and the corresponding values of the image is required. By setting a threshold value, we can look for similarity higher than a given value. Therefore, there is no need for a precise analogy. The similarity ratio can be derived as in equation 7.

$$R(i, j) = \frac{\sum_{m=1}^M \sum_{n=1}^M [s^{i,j}(m, n) * T(m, n)]}{\sum_{m=1}^M \sum_{n=1}^M [s^{i,j}(m, n)]^2} \quad (7)$$

Where  $s$  is the weld image,  $s_{i,j}$  is the searched image,  $T$  is the template image,  $i$  and  $j$  are the column and row values in an image [8].



**Figure 8.** Used Templates

Figure 8 shows the templates used. By selecting more than one template, we aim to avoid data loss and find more matches. Three of these templates represent a good weld and one represents a bad weld. In this way, it is aimed to detect both good and bad types of welds.

Figure 9 shows how the algorithm works. As can be seen, the ROI is first selected and then the image preprocessing step is applied. In this step, a filter was determined according to the type of noise. Then, it is decided whether to apply edge detection to the images according to whether the cake molds in the images are colored or not. Finally, the Template Matching algorithm was applied.

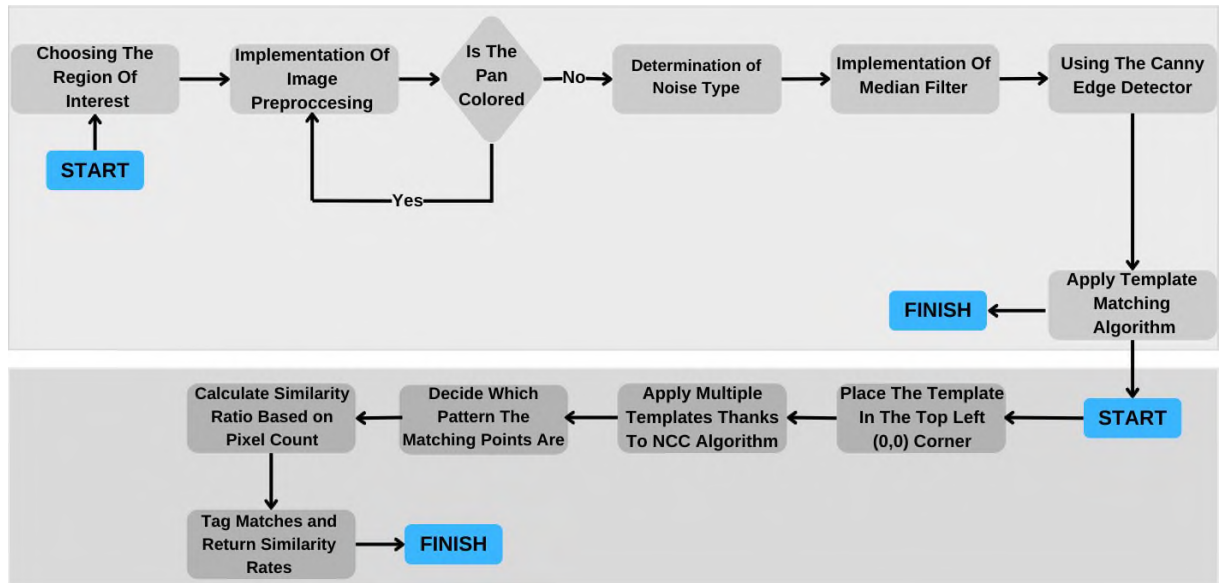


Figure 9. Algorithm's Flow Diagram

### 2.3 Normalized Cross Correlation

Since the processing load is quite high in the template matching algorithm, the algorithm runs slowly. For this reason, various types of algorithms have been created. In this study, normalized cross correlation (NCC), one of these algorithms, is used.

The Template Matching algorithm is classified into area-based and feature-based algorithms. In feature-based algorithms, edge, corner, shape and texture features of objects in the template are extracted and this information is searched for in the next frame. Given a template  $T = n \times n$  and a weld image  $S = m \times m$ , the pixels of  $T$  are denoted by  $T(i, j)$ , the pixels of  $S$  are denoted by  $S(i, j)$ ,  $r = \{0, 1, \dots, m-n\}$  and  $c = \{0, 1, \dots, m-n\}$ , the progression in row is denoted by  $r$  and the progression in column is denoted by  $c$ . The general equation of the NCC algorithm is in equation 8.

$$NCC(r, c) = \frac{\sum_{j=1}^n \sum_{i=1}^n [S(i+r, j+c) - \bar{S}(i, j)] [T(i, j) - \bar{T}]}{\sqrt{\sum_{j=1}^n \sum_{i=1}^n [S^2(i+r, j+c) - n^2 \bar{S}^2(i, j)] \sum_{j=1}^n \sum_{i=1}^n [T^2(i, j) - n^2 \bar{T}^2]}} \quad (8)$$

In the NCC algorithm,  $NCC(r, c)$  takes values between -1 and 1. If  $NCC(r, c)$  takes the value 1, matching occurs, if it takes the value -1, reverse matching occurs. For a match to occur, the value must be close to 1 [20].

### 3. RESULTS and RECOMMENDATIONS

In this study, an algorithm was developed to measure how similar the weld regions are to the specified templates and to improve time consumption and performance. According to the results obtained, the torch tip periodically overheats and becomes irritated over time, which causes deterioration in the welding process. It has also been observed that some welds slip because of incorrect initial positioning of the torch tip. Weld coordinates determined by the algorithm can be used to eliminate this shift. The proposed feature extraction algorithm processes images at an average of 200 ms according to the data obtained from image processing and obtains the result. This time can be considered good compared to the average welding speed. It was also observed that as the size of the processed image decreased, the time it took for the algorithm to respond decreased. When we process all the cake molds used in the application, the time taken is around 1500 ms, while focusing on small pieces, the time taken decreases to around 500 ms. The use of ROI has been found to be beneficial at this point. Thanks to the image preprocessing steps and the NCC algorithm, this time was reduced from 350 ms to around 200 ms.

Also with the method used in the experimental study, 784 welding points were examined. Images were taken from the weld environment after the robot finished its operations. Therefore, there is noise in the images. In this experiment, the images were first reduced to gray level and then a median filter was applied. The purpose of gray level reduction is to ensure that an edge detection algorithm is applied to the images, and the purpose of the median filter application is to eliminate noise. According to the results obtained from the noise analysis, a filter with a 5x5 kernel matrix was applied. Then, edges in the image were extracted using an edge detection algorithm that can be used for colored pans. Then, the weld images made with the Template Matching algorithm were detected. While the weld detection rate was on average 60% - 65% in images without preprocessing, this average increased to around 75% in images with image preprocessing. Again, detection rates increased from around 50% per image to 75%.

**Table 1.** The Answers of Noise in Images to Different Masks

<b>Matrix Size</b>	<b>Noise Value</b>
Unmasked Image	1.61688
Masked Image with a 3x3 Kernel	0.59702
Masked Image with a 5x5 Kernel	0.52164
Masked Image with a 7x7 Kernel	0.44577

Table 1 shows the results of the analysis for noise. Noise analysis results are shown for unmasked or masked images with various kernel matrix sizes. In the light of these results, noise decreased as the mask size increased. However, as the mask value increases, it is seen that the details in the image are lost. For this reason, the ideal mask size was determined as 5x5.

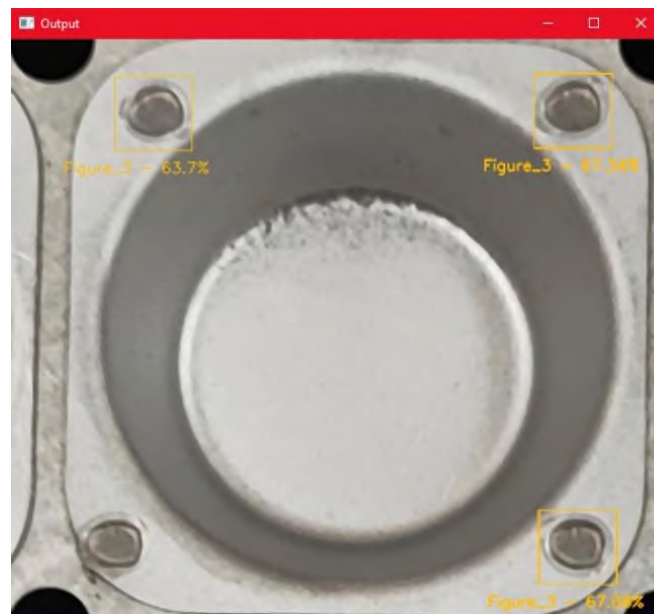


**Figure 10.** Result of Image Preprocessing

As shown in Figure 10, in the shadow of the results obtained, the results of the median filtered images give very useful results in terms of pre-processing compared to the results of the unfiltered images.

The threshold determined by the Otsu function can accurately binarize the weld region and the weld pattern. This is because the grayscale histogram of the weld region shows different features due to its differences with the original image. Of the two peaks, one peak represents the weld region and the other the background. In this way, the threshold selection is completed automatically. For each image, different thresholds are set according to the difference between the peaks in the histograms of the background and the weld region to reduce data loss as much as possible.

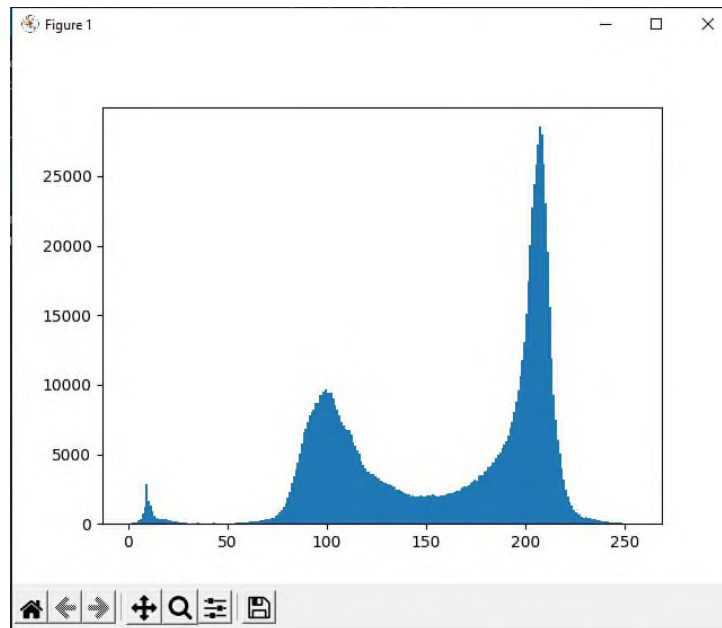


**Figure 11.** Histogram of the Original Image

As shown in Figure 11, images contain two peaks in histogram charts. Low peak welding zone and high peak background cake mold. In this way, a threshold to be determined in the region between the two peaks was to distinguish between the weld region and the cake mold.

Grey-leveled reduced images are given as input to the Otsu function for automatic threshold of images. Thus, there is no need to re-adjust the threshold for each image. It is recommended to reduce the images to gray level for auto-squeezing. This makes it easier to process cake pans produced in different colors. Template matching cannot be done correctly without graying dark pans. When images reduced to gray level were given as inputs to the Otsu function, the threshold values were determined to be 0.45 on average. Since the specified threshold value is very low, the use of the function cannot be recommended for the images used in Otsu. It is aimed to prevent data loss with the threshold value determined separately for each image [22].

Weld tracking was done by showing side weld trace lines and edge removal errors and finding the centers of these lines. Again, to acquire the weld seams, the acquisition of the weld center and laser strips by row scanning and column scanning respectively has been removed. As another example, a precise Hough program was programmed to extract the seam center. Another study proposed a two-process feature extraction method to detect the center of fillet weld seam [19]. While the edge detection algorithm used in this study gave good results in finding the edges of the weld points, it detected edges at different points affected by the lighting conditions.

In addition, the Canny edge detection algorithm was used to detect the weld points of different colored cake pans. Figure 12 shows the results of the edge detection algorithm. As can be seen in this way, the algorithm has accepted many unnecessary details as edges. Because the center of

the mold was hollow, the reflected light was detected as an edge. To overcome this problem, the mold must be vertically illuminated with an external light weld.

As a result of the study, Template Matching algorithm applied after image thresholding, gray level reduction and image preprocessing steps, the points of weld were detected. Detection rates were found depending on the similarity of the template and the weld point. Here, features of the templates such as texture and shape were utilized. These results may vary depending on the condition of the torch tip, the intensity and direction of the light. However, the results show that matches were mostly achieved. The matching results can be improved by obtaining the templates under better conditions and increasing the number of templates. In this way, the number and quality of matches obtained can be increased.



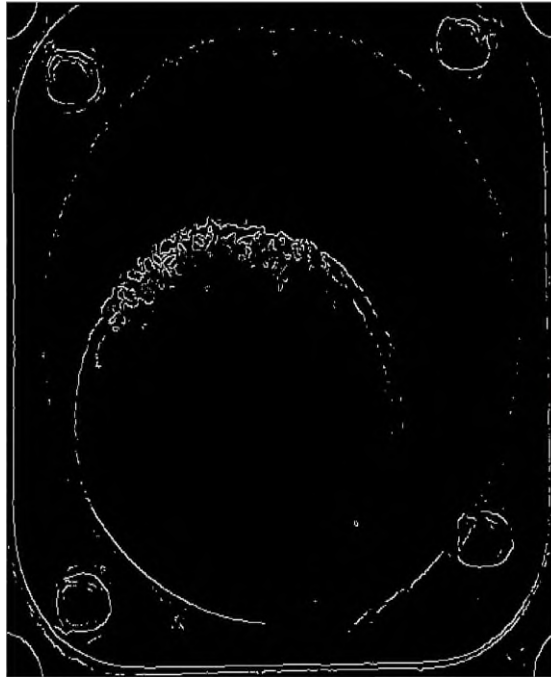


**Figure 12.** Result of Canny Edge Detection Algorithm

In addition to measuring how similar the welds are to the templates, it is also aimed to determine the type of weld. It was observed that spot type welds and I type welds could be distinguished from each other. In this way, various weld types can be distinguished and parameter settings can be adjusted according to that weld.



**Figure 13.** Weld Image of a Degraded Welding Torch Tip

Figure 13 shows how a deteriorating weld tip affects weld location and weld type. In the results shown here, the number of welds detected decreases and the locations where the weld point is sought vary considerably.



**Figure 14.** Shifted Weld Image

As shown in Figure 14, positions that may be important in detecting shifted and distorted weld points were obtained. Shifting of weld areas due to incorrect positioning makes weld detection impossible. This positioning error causes significant distortion of the weld shape. The detected coordinates can be given as feedback to the robot by taking the difference between where the welds should be and where they are and can be used for correction or maintenance purposes.

Weld points found with different templates are shown in different colors. As can be seen from the results, the goal of reducing data loss was achieved by finding the weld points with various templates. The number of templates can be increased or decreased. If the number of templates is increased, data loss will decrease, but the algorithm will take longer to run. This situation should be evaluated and decided according to the requirements. Also a template for bad weld types is defined in this application. The detection rate of bad welds can be increased by increasing the number of templates defined for bad weld points.



**Figure 15.** Template Matching Algorithm Results

As seen in Figure 15, the welds are not always aligned or where they should be. In such cases, the coordinates of the welds must be determined precisely and the place to be searched.



**Figure 16.** Result obtained with Median Filtered Image

As can be seen in Figure 16, the incorrectly detected results in the Median Filter applied image have been canceled. In addition, the accuracy of the correctly detected point of weld has increased. This can be inferred from the increase in the threshold value. Here, the threshold value is close to 74%, indicating that the filtering process can give more accurate results.



**Figure 17.** Template Matching Algorithm Results

In Figure 17, the quality of detection is erroneously degraded in the unfiltered image. Here the threshold value approached 60%.



As can be seen in Table 2, more templates were detected in the images with image preprocessing. Accordingly, it can be said that the study works more effectively. It was also observed that the number of detected points decreased as the threshold value increased. Therefore, it was also determined that the accuracy of the algorithm increased. In this study, 784 points of weld were used as the data set.

**Table 3.** Similarity Percentages of Templates Detected Without Applying Image Preprocessing Step to the Images in the Dataset

Template Name	Number of Templates	Number of Detections				Percentage of Detections			
		0.45	0.60	0.70	0.75	0.45	0.60	0.70	0.75
Template 1	149	105	98	94	90	%70.4	%65.7	%63	%60.4
Template 2	130	94	88	85	81	%72.3	%67.6	%65.3	%62.3
Template 3	292	176	169	162	155	%60.2	%57.8	%55.4	%53
Template 4	213	59	56	55	53	%27.6	%26.2	%25.8	%24.8

Table 3 shows the results of the study performed on images without the image preprocessing stage. According to these results, similarity remained at low levels. The reason for this is that images containing noise negatively affect the algorithm. The template that the welds would resemble was determined with the help of the operator. The reason why the detection rates of welds in the group called faulty welds are low is that there are many different types of faulty welds, but a template is specified. These percentages can be increased by increasing the number of welds templates of the wrong type.

**Table 4.** Similarity Percentages of Templates After Applying the Image Preprocessing Step to the Images in the Dataset

Template Name	Number of Templates	Number of Detections				Percentage of Detections			
		0.45	0.60	0.70	0.75	0.45	0.60	0.70	0.75
Template 1	149	111	109	107	104	%74.5	%73.1	%71.8	%69.8
Template 2	130	101	97	94	92	%77.7	%74.6	%72.3	%70.7
Template 3	292	193	187	182	179	%66.1	%64	%62.3	%61.3
Template 4	213	64	62	61	60	%30	%29.1	%28.6	%28.1

Table 4 shows the similarity results obtained from the images with image preprocessing. According to these results, there is an increase in detection rates in the images with image preprocessing. Again, detection rates can be increased by increasing the number of templates.

**Table 5.** Parameters of the Algorithm

Parameter	Values
Threshold	0.7
Average Algorithm Time (ms)	189,90
Size of Median Filter's Kernel Matrix	5x5

Table 5 shows some parameters of the algorithm used. The threshold value that gives the most positive results is 0.7. Here, the most effective threshold value that does not cause false weld detection was selected as the criterion. The average algorithm time was 189.9. The average time of the algorithm is the average of the times spent in each iteration. This result was achieved with the AMD Ryzen 7 5600 processor. Depending on the type of images, the most appropriate median filter kernel was selected as 5x5. The median filter kernel matrix was determined taking into account the results from the noise analysis shown in Table 1 and the fact that image blurriness increases as the matrix increases.

In line with the results obtained in the study, the high algorithm time due to the high computational load, which is one of the most important disadvantages of the Template Matching algorithm, has been overcome with the NCC Template Matching method. In this way, the application is optimized for high speeds in industrial environments. In addition, various image preprocessing and edge detection steps have been applied to reduce the impact of the harsh conditions of industrial environments. The success rate is increased by using multiple templates.

The labeled images resulting from this study can be used as a healthy dataset for machine learning algorithms in the future. In addition, they can be given as input to predictive maintenance algorithms and maintenance dates can be calculated.



**Figure 19.** Template Matching Algorithm Results Applied to Different Weld Types [21]

With this method, different weld types can be distinguished from each other as well as spot weld types. Figure 19 shows us that the type of weld made in the form of I type has been determined. Figure 19 shows the detection of type I weld with the Template Matching algorithm. From this point of view, it is also possible to detect I, U and V type welds. It is aimed to apply parameter changes by reacting instantaneously to the changing weld shape during welding [22].

#### Funding and Acknowledgements

This study is based on the master's thesis titled 'KAYNAK ROBOTLARINDA ŞABLON EŞLEŞTİRME ALGORİTMASININ KULLANIMI', accepted in the Department of Electrical and Electronics Engineering at Konya Technical University.

#### REFERENCES

- [1] Lei Yang, Yanhong Liu & Jinzhu Peng, "Advances techniques of the structured light sensing in intelligent welding robots: a review," *The International Journal of Advanced Manufacturing Technology*, 110:1027–1046, 2020.


- [2] Runquan Xiao, Yanling Xu, Zhen Hou, Chao Chen, Shanben Chen, "An adaptive feature extraction algorithm for multiple typical seam tracking based on vision sensor in robotic arc welding," *Sensors and Actuators A: Physical* 297, 111533, 2019.
- [3] Pires JN, Loureiro A, Bölmsjö G, "Welding robots: technology, system issues and Application," *Springer Science & Business Media*, [10.1007/1-84628-191-1](https://doi.org/10.1007/1-84628-191-1), 2006.
- [4] Cook GE, Andersen K, Fernandez KR, Shepard ME, Wells Jr AM, "Electric arc sensing for robot positioning control," *Robotic Welding*, IFS(Publications) Ltd, 181–216, 1987.
- [5] Fridenfalk M, "Development of intelligent robot systems based on sensor control," *Lund University*, 2003.
- [6] Brahim, B.S., Josefina J. and Nourain, N., "Fast Template Matching Method based Optimized Sum of Absolute Difference Algorithm for Face Localization". *International Journal of Computer Applications (IJCA)*, Mart. <http://eprints.utp.edu.my/4685/>, 2011.
- [7] Saravanan, C. and Surender, M. "Algorithm for Face Matching Using Normalized Cross-Correlation," *International Journal of Engineering and Advanced Technology (IJEAT) ISSN, 2249–8958*, 2013.
- [8] Jawad Muhammad & Halis Altun & Essam Abo-Serie, "Welding seam profiling techniques based on active vision sensing for intelligent robotic welding," *Int J Adv Manuf Technol*, 88:127–145, 2017.
- [9] Rongqiang Du1 & Yanling Xu1 & Zhen Hou1 & Jun Shu2 & Shanben Chen, "Strong noise image processing for vision-based seam tracking in robotic gas metal arc welding," *The International Journal of Advanced Manufacturing Technology*, 101:2135–2149, 2019.
- [10] Maini, R. and Aggarwal, H., "A Comprehensive Review of Image Enhancement Techniques," *Journal of computing, volume 2, issue 3, issn 2151-9617*, 2010.
- [11] Ferrari, V., Tuytelaars, T. and Gool, L. V., "Simultaneous Object Recognition and Segmentation by Image Exploration," *Computer Vision – ECCV, Tomás Pajdla ve Jiří Matas, 40–54. Lecture Notes in Computer Science 3021. Springer Berlin Heidelberg, 2004.* [Online]. Available: [http://link.springer.com/chapter/10.1007/978-3-540-24670-1\\_4](http://link.springer.com/chapter/10.1007/978-3-540-24670-1_4). [Accessed July 27, 2023]
- [12] Zhu, S. and Ma, K.K., "A new diamond search algorithm for fast block matching motion Estimation," *IEEE Transactions on Image Processing* 9 (2): 287–90. doi:10.1109/83.821744, 2000.
- [13] Aslıhan, M., "Nesneyi Temel Düzeyde Tespit Edebilme (Template Matching) Aşamaları," 2020. [Online]. Available: <https://medium.com/kodcular/nesneyi-temel-duzeyde-tespit-edebilme-template-matching-asmalari-6e11f8bd0a0d> [Accessed July 25, 2023]
- [14] Kettner, V. and Zabih, R. 1999. "Bayesian multi-camera surveillance". *Computer Vision and Pattern Recognition, IEEE Computer Society Conference on.*, 2:-259 Vol. 2. doi: 10.1109/CVPR.1999.784638, 1999.
- [15] Ali Değirmenci, İlyas Çankaya, Recep Demirci, 2018, "Gradyan Anahtarlamalı Gauss Görüntü Filtresi", *Düzce Üniversitesi Bilim ve Teknoloji Dergisi*, 6, 196-215, 2018.
- [16] Hanna G., "Object Tracking. Hard Cover", Publisher: In Tech, Subject: *Artificial Intelligence*, pp: 284, ISBN: 978-953-307-360-6, 2011.
- [17] Yılmaz, A., Javed, O. and Shah, M., "Object Tracking: A Survey". *ACM Comput. Surv.* 38 (4). doi:10.1145/1177352.1177355, 2006.
- [18] Xu, R.Y.D., Allen, J.G. and Jin, J.S., "Robust Real-time Tracking of Non-rigid Objects". *Proceedings of the Pan-Sydney Area Workshop on Visual Information Processing*, 95–98. VIP '05, 2004.
- [19] Fang Z, Xu D, Tan M, "Vision-based initial weld point positioning using the geometric relationship between two seams." *Int J Adv Manuf Technol*, 66(9–12):1535–1543, 2013.
- [20] Sahani, S.K., Adhikari, G. and Das, B.K. 2011. "A fast template matching algorithm for aerial object tracking," *International Conference on Image Information Processing (ICIIP)*, 1–6, 2011. doi: 10.1109/ICIIP.2011.6108841.
- [21] Dian Ary, Nurul Muhyat, Triyono, "Example Assessment Shielded Metal Arc Welding," *E3S Web of Conferences* 465, 01012, PST.04.04.07.b., 2023. [Online]. Available:

- [www.isbe.net/assessment/htmls/balanced-asmt.htm](http://www.isbe.net/assessment/htmls/balanced-asmt.htm) , Agriculture, Grade 9-12 [Accessed September 18, 2024]
- [22] M. A. Aksin, "Kaynak Robotlarında Şablon Eşleştirme Algoritmasının Kullanımı", Institute of Graduate Studies Konya Technical University, Electric Electronic Engineering, Konya, 2023.





## POSITION CONTROL OF HYDRAULIC SERVO CYLINDER FOR WAVE CHANNEL

<sup>1,2,3,\*</sup> Batın DEMİRCAN , <sup>3,4</sup> Sabri BIÇAKÇI , <sup>3,4</sup> Ersin AKYÜZ 

<sup>1</sup> Balıkesir University, Balıkesir Vocational School, Electronics and Automation Department, Balıkesir, TÜRKİYE

<sup>2</sup> Balıkesir University, Inst. of Sci., Electrical and Electronics Engineering Department, Balıkesir, TÜRKİYE

<sup>3</sup> Balıkesir University, Renewable Energy Research, Application and Development Center, Balıkesir, TÜRKİYE

<sup>4</sup> Balıkesir University, Eng. Fac., Electrical and Electronics Engineering Department, Balıkesir, TÜRKİYE




<sup>1,2,3</sup> [batin.demircan@balikesir.edu.tr](mailto:batin.demircan@balikesir.edu.tr), <sup>3,4</sup> [sbicakci@balikesir.edu.tr](mailto:sbicakci@balikesir.edu.tr), <sup>3,4</sup> [eakyuz@balikesir.edu.tr](mailto:eakyuz@balikesir.edu.tr)

### Highlights

- Hydraulic servo cylinder enables precise control of wave generation.
- Real-time wave measurement and control implemented in LabVIEW.
- 24-meter water wave channel system designed for wave generation.



## POSITION CONTROL OF HYDRAULIC SERVO CYLINDER FOR WAVE CHANNEL

<sup>1,2,3,\*</sup> Batın DEMİRCAN , <sup>3,4</sup> Sabri BIÇAKÇI , <sup>3,4</sup> Ersin AKYÜZ 

<sup>1</sup> Balıkesir University, Balıkesir Vocational School, Electronics and Automation Department, Balıkesir, TÜRKİYE

<sup>2</sup> Balıkesir University, Inst. of Sci., Electrical and Electronics Engineering Department, Balıkesir, TÜRKİYE

<sup>3</sup> Balıkesir University, Renewable Energy Research, Application and Development Center, Balıkesir, TÜRKİYE

<sup>4</sup> Balıkesir University, Eng. Fac., Electrical and Electronics Engineering Department, Balıkesir, TÜRKİYE

<sup>1,2,3</sup> [batin.demircan@balikesir.edu.tr](mailto:batin.demircan@balikesir.edu.tr), <sup>3,4</sup> [sbicakci@balikesir.edu.tr](mailto:sbicakci@balikesir.edu.tr), <sup>3,4</sup> [eakyuz@balikesir.edu.tr](mailto:eakyuz@balikesir.edu.tr)

(Received: 24.10.2024; Accepted in Revised Form: 12.02.2025)

**ABSTRACT:** This study aims to achieve position control of the hydraulic cylinder for generating a regular waveform for tsunami, flood, and coastal structure interaction studies, and to measure the generated waveform in real time to determine its conformity to the desired shape. Today, wave channel systems safeguard aquatic ecosystems and play a crucial role in understanding and mitigating natural disasters, particularly in tsunami-prone areas. The wavemaker system in the wave channel is driven by a double-acting hydraulic servo cylinder. A black-box approach is chosen for model identification, validated with real measurement data. PI parameters were initially determined using the Ziegler-Nichols method and later optimized in MATLAB using the PID Tuner and Genetic Algorithm (GA). The optimized PI parameters  $K_p$  and  $K_i$  were found [0.2989 0.0023] for GA, compared to [0.2475, 0.14] for Ziegler-Nichols, and [0.23023 0.058609] for MATLAB/PID Tuner. Real-time wave measurements were recorded with a LabVIEW-based graphical interface. The step and sinusoidal responses of the hydraulic system were analyzed using three methods for determining PI parameters. GA-optimized PI achieved the best results, with ITAE improvements of 74.82% and 69.50%, RMSE improvements of 2.15% and 3.69%, and MAE improvements of 47.02% and 49.30% compared to Ziegler-Nichols and MATLAB/PID Tuner, respectively.

**Keywords:** Closed Loop Systems, Control Theory, Fluid Flow Control, Hydraulic System, System Identification, Wave Channel

### 1. INTRODUCTION

Waves transport energy through oscillations on the air-water interface in the vast oceans and coastal regions of the Earth. The energy carried by waves is on the order of 40-60 kW/m for more than 70% of the Earth's surface [1]. An understanding and modeling of the kinematics of ocean waves is crucial in fields such as marine architecture, coastal protection, and offshore oil and gas [2], [3].

Furthermore, wave channel systems, where water waves are generated in a controlled manner, are widely used in hydraulic laboratories for wave generation. Typically, these structures consist of a hydraulic cylinder, hydraulic power unit, hydraulic valve, and an actuator submerged in water. The generated waves are used to model environmental conditions for physical experiments on scaled-down models. Physical experiments provide the opportunity to predict the behavior of full-scale objects and verify the results of numerical analyses. The primary objective of the conducted studies is to enhance human safety and the structural resilience of buildings.

The water waves obtained from a wave generator with a good control system are crucial for accurately modeling wave profiles, and they are of vital importance for conducting appropriate experimental tests of scaled physical models aimed at enhancing the safety and performance of marine structures such as ships, oil platforms, and wind turbines [4], [5]. The need to continuously enhance maritime safety is the driving force behind the continuous improvement of experimental testing techniques. Large-scale objects in the sea have a significant impact on people's lives and safety. Therefore, it is of utmost importance to conduct downscaled experiments accurately [6].

\*Corresponding Author: Batın DEMİRCAN, [batin.demircan@balikesir.edu.tr](mailto:batin.demircan@balikesir.edu.tr)

The accuracy of wave simulations is of critical importance for the design and performance evaluation of marine structures. The Pierson-Moskowitz, JONSWAP, and TMA wave spectrum models are used to ensure accuracy in wavemaker systems. The Pierson-Moskowitz model represents equilibrium sea conditions, the JONSWAP model represents growing seas, and the TMA model represents wave behavior in shallow waters. The use of these models is crucial in experimental tests aimed at enhancing the safety and performance of marine structures such as ships, oil platforms, and wind turbines [7]. In wave channel systems, the waves produced are classified into two main categories: "regular waves" and "irregular waves". Regular waves are defined as a monochromatic waveform with a single distinct frequency and wave height, while irregular waves are described as the superposition of an infinite number of monochromatic waves [8].

When examining the literature on wave generator systems used in laboratories, it is observed that hydraulic, pneumatic, electronic, and electro-hydraulic structures are used as propulsion systems. Furthermore, PLCs, microcontrollers, and DAQ cards are preferred as control structures.

As an example of a study conducted in the field of wave generation, a wave generator with a small-scale wave channel, controlled by a microcontroller and using a sinusoidal wave as the control signal, was utilized. The wave generator employed a flap-type wavemaker with a multi-pedal structure. The STM32F103 development board and DC stepper motors were used in the waveform generator system to perform tests with different periods for the signal period of the pedal. The wave amplitudes generated were examined according to the applied control signal structure [9]. When examining the literature on wave generator systems used in laboratories, it is observed that hydraulic, pneumatic, servo motor, and electro-hydraulic structures are used as propulsion systems. Furthermore, PLCs, microcontrollers, and DAQ cards are preferred as control structures. Hydraulic drive units were used to measure water waves using measurement probes and record the wave profiles with a PIV system. Various experiments were conducted, and the obtained PIV data were interpreted according to different graded wave theories to analyze wave profiles, wave conditions, and reflected waves [10]. For position control in wave makers, different control algorithms are used in the control approach of both hydraulic and electro-hydraulic systems. When the literature is examined at this point, it shows that the PID controller is sufficient to control the hydraulic actuator as desired. The feedback control system design using PID controller is adopted as it is simple and robust when applied over the specified operating range. To ensure good performance of the controller, the appropriate values for each parameter  $K_p$ ,  $K_i$  and  $K_d$  should be set optimally. PID tuning approaches such as Ziegler Nichols [11] and Nelder-Mead [12] are used to calculate the controller parameters.

Fuzzy logic controllers are used together with PID controller in position control. In a study using the STM 32 controller, fuzzy and PID controllers were compared in which the irregular waveform obtained with multiple sine signals at different frequencies was used as the reference signal. Accordingly, it was reported that the reference signal of the waveform with fuzzy controller provides higher accuracy. It is stated that fuzzy logic control is superior to PI control [13].

Ishak et al. developed and implemented a self-tuning fuzzy controller for position control of hydraulic actuator. In the study, the design of feedback control system using PID controller can be easily implemented because it is simple and robust when applied in the specified operating range. It is found that the performance of the self-tuning fuzzy PID controller is better than the conventional controller and the tracking error is effectively reduced. Another application of self-tuning fuzzy PID is described in, where the controller is used to control the position of an electro hydraulic actuator system. Accordingly, when the self-tuning fuzzy PID controller is applied to the system, the system response is faster and better tracking response is achieved than the conventional PID controller [14].

The optimization of PID controller coefficients for hydraulic cylinder position control can be effectively achieved using various methods, including fuzzy logic and hybrid techniques. The Beetle Antennae Search (BAS) algorithm applied for tuning PID parameters has been shown to significantly improve system performance and robustness against external disturbances compared to traditional tuning methods for the BAS-PID controller [15]. A hybrid algorithm combining PSO and GA has been used to

tune PID controllers in hydraulic systems, resulting in superior performance metrics compared to conventional methods [16]. This hybrid approach provides greater efficiency and effectiveness in parameter tuning by leveraging the strengths of both algorithms.”

System identification is an alternative method for obtaining a mathematical model of a system. System identification is the procedure of obtaining a model of a system using input-output data consisting of stimulus-response pairs. In order to obtain the hydraulic system model, different models of different degrees and different models are used in the literature that are most compatible with the system behavior.

The concept of system identification was first introduced by Zadeh [17] to describe the task of identifying input-output relationships using empirical data sets.

In a study by Rahmat et al. on modeling hydraulic systems, three different cosine signals were combined into a single excitation signal to identify the hydraulic system. It was reported that the best result for this system was obtained with a 4th order ARX model [18].

In another study, it was reported that the best fit was obtained with a third order ARX model using a sinusoidal signal as the excitation signal [19]. The degrees of hydraulic systems and the appropriate model for modeling or identification studies depend on the system being created. Istif used state space, arx, armax, output error and box jenkins models for hydraulic system identification and reported that the best fit was achieved with a 2nd order box jenkins model [20].

In a general review of studies on wave channel structures, this study makes a contribution to the control literature by implementing the position control of a wave generation system using a hydraulically double-rod and double-acting servo cylinder, following the hardware development of a wave channel system. Furthermore, the study distinguishes itself through the real-time measurement and recording of water waves in wave generation systems.

In this study, the position control of a wave channel containing a 24x1x1 meter flap type wave generator located in the Hydraulic Laboratory of Balıkesir University was realized using a Proportional-Integral (PI) controller. In the study, sinusoidal signals with frequencies of 0.8 Hz and 1 Hz were used to control the hydraulic drive system and the wave heights obtained for water levels of 40-50-60cm were recorded. The signal applied for the position control of the hydraulic cylinder consists of a single frequency and a single amplitude component. As a result of the position control of the hydraulic cylinder, the generated water waves exhibited a regular form. The wave height data were directly obtained from the wave measurement sensors.

The transfer function model of the wave generator system is obtained by black box method in Matlab/Simulink System Identification toolbox. The initial coefficients of the PID block were calculated using the Ziegler-Nichols method. Then the  $K_p$  and  $K_i$  parameters of the PI controller were determined using the PID Tuner tool and Genetic Algorithm (GA) in Matlab/Simulink. The determined parameters were applied experimentally. In the scope of this study, Material and Methods are presented in Section 2, experimental results are detailed in Section 3, and finally, the conclusions are discussed.

## 2. MATERIAL AND METHODS

The controlled system is located in the Balıkesir University Hydraulic Laboratory and has dimensions of 24 meters in length, 1 meter in width, and 1 meter in height. The wave generation actuator in the wave channel is of the flap type and is driven by a double-acting, double-rod hydraulic cylinder system. The cylinder has a total stroke value of 700 mm in its forward or backward movement, and the water heights for the application are selected as 40-50-60cm. A proportional hydraulic valve has been used to control the hydraulic cylinder. The hydraulic system has a capacity of 120 liters of hydraulic fluid and operates at a constant pressure of 50 bar. The hydraulic pump used in the hydraulic unit has a constant flow rate. The hydraulic valve control system utilizes the NI CRIO-9074 controller and analog input-output modules. Solid wave attenuators have been used to prevent the reflection of water waves created on both sides of the wave channel. The technical specifications of the controller used in Table 1 are provided [21].

**Table 1.** CRIO-9074 Technical Specifications

Feature	Spec
Processor	400 MHz Freescale MPC5200 real-time processor
FPGA	Xilinx Spartan-3 2M gates FPGA
Memory (RAM)	128 MB DRAM
Storage (Flash Memory)	256 MB
I/O Module Slots	8 hot-swappable C Series module slots
Operating System, Programming Languages	NI Real-Time OS, LabVIEW -C/C++

A sinusoidal input signal has been generated in the LabVIEW environment to control the stroke of the hydraulic system within the desired range. The input signal of the hydraulic cylinder is ensured to follow when amplitude, frequency, and offset parameters are entered by the user. The structure of the general control system is provided in Figure 1.

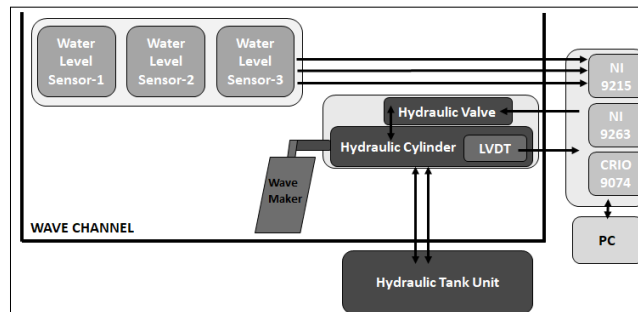
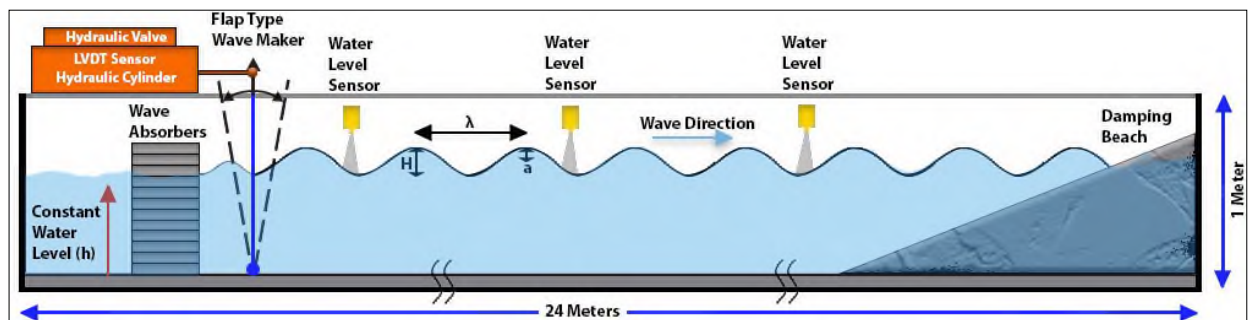
**Figure 1.** Structure of wave channel

Figure 2 presents the physical structure of the wave channel. The training of the coastal wave attenuator located at the end of the wave channel is 20%. Ultrasonic sensors have been used to measure waves at three different points on the wave channel. In the wave channel,  $h$  represents the constant water level,  $H$  represents the peak-to-peak height of the water waves created by the flap-type wave generator,  $a$  represents the peak point of the wave formed relative to the still water level, and  $\lambda$  denotes the wave period. The wave direction refers to the direction of propagation of the waves generated by the wavemaker, which is controlled by the hydraulic cylinder.

**Figure 2.** Physical structure of wave channel

The visual representation of the wave channel in the laboratory is provided in Figure 3. The visual includes a hydraulic unit, hydraulic cylinder, hydraulic valve, flap type actuator, and wave dampers.

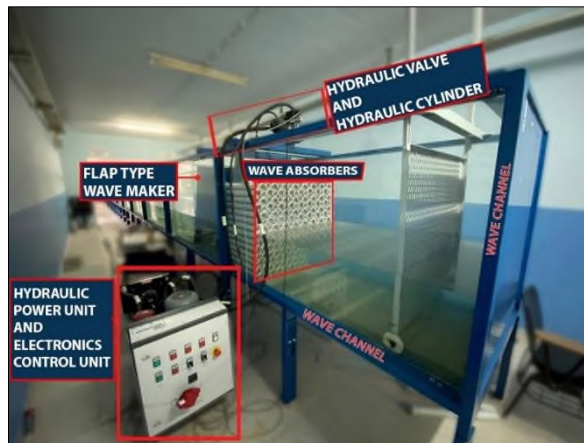


Figure 3. View of wave channel

## 2.1. System Model

It is crucial to model and understand the behaviors of hydraulic systems with complex mathematical models. Properly modeling the behaviors of such systems enhances the effectiveness of design and optimization processes. At this point, the "System Identification Toolbox" in Matlab/Simulink software provides a powerful and flexible tool for obtaining dynamic models of various systems. Particularly, the black box modeling approach is of critical importance when direct knowledge about the internal structure of the system is lacking or when the physical modeling of the system is challenging [22]. When creating a model of a physical system, the methods of white box, gray box, and black box can be used. Black box refers to the process of creating a mathematical model of a system using input-output data. This approach is particularly used in modeling systems with complex and unknown dynamics [23].

A LabVIEW interface has been developed to obtain the necessary data for creating the black box model of the system using the "System Identification Toolbox" in Matlab/Simulink. The front panel of the LabVIEW software is shown in Figure 4. "When examining the GUI presented in Figure 4, it can be observed that the following functionalities are provided for user control of the position of the hydraulic cylinder: manual control of the analog output, adjustment of the amplitude and frequency parameters for three different sinusoidal signals to be applied, notifications for the start and end of data recording, and the configuration of the test duration.

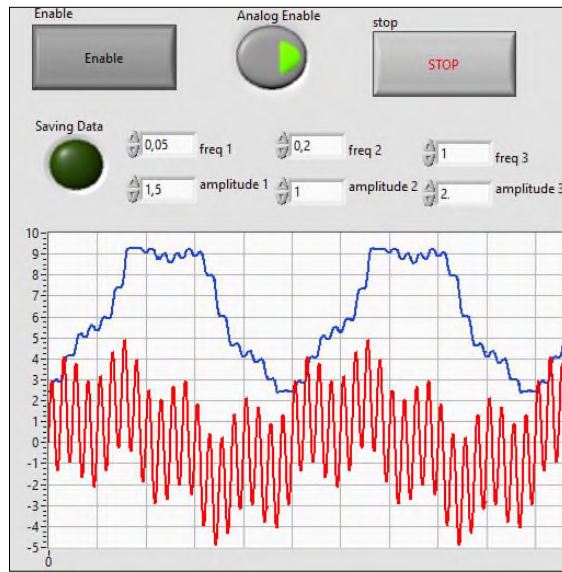


Figure 4. LabVIEW software front panel developed for system identification

The excitation signal, consisting of three different sinusoidal waveforms obtained from a sinusoidal signal generator, was applied to a hydraulic cylinder for a duration of 50 seconds without a control block, as shown in Figure 5. The positions of the hydraulic cylinder were recorded during a signal applied for 50 seconds.

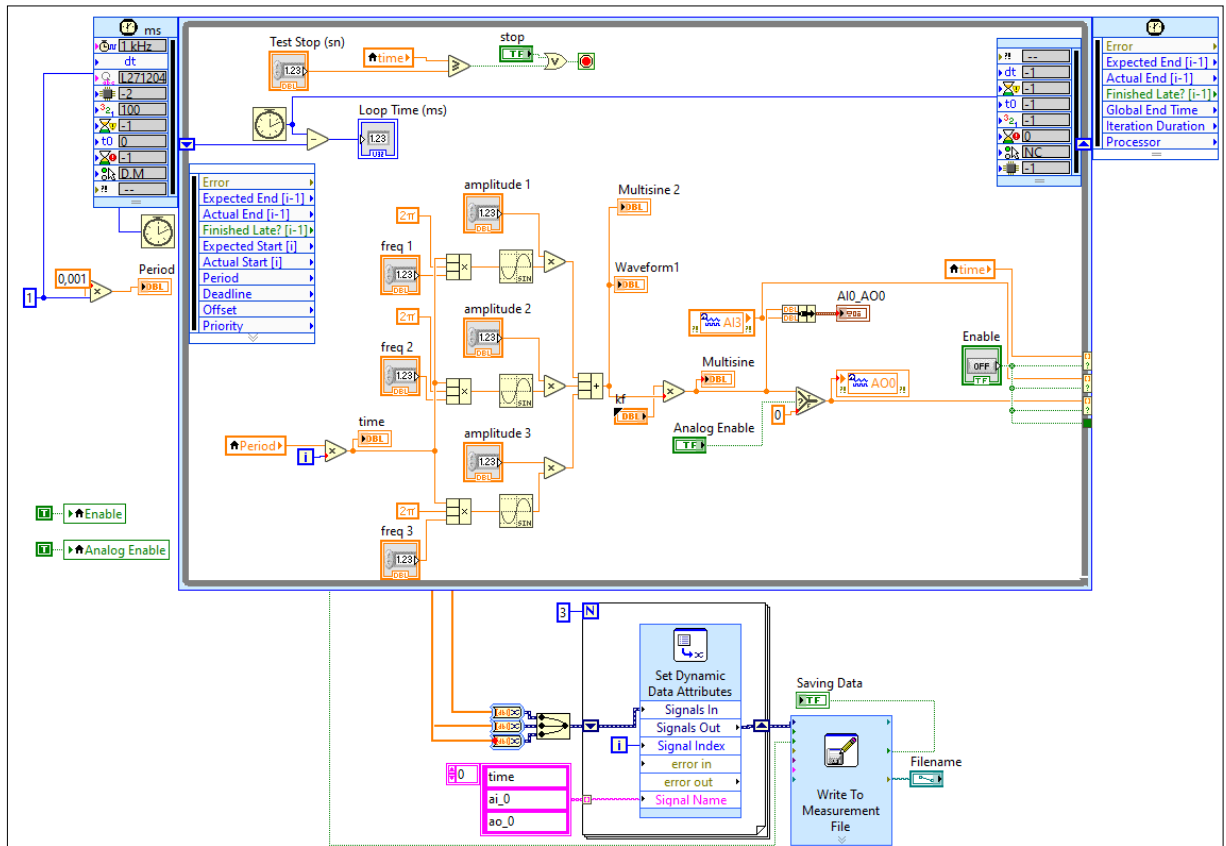


Figure 5. LabVIEW software block diagram developed for system identification

The stimulus signal applied to the hydraulic cylinder is given in equation 1. The representation of the signal in the Matlab software is given in Figure 6.

$$y = 1.5(\sin 2\pi(0.05 * t)) + 1(\sin 2\pi(0.2 * t)) + 2(\sin 2\pi(t)) \quad (1)$$

The measurement data obtained from the Linear Variable Differential Transformer (LVDT) sensor, which transmits the signal sent to the hydraulic valve and the position information of the cylinder, has been transferred to the Matlab software. Later, these signals were transferred to the "system identification toolbox" module with 1ms sampling intervals in the "Time domain" signal structure. The initial 40 seconds of measurement data, obtained for a data block, have been utilized for the prediction and construction of the model. The measurement data in the last 10-second segment was used to validate the created model. The transfer function model is provided in Equation (2).

$$y = \frac{61.34s^2 + 432s + 128.7}{s^3 + 5.892s^2 + 1.989s + 0.00164} \quad (2)$$

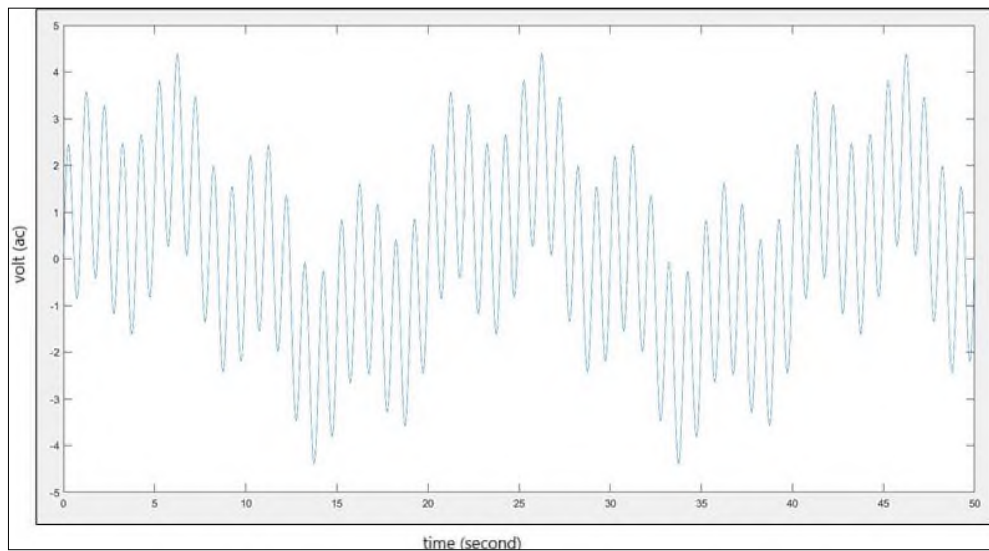
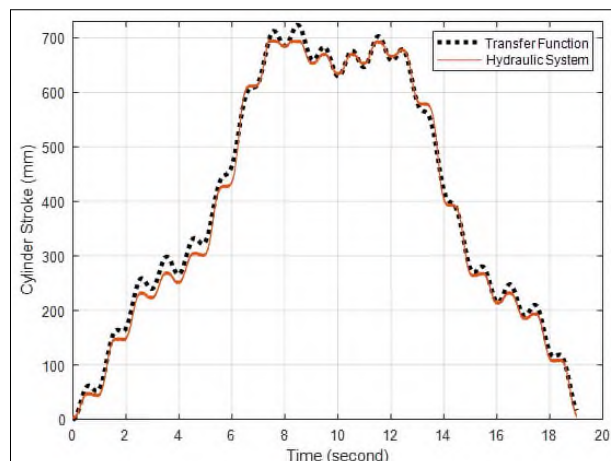


Figure 6. Stimulus signal

The obtained transfer function model has been transferred to the Matlab/Simulink software. The comparison graph in Figure 7 shows the 19-second (one period) comparison between the position information obtained from the transfer model using the same input signal and the position information obtained from the actual system. It is clearly evident that the hydraulic cylinder cannot exceed a maximum stroke value of 700 mm physically.





**Figure 7.** Transfer function output (black color), real system output (orange color)

## 2.2. Controller Design

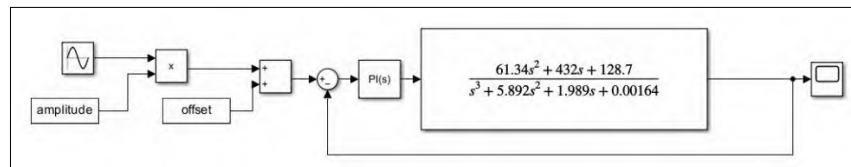
PI control method is used as a controller for position control of the hydraulic cylinder. PI controller is a simple but effective control method. In order to control a system with a PID controller, first the control coefficients " $K_p$ " and " $K_i$ " are determined. There are many methods to determine these coefficients, the method used in this study is the Ziegler-Nichols method. In this method, the " $K_i$ " term is first taken as "0" to determine these parameters. A step signal in terms of position is applied to the hydraulic cylinder. Then the " $K_p$ " coefficient is increased until the smallest " $K_p$ " coefficient is found at which the hydraulic cylinder oscillates in position. Once the " $K_p$ " coefficient is determined, the " $k_i$ " coefficient is calculated using the Table 2. "P" controller cannot provide zero steady state error and this can only be achieved with a "PI" controller. In addition, classical PD and PID controllers can lead to instability problems [24].

**Table 2.** Ziegler-Nichols Method Table [25]

Control Type	$K_p$	$K_i$	$K_d$
P	$0.5K_{cr}$	-	-
PI	$0.55K_{cr}$	$(K_p * T_{cr})/1.2$	-
PID	$0.6K_{cr}$	$(K_p * P_{cr})/2$	$(K_p * P_{cr})/8$

The Ziegler-Nichols method was employed to determine the initial PI parameters of the hydraulic system, using the fundamental initial coefficients. The initial coefficient for  $K_p$  is found to be 0.2475 and the initial coefficient for  $K_i$  is found to be 0.14. Subsequently, a transition was made to the Matlab software and an appropriate block response was determined based on the initial coefficients found.

The transfer function model created in Simulink software and the complete model with the added PI block are depicted in Figure 8.

**Figure 8.** Matlab/Simulink hydraulic system model

The PI parameters have been calculated using the PID Tuner toolbox. According to this, the " $K_p$ " coefficient has been obtained as 0.23023 and the " $K_i$ " coefficient as 0.058609. The coefficient values were used in the LabVIEW software prepared for position control of the hydraulic system. The screenshot of the PID tuner with parameter adjustment is shown in Figure 9.

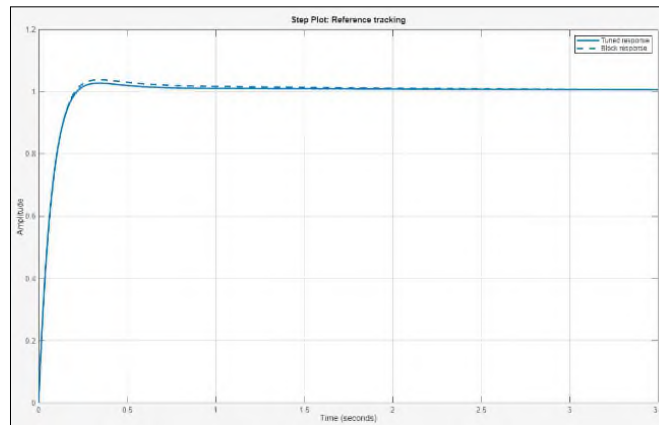


Figure 9. Matlab/Simulink PID Tuner

After determining the PI controller parameters using the Ziegler-Nichols and MATLAB/PID Tuner methods, a third approach, the meta-heuristic Genetic Algorithm (GA), was employed. The transfer function model was utilized in the MATLAB environment for determining the PI controller parameters using GA. For parameter optimization with GA, the following settings were used: population size of 50, generation count of 25, number of genes as 2, mutation rate of 0.01, crossover rate of 0.2, and ITAE as the fitness function. As a result of GA, the proportional gain  $k_p$  was determined to be 0.2989, and the integral gain  $k_i$  was found to be 0.0023. The  $k_p$  and  $k_i$  values obtained using the three methods are presented in Table 3.

Table 3. PI Parameters

Method	$K_p$	$K_i$
Ziegler-Nichols	0.2475	0.14
Matlab/ PID Tuner	0.23023	0.058609
Genetic Algorithm	0.2989	0.0023

The stability analysis of the model, whose coefficients were determined and constructed in the Simulink environment, was performed using the Simulink software environment. The poles of the system have been determined as -5.5325, -0.3586, and -0.0008, and the stability of the system is depicted in Figure 10.

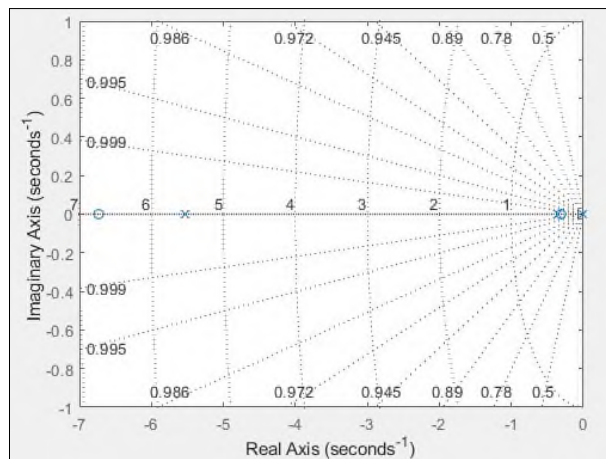


Figure 10. Stability analysis of transfer function

### 2.3. Position Control of Hydraulic System

The front panel for controlling the hydraulic cylinder at the desired frequency and voltage is provided in Figure 11. The user interface contains information about the frequency, amplitude, and offset of the sinusoidal signal to be applied to the hydraulic cylinder. There is a graphical monitoring screen available to display the applied reference signal and the obtained reference signal together. Furthermore, the user has the ability to select the data writing method for data recording.

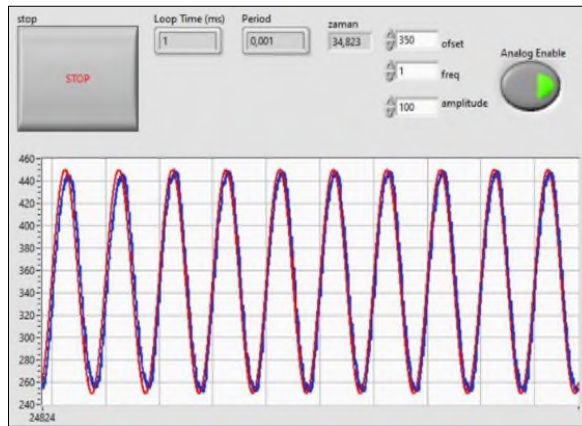


Figure 11. Developed a LabVIEW program for the front panel

The LabVIEW programming interface, which was created for the user, can be seen in Figure 12. The software loop speed has been set to 1 millisecond through the timed loop cycle. The developed software consists of four components. In the first section, a sinusoidal signal reference was generated as a function of time. The voltage signal obtained from the LVDT sensor integrated into the hydraulic cylinder was used to generate position information in the second section. The third section contains the PI block used for position control of the cylinder. A PI loop has been created in the LabVIEW software library without using the pre-built "PID" block. In the fourth section, the data has been transferred to a graphical interface for the user.

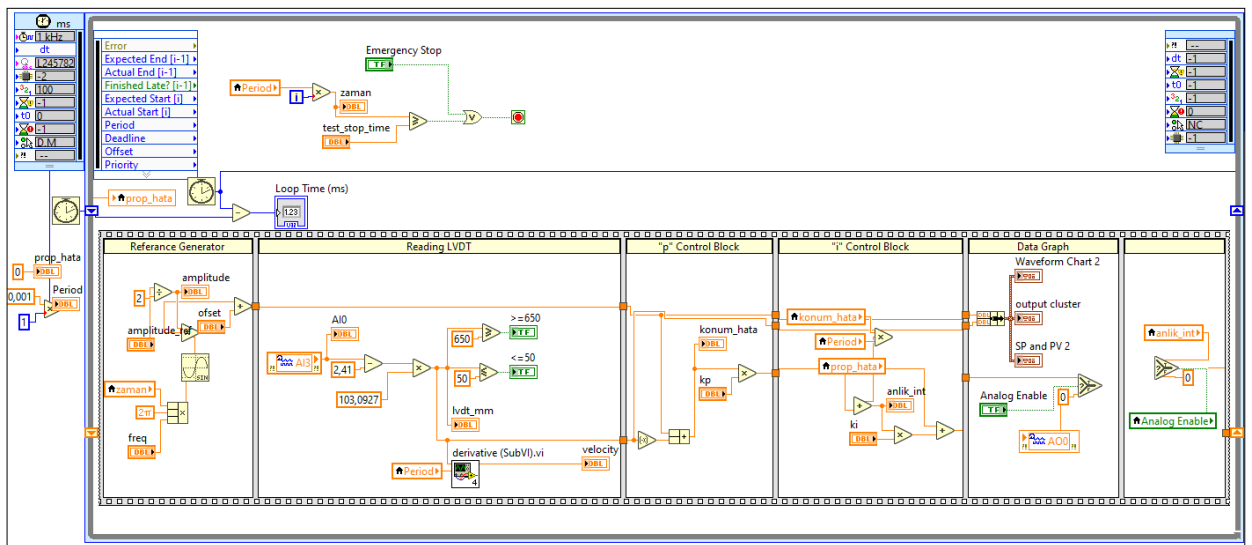
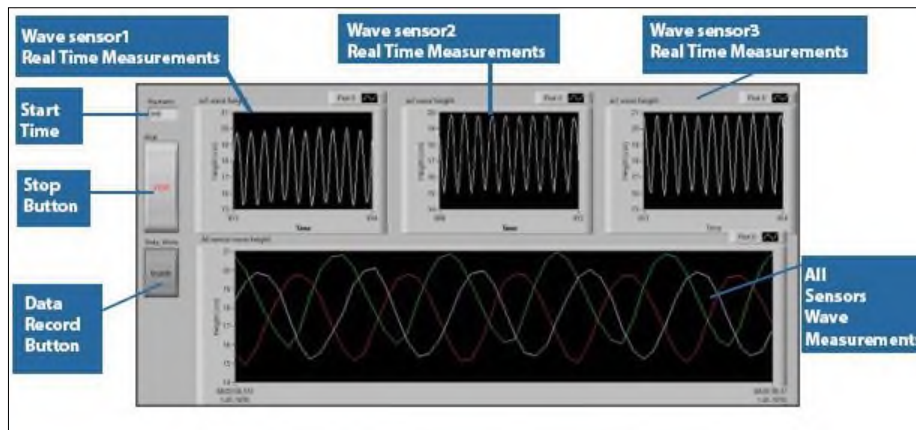


Figure 12. Developed a LabVIEW program for the back panel

## 2.4. Wave Generation

The flap-type wave generator, driven by a hydraulic cylinder located in the wave channel, has been operated at various water depths. A stimulating signal with a frequency of 0.8-1.0Hz has been sent to the hydraulic proportional valve. A program has been developed in LabVIEW software to enable real-time visualization and recording of waveforms resulting from this. This program records data from sensors at intervals of 32 milliseconds, which is the response time of the sensors. The front panel of the Labview program created for real-time wave measurement is provided in Figure 13. Three sensors are used for wave measurement in the wave channel.



**Figure 13.** LABVIEW program front panel developed for real-time wave measurement

In the program structure given in Figure 14, both real-time measurement from three channels and recording of wave data in the desired file format are ensured.

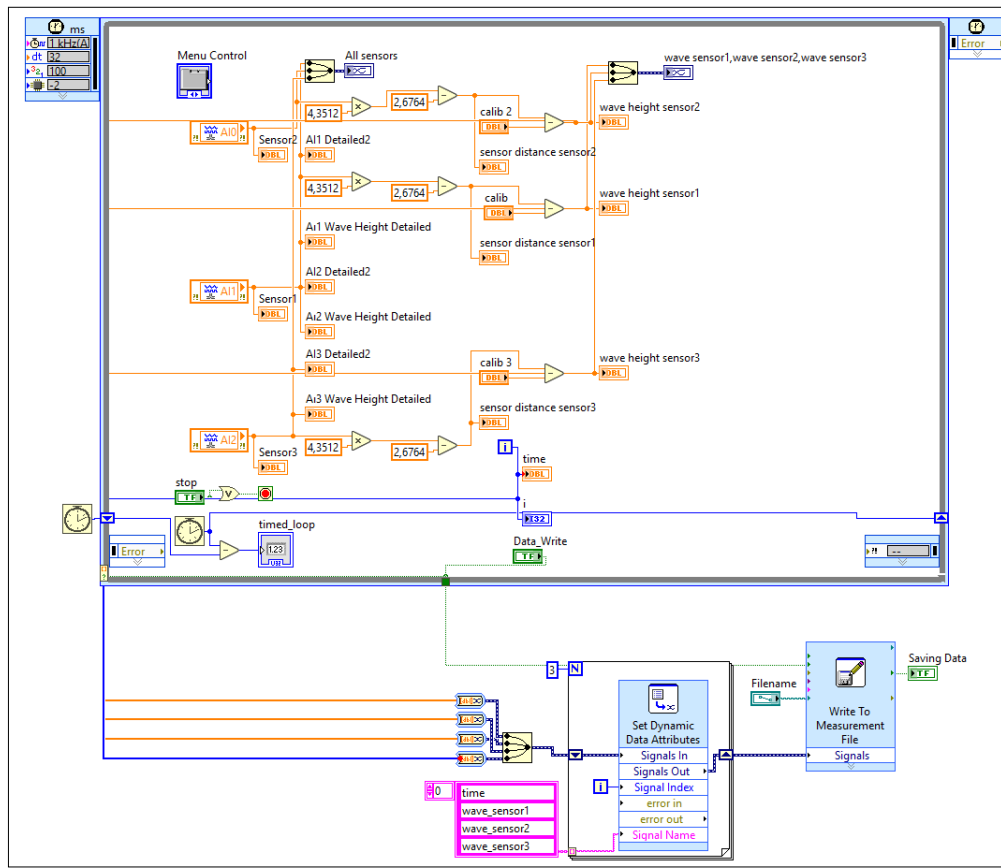


Figure 14. LABVIEW program back panel developed for real-time wave measurement

### 3. EXPERIMENTAL RESULTS

#### 3.1. Step response analysis

The PI controller parameters determined using Ziegler-Nichols, MATLAB/PID Tuner, and Genetic Algorithm were implemented on the hydraulic system via LabVIEW software. The real-time measurement results obtained are shown in Figure 15.

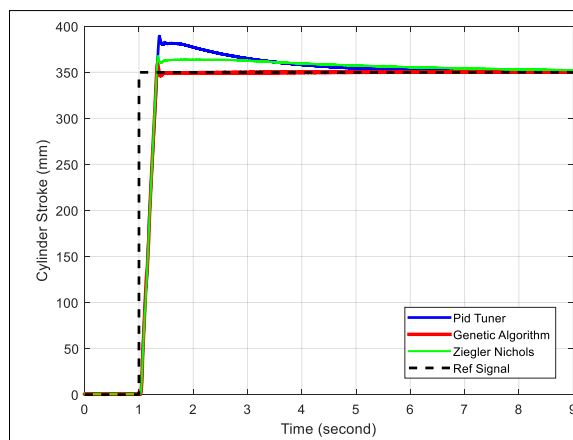


Figure 15. Step response

The controller parameters determined using Ziegler-Nichols, MATLAB/PID Tuner, and Genetic Algorithm were applied to the hydraulic cylinder system located in the wave channel, achieving position

control of the cylinder. Based on real-time measurement results obtained from the hydraulic system with the applied controller parameters, the rise time was calculated to vary between 1.282 and 1.289 seconds, the settling time ranged from 1.626 to 8.508 seconds, the steady-state error was between 0.139 and 2.24 mm, and the overshoot ranged from 2.72% to 11.42%. Additionally, to demonstrate computational indicators of control performance, the root mean square error (RMSE), the mean absolute error (MAE), and the integral of time-weighted absolute error (ITAE) criteria are utilized as defined in Equation (3). A comparison of controller performance, calculated based on real-time measurement results obtained using the three methods, is presented in Table 4.

$$RMSE = \sqrt{\frac{1}{N} \sum_{i=1}^N (e(t))^2}, \quad MAE = \frac{1}{N} \sum_{i=1}^N |e(t)|, \quad ITAE = \int_0^T t |e| dt \quad (3)$$

**Table 4.** The controller performance comparison

Control Type	Rise Time(s)	Settling Time(s)	Steady-State Error (mm)	Over Shoot (%)	RMSE	MAE	ITAE
Ziegler-Nichols	1.282	8.508	2.240	4.97	0.4556	13.7029	34.765
Matlab/PID Tuner	1.289	6.704	0.13	11.42	0.4629	14.3182	28.705
Genetic Algorithm	1.285	1.626	0.464	2.74	<b>0.4458</b>	<b>7.2593</b>	<b>8.755</b>

The ITAE based results of Genetic Algorithm based PI showed an improvement of 74.82% and 69.50%, compared with Ziegler-Nichols and Matlab/PID Tuner, respectively. The RMSE based results of Genetic Algorithm based PI showed an improvement of 2.15% and 3.69%, compared with Ziegler-Nichols and Matlab/PID Tuner, respectively. The MAE based results of Genetic Algorithm based PI showed an improvement of 47.02% and 49.30%, compared with Ziegler-Nichols and Matlab/PID Tuner, respectively.

### 3.2. Sinus response analysis

The user controls the hydraulic system with a sinusoidal signal to generate regular-form waves in the wave channel. At this point, the parameters of the 'PI' controller, determined using the genetic algorithm, were applied to both the hydraulic system and the transfer function model in the MATLAB/Simulink environment. The position responses corresponding to the desired position control signal are shown in Figure 16.

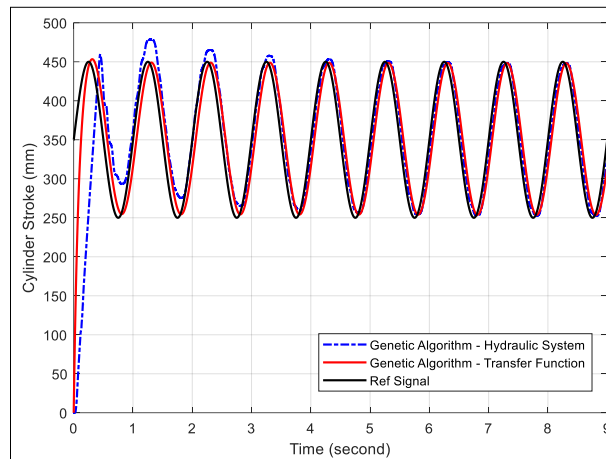


**Figure 16.** Transfer function output (red color), real system output (blue color), reference (black color)

Based on the calculations performed using the measurement results obtained from the control structure applied in real-time to the hydraulic system with the genetic algorithm, the ITAE was found to be 58.264, the MAE was 22.1941, and the RMSE was 0.5765.

### 3.3. Regular wave measurements

The hydraulic cylinder system and wave flap in the wave channel are controlled using the PI control method. The hydraulic cylinder system in the wave channel and the flap-type wave maker are controlled using the PI control method. According to the experiment presented in Table 5, the measurement results obtained from the sensor used for wave measurement, the stroke value of the hydraulic cylinder, and the constant water level data have been provided for a 1 Hz control signal.

**Table 5.** Wave Tank Experiment Results-I

Constant Water Level (h)	Hydraulic Cylinder Total Stroke	Wave Height (H), Hydraulic Cylinder Frequency
40 cm	50 mm	1 cm ,1 Hz
40 cm	100 mm	2 cm ,1 Hz
40 cm	150 mm	3 cm ,1 Hz
40 cm	200 mm	4 cm ,1 Hz
50 cm	50 mm	1 cm ,1 Hz
50 cm	100 mm	3 cm ,1 Hz
50 cm	150 mm	4 cm ,1 Hz
50 cm	200 mm	7 cm ,1 Hz
60 cm	50 mm	2 cm ,1 Hz
60 cm	100 mm	4 cm ,1 Hz
60 cm	150 mm	7 cm ,1 Hz
60 cm	200 mm	10 cm ,1 Hz

The hydraulic cylinder system in the wave channel and the flap-type wave maker are controlled using the PI control method. According to the experiment presented in Table 6, the measurement results

obtained from the sensor used for wave measurement, the stroke value of the hydraulic cylinder, and the constant water level data have been provided for a 0.8 Hz control signal.

**Table 6.** Wave Tank Experiment Results-II

Constant Water Level (h)	Hydraulic Cylinder Total Stroke	Wave Height (H), Hydraulic Cylinder Frequency
40 cm	50 mm	1 cm, 0.8 Hz
40 cm	100 mm	1,6 cm, 0.8 Hz
40 cm	150 mm	2,4 cm, 0.8 Hz
40 cm	200 mm	3 cm, 0.8 Hz
50 cm	50 mm	1 cm, 0.8 Hz
50 cm	100 mm	2 cm, 0.8 Hz
50 cm	150 mm	3 cm, 0.8 Hz
50 cm	200 mm	5 cm, 0.8 Hz
60 cm	50 mm	1,5 cm, 0.8 Hz
60 cm	100 mm	3 cm, 0.8 Hz
60 cm	150 mm	5 cm, 0.8 Hz
60 cm	200 mm	7 cm, 0.8 Hz

#### 4. CONCLUSIONS

In the conducted study, the position control of a hydraulic cylinder was utilized to generate a regular waveform in a wave channel. Water waves were created by a flap-type wave generator, which was fixed to the wave channel floor and driven by the hydraulic servo cylinder.

The parameters of the PI controller used in the position control of the hydraulic servo cylinder were determined using different methods. First, the Ziegler-Nichols method was experimentally applied directly to the hydraulic system. Second, using the model structure developed through the black-box approach, the parameters were determined via simulation in the MATLAB environment using MATLAB/PID Tuner and Genetic Algorithm. These parameters were then applied to the hydraulic system, and the accuracy of the developed model was validated.

The control signals applied to the wave channel were selected with frequencies of 0.8 Hz and 1 Hz, and the resulting wave data was recorded. The water level in the channel was maintained at a constant height of 40-50-60 cm for both signal structures, and the same control signal was applied in different frequencies. As a result, it has been determined that the effect of the generated water waveforms is dependent on the frequency of the applied control signal, even if all conditions are the same. It has been observed that as the frequency increases, the height of the water wave increases and directly affects the water level in the wave channel.

Furthermore, it has been determined that the difference between water waves generated at frequencies of 0.8 Hz and 1 Hz is at most 3 cm at water levels of 40-50-60 cm. Additionally, it has been established that a maximum wave height of 10 cm can be created with the control signal applied at a water level of 60 cm. In this study, the position control of a hydraulic servo cylinder was implemented using a PI controller to generate regular water waves in a wave channel. The position control of the hydraulic cylinder is performed in a closed loop, while the regular water wave control is performed in an open loop. In future studies, it has been evaluated that the position control of the cylinder and the wave control can be fully implemented in a closed-loop system, and the water level in the wave channel can be continuously measured and transferred to the controller as an input parameter for the wave. In this study, the



application of black-box modeling and PI control methods was carried out on a physical wave channel for controlling wave generator systems, particularly in systems where control is provided by complex hydraulic structures.

### Declaration of Ethical Standards

The authors declare that the study complies with all applicable laws and regulations and meets ethical standards.

### Credit Authorship Contribution Statement

Autor 1: Writing, design, experiments, results analysis; Autor 2: Design, experiments, results analysis; Autor 3: Writing, design, editing, supervision.

### Declaration of Competing Interest

The authors declare that they have no known competing financial interests or personal relationships that could have appeared to influence the work reported in this paper.

### Funding / Acknowledgements

The authors thank to Balıkesir University Scientific Research Projects Foundation (Project No: 2024/042) for the financial support of this study.

### Data Availability

The findings from this study are available for use by other researchers.

## 5. REFERENCES

- [1] S. Barstow, G. Mørk, D. Mollison, and J. Cruz, "The Wave Energy Resource," *Ocean Wave Energy*, pp. 93–132, Dec. 2008, doi: 10.1007/978-3-540-74895-3\_4.
- [2] O. T. Gudmestad, "Measured and predicted deep water wave kinematics in regular and irregular seas," *Marine Structures*, vol. 6, no. 1, pp. 1–73, Jan. 1993, doi: 10.1016/0951-8339(93)90009-R.
- [3] O. Yagci, V. S. O. Kirca, and L. Acanal, "Wave attenuation and flow kinematics of an inclined thin plate acting as an alternative coastal protection structure," *Applied Ocean Research*, vol. 48, pp. 214–226, Oct. 2014, doi: 10.1016/j.apor.2014.09.003.
- [4] A. Iafrati, T. Fujiwara, P. C. Mello, X. X. Zhang, and M. Drzewiecki, "Laboratory Modelling of Waves," presented at International Conf. on Fluid Dynamics, Jun. 2021.
- [5] A. Iafrati, D. Drazen, L. Xiao, and J. Henning, "Laboratory Modelling of Waves: regular, irregular and extreme events," *Proc. Int. Conf. on Coastal Eng.*, pp. 11–12, Sep. 2017.
- [6] L. Zhu, L. Zhang, X. Li, and R. Zhou, "Maritime safety assessment in the 21st-century maritime silk road under risk factors coupling," *ICTIS 2019 - 5th International Conference on Transportation Information and Safety*, pp. 411–415, Jul. 2019, doi: 10.1109/ICTIS.2019.8883809.
- [7] A. Iafrati *et al.*, "The specialist committee on modelling on environmental conditions," *J. Maritime Eng.*, vol.65, no.2, pp. 757–758, 2017.
- [8] K. Aktas, "Wave Generation and Analysis in the Laboratory Wave Channel to Conduct Experiments on the Numerically Modeled Spar Type Floating Wind Turbine," M.S. thesis, İzmir Inst. of Technol., 2020.
- [9] K. Golcek, "Gemi ve açık deniz yapıları testlerine yönelik çoklu pedal kontrollü dalga üretici tasarımı ve üretimi," Yıldız Technical Univ., Accessed: Jul. 22, 2024. [Online]. Available:

- <https://avesis.yildiz.edu.tr/yonetilen-tez/2101bf55-b8ae-46d0-9035-1a99176c2b92/gemi-ve-acik-deniz-yapilari-testlerine-yonelik-coklu-pedal-kontrollu-dalga-ureteci-tasarimi-ve-uretimi>
- [10] C. Windt, A. Untrau, J. Davidson, E. J. Ransley, D. M. Greaves, and J. V. Ringwood, "Assessing the validity of regular wave theory in a short physical wave flume using particle image velocimetry," *Exp Therm Fluid Sci*, vol. 121, p. 110276, Feb. 2021, doi: 10.1016/J.EXPTHERMFLUSCI.2020.110276.
- [11] A. A. Azman, M. H. F. Rahiman, N. N. Mohammad, M. H. Marzaki, M. N. Taib, and M. F. Ali, "Modeling and comparative study of PID Ziegler Nichols (ZN) and Cohen-Coon (CC) tuning method for Multi-tube aluminum sulphate water filter (MTAS)," *Proceedings - 2017 IEEE 2nd International Conference on Automatic Control and Intelligent Systems (I2CACIS)*, 2017, vol. 2017-December, pp. 25–30, Dec. 2017, doi: 10.1109/I2CACIS.2017.8239027.
- [12] M. Tajjudin, N. Ishak, H. Ismail, M. H. F. Rahiman, and R. Adnan, "Optimized PID control using Nelder-Mead method for electro-hydraulic actuator systems," *Proceedings - 2011 IEEE Control and System Graduate Research Colloquium (ICSGRC)*, 2011, pp. 90–93, doi: 10.1109/ICSGRC.2011.5991836.
- [13] M. Drzewiecki and J. Guziński, "Fuzzy Control of Waves Generation in a Towing Tank," *Energies* 2020, Vol. 13, Page 2049, vol. 13, no. 8, p. 2049, Apr. 2020, doi: 10.3390/EN13082049.
- [14] N. Ishak, M. Tajjudin, R. Adnan, H. Ismail, and Y. M. Sam, "Real-time application of self-tuning PID in electro-hydraulic actuator," *Proceedings - 2011 IEEE International Conference on Control System, Computing and Engineering (ICCSCE)*, 2011, pp. 364–368, doi: 10.1109/ICCSCE.2011.6190553.
- [15] Y. Fan, J. Shao, and G. Sun, "Optimized PID Controller Based on Beetle Antennae Search Algorithm for Electro-Hydraulic Position Servo Control System," *Sensors* 2019, Vol. 19, Page 2727, vol. 19, no. 12, p. 2727, Jun. 2019, doi: 10.3390/S19122727.
- [16] R. Wang, C. Tan, J. Xu, Z. Wang, J. Jin, and Y. Man, "Pressure Control for a Hydraulic Cylinder Based on a Self-Tuning PID Controller Optimized by a Hybrid Optimization Algorithm," *Algorithms* 2017, Vol. 10, Page 19, vol. 10, no. 1, p. 19, Jan. 2017, doi: 10.3390/A10010019.
- [17] L. A. Zadeh, "On the Identification Problem," *IEEE Transactions on Circuits and Systems I-regular Papers*, vol. 3, no. 4, pp. 277–281, 1956, doi: 10.1109/TCT.1956.1086328.
- [18] M. F. Rahmat, S. M. Rozali, N. A. Wahab, Zulfatman, and K. Jusoff, "Modeling and controller design of an electro-hydraulic actuator system," *Am J Appl Sci*, vol. 7, no. 8, pp. 1100–1108, 2010, doi: 10.3844/ajassp.2010.1100.1108.
- [19] *2015 IEEE International Symposium on Robotics and Intelligent Sensors (IRIS)*, IEEE, 2015.
- [20] İ. İstif, "Oransal Valf Ve Hidrolik Silindirden Oluşan Bir Sistemin Tanılanması Ve Konum Kontrolü," 2015, *Fen Bilimleri Enstitüsü*. Accessed: Aug. 09, 2024. [Online]. Available: <http://hdl.handle.net/11527/11573>
- [21] National Instruments Corp., "cRIO-9074 - NI." Accessed: Jul. 20, 2024. [Online]. Available: <https://www.ni.com/en-tr/support/model.crio-9074.html>
- [22] MathWorks®, "System Identification Toolbox - MATLAB." Accessed: Jul. 22, 2024. [Online]. Available: <https://www.mathworks.com/products/sysid.html>
- [23] J. J. Vyas, B. Gopalsamy, and H. Joshi, "System identification," in *SpringerBriefs in Applied Sciences and Technology*, Springer Verlag, 2019, pp. 47–51. doi: 10.1007/978-981-13-2547-2\_4.
- [24] L. J. Puglisi, R. J. Saltaren, C. Garcia, and I. A. Banfield, "Robustness analysis of a PI controller for a hydraulic actuator," *Control Eng Pract*, vol. 43, pp. 94–108, Oct. 2015, doi: 10.1016/j.conengprac.2015.06.010.
- [25] M. Shahrokhi and A. R. Zomorodi, "Comparison of PID Controller Tuning Methods." Accessed: Oct. 22, 2024. [Online]. Available: <https://www.semanticscholar.org/paper/Comparison-of-PID-Controller-Tuning-Methods-Shahrokhi-Zomorodi/b4ca1b81247f71593d3e60f4169f9307baa361d4>



## EXPERIMENTAL AND NUMERICAL INVESTIGATION ON THE EFFECT OF INFILL WALLS ON DYNAMIC BEHAVIOR IN RC STRUCTURES: SHAKE TABLE TESTS

<sup>1,\*</sup> Abdulhamit NAKİPOĞLU , <sup>2</sup> M. Sami DÖNDÜREN 

*Konya Technical University, Engineering and Natural Sciences Faculty, Civil Engineering Department, Konya, TÜRKİYE*

<sup>1</sup>[anakupoglu@ktun.edu.tr](mailto:anakupoglu@ktun.edu.tr), <sup>2</sup>[msdonduren@ktun.edu.tr](mailto:msdonduren@ktun.edu.tr)

### *Highlights*

- RC frame samples tested with and without infill walls.
- Shake table experiments were conducted, and numerical analysis was performed in ETABS program.
- Both experimental modal analyses and load-displacement analyses were carried out.
- Effects of infill walls on dynamic behavior were studied.
- Infill walls greatly increased stiffness and decreased displacements substantially.



## EXPERIMENTAL AND NUMERICAL INVESTIGATION ON THE EFFECT OF INFILL WALLS ON DYNAMIC BEHAVIOR IN RC STRUCTURES: SHAKE TABLE TESTS

<sup>1,\*</sup> Abdulhamit NAKİPOĞLU , <sup>2</sup> M. Sami DÖNDÜREN 

*Konya Technical University, Engineering and Natural Sciences Faculty, Civil Engineering Department, Konya, TÜRKİYE*

<sup>1</sup> [anakipoglu@ktun.edu.tr](mailto:anakipoglu@ktun.edu.tr), <sup>2</sup> [msdonduren@ktun.edu.tr](mailto:msdonduren@ktun.edu.tr)

(Received: 11.12.2024; Accepted in Revised Form: 12.02.2025)

**ABSTRACT:** Infill walls have many positive and negative effects on reinforced concrete (RC) buildings under the effect of earthquakes, but these are often not taken into consideration sufficiently. The contribution of walls to stability and stiffness in particular is considerable. In the negative sense, due to various reasons, incorrect/incomplete use of infill walls can cause extremely fatal irregularities such as short columns and soft stories. In this study, the effect of infill walls on the dynamic behavior of reinforced concrete buildings was examined. The study was conducted on a dynamic basis in order to approach the behavior under the effect of earthquakes in a more realistic way. For this purpose, a 1/3 scale 2-storey single-span reinforced concrete frame was produced for the experiments. Forced vibration tests were carried out on the shake table in the reference state (bare frame) and in the infill-walled state. The sample was subjected to an artificial ground motion with a peak ground acceleration (PGA) value of 0.54 g in both states. Experimental modal analysis, load-displacement analysis, and numerical analysis on ETABS structural analysis software were done. As a result, it was observed that the infill walls significantly enhanced the stiffness, leading to a considerable reduction in displacement values. Calculations showed that the natural frequencies increased by approximately 5-10%, while the global damping ratio decreased by about 20%.

**Keywords:** *Dynamic Behavior, Dynamic Characteristics, ETABS, Experimental Modal Analysis, Infill Wall, Shake Table*

### 1. INTRODUCTION

Earthquake resistant structural design is a very sensitive issue for Turkey. To reduce the impact of earthquakes on structures, advancements made in engineering designs and structural material technology have led to the development of lighter and stronger materials. However, the use of such materials in structural systems reduces the cross-sections and makes the systems slender. In addition, the increases obtained in strength are not at the same rate in the elasticity modulus, which is one of the most important parameters of stiffness. This situation causes significant decreases in the stiffness of the elements and systems. Therefore, the decreased stiffness creates serious vibration and stability problems in the structures and increases the interaction of the structures with their surroundings, namely the soil, under the effect of time-dependent dynamic loads such as earthquakes.

The effect of infill walls in buildings is often not given enough importance. Although infill walls do not contribute much to the structure in terms of strength, which is at most 15% according to the Turkish Building Earthquake Code TBEC 2018 [1], they provide serious gains in terms of stability. Infill walls, which greatly increase the system stiffness, also significantly limit lateral drifts. The contribution of infill walls to the system is largely in undamaged/elastic state, and the stiffness of walls decreases significantly with cracking with brittle behavior, and therefore their contribution to the strength and the stiffness decreases significantly in the plastic region. A critical issue is the correct use of infill walls. Walls should be constructed as symmetrically as possible on each story of the building. Otherwise, for example, in a building constructed with no ground story walls for commercial purposes and all other floors with infill walls, soft story irregularity (stiffness irregularity between adjacent stories) is almost

\*Corresponding Author: Abdulhamit NAKİPOĞLU, [anakipoglu@ktun.edu.tr](mailto:anakipoglu@ktun.edu.tr)

inevitable. Another example is the formation of short columns as a result of the application of band-type windows or the partial application of infill walls on the story instead of the entire story height for some other reason. Both situations cause a large part of the earthquake energy to be concentrated in these areas and often cause the structure to collapse [1], [2], [3].

Dynamic loads on structures such as earthquakes are often analyzed with static solution methods. The reason for this is usually the complexity of the solution created by the inertial forces that arise as a result of dynamic effects. However, in order to see the real behavior of a system under dynamic loads, the solution method must also be dynamic-based [4].

Although many experimental studies have been conducted on the contribution of infill walls to the behavior of the system in buildings, the vast majority of these are static-based studies. In the studies mentioned here, mostly static, or quasi-static reversed-cyclic loading type were used. Zhang et al. [5] studied on failure mechanism and seismic performance of reinforced concrete (RC) frame infilled walls structures reinforced by carbon fiber reinforced plastics (CFRP), Ou et al. [6] investigated cyclic behavior and pushover analysis of large scale two-bay, two-story reinforced concrete frames infilled with walls with openings, Jin et al. [7] investigated in-plane and out-of-plane interaction of isolated infills in reinforced concrete frames, Pradhan et al. [8] studied effects of passive confinement on out-of-plane robustness of unreinforced masonry infill walls, Monical and Pujol [9] studied the response of reinforced concrete frames with and without masonry infill walls to earthquake motions, Bhaskar et al. [10] investigated in-plane behavior of masonry infill walls with openings strengthened using textile reinforced mortar, Wang et al. [11], Wang et al. [12], Li et al. [13] investigated progressive collapse of self-centering precast concrete frame with infill walls, Ning et al. [14] studied earthquake performance of infilled reinforced concrete frames, Luo et al. [15] studied the impact of infill wall distribution on the mechanical behavior and failure patterns of multi-story RC frame structures, Li et al. [16] investigated seismic behavior of steel frame infilled with wall-panels connected by sliding joint, Zhang et al. [17] studied on improving cyclic behavior of infilled reinforced concrete frame by prefabricated wall panels with sliding joints, Balık et al. [18] investigated infill walled RC frames covered with steel sheets. On the other hand, there are also a few dynamic-based experimental studies on this subject. Nie et al. [19] studied progressive collapse of the double-layer cylindrical reticulated shell with infilled wall on shake table, Nicoletti et al. [20] studied the contribution of infill wall stiffness to steel frame structures, Yu et al. [21] investigated seismic behavior of hinged steel frames with masonry infill walls, Bahadır [22] studied band-type window spaces that can cause short-column and soft-story behaviors in RC structures on shake table experiments, Yousefianmoghadam et al. [23] investigated system identification of a two-story infilled RC building in 4 different damage states, damage was formed by removing infill walls. To summarize the literature review, there are studies on the effects of infill walls on RC structures. These are mostly static-based studies. There are a few dynamic-based studies. These studies have been conducted mainly on strengthening, strength, load carrying capacity and performance, and no research has been found on stiffness, especially on initial stiffness where the contribution of infill walls can be seen most clearly. This study addresses this gap in the literature.

In the study, the effect of infill walls on dynamic behavior in reinforced concrete structures was investigated. For this purpose, experimental modal analysis (EMA) was performed with shake table tests on the frame sample with and without infill walls. Since the main contribution of infill walls to the structure will be stiffness and it is known that the largest part of this contribution will be until the walls are damaged, no stiffness loss was desired in the sample and the experiments were performed in the elastic region. Thus, modal analysis calculations were not affected by instantaneous stiffness losses and modal parameters directly related to stiffness could be calculated clearly. Dynamic behaviors in two different states of the sample were determined by performing experimental modal analysis and load-displacement analyses and the effect of infill walls on the behavior was investigated. In addition, numerical modal analysis was performed with linear time history analysis under the same conditions for two different states of the sample using the ETABS finite element software.

## 2. MATERIAL AND METHODS

### 2.1. Sample Properties, Material Details and Construction

A 1/3 geometric scale 2-storey single-span 3D RC frame sample was constructed to be examined with vibration tests. The sample was named as (RS) in its empty-bare state (reference) and (IS) in its improved state with infill walls. The digital 3D views of the sample in RS and IS states are given in Figure 1. Some construction stages for the bare state of the sample are also shown in Figure 2. Some mistakes were made deliberately in the frame in order to represent the existing building stock. Some of these mistakes are insufficient concrete compressive strength [24], not making stirrup densification, not using stirrups in joint areas, not complying with the strong column-weak beam principle.

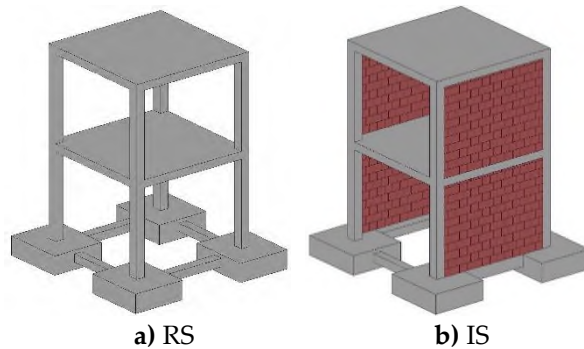


**Figure 1.** 3D views of the sample in two different states



**Figure 2.** Construction stages

The cross-section dimensions of the columns and beams are 15×15 cm. The slabs in the sample are a type of two-way slab with beams and have a thickness of 8 cm. The foundation of the frame sample is strap footing. The story heights and the span lengths in both directions of the slabs are 1 m. The dimensions and views of the frame are as shown in Figure 3. The front and side views are exactly the same.

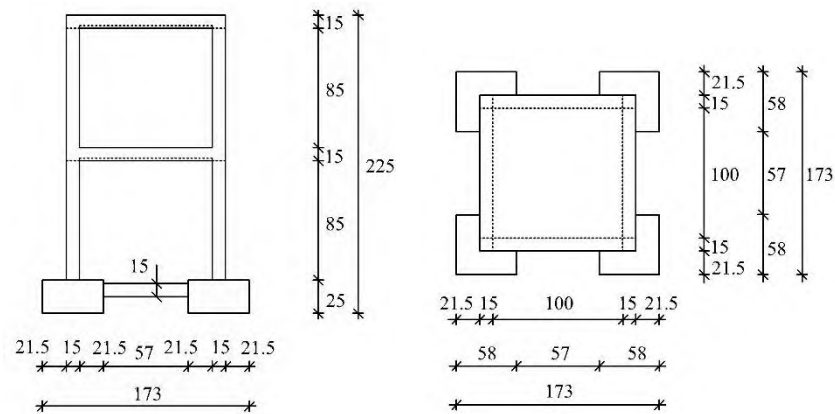


**Figure 3.** Dimensions and views of the sample; front and side view (left), top view (right) (All dimensions are in 'cm'.)

As a result of standard compression tests, the average concrete compressive strength in the stories of the sample was determined as 5.94 MPa and in the foundation as 21.11 MPa (Figure 4). Since the foundation will not be examined in the vibration tests, it is aimed to have high stiffness. [24]

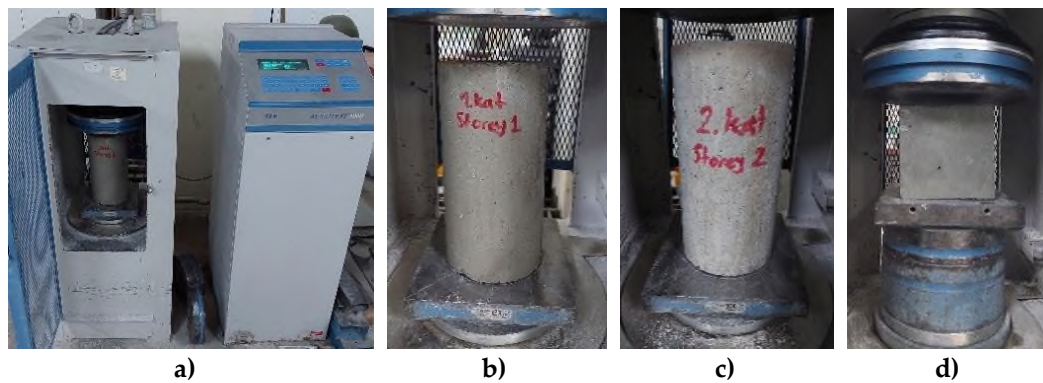


**Figure 4.** Standard compression tests; a) Test device, b) 1st story concrete sample, c) 2nd story concrete sample, d) Foundation concrete sample

The reinforcement details of the sample are given in Figure 5. The dimensions, reinforcement arrangements and details are the same in both horizontal directions. All reinforcement are ribbed steel with a yield strength of 420 MPa. The longitudinal reinforcement ratio in the columns was designed to deliberately not meet the minimum longitudinal reinforcement ratio requirement of 0.01 recommended by TBDY 2018 [1]. In the slabs, mesh reinforcement with a reinforcement diameter of 6 mm and 150×150 mm intervals was placed at the bottom and top of the section.

## 2.2. Experimental Setup

A shake table was used as an exciter in vibration experiments. The system can produce vibration in the horizontal direction by converting the rotational motion in the servo motor into linear motion. The platform dimensions of the system are 4×4 m. The shake table, which has a displacement capacity of ±153 mm in the horizontal direction, can carry a load of up to 10 tons in the vertical direction.

Responses were obtained by means of accelerometers and potentiometers. The sensors were placed in the same direction as the loading. Displacement measurements were made at a total of 3 different points, namely at the center of the foundation beam, and at the center of the beams on the 1st and 2nd stories. Similarly, acceleration measurements were made at a total of 3 points, namely 2 of them at the

center of the story beams and 1 on the platform. The digital drawing of the experimental setup is shown in Figure 6, and the actual view and sensor locations are shown in Figure 7.

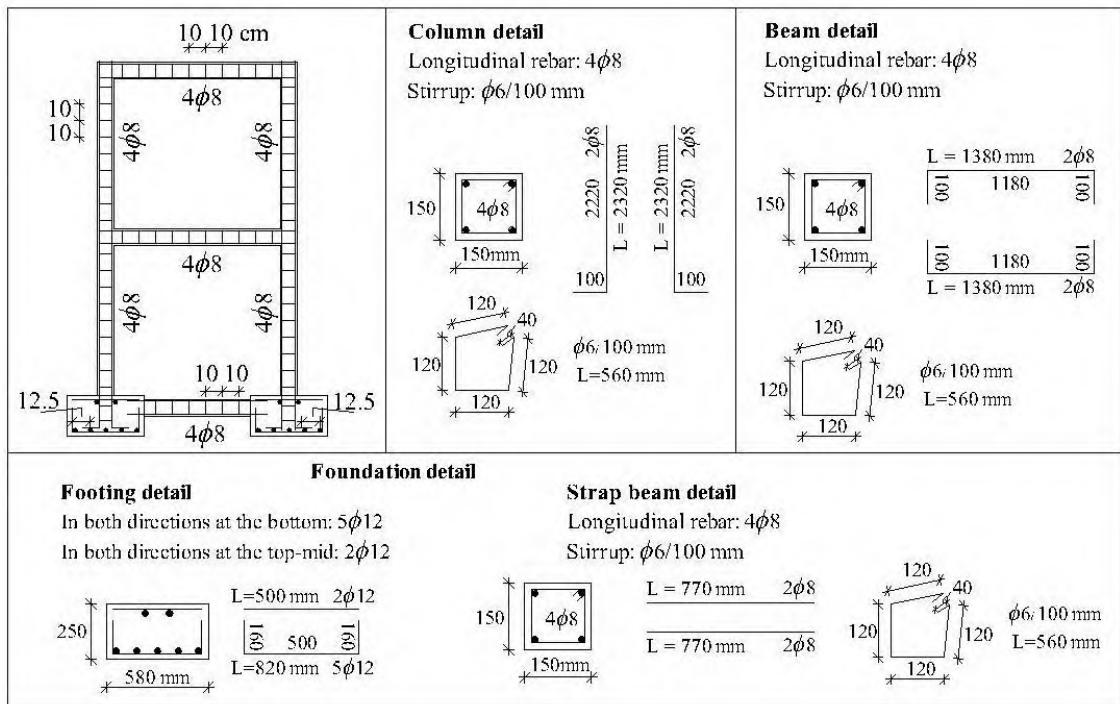


Figure 5. Reinforcement details

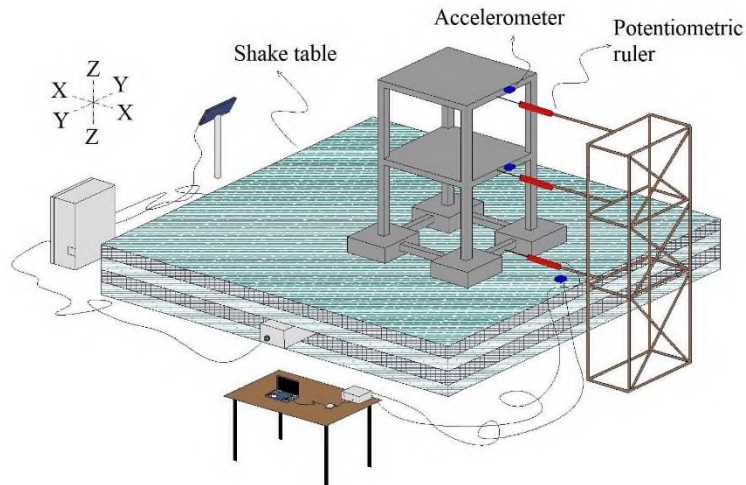
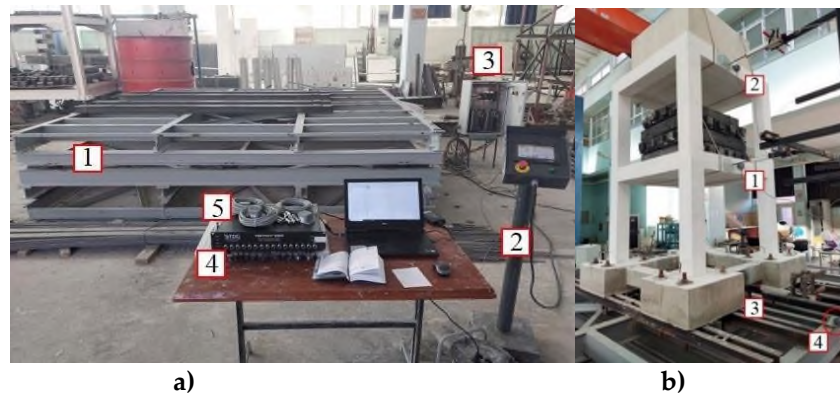


Figure 6. Digital drawing of the experimental setup





**Figure 7.** a) Experimental setup; 1) shake table, 2) control panel, 3) PLC-controlled automation system, 4) data acquisition system, 5) accelerometers, b) Sensor locations; 1) 1. story sensors, 2) 2. story sensors, 3) potentiometer on the foundation, 4) accelerometer on the shake table platform

### 2.3. Loading

In the experimental phase, approximately 1 ton weight was placed on the sample floors. Here, the vertical load carrying capacity of the shake table and the damage states that may occur in the samples are taken as basis. As dynamic loading, the 25-second part where the values are dominant in the acceleration data recorded in the 90° direction at the Kakogawa, Japan station of the 1995 Kobe, Japan earthquake was applied, but it was seen that the table could not fully reflect this data in the feedback acceleration measured on the shake table. For this reason, the excitation acceleration was not named as the Kobe earthquake, but was defined as an artificial ground motion. Accordingly, the peak ground acceleration (PGA) of this artificial motion is 0.54 g, its total duration is 21 s (Figure 8). The acceleration and displacement response spectra of this loading at 5% damping ratio are given in Figure 9.

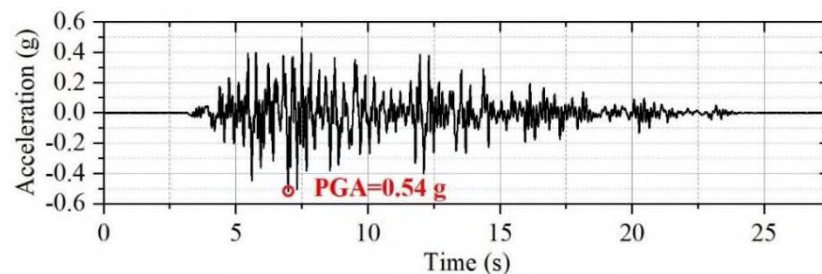


**Figure 8.** Dynamic excitation

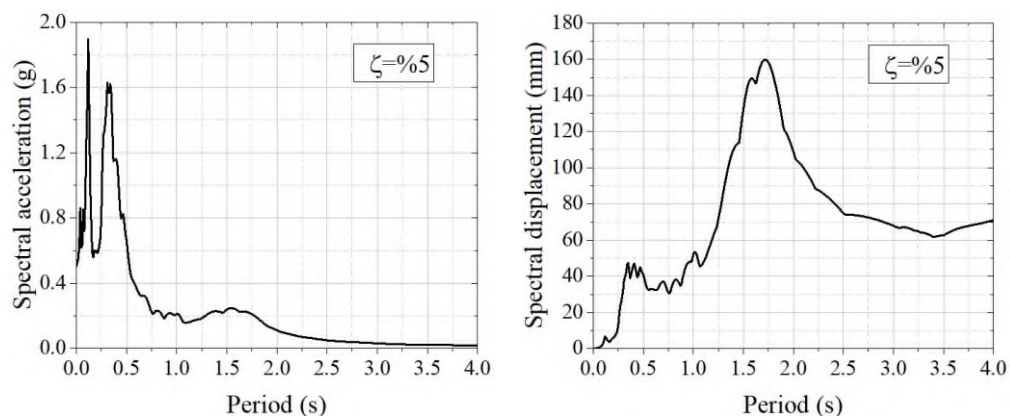


**Figure 9.** Acceleration response spectrum (left), displacement response spectrum (right)

## 2.4. Calculations Based on Experimental Data

Experimental modal analysis (EMA) was carried out using acceleration type frequency response functions (FRF, transfer function). First, signal processing was performed, and Blackman window was used to minimize the leakage error that would occur with Fast Fourier Transforms (FFT). Data were cut from appropriate frequency values with 4th order Butterworth type lowpass filter. Since no damage occurred in the sample during the experiments, at least 3 repeated tests could be performed for 2 different states of the sample. In this way, the average of FRF functions were created and, in this way, more reliable FRF graphs were obtained. Afterwards, erroneous data and noise were reduced, and nonlinear multi-degree of freedom Lorentzian type curve fitting was performed.

The natural frequencies of the 1st and 2nd modes in the loading direction were determined by the peak picking method from the resulting FRF amplitude graphs. The damping ratios were determined by the logarithmic decrement method from the top displacement-time graphs by taking into account the part where the forced vibration ends, and the free vibration begins. The mode shapes were also determined by the peak picking method from the imaginary FRF graphs.

Inertial forces occurring in the stories were taken as story shears and base shears were calculated accordingly [25], [26]. Lateral translational stiffness was determined via base shear-top displacement hysteresis curves. Here, stiffnesses were calculated by performing force/displacement on the curves obtained as a result of linear regression analysis. Since the frame was not damaged during the experiments and remained in the elastic region, these values were defined as initial lateral translational stiffnesses. [27]

In these stages, SeismoSignal v4.3.0 [28], OriginPro 2021 [29], Microsoft Excel [30], EasyTest Experimental Modal v2.1.5 [31] softwares were used.

## 2.5. Numerical Analysis

Numerical analysis was also performed for comparison with the experimental phase. Here, numerical analysis of the sample was performed under the same loading and the same conditions in the ETABS Ultimate v19.1.0 software according to the finite element method. Two different states of the sample were numerically examined with linear time history analysis. The finite element model of the sample for the RS and IS states is shown in Figure 10.

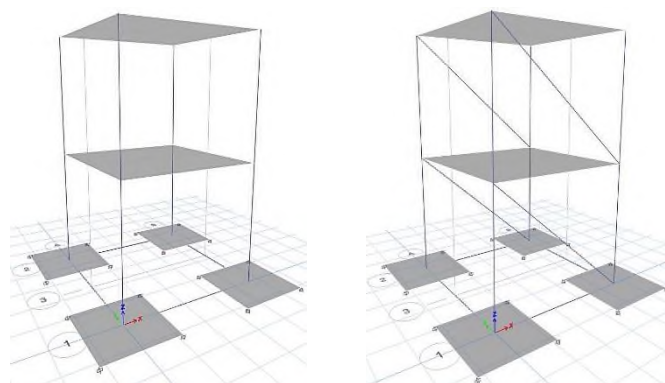


Figure 10. Finite element model of the sample; RS (left), IS (right) [32]

## 2.6. Experimental Phase

After the construction of the bare frame was completed, vibration experiments in the RS state were carried out. Experiment photos are shown in Figure 11.



Figure 11. RS state experiments

After the reference state experiments were completed, the improvement phase with infill walls was started. In this process, the frame openings of both floors in the loading direction of the sample were walled with bricks of 190×85×190 mm dimension. 1 week after the wall construction, the sample was plastered with a rough plaster of approximately 7.5 mm thickness from the inside and outside and as a result, the production of a 10 cm thick plastered infill wall was completed. The plastered areas were then cured with water for 7 days. The mortar material used in the wall and plaster consists of a mixture of cement, sand, water, and lime. Figure 12 shows the improvement process of the sample with infill walls.



Figure 12. Improvement with infill walls

After the infill wall production was completed, the tests of the sample in the improved with infill walls state (IS) were carried out in the same way. The test photos of the IS state are shown in Figure 13.



Figure 13. IS state experiments

### 3. RESULTS AND DISCUSSION

In this section, the experimentally obtained results are abbreviated as EXP, and the numerically obtained results with the ETABS program are abbreviated as NUM.

As expected, no visible damage/cracks were observed in either state of the sample during any of the tests. Accordingly, the sample remained in the elastic region in both RS and IS states and modal analysis could be carried out consistently for the initial state of the sample in both states.

Since the contribution of the infill walls to the lateral translational stiffness of the structure will decrease significantly in case of damage, the positive effect of the walls on the structure could be clearly observed without any loss of stiffness with elastic zone tests. Observations in the experiments showed that the lateral displacement of the sample decreased significantly in the IS state compared to the RS state due to the effect of the infill walls.

#### 3.1. Modal Analysis

The curve-fitted accelerance type FRF amplitude graphs of the sample in the RS and IS states obtained as a result of the experimental modal analysis are given in Figure 14 and Figure 15. The natural frequencies of the sample in the 1st and 2nd lateral translational modes in the loading direction for the RS and IS states are given in Table 1 in the unit of 'Hz' and the natural periods in the unit of 's' are given in Table 2.

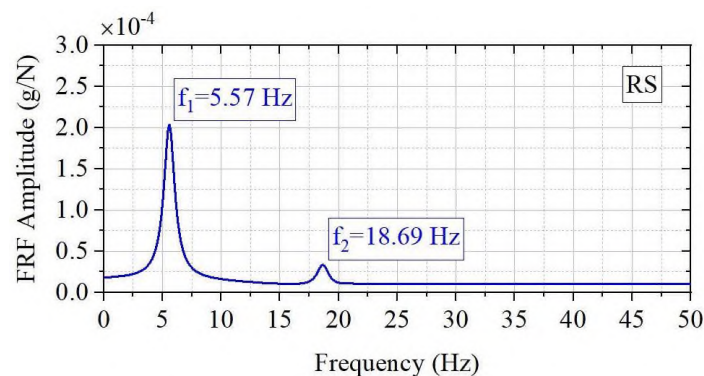


Figure 14. FRF amplitude graph of the sample in RS state

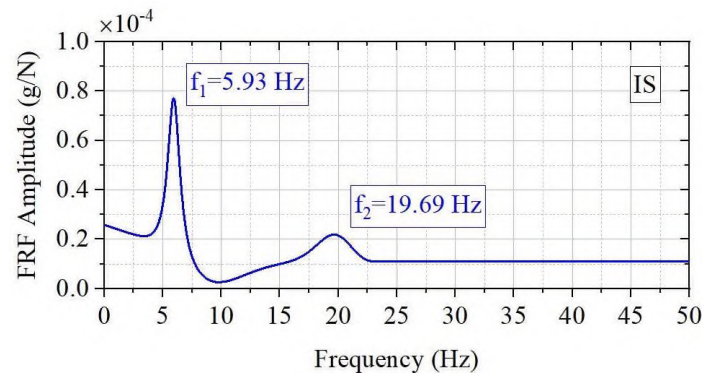


Figure 15. FRF amplitude graph of the sample in IS state

Table 1. Natural frequencies (Hz)

State	1. Mode (EXP)	1. Mode (NUM)	Difference	2. Mode (EXP)	2. Mode (NUM)	Difference
RS	5.57	5.45	2%	18.69	18.43	1%
IS	5.93	5.76	3%	19.69	18.54	6%

Table 2. Natural periods (s)

State	1. Mode (EXP)	1. Mode (NUM)	Difference	2. Mode (EXP)	2. Mode (NUM)	Difference
RS	0.180	0.184	2%	0.054	0.054	0%
IS	0.169	0.174	3%	0.051	0.052	2%

When Table 1 and Table 2 are examined, the experimentally obtained results and the numerically obtained results are quite close to each other.

The experimentally determined natural frequency and natural period values are compared in Table 3 for two different states of the sample.

Table 3. Comparison of natural frequencies and natural periods

Mode	Natural frequency (Hz) (EXP)			Natural period (s) (EXP)		
	RS	IS	Difference	RS	IS	Difference
1. Mode	5.57	5.93	+7%	0.180	0.169	-6%
2. Mode	18.69	19.69	+5%	0.054	0.051	-6%

According to Table 3, in the IS state, due to the effect of infill walls, the 1st natural frequency increased by 7% and the 2nd natural frequency increased by 5% compared to the RS state. The natural period values decreased by 6% for both modes. If Equation 1 is examined, the increase in frequency values can be achieved by increasing the stiffness or decreasing the mass. Here, it is understood that the stiffness increases because the mass is constant. In short, according to this result, the infill walls increased the stiffness of the frame.

Global damping ratios were determined by the logarithmic decrement method by considering the part where free vibration starts in the top displacement-time graphs based on experimental data. Accordingly, the damping ratios of the sample in the loading direction were calculated as 4.92% for the RS state and 4.10% for the IS state. Considering Equation 1 used in the damping ratio calculation, the decrease in the damping ratio with the increase in stiffness was a reasonable result [33]. Here, the global damping ratio decreased by 17% due to the increase in the lateral translational stiffness of the frame by the infill walls.

$$\omega_n^2 = k/m \quad \zeta = \frac{c}{2m\omega_n} \quad (1)$$

In the equation,  $\omega_n$  represents the natural frequency,  $k$  represents the stiffness,  $m$  represents the mass,  $\zeta$  represents the damping ratio,  $c$  represents the damping constant and  $c_{cr}$  represents the critical damping constant.

The 1st and 2nd lateral translational mode shapes obtained for the loading direction as a result of the numerical modal analysis are given in Figure 16.

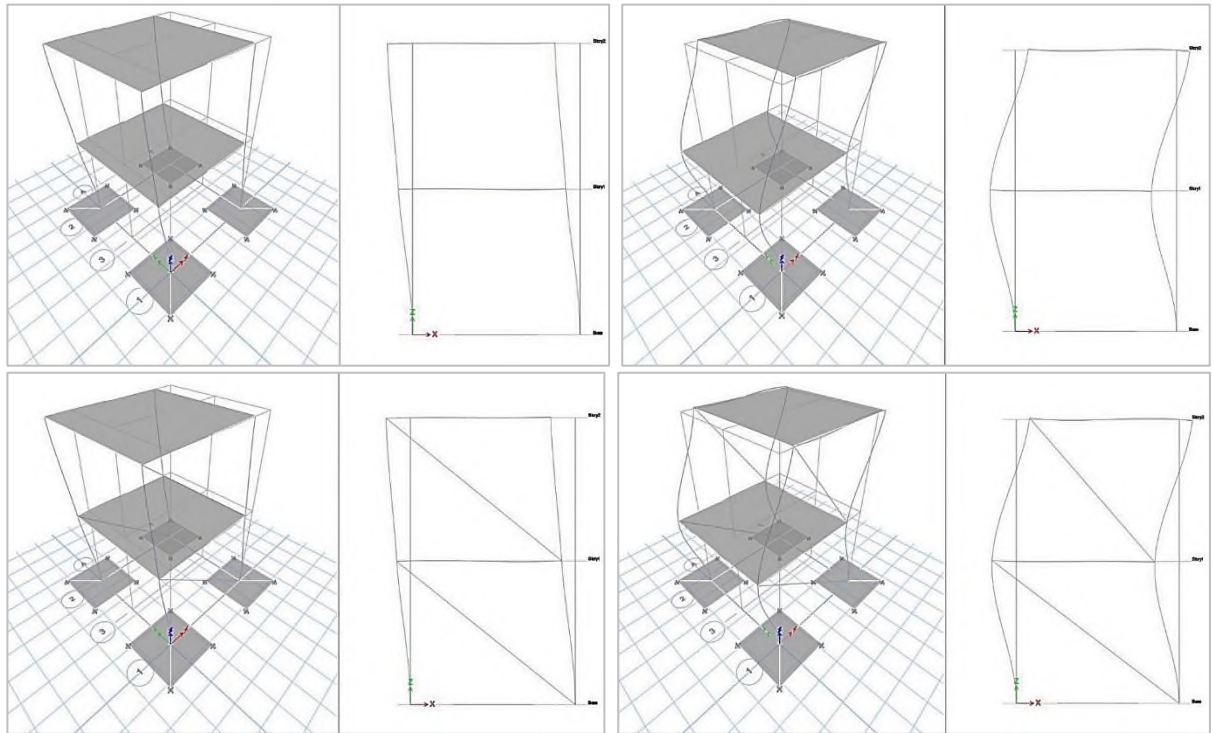


**Figure 16.** Mode shapes obtained as a result of numerical modal analysis; RS 1st Mode (top left), RS 2nd Mode (top right), IS 1st Mode (bottom left), IS 2nd Mode (bottom right) [32]

The 1st and 2nd lateral translational mode shapes determined by experimental and numerical modal analysis for the RS and IS states of the sample are compared in Figure 17 and Figure 18.

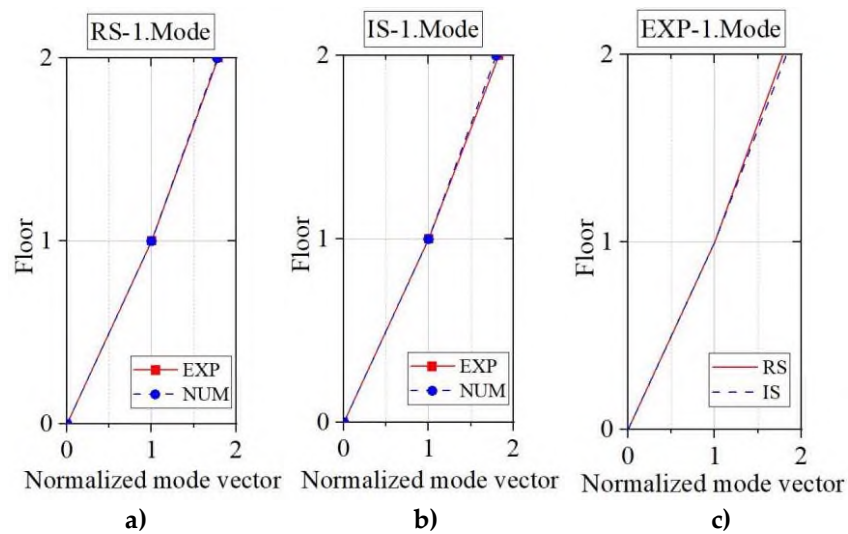


**Figure 17.** Comparison of lateral translational mode shapes; a) RS 1. Mode, b) IS 1. Mode, c) EXP 1.Mode

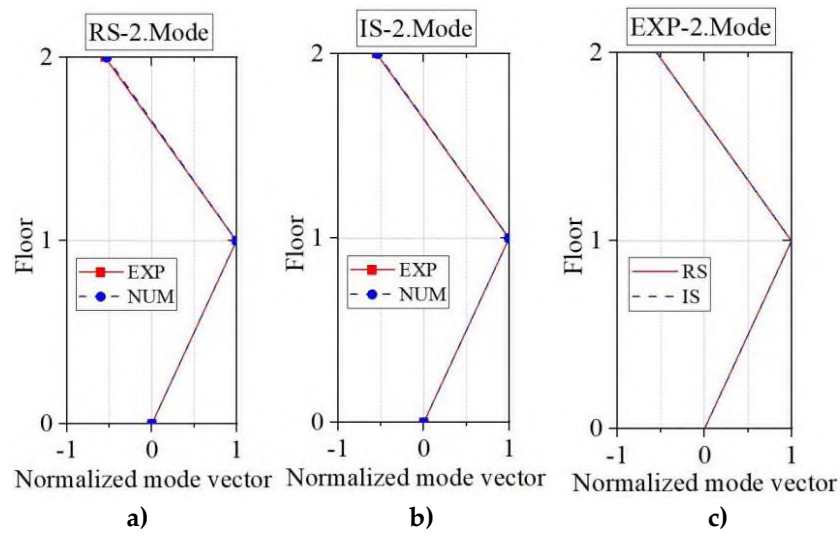


**Figure 18.** Comparison of lateral translational mode shapes; **a)** RS 2. Mode, **b)** IS 2. Mode, **c)** EXP 2. Mode

When Figure 17 and Figure 18 are examined, it is seen that the experimental and numerical results are quite compatible in terms of mode shapes. It is also seen that the infill walls do not have a significant effect on the lateral translational mode shapes.

### 3.2. Load-Displacement

The top displacement in time domain graphs obtained experimentally and numerically for the RS reference state and the IS infill walled state of the sample are given in Figure 19.

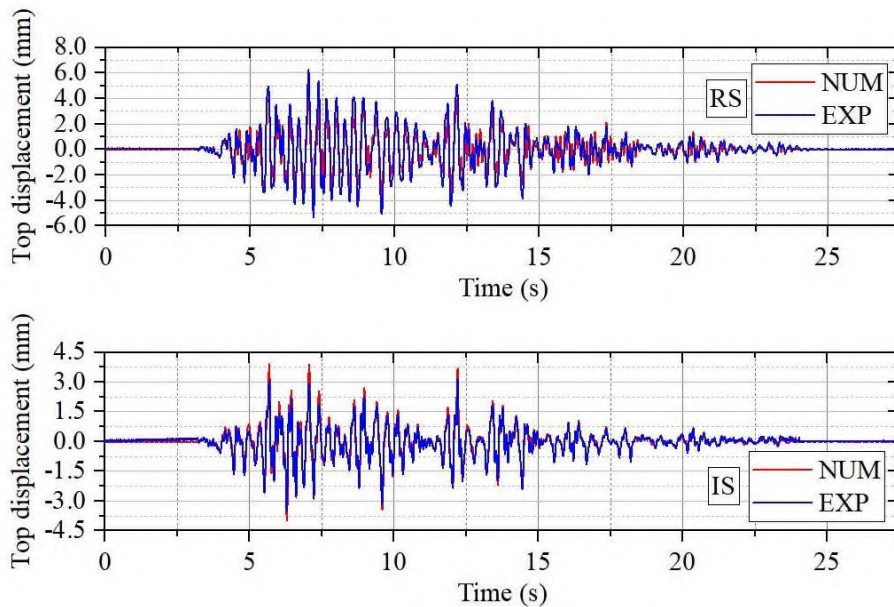


**Figure 19.** Top displacement-time graphs; RS (top), IS (bottom)

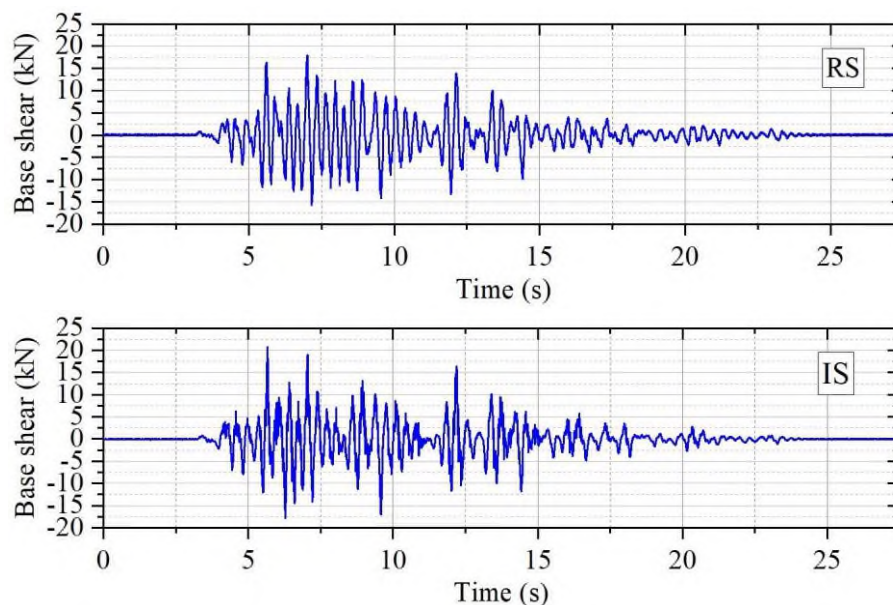
The absolute maximum top displacements of the frame determined experimentally and numerically in the RS and IS states are shown and compared in Table 4.

**Table 4.** Absolute maximum top displacements (mm)

	RS	IS	Difference
<b>EXP</b>	6.13	3.52	-43%
<b>NUM</b>	5.91	3.97	-33%
<b>Difference</b>	4%	13%	-

When Table 4 is examined, it is seen that the infill walls limit the absolute maximum top displacement to a great extent. Accordingly, the absolute maximum top displacement decreased by 43% in the IS state according to the experimental results and by 33% according to the numerical results compared to the RS state. In addition, there was a difference of 4% in the RS state and 13% in the IS state between the experimental and numerical results. These results show that infill walls significantly increase the frame stiffness and thus limit the displacements.

Experimentally obtained base shear-time graphs for the RS and IS states of the sample are given in Figure 20.

**Figure 20.** Base shear-time graphs; RS (top), IS (bottom)

The absolute maximum base shear values obtained experimentally were around 20 kN for both states of the sample.

The base shear-top displacement hysteresis curves created for the RS and IS states of the sample are shown and compared in Figure 21. In addition, curve fitting was performed on the hysteresis curves using linear regression analysis.

When Figure 21 is examined, it is seen that there is no tendency for the base shears to decrease, that is, the sample continues to receive loads without losing strength in both states and therefore remains in the elastic region. In addition, there are great differences in the slopes of the hysteresis curves. This situation is even clearer in the curves obtained as a result of linear regression analysis. The slope of the hysteresis curve is greater in the IS state than in the RS state. Since the slope here shows the force/displacement ratio, it directly corresponds to the lateral translational stiffness. In other words, the initial lateral translational stiffness of the sample has increased due to the effect of the infill walls. If we express it numerically, the stiffness value, which was 2.57 kN/mm in the RS state, became 4.82 kN/mm in the IS state. Thus, an 88% increase in stiffness has occurred thanks to the positive effect of the infill walls on the structure.



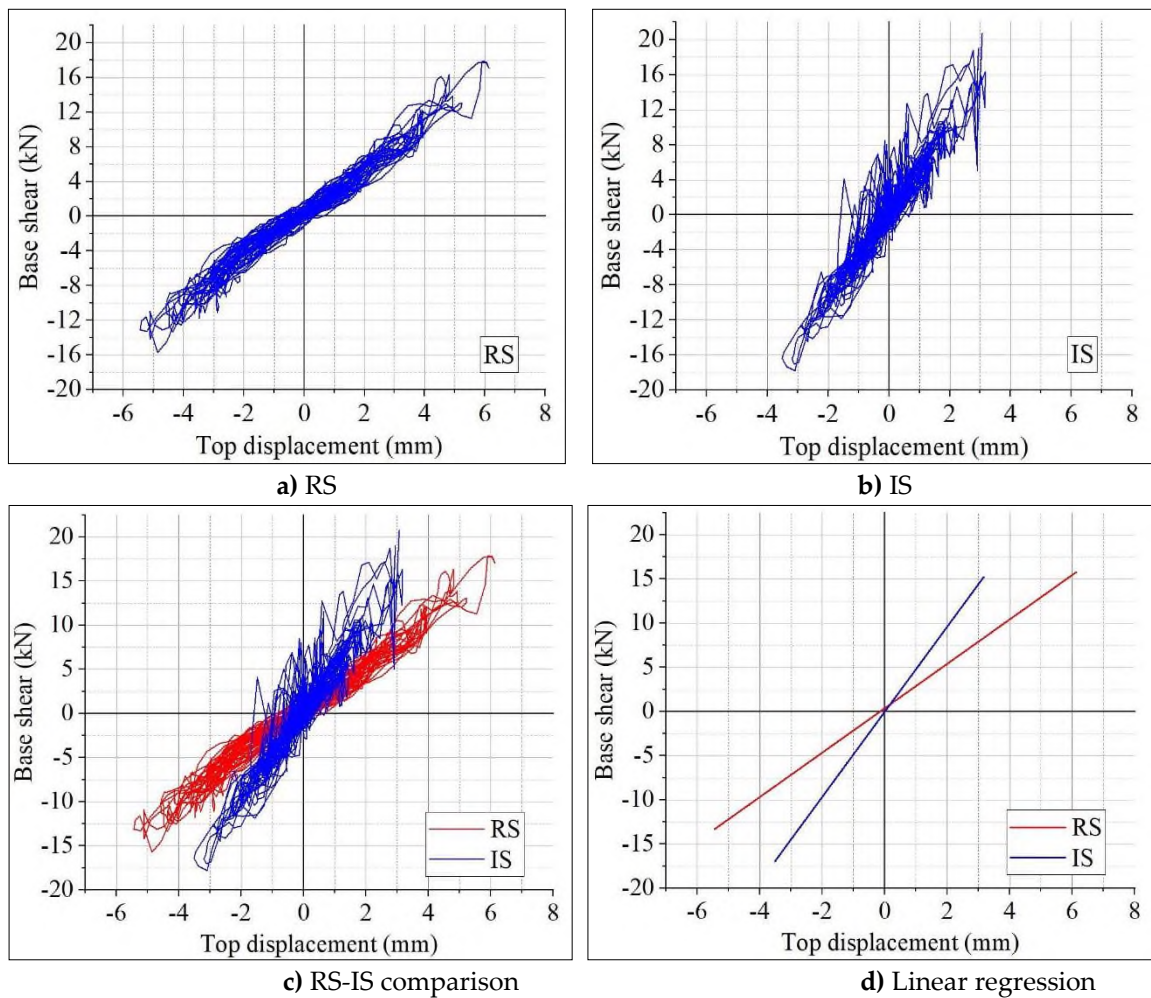


**Figure 21.** Base shear-top displacement hysteresis curves; **a)** RS, **b)** IS, **c)** RS-IS comparison, **d)** Linear regression

#### 4. CONCLUSIONS

In this study, the effect of infill walls on dynamic behavior in RC structures was investigated experimentally and numerically. Shake table tests were performed on a 3D RC frame with 1/3 scale 2 stories and single-span with and without infill walls. Dynamic parameters were determined for these two different states through experimental modal analysis and load-displacement analyses were performed using experimental data. In addition, numerical analysis was performed under the same conditions with the ETABS finite element software.

The results and comparisons obtained as a result of experimental and numerical studies are given below.

1. Infill walls increased the lateral translational stiffness of the frame and in this way, the modal parameters and displacements which are directly related to stiffness were significantly changed. Here, thanks to the stiffness gain, frequency values increased, periods, damping ratios, top displacements decreased, and thus significant contributions were made to the dynamic behavior of the frame.
2. Mode shapes and base shear are not affected much by the addition of infill walls. The fact that the base shear is similar in the cases with and without infill walls indicates that the contribution of the walls to the strength in the elastic region is very limited. If the behavior in the plastic

region is also considered, the expected increase to the strength according to TBEC 2018 [1] is already at most 15%.

3. In the experiments, it was observed that the lateral displacement of the sample decreased significantly in the IS state compared to the RS state due to the effect of infill walls.
4. In the IS state, the 1st natural frequency of the sample increased by 7% (5.57 Hz to 5.93 Hz) and the 2nd natural frequency increased by 5% (18.69 Hz to 19.69 Hz) compared to the RS state.
5. 1st natural periods are 0.180 s and 0.169 s, 2nd natural periods are 0.054 s and 0.051 s for RS and IS states, respectively. There is a 6% difference in the 1st and 2nd natural period values between the states of the sample.
6. According to logarithmic decrement method, in the IS state, the global damping ratio was determined to be 17% less than in the RS state (4.92% to 4.10%). According to this result, it is seen that there is an inverse proportion between stiffness and damping ratio.
7. According to the experimental results, infill walls reduced the top displacement by 43% (6.13 mm to 3.52 mm) and according to the numerical results, by 33% (5.91 mm to 3.97 mm). These values indicate a significant gain in stiffness.
8. There was a great difference in the slopes of the base shear-top displacement hysteresis curves (force/displacement), i.e. lateral translational stiffnesses, between the RS and IS states. Infill walls increased the initial lateral translational stiffness of the sample by 88%.
9. Numerical analysis yielded results that were remarkably close to the experimental results.

Considering these results, it has been determined that infill walls provide a significant increase in the initial lateral translational stiffness, thus limiting the displacement demand to a great extent, increasing the natural frequencies substantially and reducing the damping ratio significantly. Thus, it is obvious that infill walls have a significant effect on the dynamic behavior of RC structures under earthquake effects and their contributions, especially in the elastic region, should not be ignored.

### **Declaration of Ethical Standards**

The authors declare that they followed all ethical guidelines including authorship, citation, data reporting, and publishing original research.

### **Credit Authorship Contribution Statement**

Author 1: conceptualization, methodology, formal analysis and investigation, writing-original draft preparation, writing-review and editing.

Author 2: conceptualization, writing-review and editing, funding acquisition, resources, supervision.

### **Declaration of Competing Interest**

The authors declare that they have no financial conflicts of interest or personal relationships that could have influenced the work presented in this manuscript.

### **Funding / Acknowledgements**

This study is part of the doctoral dissertation of the first author, which was accepted by the KTUN Graduate Education Institute in 2024. The dissertation was funded by the KTUN Coordinatorship of the Instructor Training Programme (2018-ÖYP-42). The authors wish to express their gratitude to the KTUN Coordinatorship of the Instructor Training Programme for their collaboration.

## 5. REFERENCES

- [1] Republic of Türkiye Ministry of Interior Disaster and Emergency Management Presidency, *TBEC 2018 – Turkish Building Earthquake Code 2018*. Ankara, Türkiye, 2018.
- [2] A. S. Aljawadi, M. Vafaei, S. C. Alih, "Seismic strengthening of deficient ground soft-story RC frames with inadequate lap splice using chevron brace," *Structures*, vol. 61, pp. 106029, 2024. <https://doi.org/10.1016/j.istruc.2024.106029>.
- [3] S. Yang, S. Zheng, L. Dong, L. Liu, Y. Xiao, W. Zhao, "Seismic performance of corroded reinforced concrete short columns: Experiment and theoretical analysis," *Structures*, vol. 70, pp. 107665, 2024. <https://doi.org/10.1016/j.istruc.2024.107665>.
- [4] Z. Celep, *Structural dynamics*, 4<sup>th</sup> ed., İstanbul: Beta Printing and Publishing, 2011. (in Turkish)
- [5] X. Zhang, Y. Zhou, X. Liu, C. Wang, Z. Sun, "Study on failure mechanism and seismic performance of RC Frame-Infilled walls structures reinforced by CFRP," *Eng Fail Anal*, vol. 168, pp. 109114, 2025. <https://doi.org/10.1016/j.engfailanal.2024.109114>.
- [6] Y. C. Ou, N. V. B. Nguyen, L. Hoang, "Cyclic behavior and pushover analysis of large scale two-bay, two-story reinforced concrete frames infilled with walls with openings," *Eng Struct*, vol. 317, pp. 118663, 2024. <https://doi.org/10.1016/j.engstruct.2024.118663>.
- [7] W. Jin, C. Zhai, M. Zhang, W. Liu, Y. Wei, L. Xie, "Experimental investigation on the in-plane and out-of-plane interaction of isolated infills in RC frames," *Eng Struct*, vol. 293, pp. 116569, 2023. <https://doi.org/10.1016/j.engstruct.2023.116569>.
- [8] S. Pradhan, Y. Sanada, Y. Rokhyun, H. Choi, K. Jin, "Effects of passive confinement on out-of-plane robustness of unreinforced masonry infill walls," *Structures*, vol. 65, pp. 106676, 2024. <https://doi.org/10.1016/j.istruc.2024.106676>.
- [9] J. Monical, S. Pujol, "A study of the response of reinforced concrete frames with and without masonry infill walls to earthquake motions," *Structures*, vol. 63, pp. 106345, 2024. <https://doi.org/10.1016/j.istruc.2024.106345>.
- [10] J. K. Bhaskar, D. Bhunia, L. Koutas, "In-plane behaviour of masonry infill walls with openings strengthened using textile reinforced mortar," *Structures*, vol. 63, pp. 106439, 2024. <https://doi.org/10.1016/j.istruc.2024.106439>.
- [11] H. Wang, S. Li, C. Zhai, "Experimental and numerical investigation on progressive collapse of self-centering precast concrete frame with infill walls," *J Build Eng*, vol. 78, pp. 107472, 2023. <https://doi.org/10.1016/j.jobe.2023.107472>.
- [12] H. Wang, S. Li, C. Zhai, "Effect of infill walls on progressive collapse behavior of self-centering precast concrete frame," *Structures*, vol. 59, pp. 105729, 2024. <https://doi.org/10.1016/j.istruc.2023.105729>.
- [13] S. Li, H. Wang, H. Liu, S. Shan, C. Zhai, "Experimental study on progressive collapse of self-centering precast concrete frame with infill walls," *Eng Struct*, vol. 294, pp. 116746, 2023. <https://doi.org/10.1016/j.engstruct.2023.116746>.
- [14] N. Ning, Z. J. Ma, P. Zhang, D. Yu, J. Wang, "Influence of masonry infills on seismic response of RC frames under low frequency cyclic load," *Eng Struct*, vol. 183, pp. 70-82, 2019. <https://doi.org/10.1016/j.engstruct.2018.12.083>.
- [15] R. Luo, X. Guo, B. Wang, X. Dong, Q. Zhang, Z. Quyang, "The impact of infill wall distribution on the mechanical behavior and failure patterns of multi-story RC frame structures: An acceleration strain coupled testing approach," *Structures*, vol. 59, pp. 105737, 2024. <https://doi.org/10.1016/j.istruc.2023.105737>.
- [16] Y. Li, Z. Ning, H. L. Shan, C. M. Gao, S. Huang, "Seismic behavior of steel frame infilled with wall-panels connected by sliding joint," *J Constr Steel Res*, vol. 212, pp. 108253, 2024. <https://doi.org/10.1016/j.jcsr.2023.108253>.
- [17] C. Zhang, Z. Yang, T. Yu, W. Huang, X. Deng, Z. Lin, S. Wu, "Experimental and numerical studies of improving cyclic behavior of infilled reinforced concrete frame by prefabricated wall

- panels with sliding joints," *J Build Eng*, vol. 77, pp. 107524, 2023. <https://doi.org/10.1016/j.jobbe.2023.107524>.
- [18] F. S. Balık, F. Bahadır, M. Kamanlı, "Seismic behavior of lap splice reinforced concrete frames with light-steel-framed walls and different anchorage details," *Struct Eng Int*, vol. 33, no. 3, pp. 488-497, 2023. <https://doi.org/10.1080/10168664.2022.2073941>.
- [19] G. B. Nie, Y. J. Shi, C. X. Zheng, Z. Y. Wang, W. Wang, Q. S. Yang, "Shaking table test on progressive collapse of the double-layer cylindrical reticulated shell with infilled wall," *Structures*, vol. 67, pp. 106946, 2024. <https://doi.org/10.1016/j.istruc.2024.106946>.
- [20] V. Nicoletti, L. Tentella, S. Carbonari, F. Gara, "Stiffness contribution and damage index of infills in steel frames considering moderate earthquake-induced damage," *Structures*, vol. 69, pp. 107581, 2024. <https://doi.org/10.1016/j.istruc.2024.107581>.
- [21] Q. Q. Yu, J. Y. Wu, X. L. Gu, L. Wang, "Seismic behavior of hinged steel frames with masonry infill walls," *J Build Eng*, vol. 77, pp. 107536, 2023. <https://doi.org/10.1016/j.jobbe.2023.107536>.
- [22] F. Bahadır, "Experimental study on three-dimensional reinforced concrete frames subjected to dynamic loading," *Structures*, vol. 24, pp. 835-850, 2020. <https://doi.org/10.1016/j.istruc.2020.01.045>.
- [23] S. Yousefianmoghadam, M. Song, A. Stavridis, B. Moaveni, "System identification of a two-story infilled RC building in different damage states," *Improving the Seismic Performance of Existing Buildings and Other Structures*, pp. 607-618, 2015. <https://doi.org/10.1061/9780784479728.050>.
- [24] M. Inel, S. M. Senel, H. Un, "Experimental evaluation of concrete strength in existing buildings," *Magazine of Concrete Research*, vol. 60, pp. 279-289, 2008. <https://doi.org/10.1680/macr.2007.00091>.
- [25] I. Khan, K. Shahzada, T. Bibi, A. Ahmed, H. Ullah, "Seismic performance evaluation of crumb rubber concrete frame structure using shake table test," *Structures*, vol. 30, pp. 41-49, 2021. <https://doi.org/10.1016/j.istruc.2021.01.003>.
- [26] S. Gavridou, J. W. Wallace, T. Nagae, T. Matsumori, K. Tahara, K. Fukuyama, "Shake-table test of a full-scale 4-story precast concrete building. I: Overview and experimental results," *J Struct Eng*, vol. 143, no. 6, pp. 04017034, 2017. [https://doi.org/10.1061/\(ASCE\)ST.1943-541X.0001755](https://doi.org/10.1061/(ASCE)ST.1943-541X.0001755).
- [27] A. G. El-Attar, R. N. White, P. Gergely, "Shake table test of a 1/8 scale three-story lightly reinforced concrete building," National Center for Earthquake Engineering Research, Cornell University, USA, Tech. Report. 1991:NCEER-91-0018.
- [28] *SeismoSignal v4.3.0*. Seismosoft Ltd., 2011.
- [29] *OriginPro*, Northampton, Massachusetts: OriginLab Corporation, 2021.
- [30] Microsoft Office 365, *Microsoft Excel*, Redmond, Washington: Microsoft Corporation.
- [31] *EasyTest Experimental Modal v2.1.5*, Ankara: Teknik Destek Grubu Ltd., 2023.
- [32] *ETABS Ultimate v19.1.0*, Berkeley, California: Computers and Structures Inc., 2021.
- [33] A. K. Chopra, *Dynamics of structures: Theory and applications to earthquake engineering*, 4<sup>th</sup> ed., London: Pearson Education Ltd., 2012.



## COPPER EXTRACTION FROM DEEP EUTECTIC SOLVENT AS ATACAMITE BY HYDROLYSIS METHOD

\* Mehmet Ali TOPÇU 

*Karamanoğlu Mehmetbey University, Engineering Faculty, Metallurgical and Materials Engineering  
Department, Karaman, TÜRKİYE  
[topcumali@kmu.edu.tr](mailto:topcumali@kmu.edu.tr)*

### *Highlights*

- Copper was extracted from deep eutectic solvent with hydrolysis method.
- Atacamite particles with irregular shape was obtained by easy and applicable method.
- Experimental analysis confirmed the crystallinity with and orthorhombic structure.
- Optical analysis revealed a band-gap energy of 2.72 eV for atacamite particles.



## COPPER EXTRACTION FROM DEEP EUTECTIC SOLVENT AS ATACAMITE BY HYDROLYSIS METHOD

\* Mehmet Ali TOPÇU 

*Karamanoğlu Mehmetbey University, Engineering Faculty, Metallurgical and Materials Engineering  
Department, Karaman, TÜRKİYE  
[topcumali@kmu.edu.tr](mailto:topcumali@kmu.edu.tr)*

(Received: 30.12.2024; Accepted in Revised Form: 13.02.2025)

**ABSTRACT:** Deep eutectic solvents (DESs) have garnered as promising alternatives to conventional solvents for metal extraction due to their facile synthesis, high chloride concentration, non-aqueous nature, and low cost. This work explores a green route for ultrafast extraction of atacamite [Cu<sub>2</sub>Cl(OH)<sub>3</sub>] from a deep eutectic solvent at room temperature in a short time using copper (II) sulfate pentahydrate as a precursor. The phase, chemical, morphological, and structural properties of the extracted atacamite were investigated using XRD, Rietveld method, SEM-EDX, and FTIR techniques. As a result of XRD analysis, it was determined that the atacamite with an average diameter of 85.59 µm has an orthorhombic crystal structure. Also, it was determined that the crystal structure parameters obtained from XRD and the theoretical calculations of these values were in good agreement according to the Rietveld refinement. SEM/EDX analysis showed that the extracted atacamite particles exhibited heterogeneity in terms of size and morphology, while elemental composition was found to be homogeneous throughout the particles. UV-Vis analysis and theoretical calculations, the optical band of atacamite particles was found as 2.72 eV. Also, this study demonstrates that the hydrolysis method can serve as an efficient, low-energy pathway for the recovery of metals from DESs, highlighting its potential as a novel approach in copper metallurgy.

**Keywords:** *Deep Eutectic Solvent, Copper Extraction, Atacamite, Rietveld Refinement, Hydrolysis, Characterization*

### 1. INTRODUCTION

Copper extraction predominantly occurs from sulfide ores, with notable examples including chalcopyrite, bornite, covellite, digenite, and chalcocite. Chalcopyrite represents the most abundant copper mineral, comprising approximately 70% of global copper reserves. Pyrometallurgy has historically been the primary method for copper extraction, but this method is economically viable only for high-grade ores and poses significant environmental challenges due to substantial SO<sub>2</sub> emissions. Therefore, hydrometallurgy has emerged as an alternative method for extracting copper from sulfidic copper ores, which is particularly advantageous for processing low-grade copper ores due to its lower operational expenditures [1], [2].

Hydrometallurgy is an aqueous-based metallurgical process utilized for the recovery of metals from ores or industrial residues. The process involves the leaching of metal-bearing materials using suitable aqueous reagents, including acidic, basic, or saline solutions, to extract metal ions into the solution. Subsequently, the metal ions in the solution are recovered in their metallic or compound form through various techniques such as precipitation, ion exchange, cementation, and electrodeposition. Because it consumes less energy and is more environmentally friendly than pyrometallurgical methods, hydrometallurgical methods have gained popularity, they are not without drawbacks. These processes often involve lengthy procedures, lower metal recovery rates, and significant consumption of strong acids. Additionally, wastewater discharge can lead to secondary pollution. The shortcomings of the conventional methods have spurred the development of solvometallurgy as a novel and attractive approach [3], [4].

\*Corresponding Author: Mehmet Ali TOPÇU, [topcumali@kmu.edu.tr](mailto:topcumali@kmu.edu.tr)

Despite the solvent-related differences between solvometallurgy and hydrometallurgy, many of the unit operations show similarities. Solvometallurgy is a process that uses non-aqueous solvents such as ionic liquids, deep eutectic solvents (DESs), liquefied ammonia, concentrated sulfuric acid or, supercritical carbon dioxide to dissolve minerals or wastes at lower temperatures, enabling metal recovery [5], [6]. Over the past few years, in search of green solvents that can replace harmful and volatile organic solvents, researchers have shown great interest in deep eutectic solvents (DESs) which stand out with their low melting point, low vapor pressure, high solubility, non-flammability, negligible toxicity, and easily recyclable properties [7]. DESs are defined as a stable eutectic system formed by mixing two or more components, resulting in a significantly lower eutectic point temperature compared to an ideal liquid mixture. They are generally produced by the formation of strong hydrogen bonds between hydrogen bond donor molecules (HBDs) and hydrogen bond acceptor molecules (HBAs). Charge delocalization from the interaction of HBDs with quaternary ammonium salts triggers the formation of DES, causing a significant decrease in the melting point. The melting point of the eutectic mixture is lower than the melting point of its constituent pure HBDs and HBAs components or an ideal liquid mixture. Various DESs can be synthesized including binary, ternary, and quaternary DESs can be synthesized by combining a large number of HBAs and HBDs components. The first DES synthesized by Abbott et al., was obtained by mixing the components choline chloride as HBA with a melting point of 302 °C and urea as HBD with a melting point of 133 °C in specific proportions. The melting point of this mixture is 12 °C and it forms a stable, transparent liquid at room temperature [8]. DESs are typically represented by the general formula  $\text{Cat}^+\text{X}^-\text{zY}$ , where  $\text{Cat}^+$  denotes an organic cation (e.g., ammonium, sulfonium, or phosphonium);  $\text{X}^-$  is a halide anion acting as Lewis's base,  $\text{Y}$  is Brønsted or Lewis acid, and  $z$  signifies the number of  $\text{Y}$  molecules interacting with the  $\text{X}^-$  anion. For example, choline chloride ( $\text{ChCl}$ ,  $[\text{HOCH}_2\text{CH}_2\text{N}(\text{CH}_3)_3^+\text{Cl}^-]$ ), the most commonly used HBA, forms complexes with HBDs of the following reaction [9], [10].



Due to their unique physicochemical properties, deep eutectic solvents (DESs) have emerged as promising alternatives to conventional solvents for metal recovery and other applications [11], [12]. Thanks to the customizable structures of DESs, special solvers can be designed for different applications. DESs have potential applications in many fields such as metal extraction, extraction of biological molecules, catalysis, electrochemistry, and materials science. In particular, important studies are being carried out in areas such as selective separation and recovery of metal ions, extraction of active ingredients in the pharmaceutical industry, and synthesis of nanomaterials [13], [14].

The increasing demand for metals is driven by technological advancements, and the development of more efficient and greener methods for metal recovery from low-grade ores, industrial waste, and by-products. Thus far, numerous studies have been conducted on the recovery of various metals such as lead, zinc, cobalt, lithium etc., from different sources including ore or metallurgical waste, using solvometallurgical leaching [15], [16]. The applications of DESs to copper recovery have yielded promising results in copper metallurgy. Angarra et al., investigated the electrochemical dissolution and recovery of chalcopyrite mineral in different DESs. A mixed DES, comprising 20 wt%  $\text{ChCl}$ -oxalic acid and 80 wt%  $\text{ChCl}$ -ethylene glycols, yielded the highest selective copper recovery (99%) from chalcopyrite, as reported by researchers [17]. Zhao et. al., investigated the extraction of copper from an end-of-life circuit board using three  $\text{ChCl}$ -based DESs synthesized with ethylene glycol, oxalic acid, and glycol acid. The results indicated that 90.35% Zn, 87.47% Pb, and 16.77% Cu were extracted from the blended metal powder through calcination and leaching with  $\text{ChCl}$ -glycol acid [18]. Topçu et. al., studied copper recovery from copper smelting slag with  $\text{ChCl}$ -urea DES as a green reagent. Experimental findings showed that 80% of copper leaching can be achieved at 48 h, 95 °C, 1/25 g·ml<sup>-1</sup>, and -33 μm [19]. Although studies on copper recovery from various sources have yielded promising results, research on copper extraction from DESs solutions remains limited.

In addition to the extraction of copper from natural sources, synthetic production of copper minerals has been investigated previously. Atacamite, widely utilized in catalysis, pigment and dye production, and the pharmaceutical industry due to its antifungal properties, has been synthesized using various techniques [20]. Xie et al., have synthesized atacamite as precursor for the production of CuO. The synthesis of the atacamite precursor commenced by the dropwise addition of 50 mL of a 0.7 M mixed solution of KOH and  $K_2CO_3$  to 20 mL of a vigorously stirred, hot 3.5 M  $CuCl_2$  solution. The reaction was accompanied by the evolution of gas bubbles and the formation of a bluish-green precipitate. The precipitate was subsequently isolated through successive centrifugation and washing steps, employing distilled water and ethanol as washing solvents. The collected precipitate was then dried overnight at 60 °C in a desiccator. In the subsequent step, 20 mL of a 2 M KOH aqueous solution was added dropwise to a 5 mL suspension containing 0.3 g of the previously synthesized atacamite precursor under continuous stirring. This addition resulted in the formation of a blue precipitate [21]. Zhu et al., prepared atacamite nanoribbons following three step reaction process. Aqueous solutions of  $CuCl_2 \cdot 2H_2O$  and  $(NH_4)_2CO_3$  were prepared at specific concentrations. Subsequently, the  $CuCl_2$  solution was added dropwise to a vigorously stirred solution of  $(NH_4)_2CO_3$ . Upon mixing, an initial white precipitate formed, which subsequently dissolved. As the molar ratio of  $CuCl_2 \cdot 2H_2O$  to  $(NH_4)_2CO_3$  approached 1:2, a characteristic deep blue complex solution was observed. This solution was then aged for 2-7 days, resulting in the formation of a jade-green precipitate of  $Cu_2Cl(OH)_3$ . The precipitate was isolated by centrifugation, washed thoroughly with distilled water and ethanol, and finally dried in an oven at 60 °C for 12 hours [22]. Nascimento et al., investigated the structural and antifungal properties of  $\beta$ -atacamite samples synthesized via a sonochemical driven route. The synthesis of atacamite was initiated by dissolving 1 mmol of copper chloride dihydrate and 2 mmol of sodium chloride in 40 mL of distilled water. Simultaneously, 0.5 mmol of calcium carbonate ( $CaCO_3$ ) was dissolved in a separate container. Subsequently, the solution containing copper and chloride ions was poured into a beaker containing 50 mL of a freshly prepared urea hydrolysis solution. The mixture was sonicated at 2000 W, 20 kHz, with an amplitude of 60%, using a pulse cycle of 5 seconds on and 10 seconds off. The mixture was then added dropwise to the solution containing calcium ions, resulting in the immediate formation of a light green suspension under sonication at room temperature [23].

This study investigated copper extraction from a DES formulated with ChCl and urea, two readily available, cost-effective, and biocompatible components, exhibiting high copper solubility and metal-free composition. After dissolving the copper bearing mineral, hydrolysis method was performed to obtain copper as atacamite particles at room temperature. Also, the chemical, mineralogical, and optical properties of extracted particles were revealed by detailed quantitative analyses.

## 2. MATERIAL AND METHODS

Copper (I) sulfate pentahydrate ( $CuSO_4 \cdot 5H_2O$ , >98%) was used in this work provided from Sigma Aldrich. Deep eutectic solvent was prepared using commercially available choline chloride ChCl,  $C_5H_{14}ClNO$  and urea ( $CO(NH_2)_2$ , >99% purity) supplied by Merck without any prior purification steps. The deionized water used in the hydrolysis experiment was obtained from the MP MINIPure brand water device.

40 mmol ChCl (5584.8 mg ChCl) and 80 mmol urea (4804.8 mg) (stoichiometric molar ratio of 1:2) were mixed in a 50 ml glass bottle. Then, the mixture was subjected to gentle heating to 50 °C using a temperature-controlled hot plate and stirred (250 rpm) continuously until a homogeneous colourless liquid was obtained. The solution was subsequently cooled and placed in a desiccator for further metal extraction experiments. The formation of deep eutectic solvent is illustrated in **Fig.1.a**.

The dissolving process of  $CuSO_4 \cdot 5H_2O$  was carried out in DES solution at 50 °C. 2 g of  $CuSO_4 \cdot 5H_2O$  was added to 25 mL of DES solution and the mixture was stirred until the sample was completely dissolved. Then, the distilled water was added dropwise until the solution became turbid and white particles were produced. After the hydrolysis experiment, solid and liquid parts were separated using a centrifuge. Following separation, the green solid particles were washed with acetone to eliminate



organic contaminants and dried at 50 °C before characterization.

The phase analysis of the precipitated sample was detected with X-ray diffraction analysis (XRD, Bruker Advance D8). Phase identification and quantification were conducted using Panalytical HighScore Plus®, which utilizes the International Centre for Diffraction Data (ICDD) database. A scanning electron microscope (SEM, Hitachi SU5000) with an energy dispersive X-ray module (EDX) was used to monitor the morphological properties and chemical composition of the samples. The structural properties of copper precipitates were detected with fourier transform infrared spectroscopy (FT-IR). FT-IR analysis was carried out using Bruker Vertex 70 ATR-FTIR over the range 4000 – 400  $\text{cm}^{-1}$  with a nominal resolution of 8  $\text{cm}^{-1}$ . The optical properties of atacamite particles were examined by UV-Vis absorption spectroscopy recorded on a Shimadzu UV 2600 UV-Vis spectrometer. The experimental works are illustrated in Fig. 1.b.

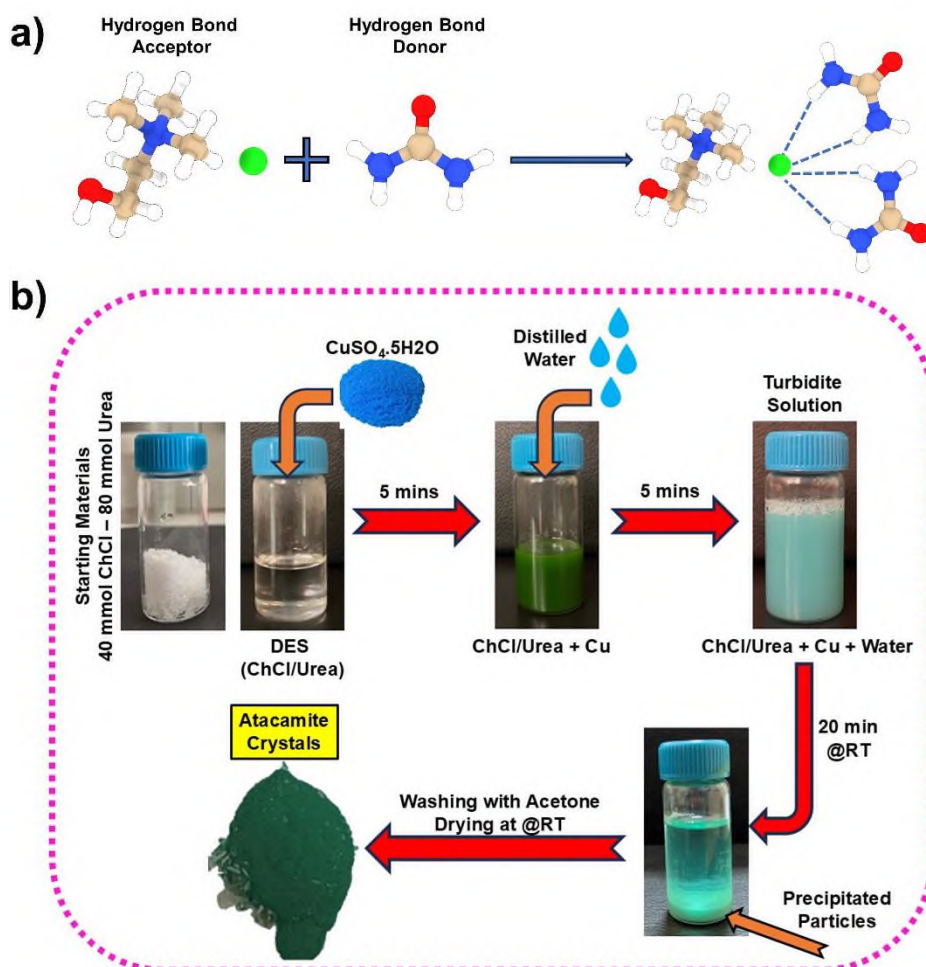


**Figure 1.** a) Formation of deep eutectic solvent and b) flow chart of experimental processes

### 3. RESULTS AND DISCUSSION

Phase properties of extracted particles from DES solution were investigated by X-ray diffraction technique. As seen from the XRD pattern (Fig 2a.), the particles extracted from DES solution at room temperature were  $\text{Cu}_2\text{Cl}(\text{OH})_3$  according to the JCPDS card number 96-900-7719. The position of main diffraction peaks at 16.15°, 16.63°, 32.19°, 39.67°, 50.04°, 52.62°, and 67.86° are indexed with (011), (101), (013), (004), (033), (105), and (026) planes of the orthorhombic crystal structure with space group Pnma 62.

The mechanisms underlying metal dissolution using DESs have been the subjects of recent

investigations. A two-step mechanism is commonly proposed for the dissolution of metal oxides in DES. (i) the dissolution mechanism of metal oxides in DES is considered to initiate with an interaction between the protons of the functional groups within HBD (e.g., carboxyl groups in organic acids, hydroxyl groups in alcohols) and the active hydroxyl sites on the hydrated metal species surface, leading to the formation of intermediate species with protonated oxide, which can be expressed by the following equation [15], [24] :

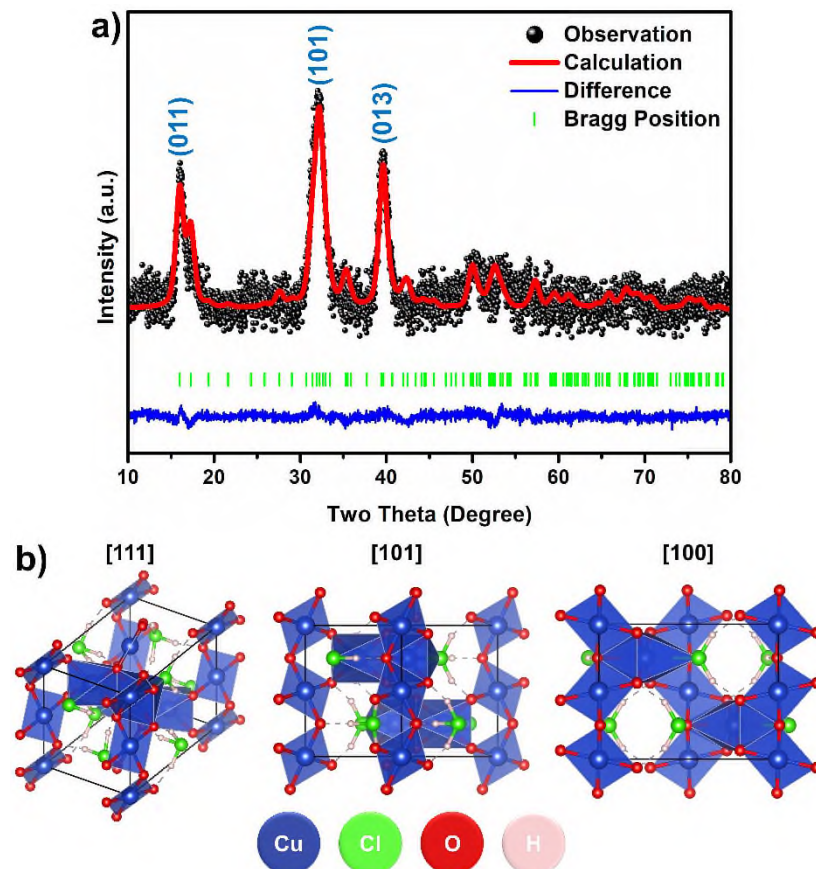
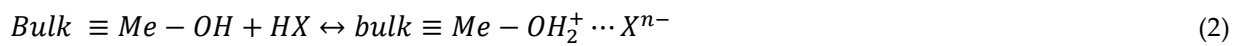
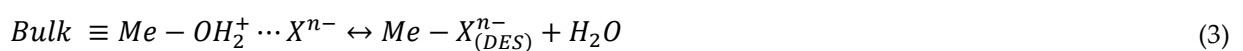


**Figure 2.** a) Rietveld refinement XRD graph and b) illustration of the crystal structure of atacamite

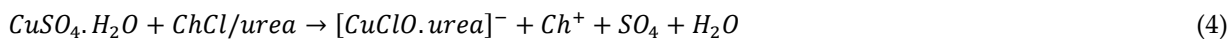
where Bulk  $\equiv$  Me-OH denotes a hydrated metal oxide with active OH sites; HX is the HBDs of DES.

(ii) If the metal-ligand complexes are thermodynamically more stable than the metal-hydroxide complexes, the protons would preferentially interact with the oxide anions, leading to the cleavage of metal oxide bonds. Deprotonated HBD ligands can substitute the active hydroxyl sites of the metal oxide, promoting metal-ligand complexation. Subsequently, anionic species ( $\text{Cl}^-$ ) within the bulk DES may engage in ligand exchange anions reactions.



The dissolution process of metal species involves the availability of protons from HBD in the DES prepared with ChCl and urea. The protons facilitate the dissolution of metal species by weakening the metal-oxygen bonds through the protonation of the oxide anions. Furthermore, the chloride anions supplied by the HBA can significantly contribute to the stabilization of the dissolved metal ions through

the formation of metal-chloro complexes. It has been previously reported that the dissolution of both oxide and sulfide metal species in ChCl-urea DES invariably results in the formation of metal complexes in the final solution. Consequently, it can be inferred that the dissolving of  $\text{CuSO}_4 \cdot 5\text{H}_2\text{O}$  using the ChCl-urea mixture results in the formation of  $[\text{CuClO} \cdot \text{urea}]^-$  complex anions within the solution.



Upon the addition of water to the DES solution, the decomposition of urea in the CuClO/urea complex will hydroxide anions (Eq 5). Subsequently, atacamite particles will form in the presence of high concentration of chloride and hydroxide anions (Eq. 6) [25].



Rietveld refinement analysis was employed to comprehensively determine the crystallographic parameters of the precipitated using Panalytical HighScore Plus software. **Fig. 2.b** also illustrates the outcome of Rietveld refinement, displaying the experimentally observed XRD pattern ( $Y_{\text{obs}}$ ), the calculated diffraction pattern ( $Y_{\text{calc}}$ ), the difference plot between the observed and calculated intensities ( $Y_{\text{obs}} - Y_{\text{calc}}$ ), and the position of Bragg reflections. Theoretical calculations were performed to investigate the crystal structure, which was assigned to the Pnma 62 space group. The Rietveld refinement procedure yielded a set of goodness-of-fit parameters, including the weighted profile factor ( $R_{\text{wp}}$ ), the expected weighted profile factor ( $R_{\text{exp}}$ ), the Bragg R-factor ( $R_{\text{Bragg}}$ ), the crystallographic R-factor ( $R_{\text{cryst}}$ ), the chi-square value ( $\chi^2$ ), and the overall goodness-of-fit index (GoF). These values are presented in **Table 1**.

The  $\chi^2 [(R_{\text{wp}}/R_{\text{exp}})^2]$  and GoF ( $R_{\text{wp}}/R_{\text{exp}}$ ) values were obtained as 0.01326 and 0.1151, respectively, and these parameters show the quality of refinement. The goodness fit parameters  $\chi^2$  and GoF are below 1, indicating the reliability of the refinement method [26], [27]. Also, a comparative analysis of the lattice parameters, as determined by Rietveld refinement, is provided in **Table 1**. A comparison between the lattice parameters derived from Rietveld refinement and XRD patterns with theoretical values reveals an excellent agreement. The crystallographic illustration of the orthorhombic structure belonging to atacamite is presented in **Fig.3(b)**. The unit cell of the orthorhombic crystal system consists of 95 atoms, 120 bonds, and 19 polyhedra. There are two inequivalent  $\text{Cu}^{+2}$  sites in orthorhombic crystallizes structure. In the first  $\text{Cu}^{2+}$  site, the copper cation ( $\text{Cu}^{2+}$ ) is coordinated in a distorted square plane geometry by four oxygen anions and two equivalent chloride anions. The Cu-O bonds display a distinct asymmetry, featuring two shorter bonds of 1.95 Å and two longer bonds of 1.99 Å. In contrast, the two Cu-Cl bonds are of equal length at 2.91 Å. The second  $\text{Cu}^{2+}$  ion occupies a six-coordinate site, being bonded to five oxygen anions and one chloride ion. The Cu-O bonds display a heterogeneity in bond lengths, varying from 2.01 Å to 2.38 Å. The Cu-Cl bond, however, exhibits a more uniform length of 2.88 Å. Besides the copper ion sites, there are two inequivalent  $\text{H}^{+1}$  sites. The primary hydrogen center exhibits a linear coordination geometry, wherein it is coordinated to one oxide ion and one chloride ion. The H-O bond length is determined to be 0.99 Å, and the H-Cl bond length is experimentally determined to be 2.06 Å. The secondary hydrogen cation ( $\text{H}^+$ ) occupies a linear coordination site, bonded to one oxygen anion ( $\text{O}^{2-}$ ) and one chloride anion ( $\text{Cl}^-$ ). The H-O bond length is 1.00 Å, while the H-Cl bond length is 2.05 Å. Two distinct oxygen anion sites are observed. The primary  $\text{O}^{2-}$  site exhibits a distorted coordination geometry, bonded to three  $\text{Cu}^{+2}$  cations and one  $\text{H}^+$  cation. Similarly, the secondary  $\text{O}^{2-}$  site is also distorted, coordinating to three  $\text{Cu}^{+2}$  cations and one  $\text{H}^+$  cation. The chloride anion ( $\text{Cl}^-$ ) adopts a six-coordinate geometry, forming bonds with three  $\text{Cu}^{+2}$  cations and three  $\text{H}^+$  cations.

**Table 1.** Rietveld refinement parameters and lattice constant of atacamite

$R_{wp}$	$R_{exp}$	$R_{Bragg}$	$R_{Cryst}$	$\chi^2$	Gof
9.76	84.76	4.21	3.7	0.01326	0.1151
Lattice Constant		Theoretical	Rietveld	XRD	
a (Å)		6.02797	6.08314	6.05288	
b (Å)		6.86383	6.80939	6.78210	
c (Å)		9.11562	9.01706	9.01193	
Volume (Å) <sup>3</sup>		377.158	373.509	369.950	

The extraction efficiency of the proposed method was determined by comparing the initial mass of the starting material,  $CuSO_4 \cdot 5H_2O$  (2 g), with the final mass of the extracted atacamite (1.334 g). The copper content of the  $CuSO_4 \cdot 5H_2O$ :

$$= \frac{[2 \text{ g } CuSO_4 \cdot 5H_2O] \times [65.546 \text{ g/mol } Cu]}{[294.685 \text{ g/mol } CuSO_4 \cdot 5H_2O]} = 0.445 \text{ g } Cu \quad (7)$$

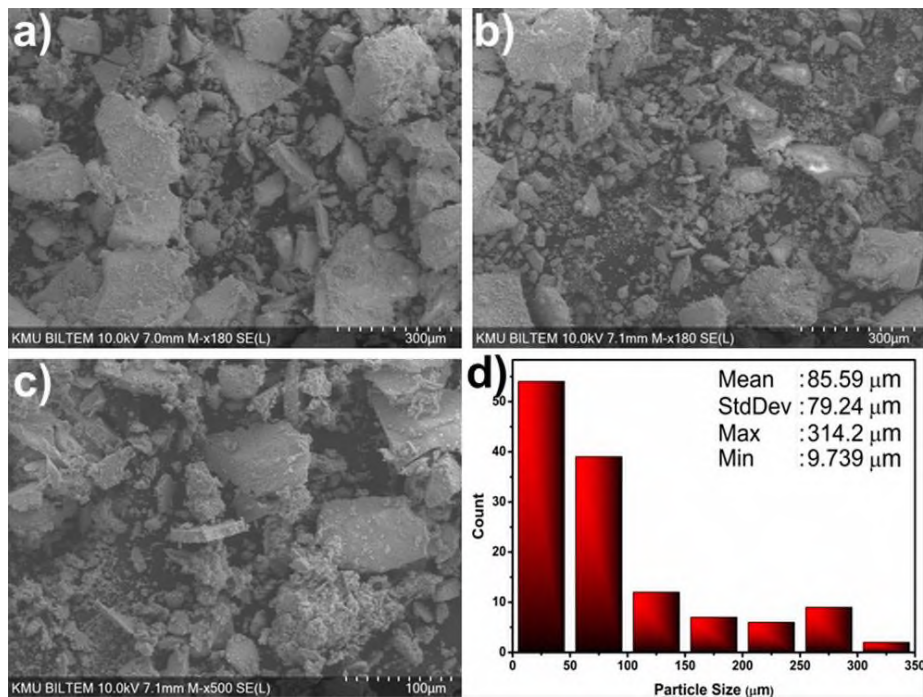
The copper content of the extracted atacamite:

$$= \frac{[0.670 \text{ g } Cu_2Cl(OH)_3] \times [2 \times 65.546 \text{ g/mol } Cu]}{[213.57 \text{ g/mol } Cu_2Cl(OH)_3]} = 0.410 \text{ g } Cu \quad (8)$$

The extraction efficiency of the proposed method:

$$= \left( \frac{0.410 \text{ g } Cu}{0.445 \text{ g } Cu} \right) \times 100 = 92.1\% \quad (9)$$

The morphological properties of the extracted atacamite were analyzed by SEM/EDX as shown in Fig. 3(a-d).

**Figure 3.** (a-c) SEM images and d) particle size distribution of atacamite particles

The atacamite particles extracted from the DES medium exhibited a variety of sizes and morphologies, as observed in SEM images. SEM analysis indicated the presence of particles with diverse

morphologies, encompassing plate-like, spherical, and rod-like structures. According to the particle size analysis, the average size of the atacamite particles was determined to be 85.59  $\mu\text{m}$ . Despite the presence of particles as large as 314.2  $\mu\text{m}$ , particle size analysis revealed that a majority of the atacamite particles obtained from the DES solution were smaller than 50  $\mu\text{m}$  (Fig. 3.d).

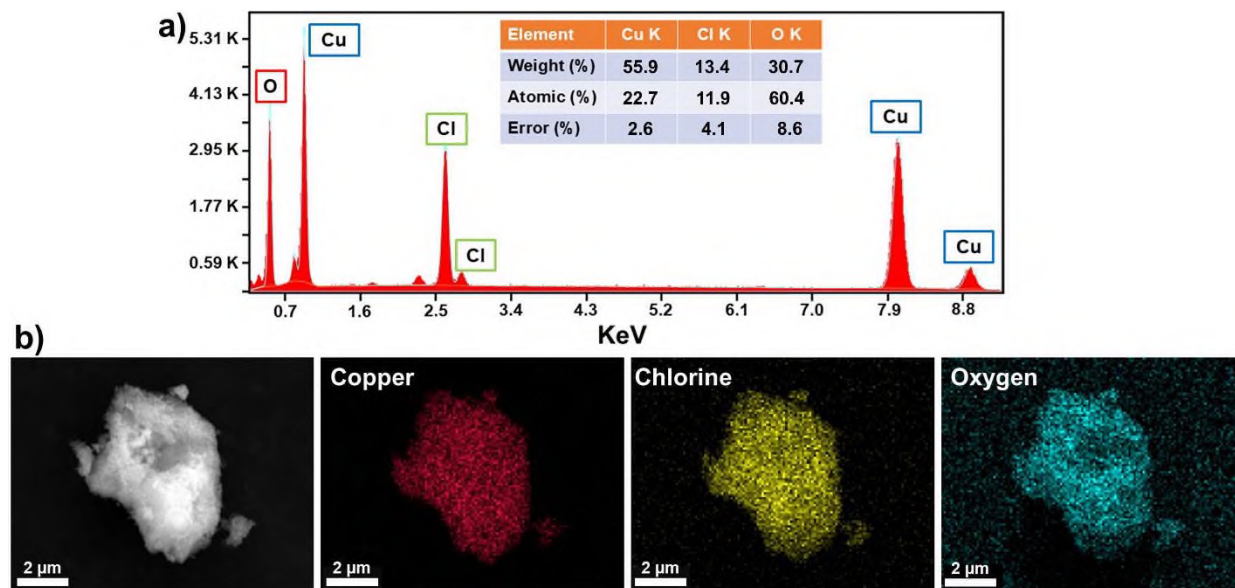


Figure 4. b) EDX analysis and b) elemental mapping of atacamite powders

The chemical composition and elemental mapping results obtained with EDX analysis are shown in Fig. 4(a-b). The EDX spectrum exhibits intense peaks corresponding to copper, chlorine, and oxygen (Fig. 4.a). The elemental composition of atacamite, as determined by EDX analysis, is inconsistent with theoretical values. Stoichiometrically, the atacamite mineral is composed of 59.51% copper, 22.47% oxygen, 16.60% chlorine, and 1.42% hydrogen. In the elemental mapping, copper, chlorine, and oxygen are represented by red, yellow, and blue, respectively. It is apparent from Fig. 4.b that copper, chlorine, and oxygen have been homogeneously distributed throughout the particles.

FTIR spectroscopy was utilized to investigate the chemical composition and bonding characteristics of atacamite particles. Fig. 5. shows the typical FTIR spectra of the extracted atacamite particles. The atacamite particles exhibited high-intensity infrared bands in the region of 3346 – 3324  $\text{cm}^{-1}$ , attributable to hydroxyl stretching vibration groups with different Cu-O distances. The bands observed at 1644 and 1631  $\text{cm}^{-1}$  are attributed to O-H bending vibrations. Additionally, The FTIR spectrum also revealed six distinct infrared bands at 983, 948, 918, 894, and 846  $\text{cm}^{-1}$ , corresponding to vibrational modes influenced by interactions between Cu-O-H and O-H...Cl groups. The intense bands observed below 820  $\text{cm}^{-1}$  are assigned to the Cu-O stretching vibrational modes within the crystal structure [23], [25].

UV-Vis analysis was employed to investigate the optical properties of extracted atacamite particles with the results presented in Fig. 6(a-d). Fig. 6.a demonstrates a gradual increase in reflectivity for atacamite derived from DES solution as the wavelength increases from the ultraviolet to the visible range. The maximum reflectivity was observed in the near-infrared region. The band gap and its nature in atacamite particles were determined using diffuse reflectance spectroscopy data. Initially, the absorption, expressed as the Kubelka-Munk function  $F(R_\infty)$  was calculated using Eq. 10.

$$F(R_\infty) = \frac{(1 - R)^2}{2R} \quad (10)$$

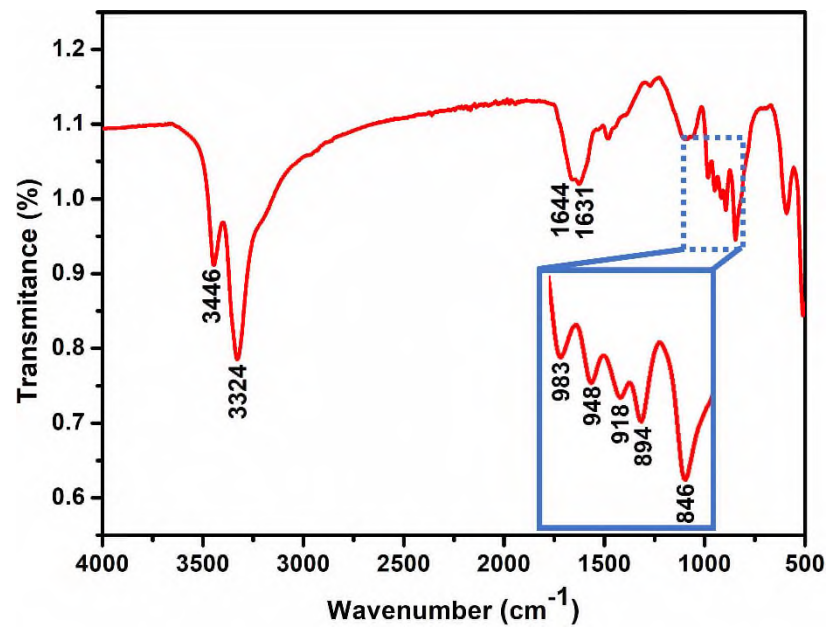


Figure 5. FTIR spectra of atacamite particles

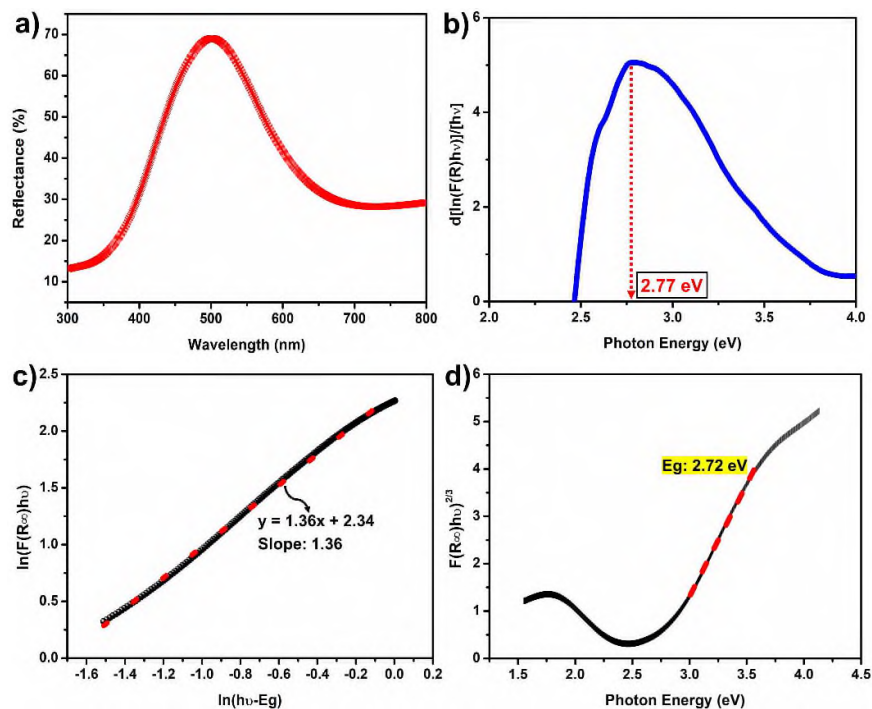


Figure 6. (a) Diffuse reflectance, (b)  $d[\ln(F(R_\infty)hv)]/[hv]$  vs. photon energy graph, (c)  $\ln(F(R_\infty)hv)$  vs.  $\ln(hv-E_g)$  graph, and (d) band-gap energy diagram of atacamite particles

where  $F(R_\infty)$  is the Kubelka-Munk function relates to absorption and  $R$  represents the percent.

According to the  $d[\ln(F(R_\infty)hv)]/[hv]$  vs. photon energy graph (Fig. 6.b), the band gap was estimated to be approximately 2.77 eV based on absorption data. The Tauc's equation (Eq. 11) was employed to determine the  $m$  exponent, obtained from the slope of the  $\ln(F(R_\infty)hv)-\ln(hv-E_g)$  plot (Fig. 6.c), which provides information about the type of electron transitions. The  $m$  value was found to be 1.36 and this

reveals that atacamite particles have forbidden direct transition type.

$$F(R_{\infty})hv = A(hv - EG)^m \quad (11)$$

where  $hv$  represents the photon energy,  $A$  is the material-specific constant,  $Eg$  is the optical band gap and  $m$  is the exponent that characterizes the type of band gap.

Thus, the optical band-gap of atacamite particles was estimated as 2.72 eV by fitting the linear part of the  $(F(R_{\infty})hv)^{2/3}$  vs. the photon energy graph (Fig. 6.d). When the optical properties of atacamite extracted from DES solution were compared to those reported in the literature, a good agreement was found [23], [28].

The experimental results presented herein strongly support the feasibility of employing the proposed methods in copper metallurgy. Given its simplicity, cost-effectiveness, and minimal environmental impact, the hydrolysis method offers a sustainable and energy-efficient approach for recovering copper from DES leach solution resulting in the formation of atacamite. Copper-containing materials exhibit a wide range of properties making them suitable for applications such as photocatalysis, antibacterial coating, and the development of biosensors and electrochemical sensors. The rich chemistry of copper has facilitated its incorporation into a diverse range of natural minerals and biological systems. The tribasic copper chloride mineral family  $[\text{Cu}_2(\text{OH})\text{Cl}]$  has attracted considerable interest owing to its structural diversity and potential applications in various technological domains. Stoichiometric  $\text{Cu}_2(\text{OH})_3\text{Cl}$  exists in multiple polymorphs including atacamite (orthorhombic), botallackite (monoclinic), and clinoatacamite (monoclinic). The unique combination of geometric frustration and unconventional magnetic properties in  $\text{Cu}_2(\text{OH})_3\text{Cl}$  has driven significant interest in this material for fundamental studies [28], [29].  $\text{Cu}_2(\text{OH})_3\text{Cl}$  materials with diverse crystal structures are commonly synthesized via hydrothermal methods involving the use of aqueous solvents and mineralizers under high temperatures and pressure, requiring additional equipment and energy [28], [30]. The proposed hydrolysis method in this study offers a simple, low-cost, and environmentally friendly approach to synthesizing atacamite particles at room temperature, eliminating the need for additional equipment.

#### 4. CONCLUSIONS

Atacamite was successfully recovered from DES solution using a simple, low-cost, and fast route at ambient temperature. XRD analysis confirmed the formation of highly crystalline  $\text{Cu}_2(\text{OH})\text{Cl}$  with an orthorhombic structure (Pnma), demonstrating rapid and efficient synthesis within a short extraction time. SEM images show the presence of particles with an average size of 89.5  $\mu\text{m}$  with irregular morphologies. EDX spectra indicate that the extracted particles contain predominantly copper, chlorine, and oxygen elements. FTIR analysis showed the presence of typical characteristic bands of atacamite. Diffuse reflectance spectroscopy measurements and mathematical calculations determined the optical bandgap of atacamite microparticles to be 2.77 eV. The facile nature of the hydrolysis method positions it as a viable strategy for the solvometallurgical recovery of valuable metals from complex matrices such as DES. Furthermore, this work offers a practical approach to the synthesis of atacamite at room temperature with simple, fast, and environmental compatibility.

#### Declaration of Ethical Standards

The author followed all ethical guidelines, including authorship, citation, data reporting, and publishing original research.

#### Declaration of Competing Interest

The author declares that they have no known competing financial interest or personal relationships

that could have appeared to influence the work reported in this paper.

### Funding / Acknowledgements

The authors declares that there is no financial support.

### Data Availability

No data was used for the research described in the article.

### REFERENCES

- [1] J. Hu, F. Zi, and G. Tian, "Extraction of copper from chalcopyrite with potassium dichromate in 1-ethyl-3-methylimidazolium hydrogen sulfate ionic liquid aqueous solution," *Minerals Engineering*, vol. 172, p. 107179, 2021, doi: <https://doi.org/10.1016/j.mineng.2021.107179>
- [2] G. Ji, Y. Liao, Y. Wu, J. Xi, and Q. Liu, "A review on the research of hydrometallurgical leaching of low-grade complex chalcopyrite," *Journal of Sustainable Metallurgy*, vol. 8, no. 3, pp. 964–977, 2022, doi: <https://doi.org/10.1007/s40831-022-00561-5>
- [3] L. Xiao et al., "An environmentally friendly process to selectively recover silver from copper anode slime," *Journal of Cleaner Production*, vol. 187, pp. 708–716, 2018, doi: <https://doi.org/10.1016/j.jclepro.2018.03.203>
- [4] K. Binnemans and P. T. Jones, "The twelve principles of circular hydrometallurgy," *Journal of Sustainable Metallurgy*, vol. 9, no. 1, pp. 1–25, 2023, doi: <https://doi.org/10.1007/s40831-022-00636-3>
- [5] X. Li, W. Monnens, Z. Li, J. Fransaer, and K. Binnemans, "Solvometallurgical process for extraction of copper from chalcopyrite and other sulfidic ore minerals," *Green Chemistry*, vol. 22, no. 2, pp. 417–426, 2020, doi: <https://doi.org/10.1039/C9GC02983D>
- [6] K. Kurniawan, S. Kim, M. Bae, A. Chagnes, and J. Lee, "Investigation on solvometallurgical processes for extraction of metals from sulfides," *Minerals Engineering*, vol. 218, p. 109005, 2024, doi: <https://doi.org/10.1016/j.mineng.2024.109005>
- [7] K. A. Omar and R. Sadeghi, "Physicochemical properties of deep eutectic solvents: A review," *Journal of Molecular Liquid*, vol. 360, p. 119524, 2022, doi: <https://doi.org/10.1016/j.molliq.2022.119524>
- [8] A. P. Abbott, G. Capper, D. L. Davies, R. K. Rasheed, and V. Tambyrajah, "Novel solvent properties of choline chloride/urea mixtures," *Chemical Communications*, no. 1, pp. 70–71, 2003, doi: <https://doi.org/10.1039/B210714G>
- [9] A. P. Abbott, G. Capper, D. L. Davies, K. J. McKenzie, and S. U. Obi, "Solubility of metal oxides in deep eutectic solvents based on choline chloride," *Journal of Chemical & Engineering Data*, vol. 51, no. 4, pp. 1280–1282, Jul. 2006, doi: <https://doi.org/10.1021/je060038c>
- [10] A. P. Abbott, D. Boothby, G. Capper, D. L. Davies, and R. K. Rasheed, "Deep eutectic solvents formed between choline chloride and carboxylic acids: Versatile alternatives to ionic liquids," *Journal of the American Chemical Society*, vol. 126, no. 29, pp. 9142–9147, Jul. 2004, doi: <https://doi.org/10.1021/ja048266j>
- [11] N. Peeters, K. Binnemans, and S. Riaño, "Solvometallurgical recovery of cobalt from lithium-ion battery cathode materials using deep-eutectic solvents," *Green Chemistry*, vol. 22, no. 13, pp. 4210–4221, 2020, doi: <https://doi.org/10.1039/D0GC00940G>
- [12] Q. Zhang, K. De Oliveira Vigier, S. Royer, and F. Jérôme, "Deep eutectic solvents: syntheses, properties and applications," *Chemical Society Reviews*, vol. 41, no. 21, pp. 7108–7146, 2012, doi: <https://doi.org/10.1039/C2CS35178A>



- [13] B. B. Hansen et al., "Deep eutectic Solvents: A review of fundamentals and applications," *Chemicals Reviews*, vol. 121, no. 3, pp. 1232–1285, Feb. 2021, doi: <https://doi.org/10.1021/acs.chemrev.0c00385>
- [14] T. El Achkar, H. Greige-Gerges, and S. Fourmentin, "Basics and properties of deep eutectic solvents: a review," *Environmental Chemistry Letters*, vol. 19, no. 4, pp. 3397–3408, 2021, doi: <https://doi.org/10.1007/s10311-021-01225-8>
- [15] S. Suffia and D. Dutta, "Applications of deep eutectic solvents in metal recovery from E-wastes in a sustainable way," *Journal of Molecular Liquid*, vol. 394, p. 123738, 2024, doi: <https://doi.org/10.1016/j.molliq.2023.123738>
- [16] M. I. Martín, I. García-Díaz, and F. A. López, "Properties and perspective of using deep eutectic solvents for hydrometallurgy metal recovery," *Minerals Engineering*, vol. 203, p. 108306, 2023, doi: <https://doi.org/10.1016/j.mineng.2023.108306>
- [17] S. Anggara et al., "Direct extraction of copper from copper sulfide minerals using deep eutectic solvents," *Green Chemistry*, vol. 21, no. 23, pp. 6502–6512, 2019, doi: <https://doi.org/10.1039/C9GC03213D>
- [18] Q. Zhao, S. Ma, W. Ho, Y. Wang, J. Y. T. Ho, and K. Shih, "Simple and environmentally friendly metal recovery from waste printed circuit boards by using deep eutectic solvents," *Journal of Cleaner Production*, vol. 421, p. 138508, 2023, doi: <https://doi.org/10.1016/j.jclepro.2023.138508>
- [19] M. A. Topçu, S. A. Çelteç, and A. Rüşen, "Green leaching and predictive model for copper recovery from waste smelting slag with choline chloride-based deep eutectic solvent," *Chinese Journal of Chemical Engineering*, vol. 75, pp. 14–24, 2024, doi: <https://doi.org/10.1016/j.cjche.2024.07.005>
- [20] D. Haro, P. García-Muñoz, M. Mola, F. Fresno, and J. Rodríguez-Chueca, "Atacamite ( $\text{Cu}_2\text{Cl}(\text{OH})_3$ ) as catalyst of different AOPs for water disinfection," *Catalysis Today*, vol. 429, p. 114496, 2024, doi: <https://doi.org/10.1016/j.cattod.2023.114496>
- [21] H. Xie, L. Zhu, W. Zheng, J. Zhang, F. Gao, and Y. Wang, "Microwave-assisted template-free synthesis of butterfly-like  $\text{CuO}$  through  $\text{Cu}_2\text{Cl}(\text{OH})_3$  precursor and the electrochemical sensing property," *Solid State Sciences*, vol. 61, pp. 146–154, 2016, doi: <https://doi.org/10.1016/j.solidstatesciences.2016.09.017>
- [22] C. Zhu, C. Chen, L. Hao, Y. Hu, and Z. Chen, "Template-free synthesis of  $\text{Cu}_2\text{Cl}(\text{OH})_3$  nanoribbons and use as sacrificial template for  $\text{CuO}$  nanoribbon," *Journal of Crystal Growth*, vol. 263, no. 1, pp. 473–479, 2004, doi: <https://doi.org/10.1016/j.jcrysgro.2003.11.003>
- [23] M. V. B. do Nascimento et al., "Sonochemical-driven synthesis of synthetic Atacamite -  $\beta\text{-Cu}_2(\text{OH})_3\text{Cl}$ : Structure, and its antifungal activity," *Nano-Structure and Nano-Objects*, vol. 34, p. 100958, 2023, doi: <https://doi.org/10.1016/j.nanoso.2023.100958>
- [24] Z. Yuan, H. Liu, W. F. Yong, Q. She, and J. Esteban, "Status and advances of deep eutectic solvents for metal separation and recovery," *Green Chemistry*, vol. 24, no. 5, pp. 1895–1929, 2022, doi: <https://doi.org/10.1039/D1GC03851F>
- [25] Z. Jie et al., "Fabrication of octahedral Atacamite microcrystals via a hydrothermal route," *Micro and Nano Letters*, vol. 6, no. 3, pp. 119–121, Mar. 2011, doi: <https://doi.org/10.1049/mnl.2010.0217>
- [26] Z. Liu, Y. Zong, H. Li, D. Jia, and Z. Zhao, "Selectively recovering scandium from high alkali Bayer red mud without impurities of iron, titanium and gallium," *Journal of Rare Earths*, vol. 35, no. 9, pp. 896–905, 2017, doi: [https://doi.org/10.1016/S1002-0721\(17\)60992-X](https://doi.org/10.1016/S1002-0721(17)60992-X)
- [27] C.-Z. Liao, L. Zeng, and K. Shih, "Quantitative X-ray Diffraction (QXRD) analysis for revealing thermal transformations of red mud," *Chemosphere*, vol. 131, pp. 171–177, 2015, doi: <https://doi.org/10.1016/j.chemosphere.2015.03.034>
- [28] X. Liu, L. Xu, Y. Huang, H. Cheng, and H. J. Seo, "Paratacamite phase stability and improved optical properties of  $\text{Cu}_2(\text{OH})_3\text{Cl}$  crystal via Ni-doping," *Materials & Design*, vol. 121, pp. 194–201, 2017, doi: <https://doi.org/10.1016/j.matdes.2017.02.071>

- [29] M. R. Bisengalieva, I. A. Kiseleva, L. V. Melchakova, L. P. Ogorodova, and A. M. Gurevich, "The molar heat capacity of hydrous copper chloride: atacamite  $\text{Cu}_2\text{Cl}(\text{OH})_3$ ," *The Journal of Chemical Thermodynamics*, vol. 29, no. 3, pp. 345–352, 1997, doi: <https://doi.org/10.1006/jcht.1996.0162>
- [30] S. Chu, P. Müller, D. G. Nocera, and Y. S. Lee, "Hydrothermal growth of single crystals of the quantum magnets: Clinoatacamite, paratacamite, and herbertsmithite," *Applied Physics Letters*, vol. 98, no. 9, 2011, doi: <https://doi.org/10.1063/1.3562010>

## URETHANE-MODIFIED ALKYD RESIN BASED PAINT PRODUCTION: DETERMINATION OF PAINT PROPERTIES

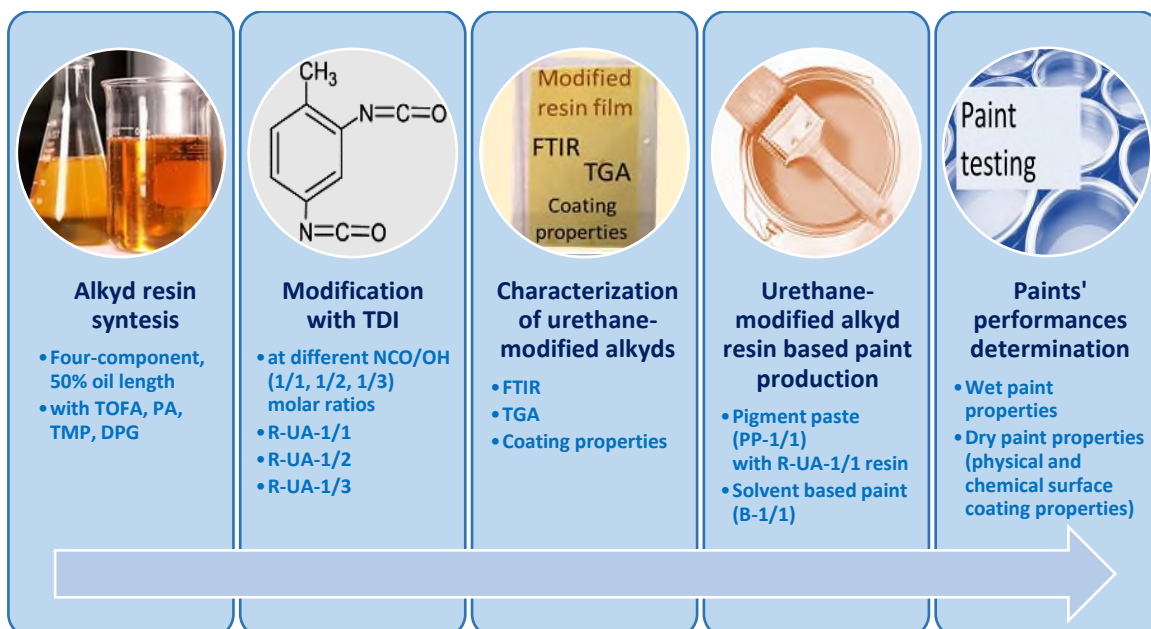
<sup>1,\*</sup> Ferda CİVAN ÇAVUŞOĞLU , <sup>2,\*</sup> Işıl ACAR 

<sup>1</sup> İstanbul Beykent University, Chemical Engineering Department, İstanbul, TÜRKİYE  
<sup>2</sup> İstanbul University-Cerrahpaşa, Chemical Engineering Department, İstanbul, TÜRKİYE  
<sup>1</sup> ferdacavusoglu@beykent.edu.tr, <sup>2</sup> acar@iuc.edu.tr

### Highlights

- Urethane-modified alkyds were prepared at NCO/OH molar ratios of 1/1, 1/2, and 1/3 using TOFA-alkyd with a 50% oil length and TDI.
- Good physical/chemical coating and good thermal properties were observed in modified alkyds.
- A stable paint system was created successfully using the best resin (NCO/OH mole ratio: 1/1) as a binder in solvent-based paint.
- The wet paint properties of urethane-modified alkyd-based paint were quite suitable for production.
- The paint films exhibited high abrasion resistance, superior adhesion strength, excellent environmental resistance, gloss, and high resistance to acid, water, and household chemicals.

### Graphical Abstract



Flowchart of this study

\*Corresponding Authors: The authors have contributed equally to this work.

Ferda CİVAN ÇAVUŞOĞLU and Işıl ACAR, [ferdacavusoglu@beykent.edu.tr](mailto:ferdacavusoglu@beykent.edu.tr), [acar@iuc.edu.tr](mailto:acar@iuc.edu.tr)



## URETHANE-MODIFIED ALKYD RESIN BASED PAINT PRODUCTION: DETERMINATION OF PAINT PROPERTIES

1.\* Ferda CİVAN ÇAVUŞOĞLU , 2.\* Işıl ACAR 

<sup>1</sup> İstanbul Beykent University, Chemical Engineering Department, İstanbul, TÜRKİYE  
<sup>2</sup> İstanbul University-Cerrahpaşa, Chemical Engineering Department, İstanbul, TÜRKİYE  
<sup>1</sup> [ferdacavusoglu@beykent.edu.tr](mailto:ferdacavusoglu@beykent.edu.tr), <sup>2</sup> [acar@iuc.edu.tr](mailto:acar@iuc.edu.tr)

(Received: 16.11.2024; Accepted in Revised Form: 17.02.2025)

**ABSTRACT:** Alkyd resins have an important place among the binders used in the paint industry. One of the major advantages of alkyd resins is that they are susceptible to various modifications to gain the desired properties. In this study, urethane-modified alkyd resins were synthesized at different modification ratios using toluene diisocyanate as a modifier. The resin with the determined optimum modification ratio was used as the binder resin in the paint formulation. In the synthesis of four-component alkyd resin with 50% oil length, phthalic anhydride, tall oil fatty acid, trimethylolpropane, and dipropylene glycol were used. The synthesis of urethane-modified alkyd resins (R-UA-1/1, R-UA-1/2, and R-UA-1/3) was carried out by modification reactions of the prepared alkyd resin with TDI at different NCO/OH (1/1, 1/2, 1/3) molar ratios. Characterization of modified resins was performed by Fourier transform infrared spectroscopy. Subsequently, the optimum NCO/OH ratio was determined due to the physical and chemical surface coating properties and thermogravimetric analysis results of the resin films. The best results were obtained in the resin, where the modification ratio was NCO/OH: 1/1. Then, the urethane-modified alkyd resin (R-UA-1/1) prepared in this ratio was used as a binder in the solvent-based paint formulation. The wet/dry paint properties and household chemical resistance properties of solvent-based paint (B-1/1), prepared using urethane-modified alkyd resin, were examined with tests according to the standards, and the coating performance of this paint was determined in detail. As a result, durable coatings that are suitable for interior applications and can compete with alkyd paints were obtained from the paint prepared with urethane-modified alkyd resin.

**Keywords:** Alkyd, Coating Properties, Modification, Synthetic Paint, Urethane-Modified Alkyd Resin, Wet/Dry Paint Properties

### 1. INTRODUCTION

In recent times, there has been a rapid increase in industrialization and improvements in the global economy, leading to a rise in production and demand in the paint industry. Since coating/paint products provide resources to a wide area, especially the construction and manufacturing industry, the paint sector significantly affects other sectors and is affected by all sectors. The paint sector has a wide range of products that address many areas such as interior, exterior, marine, automobile, furniture, heavy industry, road-marking, and heat-resistant paints. In this context, the performance of the paint should be appropriate for the intended application area, ensuring durability and long life, while also being cost-effective and easy to apply. The most crucial component that offers various properties to the paint according to its usage area and determines its performance is the binder resin, which constitutes the majority of the paint's composition. In paint formulations, mostly alkyd, polyester, polyurethane, epoxy, silicone, acrylic, etc. resins are used as binder resins.

Alkyd resins are products of the condensation reaction of polyacids, polyols, and monofunctional fatty acids or oils. They are suitable for producing coating materials due to their compatibility with most polymers and wide formulation choices. Alkyds are mostly preferred as binders in surface coatings such

\***Corresponding Authors:** The authors have contributed equally to this work.

Ferda CİVAN ÇAVUŞOĞLU and Işıl ACAR, [ferdacavusoglu@beykent.edu.tr](mailto:ferdacavusoglu@beykent.edu.tr), [acar@iuc.edu.tr](mailto:acar@iuc.edu.tr)

as paints and varnishes that form a hard and continuous film [1], [2]. It can be modified with various chemicals to gain the desired properties for use in different areas [3]. Alkyd resin, which is frequently used as a binder in the paint industry, affects not only the physical properties of the paint, such as hardness, flexibility, abrasion, impact resistance, and gloss, but also its chemical properties, such as acid, alkali, water, and solvent resistance [4], [5]. In conclusion, alkyd resins hold a significant position among binders in the paint industry due to superior coating properties, favorable manufacturing conditions, cost-effective raw material prices, high storage stability, and adaptability for various modifications [6], [7], [8].

Urethane-modified alkyd resins (uralkyds), prepared by modifying alkyd resins with toluene diisocyanate (TDI), have advantages such as fast drying, high resistance to chemical factors, compatibility on various surfaces, formation of glossy films on wooden surfaces, and formation of hard/non-flexible films. At the present time, urethane alkyds have a wide range of applications as binders in construction paints and varnishes. Urethane-modified alkyd resins provide better abrasion and hydrolysis resistance than alkyd coatings [3]. There are studies in the literature on the use of various alkyd and modified alkyd resins as binders in paint formulations. Soybean oil-based alkyd resins [7] and acrylic-modified water-reducible alkyd resin [8] obtained from waste PET intermediates, modified alkyd resins based on a new source of dicarboxylic acid [9], indicum seed oil modified alkyd resin [10] were used as a binder in paint formulations.

In this study, urethane-modified alkyd resins were synthesized at various modification ratios using TDI as a modifier. Then, the modified alkyd resin, prepared at the optimum modification ratio, was used as a binder component in the paint formulation. For this, firstly, the surface coating properties of urethane-modified alkyd resins synthesized at various modification ratios were determined, and their thermal behaviors were examined by the TGA method. Then, the wet/dry paint properties and household chemical resistance properties of the solvent-based paint, prepared using the urethane-modified alkyd resin with optimum ratio, were examined with tests in accordance with the standards, and the coating performance of the prepared paint was determined.

## 2. MATERIAL AND METHODS

### 2.1. Materials

TOFA, used in alkyd resin synthesis, was supplied by Arizona Chemicals (USA). TMP and PA were provided by Perstorp (Sweden) and Sigma-Aldrich (USA), respectively. Toluene 2,4 diisocyanate (TDI), used in modification, is a Sigma-Aldrich product. Dispersion and wetting agent (DISPERBYK-108), used for paint systems, is a BYK (Germany) product. Bentone, used as additive, was supplied by Boysan Boya (Turkey). Titanium dioxide (TiO<sub>2</sub>), butylglycol and soy lecithin were purchased by Sigma Aldrich. Pigment (Eisenoxydgelb 920) is a product of Bayer (Germany). Driers (cobalt naphthenate and manganese naphthenate as primary driers, 6% solution, zirconium naphthenate, and calcium naphthenate as auxiliary or secondary driers, 6% solution) were provided by Akpa Kimya (Turkey). Acetone, ethanol, methanol, xylene, toluene, and ethyl acetate, used in reactions and tests, are products of Merck (Germany). All other materials are of analytical or synthesis purity. Distilled water was used in all experimental studies.

### 2.2. Methods

#### 2.2.1. Synthesis and characterization of urethane-modified alkyd resins

Alkyd resin formulation calculations were performed using the K alkyd constant system. Tall oil fatty acid (TOFA), phthalic anhydride (PA), trimethylolpropane (TMP), and dipropylene glycol (DPG) were used in the synthesis of a four-component, 50% oil-content alkyd resin. Afterward, urethane-modified alkyd resins were synthesized by the modification reactions of alkyd resin with TDI at various (NCO/OH: 1/1, 1/2, and 1/3) molar ratios. These modified resins were symbolized as "R-UA-1/1", "R-UA-1/2" and "R-UA-1/3", respectively.

The alkyd synthesis and urethane-modification reactions were carried out in the five-necked glass reactor in a heating mantle. In alkyd synthesis, the glass reactor was equipped with a mechanical stirrer, gas inlet, thermometer, reflux condenser + Dean-Stark part. On the other hand, in modification reactions, the reaction system included a mechanical stirrer, gas inlet, thermometer, and dropping funnel.

The modification reaction temperature was kept constant at around 40°C during the TDI addition. The progress of the reactions and the isocyanate group contents were followed by isocyanate determination (ASTM D 2572) of samples taken from the reactor at certain time intervals [3]. The structural characterizations of the synthesized urethane-modified alkyd resins were performed using Agilent brand Cary 630 model Fourier Transform Infrared Spectroscopy (FTIR).

### 2.2.2. Surface coating tests and thermal analyses of urethane-modified alkyd resins

The optimum NCO/OH ratio of the modified resins was determined according to their physical/chemical surface coating and thermal properties. The NCO/OH ratio in the resin that was best in terms of coating performance and thermal properties was specified as the optimum ratio.

The physical and chemical surface coating properties of the films prepared from modified resins were tested according to the related standards. Details about these tests are presented in the relevant section below.

Thermal properties of the modified resin films were investigated using the Linseis brand STA PT 1750 model Thermogravimetric Analysis (TGA) device. Samples (~10 mg) were prepared from oven-dried films. Measurements were carried out by heating from room temperature to 650°C at a rate of 10°C/min in air atmosphere.

### 2.2.3. Urethane-modified alkyd resin based paint production

Preparation of the solvent-based paint was carried out in two stages using a high-speed laboratory-type disperser (Yökeş brand VBR-12 model, Turkey). In the first stage, urethane-modified alkyd resin diluted to 65% (wt.) solids, pigment, and wetting agent were mixed homogeneously with low-speed mixing to prepare the pigment paste. In the second stage, after adding other paint components and additives to the prepared paint paste, the mixing speed was gradually increased and mixing was realized at the necessary speed (peripheral speed: ~20 m/s) for complete dispersion. Thus, a urethane-modified alkyd resin-based paint system was prepared by ensuring that the pigments were completely wetted by the binder.

### 2.2.4. Surface coating / paint tests applied to resins and paint

The surface coating properties of the synthesized resins and the wet/dry paint properties with the household chemicals resistances of the paint were determined by tests conducted according to standards.

#### 2.2.4.1. Wet Paint Tests

The solids content% (ASTM-D 1259), density (with BYK density-cup, according to ISO 2811), viscosity (with Brookfield DV2T rotary viscometer, according to ASTM-D 2196), flow time (with BYK flow-cups, according to ISO 2431), particle size (with BYK grindometer, according to ASTM-D 1210-05) and hiding power property (with BYK Byko-charts, according to ISO 6504) were tested for determination of wet paint properties of prepared urethane-modified alkyd resin based synthetic paint.

**Solids content:** After weighing the paint in the petri dish, it was placed in the oven at 110°C and kept there until it reached a constant weight. The final weighing was then recorded. The solids content was calculated as a percentage based on the weighing measurements.

**Density:** The density of the paint was determined by filling the tared density-cup and weighing it again. The density was calculated based on the weighing measurements.

**Viscosity:** In a rotary viscometer, to determine dynamic viscosity values, measurement was taken when the torque value reached 50% of the appropriate speed set for the selected spindle, based on the viscosity value at room temperature (20-25°C).

**Flow time:** The time taken for the flow-cup, which was 8 mm in orifice diameter and filled with paint, to empty with a continuous and uninterrupted paint flow at room temperature was determined in seconds.

**Particle size:** 1 mL of paint was dropped onto the deep edge of the grooves on the 100 µm grindometer, and the paint was spread along the grindometer using the applicator. The value corresponding to the point where the homogeneous image disappeared and dots began to appear in the paint film on the grindometer was determined as the particle size of the paint, and results were given in micron (µ) and Hegman (NS).

**Hiding power:** Hiding power cards (BYK, Byko-charts) cut into squares were weighed. The paint was applied with a brush to the card in such a way that the checkerboard pattern substrate was not visible and the card was weighed again. The hiding power value was calculated in g/cm<sup>2</sup> according to the first and final weighing of the cards with known surface area and weight.

#### 2.2.4.2. Dry Paint / Surface Coating Tests

Dry paint / surface coating tests were carried out in two groups, and thus (I) Physical coating properties and (II) Chemical coating properties were determined.

##### (I) Physical coating properties

To determine the physical surface coating properties of resin films (50 µ) and the dry paint properties of the paint film (100 µ), "drying degree" (Erichsen 415/E drying-time tester), "pendulum hardness" (Sheen König pendulum), "adhesion strength" (Erichsen GS 10 cross-cut), "impact resistance" (BYK Gardner PF-1115 impact tester), "abrasion resistance" (Erichsen 2511-11 falling sand tester), and "gloss" (Sheen 101 N gloss meter) measurements were performed based on related standards.

**Drying degree (DIN 53150):** In this standard, the drying degree is performed according to the "Modified Bandow Wolf method". In this method, 7 drying degrees are defined between 1-7. The 1<sup>st</sup> drying degree is determined by whether the 0.2 mm diameter glass beads poured on the film adhered to the surface after 10 s. On the other hand, drying degrees between 2 and 6 are determined by whether the Kraft paper adhered to the film surface after applying 5, 50, 500 and 5000 g/cm<sup>2</sup> pressure for 60 s. In addition, the dry-to-touch stage (the paint does not stick to the finger when touched) of these films was also determined according to the ASTM D 1640 standard.

**Pendulum hardness (DIN 53157):** For the measurement, the film-coated glass plate is placed on the König pendulum. Then, the damping time of the pendulum oscillating in the specified amplitude (from 6° to 3°) is determined. The results are given in "König seconds".

**Adhesion strength (ASTM D 3359-76):** The film on the glass plate is cut at right angles with a cross-cut cutter to create a lattice pattern (6 x 6 = 36), and this pattern is swept with a brush. The appearance of the lattice pattern is compared with the standard, which is classified according to the amount of squares remaining intact. The results are given in "% adhesion".

**Impact resistance (ASTM D 2794-69):** The test is based on the principle of observing the deformation on the film surface as a result of dropping a standard cylindrical steel weight through a guide tube onto a film-coated metal plate. The results are determined as "kg x cm" according to the standard weight used and the height of the drop.

**Abrasion resistance (ASTM D 968-05):** First, a film-coated glass plate is placed at a 45° angle in the device. The hard sand that passes through sieve no. 25 and remains in sieve no. 30 is allowed to pour freely onto the film surface via a vertical tube due to the gravity effect. The test continues until the volume of sand required to create a ~4 mm diameter erode gap on the film surface is reached. The results are reported as "mL sand".

**Gloss (ASTM D 523):** This test method is based on the principle of measuring the specular reflectance of light on the surface of the film-covered glass plate and comparing it with that of black glass. The results are expressed as "gloss unit (GU)".

### (II) Chemical coating properties

To determine the chemical surface coating properties of the resin films (50  $\mu$ ), water, acid, salt, alkali, solvent and environmental resistance tests, and for the chemical dry paint properties of the paint films (100  $\mu$ ), household chemicals, solvent, and environmental resistance measurements were performed according to relevant standards/literature.

**Water, acid, salt and alkali resistance (ASTM D 1647-89):** The film-coated tin plate, prepared by casting method, was immersed in a beaker filled with distilled water at room temperature, and kept for 18 h. After 18 h, the plate was examined after being wiped dry, and 20 min, 1 h and 2 h later.

The film, prepared on the glass plate by the film applicator, was immersed in a beaker containing 3% (wt.) sulfuric acid ( $H_2SO_4$ ), and the changes on the film surface were examined for 72 h.

The film prepared on the glass plate by the film applicator, was immersed in a beaker containing 5% (wt.) sodium chloride (NaCl), and the changes on the film surface were examined for 72 h.

The alkali resistance test was carried out using the films which prepared by immersion method on glass tubes. The films were immersed in beakers containing dilute sodium hydroxide (0.1 M NaOH) solution, and the changes on the surfaces of the films were examined for 72 h. Then, this test was repeated by immersing the films, which were resistant to dilute solution, in beakers containing concentrated NaOH solution (3% wt.)

**Solvent resistance [11]:** 1x1 cm gauze pieces impregnated with methanol, toluene, ethyl acetate, and acetone were placed on the film surface of glass plate after removing excess solvent with filter paper and covered with Petri dishes. After 30 minutes, the Petri dishes were removed, and changes on the film surfaces were observed.

**Environmental resistance [11]:** First, the film prepared on the glass plate was kept in a beaker containing distilled water at room temperature for 18 h, then in a deep freezer at  $-20\pm 2^\circ C$  for 3 h, and then in an oven at  $50\pm 2^\circ C$  for 3 h. At the end of all these stages, 1 cycle was completed, and the film was examined visually at the end of each cycle.

**Household chemical resistance (ASTM-D 1308-02):** In this tests applied to the dry paint film, 3%  $H_2SO_4$  (wt.), 0.1 M NaOH, 3% NaOH (wt.), cold water ( $25^\circ C$ ), hot water ( $80^\circ C$ ), 8 g/L soft soap solution and 1 g/L dishwashing detergent solution were used to determine acid, alkali, distilled water, soap, and detergent resistances of the paint by the immersion method. According to the immersion method, paint-coated metal plates (or glass plates for distilled water resistance) were immersed in beakers containing the test solution at room conditions. Changes on the film surface were observed for 72 h.

Alcohol, vinegar, and beverage resistances were determined by spot test using 50% ethyl alcohol (v/v), 3% acetic acid by weight, 1 tea bag brewed for 5 min/100 mL distilled water, 2.5 g coffee/100 mL distilled water, and cola. According to the spot test method, 1 mL of test solution was dropped on the paint-coated metal plate and covered with a watch glass. Drops were wiped at certain intervals, and changes on the surface of the paint were observed.

## 3. RESULTS AND DISCUSSION

### 3.1. FTIR Analysis of Urethane-Modified Alkyd Resins

FTIR spectra of urethane-modified alkyd resins (R-UA-1/1, R-UA-1/2, R-UA-1/3) synthesized at different NCO/OH modification ratios are presented in Figure 1. As given in the literature, the FTIR spectrum of TDI has a sharp absorption peak at  $2250\text{ cm}^{-1}$  belonging to the stretching vibration of the isocyanate ( $-N=C=O$ ) group [3], [12], [13], [14]. When the spectra of urethane-modified alkyd resins in Figure 1 were examined, it was seen that this sharp peak belonging to the  $-N=C=O$  group of TDI was not observed in the resin spectra. This situation confirms that the  $-NCO$  groups of TDI and the free  $-OH$  groups [15], [16], [17] of the alkyd resin have completely reacted. In addition, the presence of characteristic peaks



belonging to the urethane structure observed in the FTIR spectra of all modified resins (-NH stretching peak at  $3355\text{ cm}^{-1}$  belonging to urethane bonds [14], [18], stretching vibration in  $2850\text{-}3000\text{ cm}^{-1}$  region of the aliphatic C-H bond [15], [16], [17], [19], [20], the vibration of the carbonyl (-C=O) group at  $1730\text{ cm}^{-1}$  belonging to the urethane bond [15], [16], [17], [18], [19], [20], -NH deformation peak at  $1534\text{ cm}^{-1}$  [16], [17], -NH bending vibration at  $1599\text{ cm}^{-1}$  [18], -CN stretching vibration in  $1386\text{-}1278\text{ cm}^{-1}$  [20] region attributed to the amide II band) indicates the formation of urethane alkyd structure.

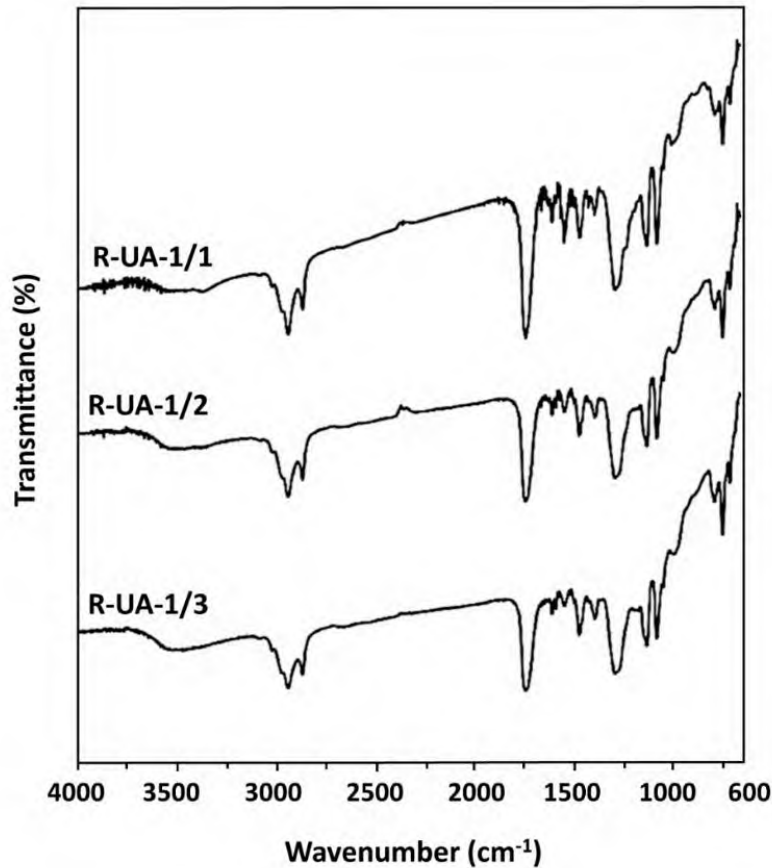


Figure 1. FTIR spectra of urethane-modified alkyd resins.

### 3.2. Surface Coating Properties of Urethane-Modified Alkyd Resins

Before physical and chemical surface coating tests for resins, driers were added to the diluted resin in proportion to 1% Zn and 0.1% Co by weight based on the amount of urethane-modified alkyd resin. Then, the resin films were prepared using the BYK film applicator ( $50\ \mu$ ) for tests.

#### 3.2.1. Physical surface coating properties

First of all, the drying degrees of the modified resin films were monitored in the air. By the end of 72 h, the films reached the 4<sup>th</sup>, 5<sup>th</sup>, and 6<sup>th</sup> drying degrees. Prior to testing their physical and chemical surface coating properties, the films were oven-cured at  $110^{\circ}\text{C}$  for 2 h. This process resulted in all films achieving the 7<sup>th</sup> drying degree, indicating that they were fully dried throughout their thickness according to the standard.

The physical surface coating test results of urethane-modified alkyd resin films, which were determined after oven-curing at  $110^{\circ}\text{C}$  for 2 h, are presented in Table 1.

**Table 1.** Physical surface coating properties of urethane-modified alkyd resin films.

Physical Coating Tests	Urethane-Modified Alkyd Resins		
	R-UA-1/1	R-UA-1/2	R-UA-1/3
Drying degree (in the air for 72 h)	6	5	4
Drying degree (at 110°C for 2 h)	7	7	7
Hardness (König second)	179	128	109
Adhesion strength (%)	100	100	100
Impact resistance (kg x cm)	200	100	75
Abrasion resistance (mL sand)	6000	5000	4000
Gloss (GU)	116	121	119

As seen in Table 1, hard and glossy films with excellent adhesion strength were obtained from the synthesized urethane-modified alkyd resins. Moreover, it is observed that hardness, abrasion, and impact resistance values increase with increasing NCO/OH ratio. Among the urethane-modified alkyd resins with different NCO/OH molar ratios, the best physical surface coating properties were observed in the resin with 1/1 NCO/OH ratio (R-UA-1/1) with hardness of 179 König seconds, abrasion resistance of 6000 mL sand, impact resistance of 200 kg x cm, and adhesion strength of 100%.

### 3.2.2. Chemical surface coating properties

The chemical surface coating test results of urethane-modified alkyd resin films, which were determined after oven-curing at 110°C for 2 h, are presented in Table 2.

As seen in Table 2, urethane-modified alkyd resin films have excellent acid, salt, water, solvent, and environmental resistance. However, the alkali resistances of these films varied according to the modification ratio (NCO/OH ratio). For example, R-UA-1/1 resin film was resistant to dilute alkali solution (0.1 M NaOH) for 72 h whereas R-UA-1/2 and R-UA-1/3 resin films were able to resist 6 and 3 h, respectively. For the R-UA-1/1 resin film, that was resistant to 0.1 M NaOH solution, the alkali resistance test was repeated with a concentrated alkali solution (3 wt.% NaOH). R-UA-1/1 resin film started to be affected by 3% NaOH solution after 24 h, and it was completely separated from the surface after 72 h. As can be seen from these results, the alkali resistance of alkyd resins known to have poor alkali resistance [21] was slightly increased with urethane modification. Especially, the alkali resistance of urethane-modified alkyd resin with an NCO/OH ratio of 1/1 is good according to the literature and can be improved further.

According to the physical and chemical surface coating test results of the resin films modified at different ratios, it was observed that the R-UA-1/1 resin with an NCO/OH molar ratio of 1/1 had the best coating performance.

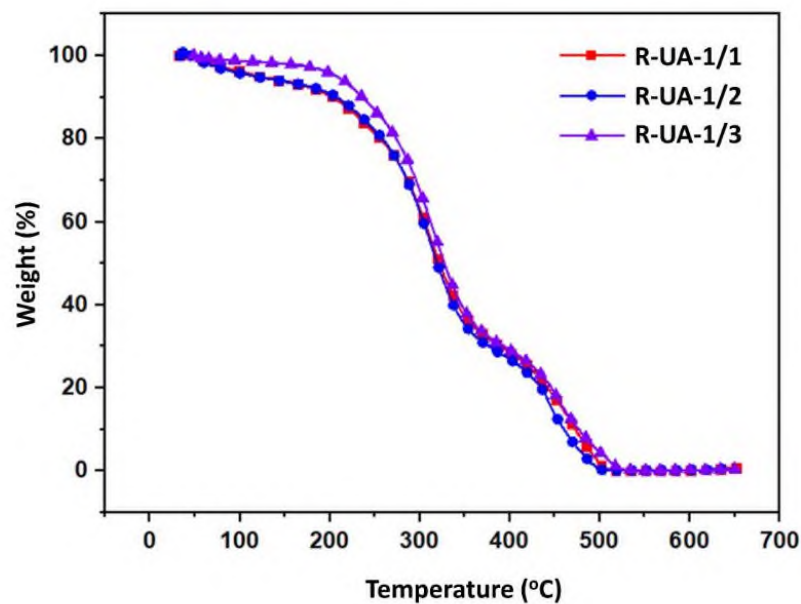
### 3.3. Thermal Properties of Urethane-Modified Alkyd Resins

Thermogravimetric analyses were performed to determine the thermal properties of the urethane-modified alkyd resin films. The TGA curves obtained from the thermal analyses are presented comparatively in Figure 2.

As seen in Figure 2, the urethane-modified alkyd resins showed similar thermal behavior profiles. The final thermal oxidative decomposition temperatures of R-UA-1/1, R-UA-1/2, and R-UA-1/3 resins were found to be 506°C, 499°C, and 518°C, respectively, indicating their high thermal resistance. According to the thermal analysis and all other surface coating test results, optimum results were obtained in the resin where the modification ratio was NCO/OH: 1/1. The urethane-modified alkyd resin (R-UA-1/1) prepared in this ratio was used as a binder in the solvent-based paint formulation.

**Table 2.** Chemical surface coating properties of urethane-modified alkyd resin films.

Chemical Coating Tests	Urethane-Modified Alkyd Resins		
	R-UA-1/1	R-UA-1/2	R-UA-1/3
Alkali resistance 0.1 M NaOH	24 h No change on the film surface (slight yellowing in solution)	1.5 h The film surface began to be affected	1 h The film surface began to be affected
	72 h No change on the film surface (slight yellowing in solution)	6 h The film completely separated from the substrate	3 h The film completely separated from the substrate
Alkali resistance 3% NaOH	24 h The film surface began to be affected	-	-
	72 h The film completely separated from the substrate	-	-
Acid resistance 3% H <sub>2</sub> SO <sub>4</sub>	72 h No change	72 h No change	72 h No change
Salt resistance 5% NaCl	72 h No change	72 h No change	72 h No change
Water resistance Distilled water	18 + 2 h No change	18 + 2 h No change	18 + 2 h No change
Solvent resistance methanol, toluene, ethyl acetate, acetone	30 min No change	30 min No change	30 min No change
Environmental resistance wet-dry-heat cycle	10 cycles No change	10 cycles No change	10 cycles No change

**Figure 2.** TGA curves of urethane-modified alkyd resin films.

### 3.4. Urethane-Modified Alkyd Resin Based Paint Production

To prepare the B-1/1 paint, a process was carried out in two stages using the urethane-modified alkyd resin (R-UA-1/1) with an NCO/OH:1/1 as a binder. The pigment paste was combined with other paint components and additives to create a stable dispersion system. The composition of the pigment paste (PP-1/1), and the formulation of the solvent-based urethane-modified alkyd paint (B-1/1), prepared with R-UA-1/1 resin diluted to 65% solids with xylene, are presented in Table 3 and Table 4, respectively.

**Table 3.** The composition of the pigment paste (PP-1/1).

Component	Ratio (wt.%)
Binder, R-UA-1/1 resin (65% in xylene)	71.29
White pigment/filler, TiO <sub>2</sub>	14.26
Colored pigment (Bayer, iron oxide yellow)	14.26
Additive, bentone (rheological agent, anti-slump and anti-slip additive)	0.18
Dispersion and wetting agent (DISPERBYK-108)	0.02

**Table 4.** The formulation of the solvent-based urethane-modified alkyd paint (B-1/1).

Component	Ratio (wt.%)
Pigment paste (PP-1/1)	18.68
Binder, R-UA-1/1 resin (65% in xylene)	78.60
Additive, butyl alcohol (brushability and flow improving agent)	1.87
Additive, soy lecithin (wetting and dispersing agent additive)	0.40
Additive, bentone (rheological agent, anti-slump and anti-slip additive)	0.23
Dispersion and wetting agent (DISPERBYK-108)	0.23

The preparation of B-1/1 paint occurred in two stages. In the first stage, a pigment paste (PP-1/1) was prepared. For this, the components listed in Table 3 were loaded into the mixing chamber of the high-speed laboratory-type disperser. This composition was mixed at a peripheral speed of 12-14 m/s, and homogenization was achieved. In the second stage, the other paint components and additives in Table 4 were added to the prepared PP-1/1 pigment paste. The mixing speed was gradually increased, and finally, the system was continuously mixed at a peripheral speed of 20 m/s, which was sufficient for complete dispersion. At the end of this process, which lasted for a total of 70 min, a urethane-modified alkyd resin-based paint system (B-1/1) was successfully prepared. After preparation of the paint, it was diluted to 75% solids content using xylene.

### 3.5. Wet Paint and Dry Paint Properties of Urethane-Modified Alkyd Resin Based Paint

The properties of urethane-modified alkyd resin-based paint were determined by “wet paint tests”, “dry paint tests (physical coating tests)”, and “household chemical resistance tests (chemical coating tests)”.

#### 3.5.1. Wet paint properties

Wet paint test results applied to B-1/1 paint under room conditions are presented in Table 5.

**Table 5.** Wet paint test results of B-1/1 paint.

Wet paint tests	Results
Solids content	75% (wt.)
Flow time (with DIN Cup, 8 mm/21°C)	42 seconds
Dynamic viscosity (with Brookfield DV2T rotary viscometer)	33270 cP
Density (with BYK density-cup)	1.07 g/cm <sup>3</sup>
Hiding power (with BYK Byko-chart)	0.0269 g/cm <sup>2</sup>
Particle size (with 100 $\mu$ BYK grindometer)	7.5 Hegman / 6.5 $\mu$

As the viscosity value of paints increases, the flow time also increases. The dynamic viscosity of the prepared urethane-modified alkyd resin-based paint was found to be 33270 cP, and the flow time was 42 seconds. The density, hiding power, and particle size values of the paint are in the suitable range for paint applications [8, 22].

### 3.5.2. Dry paint properties

Before dry paint tests of B-1/1 paint, a mixture of driers was added to the diluted paint formulation at a ratio of 1.12% (0.28% Co + 0.14% Mn + 0.42% Zr + 0.28% Ca) by weight of the total formulation [22] and mixed in the disperser at 20 m/s peripheral speed for 10 min. Then, 100  $\mu$  paint films were prepared with the BYK applicator.

Primarily, the drying degrees of the solvent-based paint film were determined in the air, and the results are presented in Table 6. The physical dry paint properties of the paint film oven-cured at 110°C for 2 h are presented in Table 7. In addition, the solvent and environmental resistance test results are also presented in Table 8.

**Table 6.** Drying degree test results of B-1/1 paint in the air.

Time	Drying degree
1.5 h	Dry to touch
3 h	1 <sup>st</sup> stage
4 h	2 <sup>nd</sup> stage
7 h	3 <sup>rd</sup> stage
24 h	4 <sup>th</sup> stage
48 h	5 <sup>th</sup> stage
72 h	5 <sup>th</sup> stage

At the end of the drying time test applied to the 100  $\mu$  paint film, it was observed that the paint film reached the 4<sup>th</sup> stage after 24 h, and the 5<sup>th</sup> stage after 72 h. The paint film, which reached the dry-to-touch stage in 1.5 h in the air under room conditions, achieved the highest drying degree (7<sup>th</sup> stage) after 2 h of oven-cured at 110°C after remaining in these conditions for 72 h. All other physical and chemical surface coating tests were applied to oven-cured films.

**Table 7.** Physical dry paint test results of B-1/1 paint.

Dry Paint Tests	Results
Drying degree (Modified Bandow Wolf test method)	7 <sup>th</sup> stage
Abrasion resistance (Falling sand test method)	18000 mL sand
Adhesion strength (Cross-cut test method)	%100
Impact resistance (Falling weight test method)	50 kg x cm
Pendulum hardness (König Pendulum method)	66 König seconds
Gloss (specular reflection at 60° angle)	84 GU

When Table 7 is examined, it is seen that a film with excellent adhesion and high abrasion resistance was obtained from urethane-modified alkyd resin-based synthetic paint. The pendulum hardness of the B-1/1 paint was found to be 66 König seconds. For the König pendulum, the period of oscillation (damping time) of the standard glass plate is 250 König seconds [23]. This indicates that the paint film was relatively soft. Impact resistance was also slightly lower in proportion to hardness. In the standards, 70-85 GU values in gloss measurements at 60° correspond to gloss coatings (6<sup>th</sup> gloss level) [24]. Accordingly, a glossy film with a value of 84 GU was obtained from B-1/1 paint.

**Table 8.** Solvent and environmental resistance test results of B-1/1 paint.

<b>Solvent resistance</b>	<b>Time</b>	<b>Results</b>
Acetone	30 min.	No change
Ethyl Acetate	30 min.	Slight swelling on the film surface
Methanol	30 min.	Slight swelling on the film surface
Toluene	30 min.	Swelling on the film surface
<b>Environmental resistance</b>	10 cycle	No change

As seen in Table 8, when toluene, an aromatic and non-polar solvent known as an effective solvent due to the reactivity of its methyl group, was applied, swelling occurred on the film surface. In contrast, when ethyl acetate, a moderately polar aliphatic solvent, and methanol, an aliphatic and polar solvent having a methyl group, were used, only slight swelling was noted on the film surface. Whereas, the paint film showed no signs of damage when exposed to acetone, which is also an aliphatic and polar solvent. In the environmental resistance test (Table 8), which was performed as an accelerated simulation of periodical/circular ambient conditions in nature, it was observed that the paint film was not affected in any way after 10 cycles (1 cycle: 18 h in distilled water at room temperature + 3 h in the refrigerator at -16°C + 3 h in the oven at 50°C). The paint film has excellent environmental resistance.

Within the scope of household chemical resistance tests, the alkali resistance (0.1 M NaOH and 3% NaOH) test results applied by the immersion method are presented in Table 9. The results of the resistance tests against to acid (3% H<sub>2</sub>SO<sub>4</sub>), hot distilled water (80°C), cold distilled water (room conditions, 25°C), soap, and detergent applied by the immersion method are also presented in Table 10.

**Table 9.** Alkali resistance test results of B-1/1 paint.

<b>Time</b>	<b>Dilute alkali solution</b>	<b>Concentrated alkali solution</b>
	<b>0.1 M NaOH</b>	<b>3% NaOH</b>
1 h	No change	Surface roughness
3 h	No change	Slight wrinkle
4 h	No change	Partial separation from the substrate
6 h	Surface roughness	Partial separation from the substrate
24 h	Partial separation from the substrate	Complete separation from the substrate
48 h	Complete separation from the substrate	-

As seen in Table 9, the B-1/1 paint film started to be affected by the dilute alkali solution after 6 h, and the film was completely removed from the substrate after 48 h. In the concentrated alkali solution, the film began to be affected by the alkali after 1 h. After 4 h, the film was partially separated from the substrate, and after 24 h, the film was completely dissolved and separated from the substrate.

Urethane-modified alkyd resin-based paint films showed sensitivity to alkali solution due to the hydrolysable ester bonds in their structure [15]. However, the ability of the paint film to withstand dilute alkali solution for 48 h and concentrated alkali solution for 24 h shows that this property is relatively acceptable according to the literature, and it can be improved.

**Table 10.** The acid, hot-cold distilled water, soap, and detergent resistance tests results of B-1/1 paint.

Test	Time	Results
Acid resistance (3% H <sub>2</sub> SO <sub>4</sub> )	72 h	No change
Cold distilled water (25°C)	72 h	No change
Hot distilled water (80°C)	48 h	No change
	72 h	Surface roughness
Soap resistance (8 g/L soft soap solution)	72 h	No change
Detergent resistance (1 g/L dishwashing detergent solution)	72 h	No change

In the acid resistance test presented in Table 10, which was performed by the immersion method, no effect was observed on the film surface after 72 h. The paint film, which was not affected by cold distilled water for 72 h, withstands for 48 h in hot distilled water. However, at the end of 72 h, small bubbles formed on the surface without compromising the integrity of the film. In soap and detergent resistance tests, there was no effect on the film at the end of 72 h.

Within the scope of household chemical resistance tests, the results of the alcohol, vinegar, and beverage resistance tests, which were applied spot-on and were performed using ethyl alcohol (50%, v/v), acetic acid (3% (wt.)), tea (1 tea bag brewed for 5 min/100 mL distilled water), coffee (2.5 g coffee/100 mL distilled water), and cola drink, are presented in Table 11.

**Table 11.** The beverage, vinegar, and ethyl alcohol resistance tests results of B-1/1 paint.

Time	Beverages			Acetic acid	Ethyl alcohol
	Tea	Coffee	Cola		
1 h	No change	No change	No change	No change	No change
2 h	No change	No change	No change	No change	No change
3 h	No change	No change	No change	No change	No change
4 h	No change	No change	No change	No change	No change

When Table 11 is examined, no change/deterioration/effect was observed in the paint film after 4 h in contact with beverages such as tea, coffee, cola, vinegar (acetic acid), and ethyl alcohol. It is seen that the paint film was resistant to household chemicals.

#### 4. CONCLUSIONS

In this study, high-performance films with hard, glossy, superior adhesion strength, high chemical, and excellent environmental resistance with good thermal properties were obtained from modified alkyd resins prepared by modification reactions of the synthesized four-component tall oil fatty acid-based and 50% oil alkyd resin with TDI at different NCO/OH (1/1, 1/2 and 1/3) molar ratios. Moreover, as the NCO/OH ratio increased, hardness, abrasion, and impact resistance values increased. At the end of all coating tests and thermogravimetric analyses, the best coating properties were observed in the R-UA-1/1 resin with an NCO/OH ratio of 1/1 among the urethane-modified alkyd resins with different NCO/OH molar ratios. R-UA-1/1 urethane-modified alkyd resin having the optimum ratio was used as a binder in the solvent-based paint formulation, and a stable paint-dispersion system without any phase separation was successfully created by combining other paint components and additives. Wet paint and dry paint tests of the prepared B-1/1 paint were performed, and it was observed that the wet paint properties were suitable for paint production. Further, paint films with high abrasion resistance, superior adhesion strength, excellent environmental resistance, glossy, and high resistance to acid, water, and household chemicals were obtained from B-1/1 paint. Considering that the paint industry needs coatings with very different properties for various purposes, even the improvable preliminary results obtained in this study are an achievement in themselves.

As a result, the production of paint with high coating performance and durability was successfully achieved by using the synthesized urethane-modified alkyd resin as a binder component in solvent-based paint production. This paint can be used as an alternative to durable coatings and alkyd paint systems suitable for interior applications.

## 5. FUTURE PERSPECTIVES

Our future study aims to produce sustainable, economical, and environmentally friendly waste-based paints that can compete with alkyd and modified alkyd-based paints by using the results obtained in this study and the approach of recycling and re-evaluation of waste PET.

### Declaration of Ethical Standards

The authors declare that they comply with all ethical standards.

### Credit Authorship Contribution Statement

The authors have contributed equally to this work.

Ferda CİVAN ÇAVUŞOĞLU: Investigation, formal analysis (all experiments, tests and analyses), validation, visualization, data curation, writing - original draft, writing - review & editing.

Işıl ACAR: Conceptualization, methodology, investigation, supervision, resources, formal analysis (support), validation, visualization, data curation, writing - original draft, writing - review & editing.

### Declaration of Competing Interest

The authors declare that there is no conflict of interest.

### Funding / Acknowledgements

The authors declare that no funds or grants were received during the preparation of this manuscript.

This study includes a part of the PhD thesis titled "Production of Urethane Modified Alkyd Resin from Waste PET Intermediates" prepared at Istanbul University-Cerrahpaşa in 2019.

### Data Availability

All data regarding the study are presented in this article.

## REFERENCES

- [1] A. Hofland, "Alkyd resins: From down and out to alive and kicking," *Progress in Organic Coatings*, vol. 73, no. 4, pp. 274–282, 2012.
- [2] R. Ploeger, D. Scalarone, and O. Chiantore, "The characterization of commercial artists' alkyd paints," *Journal of Cultural Heritage*, vol. 9, no. 4, pp. 412–419, 2008.
- [3] F. Civan Çavuşoğlu and I. Acar, "Synthesis of PET-based urethane-modified alkyd resins from depolymerization intermediates of post-consumer PET bottles: coating properties and thermal behaviors," *Journal of Coatings Technology Research*, vol. 20, no. 2, pp. 741–761, 2023.
- [4] I. H. Ifijen, M. Maliki, I. J. Odiachi, O. N. Aghedo, and E. B. Ohiocheoya, "Review on solvents based alkyd resins and water borne alkyd resins: impacts of modification on their coating properties," *Chemistry Africa*, vol. 5, pp. 211–225, 2022.
- [5] S. N. Gan and B. Y. Tan, "FTIR studies of the curing reactions of palm oil alkyd-melamine enamels," *Journal of Applied Polymer Science*, vol. 80, no. 12, pp. 2309–2315, 2001.
- [6] T. Erol, D. H. Özaltun, F. Civan Çavuşoğlu, I. Acar, and G. Güçlü, "The effect of linseed oil/canola oil blend on the coating and thermal properties of waste PET-based alkyd resins," *Anais da*



- Academia Brasileira de Ciências*, vol. 96, no. 1, 2024.
- [7] E. Bulak and I. Acar, "The use of Aminolysis, Aminoglycolysis, and simultaneous Aminolysis-hydrolysis products of waste pet for production of paint binder," *Polymer Engineering & Science*, vol. 54, no. 10, pp. 2272–2281, 2014.
- [8] Ö. N. Büyükyonga, N. Akgün, I. Acar, and G. Güçlü, "The usage of novel acrylic-modified water-reducible alkyd resin obtained from post-consumer PET bottles in water-based paint formulation," *Journal of Material Cycles and Waste Management*, vol. 22, no. 1, pp. 187–196, 2020.
- [9] H. F. Al-Shareef, A. M. Yousif, R. Eleisawy, A. M. Mahmoud, and H. Abdelwahab, "A wide range of modified alkyd resins based on a new source of dicarboxylic acid as a binder for anticorrosive paint," *Pigment & Resin Technology*, vol. 54, no. 3, pp. 444–453, 2025.
- [10] K. M. Kalu, R. Kenneth, E. K. C. Luntsi, J. U. Titus, F. Garba, and N. A. Haruna, "Formulation of a semi-gloss paint using sesamum indicum seed oil-modified alkyd resin as a binder," *International Journal of Innovative Research and Advanced Studies*, vol. 10, no. 6, pp. 34–38, 2023.
- [11] T. Mizutani, K. Arai, M. Miyamoto, and Y. Kimura, "Application of silica-containing nanocomposite emulsion to wall paint: A new environmentally safe paint of high performance," *Progress in Organic Coatings*, vol. 55, no. 3, pp. 276–283, 2006.
- [12] F. S. Güner, A. Gümüşel, S. Calica, and A. T. Erciyes, "Study of film properties of some urethane oils," *Journal of Coatings Technology*, vol. 74, no. 6, pp. 55–59, 2002.
- [13] O. Eksik, T. Erciyes, "A new modification method for triglyceride homopolymerization," *Journal of İTÜ, Serie D: Engineering*, vol. 9, no. 4, pp. 97–102, 2010.
- [14] V. D. Athawale and P. S. Pillay, "Interpenetrating polymer networks based on uralkyd-butylmethacrylate," *Reactive & Functional Polymers*, vol. 50, no. 1, pp. 1–8, 2002.
- [15] O. Saravari and S. Praditvatanakit, "Preparation and properties of urethane alkyd based on a castor oil/jatropha oil mixture," *Progress in Organic Coatings*, vol. 76, no. 4, pp. 698–704, 2013.
- [16] O. Saravari, K. Pathomwattanasak, and V. Pimpan, "Synthesis of urethane oils from palm oil and waste PET bottles," *Journal of Applied Polymer Science*, vol. 105, no. 4, pp. 1802–1807, 2007.
- [17] O. Saravari, B. Vessabutr, and V. Pimpan, "Synthesis of urethane oils from waste poly(ethylene terephthalate) bottles," *Journal of Applied Polymer Science*, vol. 92, no. 5, pp. 3040–3045, 2004.
- [18] J. S. Ling, I. Ahmed Mohammed, A. Ghazali, and M. Khairuddean, "Novel poly(alkyd-urethane)s from vegetable oils: Synthesis and properties," *Industrial Crops and Products*, vol. 52, pp. 74–84, 2014.
- [19] I. O. Bakare, C. Pavithran, F. E. Okieimen, and C. K. S. Pillai, "Synthesis and characterization of rubber-seed-oil-based polyurethanes," *Journal of Applied Polymer Science*, vol. 109, no. 5, pp. 3292–3301, 2008.
- [20] Marlina, Saiful, Rahmi, S. Saleha, and S. Nurman, "Synthesis and characterization new polyurethane membrane from hydroxylated rubber seed oil," *Oriental Journal of Chemistry*, vol. 33, no. 1, pp. 199–206, 2017.
- [21] M. Boruah, P. Gogoi, B. Adhikari, and S. K. Dolui, "Preparation and characterization of Jatropha Curcas oil based alkyd resin suitable for surface coating," *Progress in Organic Coatings*, vol. 74, no. 3, pp. 596–602, 2012.
- [22] K. C. Ünlü, K. Bal, I. Acar, G. Güçlü, "Fabrication of Solvent-based Alkyd Paint from Disposable PET Water Bottles: A Comparative Study," *Acta Scientiarum. Technology*, vol. 47, e69864, pp. 1–16, 2025.
- [23] O. M. Balci and T. B. Iyim, "Preparation and Application of Novel Nanocomposite Coating Materials Based on Phenolic Resin," *Asian Journal of Chemistry*, vol. 26, no. 11, pp. 3191–3196, 2014.
- [24] S. Sönmez, "Gloss of Paper. In: Current Researches in Engineering Sciences," Ed. B. Kıran, *Duvar Publishing*, pp. 77–89, 2020. Accessed: Nov., 2024. [Online]. Available: [https://www.researchgate.net/publication/348325900\\_gloss\\_of\\_paper](https://www.researchgate.net/publication/348325900_gloss_of_paper).



## IMPACT OF PARTIAL SHADING GEOMETRY ON THE ENERGY AND EXERGY PERFORMANCE OF PV MODULES

<sup>1</sup> Saleh Musaed Saleh Musaed ALNAKHLANI , <sup>2,\*</sup> Selcuk SELIMLI 

*Karabuk University, Energy Systems Engineering Department, Karabuk, TÜRKİYE*  
<sup>1</sup> [salehmusaedalnakhlani10@gmail.com](mailto:salehmusaedalnakhlani10@gmail.com), <sup>2</sup> [selcukselimli@karabuk.edu.tr](mailto:selcukselimli@karabuk.edu.tr)

### *Highlights*

- The impact of shader form on PV module energy performance is studied.
- The rectangular form causes the greatest reduction in 1<sup>st</sup> and 2<sup>nd</sup> law efficiencies.
- The lowest diminish in the efficiencies has been obtained by triangular form.
- The highest efficiency decrease is 7.22% energetically, and 9.04% exergetically.



## IMPACT OF PARTIAL SHADING GEOMETRY ON THE ENERGY AND EXERGY PERFORMANCE OF PV MODULES

<sup>1</sup> Saleh Musaed Saleh Musaed ALNAKHLANI , <sup>2,\*</sup> Selcuk SELIMLI 

Karabuk University, Energy Systems Engineering Department, Karabuk, TÜRKİYE

<sup>1</sup> [salehmusaedalnakhlani10@gmail.com](mailto:salehmusaedalnakhlani10@gmail.com), <sup>2</sup> [selcukselimli@karabuk.edu.tr](mailto:selcukselimli@karabuk.edu.tr)

(Received: 24.10.2024; Accepted in Revised Form: 22.02.2025)

**ABSTRACT:** In this experimental study, the impact of the geometric shape of partial shading on the energy and exergy performance of photovoltaic (PV) modules was evaluated using quadrant, triangular, and rectangular shaped shaders located on PV<sub>1</sub>, PV<sub>2</sub>, and PV<sub>3</sub> modules. The change in power output as well as the first and second efficiency of the PV modules was examined. In addition, fluctuations in the cost of exergy destruction (*COEx*) and the sustainability index (*SI*) were also observed. As a result, while the first law efficiencies of the PV<sub>1</sub>, PV<sub>2</sub>, and PV<sub>3</sub> modules were determined to be 5.33%, 6.85%, and 4.97%, respectively, the second law efficiencies were calculated as 2.06%, 3.99%, and 1.38%, respectively. The decrease rate of the first law efficiencies of the PV<sub>1</sub>, PV<sub>2</sub>, and PV<sub>3</sub> modules compared to the PV module was 6.86%, 5.34%, and 7.22%, respectively. Likewise, the decline in the second law efficiencies of the PV<sub>1</sub>, PV<sub>2</sub>, and PV<sub>3</sub> modules was 8.36%, 6.43%, and 9.04%, respectively. The *COEx* for them was \$29.89/year, \$29.34/year, and \$30.11/year, respectively, while for the PV module it was \$29.01/year. The *SI* of the PV<sub>1</sub>, PV<sub>2</sub>, and PV<sub>3</sub> modules is 8.92%, 7.14%, and 9.82% lower than that of the PV module.

**Keywords:** Energy, Exergy, First And Second Law Efficiency, Partial Shader Geometry, *SI*

### 1. INTRODUCTION

Currently, 81% of the world's energy needs are met by fossil fuels. The fossil fuel demand provided by 26.8% coal, 23.2% natural gas and 30.9% petroleum. The share of renewable energy sources is below 15% [1]. Population growth increases energy demand, but political and economic crises limit access to energy sources. Because of the threat to their national energy security, nations are turning their attention to alternatives like renewable energy sources [2]. The most common, widely accessible and easily convertible renewable energy source is solar energy [3]. Compared to other energy sources, solar energy is incredibly affordable because of its low initial investment, ongoing maintenance, and operating costs. [4]. Systems that run on solar energy have nearly zero CO<sub>2</sub> emissions, making them significantly better for the environment than systems that use carbon-intensive energy sources. PV cells, semiconductor structures that convert sunlight directly into electricity, are a widely used technology [5]. The energy conversion efficiency of a PV module can be increased to a limited extent by reducing its temperature. In addition, this enhancing effect further increases effectiveness with increased sunlight [6]. A few examples of dynamic environmental factors that impact PV module performance are temperature variations, partial shading, and fluctuating solar irradiance [7]. Shade drastically lowers PV power output by blocking sunlight from reaching the PV module [8]. The energy conversion of PV modules can be influenced by two types of shading: static and dynamic. While static shading can be produced by things like buildings, trees, and signs, dynamic shading can be produced by clouds, birds, or flying objects in the air [9]. To achieve high voltage, PV cells in PV modules must be connected in series; However, this also limits the system current because the cell with the lowest current among the cells connected in series also acts as a current limiter. This is why shading a PV cell can limit the total current of the series. Connecting a string of parallel bypass diodes to a cell string will eliminate this restriction [10]. Partial shading has no discernible effect on the total voltage of the cells connected in series, which is the sum of all the voltages [11]. Shaded PV cells also produce lower current and are forced to carry higher current resulting from unshaded cells. When the operating current exceeds the short-circuit current in shaded cells, hotspot

\*Corresponding Author: Selcuk SELIMLI, [selcukselimli@karabuk.edu.tr](mailto:selcukselimli@karabuk.edu.tr)

heating occurs, an area of PV modules that becomes overheated due to shading, resulting in premature degradation and permanent damage to the shaded cells [12], [13]. PV cells that are partially shaded produce a resistance that acts as a load rather than generating electricity. Bypass diodes are used to eliminate these shaded cells and facilitate easy transfer of the current generated by the non-shaded cells [14]. The following lines provide a detailed overview of the studies that address the effects of shading on the module performance. A study conducted by Sathyanarayana et al. examined how shading affects the output power and energy efficiency of a PV module. It was found that a 2.46% reduction in energy efficiency was caused by almost 19.82% shading of the module surface [15]. The study by Bayrak et al. investigated the effects of shading size on the performance of a PV module. It was found that the module efficiency decreases by 0.78%, 4.16%, 4.45% and 5.26% at shading rates of 25%, 50%, 75% and 100%, respectively [16]. Belhus's et al. have found that partial shading can significantly reduce the power output of PV module arrays. They added that the shading pattern may be more important in this case than the shading area alone [17]. Hariharasudhan et al. conducted an experiment to study the performance of PV modules under different partial shading conditions for individual PV cells. They found that the performance drop is almost 26% [18]. A study by Trammel et al. examined energy losses from PV modules due to shading or pollution. Partial shading of a PV module, they explained, is not as bad as shading the entire cell, which can cause the system to lose up to 25% of its power [19]. An article by Bellhouse et al. investigated the close relation between the effects of partial shading and the performance of PV modules. They tried to mitigate the effects of partial shading on the energy efficiency of the PV systems [20]. In a study, Tian et al. concluded that even minimal shading can significantly reduce the electrical output of a PV system [21]. In a study by Mamun et al. investigated the effect of partial shading on the energetic performance of a PV module. It has been reported that a 10% increase in shaded module area results in a 2.3% reduction in electrical efficiency [22]. In an experimentally validated computational study by Cameron et al., it was found that partial shading can lead to a decrease in the exergy efficiency of a PV module by approximately 3.5% [23]. Bayrak and Oztop investigated the influence of the shading size of both static and dynamic shading on the performance of the PV module. They evaluated hotspot formation and compared the performance degradation [24]. In an experimental study by Keskin, partial shading of a PV string was found to reduce exergy efficiency by approximately 6.87% [25]. A study by Dolara et al. investigated how partial shading affects the energetic performance of the PV modules. Their findings indicate that power output is lowered by over 30% when a single cell is shaded by 50% [26]. In an experimental study, Tripathi et al. found that the power reduction was almost 70.27% when half of the PV module area was shaded [27]. The studies mentioned so far, along with many others in the literature, address the decline in the energetic performance of PV systems due to shading. A large part of it specifically addressed the question of whether shadow size has a serious impact on performance degradation. Few of them have considered that in addition to shadow size, shadow geometry can also have an impact on performance degradation. Through this consideration, this study, conducted with shadders with identical shadow areas and different geometric forms, attempts to contribute to the literature on the impact of shadow geometry on performance degradation.

## 2. MATERIALS AND METHODS

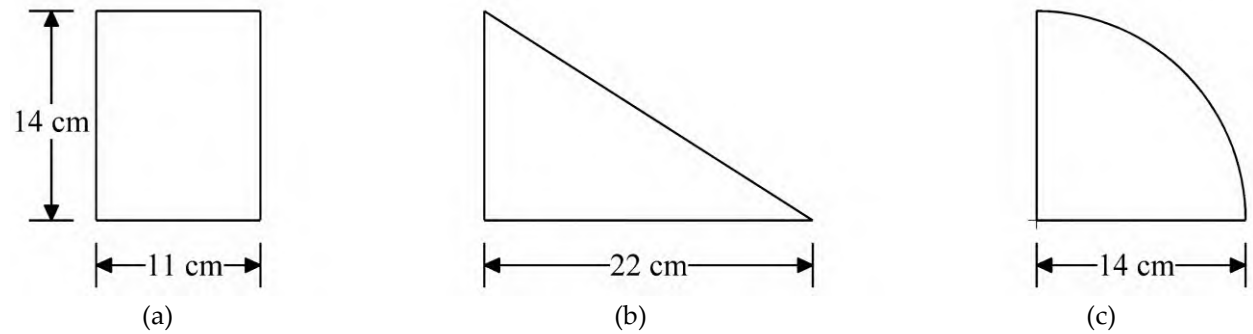
The effects of partial shading geometry on the energy and exergy performance of PV modules were experimentally investigated in this study. The study was conducted in the city of Karabuk in the western part of the Black Sea region of Türkiye. The test was conducted on a bright, cloudless day in January 2024. The test took place between 11:00 and 16:30. Four identical PV modules with a peak output of 50 W are used for the test. In Table 1, the PV module specifications were shown.

**Table 1.** PV module specifications.

<b>Module type</b>	Monocrystalline
<b>Dimensions (cm)</b>	67.4 x 42.4 x 2.5
<b>Rated peak power (<math>W_p</math>)</b>	50
<b>Tolerance (%)</b>	$\pm 5$
<b>Peak power voltage (V)</b>	20.6
<b>Peak power current (A)</b>	2.43
<b>Circuit voltage [open] (V)</b>	22.68
<b>Circuit current [short] (A)</b>	2.37

All data is for standard conditions of testing; AM 1.5,  $T_c=25^\circ\text{C}$ ,  $F=1000\text{ W/m}^2$

The PV modules in the test setup were optimally oriented to the south with a fixed tilt angle of  $40^\circ$ , which was the ideal position in Karabuk. To create the shading effect, three differently shaped shaders (quadrant, triangular, and rectangular) were cut out of thick paper with the same surface area. Figure 1 shows the dimensions of the shaders. The area of each piece is  $154\text{ cm}^2$ . Each piece was placed in an identical position on the PV modules. The first PV module is the reference module. The shaders in the shape of a quadrant, a triangular and a rectangular were positioned at the same locations of the  $PV_1$ ,  $PV_2$  and  $PV_3$  module surface, respectively.

**Figure 1.** Dimensional details of shading form a) rectangle, b) triangle, c) quadrant.

The electric outputs of the PV modules were linked to a load circuit equipped with resistors and digital voltmeters/ammeters. To test each module under load,  $50\text{ W } 14.7\Omega$  resistors were used. Solar irradiance was measured using the TES 1333R solar power meter. K-type thermocouples were attached to the rear of each module to monitor its temperature. Two of the thermocouples were positioned at opposite corners of the module, with the third in the middle. Due to the uneven temperature distribution of the modules during testing, we estimated the temperature of each module by averaging its three-point data. The ambient temperature was measured using a K-type thermocouple. Data collected from thermocouples using an Elimko E680 data logger were recorded on a computer. Every second, the data logger transmitted temperature readings to a computer. For evaluation, half-hourly time averages of the data were calculated. Voltage, current and solar irradiance data were recorded every 30 minutes throughout the test. The test setup was shown in detail in Figure 2.

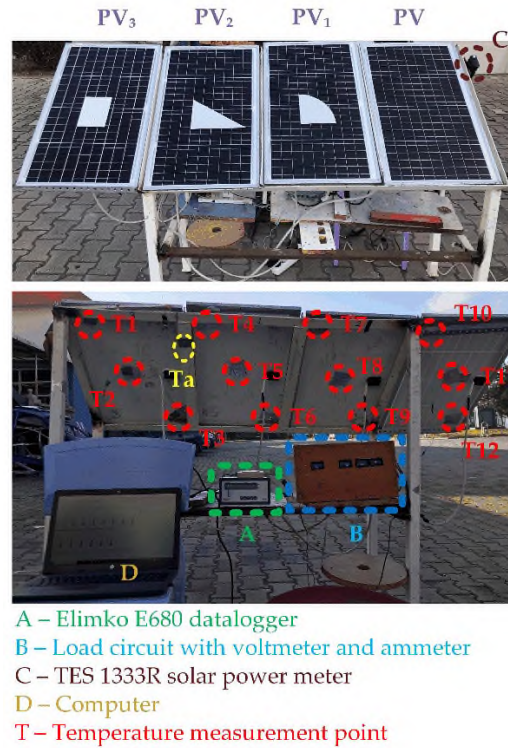


**Figure 2.** An illustration of the experimental setup in detail.

Table 2 lists the measuring devices with their technical specifications.

**Table 2.** Measuring instruments and their technical capabilities

Device / Sensor	Data type	Measurement point	Specifications	Uncertainty (%)
Elimko E680 data logger / Picotech, K-type thermocouple	Temperature	T1, T2, T3, T4, T5, T6, T7, T8, T9, T10, T11, T12, Ta	Measurement range: -200 to +1300°C / -40 to 1200°C	±0.5 / ±2.5
Load circuit with voltmeter and ammeter	Voltage and current	Module electrical outputs	Measurement range: DC 0 to 100 V, 0 to 10 A	±1
TES 1333R solar power meter	Solar irradiance	C	Measurement range: 0 to 2000 W/m <sup>2</sup>	±5

The experimental uncertainty of the study was determined using the terminology described in the “Uncertainty Model” section below.

## 2.1. Uncertainty Model

The uncertainty of the results, which depends on the uncertainty of the measurement data, was determined by uncertainty analyzes using the Kline and McClintock method, which is given in Eq. (1) [16].

$$w_R = \sqrt{\left(\frac{\partial R}{\partial x_1} w_1\right)^2 + \left(\frac{\partial R}{\partial x_2} w_2\right)^2 + \dots + \left(\frac{\partial R}{\partial x_n} w_n\right)^2} \quad (1)$$

In Eq. (1),  $R$  is the functional relationship of the independent variables  $x_1, x_2, \dots, x_n$ . The resulting uncertainty is denoted by  $w_R$ .  $w_1, w_2, \dots, w_n$  are the uncertainty of independent variables. The calculated

overall uncertainty of the test was determined to be 5.92%. The data evaluation of the experimental measurements was carried out based on the theoretical relationships specified in the following “Mathematical Model” section.

## 2.2. Mathematical Model

Using the relationships found in Eqs. (1–9), PV modules can be examined from an energy perspective. The energy balance of the PV modules is given by Eq. (2) [28].

$$\dot{P}_s = \dot{P}_e + \dot{P}_{th,l} + \dot{P}_{oth,l} \quad (2)$$

In Eq. (2),  $\dot{P}_s$  and  $\dot{P}_e$  denote the solar and electrical energy rates.  $\dot{P}_{th,l}$  is the thermal energy lost to the environment in the test configuration.  $\dot{P}_{oth,l}$  symbolize the other losses of the PV module to the environment. Eq. (3) presents solar energy [28].

$$\dot{P}_s = G_s A f_{act} \quad (3)$$

Where  $A$  is the PV module surface area,  $G_s$  is the solar irradiance. Active module surface fraction is represented by  $f_{act}$ . Eq. (4) relates to the electrical power that a PV module produces [29].

$$\dot{P}_e = IV \quad (4)$$

Where  $I$  and  $V$  represent the current and voltage outputs of a PV module. Eq. (5) indicates the thermal losses of a PV module [29].

$$\dot{P}_{th,l} = hA\Delta T \quad (5)$$

The overall heat transfer coefficient ( $h$ ) is determined using Eq. (6) [29].

$$h = h_c + h_r \quad (6)$$

Equation for the convection heat transfer coefficient ( $h_c$ ) as in Eq. (7) [29].

$$h_c = 2.8 + 3V_w \quad (7)$$

Where  $V_w$  symbolizes the local wind speed. Eq. (8) is used to calculate the radiative heat transfer coefficient ( $h_r$ ) [29].

$$h_r = \varepsilon\sigma(T_{sky} + T_m)(T_{sky}^2 + T_m^2) \quad (8)$$

In Eq. (8), emissivity constant, Stefan-Boltzmann constant and module temperature are indicated by the symbols  $\varepsilon$ ,  $\sigma$ , and  $T_m$ . Eq. (9) can be used to estimate the effective temperature of the sky ( $T_{sky}$ ) [29].

$$T_{sky} = T_a - 6 \quad (9)$$

Where the ambient temperature is denoted by  $T_a$ . First law efficiency ( $\eta_I$ ) of a PV module is determined by the relationship according to Eq. (10) [29].

$$\eta_I = \frac{\dot{P}_e}{\dot{P}_s} \quad (10)$$

Eqs. (10–15) are used to examine PV modules from an exergy perspective. The exergy balance of the PV module is defined using Eq. (11) [29].

$$\sum \dot{E}x_i = \sum \dot{E}x_o + \sum \dot{E}x_l + \sum \dot{E}x_{ir} \quad (11)$$

Where,  $\dot{E}x_i$ ,  $\dot{E}x_o$ ,  $\dot{E}x_l$  and  $\dot{E}x_{ir}$  indicates input, output, loss exergy rates and the irreversibility rate. Solar exergy rate ( $\dot{E}x_s$ ) is shown in Eq. (12) [29].

$$\dot{E}x_s = \dot{P}_s \left[ 1 - \frac{4}{3} \left( \frac{T_a}{T_s} \right) + \frac{1}{3} \left( \frac{T_a}{T_s} \right)^4 \right] \quad (12)$$

Where, ( $T_s$ ) denotes the sun temperature. Electrical exergy rate ( $\dot{E}x_e$ ) is defined by Eq.(13) [29].

$$\dot{E}x_e = \dot{P}_e \quad (13)$$

In this study, the thermal exergy rate ( $\dot{E}x_{th}$ ) is lost to the environment and cannot be used. For this reason, it is related to heat loss and is expressed as in Eq. (14) as follows [29].

$$\dot{E}x_{th} = \dot{P}_{th,l} \left( 1 - \frac{T_a}{T_m} \right) \quad (14)$$

The exergy loss can be calculated by Eq. (15) [30].

$$\dot{E}x_l = \dot{E}x_s (1 - \eta_{II}) \quad (15)$$

Eq. (16) provides the PV module efficiency ( $\eta_{II}$ ) based on the second law of thermodynamics [16], [31]–[34].

$$\eta_{II} = \frac{\dot{E}x_o}{\dot{E}x_i} = \frac{\dot{E}x_e - \dot{E}x_{th}}{\dot{E}x_s} \quad (16)$$

Where input and output exergies are indicated by the symbols  $\dot{E}x_i$  and  $\dot{E}x_o$ . Eq. (17) shows the relationship between the *SI*, the evaluation parameter of exergy applications to reduce resource waste and environmental damage, and the second law efficiency [35].

$$SI = \frac{1}{1 - \eta_{II}} \quad (17)$$

The *COEx* can be computed using Eq. (18) [32].



$$COEx = \text{unit price of electricity} \times \text{destructured exergy} \quad (18)$$

The measured and calculated energy and exergy-based data related to the stated theoretical basis in this section were evaluated in the next section “Results and Discussions”.

### 3. RESULTS AND DISCUSSIONS

This experimental study investigated the effects of partial shading with identical area but different shadow shape on the energy and exergy performance of PV modules. In the following section, authors visualized, and evaluated the measured and calculated electrical, thermal, and energetic parameters. The solar irradiance, ambient temperature, and PV module temperatures are shown in Figure 3. As indicated by the graphic curves in Figure 3, the solar irradiance was 525.4 W/m<sup>2</sup> at 11:00, the start of the test. At 14:30, the irradiance reached its maximum value of 1124 W/m<sup>2</sup>, after increasing gradually until midday. The irradiance decreased with a more noticeable decreasing trend from 14:30 to 16:30, reaching the value of 646 W/m<sup>2</sup>, in contrast to the increase that was seen until 14:30. The test mean value of solar irradiance was 842.7 W/m<sup>2</sup>. The average ambient temperature for the test day was calculated to be 6°C using the data shown in Figure 3. Before testing, the setup was kept in a dark, closed environment. For this reason, at the start of the test, the test setup was close to ambient temperature and the PV modules were at the same temperature. PV modules start converting energy as soon as they are exposed to sunlight and their temperature increases accordingly. PV cells that are partially shaded produce less current than those that are not. By blocking the high current that tries to pass through them, shaded cells function as a reverse p-n junction, lowering the circuit voltage, heating up, producing hot spots, and releasing energy [36]. As shown in Figure 3, hotspots caused by different current resistances due to different shading geometries under the same conditions resulted in temperature fluctuations between the partially shaded PV<sub>1</sub>, PV<sub>2</sub> and PV<sub>3</sub> modules compared to the unshaded PV module. Compared to the unshaded PV module, the temperatures of the shaded modules were even higher. The average PV module temperature was found to be 22°C, while the average PV<sub>1</sub>, PV<sub>2</sub>, and PV<sub>3</sub> temperatures were 25°C, 24°C, and 26°C, respectively. Partial shading limited the solar irradiance on the PV cells and the hotspots resulted in differences in the module temperatures, which affected the current and voltage outputs of the PV modules.

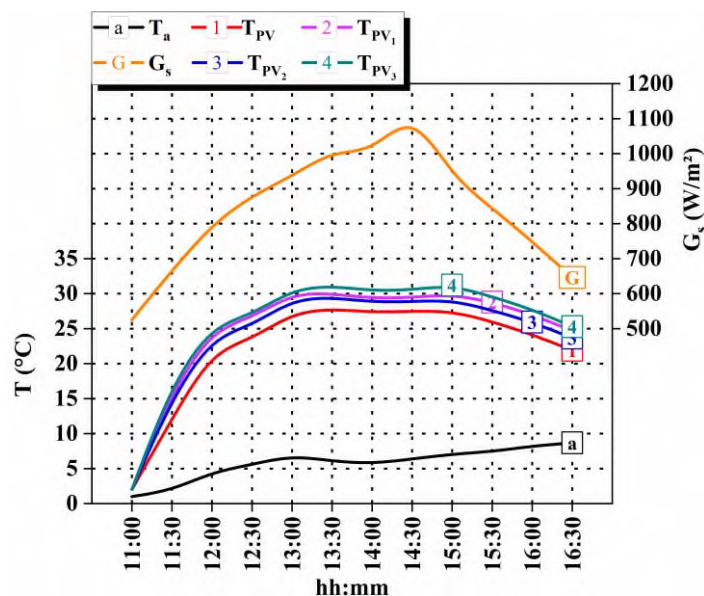


**Figure 3.** The solar irradiance on test day and the temperatures of the modules and surroundings.

As show in Figure 4, the output voltage and current of the PV modules. Figure 4 shows that module outputs tended to increase until midday as solar irradiance increased. A downward trend in the outputs

was noted as the irradiance intensity incident on the panels began to decrease over the following hours of testing. Based on the data in Figure 4, the average voltage and current outputs for the PV were determined to be 20.74 V and 1.39 A. The partially shaded PV<sub>1</sub>, PV<sub>2</sub> and PV<sub>3</sub> modules had average output voltages of 13.46 V, 15.18 V and 12.89 V, respectively. Their respective average output currents were 0.9 A, 1.02 A, and 0.88 A. It was found that the electrical performance of partially shaded modules is significantly lower than that of unshaded module. Compared to the PV module, the voltage outputs of the PV<sub>1</sub>, PV<sub>2</sub> and PV<sub>3</sub> modules decreased by about 35.11%, 26.79% and 37.84%, respectively. In that order, current production fell by 34.93%, 26.35% and 36.73%. The shader with the rectangular shape reduced voltage and current the most, while the shader with the triangular shape reduced them the least. Since the PV module was not shaded, sunlight could reach the PV cells unhindered, exposing the entire surface to the sun. All of the solar irradiance and, thus, all of the solar power could not reach the PV cells due to the partial shading of the PV<sub>1</sub>, PV<sub>2</sub>, and PV<sub>3</sub> modules.

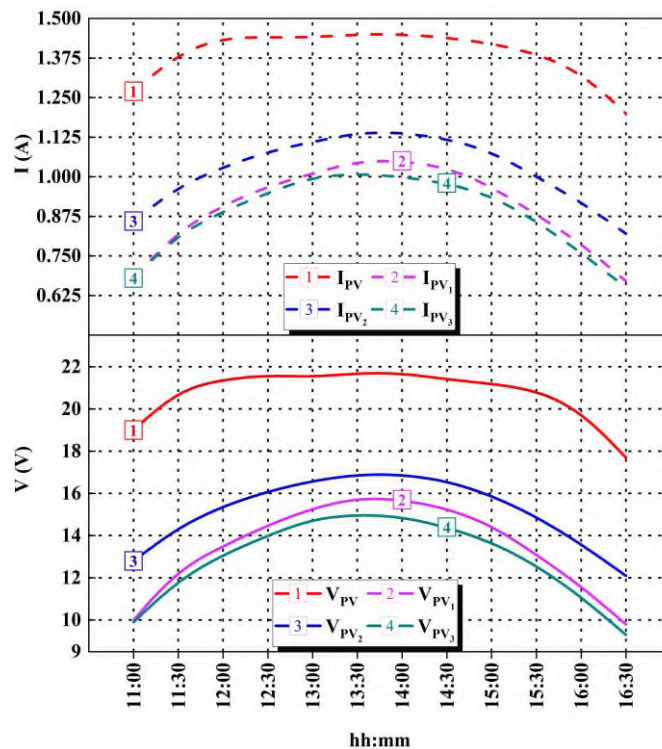


Figure 4. Current and voltage outputs of PV modules.

The half-hourly values of solar power reaching the module cells and the electrical power outputs of the module are shown in Figure 5. Solar irradiance increased, the solar power on the PV modules increased with a decreasing trend until 14:30, and then showed a stable decreasing trend until the end of the test as shown in Figure 5. The PV module received an average of 242.78 W of solar power because it was not shaded, while the PV<sub>1</sub>, PV<sub>2</sub> and PV<sub>3</sub> modules only received an average of 229.81 W due to the shade. On average, 28.89W of solar energy could be converted into electricity by the PV module, while 12.42W, 15.69W and 11.55W could be converted by PV<sub>1</sub>, PV<sub>2</sub> and PV<sub>3</sub>, respectively. Partial shading of modules with shaders of the same size, which reduced the amount of solar irradiance reaching the module cells by approximately 5.34%. However, the loss of electrical power was significantly higher due to the resulting current resistance and hotspots in the shaded cells. The average electrical power output of PV<sub>1</sub>, PV<sub>2</sub> and PV<sub>3</sub> recorded a decrease of 57%, 45.68% and 60.01%, respectively. In an experimental study by

Abdulmawjood et al., a reduction in output power ranging from 45.8% to 72.6% was observed by changing the shading area [37].

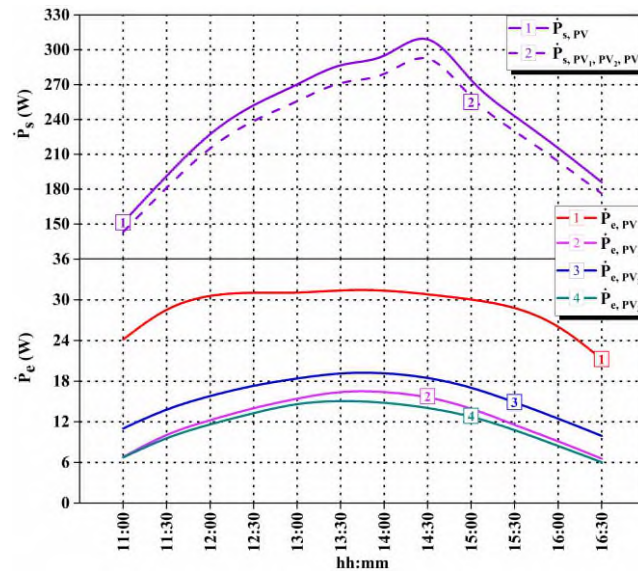


Figure 5. The solar power and the electrical power outputs

In terms of electrical power output, the triangular shader had the smallest reduction and the rectangular shader had the largest. Figure 6 shows the input, output and loss exergies of PV modules. The input exergy rate of the PV module was 227.14 W, the output exergy rate was 22.57 W, and the loss exergy rate was calculated to be 204.58 W, as shown in Figure 6. The input exergy rate of the PV<sub>1</sub>, PV<sub>2</sub> and PV<sub>3</sub> modules decreased to 215.01 W due to partial shade. All three partially shaded modules experienced an equal decrease in input exergy rate of approximately 5.34% compared to the PV module. The PV<sub>1</sub>, PV<sub>2</sub> and PV<sub>3</sub> modules were found to have output exergy rates of 4.21 W, 8.12 W and 2.65 W, respectively. According to the calculations, the exergy loss rates were 210.8 W, 206.88 W and 212.35 W in that order. Compared to the PV module, the output exergy rates of the PV<sub>1</sub>, PV<sub>2</sub> and PV<sub>3</sub> modules shaded by a quadrant, a triangular and a rectangular partial shaders decreased by 81.34%, 64.02% and 88.25%, respectively. The hotspot created due to the shading increased the loss exergy by about 3.04%, 1.08% and 3.79% in PV<sub>1</sub>, PV<sub>2</sub> and PV<sub>3</sub>, respectively. In an experimental study of Khajen and Keskin, the maximum increase in exergy loss due to the shading effect was found to be 23.32% [38]. The triangular formed partial shader displayed the least amount of reducing effect, whereas the rectangular formed partial shader decreased the exergy output rate in the maximum rate despite having equal surface areas.

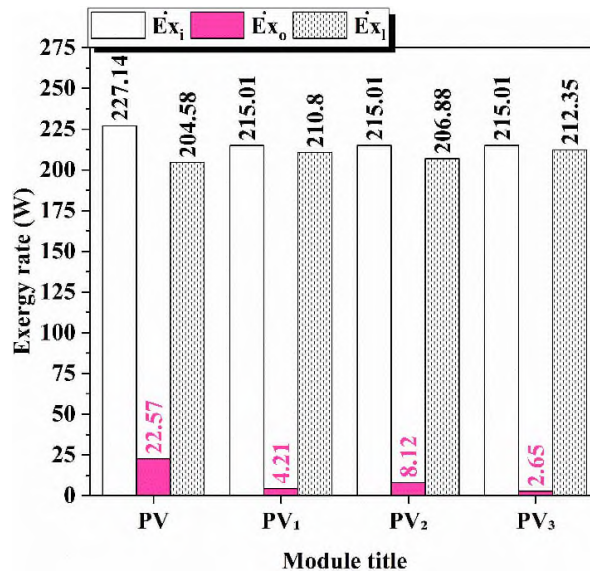


Figure 6. Input, output and loss exergy of PV modules.

The energy and exergy efficiencies of the modules are shown comparatively in Figure 7. The first and second efficiencies of the PV module reached 12.19% and 10.42% in the test, respectively, as shown in Figure 7. In addition, Figure 7 shows that the first law efficiency of the PV<sub>1</sub>, PV<sub>2</sub> and PV<sub>3</sub> modules compared to the PV module was affected to different extents by partial shades with different geometric shapes, equivalent surface areas and the same positioning on the module surfaces. PV<sub>1</sub>, PV<sub>2</sub>, and PV<sub>3</sub> modules had first law efficiencies of 5.33%, 6.85%, and 4.97%, respectively; second law efficiencies were 2.06%, 3.99%, and 1.38%, in that order. The first law efficiency of PV<sub>1</sub>, PV<sub>2</sub> and PV<sub>3</sub> modules decreased by 6.86%, 5.34% and 7.22%, respectively, compared to the PV module. The second law efficiency values for the PV<sub>1</sub>, PV<sub>2</sub> and PV<sub>3</sub> modules decreased by 8.36%, 6.43% and 9.04%, respectively. PV<sub>2</sub> and PV<sub>3</sub> modules shaded by triangular and rectangular shades showed the lowest and highest changes in first and second law efficiency, respectively.

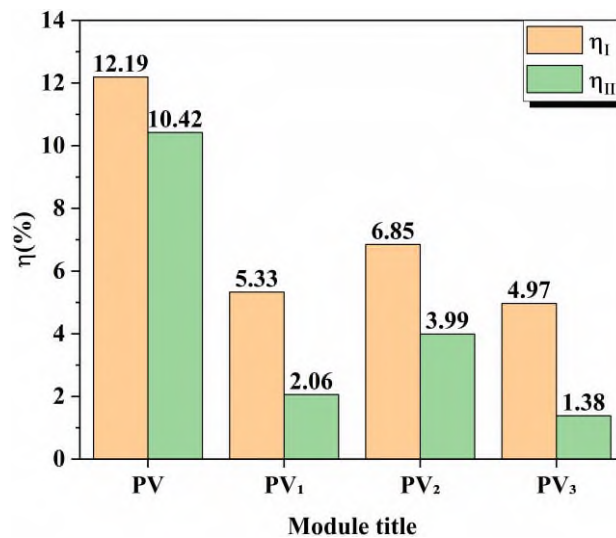


Figure 7. The first and second law efficiencies of modules.

Another notable aspect besides the variation in energy and exergy efficiency values is that the energy efficiency values for each module are greater than the exergy efficiency values. The reason for this common situation is explained in detail in Refs. [34], [39]–[43] as follows: Energy efficiency, based on the first law of thermodynamics, deals with the quantity of energy and does not consider irreversibility. However, exergy efficiency, which is associated with the second law of thermodynamics, evaluates the quality of energy and is only interested in the energy that can be used for useful purposes at the end of the process. When evaluating exergy efficiency, the part of solar energy that is converted into electrical energy in PV cells is evaluated as output energy, and the part that is converted into heat is evaluated as a loss, not as output. At this point, it is concluded that the exergy efficiency of a PV module is always lower than the energy efficiency, which is because of irreversibilities. The energy and exergy efficiencies of this study were summarized in Table 3 by comparing the results of similar studies from literature.

**Table 3.** Comparison of energy and exergy efficiency based on similar study results in literature.

Study	Method	Type of shading	$\eta_I$ (%)		$\eta_{II}$ (%)	
			Unshaded	Shaded	Unshaded	Shaded
This study	Experimental	Static shading	12.19	6.85	10.42	3.99
Bayrak et al. [16]			8.19	5.3	8.05	4.86
Gurturk et al. [44]		2.53	2.19	1.7	1.46	
Khalejan and Keskin [38]		Dynamic shading	9.12	8.79	7.82	6.87

The energy and exergy efficiency results of this study tend to vary similarly to the results of the literature supporting the results and presented in Table 3. The electricity tariff fee set by the Energy Market Regulatory Authority of the Republic of Türkiye that energy suppliers charged for residential customers from January 1, 2024 is 5.8 cents/kWh [45]. The authors calculated the cost of exergy loss based on the electricity price. They visualized the  $SI$  and  $COEx$  in Figure 8. The estimated annual  $COEx$  for a PV module was \$29.01, as shown in Figure 8.  $PV_1$ ,  $PV_2$ , and  $PV_3$  had  $COEx$  values of \$29.89, \$29.34, and \$30.11 annually, respectively. The triangular shader caused a minimal increase in the  $COEx$ , while the rectangular shader caused a maximal increase. The PV module had a  $SI$  of 1.12, while the  $PV_1$ ,  $PV_2$ , and  $PV_3$  modules had  $SI$  of 1.02, 1.04, and 1.01, respectively. Compared to the PV module, the  $SI$  of the  $PV_1$ ,  $PV_2$  and  $PV_3$  modules decreased by 8.92%, 7.14% and 9.82%, respectively. The decline effect was observed in the  $SI$  through the shading effect in an experimental study by Khan et al. [46]. The triangular shader caused the smallest drop in the  $SI$  due to shading, while the rectangular shader caused the largest drop. The decline in the  $SI$  can be related to the increase in  $COEx$ .

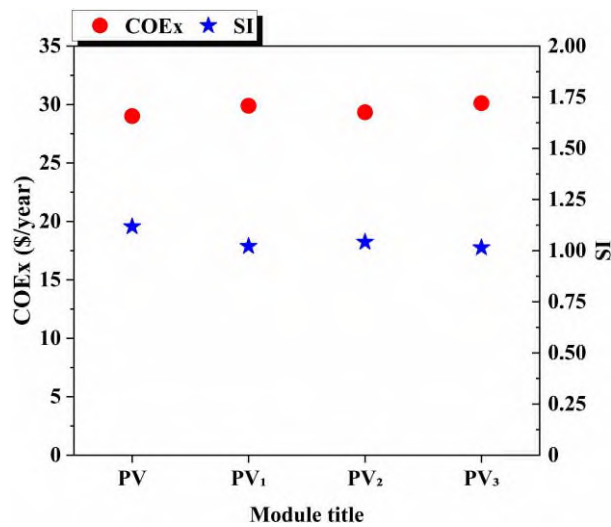


Figure 8. The *COEx* and *SI* of the modules.

The general judgment obtained from all these evaluations is summarized and presented in the last section, "Conclusions".

#### 4. CONCLUSIONS

In this experimental study, the effect of the geometric shape of partial shading on the energy and exergy performance of PV modules was examined using a four-module test setup. One module was unshaded (referred to as a PV module), the others were shaded with quadrant, triangular, and rectangular shaped shaders and called PV<sub>1</sub>, PV<sub>2</sub>, and PV<sub>3</sub>, respectively. The test conducted in Karabuk, Türkiye found that the shaded panels (PV<sub>1</sub>, PV<sub>2</sub> and PV<sub>3</sub>) received less solar power. Shading reduced the power generation of the shaded cells, increased resistance in the circuit, and limited current flow, which in turn reduced the performance of the modules. Furthermore, local hotspots caused by resistance in shaded cells could potentially lead to long-term irreparable damage. Below is a detailed numerical summary of the effects of shading geometry on the energy and exergy performance of PV modules based on experimental measurements and calculations.

- The first and second efficiencies of the PV module were 12.19% and 10.42%, respectively.
- The PV<sub>1</sub>, PV<sub>2</sub>, and PV<sub>3</sub> modules had first law efficiencies of 5.33%, 6.85%, and 4.97%, respectively.
- The second law efficiencies of the PV<sub>1</sub>, PV<sub>2</sub>, and PV<sub>3</sub> modules were 2.06%, 3.99%, and 1.38%, respectively.
- In the PV<sub>1</sub>, PV<sub>2</sub>, and PV<sub>3</sub> modules, the first law efficiencies decreased by 6.86%, 5.34%, and 7.22%, respectively.
- The second law efficiencies for modules PV<sub>1</sub>, PV<sub>2</sub>, and PV<sub>3</sub> decreased by 8.36%, 6.43%, and 9.04%, respectively.
- The annual value of *COEx* for PV<sub>1</sub>, PV<sub>2</sub>, and PV<sub>3</sub> was \$29.89, \$29.34, and \$30.11, respectively, while the value for PV module was \$29.01.
- The *SI* decreased by 8.92%, 7.14%, and 9.82% for PV<sub>1</sub>, PV<sub>2</sub>, and PV<sub>3</sub> modules compared to PV module, respectively.

#### Declaration of Ethical Standards

There are no ethical issues regarding the publication of this study.

### Credit Authorship Contribution Statement

**Saleh Musaed Saleh ALNAKHLANI** : Resources, Methodology, Experimentation, Investigation.

**Selcuk SELİMLİ**: Methodology, Writing – original draft, Visualisation, Supervision, Investigation, Conceptualization.

### Declaration of Competing Interest

The authors declare that they have no known competing financial interests or personal relationships that could have appeared to influence the work reported in this paper.

### Funding / Acknowledgements

The authors gratefully acknowledge that this article is derived from the MSc thesis titled “Experimental Investigation of the Effect of Shading Geometry on the Energy Performance of a PV Module,” completed by Saleh Musaed Saleh Musaed ALNAKHLANI with the scholarship of the Türkiye Scholarships and the Islamic Development Bank ISDB-YTB Joint Scholarship Program (Application No. 21YE031292, 2021).

### Data Availability

The research data has not been made available in the repository.

### REFERENCES

- [1] L. Xu, P. Ding, Y. Zhang, Y. Huang, J. Li, and R. Ma, “Sensitivity analysis of the shading effects from obstructions at different positions on solar photovoltaic panels,” *Energy*, vol. 290, p. 130229, 2024.
- [2] B. A. Kazancı, O. F. F. Arslan, and S. Dincer, “Climate Crisis and The Future of Renewable Energy in the Turkic Republics,” in *Analyzing Energy Crises and the Impact of Country Policies on the World*, M. S. O. Ozcan, Ed., 1st ed. IGI Global, 2023, pp. 178–194.
- [3] N. L. Panwar, S. C. Kaushik, and S. Kothari, “Role of renewable energy sources in environmental protection: A review,” *Renew. Sustain. Energy Rev.*, vol. 15, no. 3, pp. 1513–1524, 2011.
- [4] M. K. H. Rabaia *et al.*, “Environmental impacts of solar energy systems: A review,” *Sci. Total Environ.*, vol. 754, p. 141989, 2021.
- [5] L. Etgar, “Semiconductor nanocrystals as light harvesters in solar cells,” *Materials (Basel)*, vol. 6, no. 2, pp. 445–459, 2013.
- [6] S. P. Aly, S. Ahzi, and N. Barth, “Effect of physical and environmental factors on the performance of a photovoltaic panel,” *Sol. Energy Mater. Sol. Cells*, vol. 200, p. 109948, 2019.
- [7] K. Suresh Kumar and P. Winston David, “Performance analysis of winnowing dynamic reconfiguration in partially shaded solar photovoltaic system,” *Sol. Energy*, vol. 268, p. 112309, 2024.
- [8] K. Hasan, S. B. Yousuf, M. S. H. K. Tushar, B. K. Das, P. Das, and M. S. Islam, “Effects of different environmental and operational factors on the PV performance: A comprehensive review,” *Energy Sci. Eng.*, vol. 10, no. 2, pp. 656–675, 2022.
- [9] S. K. Das, D. Verma, S. Nema, and R. K. Nema, “Shading mitigation techniques: State-of-the-art in photovoltaic applications,” *Renew. Sustain. Energy Rev.*, vol. 78, pp. 369–390, 2017.
- [10] S. Gallardo-Saavedra and B. Karlsson, “Simulation, validation and analysis of shading effects on a PV system,” *Sol. Energy*, vol. 170, pp. 828–839, 2018.
- [11] P. dos Santos Vicente, E. M. Vicente, M. G. Simoes, and E. R. Ribeiro, “Shading position effects on photovoltaic panel output power,” *Int. Trans. Electr. Energy Syst.*, vol. 30, no. 1, pp. 1–19, 2020.
- [12] M. Khodapanah, T. Ghanbari, E. Moshksar, and Z. Hosseini, “Partial shading detection and

- hotspot prediction in photovoltaic systems based on numerical differentiation and integration of the P – V curves," *IET Renew. Power Gener.*, vol. 17, no. 2, pp. 279–295, 2023.
- [13] K. Osmani, A. Haddad, H. Jaber, T. Lemenand, B. Castanier, and M. Ramadan, "Mitigating the effects of partial shading on PV system's performance through PV array reconfiguration: A review," *Therm. Sci. Eng. Prog.*, vol. 31, p. 101280, 2022.
- [14] S. Hamdi, D. Saigaa, and M. Drif, "Modeling and simulation of photovoltaic array with different interconnection configurations under partial shading conditions for fill factor evaluation," in *Proceedings of 2014 International Renewable and Sustainable Energy Conference*, 2014, pp. 25–31.
- [15] P. Satyanarayana, R. Ballal, L. P. Sagar S, and G. Kumar, "Effect of shading on the performance of solar PV panel," *Energy and Power*, vol. 5, no. 1A, pp. 1–4, 2015.
- [16] F. Bayrak, G. Ertürk, and H. F. Oztop, "Effects of partial shading on energy and exergy efficiencies for photovoltaic panels," *J. Clean. Prod.*, vol. 164, pp. 58–69, 2017.
- [17] N. Belhaouas *et al.*, "PV array power output maximization under partial shading using new shifted PV array arrangements," *Appl. Energy*, vol. 187, pp. 326–337, 2017.
- [18] T. Hariharasudhan, D. Prince Winston, M. Palpandian, and M. Pravin, "A comparative analysis of polycrystalline and bifacial photovoltaic module under various partial shading condition," *Energy Convers. Manag.*, vol. 270, p. 116223, 2022.
- [19] G. Trzmiel, D. Głuchy, and D. Kurz, "The impact of shading on the exploitation of photovoltaic installations," *Renew. Energy*, vol. 153, pp. 480–498, 2020.
- [20] N. Belhaouas *et al.*, "A new approach of PV system structure to enhance performance of PV generator under partial shading effect," *J. Clean. Prod.*, vol. 317, p. 128349, 2021.
- [21] H. Tian, F. Mancilla-David, K. Ellis, E. Muljadi, and P. Jenkins, "Determination of the optimal configuration for a photovoltaic array depending on the shading condition," *Sol. Energy*, vol. 95, pp. 1–12, 2013.
- [22] M. A. Al Mamun, M. Hasanuzzaman, and J. Selvaraj, "Experimental investigation of the effect of partial shading on photovoltaic performance," *IET Renew. Power Gener.*, vol. 11, no. 7, pp. 912–921, 2017.
- [23] W. J. Cameron, M. M. Alzahrani, J. Yule, K. Shanks, K. S. Reddy, and T. K. Mallick, "Effects of partial shading on thermal stress and exergetic efficiency for a high concentrator photovoltaic," *Energy*, vol. 288, p. 129818, 2024.
- [24] F. Bayrak and H. F. Oztop, "Effects of static and dynamic shading on thermodynamic and electrical performance for photovoltaic panels," *Appl. Therm. Eng.*, vol. 169, p. 114900, 2020.
- [25] V. Keskin, "Exergoeconomic analysis of a photovoltaic array affected by dynamic shading," *J. Sci. Reports-A*, no. 052, pp. 35–50, 2023.
- [26] A. Dolara, G. C. Lazaroiu, S. Leva, and G. Manzolini, "Experimental investigation of partial shading scenarios on PV (photovoltaic) modules," *Energy*, vol. 55, pp. 466–475, 2013.
- [27] A. K. Tripathi, M. Aruna, and C. S. N. Murthy, "Performance of a PV panel under different shading strengths," *Int. J. Ambient Energy*, vol. 40, no. 3, pp. 248–253, 2019.
- [28] M. Abou Houran *et al.*, "Energy and exergy analysis of a novel solar-based system merged with power cycle," *Appl. Therm. Eng.*, vol. 240, p. 122080, 2024.
- [29] C. Manjunath, J. Reddy, K. S. R. Reddy, I. R. G. Kumar, and S. Sanketh, "Energy, exergy performance and analysis of 50W solar photovoltaic module," *Mater. Today Proc.*, vol. 54, pp. 531–536, 2022.
- [30] W. Zou, G. Yu, and X. Du, "Energy and exergy analysis of photovoltaic thermal collectors: Comprehensive investigation of operating parameters in different dynamic models," *Renew. Energy*, vol. 221, p. 119710, 2024.
- [31] K. Sopian, A. H. A. Al-Waeli, and H. A. Kazem, "Energy, exergy and efficiency of four photovoltaic thermal collectors with different energy storage material," *J. Energy Storage*, vol. 29, p. 101245, 2020.
- [32] S. Sukumaran and K. Sudhakar, "Performance analysis of solar powered airport based on energy and exergy analysis," *Energy*, vol. 149, pp. 1000–1009, 2018.



- [33] W. Kuczynski and K. Chlischcz, "Energy and exergy analysis of photovoltaic panels in northern Poland," *Renew. Sustain. Energy Rev.*, vol. 174, p. 113138, 2023.
- [34] A. S. Joshi, I. Dincer, and B. V. Reddy, "Thermodynamic assessment of photovoltaic systems," *Sol. Energy*, vol. 83, no. 8, pp. 1139–1149, 2009.
- [35] M. Abid and A. Hepbasli, "Dynamic exergetic analysis and evaluation of photovoltaic modules," *Energy Sources, Part A Recover. Util. Environ. Eff.*, vol. 37, no. 21, pp. 2271–2284, 2015.
- [36] A. Saha, N. N. Nipu, and M. F. Khan, "Effect of partial shading on the performance of solar PV module and impact of bypass diode in performance enhancement," in *2019 5th International Conference on Advances in Electrical Engineering (ICAEE)*, 2019, pp. 891–896.
- [37] K. Abdulmawjood, S. Alsadi, S. S. Refaat, and W. G. Morsi, "Characteristic study of solar photovoltaic array under different partial shading conditions," *IEEE Access*, vol. 10, pp. 6856–6866, 2022.
- [38] S. H. Pour Rahmati Khalejan and V. Keskin, "Effects of dynamic shading on thermal exergy and exergy efficiency of a photovoltaic array," *Teh. Vjesn. - Tech. Gaz.*, vol. 29, no. 6, pp. 1889–1895, 2022.
- [39] M. Yaghoubirad, N. Azizi, A. Ahmadi, Z. Zarei, and S. F. Moosavian, "Performance assessment of a solar PV module for different climate classifications based on energy, exergy, economic and environmental parameters," *Energy Reports*, vol. 8, pp. 15712–15728, 2022.
- [40] A. Pandey, P. Pant, O. Sastry, A. Kumar, and S. Tyagi, "Energy and exergy performance evaluation of a typical solar photovoltaic module," *Therm. Sci.*, vol. 19, no. 2, pp. 625–636, 2015.
- [41] A. R. Hakim, W. T. Handoyo, and P. Wullandari, "An energy and exergy analysis of photovoltaic system in Bantul Regency, Indonesia," *J. Mechatronics, Electr. Power, Veh. Technol.*, vol. 9, no. 1, pp. 1–7, 2018.
- [42] D. Rusirawan, "Energetic modelling of photovoltaic modules in grid-connected systems," Ph.D. dissertation, Dept. of Mech. Eng., Szent István Univ., Gödöllő, Hungary, 2012.
- [43] K. N. Shukla, S. Rangnekar, and K. Sudhakar, "A comparative study of exergetic performance of amorphous and polycrystalline solar PV modules," *Int. J. Exergy*, vol. 17, no. 4, pp. 433–455, 2015.
- [44] M. Gurturk, H. Benli, and N. K. Erturk, "Effects of different parameters on energy - Exergy and power conversion efficiency of PV modules," *Renew. Sustain. Energy Rev.*, vol. 92, pp. 426–439, 2018.
- [45] Energy Market Regulatory Authority (EMRA), "Activity-based tariffs approved by EMRA and will be applied as of January 1, 2024," 2024. [Online]. Available: <https://www.epdk.gov.tr/Detay/DownloadDocument?id=59UJUGOnkMs=>. [Accessed Sept. 17, 2024].
- [46] M. A. Z. Khan, A. Wahab, F. Ali, N. Ahmad, M. A. Kamran, and A. Hassan, "Performance of solar roof top panels with disparate particulate accumulation: Exergy analysis on an indoor lab study," *PLoS One*, vol. 18, no. 9, pp. 1–22, 2023.